U.PORTO

FEUP FACULDADE DE ENGENHARIA
UNIVERSIDADE DO PORTO

VIBRATION-BASED STRUCTURAL HEALTH MONITORING OF WIND TURBINES

Gustavo Miguel Cameira da Silva Oliveira

A dissertation presented to the Faculty of Engineering of the University of Porto
for the degree of Doctor of Civil Engineering

Supervisors: Álvaro Cunha (Full professor); Filipe Magalhães (Assistant professor);
Elsa Caetano (Associate professor)

April 2016

POPH QUALIFICAR É CRESCER.
QUADRO DE REFERÊNCIA ESTRATÉGICO NACIONAL PORTUGAL 2007.2013
GOVERNO DA REPÚBLICA PORTUGUESA
UNIÃO EUROPEIA Fundo Social Europeu

To my parents

ABSTRACT

Wind power is one of the most attractive and reliable options for renewable and clean energy. In the last years, the installed capacity for exploitation of wind energy has consistently increased worldwide. Alongside, the technological evolutions of this sector have been based on the development of multi-MW systems with increasingly larger structures elements, such as support structures and rotor blades. These wind turbines present considerable advantages considering the power production; however, they also represent several structural challenges: these wind turbines have become increasingly flexible structures, prone to resonance phenomena and to rapid wear.

In that sense, the structural integrity and proper operation of large wind turbines is a concern for owners and operators, specially in turbines installed offshore. Monitoring systems capable of evaluating the condition of structural elements such as foundation, tower and blades, are seen as a suitable response to address this problem. Among the several techniques available, vibration-based systems reveal a great potential for structural monitoring.

Therefore, this thesis is focused on the development and implementation of a vibration-based dynamic monitoring system for wind turbines. This system is based on Operational Modal Analysis tools, capable of accurately estimate the modal properties of wind turbine structures from their dynamic response. The efficiency of these tools in the modal identification of wind turbines was validated with the analysis of vibrational data collected during a short period from onshore (Izar Bonus 1.3MW/62) and offshore (Vestas V90-3.0MW) models.

Afterwards, a vibration-based monitoring system was implemented on a 2.0 MW Senvion MM82 wind turbine allowing the collection of data during more than one year. Throughout this program, the system was defined with two main purposes: detection of structural anomalies (based on the continuous estimation and statistical analysis of the variations of the modal properties) and fatigue assessment (based on a reduced number of installed sensors). The program was complemented with the analysis of alternative solutions for optimization of the number of installed sensors. The usefulness of the system was tested with different damage scenarios. It was concluded that the monitoring system is capable of detecting small damages in the support structure of both onshore and offshore wind turbines. The tools developed for fatigue evaluation using the estimated modal responses showed promising results but a complete validation of their accuracy need further research.

RESUMO

Energia eólica é uma das mais atrativas e fiáveis opções para energia renovável e limpa. Nos últimos anos, a capacidade instalada para aproveitamento do recurso eólico tem crescido de forma consistente em todo o mundo. Ao mesmo tempo, a evolução tecnológica do sector tem sido baseada no desenvolvimento de sistemas com múltiplos MW, recorrendo a elementos estruturais de dimensões cada vez maiores, tais como estruturas de suporte e pás. Estas torres eólicas apresentam vantagens consideráveis do ponto de vista da produção; no entanto, representam também diversos desafios estruturais: estes aerogeradores tornaram-se estruturas cada vez mais flexíveis, propensos a fenómenos de ressonância e a um desgaste rápido.

Nesse sentido, a integridade estrutural e a correta operação de modernas torres eólicas é uma preocupação para donos e operadores, especialmente em turbinas instaladas em *offshore*. Sistemas de monitorização capazes de avaliar a condição de elementos estruturais, tais como fundação, torre e pás, são vistos como uma resposta adequada para lidar com este problema. De entre as várias técnicas disponíveis, sistemas baseados na análise de vibrações revelam um grande potencial para monitorização estrutural.

Assim, esta tese foca-se no desenvolvimento e implementação de um sistema de monitorização dinâmico baseado na análise de vibrações para torres eólicas. Este sistema é baseado em ferramentas de Análise Modal Operacional, capazes de estimar com precisão as propriedades modais das estruturas de aerogeradores a partir da sua resposta dinâmica. A eficácia destas ferramentas na identificação modal de torres eólicas foi validada com a análise de dados de vibração colhidos durante um curto período de tempo para uma torre instalada em terra (Izar Bonus 1.3MW/62) e uma outra em *offshore* (Vestas V90-3.0MW).

Posteriormente, um sistema de monitorização foi implementado numa torre eólica Senvion MM82, permitindo a recolha de dados duranta mais de um ano. Ao longo deste programa, o sistema foi definido com dois objetivos principais: deteção de anomalias estruturais (baseado na estimativa contínua e análise estatística das variações das propriedades modais) e avaliação da condição de fadiga (com base num reduzido número de sensores instalados). O programa foi complementado com a análise de soluções alternativas para otimização do número de sensores instalados. A utilidade do sistema foi testada com diferentes cenários de dano. Foi concluído que o sistema de monitorização é capaz de detetar danos reduzidos na estrutura de suporte de torres instaladas em terra e em *offshore*. As ferramentas desenvolvidas para avaliação de fadiga, através de estimativas de respostas modais, mostraram resultados promissores, no entanto uma validação completa da sua precisão requere desenvolvimentos adicionais.

ACKNOWLEDGEMENTS

This thesis would not be possible without the help and support of several people. Here I present my sincere gratitude:

- to Prof. Álvaro Cunha, my advisor, for challenging me with such an interesting topic, for all the support given during this period and for his care to ensure all the conditions and means for the proper development of this thesis;
- to Prof. Filipe Magalhães, my co-advisor, for all the support, for the endless hours he received me in his office and for the patience and sympathy to clarify unscheduled problems;
- to Prof. Elsa Caetano, my co-advisor, for her support whenever needed and for the opportunity to cooperate on interesting projects;
- to Eng. José Carlos Matos, Eng. Miguel Marques and Eng. Silvina Guimarães from INEGI, for the opportunity to work within the Rotor Blade Extension project;
- to Prof. Christof Devriendt and Doctor Wout Weijtjens from OWI-Lab, for the interesting conversations about modal identification and for the opportunity to use the data of the Vestas V90-3.0MW wind turbine;
- to Eng. José Saraiva from Senvion and to Eng. Carlos Cardoso and Eng. Frederick Saborano from Cavalum, for all the support given within the study of the Senvion MM82 wind turbine;
- to Prof. Álvaro Rodrigues and Prof. Fernando Marques da Silva, for the interesting suggestions and conversations that helped improve this thesis;
- to my work colleagues and friends Nuno, Joana(s), Celeste, Berawi, Sandro, Fernando, Aires, Ana, André, Ricardo and Sérgio, for the fun that was working in our H304;
- to my parents and brother, to whom I owe who I am;
- to Paulina, for putting up with my bad mood and, even thus, always cheer me up;
- to Fundação para Ciência e Tecnologia, for the financial support through the PhD fellowship SFRH/BD/79328/2011.

NOMENCLATURE

A	Area of cross section
A, B, C, D	State-space model matrices
C_1	Damping matrix
C_D	Drag coefficient
C_L	Lift coefficient
C_P	Power coefficient
C_T	Thrust coefficient
D	Diameter, Damage
E	Young modulus
F	Excitation force
G	Next-state output correlation matrix, Gyroscopic matrix
H	Frequency response function
H_s	Significant wave height
I	Identity matrix, Second moment of inertia of the cross section
K	Stiffness matrix, Kalman gain
K_C	Geometric stiffness matrix
K_m	Modal Kalman gain
M	Mass matrix, Bending moment
N_B	Number of blades
O	Extended observability matrix
P	Power
Q, R, S	Noise covariance matrices
R	Correlation matrix, Radius, Rotation matrix
S	Spectrum matrix, Scour depth
T	Torque, Period of time

T_p	Peak period
T_z	Mean zero-crossing period
U	wind speed
V	Modal output matrix
Z	Matrix with predictor variables

a	Axial induction factor
a'	Angular induction factor
c	Airfoil chord
e_k	Innovation sequence
f	Natural frequency
l	Number of outputs sensors
$\dot{m}$	Mass flow rate
n_r	Number of reference outputs
p	Pressure
q	Modal coordinates
r	Position of the blade under consideration
u	Input vector
v	Vectors containing noise due to sensor inaccuracy
w	Vector containing noise due to disturbances and modelling inaccuracies
x	State vector (which contains the displacement and velocity vectors of the system)
$x_{m,k}$	Modal state vector at k instant
$\bar{x}$	Mean value of the distribution
y	Output vector, displacement (in time domain)
z_k	State vector
$z_{m,k}$	Modal state vector

Γ	Reversed extended stochastic controllability matrix
Λ	Modal state matrix
Ψ	Matrix with eigenvectors
Ω	Rotational frequency of the rotor

α	Angle of attack
β	Vector with weight parameters of the predictor variables
$\hat{\varepsilon}$	Residual error
θ	Pitch angle
λ	Tip speed ratio, system poles
ξ	Damping ratio
ρ	Mass density
σ	Standard deviation
σ'	Local solidity
ϕ	Matrix with the mode shape configurations at the measured degrees of freedom, angle of inflow
ω	Circular frequency, angular velocity of the wake

$(*)_D$	Diagonal elements of a matrix
$*^{\dagger}$	Moore-Penrose pseudo-inverse
$*^{T}$	Transpose operator
$\otimes$	Kronecker product operator
$Abs(*)$	Absolute value
$Cov[*]$	Covariance
$E[*]$	Expectation value
$Re(*)$	Real part
$tr(*)$	Trace of a matrix

CAPEX	Capital Expenditure
CM	Condition Monitoring
FA	Fore-Aft
FEM	Finite Element Model
LCL	Lower Control Limit
MAC	Modal Assurance Criterion
MBC	Multi-Blade Coordinate
OMA	Operational Modal Analysis
OPEX	Operational Expenditure
PDF	Probability Density Function
RBE	Rotor Blade Extension

RMS	Root Mean Square
SCADA	Supervisory Control And Data Acquisition
SHM	Structural Health Monitoring
SS	Side-Side
SSI-COV	COVariance-driven Stochastic Subspace Identification
SSI-DATA	DATA-driven Stochastic Subspace Identification
UCL	Upper Control Limit

p-LSCF	poly-reference Least Squares Complex Frequency Domain

CONTENTS

1 INTRODUCTION

1.1 RESEARCH CONTEXT

The electricity sector has undergone profound changes in the last years. The awareness for the environmental conservation, in particular to the greenhouse effect, alongside with the desire of higher energy independence by importing countries on fossil fuels, has led to the investment in the exploitation of renewable energy sources. In fact, renewable sources are in the focus of current energy policies. Almost all major world economies have developed studies and programs to introduce more clean energy into their energy mix. In particular, The European Union has been implementing a program with challenging objectives for 2020, known as "20-20-20" targets (Commission of the European Communities, 2008). Among them, it was defined a 20 % share of renewable energies in overall European Union energy consumption by 2020 (European Commission, 2013), including a target of 34 % of the electricity demand supplied by renewable sources (European Commission, 2015c). Subsequent programs for 2030 (European Commission, 2015a) and 2050 (European Commission, 2015b) are already under development.

In Portugal, until a few decades ago, the hydroelectric production represented almost the whole renewable contribution to the energy mix. From the 1990s, wind energy began to arouse some interest and the initial wind farms were installed. In the next decade, large investments in the implementation of wind turbines were made, which increased the importance of this source in the national electricity mix. Successively, wind power has gained importance in the national panorama, recently achieving power production numbers close (or even higher) to the hydropower generation. Currently, Portugal has been presenting very good results in the introduction of energy from renewable sources in its electrical system. The results obtained in 2015 are very good indicators: 50 % of the electrical energy demand was supplied from renewable sources, with wind power accounting for 22 % (Portuguese Renewable Energy Association (APREN), 2015). This value confirms the importance of this source in the national electric system.

Apart from these aspects, two additional perspectives may promote (once again) the installation of new wind turbines in Portugal (Government of Portugal, 2015). The first one is related to the future prospects from the national government of achieving a share of 40 % of the gross final consumption of energy from renewable sources by 2030, including a strong participation of wind power for electric power demand. The second perspective is related to the future possibility of establishment of European electric power interconnections. This possibility is related to the export of energy produced by renewable sources to countries with difficulties to meet the targets agreed with the European

Commission. This interconnection, which could achieve 15 % of the total installed capacity by 2030, would lead to a considerable boost of implementation of new wind power plants. Alongside, an important portion of the installed wind power capacity in Portugal is achieving its design lifetime, with repowering operations being expected in the next years.

Given this policy background, it is consensually accepted that wind power is a key element in the present and future electric energy strategy. New wind turbines are expected to be installed in the next few years with power outputs considerably higher than the nowadays common values, mainly due to cost aspects. In addition, offshore locations are becoming very attractive to install turbines due to their higher production yields. Three significant difficulties will be faced by this new wind turbine models:

- The increase of the wind turbines dimension, particularly the increase of the height of tower and blades length, will turn the wind turbine into more flexible structural systems. Consequently, the study of the dynamic characteristics of the structure will be of major importance in order to avoid resonance problems and rapid wear of the components;
- The installation of wind turbines in offshore locations is still shrouded in some uncertainty concerning the real wear suffered by the structures. On the other hand, the costs associated with offshore wind turbines are still high, which demand for optimization in their design;
- Apart from reducing the cost of installation of the wind power plants (CAPEX), the reduction of the costs over the period of its operation (OPEX) also represents an important vector for competitiveness. A crucial aspect to lower this cost is the optimization of the maintenance strategy. Considering the high power outputs of new models, the downtime of a single wind turbine may represent a significant income loss. In that sense, several monitoring system are being developed to remotely assess the condition of several components of the wind turbine, allowing to optimize the maintenance interventions according to expected loss of production during downtime, availability of replacing components and meteorological conditions (in the case of offshore wind farms or onshore wind farms in mountains).

These facts address the new challenges that, from a structural point of view, will concern the owners of wind farms. In that sense, a real-time monitoring system capable of assessing the structural integrity of the support structure of wind turbines (including tower and foundation) can be a very useful tool to aid decision-making. With a monitoring system, the wind farm owner can analyse the structural health of the wind turbines in remote locations and adapt the maintenance strategy according to the received data. In short, in possession of this information, the owner could maximize the investment.

In order to be effective, a monitoring system installed at a wind turbine support structure should be able to answer two important questions:

- Is the structure damaged?
- How is the fatigue condition of the structure? Is the structure able to fulfil its period of life? Or should the structure be disassembled before (or after) this period?

To meet these two aspects, different modules need to be integrated into one vibration-based structural health monitoring (SHM) system: a structural anomalies detection monitoring system and a fatigue monitoring system.

The structural anomalies detection monitoring system is a tool with the aim of detecting damage. It can be based on the continuous tracking of the modal properties of the structure. For this purpose,

tools already tested on civil engineering structures can be used in wind turbines in order to extract the monitored features. These tools, from a branch of the experimental modal analysis field named as Operational Modal Analysis (OMA), permit to identify the modal characteristics of structures during the various operating conditions of the turbines. Thus, considering that damage is usually associated with stiffness reductions, the natural frequencies of the various vibration modes can be used as damage indicators. The study of the evolution and variation of these indicators indirectly evidence the existence of damage in the structure.

The second module comprises the fatigue analysis of the structure. Fatigue assessment is a key point in wind turbines, since these structures are mainly subjected to dynamic loads. Thereby, this module permits to assess the evolution of the wear of the wind turbine support structure over time. This information can then be compared with the estimated lifetime of the structure in order to validate the suitability of this period.

1.2 OBJECTIVES AND MAIN CONTRIBUTIONS

The main goal of this thesis consists on the development of a complete vibration-based monitoring system capable of delivering useful results to assess the integrity of the wind turbine support structure.

To achieve this goal, this thesis addresses the following objectives:

- Implementation of output-only modal identification algorithms in the context of wind turbines and development of strategies for continuous identification of the modal properties of these structures;
- Development of a monitoring system to identify structural changes in the support structure of wind turbines based on the identified modal properties;
- Development of a methodology to estimate the fatigue damage at the support structure of wind turbines based on a small number of sensors;
- Integration of the two components (damage identification and estimation of the fatigue wear) of the vibration-based dynamic monitoring system in a single software package, demonstrating with full-scale applications the usefulness of the system in the management of wind farms.

It is expected that the outcomes presented in this thesis may represent a step forward in the development of global systems to monitor the most important components of wind turbines. In that sense, the main contributions of this thesis are the following:

- Synthesis of the major technical progresses of wind turbines and current state of evolution (Chapter 2);
- Description of the main components of a wind turbine, with a main focus on the different types of support structure, including costs breakthrough and reliability (Chapter 3);
- Description of the main characteristics related to the dynamic behaviour of wind turbine structures (Chapter 4);
- Analysis of the implications of the application of output-only modal identification algorithms to vibration signals from wind turbines (sections 5.3 and 5.7);
- Adaptation of the post-processing tool originally developed to the SSI-DATA algorithm to decompose the vibration signals into modal responses to be used together with the SSI-COV and p-LSCF algorithms (section 5.5.2);
- Application of the developed algorithms to data sets recorded on the blades and tower of a Izar Bonus 1.3MW/62 wind turbine using two different measurement systems: based on fibre Bragg grating sensors and accelerometers (section 5.8);
- Application of the developed algorithms to data sets collected during a short period on the support structure of an offshore Vestas V90-3.0MW wind turbine;
- Development of a strategy to estimate the fatigue state along the support structure of a wind turbine based on a reduced number of sensors (section 6.4.1);
- Creation of a vibration-based dynamic monitoring system, specially designed to meet the requirements of a wind turbine, able to perform, in a first module, the online automatic

identification of the modal parameters under all operating conditions, to remove the influence of operational and environmental effects and to compute indices permitting to detect the presence of small structural anomalies; and, in the second module, estimate the fatigue conditions along the support structure of a wind turbine (section 7.2);

- Conception, assembly and operation of a monitoring system on a Senvion MM82 wind turbine for a period of one year, where the developed routines were tested, demonstrating the ability of the system to detect the occurrence of small damages (section 7.3);
- Optimization analysis concerning the ability (and loss of accuracy) of the dynamic monitoring system to operate with a reduced number of installed sensors (section 7.3.8).

1.3 ORGANIZATION OF THE THESIS

The present thesis is divided in 9 chapters. It was the intention of the author to start from a global perspective of the wind energy industry to adequately frame the problem of wind turbine monitoring based on modal analysis. The text is then progressively oriented towards more detailed aspects of the implementation of the vibration-based monitoring system. A description of the contents addressed in each chapter is presented in the following paragraphs.

Chapter 1 introduces the present work. A small contextualization of the work is presented followed by a brief description of the organization of the text throughout the chapters.

Chapter 2 describes the evolution of the wind turbines from the initial models to the current offshore solutions. In addition, some important aspects of the wind energy market are introduced and some potential future trends are also analysed.

Chapter 3 is essentially dedicated to the description of the components of current wind turbine models. The operation of a wind turbine is explained according to the Blade Element Theory, serving as a mean for a better understanding of some operational aspects of these power plants.

Chapter 4 introduces important aspects concerning the dynamic characteristics of wind turbines. The typical dynamic behaviour of the tower and rotor blade elements is described, as well as some aspects regarding the different contributions to the damping of the structure.

Chapter 5 addresses the topic of the Operational Modal Analysis, which is a core aspect of the dynamic monitoring system. Some output-only algorithms are introduced, namely the SSI-COV, the SSI-DATA and the p-LSCF methods, and the main challenges associated with their application to wind turbines are addressed. In addition, some capabilities of these algorithms are introduced, namely post-processing tools to decompose the dynamic response into modal and harmonic responses. Then, the algorithms previously introduced are used to analyse vibrational data from two case studies: the Izar Bonus 1.3MW/62 and the Vestas V90-3.0MW wind turbines.

Chapter 6 begins with a brief description of the main dynamic loads acting on a wind turbine and the particularities of the fatigue design of these structures. The chapter continues with the description of a methodology to estimate the fatigue condition of the support structure based on a reduced number of sensors and with the presentation of a virtual sensors technique to estimate the acceleration at unmeasured locations.

Chapter 7 presents the bridge between the algorithms and methodologies described in Chapter 5 and 6 and the developed dynamic monitoring system. The methodologies implemented for removing the environmental effects on the damage indicators are introduced, as well as the statistical procedure to identify structural damage. Alongside, the estimation of the remaining fatigue lifetime based on a reduced monitoring time is also addressed. Then, a detailed description of the monitoring program of the Senvion MM82 wind turbine is introduced. The main results obtained with the routines developed in the scope of the monitoring system are presented

Finally, **Chapter 8** summarizes the main conclusions of this thesis and highlights some potential future research topics.

2
FROM WINDMILLS TO THE MODERN WIND TURBINES

2.1 TECHNOLOGICAL DEVELOPMENT

2.1.1 THE ONSHORE DEVELOPMENT

Wind power has been exploited for several centuries, from mechanical to, more recently, electrical purposes. The first wind turbines came almost directly from wind mill concepts. From these models, several technological progresses were made, which led to current multi-MW turbines. Thus, in this section, an overview of the most important steps in the technological development of wind turbines is presented.

2.1.1.1 The First Attempts

The first references to the development of electricity generator windmills are shared between Charles F. Brush in 1888 (Shepherd, 1990) and Poul LaCour in 1891 (Gasch and Twele, 2012). It is interesting to note that, even in the beginning of its technological development, different strategies from a conceptual point of view were followed. The Brush wind turbine (Figure 2.1), installed in Ohio, Cleveland, in 1888, was an adaptation of the American windmill. It presented a power output of 12 kW based on a low-speed, multi-blade design. On the other hand, the LaCour wind turbine, erected in 1891 in Askov, Denmark, was designed following the principles of the new engineering science of aerodynamics (Figure 2.2). In that sense, it stepped away from the low tip-speed ratio design (ratio between the blade tip speed and the wind speed) of the Brush model since it was not suitable for electric generation (Gasch and Twele, 2012). The LaCour model was based on the European windmill and presented some aerodynamic refinements, such as low solidity rotor (ratio between the blade area and the swept area), leading-edge camber and a low drag coefficient (Shepherd, 1990). This design was later adapted for commercial purposes, being characterized by its reliability and efficiency (Hau, 2006).

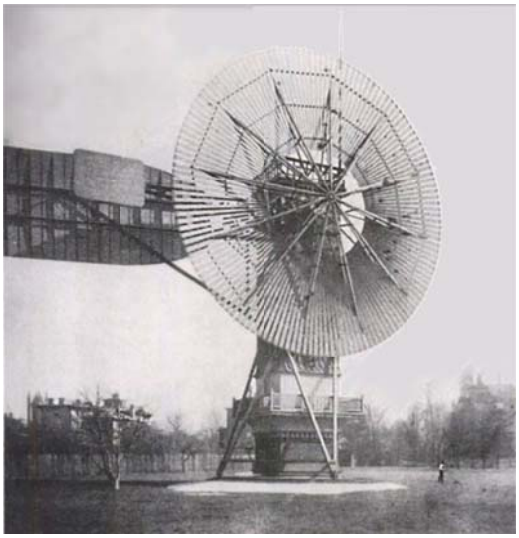

Figure 2.1 - The Brush wind turbine (Anon, 1890)

Figure 2.2 - LaCour wind turbine (Hau, 2006)

After the First World War (1914-1918), some important developments took place. In the theoretical field, Albert Betz presented in 1920 the actuator disc theory to the wind turbine (Betz, 1920). In his paper (later edited in a book (Betz, 1926)), Betz presents his considerations about the ideal maximum factor of kinetic energy extractable from the flux of energy from wind (also called "Betz Limit" – see Chapter 3).

Some new models were presented during this period. From those, the one developed by the brothers Marcellus and Joseph Jacobs, whose development started in 1922 in the USA, stands out. The model was designed with a three-bladed rotor (the nowadays standard design) with a 4 m diameter rotor (Figure 2.3). One of the most interesting aspects in to the development of this wind turbine is related to the severe vibration problems detected when an initial rotor solution based on two blades was tested. It was noted that, during yawing operations of the turbine, abnormal vibrations were detected due to changes in gyroscopic inertia (Shepherd, 1990). This is one of the first descriptions of dynamic problems related to wind turbines and led to a different design solution, based on a three-bladed rotor. This wind turbine was a great commercial success, with models with power output ranging from 1.8 to 3.0 kW (Hau, 2006).

Figure 2.3 - Jacobs wind turbine (Hau, 2006)

Two innovative concepts of wind energy exploitation were presented during this period. The first is referred to the Savonius rotor, introduced in 1925 (Savonius, 1931). It was characterized by a vertical axis turbine, which S-shaped cross sections working by lift (Figure 2.4). This type of turbine achieved some popularity due to its simple construction and its ability to operate with wind from any direction. However its low efficiency prevented its commercial success (Shepherd, 1990). Nevertheless, this concept is still seen in some small-scale wind exploitation devices.

The second concept was presented by Georges Jean Darrieus in 1926 (Darrieus, 1931). The Darrieus Rotor had two or three blades connected at the top and at the bottom to the central shaft (Figure 2.5). This concept presented some advantages, such as the placement of the power train near the ground level (where maintenance is easier) and the exemption of a yaw system. Furthermore, the curved-shape of the blades was designed to minimize the bending stress along its length (Shepherd, 1990). For this reason, the blades could be cheaper. This concept was later employed in an utility-scale model.

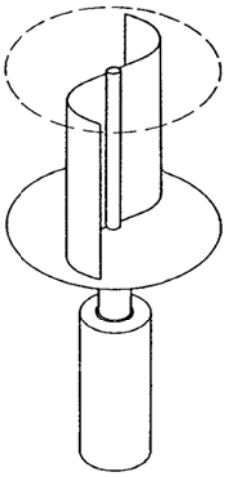

Figure 2.4 - Savonius Rotor

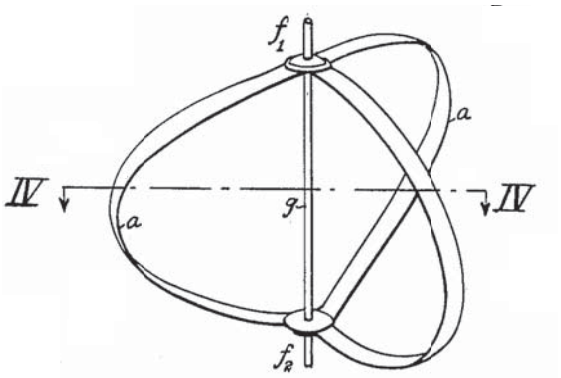

Figure 2.5 - Darrieus Rotor (Darrieus, 1931)

In the decade of 1930s, the typical wind turbine was composed by a horizontal upwind rotor (the rotor is placed in front of the tower, orientated to the wind – see Chapter 3) with two or three blades with low solidity. The rotor blades operated at a variable speed with a fixed pitch (angle of blades along its longitudinal axis). Its electrical system was composed by a 12 or 32 V DC generator. This typical unit worked unattended and was said to be very reliable and long-lived (Shepherd, 1990).

The Great Depression in the 1930s alongside with the extension of the Rural Electrification Act in the USA (a program in which loans were provided to the installation of electrical distributions systems in rural areas), led to the demise of the small turbines. Furthermore, the small turbines up to this date were not cost effective to compete with the investments in central power plants. At this point in the history of wind turbines, the investments would be turned over to larger wind turbines connected to the electric grid in order to reduce the cost of wind energy and to prevent future problems of worldwide energy shortages (Shepherd, 1990).

2.1.1.2 The First Large Machines

One of the first large projects was the 100 kW, 30 m diameter Balaclava wind turbine in 1931 (Sectorov, 1973) (Figure 2.6). It had a 30 m height steel lattice tower and was located at Balaclava, on Crimea, near the Black Sea. It had a three-bladed rotor with an automatic yaw system and pitch control (adjustment over the angle of the blade facing the wind – see Chapter 3). Although it had some primitive solutions (such as gears made of wood and simple blade surface treatment), it achieved good results. This machine was connected to a steam power station and is considered the first wind turbine to be interconnected to an AC utility system (Shepherd, 1990).

Figure 2.6 - Balaclava wind turbine (Shepherd, 1990)

Figure 2.7 – Smith-Putnam wind turbine (Hau, 2006)

In late 1939, the American Engineer Palmer C. Putnam approach the S. Morgan Smith Company of York with a new wind turbine with the latest technology (Voaden, 1943). The construction of this new project started in 1941 on the top of a mountain called "Grandpa's Knob" (near Vermont, USA) and it is considered a landmark in the wind energy history. This model reflects the demand for reducing production costs with large wind turbines with high power outputs.

Technically, the Smith-Putnam wind turbine was a remarkable and giant project for that time. It had a 53.3 m diameter, 2-bladed upwind rotor that generated a power output of 1.25 MW with a synchronous (AC) generator (Shepherd, 1990) and a steel lattice tower with a height of 33.5 m (Voaden, 1943) (Figure 2.7). It included some technological innovations such as (Shepherd, 1990):

- Full span active control of the blade pitch (the blades were made of stainless-steel);
- The use of individual flapping hinges on the blades to reduce gyroscopic loads on the shaft (a similar problem previously faced in the development of the Jacobs turbine);
- Active yaw control by mean of a servomotor turning a pinion meshing with a large bull gear between the machinery house (or nacelle) and the tower.

The generator was connected to the electrical system at wind speeds higher than 8 m/s, reached its rated power at 13.4 m/s (Voaden, 1943) and it ran until the maximum wind speed of 32 m/s (Johnson, 2001). The Smith-Putnam wind turbine is considered the first large wind turbine with two blades (Johnson, 2001) and it was the largest wind turbine for almost 40 years. Notwithstanding, it faced some important drawbacks. From the technical point view, it was concluded that the blades were undersigned, presenting several cracks after some operating time. From the economic point of view, it demonstrated that some improvements would have to be taken in order to be become cost effective with respect to the conventional power generation processes (Gasch and Twele, 2012).

At this time, the increase of the capacity of the wind turbines was already a confirmed trend. Although the Smith-Putnam wind turbine had been a one-off project, some previous and future projects confirmed this trend, some of them with utopic designs (like the design of Hermann Honnef with a power output of 20 MW (Hau, 2006)).

In 1939, the World War II began. From the end of World War I (1918) to 1939, the interest in wind power in Denmark decreased (Vestergaard, Brandstrup et al., 2004). The price of coal and oil had become sufficiently low to decelerate the interest in wind energy. However, with the beginning of the World War II, the increase in the price of fossil fuels led, once again, to the rise of wind energy interest. Some old commercial LaCour machines were reactivated and some new wind turbines were built.

Also in Denmark, a new company (F.L. Smidth Company) developed a new model during this period, relying in a small, conservative design. In addition, new concepts of modern aerodynamics (modern airfoils) were applied to the blades (Ackermann and Söder, 2002). Under this philosophy, reliable models with power outputs ranging from 50 kW to 70 kW were developed, with rotor diameters of 17.5 m and 24 m, respectively. It is interesting to note that the model with the higher power output was designed with a concrete tower, not a very common solution at the time.

The models developed by the Smidth Company are an example of a development trend, choosing simple designs over heavy and complicated models, in opposition to the Smith-Putnam turbine design. In fact, the Smidth wind turbines are considered the forerunners of modern wind turbine generators by some authors and one of the pioneers of the Danish wind energy market (Shepherd, 1990; Ackermann and Söder, 2002). By the first half of the 20th century, the wind energy market was already a reality due to the number of small wind turbines installed, being the primary energy source in some areas (Hau, 2006).

a) b)

Figure 2.8 – Smith wind turbines (Hau, 2006): a) 50 kW model with steel lattice tower; b) 70 kW model with concrete tower

During the 1930s and 1940s, much theoretical and design activity in the wind energy field was held in Germany. This development was undertaken by the German Reich with the aim of a self-sufficiency in fuel power (Hau, 2006). For this purpose, the "Reichsarbeitsgemeinschaft Windkraft" (RAW) was created with renowned scientists, technicians and industrials. Among the projects developed under the RAW program, the project led by the engineer Franz Kleinhenz, in 1937, stands out, reflecting the ambition of building large machines to reduce the cost of energy production. This wind turbine had remarkable characteristics like a 130 m rotor diameter with a three or four-bladed downwind rotor. This rotor would have a power output of 10 MW at a tip speed of 5 and the generator would have been from the direct drive type. The designed tower was a guyed tubular steel tower, with the upper part yawing with the rotor. The concept was improved from 1938 to 1942 and was ready for construction. However, the war prevented its construction (Hau, 2006). It is interesting to note that, even nowadays, some of these characteristics are still not widely implemented in commercial wind turbines

Apart from Denmark and USA, other regions also showed some interest in the exploitation of wind energy, although in a small scale. In the United Kingdom, there was a wind energy program running from 1948 to the early 1960s (Spera, 1994). Among some different designs developed during the program, the Enfield-Andreau wind turbine project stands out from the others due to its innovative design, although associated with low efficiency (Hau, 2006)).

Also in France, there was some interest in the development of experimental wind turbines during this time. The 30.1 m rotor diameter, 800 kW Best-Romani turbine and the 35 m rotor diameter, 1.0 MW Vadot turbine are examples of projects from this time (Hau, 2006).

During the post-war period in Germany, Ulrich Hutter was the main name in the field of wind power. Hutter, who had already been distinguished on previous papers on the theory of wind turbines (Hau, 2006), conducted some experimental tests during the 1950s. His studies culminated in the 34 m rotor diameter W-34 wind turbine with an AC synchronous generator (Gasch and Twele, 2012) with a rated power output of 100 kW at a wind speed of 8 m/s (Figure 2.9) (Johnson, 2001). This turbine, erected in

1957, had a two-bladed, downwind rotor with a simple hollow pipe tower with 22 m of height supported by guy wires (Johnson, 2001). One of Hutter's main priorities was the lightweight construction. For this reason, the blades were made of an advanced glass-fibre composite material (Hau, 2006) and they were aerodynamically refined, being connected to a teetering hub (see Figure 3.6). The solution found for this connection was another innovation: instead of a more complex design like the one used in the Smith-Putnam wind turbine, the teetering movements of the rotor were aerodynamically damped by mechanically coupling the teetering angle to the blade-pitch angle (Hau, 2006). The pitch mechanism of the blades changed their angles at higher wind speed to keep a constant speed of rotation of the rotor (Vargo, 1974). This wind turbine is considered as an example of a third design philosophy, relying on the reduction of the structure weight and on the optimization of its aerodynamics.

Figure 2.9 – W-34 wind turbine (Hau, 2006)

Figure 2.10 – Gedser wind turbine (Hau, 2006)

One of most innovative and reliable wind turbines built during this time was the Gedser wind turbine (Figure 2.10), designed by Johannes Jull and located in Denmark. This wind turbine was in operation between 1958 and 1967 (Lundsager, Frandsen et al., 1980), connected to the Danish public power system (Johnson, 2001). The Gedser wind turbine had a 24 m diameter, three-bladed, upwind rotor with an induction generator (rather than the more conventional, at that time, synchronous generator) (Manwell, McGowan et al., 2010) achieving a power output of 200 kW at a wind speed of 15 m/s (Lundsager, Frandsen et al., 1980). The tower had a height of 24 m and was made of concrete. Although these characteristics were not so impressive, this wind turbine had some major innovations, such as the power control through aerodynamic stall: its blades had an aerodynamic design which caused flow separation under strong wind conditions, acting as a completely passive power limitation, avoiding the need for pitch control, like the Smidth wind turbine. For aerodynamic braking, the turbine was equipped with turnable blade tips which were activated by centrifugal forces at a grid failure (Gasch and Twele, 2012). Compared to the Smith-Putnam wind turbine, the Gedser was much less complex, from a mechanical point of view (Vestergaard, Brandstrup et al., 2004). All these characteristics and innovations led to a period of operation without major maintenance (Vestergaard, Brandstrup et al., 2004). The Gedser wind turbine was decommissioned in 1967 and it was later

refurbished in the mid-1970s at the request of NASA for measurements, in the framework of an American program (Hau, 2006).

Although Hutter and Juuls' projects were considered a success, the wind turbine projects in general were not yet reliable, with numerous problems and faults to be dealt with (Hau, 2006). Besides these reasons, the extremely low prices of primary fuels after the World War II, along with the increased investments in nuclear energy, demonstrated that the wind generated electricity was too expensive to compete with other sources (Gasch and Twele, 2012). Due to this, the wind energy industry suffered another breakdown during the 1960s.

2.1.1.3 The Modern Wind Turbine Concept

In the late 1960s - beginning of 1970s, the awareness of dependency on the oil exporting countries started to take place. The oil crisis in 1973 and 1979 confirmed this misgiving, having led to supply problems and an increase in the oil prices in the western economies. With the aim of reducing this situation, national programs for the development of renewable energy sources were created.

In the USA, the Federal Wind Energy Program began in 1972 (Ramler and Donovan, 1979). The National Aeronautics and Space Administrator (NASA) was selected to manage the technology development and initial deployment of large wind turbines in the Lewis Research Center. This project represents one of the most extensive development program in the wind energy field, in which several variations of structural configurations and mechanisms were tested.

The first wind turbine developed and built by this program was the NASA/DOE Mod-0 in 1975. This wind turbine was a two-bladed, 38 m rotor diameter with a power output of 100 kW at a wind speed of 8 m/s (Ramler and Donovan, 1979). This turbine had a 30 m high tower. The Mod-0 wind turbine was extensively tested with a large number of modifications along its operation life: with a teeter and rigid hub, different blade materials, with pitch and stall control, with stiff and more flexible supporting towers, different kinds of generators, among others (Spera, 1994) (Figure 2.11). The turbine operated, in most of the time, as a downwind rotor, although the upwind solution had also been tested, as well as a one-bladed rotor solution (Corrigan and Ernsworth, 1986). One of the most noticeable characteristic of this wind turbine was the influence of the tower in the blade vibration when the rotor was downwind, one important dynamic characteristic of this type of turbines. The Mod-0 was dismantled in 1987 (Spera, 1994).

Figure 2.11 – MOD-0 wind turbine variations

The second development of the NASA/DOE program was the Mod-0A wind turbine. The purpose of this model was to study, identify and solve technical and operational utility interconnection issues (Spera, 1994). This model was basically a version of the Mod-0 with a larger gearbox and generator (200 kW) (Ramler and Donovan, 1979). Four prototypes were built for four different locations between 1977 and 1980. Each location represented a different scenario both for grid integration and wind conditions. From this project, it was proven that, while not yet cost-effective, wind turbines could be successfully integrated into the normal operations of a utility, producing high-quality AC power (Spera, 1994). The MOD-0A project ended in 1982 (Spera, 1994).

The MOD-1 project entered in service in 1979. The wind turbine had a 61 m diameter downwind rotor (the largest ever built (Spera, 1994)) with two steel blades (Ramler and Donovan, 1979) (Figure 2.12). This model had a rated power of 2.0 MW at a wind speed of 14.6 m/s (Johnson, 2001). The tower had a steel truss design and was 42.7 m high. This wind turbine was considered the first operational megawatt sized wind turbine in the world (Collins, Shaltens et al., 1982). However, the MOD-1 model faced some problems. It was too heavy and, consequently, too expensive, mainly due to its stiff tower, to its heavy, complex and large full span pitch controlled blades and to its bedplate (Ramler and Donovan, 1979). The effect of the tower on the blades created high impulsive loads to the rigidly mounted blades, becoming clear that this design philosophy would not be suitable for a 20 - 30 years period of life (Spera, 1994). A new model, MOD-1A, was designed with some solutions aiming to avoid these problems but, due to funding issues, it was not built (Collins, Shaltens et al., 1982). Besides technical and economic problems, there were also some complaints from local residents about noise and television interference (Collins, Shaltens et al., 1982). The MOD-1 project ended in 1988 with the disassemble of the wind turbine (Johnson, 2001).

Figure 2.12 – MOD-1 wind turbine (Wikipedia, 2009)

The next iteration of the NASA program started in 1977 with the MOD-2 project (Gordon, Andrews et al., 1983) (Figure 2.13). This project was designed as a sequence of the findings and developments of the previous NASA/DOE projects (MOD-0, MOD-0A and MOD-1) and, for that reason, it is referred to as a second generation machine (Ramler and Donovan, 1979). The project of the MOD-2 wind turbine was a design evolution of the proposed design for the MOD-1A model. The MOD-2 wind turbine was a two-bladed, upwind rotor with a diameter of 91.4 m. This model had a power output of 2.5 MW at a wind speed of 12.3 m/s and used a synchronous generator (Gordon, Andrews et al., 1983). Three of the major modifications from the MOD-1 design were (Ramler and Donovan, 1979):

- The power control. Instead of the heavy and complex full-span pitch control of the blades, power control of the wind turbine was handled through the pitch of just the outer 30 % the blade span;
- The tower design philosophy. The designed tower was considerably more flexible than those used in previous projects. It consisted in a 61 m high steel tower with a cylindrical shell design. In this design, the natural frequency of the tower is lower than the frequency of rotation of the blades. For this reason this design is called "soft-soft" (see 3.3.4);
- The load reduction. The rotor was designed to allow teeter of up to 5º in and out of the plane of the rotor.

This design approach permitted to save weight and, consequently, reduce costs. Comparing to the MOD-1 design (which was smaller), the MOD-2 was around 10 % lighter (Ramler and Donovan, 1979).

Three MOD-2 machines were built and tested in a cluster in 1980 in Goodnoe Hills, Washington. The disposition of the three wind turbines was defined in order to study possible aerodynamic interferences between large turbines in downwind (wake effects) (Spera, 1994). Two other machines were also built for utility companies. The MOD-2 machines suffered some technical problems and economic studies showed that the costs were still not competitive. However, this project proved that a group of large wind turbines could operate in a totally automatic and unattended mode (Spera, 1994).

The third generation of horizontal-axis wind turbines from the NASA/DOE program included four projects: MOD-3, MOD-4, MOD-5A and MOD-5B (although the MOD-3 and MOD-4 projects stopped in an initial phase) (Spera, 1994). The main goal of the MOD-5 program, started in 1980, was, once again, to develop cost competitive, large wind turbines (Baldwin and Kennard, 1985).

The MOD-5A design, developed by General Electric Company for NASA/DOE, had a 122 m diameter rotor with two blades and the hub was placed 76 m above the ground (Baldwin and Kennard, 1985). The power output of this machine was 7.2 MW with a rotor rotation of 13 or 17 rpm, depending on wind conditions (Johnson, 2001). However, this machine was not built due to low perspectives of a commercial success from General Electric which withdrew from the project. Nevertheless, this wind turbine would represent, for nowadays state-of-art, one of the most powerful projects.

The MOD-5B, developed by Boeing for NASA/DOE, was built in 1987 (Spera, 1995). This wind turbine followed the design concept of the MOD-2 machine: a two-bladed, upwind, teetered rotor with a partial span pitch control of the blades (Spera, 1995). The turbine was supported by a cylindrical steel shell and had a rated power of 3.2 MW and a rotor diameter of 97.5 m (Figure 2.14). The major innovation of the model was the ability of its turbine to operate successfully at variable speed (from 13 to 17.3 rpm).

Figure 2.13 – MOD-2 wind turbines (Wikipedia, 2009)

Figure 2.14 – MOD-5B (Wikipedia, 2009)

Alongside with the NASA/DOE, the Department of the Interior of the USA (DOI) was also interested in wind energy to operate with its hydroelectric turbines (Spera, 1995). For this reason, the DOI asked NASA for project management and technical support and a joint-venture of two companies (one American and other Swedish) was selected to design, fabricate and install two megawatt scale wind turbines (designated as "system verifications units" - SVUs). In 1982, the WTS-4 wind turbine began to operate. This machine was a horizontal axis wind turbine with a 79.2 m diameter, downwind rotor (Figure 2.15). It had two fiberglass blades mounted on a teetered hub with full-blade pitch control. The steel shell tower followed a "soft-soft" design with 80 m of height. This wind turbine was, at that time, the most powerful ever made, with a power output of 4.0 MW. The second SVU installed was a 2.5 MW MOD-2.

Figure 2.15 – WTS-4 wind turbine (Wikipedia, 2009; Schwerin, 2010)

During the 1970s, there was also some relevant research in wind power outside the USA. In Canada, the research efforts were towards the vertical axis wind turbines (VAWT), specifically with the Darrieus design. Among others (small) turbines, the National Research Council (NRC) developed the Éole VAWT. The installation of this turbine was complete in 1987 in Quebec, Canada (Spera, 1994). It was the first megawatt-class Darrieus turbine, with a 64 m diameter and with an original power output of 4.0 MW, operating at variable speed (Figure 2.16). However, to ensure the longevity of the machine, the rated power was lowered to 2.5 MW. The experience gained and the results achieved were not very encouraging and the Canadian program was terminated (Hau, 2006). Some research in the Darrieus concept field was also performed in the USA in the Sandia National Laboratories in Albuquerque.

a) b)

Figure 2.16 – Éole VAWT: a) general view (Wikipedia, 2005); b) illustration (Spera, 1994)

In Europe, some Governments from Nordic and Central European countries also developed research programs during this period. In Denmark, an ambitious program started in 1974. The main goal was "*that it should be possible to generate 10% of the Danish power requirement from wind energy without creating particular problems in the public power grid*" (Hau, 2006). For this purpose, the 200 kW Gedser wind turbine was refurbished for a joint study with NASA. Furthermore, two 630 kW wind turbines with 40 m diameter were built in Nibe, which had their first rotation in 1979 and 1980 (International Energy Agency (IEA), 1984). These wind turbines had a three-bladed, upwind rotor with steel blade spars and both had a concrete tower (Spera, 1994) (Figure 2.17). Each of the wind turbines had a different power control mechanism: one had a tip-controlled rotor while the other had a full-span pitch control. These wind turbines operated for 15 years.

Previously in 1975, a 2.0 MW wind turbine was built in Tvind, Denmark (Hau, 2006) (Figure 2.18).

Figure 2.17 – Nibe A wind turbine

Figure 2.18 – Tvind wind turbine

Another Nordic country with important developments was Sweden. The National Swedish Board for Energy Source Development was founded in 1975 and two large wind turbines were built (Hau, 2006). The 2.0 MW, 75 m diameter WTS-75 Nasudden wind turbine with two blades on a rigid hub upwind of the cylindrical concrete tower had its first rotation in 1983 (Figure 2.19) (International Energy Agency (IEA), 1984). This turbine had an unusual feature: a carriage assembly mounted on vertical rails on the side of the tower, for raising or lowering major components. This feature eliminated the need for a large crane (Spera, 1994). The second large wind turbine erected in Sweden was the WTS-3 Maglarp wind turbine in 1982 (International Energy Agency (IEA), 1984). This machine was built by the same consortium that built the WTS-4 for the NASA/DOI program. The WTS-3 had a rated power of 3.0 MW with a 78 m diameter, two-bladed, downwind rotor (Figure 2.20). It also had a "soft-soft" tower with a height of 80 m (International Energy Agency (IEA), 1984).

Figure 2.19 – Nasudden wind turbine

Figure 2.20 – Maglarp wind turbine

The German state subsidized program on the development of wind energy started in 1974 (International Energy Agency (IEA), 1984). The most emblematic project was the Growian wind turbine, which was assembled in 1982 (Thiele, 1984). This wind turbine was, at that time, the largest ever built (Figure 2.21). It had a 100 m diameter, two-bladed, downwind rotor which was supported by a 100 m tall steel tower stabilized by several guy cables (Spera, 1994). The carbon-filament blades had a full-span pitch control. The Growian machine was also the first wind turbine to attempt variable-speed operation although it was not well succeed. Additionally, the Growian wind turbine suffered other problems, including fatigue in major components which conducted to its disassemble in 1987 (International Energy Agency (IEA), 1989). Despite of the low success of the Growian project, some smaller machines operated satisfactorily (such as the 370 kW Monopteros with a one-bladed, 48 m diameter rotor (Figure 2.22) (Spera, 1994).

Figure 2.21 – Growian wind turbine

Figure 2.22 – Monopteros wind turbine

The large wind turbines developed during the 1970s and 1980s failed, in general, one of their main purposes: to produce energy at a competitive price. They were not as reliable as expected, with short life periods due to several failures. In (Johnson, 2001), it is referred the fact that smaller turbines (in the 100 kW range) could be built at lower costs and with better performance than the larges turbines as one of the reasons to the end of the American program. In fact, the seek for larger and powerful wind turbines underestimated the difficulty of building reliable machines of this size. The Growian wind turbine is an example in which the size of the turbine is too large for the time in which it was built.

On the other hand, for the first time in the history of the wind energy, there was a consistent experimental and theoretical knowledge of wind turbines. This knowledge was fundamental for the beginning of the commercial market of wind turbines as it is known today.

In hindsight, it is possible to evidence three distinct groups of approaches on the structural and control level over the evolutionary history of wind turbines (Thresher and Dodge, 1998):

- Turbines designed to withstand high wind loads. These models were considerably robust, with low rated power and were optimized for reliability. An example of this philosophy was the Gedser wind turbine;
- Turbines designed to be compliant and shed loads. These models were optimized for performance. Their design had an important concern with the reduction of weight and with the optimization of the aerodynamic profile of the blades. An example of this design concept was the W-34 wind turbine;
- Turbines designed to manage loads mechanically and/ or electrically. These turbines were optimized for control, with several mechanical and electrical innovations (such as hinged blade connections and variable speed generators). An example of this concept was the Smith-Putnam turbine.

The first approach was indubitably the most durable and reliable. However, the increase of knowledge in the industry has led to less conservative designs, with the aim of weight reduction (to reduce cost) and control (to optimize the production). Thus, a joint of the second and third approaches is currently the main driver of the design concepts.

An illustration of the principal projects held during this period of development is shown in Figure 2.23. The evolution of the dimension of the wind turbines is notorious.

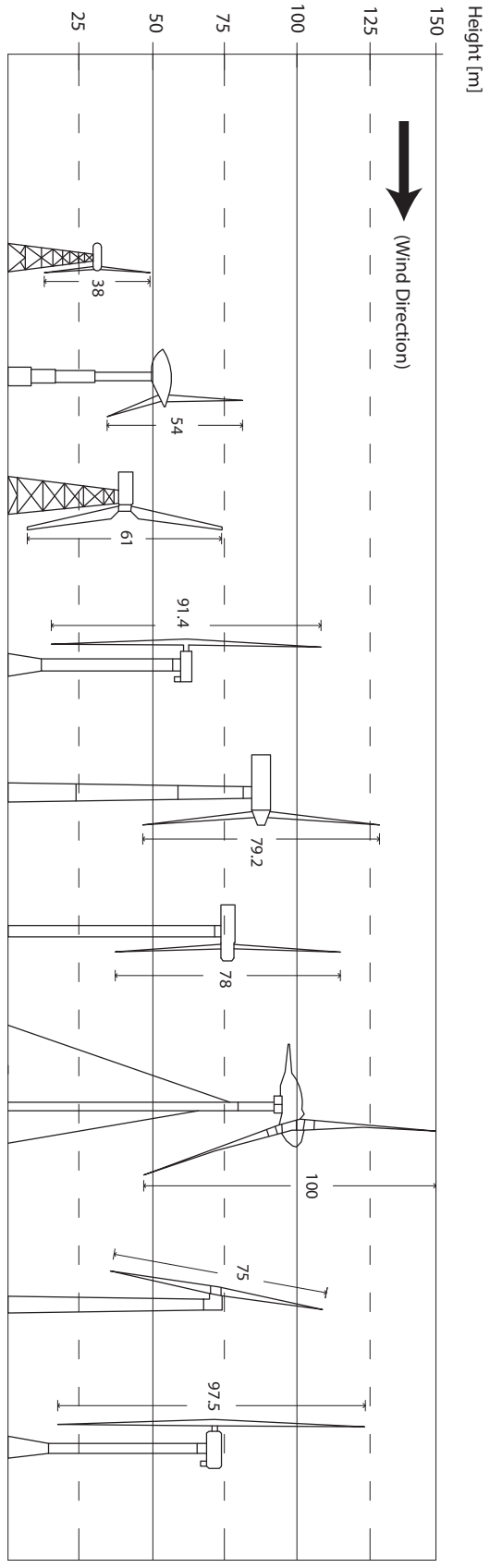

Name	Year	Rated Power [MW]
MOD-0	1975	0.20
Tvind	1975	2.00
MOD-1	1979	2.00
MOD-2	1980	2.50
WTS-4	1982	4.00
WTS-3	1982	3.00
Growian	1982	3.00
WTS-75	1983	2.00
MOD-5B	1987	3.20

Figure 2.23 – Main projects developed during the 1970s and 1980s (adapted from (Spera, 1995; Gasch and Twele, 2012))

2.1.1.4 Current situation and future trends

Nowadays, wind turbines present a mature state of technology. In fact, wind is considered the renewable source of energy with the widest and most successful deployment over the last two decades (Arántegui, Corsatea et al., 2013). The current state-of-art of onshore wind turbine is composed of:

- Horizontal axis turbines;
- Steel, concrete or hybrid shell towers;
- Upwind rotor, with three blades;
- Rotor with variable speed (this feature enhances the efficiency of the system);
- Yaw system for rotor orientation according to wind direction;
- Active pitch control of blades (for high wind speed regulation);
- Synchronous or induction generator;
- Utilization of a gearbox (although some models with direct-driven generators are available).

In order to better understand the state of technical evolution of the wind energy industry, a survey about the currently available wind turbine models was conducted. In this research, the onshore models presented in the portfolio of the most relevant manufacturers were considered[1].

Figure 2.24 presents the main results obtained, namely the relationship between rotor diameter and rated power for available wind turbines. As can be seen, the majority of the models available have a rated power below 4.0 MW, although there are already some models with higher power outputs (achieving a maximum value of 7.58 MW). One interesting aspect is the apparent stagnation of the rotor size of the largest wind turbines. However, due to the limited number of models with power outputs higher than 4.0 MW currently available, this is a trend that will need further investigation. Another relevant characteristic is the large variation of rotors size for the same rated power. This is partly explained by the development of models designed for sites characterized by low-wind speed conditions. These models usually present high towers (around 120 m to 146 m of height) and larger rotor diameters.

The data collected is also used to illustrate the "position" of the two onshore models studied in this work, the 2.0 MW Senvion MM82 and the Izar Bonus 1.3MW/62 (indicated with a red circle in Figure 2.24). It is visible that, while the latter is located in the low range of power capacity, the Senvion model is more in line with the common available models between 2.0 MW and 3.0 MW.

[1] In this study, the manufacturers considered were: Alstom, AMSC, Darwin, Enercon, Gamesa, GE Energy, GoldWind, MY Wind, Nordex, Samsung, Senvion, Siemens, Sinovel, Suzlon and Vestas.

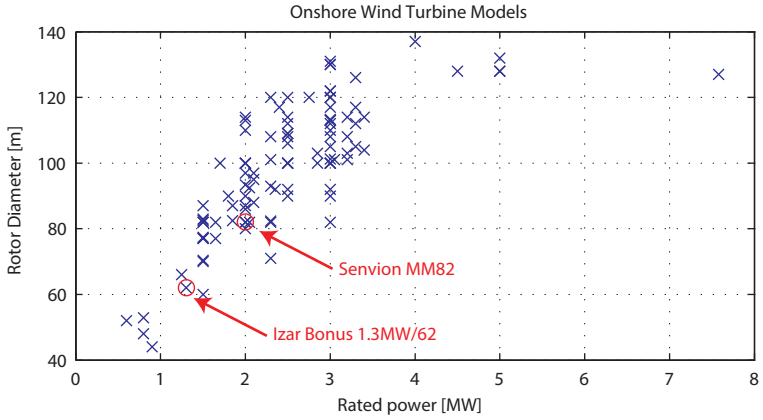

Figure 2.24 – Rated power and rotor diameter of onshore wind turbines

2.1.2 The Offshore Development

The transfer of wind energy technology from land to the sea was a natural development. The implementation of wind turbines at sea presents some important advantages (Henderson, Morgan et al., 2003):

- Wide continuous areas available for large wind farm projects;
- Higher wind speed, which generally increases with the distance from the shore;
- Less turbulence, which allows the turbines to harvest the available energy more effectively, with reduced fatigue loads on the turbine;
- Lower wind shear (i.e. the boundary layer of slower moving wind close to the surface is thinner), thus allowing the use of shorter towers;
- Possibility of faster rotational speeds than on land, due to lower noise restrictions.

On the other hand, some disadvantages are naturally present in offshore turbines:

- Being a more recent technology, the design of wind turbines is still in an initial phase. Consequently, the costs are still quite high when compared to onshore technology;
- The structures are subjected to a higher variety of dynamic loads;
- The maintenance is more difficult and costly.

A description of the offshore evolution is briefly presented in the next sections.

2.1.2.1 The first offshore projects

The first turbines were installed at sea in the early 1990s. At that time the developed machines already presented some reliability, with power outputs in the 500 kW range.

The countries bordering the Baltic and North Sea were the first to install offshore wind turbines. Both the Baltic and the North Sea present very good conditions for the implementation of offshore technology: they both have shallow waters and good wind speeds.

The first offshore turbine was a single demonstration erected in Nogersund, Sweden, in 1991. However it was abandoned due to a fire in 1998 (Henderson, Morgan et al., 2003). The first offshore wind farm was the Vindeby wind farm, commissioned in 1991 at the Baltic Sea (Denmark) (Henderson, Morgan et al., 2003). This wind farm consisted in 11 turbines with a rated-power of 450 kW each, implemented in very low water depth.

During the following years, 4 more wind farms were built in Sweden, the Netherlands and Denmark, with wind turbines with individual power output of around 500 kW.

In 2000, a new dimension started for offshore wind energy with the implementation of the first megawatt class wind turbines. During this year, three new offshore wind farms were commissioned (including the first in the UK) (Henderson, Morgan et al., 2003). Among these, the Middelgrunden wind farm, in Denmark, deserves greater prominence. It was composed of 20 wind turbines with an individual power output of 2 MW located, once again, in very shallow waters.

During the next years, the construction of new multi-megawatt sized wind farms continued. Special relevance must be given to the Horns Rev (Figure 2.25) and Nysted wind farms (both in Denmark) commissioned in 2002 and 2003, respectively. These wind farms represented a big step in the offshore industry, with rated powers of around 160 MW.

Figure 2.25 – Horns Rev offshore wind farm

2.1.2.2 Current situation and future trends

Nowadays, the offshore wind turbine sector is already an implemented industry. The development of offshore wind turbines is, in its essence, an adaptation and evolution of the land-based models. Among others, some technical modifications concerning offshore-oriented design include:

- Strengthening of the tower to handle the additional loads (Musial and Ram, 2010);
- Higher power outputs and tips speeds;
- Higher component redundancy (Henderson, Morgan et al., 2003);
- Improved protection against harsh marine environment (including corrosion);

- Personnel access platforms;
- Special design of the foundation and the transition piece (component between the foundation and the tower – see Chapter 3).

Some other technical features are often also included (Musial and Ram, 2010):

- Monitoring systems for better diagnostic information of the structure and turbine;
- Onboard service cranes;
- Bearing-lubrication and oil-temperature regulation systems;
- Sometimes a heliport is included at the top the structure.

The current state-of-art is similar to the onshore model in terms of mechanical solutions, although the dimensions of rotor diameter and the rated power tend to be higher. This is justified by the absence of some limitations present on the transportation on land (such as bridges height, road bends and short transition curves in vertical alignments). Beside these limitations, the installation of wind turbines with higher rated power allows to reduce the cost per MW, which is an important aspect to counterbalance the high costs associated with the installation of offshore turbines. Another feature of offshore models is the lower hub height due to the lower wind shear. In most of the times, tower height is defined for the specific site of installation. However, the smaller experience in offshore installations still leads to a lower standardization of the models compared with the onshore variant. For this reason, there is still a wide variety of offshore wind turbine foundations (see Chapter 3).

The same market study presented in section 2.1.1.4 for onshore wind turbines was also developed for the offshore models. The offshore models were characterized once again by their rotor diameter and rated power. The main results are presented in Figure 2.26 (including the Vestas offshore model studied in this work).

As can be observed, the current offshore models present larger rotor diameters and higher power output than the onshore models (Figure 2.24), with several models in the 4.0 MW – 6.5 MW range. Nevertheless, there are already some models presenting capacities higher than 7.0 MW.

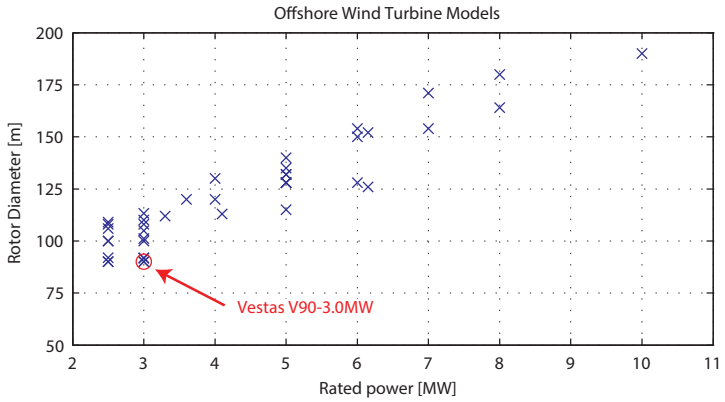

Figure 2.26 – Rated power and rotor diameter of offshore wind turbines

Another important aspect in the offshore development is related to the distance to the shore and water depth at which the wind farms are installed. Figure 2.27 presents the average distance to shore and water depth of European wind farms, alongside with their dimension (defined by the size of the

circles). Over the years, the distance to shore has increased, as well as the water depth of the sites of the projects. The average distance to shore was 32.9 km and the average water depth of wind farms was 22.4 m, at the end of 2014 (European Wind Energy Association (EWEA), 2015a). Looking at Figure 2.27, it is possible to assume that the trend of installation of wind farms away from the shore will continue.

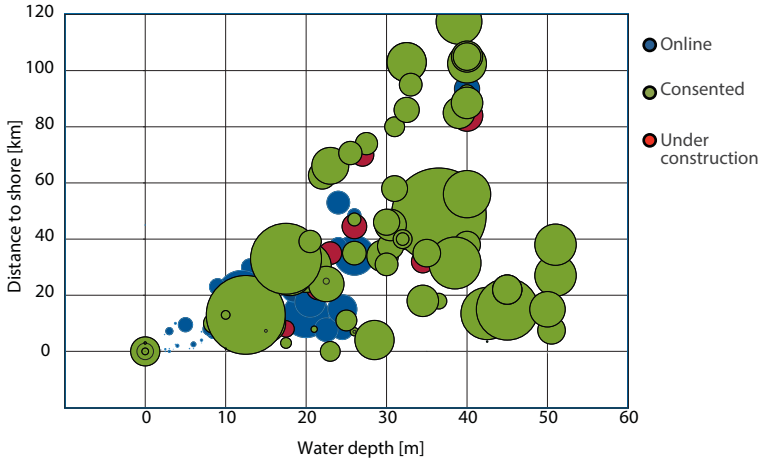

Figure 2.27 – Average water depth and distance to shore of online, under construction and consented European wind farms, at the end of 2014 (adapted from (European Wind Energy Association (EWEA), 2015a))

The main design drivers for the future of offshore wind turbines will be the cost reduction and the implementation of turbines at higher water depths. Furthermore, the increase of the turbine power output and of their reliability will continue, alongside with a better understanding of the influence of the environment on the structure of the wind turbine.

Currently, the levelized cost of offshore energy is slightly higher than twice the onshore cost (World Energy Council (WEC), 2013; Bloomberg New Energy Finance, 2015; U.S Energy Information Administration, 2015). In order to become viable, the capital and operational expenditure of offshore investments need to be reduced. A part of the reduction of the initial investment is achieved with the decrease of the structure weight (Butterfield, Musial et al., 2007). With light-weight structures, the loads tend to decrease through all the structure, including in the foundation. Some new and more expensive materials might be used for this purpose, such as, in special cases, carbon in the blades (Butterfield, Musial et al., 2007). However, less material (and then less stiffness and mass) leads to a more flexible structure which, considering the dynamic loads, requires a thorough understanding of the dynamic behaviour of the structural system.

Another possibility for weight reduction is the adoption of two-bladed rotors (Butterfield, Musial et al., 2005). This solution was almost abandoned for the onshore turbines due to lower yield and for aesthetic reasons, as well as some technical problems that were not solved in the past - like the one described for the Jacobs wind turbine (Butterfield, Musial et al., 2007). However, the reduction of one blade (with the consequent weight decrease) could be balanced by the increase in blade tip speed of the offshore turbines. In addition, the higher rotor speeds lead to a lower input torque and lower gear ratios, which permit to reduce some mechanical components located in the nacelle. The increase in rotor tip speed could also lead to the utilization of direct-drive generators (drivetrains without gearboxes) (Musial and Ram, 2010).

In the future, another major change may take place for the offshore turbines. The continuous increasing of rotor diameters may lead to a definition of the blade design by a deflection limit in upwind rotors, instead of a load limit criterion (Butterfield, Musial et al., 2007). This is due to the increased levels of strength and flexibility achieved in blades. For this reason, downwind rotors may be an option for future offshore wind turbines because, contrary to the upwind solution, the blades deflect away from the tower. The downwind solution was abandoned in the past due to vibrations and noise problems (Butterfield, Musial et al., 2007) with the blades passing through the tower shadow. Nevertheless, for large distances from the shore, noise disturbances are not a problem.

Some other perspectives for future developments of wind turbines are presented in (European Commission, 2011). In the report of the UpWind program, some considerations are made for the design of a giant 20 MW wind turbine. Although the program was not exclusively for the offshore market, the dimensions of the turbines under analysis make them suitable for the implementation at offshore locations. Among other considerations, some important aspects are referred for the feasibility of turbines with this dimension:

- Reduction of the magnitude of fatigue loads. For this, advanced rotor control strategies are required (the concept of "smart turbine" is introduced);
- Implementation of control systems for detection and evaluation of upcoming wind loads (gusts or vortex) with the aim of load alleviation (such as LIDAR systems mounted at the nacelle);
- Individual pitch control of each blade;
- Application of materials with lower mass to strength ratio;
- Introduction of monitoring technologies to assess the structural integrity of the system;
- Due to transportation issues, the blades might have to be splitted into two pieces since the rotor of the studied 20 MW wind turbine has a diameter of 252 m. For this reason, this joint might be an important focus of attention;
- The need for optimization of the offshore substructure (foundation and transition piece).

The offshore substructure is another important topic for the future of offshore wind turbines. Nowadays there is a large variety of commercially implemented, tested and concept designs (see Chapter 3). The future trend, as stated earlier, is to increase the distance from the shore. In this situation, due to a larger water depth, floating structures seem to be the most suitable option. Until today, a few number of experimental projects have been deployed. For the next years, many floating wind turbine projects are schedule to start in several countries (Main(e) International Consulting LLC, 2012).

2.2 BRIEF MARKET ANALYSIS

2.2.1 THE START OF THE DANISH AND AMERICAN MARKET

The wind energy market gained relevance in the second half of the 20th century (Hau, 2006). In Denmark in the early 1980s, some small manufacturers of agricultural machines entered in the market with simple wind turbines with power outputs around 30 - 75 kW (Hau, 2006; Gasch and Twele, 2012). These machines followed the Juul's concept with a three-bladed, stall-regulated, upwind rotor working at a fixed speed with an induction generator (Burton, Sharpe et al., 2001). This market was initially sustained by an appropriate feed-in tariff set by the government (Gasch and Twele, 2012). A consequence of the development of the Danish market was the creation of a certificate by the Wind Turbine Test Station in Risø to attest the maturity and safety of the wind turbines.

On the other hand, the American market was created mainly due to politic measures. Consecutive measures took by the Senate that culminated in the Public Utilities Regulatory Policy Act (PURPA) in 1978 (Hau, 2006), conducted to a favourable situation of subsidies for wind energy investments. The state which provided the best incentives, and which also had good wind conditions, was California (Manwell, McGowan et al., 2010). Thus, the first wind farms were built there between 1979 and 1980. Due to economic viability, these wind farms were constituted by 100 or more turbines (Johnson, 2001). These small wind turbines, with power outputs up to 100 kW, were initially manufactured by American companies. However, the initial operation of these wind turbines was characterized by several difficulties due to the technological immaturity of the models (Manwell, McGowan et al., 2010). Sometime later, Danish wind turbines entered in the American market and became more successfully than native companies, mainly due to their larger experience.

After the initial problems, the number of wind farms increased very quickly around 1981, with an installed capacity over 1500 MW (Johnson, 2001). However, in the years between 1986 and 1987, the economic situation changed in California (Hau, 2006). The conjugation of the expiration of the tax credits for the investors, alongside with the lower supply tariffs offered by the utilities, led to a slowdown (and, sometime later, to the stagnation) of the growth of wind farms (Hau, 2006).

In the rest of Europe, the wind energy market started in the 1990s with a support scheme mainly based in feed-in tariffs for wind power generation (Ackermann and Söder, 2002).

2.2.2 ONSHORE WIND TURBINE MARKET

The analysis of the evolution of the wind energy market and its current situation is a clear way to attest the success of this industry in the last 15 years. In this section, a brief market analysis is made for the entire market (onshore together with offshore), since the latter still has a minor importance in terms of total installation numbers (around 2.4 % of the total installed capacity).

Analysing the cumulative installed capacity in the world (Figure 2.28), it is possible to observe the consistent growth of the wind energy market, with a total installed capacity already exceeding the 350 GW. Qualitatively, it is also possible to observe that Europe and Asia are the leaders in the installed capacity. In fact, Asia became the region in the world with the largest installed wind park during 2014. The main driver of this situation is China, which has become the world leader in installed capacity when it surpassed the USA during 2010 (Global Wind Energy Council (GWEC), 2011). The top 10 countries with the largest cumulative installed capacity are presented in Figure 2.29.

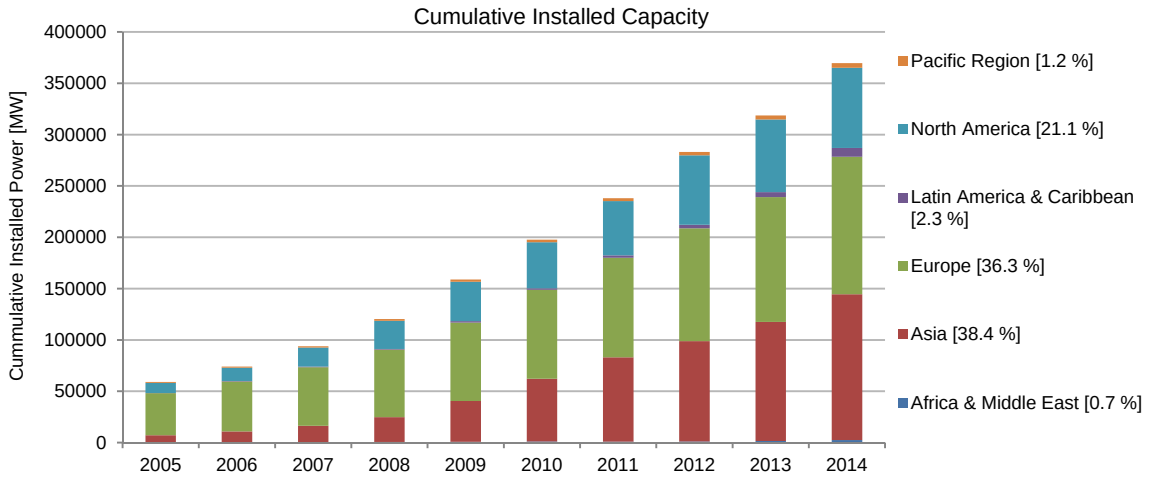

Figure 2.28 – Cumulative installed capacity (the share at the end of 2014 results is presented in brackets) (EWEA 2007, 2008, 2009, 2010, 2011b, 2012b, 2013c, 2014b, 2015b) (GWEC 2007, 2008, 2009, 2010, 2011, 2012, 2013, 2014, 2015)

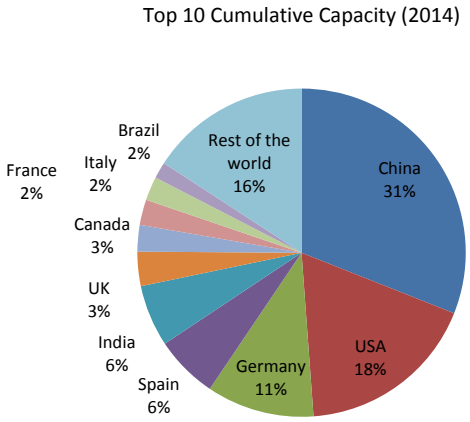

Figure 2.29 – Top 10 Countries in cumulative installed capacity in the end of 2014 (European Wind Energy Association (EWEA), 2015b; Global Wind Energy Council (GWEC), 2015)

On the other hand, European investments stagnated during the last years which can be justified by the financial crisis installed in this continent (Figure 2.30). In the opposite side, China was responsible, during 2013 and 2014, by more than 45 % of the new installations (Figure 2.31). These recent investments led China to a position of market domination.

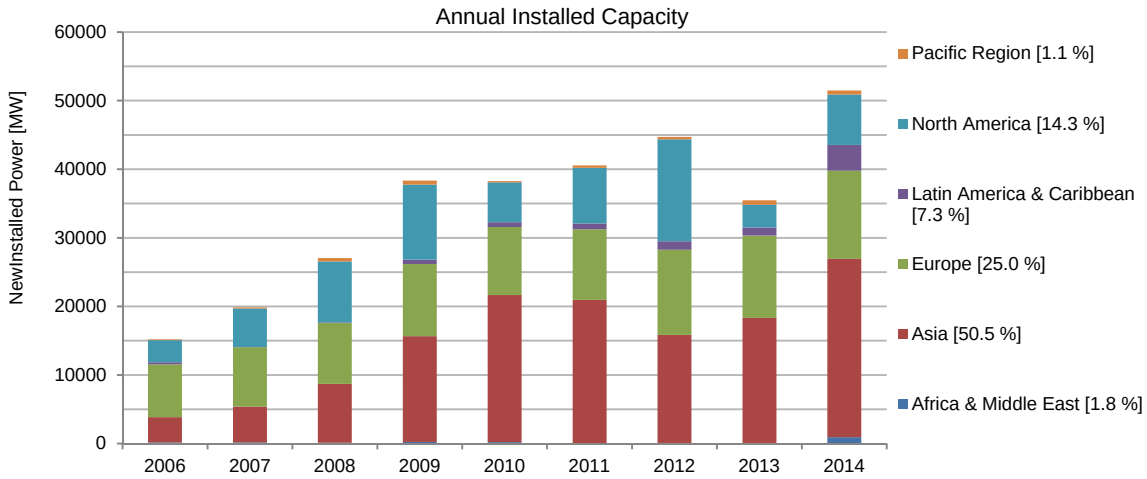

Figure 2.30 – Annual installed capacity (the share at the end of 2014 results is presented in brackets) (EWEA 2007, 2008, 2009, 2010, 2011b, 2012b, 2013c, 2014b, 2015b) (GWEC 2007, 2008, 2009, 2010, 2011, 2012, 2013, 2014, 2015)

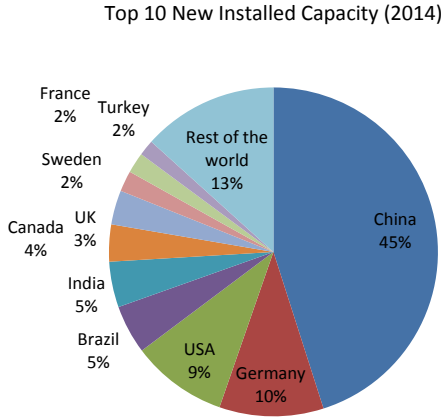

Figure 2.31 – Top 10 Countries in new installed capacity in the 2014 (European Wind Energy Association (EWEA), 2015b; Global Wind Energy Council (GWEC), 2015)

In Portugal, large investments were done in wind energy since the first wind farm was commissioned at Madeira in 1986. Portugal is the 12th country in the world with largest installed power and the 8th in Europe with a cumulative installed capacity of 4 914 MW (European Wind Energy Association (EWEA), 2015b; Global Wind Energy Council (GWEC), 2015) (Figure 2.32).

However, the investments have been declining in recent years. This situation may be explained by the financial crisis, by the minor incentives given by the Government and by some limits imposed for penetration in the national electrical system.

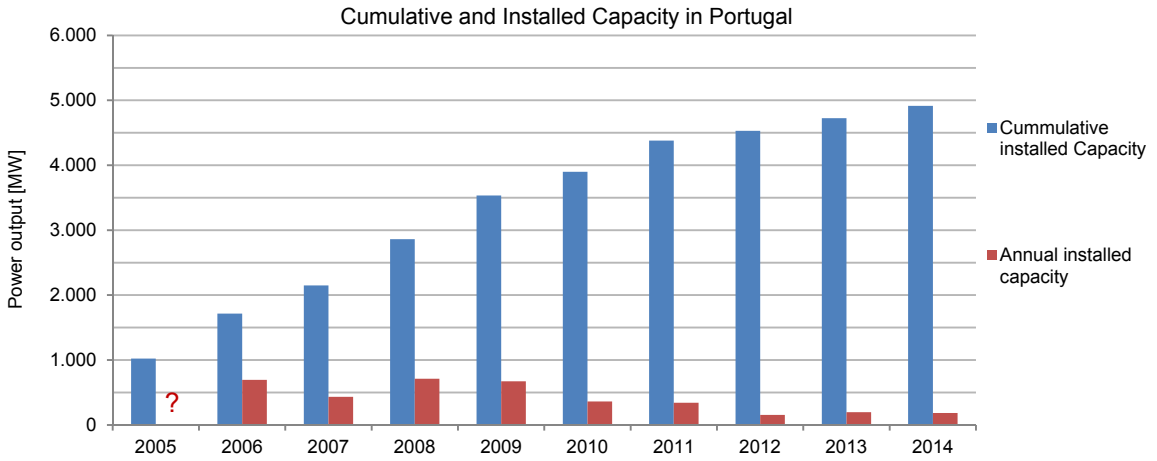

Figure 2.32 – Annual cumulative and installed capacity in Portugal (since 2005) (EWEA 2007, 2008, 2009, 2010, 2011b, 2012b, 2013c, 2014b, 2015b)

Figure 2.33 shows the geographical distribution of wind farms in the continental territory of Portugal. As can be observed, the major part of wind farms is located in the north and centre of the country, mainly in interior highlands.

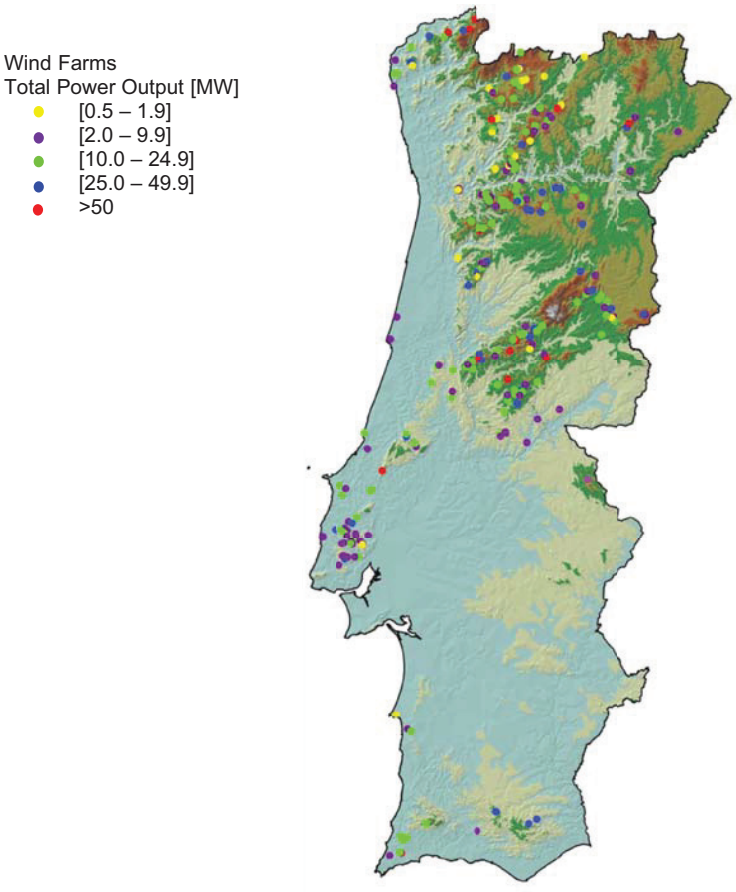

Figure 2.33 – Installed wind farms in Portugal at the end of 2014 (Institute of Mechanical Engineering and Industrial Management (INEGI) and Portuguese Renewable Energy Association (APREN), 2015)

2.2.3 Offshore Wind Turbine Market

Compared to the onshore market, offshore wind power is still in the beginning, with slightly less than 9 GW installed, corresponding to 2.4 % of the total installed capacity worldwide (Figure 2.34). At the end of 2014, there were only 17 countries in the world with offshore wind turbines installed. From these, the major part is from Europe. The implementation in this continent represents more than 90 % of the world installed capacity.

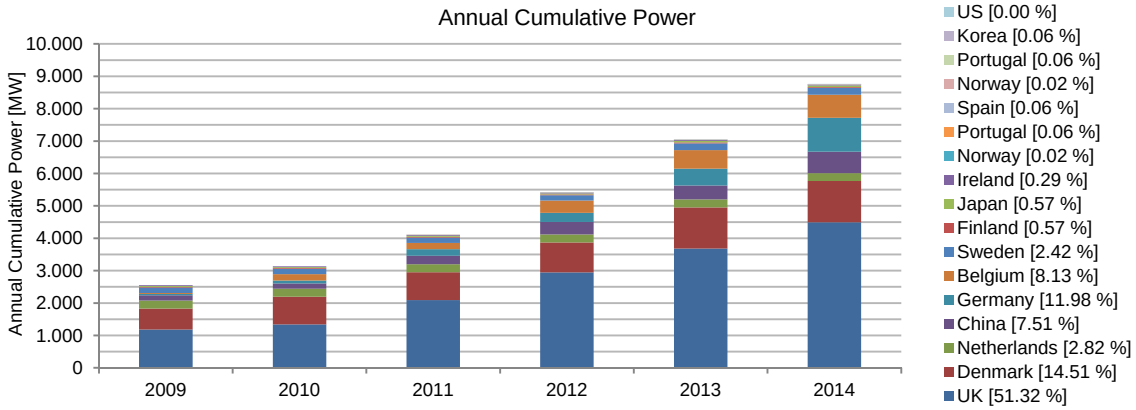

Figure 2.34 – Annual cumulative capacity of offshore wind turbines .The share values in brackets are referred to the end of 2014 (EWEA 2011a, 2012a, 2013b, 2014a, 2015a) (GWEC 2012, 2013, 2014, 2015)

In today's market, the UK is clearly dominant with more than 50 % of the entire global capacity. The UK has been doing a large investment in the offshore market in the last years, as can be seen in Figure 2.35. Portugal has a small portion of the entire market with just one 2.0 MW experimental floating offshore wind turbine.

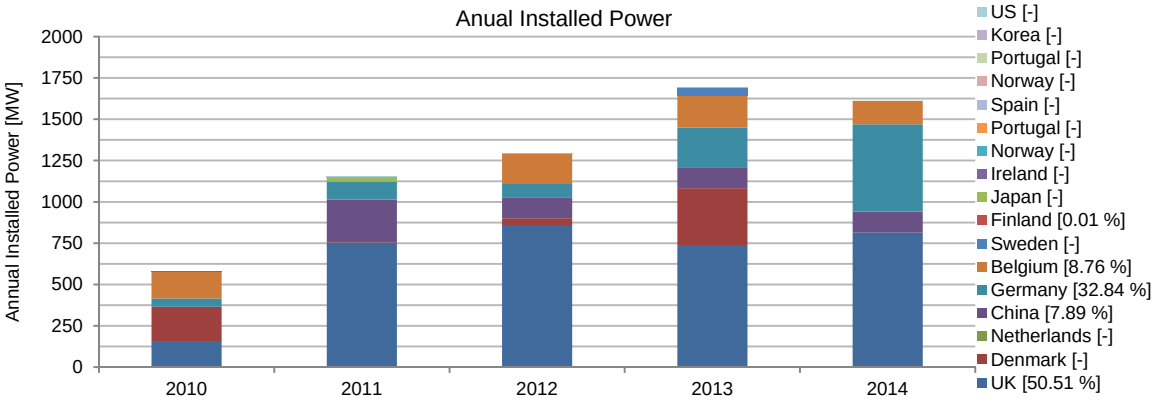

Figure 2.35 – Annual installed capacity of offshore wind turbines (data from 2013 is only referred to European countries). The share values in brackets are referred to the end of 2012 (EWEA 2011a, 2012a, 2013b, 2014a, 2015a) (GWEC 2012, 2013, 2014, 2015)

The dominance of the offshore market by the Northern countries of Europe is a clear evidence. For this fact, the water depth conditions present in these countries should be considered as an important driver. Analysing Table 2.1, it is evident the large portion of shallow waters present in the north of Europe, in opposition to the situation at the south regions, where the water depth increases rapidly

with the distance from the coast. In addition, it is also possible to note the apparent good conditions for the USA to install offshore wind farms. However, in the last years, investments in this area were not considered a priority by this country.

Table 2.1 – Percentage of water depths in different regions up to 100 km offshore (Henderson, 2003)

Region	Water Depth			
	< 25 [m]	25 – 50 [m]	50 – 100 [m]	100 – 300 [m]
North Europe	21	26	32	20
South Europe	16	11	23	49
Japan	22	9	18	51
USA	50	26	13	11

2.3 FINAL CONSIDERATIONS

This chapter described the evolution of wind turbines, since the first attempts to modern utility-scale models. In the same manner, the emergence and development of offshore turbines, from land-based models to especially designed models to be installed offshore, was covered. Apart from the efficiency in the exploitation of energy from the wind, two important aspects defined the success of some models over others: reliability and cost effectiveness.

The second part of the chapter briefly introduced the wind energy market. It was attested the importance of this sector, with a consistent growth sustained by both consolidated and emergent markets. In addition, the potential growth of the offshore market, still in an early phase of deployment, was referred.

This chapter is especially important to frame the scope of the present work. A monitoring system, able to detect structural damages at an early stage and perform an estimation of the fatigue condition of the support structure, represents an important tool to remotely control the condition of the wind turbine and, thus, its reliability. At the same time, this continuous assessing provides helpful information to timely prepare maintenance actions, as well as possible retrofitting needs, allowing to optimize the reduction of OPEX (cost over the period of operation – see Chapter 3).

3
BASICS OF WIND TURBINES

3.1 General Layout

3.1.1 Wind Turbine Typology

Historically, wind turbines can be defined according to several design configurations. Concerning conceptual design aspects, a major distinction is made according to the position of the axis of rotation of the wind rotor: the axis can be positioned vertically or horizontally.

Vertical-axis wind turbines, such as the Savonius and Darrieus rotor (Figure 2.4 and 2.5), are rarely used in modern large wind turbines. Although this kind of turbines presents some advantages, some negative aspects such as the low tip-speed ratio, the inability to self-start and the difficulty to control the rotor speed (Hau, 2006) led to low interest in their development during the 1970s and 1980s.

The horizontal-axis wind turbine is the most common solution. This type of wind turbines can be subdivided into two main groups considering the configuration of the rotor with respect to the wind flow direction: upwind and downwind rotors (being the latter almost not used nowadays).

In this work, the main focus is oriented towards the horizontal-axis upwind turbines, the typical nowadays configuration. Notwithstanding, some considerations are made about other solutions. The layout of a nowadays common onshore and offshore wind turbine is shown in Figure 3.1. The represented offshore example refers to a monopile foundation solution (see section 3.1.1.5). In Figure 3.2 the terminology for the translational and rotational degrees of freedom of a wind turbine is introduced.

A brief description of the main components of nowadays onshore and offshore wind turbines is presented in the following sections.

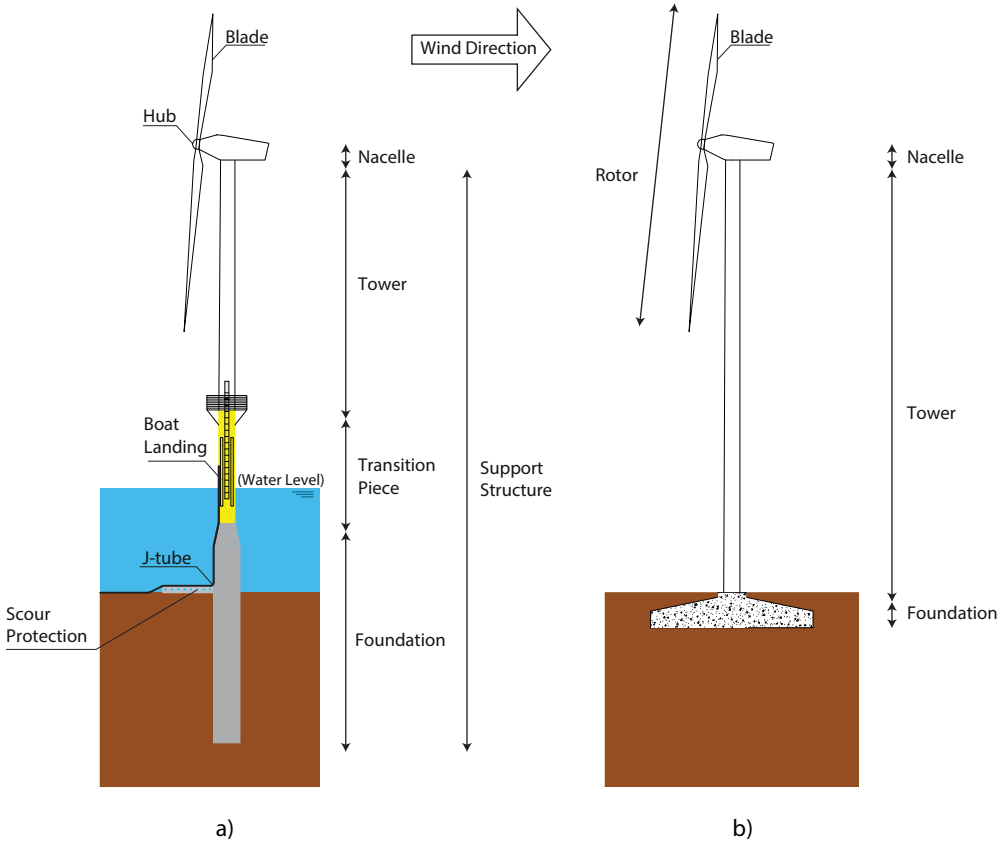

Figure 3.1 – Main wind turbine components of horizontal-axis upwind wind turbines: a) offshore; b) onshore

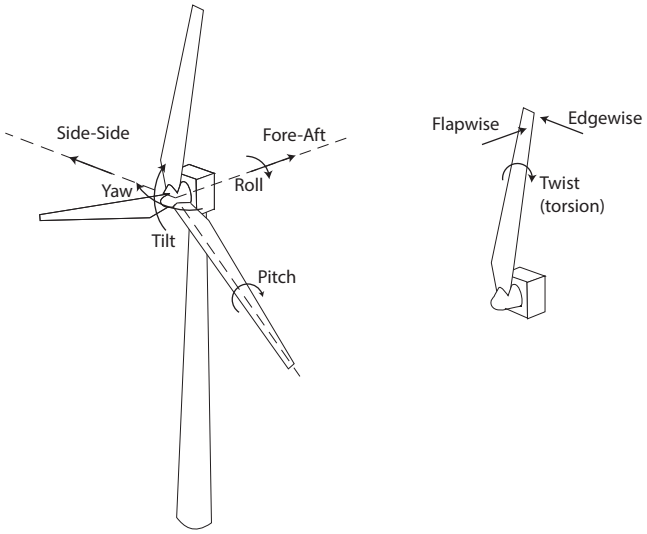

Figure 3.2 – Terminology of the principal axes of translation and rotation of a wind turbine structure

3.1.1.1 Rotor

The rotor is the key component of a wind turbine, converting the kinetic energy of the wind into mechanical energy. It is composed by the blades which are connected to the hub.

The design of a blade is one of the most complex tasks in the development of a wind turbine. Blades have to be designed in order to optimize the energy extraction from the wind flow. However, at the same time, the progressive increase in the power output of the turbines demands increasingly larger blades (with models of 83.5 m already being produced (Quilter, 2013)).

For these reasons, blades present complex cross sections (named airfoils) which vary along their length (Figure 3.3). In addition, blades have to be sufficiently light, stiff and strong, at the same time, to not contribute with enormous gravitational loads (for the blade itself and for the tower), to not deflect too much (which would drive to loss of efficiency and, even more important, could lead to a collision with the tower) and to resist to a very high number of cycles during their lifetime (of around 10^7 to 10^8 (Hau, 2006)). In order to accomplish all these prerequisites, composite materials are used (usually epoxy resins with glass fibres, although carbon fibres may be also used in the blade composition).

In Figure 3.4 two common solutions for the structure of a blade are presented.

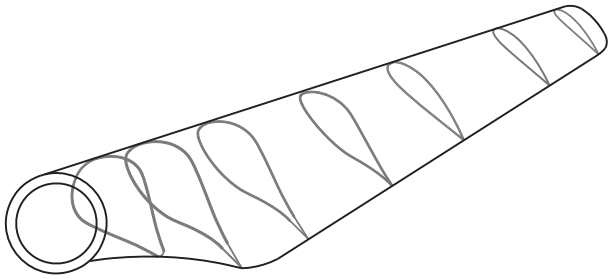

Figure 3.3 – Variation of the airfoil along blade length

Considering the rotor position, wind turbines may have a wide variety of configurations. As previously referred, the rotor can be placed in front (upwind) or behind (downwind) the tower. This latter solution is rarely used today because of noise, vibrations and efficiency problems. Due to the presence of the tower upstream of the rotor, the flow is disturbed before it reaches the blades and, every time a blades pass behind the tower, the momentary absence of aerodynamic force leads to additional vibrations (shadow effects). In addition, large downwind rotors also need a yaw system (which is not necessary in small downwind turbines). Several examples of downwind wind turbines were presented in Chapter 2.

The number of blades is another aspect that contributes for the variety of rotor configurations. Historically, wind turbines have one, two or three blades. The difference between two or three-bladed rotors implies, besides differences in tip-speed and efficiency, different vibration problems. Figure 3.5 presents an example of the yaw moment created by an asymmetrical wind flow on wind turbines with different rotor solutions (Hau, 2006). As can be seen, one and two-bladed rotor wind turbines suffer from a noteworthy time-varying yaw moment while this excitation is almost undetected with rotors with three or more blades. This effect is due to the variation of the rotor moment of inertia with the blades revolution. Whereas in one or two-bladed rotors, this asymmetry in the moment of inertia is

relevant and leads to a pulsating load profile during a revolution (Hau, 2006), three or more blades confer an almost symmetrical moment of inertia to the rotor.

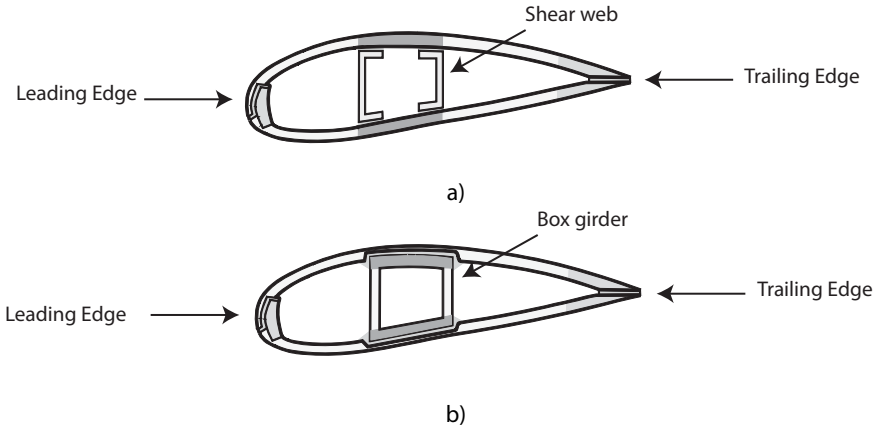

Figure 3.4 – Two common design concepts for blade cross sections with different load-carrying solutions (adapted from (Tong, 2010)): a) shear web; b) box girder

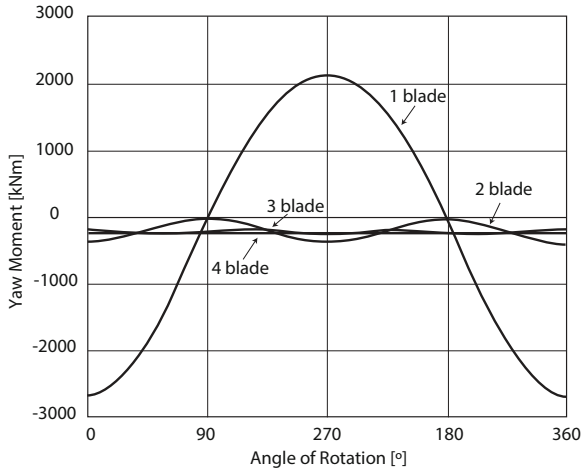

Figure 3.5 – Yaw moment caused by asymmetrical wind flow on wind turbines with different number of blades (adapted from (Hau, 2006))

With the aim of alleviating these loads created by two-bladed rotors, some solutions were developed. These solutions focus on the flexibility of the connections between blades and the hub (Figure 3.6).

The simplest solution is the rigid hub connection. This solution connects the blades to the hub at fixed positions and, consequently, the loads are directly transmitted to the drive train by the hub. This is the common solution for three-bladed rotors and for some rotors with two blades (such as the 1983 WTS-75 Nasudden, see Figure 2.19)).

A more flexible solution is the teetering hub. This hub connection allows the rotor to teeter about the rotor shaft due to a hinge located at the hub. This solution permits to balance out some asymmetrical loads. This solution is intended for two-bladed rotors (and was used in the 1982 Growian wind turbine, see Figure 2.21).

Another flexible solution is the flapping hinge rotor. In this solution, a hinge is installed in each blade allowing the individual rotation of the blades (the 1941 Smith-Putnam wind turbine used this solution, see Figure 2.7)).

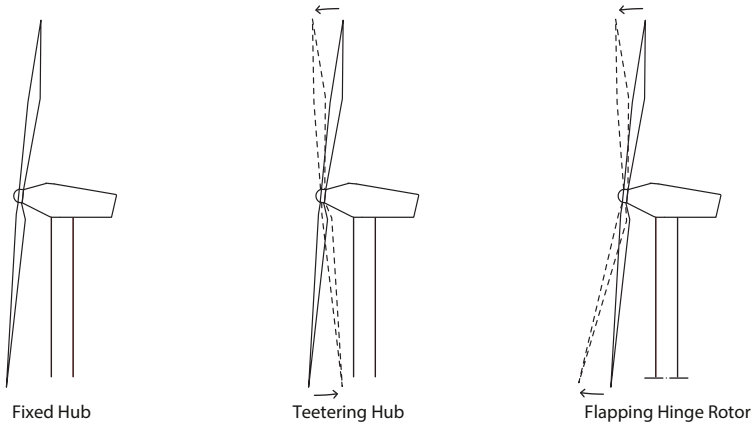

Figure 3.6 – Hub solutions

3.1.1.2 Nacelle

The nacelle is the component of a wind turbine which encloses the mechanical and some electrical elements (Figure 3.7).

In the nacelle, the rotor shaft (or main shaft) receives the torque (mechanical energy) from the hub. In nowadays most common turbines, this shaft is connected to a gear box. The gear box increases the rotational speed from the rotor shaft to a more convenient speed to the generator. The connection between the gearbox and the generator is made by the generator drive shaft. The generator produces electric energy from the mechanical energy. There is also a mechanical brake with the aim of stopping the turbine when necessary and a yaw system that mechanically orients the nacelle to the wind direction. The components of the nacelle are supported by the bedplate.

Although the previous description refers to the most common nacelle layout, there are also some different concepts, such as the absence of a gear box (direct-driven generators).

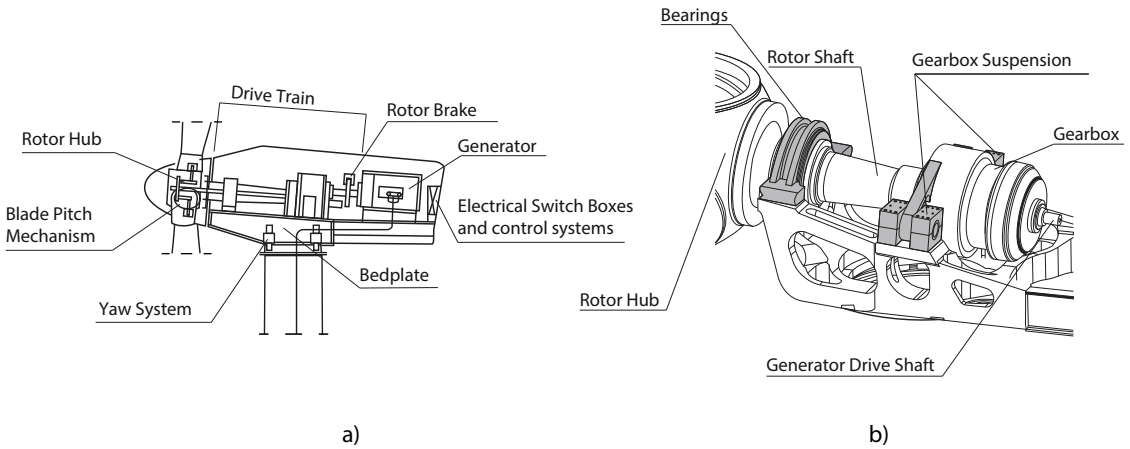

a) b)

Figure 3.7 – a) Main components inside the nacelle. b) Detail of the drive train (adapted from (Hau, 2006))

3.1.1.3 Tower

Wind turbine tower elevates the rotor to the desire height. Since the wind flow presents higher speed and lower turbulence at higher heights, the towers tend to be very tall. In addition, wind turbine towers are also very slender which, alongside with the rotor motion, leads to complex dynamic problems.

The more common towers are of four types: steel tubular, steel lattice, concrete tubular and hybrid solutions. There are also some special designs, such as guyed supported towers. However, since these are almost not used nowadays, they are not covered in this work.

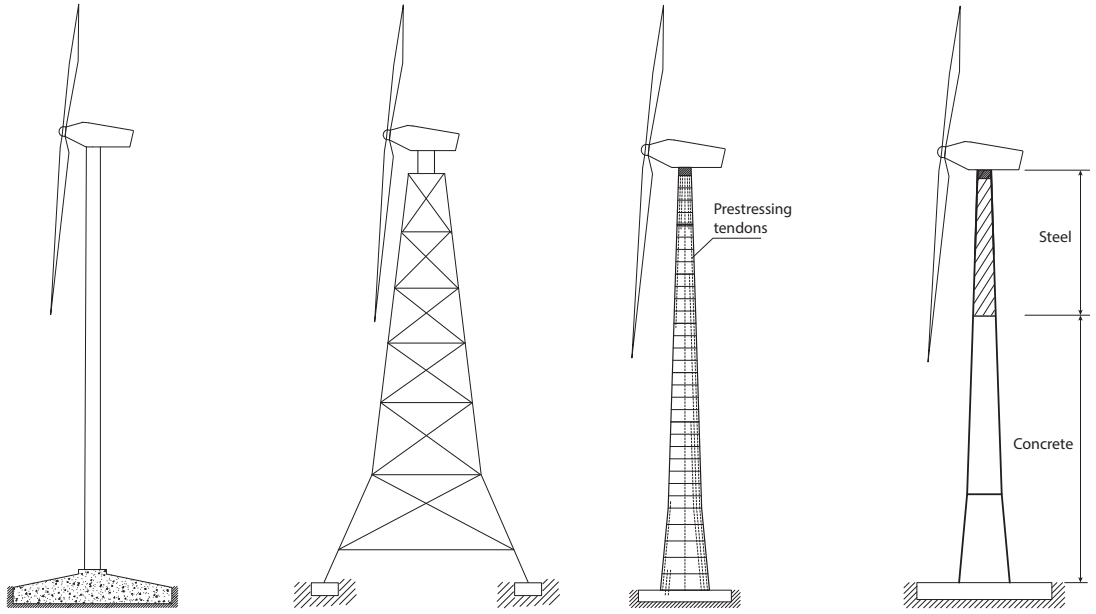

Figure 3.8 – Various wind turbine tower types: a) steel tubular; b) lattice; c) concrete tubular; d) hybrid solution (adapted from (Tricklebank, Halberstadt et al., 2007))

Steel Tubular Tower

The most currently used solution is the steel tubular tower. It is composed by steel sheets which are rolled into a circular shape and then welded together to form a circular section with a length of around 20 m – 30 m. These sections are assembled on-site by bolted connections. Thus, no on-site welding processes are needed.

The main advantages of this solution are its short on-site assembly and erection time. From a design point of view, steel tubular towers also present some benefits, such as an uniform behaviour for all yaw directions (due to the circular cross section) and a good control over the dynamic characteristics, since it is a solution with a large accumulated experience.

On the other hand, steel tubular tower have shown some difficulties in following the growth in dimensions for onshore wind turbines. With higher tower height, also a larger tower base diameter is usually required. Since a diameter of around 4.0 m – 4.5 m is the common limit for road transportation, alternative solutions need to be considered. Besides this, the increase in height also

introduces some difficulties concerning the stiffness of the tower. For that reason, this solution is not used in some models due to the required structural stiffness that a steel tubular tower cannot deliver.

Steel Lattice Tower

Steel lattice towers were the preferred solution of the first experimental turbines and of the first smaller commercial turbines (see for example Figure 2.6 and 2.7) (Hau, 2006). This solution is constituted by legs and bracings connected by bolted or welded joints.

Lattice towers can be a solution for high towers, since they can be transported disassembled. They present a satisfactory stiffness and strength with regard to the material consumed. They are also lighter than the tubular solutions and usually present a higher structural damping due to the numerous joints of the structure.

In contrast, the assembling of the structure is very time-consuming and complex. Also the expenditure with maintenance is considerably higher than for tubular sections due to the high number of joints. In the past, this solution was considered as "ugly", not being endorsed by populations. This solution is not very common in nowadays installations.

Concrete Tubular Tower

Concrete solutions for wind turbine towers have a long tradition in some countries, such as Denmark (Hau, 2006). It is generally used with precast concrete, alongside with pre or post-stressed tendons, although concrete mixed on-site is also used.

Concrete towers present the main advantage of higher stiffness and damping than steel tubular. This is the reason why some very large wind turbines use this solution. Also, if the concrete is mixed on-site, the problem of transportation of large components does not arise.

Some disadvantages are also inherent to this solution. If the concrete is mixed on-site, the construction process is time consuming and might be dependent on the weather conditions. Also, the post and pre-stressing operations are complex and require special precautions. From a design perspective, the fatigue analysis is difficult to handle, leading to conservative designs in many situations.

Hybrid Tower

A compromise solution is obtained with tubular hybrid towers. This solution is characterized by a concrete tower for the lower part of the tower (usually mixed on-site), while the upper portion is made of steel. Thus, it is possible to increase the stiffness of the structural system with a short period of concrete curing and without transportation of large steel components. This is a solution mainly for high wind turbine towers (100 m or higher).

3.1.1.4 Transition Piece

The transition piece only exists in offshore wind turbines. It connects the foundation to the tower. This element is considered one of the most critical points of the structural integrity of offshore wind turbines.

This element is grouted on the top of the foundation and, in this operation, any lack of verticality is corrected (Figure 3.9). The transition piece usually attaches a structure for boat landing, platforms, ladders and the j-tube (a metallic tube that guides the cables to the seabed).

Although the transition piece is utilized in several types of foundations for offshore wind turbines, other offshore solutions may not need this element.

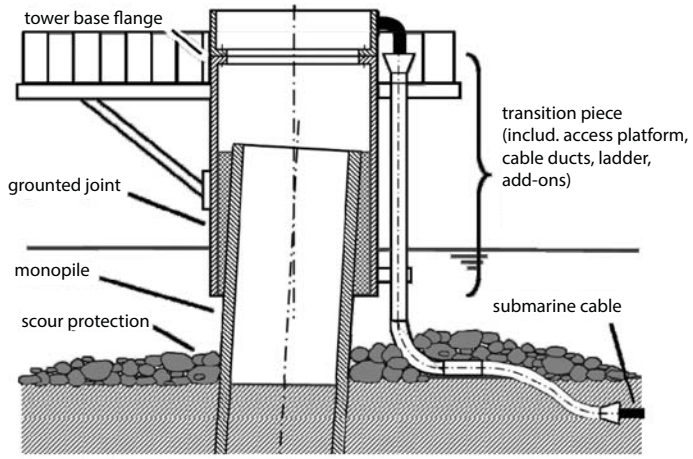

Figure 3.9 – Grouted joint for the connection between the foundation (monopile) and the transition piece. In this situation, the verticality is corrected by the connection (Gasch and Twele, 2012)

3.1.1.5 Foundation

The foundation is the component that best distinguishes onshore and offshore wind turbine structures. While onshore turbine foundations follow traditional in-land civil engineering solutions, offshore models have been progressively adopting solutions from oil and gas offshore industry.

However, both onshore and offshore foundations have the same function: to ensure stability and drive the loads from the structure to the ground, which means, to prevent the structure from sinking due to gravitational loads, from sliding due to horizontal loads and from fall over due to base overturning moments. Besides this, it is important to bear in mind that the definition and implementation of the designed foundation will influence the dynamic behaviour of the entire structural.

Onshore Solutions

The foundations for onshore wind turbines employ well-known and controlled solutions. There are mainly two possibilities: slab foundations or pile foundations (Figure 3.10).

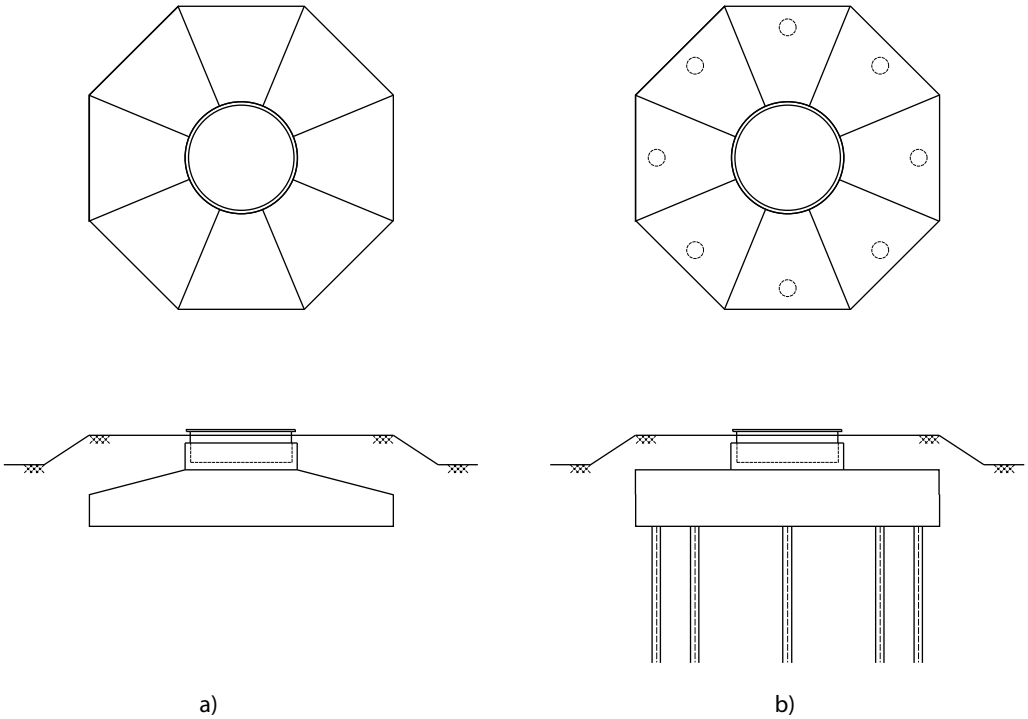

Figure 3.10 – Examples of foundations for onshore wind turbines: a) slab foundation; b) pile foundation

Slab foundations are used when the ground near the top is of good quality. They consist on reinforced concrete slabs which usually have a polygonal geometry (such as an octagonal shape) with a tapered or constant thickness.

This kind of foundation resists to the overturning moment with the eccentricity of the reaction. The vertical and horizontal loads are resisted by the dispersion of the load through the foundation area and by the friction between the ground and the foundation, respectively.

Pile foundations are used for weaker soils. They are constituted by a pile cap from which a certain number of piles are connected and extended until a good soil layer is reached. In this situation, the loads are absorbed by the soil through axial and lateral pile resistance against the soil. Once again, reinforced concrete is used in this solution.

Offshore Solutions

In contrast to onshore turbines, there is the need for diversified offshore solutions, depending on the water depth. In addition, these solutions are considered far more complex than for onshore.

Offshore solutions for wind turbines can be divided in three categories: for shallow waters (up to 25 – 30 m), for transitional waters (from around 30 to around 60 m) and for deep waters (more than 60 m). The most appropriate solutions for each water depth are presented in Table 3.1.

Table 3.1 – Offshore foundation solutions concerning water depth

Solution	Shallow waters (0 – 30 m)	Transitional waters (30 – 60 m)	Deep waters (+ 60 m)
Gravity-based	✓		
Monopile	✓		
Tripod		✓	
Jacket		✓	
Tripile		✓	
Floating			✓

Gravity-based foundation is the second most used solution for current offshore wind turbine projects (Figure 3.11). It consists on a caisson (usually made of concrete) which is filled with material to achieve the required weight. Therefore, a large footprint is used to absorb moments due to environmental loads. The caisson is fabricated on land and then transported to the site, where it is submerged and filled with ballast. For the operation on the site, heavy vessels are required to set the foundation. Besides the need for heavy machinery, another disadvantage is the necessary preparation of the seabed. This operation ensures compaction and homogenization of the soil to prevent uneven settling.

This solution is considered, with regard to the vibrational characteristics, as "stiff". For this reason, the aerodynamic damping of the rotor do not contribute in large measure to alleviate the response of the structure due to the dynamic loads (see section 4.5) (Hau, 2006).

Gravity foundations are indicated for very shallow waters (around up to 10 m – e.g. the Nysted wind farm in Denmark). However, there are examples of implementation at deeper waters (around 27 m – e.g. the Thornton Bank wind farm, in Belgium (Thomsen, Forsberg et al., 2007)).

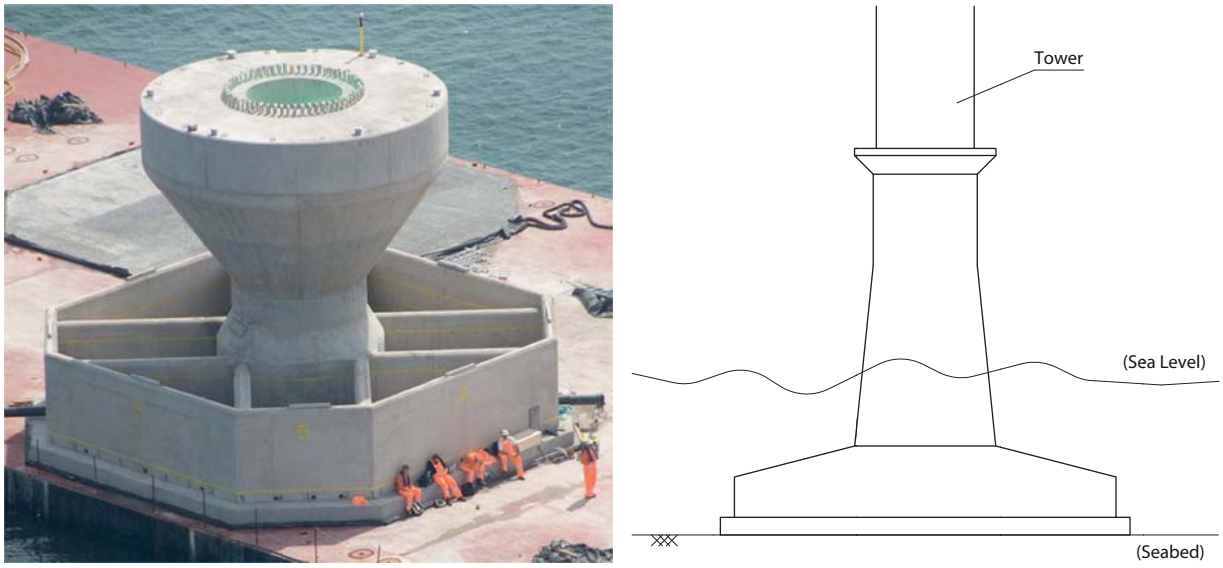

Figure 3.11 – Gravity-based foundation (photo (Scots Renewables, 2011) and illustration)

Monopile foundation is another alternative solution for shallow waters and is, nowadays, the most used solution in offshore wind turbines (Figure 3.12). It consists on a free-standing steel pipe which is driven or drilled (depending on soil quality) into the seabed by means of special and heavy equipment. In situations in which the monopile is implemented by driving, hydraulic hammers are used for penetration. Since the pressure introduced by the hammers is very high, appurtenances (such as outside ladders and the j-tube) cannot be installed directly on the monopile. For this reason, they are installed on the transition piece. The previous preparation of the seabed is not necessary for monopiles although significant boulders should be avoided on the foundation area.

Contrary to the gravity-based solution, monopile foundations are considered as "soft", in respect of their dynamic behaviour (Hau, 2006).

Monopile foundations are used in deeper waters than gravity-based solutions. However, a water depth of around 25 m to 30 m is a consensual limit for the implementation of this foundation. This type of foundation was used in the Horns Rev wind farm (in Denmark).

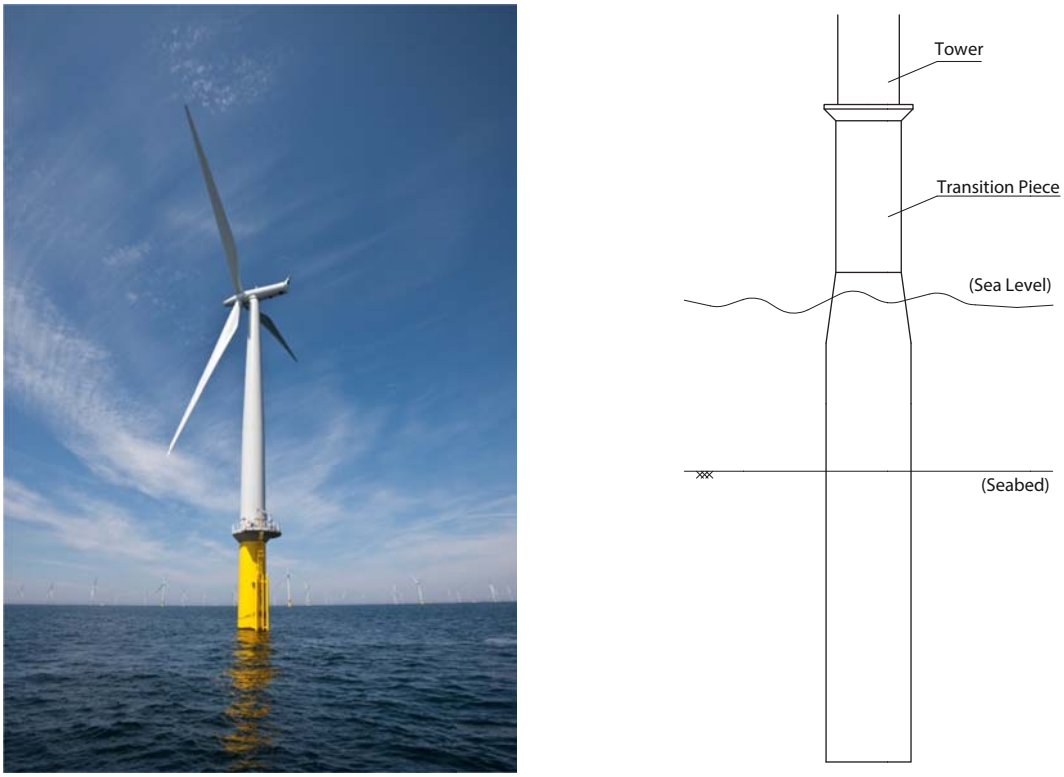

Figure 3.12 – Monopile foundation (photo (LORC, 2012b) and illustration)

A different approach under development for the foundation of turbine towers is the suction bucket, a technology already used in the oil and gas industry (Figure 3.13) (Byrne, Houlsby et al., 2002). This technology consists of skirted shallow foundations, which inside water is pumped out, resulting in the sinking of the bucket into the soil due to the created pressure differential. Suction buckets present a saving in material (compared to common monopiles), and a faster and simpler installation, in which hammering is avoided (Byrne, Houlsby et al., 2002). However, there is some concern regarding the lateral stability and the verticality of the tower (Tong, 2010).

This type of foundation is still in an experimental phase. There are already some examples implemented (in Frederikshavn, Denmark) (Ibsen, Liingaard et al., 2005) and more recently at the Dogger Bank (UK) (Carbon Trust, 2013)). However a project was cancelled due to installation problems in 2005 (Enercon GmbH, 2005).

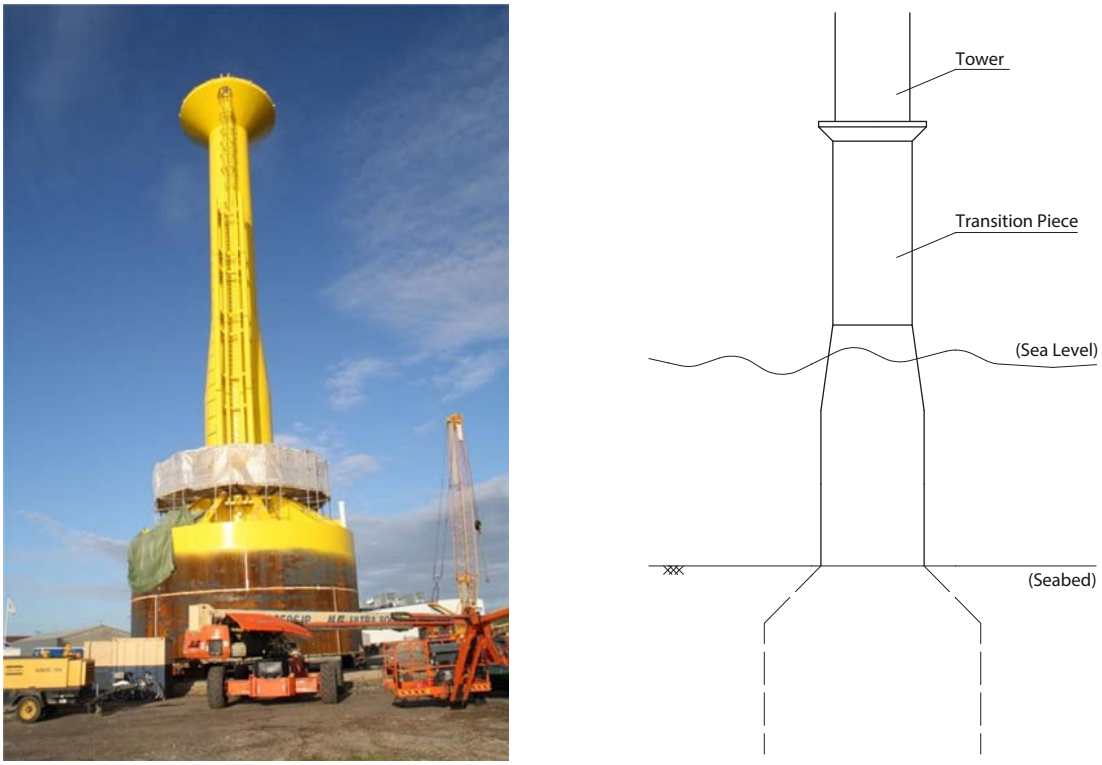

Figure 3.13 – Suction bucket foundation (photo and illustration)

Water depths of around 25 m – 30 m are the limit of current common commercial offshore wind turbines. Beyond this limit, the applicability of the presented solutions becomes very expensive and demanding on material weight and on machinery for implementation. For this reason, new foundation technologies are under development nowadays (for transitional and deep waters).

Tripod foundation is one of the alternatives for transitional waters. It is an expansion of the monopile concept with a larger footprint (Figure 3.14). Tripods consist on a structure with three legs which diverge from a single node. These three points are anchored in the seabed.

The tripod geometry allows this solution to be light-weight and "stiff". Since the loads are mainly axial in the legs, scour protection is generally not needed (Tong, 2010). In addition, only reduced seabed prearrangement is required. On the other hand, these structures are complex to build (leading to a high production expenditure) and difficult to transport (Hau, 2006). Also, the main joint of the three legs is complex and a potential focus of fatigue problems.

Tripod foundations are suitable for water depths up to around 50 m – 60 m. This kind of foundations has been already implemented on the Alpha Ventus wind farm, in Germany (Bartsch, 2012).

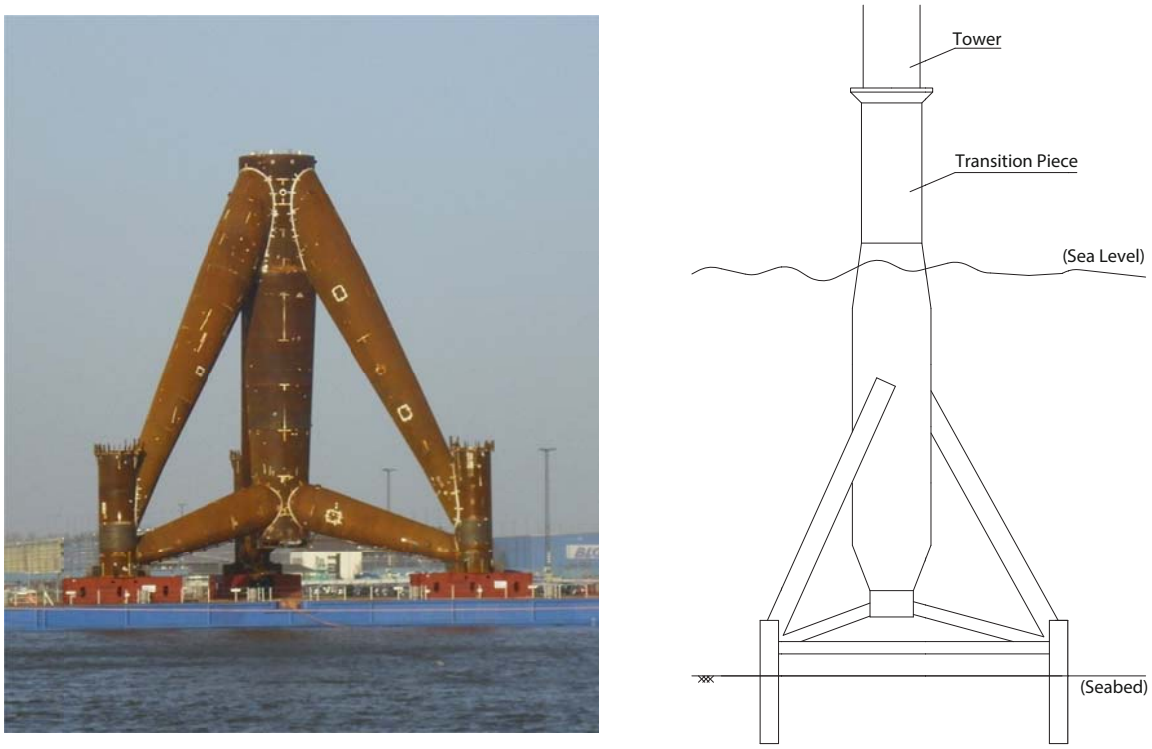

Figure 3.14 – Tripod foundation (photo (Wikipedia, 2012) and illustration)

Another alternative for transitional water depths is the jacket foundation (Figure 3.15). This solution is an application of a common design employed by the oil and gas industry for offshore structures. It consists on a truss tower with three or four legs connected to each other by bracings.

Jacket foundations are light-weight and efficient structures, with a very good resistance to overturning moments. Although they represent a notable reduction of material (steel), they are expensive due to the necessary weldings. Its installation process is similar to the tripod. The jacket is transported to the desire site where the structure is implemented. The anchoring of the structure is also realized through piles or with suction buckets (LORC, 2012a).

This type of structures is nowadays idealized for water depths up to around 50 m – 60 m. However, this technology is employed for deeper waters on the oil and gas industry, so it can be also potentially used for implementation of offshore turbines in deeper waters. The Beatrice wind farm (in Germany) is an example of implementation of wind turbines on jacket foundations.

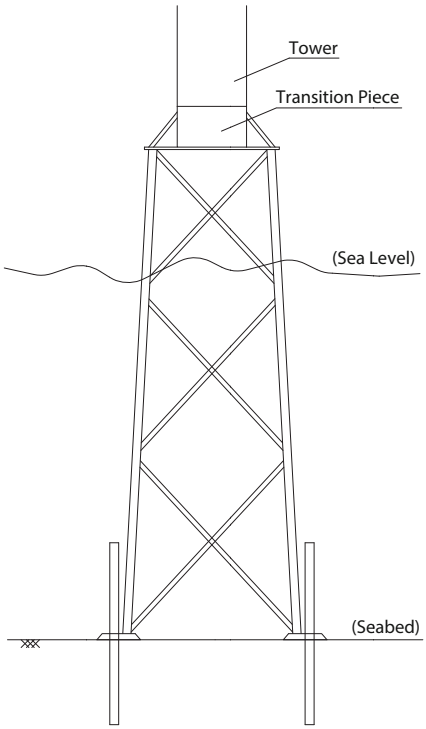

Figure 3.15 – Jacket foundation (photo (LORC, 2012a) and illustration)

The tripile is other foundation technology installed nowadays for medium water depth (Figure 3.16). It consists on a natural evolution from the monopile: instead of just one steel pile, three monopiles are installed and connected at the top by a transition piece.

This design has the advantage of increasing the stiffness of the monopile solution. However, the installation of the three piles is of major importance and needs a rigorous approach. In addition, each pile needs to be hammered which is extremely noisy (LORC, 2012c).

The tripile solution is indicated for water depths up to 50 m. This technology has already been implemented in the BARD Offshore 1 wind farm and in the Hooksiel wind farm (BARD Engineering GmbH).

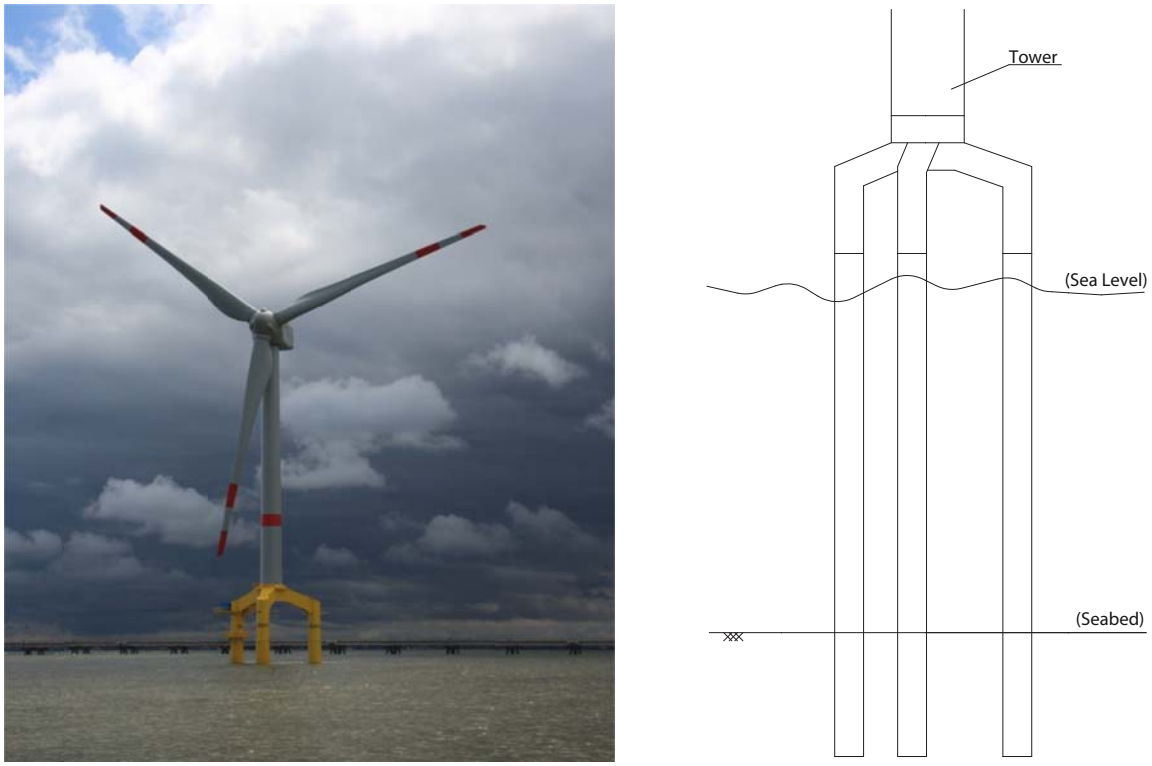

Figure 3.16 – Tripile foundation (photo (BARD Engineering GmbH) and illustration)

As referred in Chapter 2, one of the today's main fields of development in the offshore wind turbine industry is the floating structure for deep water depths. Nowadays, there are already some experimental projects under development, however there is still a long way of development for the feasibility of commercial offshore wind turbines based on floating foundations.

Besides the possibility of introduction of wind turbines at deep water depths, floating concepts enable a mass-production of structures since they can achieve a high independence from the seabed conditions. Another advantage of floating platforms is the possibility of being towed to their location.

The design of floating structures follows mainly three different concepts to achieve stability (Butterfield, Musial et al., 2005):

- Ballast – This kind of solution uses the weight of ballast below a central buoyancy tank to create a righting moment and high inertial resistance to pitch and roll. The elongated shape of the structure helps to minimize the heave motion. This solution has been used in the offshore oil industry for many years (Musial, Butterfield et al., 2004);
- Mooring Lines - Platforms using this technology achieve stability through the use of mooring lines under tension;
- Buoyancy – This last concept relies on a distributed buoyancy, achieved through the use of a weighted plane area for righting moment (Butterfield, Musial et al., 2005).

Although each described concept presents a different physical principle to achieve stability, in reality floating platforms usually present a hybrid system. Commonly, solutions are designed based on all of

the three concepts, although generally relying on one primary source for stability (Butterfield, Musial et al., 2005).

A representative design of each of the listed concepts is presented in Figure 3.17.

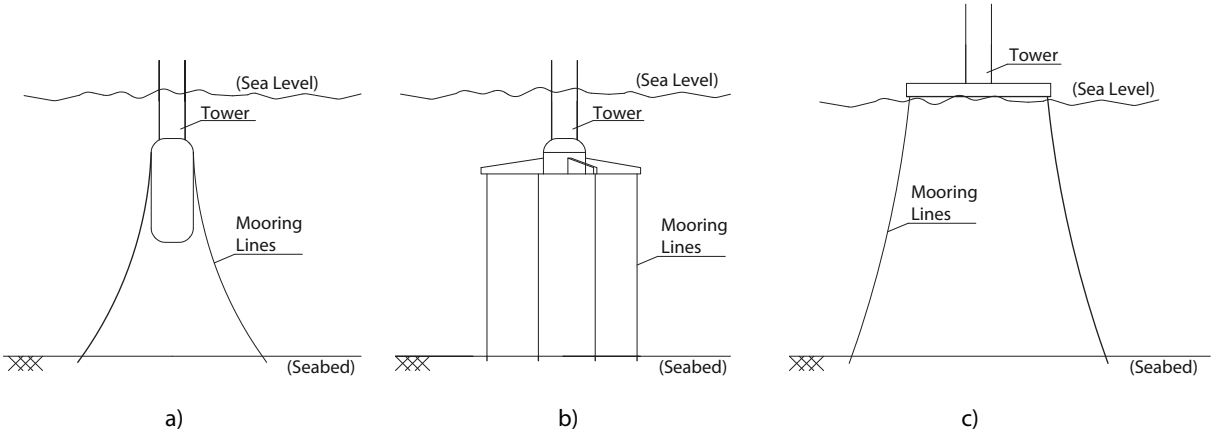

Figure 3.17 – Floating solutions for offshore wind turbines(adapted from (Butterfield, Musial et al., 2005)): a) ballast; b) mooring lines; c) buoyancy

3.1.1.6 Monitoring and Control System

Modern wind turbines are usually equipped with a monitoring and control system named SCADA (Supervisory Control and Data Acquisition system). This system consists of a microprocessor, together with several sensors, to control the operation and monitor the performance of the turbine.

Under this system, several data is registered through sensors that record, among others:

- Wind speed and direction;
- Rotor speed;
- Nacelle orientation;
- Generator speed;
- Pitch angle.

With this data, the control system is responsible for operations like the start and stop of rotor rotation, emergency shut-down, adjustment of nacelle orientation and pitch angle. The system is also used to monitor the power production from a remote location, since it is usually connected through any means of communication (such as internet network). The information provided by the SCADA system can be also used to monitor the condition of several components (see Chapter 5). This data represents an important part in the architecture of the developed monitoring system (see Chapter 7).

3.1.2 COSTS BREAKTHROUGH

The investment costs of wind farms are of paramount importance for the feasibility of wind energy. These costs are divided into capital costs (CAPEX - including all the costs for the implementation of the farm) and variable costs (OPEX - including all the costs over the period of its operation – e.g. operation and maintenance, land rental, insurance, among others).

The NREL study present in (Tegen, Hand et al., 2012) describes some costs related to onshore models of U.S. wind projects during 2010. Figure 3.18 presents the principal results of this study, namely the capital cost share of the principal components of a wind turbine located in wind farm. These costs are grouped in larger groups, namely:

- Turbine – comprises the wind turbine itself, which includes the tower, nacelle and rotor components (Blanco, 2009);
- Balance of plant – including all the infrastructure except the turbine (foundations, buildings, roads, among others) (Department of Energy & Climate Change, 2010);
- Installation and commissioning – including the installation and commissioning of the turbine and balance of plant (Department of Energy & Climate Change, 2010);
- Development and consent – includes the multifaceted process of taking a wind farm from inception through to the point of financial close or commitment to build, depending on the contracting model, including several studies and contracts (Department of Energy & Climate Change, 2010).

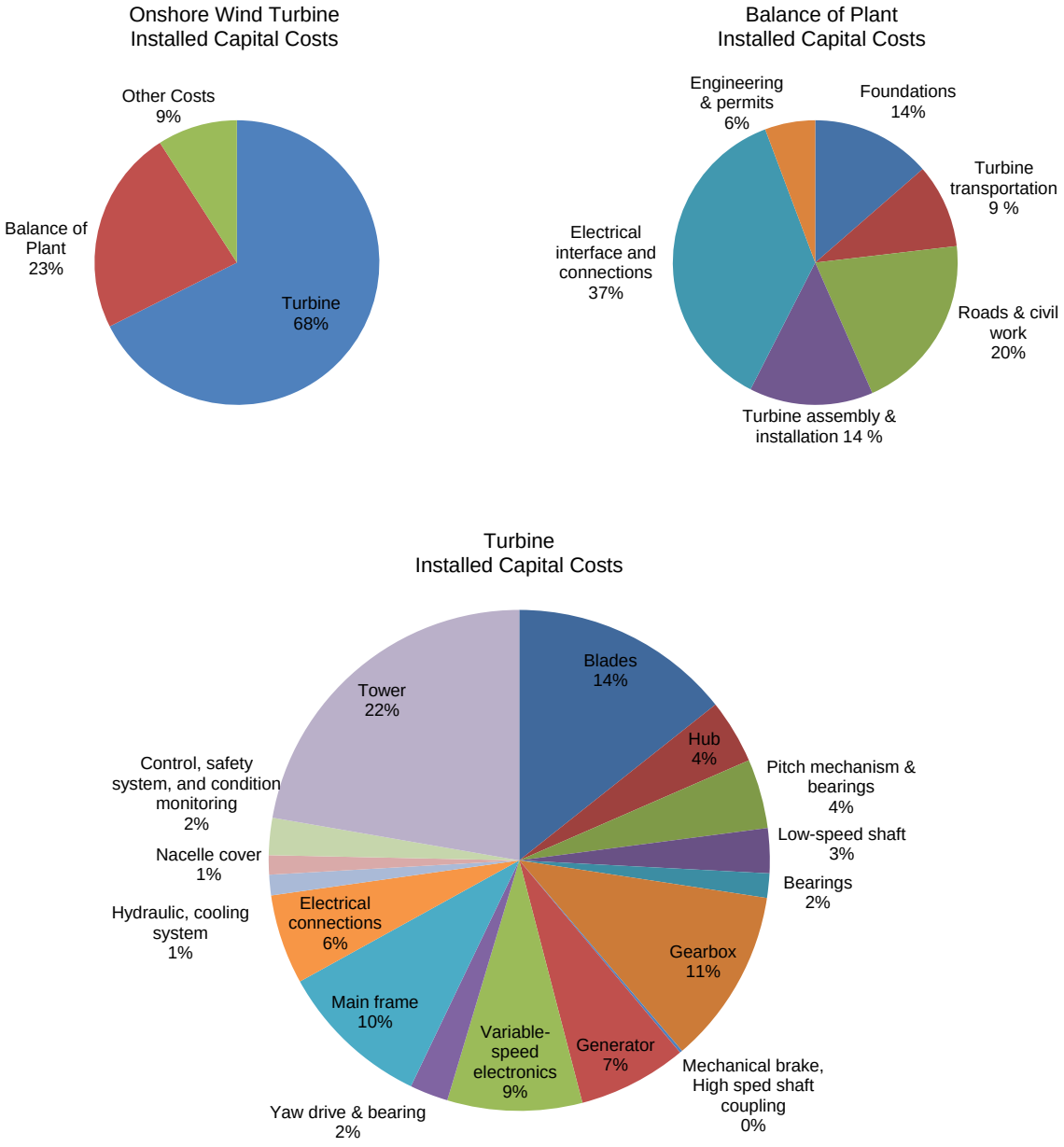

Figure 3.18 – Installed capital costs for onshore wind turbine farms (Tegen, Hand et al., 2012)

The main installed capital costs of offshore wind turbines are shown in Figure 3.19 (Department of Energy & Climate Change, 2010). These values are adjusted in order to give representative results for a 500 MW+ wind farm of approximately 5 MW turbines on jacket foundations in typical UK east coast conditions around 80 km from shore in water depth of 30 m and considering market dynamics prevailing at the start of 2010.

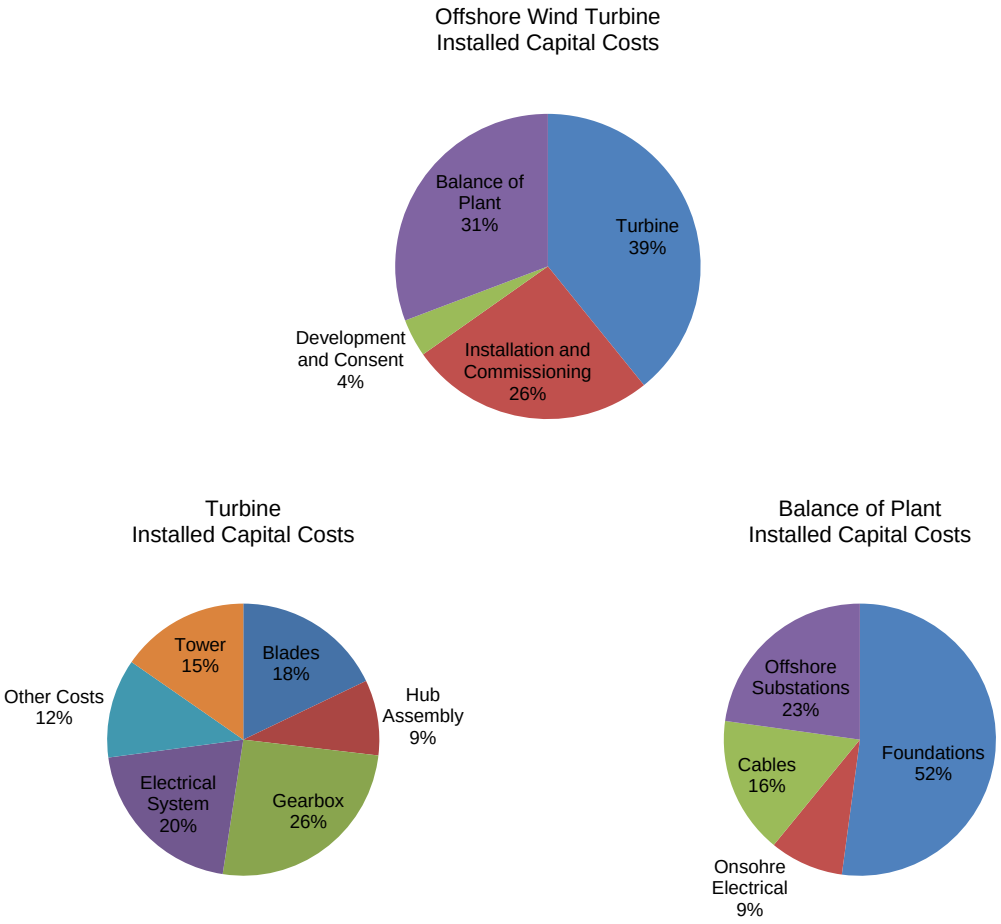

Figure 3.19 – Installed capital costs for offshore wind turbine farms (Department of Energy & Climate Change, 2010)

Since offshore models are largely dependent on the water depth of implementation, a qualitative representation of costs for different substructures is presented in Figure 3.20 (Musial and Ram, 2010).

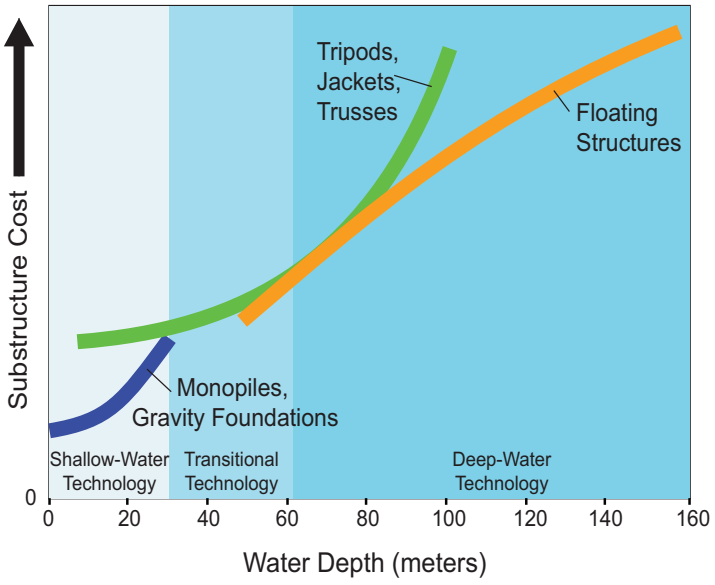

Figure 3.20 – Cost of offshore wind turbine substructures with water depth (adapted from (Musial and Ram, 2010))

As can be seen from the previous figures, the main costs come from the turbine group. However, for offshore turbines, the costs are more evenly distributed mainly due to the increased cost of foundations and installation of the turbines (Department of Energy & Climate Change, 2010).

Another interesting aspect is the high relative cost importance of the tower, blades and gearbox. This is highlighted in Figure 3.21 (capital costs of a 5.0 MW turbine from Senvion).

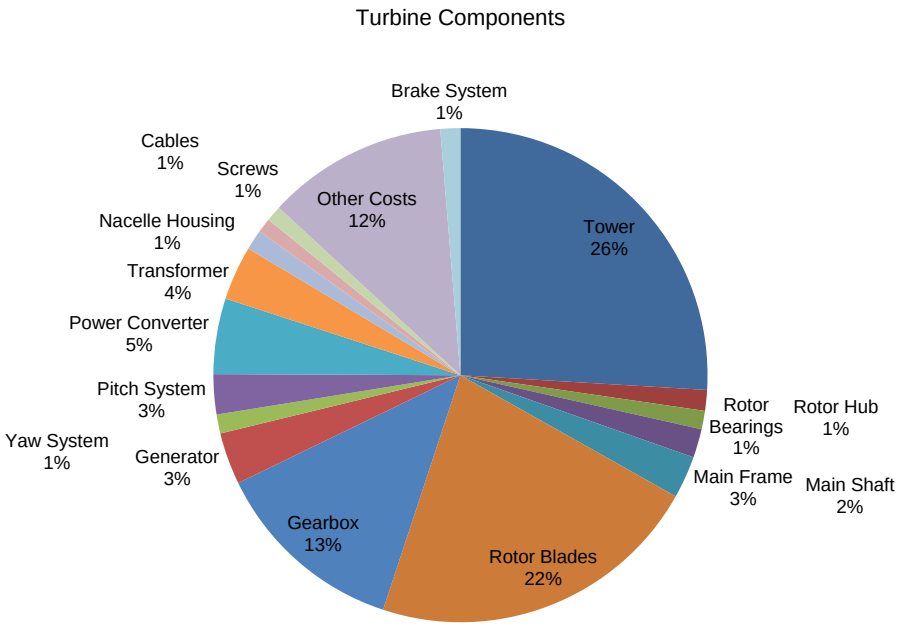

Figure 3.21 – Share of capital costs of the Senvion 5M wind turbine (Wind Directions, January/ February 2007)

3.1.3 Wind Turbine Components Reliability

Wind turbines are located, to a large extent, in remote sites. Considering the case of Portugal as an example (see Figure 2.33), most onshore wind farms are located on mountainous locations, with difficult access. This fact makes the access of people and necessary machinery/ equipment for maintenance and/ or reparation much more difficult and costly. If the offshore situation is considered, in addition to the higher costs compared to the onshore solutions, the access to the structure is also dependent on the weather conditions (Nielsen and Sørensen, 2011).

Considering all these constraints, a rigorous reliability analysis is necessary to optimize power production (and profitability). Several strategies for maintenance exist today (Faulstich, 2010), from simple derivation from past experience to more complex models with the help of installed sensors. However, a simple separation of strategies can be used (Sørensen and Sørensen, 2011):

- Corrective maintenance – this model follows a reactive approach, which means that maintenance is performed if a component has failed;
- Proactive maintenance – this strategy aims to anticipate and avoid the failure of components. This kind of maintenance can be subdivided into two categories: preventive and predictive. Preventive maintenance (also known as time-based) is referred to a strategy based on

scheduled activities defined according to statistical models based on the historic of failures. On the other hand, predictive maintenance is a strategy based on the assessment of the components health through sensors installed in the components/ structure. The monitoring system developed and described in this work falls in this category. This is the strategy expected for future large onshore and offshore wind turbines.

Modern wind turbines achieve a high availability[1], of around 97 %, when the maturity and teething problems of the turbines are solved (Harman, Walker et al., 2008). However, several failures still occur, implying unscheduled down times (Faulstich, 2010).

The UpWind project (Faulstich, 2010) analysed wind turbine failures in the German market between 1989 and 2006. It presents two major groups of failure causes:

- External causes (such as lightning, grid outage, icing, storm). These failures mostly affect electric subassemblies and occur more frequently. However, the downtime associated with each occurrence is usually short. For these cases, design optimization is suggested as solution for prevention;
- Operation causes (such as wear out and relaxation). This type of failure mainly affects mechanical components and, although seldom, usually implies large downtimes. An assessment of the condition of the components through the use of sensors is recommended for prevention of these failures.

Among different components, electrical systems represent the most common failures for onshore wind turbines (Figure 3.22). However, rotor blades (including pitch system), the yaw system, the gearbox and also electrical systems are the ones which imply longer downtime, according to Figure 3.23 (Faulstich, 2010; Wilkinson and Hendriks, 2011).

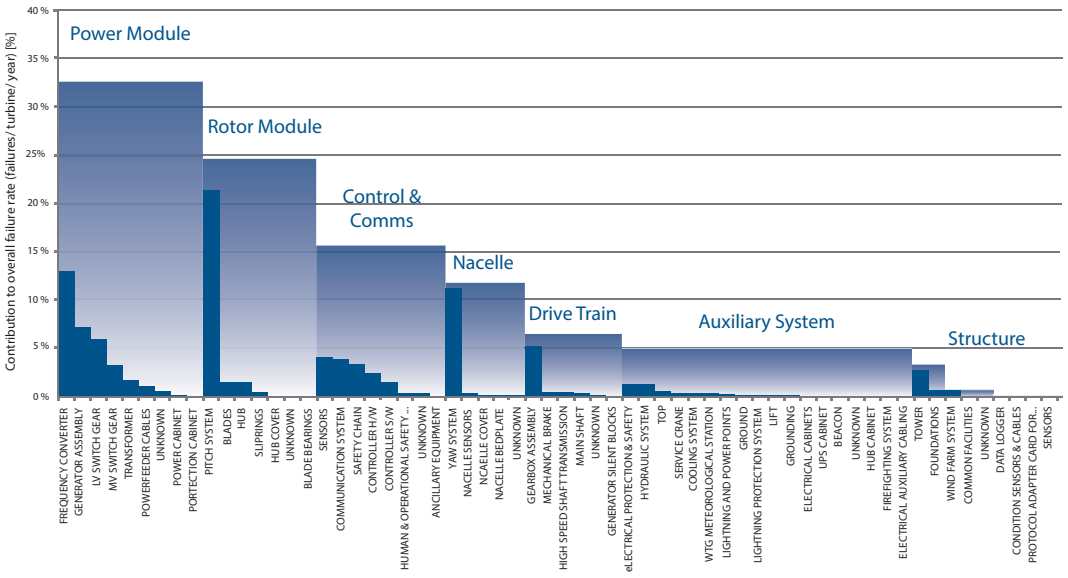

Figure 3.22 – Normalized failure rate of sub-systems and assemblies for turbines of multiple manufacturers (for onshore wind turbines) (adapted from (Wilkinson and Hendriks, 2011))

[1] Availability time is defined as the ratio between the time during which the wind turbine is available to produce (with none component failure) and the entire time under analysis.

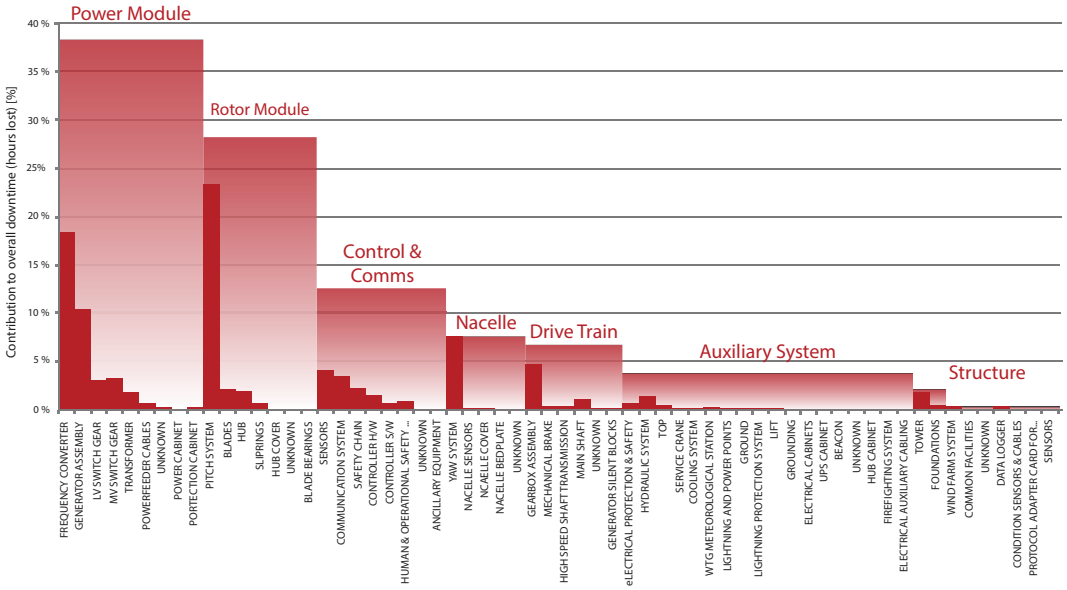

Figure 3.23 – Normalized hours lost per turbine per year due to faults in sub-systems and assemblies for turbines of multiple manufacturers (for onshore wind turbines) (adapted from (Wilkinson and Hendriks, 2011))

Although the tower is not considered as a major source of problems, some aspects must be analyzed, since the support structure of a wind turbine is fundamental for the integrity of the whole system. The main problems assigned to the tower refer to corrosion and cracking (Liu, Tang et al., 2010), alongside with more routine maintenance tasks, such as bolt tightening.

Some dramatic failures are registered in literature. In Devon, England, a small 50 kW wind turbine collapsed in 2013. The cause was said to be the lack of resistance of the tower to the registered high wind speeds (Gray, 2013). In Taiwan, a large wind turbine collapsed in 2008 due to insufficient strength of bolts (Chou and Tu, 2011). Other cases of tower buckling due to a typhoon are reported in (Li, Chen et al., 2013). A list of tower collapses is presented in (Chou and Tu, 2011), however, in some cases, the causes are not available. In all these cases, the wind turbine was completely destroyed. The share of wind turbine accident causes up to 2009 is presented in Figure 3.24. As can be seen, structural failure represents a significant portion.

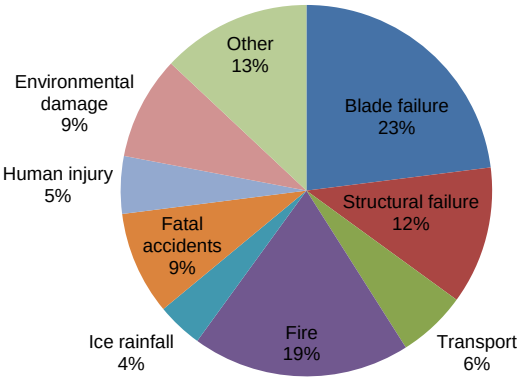

Figure 3.24 – Failure types of wind turbine accidents (Chou and Tu, 2011)

Figure 3.25 presents the estimated maintenance, repair and replacement costs of wind turbines (Gasch and Twele, 2012). It classifies the support components (tower and foundations) as the elements with the higher number of years between significant investments. This is expectable, since tower and foundations are designed to maintain their structural integrity during the entire life period of the wind turbine. However, this figure also demonstrates the high investment expected for the tower before the expected period of 20 - 25 years, which means that, in average terms, this expenditure would have to be considered.

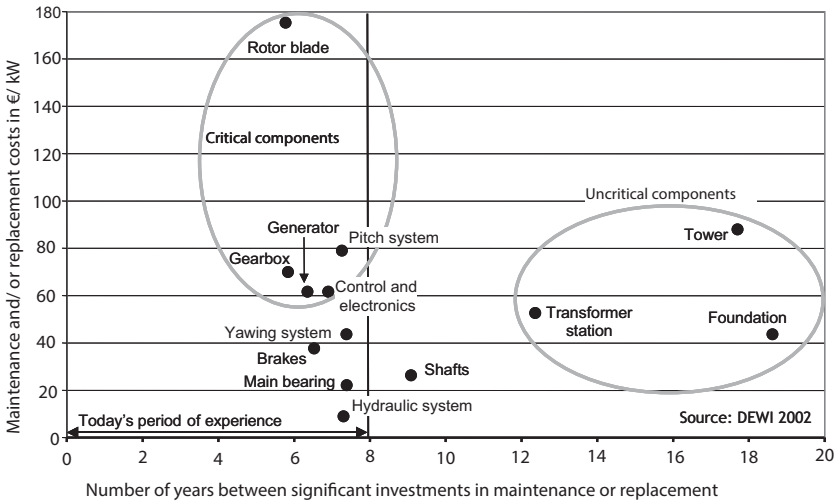

Figure 3.25 – Estimated maintenance, repair and replacement costs of wind turbines (adapted from (Gasch and Twele, 2012))

3.2 WIND TURBINE PERFORMANCE

3.2.1 ROTOR POWER CHARACTERISTICS (PHYSICS)

The understating of the operation of a wind turbine has been continuously improved. The *axial momentum theory*, initially developed by Rankine in 1865 (Rankine, 1865), was the first explanation of power extraction at a rotor from a free-stream. In 1878, Froude originally developed the *blade element theory*, where he studied the effects of the flow on blades. Based on the axial momentum theory, Betz in 1920 (Betz, 1920) (and also, independently, Lanchester in 1915 and Joukowsky in 1920 (van Kuik, 2007)) calculated the maximum efficiency of an ideal wind turbine rotor, known as the *Betz limit*. Besides these initial works, other authors such as Glauert and Prandtl also contributed with subsequent developments (Burton, Sharpe et al., 2001). In this section, the combination of the *axial momentum theory* with the *blade element theory* is presented, which constitute the base of the nowadays procedure to analyze the wind turbine system aerodynamic performance.

3.2.2 AXIAL MOMENTUM THEORY (THE ACTUATOR DISC)

The *axial momentum theory* (also known as the *actuator disc theory*) assumes that a stream tube passes through a disc, where the kinetic energy of the flow is extracted. In this theory, it is assumed that just the mass of air that passes through the disc is affected (Figure 3.26). The mass flow rate remains constant during the whole process. So, with the approach to the disc, the air stream slows down and, consequently, expands its cross section area (due to the principle of linear momentum).

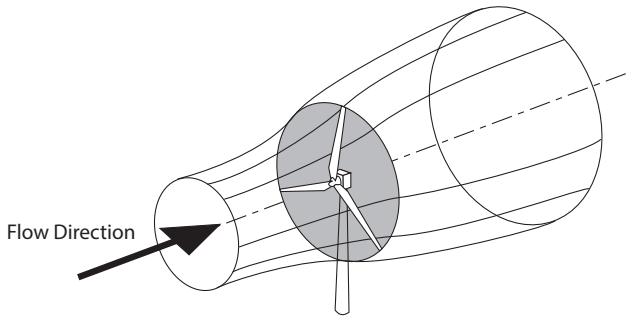

Figure 3.26 – The energy extracting stream tube of a wind turbine (adapted from (Burton, Sharpe et al., 2001))

This theory considers the following assumptions (Manwell, McGowan et al., 2010):

- Homogenous, incompressible, steady state fluid flow;
- No frictional drag;
- An in-plane continuous disc (similar to an infinite number of blades);
- Uniform thrust over the disc;
- A non-rotating wake;
- The static pressure far upstream and far downstream of the rotor is equal to the undisturbed ambient static pressure.

A schematic illustration of the flow mechanism according to this theory is presented in Figure 3.27.

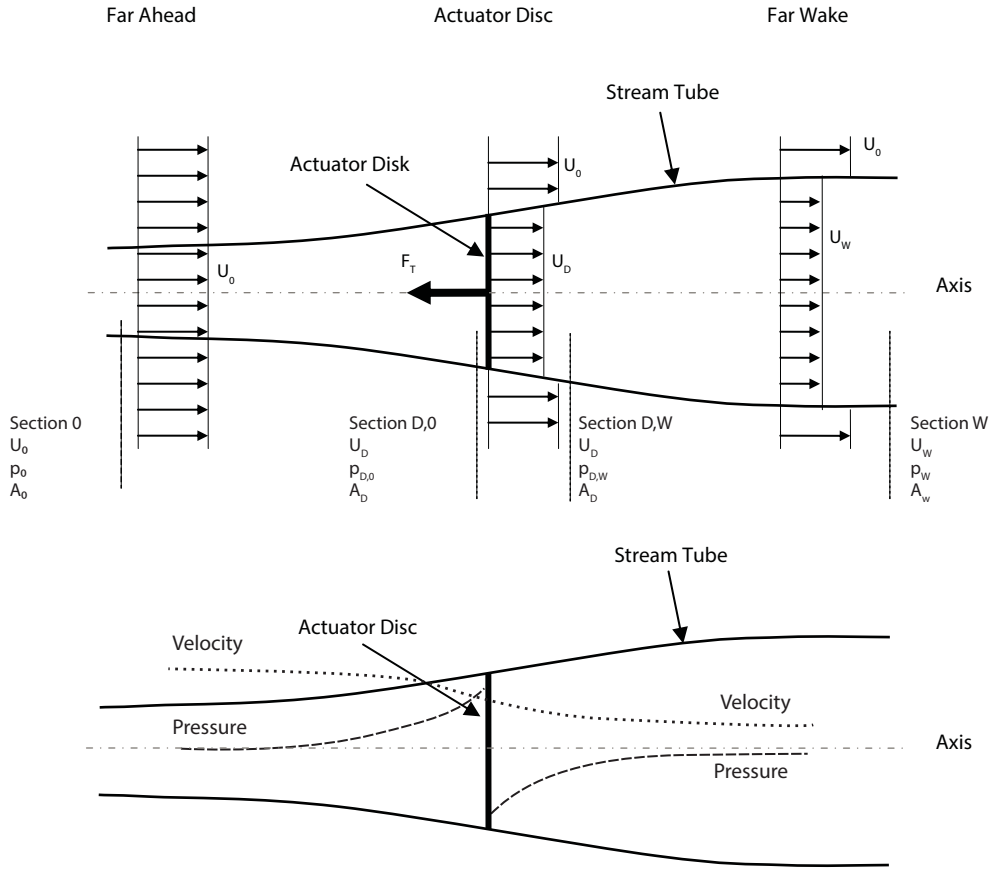

Figure 3.27 – Actuator disc with stream tube. Velocity and pressure development along the stream tube (adapted from (Tempel, 2006))

Considering the variation of linear momentum of the volume of air in the stream tube and the mass conservation principle, it is possible to calculate the axial thrust force of the rotor (F_A), considering the variation of the cross section between 0 and W), represented in Figure 3.27:

$$F_A = U_0(\rho_{air}.A.U)_0 - U_w(\rho_{air}.A.U)_w \tag{3.1}$$

with:

F_A	Axial thrust force of the rotor
ρ_{air}	Mass density of air
U_*	wind velocity (in section *)
A_*	Area of cross section (in section *)
$*_0$	Section far ahead of the rotor
$*_w$	Section far wake of the rotor

Since the flow is considered as in a steady state, it is possible to consider:

$$\dot{m} = (\rho_{air}.A.U)_0 = (\rho_{air}.A.U)_w \tag{3.2}$$

with:

$\dot{m}$	Mass flow rate

The thrust force can then be defined as:

$$F_A = \dot{m}(U_0 - U_w) \tag{3.3}$$

Applying the Bernoulli equation between the sections far ahead and in the vicinity ahead of the rotor ($*_{D,0}$), and between the vicinity of the rotor wake ($*_{D,W}$) and the far wake of the rotor, it becomes:

$$\begin{aligned} p_0 + \frac{1}{2}.\rho_{air}.U_0^2 &= p_{D,0} + \frac{1}{2}.\rho_{air}.U_{D,0}^2 \\ p_{D,w} + \frac{1}{2}.\rho_{air}.U_{D,w}^2 &= p_w + \frac{1}{2}.\rho_{air}.U_w^2 \end{aligned} \tag{3.4}$$

with:

p_*	Pressure (in section *)

As exposed in Figure 3.27, the flow velocity is the same immediately before (section $D,0$) and after (section D,W) the actuator disc and the pressure is identical far away of the rotor disc (ahead and after).

So, defining the thrust force according to the variation of pressure on each vicinity of the disc:

$$F_A = A_D(p_{D,0} - p_{D,W}) \tag{3.5}$$

and introducing (3.4) in equation (3.5), one obtains:

$$F_A = \frac{1}{2}.\rho.A_D(U_0^2 - U_W^2) \tag{3.6}$$

From equation (3.6) and considering $\dot{m} = (\rho . A . U)_D$ in equation (3.3), it is possible to conclude that the velocity in the disc section is the average value of the upstream and downstream flow speed:

$$U_D = \frac{U_0 + U_W}{2} \tag{3.7}$$

Introducing the axial induction factor (a) as:

$$a = \frac{U_0 - U_D}{U_0} \tag{3.8}$$

it is possible to rewrite equation (3.7) as:

$$\begin{aligned} U_D &= U_0(1 - a) \\ U_W &= U_0(1 - 2.a) \end{aligned} \tag{3.9}$$

As shown in the previous equations, a defines the degree of slowdown of the wind at the actuator disc. From equation (3.9), it is concluded that, in the extreme case, the induction factor can be a = 1/2. However, in this situation, the flow would cease and, thus, the flow mechanism would not be possible.

Since the power output (P) is obtained as the rate of work done by the force at the actuator disc, it can be written as:

$$P = F_A . U_D = \left[\frac{1}{2} . \rho . A_D . U_0^3\right] . [4 . a(1 - a)^2] \tag{3.10}$$

where the term defined in the first square brackets represents the power that is present in the flux, while the second square brackets represents the efficiency of the power capturing.

Considering equations (3.6) and (3.9), the thrust force is defined as:

$$F_A = \frac{1}{2} . \rho . A_D . U_0^2 . 4 . a(1 - a) \tag{3.11}$$

Usually, both P and F_A parameters are characterized by non-dimensional coefficients: the power coefficient (C_P) and the thrust coefficient (C_T), respectively:

$$C_P = \frac{Power\ Extracted}{Power\ Available} = \frac{\frac{1}{2}.\rho.A_D.U_0^3.4.a(1-a)^2}{\frac{1}{2}.\rho.A_D.U_0^3} = 4.a(1-a)^2 \tag{3.12}$$

$$C_T = \frac{Thrust\ Force}{Dynamic\ Force} = \frac{\frac{1}{2}.\rho.A_D.U_0^2.4.a(1-a)}{\frac{1}{2}.\rho.A_D.U_0^2.} = 4.a(1-a) \tag{3.13}$$

In Figure 3.28 both coefficients are represented. As expected, the maximum values of the coefficients are attained for different values of a (as already referred, values of a greater than 1/2 are unrealistic).

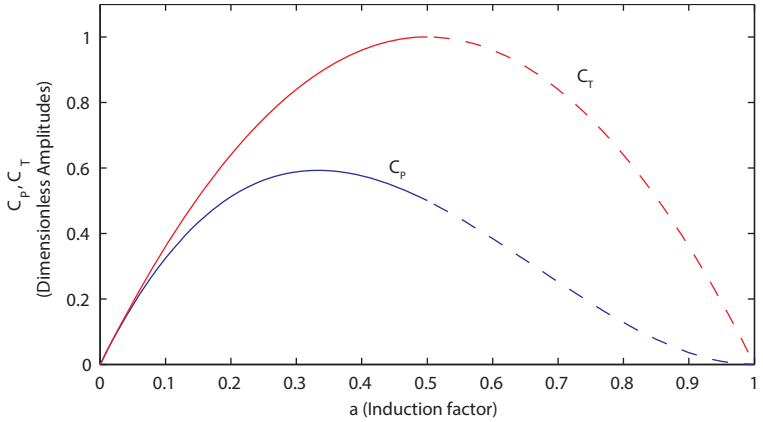

Figure 3.28 – Variation of C_P and C_T with the axial induction factor

The calculation of the induction factor for the maximum values of the coefficients is obtained with:

$$\frac{dC_P}{da} = 0 \rightarrow C_{P,MAX} = \frac{16}{27} \cong 0.593, a = \frac{1}{3} \tag{3.14}$$

$$\frac{dC_T}{da} = 0 \rightarrow C_{T,MAX} = 1, a = \frac{1}{2} \tag{3.15}$$

While the results obtained for the thrust coefficient are not of too much importance (due to the fact that the maximum value is obtained for an unrealistic situation), the result of equation (3.14) represents an important achievement. The value of 16/27, named as *Betz Limit*, is considered the theoretical maximum limit for power extraction from the flow. This means that, no matter the efficiency of the machine, no wind turbine can extract more than 59.3 % of the kinetic energy of the wind.

Obviously, this theory does not accurately characterize the real physical situation: the rotor is not composed by a uniform disc with only axial thrust acting on it and the wind does not continue as an undisturbed axial flow after passing through the rotor, among other things. To overcome these

simplifications, the variation of angular momentum in the flow is considered in the theory presented in the next section.

3.2.3 Angular Momentum Theory

The *angular momentum theory* also studies the extraction of power from the wind flow. However, this theory, unlike the *axial momentum theory*, assumes the rotation of the rotor and, consequently, the creation of a rotational wake flow. This rotational wake flow has an opposite direction from the rotor rotation in reaction to the torque exerted by the flow on the rotor.

An important difference from the *axial momentum theory* is that the energy extracted from the flow is lower. This is due to the energy employed in the rotor and wake rotation. It is assumed that the angular velocity of the rotor (Ω) is high when compared to the angular velocity of the wake flow (ω). Since the tangential speed of the rotor is not the same for all radial positions, annular rings of radius r and thickness dr are considered, defining areas of $2.\pi.r.\mathrm{d}r$ (Figure 3.29).

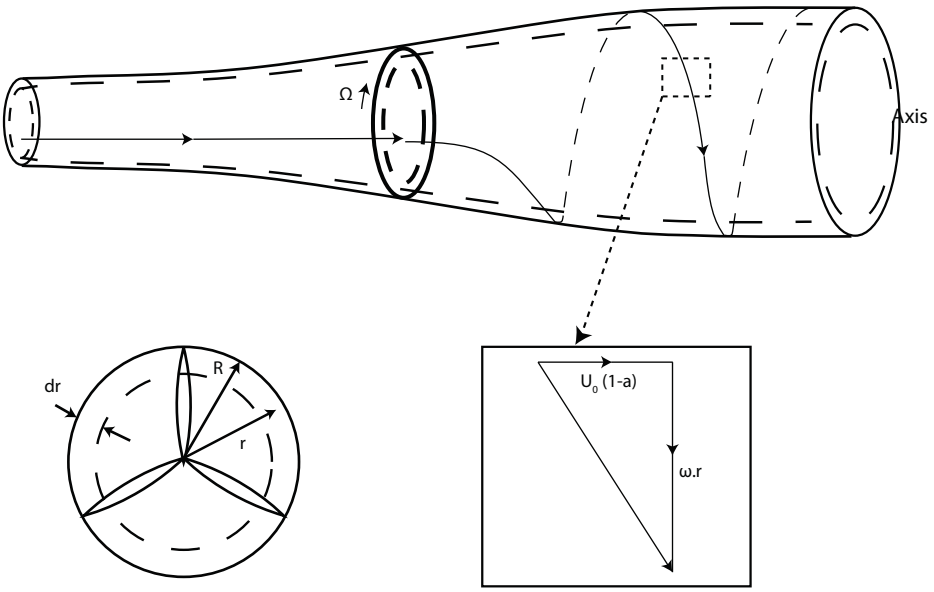

Figure 3.29 – Annular ring in the stream tube and decomposition of wake wind speed (adapted from (Manwell, McGowan et al., 2010))

As shown in Figure 3.29, the wake flow has an axial speed of $U_0(1-a)$ (like in the *axial momentum theory*) and a rotational speed of ω.

Defining an angular induction factor as:

$$a' = \frac{\omega}{2.\Omega} \tag{3.16}$$

the angular velocity of the wake flow can be written as:

$$\omega = 2.\Omega.a' \tag{3.17}$$

The torque of the annular stream is defined as the rate of change of angular momentum (due to the rotational speed):

$$\begin{aligned} \mathrm{d}T &= \rho.2.\pi.r.\mathrm{d}r.U_0(1-a).2.\Omega.a'.r^2 = \\ &= 4.a'.U_0(1-a).\rho.\Omega.r^3.\pi.\mathrm{d}r \end{aligned} \tag{3.18}$$

with:

T	Torque on the actuator disc

With the defined rotor torque, it is possible to calculate the power output due to it:

$$\mathrm{d}P = \mathrm{T}.\Omega \tag{3.19}$$

Defining the relationship between the tangential speed of the rotor at a radial distance r and the wind speed as the *local speed ratio* (or *tip speed ratio*, for the case of $r = R$):

$$\begin{aligned} \frac{\Omega.r}{U_0} &= \lambda_r \\ \frac{\Omega.R}{U_0} &= \lambda \end{aligned} \tag{3.20}$$

The power output (3.19) for each ring of radius r and thickness $\mathrm{d}r$ can be written as:

$$\mathrm{d}P = \left[\frac{1}{2}.\rho.U_0^3.2.\pi.r.\mathrm{d}r\right].[4.a'(1-a).\lambda_r^2] \tag{3.21}$$

Once again, the term defined in the first square brackets represents the power of the flux, while in the second square brackets, the efficiency of the capturing element is quantified (also known as blade element efficiency (Burton, Sharpe et al., 2001)).

As shown in (3.21), the power output extracted from the wind when the rotational wake is considered, depends not only on a and a', but also on the *tip speed ratio*. The power coefficient is defined by:

$$\mathrm{d}C_P = \frac{\mathrm{d}P}{\frac{1}{2}.\rho.A.U_0^3} \Rightarrow C_P = \frac{8}{\lambda^2}\int_0^{\lambda} a'(1-a)\lambda_r^3 \,\mathrm{d}\lambda_r \tag{3.22}$$

Although the calculation of the integral in the equation (3.22) is not presented in this work (it can be consulted in (Manwell, McGowan et al., 2010)), it is important to note two things:

- The power coefficient (C_P) depends on the tip speed ratio (λ);
- The maximum power that can be extracted from the wind tends to the *Betz Limit* (16/27).

Figure 3.30 illustrates the previous statements.

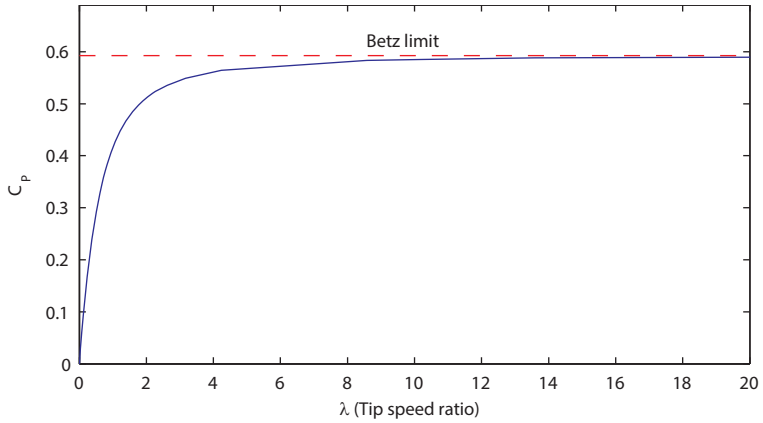

Figure 3.30 – Evolution of C_P with λ according to angular momentum theory

Considering the previous statements, it is possible to conclude that the evolution from rotors with fixed-speed to rotors with variable-speed was a major evolution step for the efficiency in energy harvesting. Whereas in a fixed-speed, the optimum tip-speed ratio is only achieved for a specific wind speed, with a variable-speed turbine, it is possible to have different optimum points of operation for each wind speed (Figure 3.31).

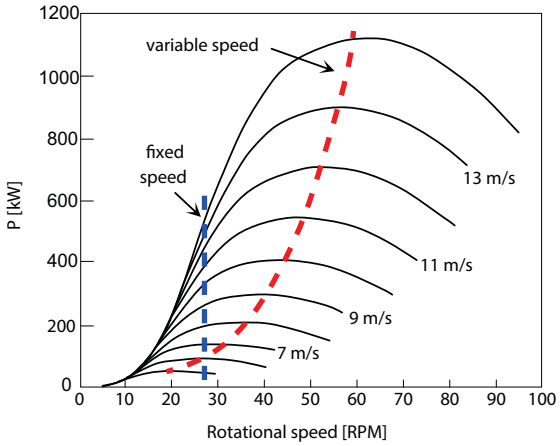

Figure 3.31 – Power output as function of rotational speed for a fixed- and variable-speed wind turbine for different wind speed classes (adapted from (Tempel, 2006))

Although the previous *momentum theories* already explain the power extraction from a wind flow, the problem is still not solvable yet due to unknown axial and angular induction factors (a and a'). For this reason, an additional approach to this problem is needed: the *blade element theory*.

3.2.4 Blade Element Theory

In this theory, the forces acting on the blades are expressed as a function of their shape and orientation. The following assumptions are adopted:

- Each blade is divided into n elements along its longitudinal axis;
- There is no radial flow (the aerodynamic interaction between elements is ignored);
- The forces acting on the blades are determined only according their airfoil characteristics: lift (C_L) and drag (C_D) coefficients;
- Three-dimensional effects are neglected.

Figure 3.32 presents a different perspective of the rotor annular ring of the Figure 3.29. It also presents a detailed illustration of a blade, with an arbitrary airfoil and the wind and rotor velocities associated with one element (grey area).

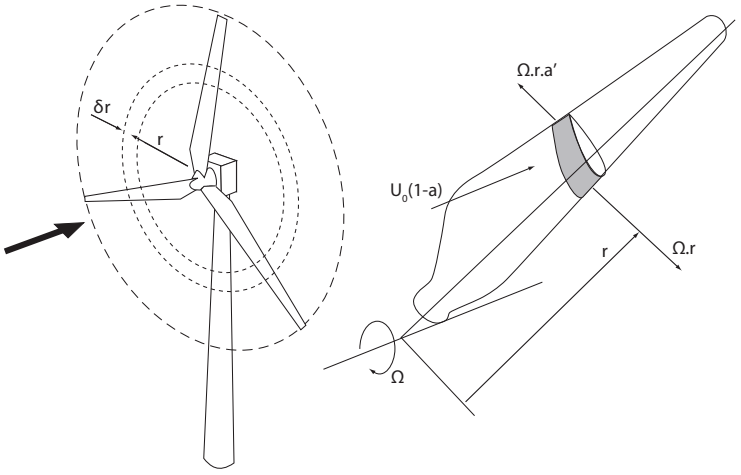

Figure 3.32 – Rotor annular ring and detail of a blade element (adapted from (Burton, Sharpe et al., 2001))

As previously introduced, a blade element with a radius r and a radial width dr is subjected to an axial wind speed of $U_0(1-a)$ and a rotational wind speed[2] of $\Omega.a'$ created by a rotor angular speed of Ω. Since tangential speeds are obtained from rotational speed multiplied by r, the resultant relative velocity between the blade element and the wind is:

$$U_{Rel} = \sqrt{[U_0(1-a)]^2 + [\Omega.r(1+a')]^2} \tag{3.23}$$

An illustration of the relative velocity, its components and the associated lift (F_L) and drag (F_D) forces is presented in Figure 3.33 (where the chord of the airfoil is represented by c, θ represents the pitch angle and ϕ represents the angle of inflow).

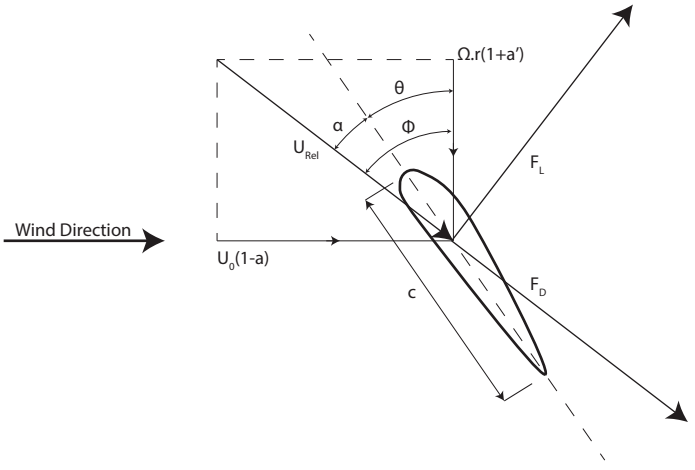

Figure 3.33 – Relative wind velocity applied to the airfoil and the subsequent lift and drag forces

[2] The rotational speed of the blade element is obtained assuming a linear increase from 0 (at the far ahead location) to 2. Ω. a' (in the far wake location).

Having in mind the relative velocity defined in equation (3.23), it is possible to define the drag and lift forces:

$$\mathrm{d}F_D = \frac{1}{2}.C_D(\alpha).\rho.U_{Rel}^2.c.\mathrm{d}r \tag{3.24}$$

$$\mathrm{d}F_L = \frac{1}{2}.C_L(\alpha).\rho.U_{Rel}^2.c.\mathrm{d}r \tag{3.25}$$

with:

F_D	Drag force
F_L	Lift force
α	Angle of attack

3.2.5 Blade Element Momentum

The *Blade Element Momentum* (BEM) is defined as a joining of the *momentum* and *blade element theories*, in order to solve the blade load problem.

Summarizing the results obtained with the previous deductions, one gets from the *axial momentum theory*:

$$\mathrm{d}F_A = 4.a(1-a)\rho.U_0^2.\pi.r.\mathrm{d}r, \quad \text{Considering: } \mathrm{d}A_{Annular\ ring} = 2.\pi.r.\mathrm{d}r \tag{3.26}$$

and from the *angular momentum theory*:

$$\mathrm{d}T = 4.a'.U_0(1-a).\rho.\Omega.r^3.\pi.\mathrm{d}r \tag{3.27}$$

Considering now the results presented for the blade element theory (equations (3.24) and (3.25)) and calculating their effects on the rotor, the following expressions for $\mathrm{d}F_A$ and dF_T are obtained:

$$\mathrm{d}F_A = N_B.\frac{1}{2}\rho.U_{Rel}^2[C_L cos(\phi) + C_D sin(\phi)]c.\mathrm{d}r \tag{3.28}$$

$$\mathrm{d}T = N_B.\frac{1}{2}\rho.U_{Rel}^2[C_L sin(\phi) - C_D cos(\phi)]c.r.\mathrm{d}r \tag{3.29}$$

with:

N_B	Number of blades

Taking into account the following relationships:

$$\sigma' = \frac{N_B . c}{2 . \pi . r} \tag{3.30}$$

$$U_{Rel} = \frac{U_0 (1 - a)}{sin(\phi)} \tag{3.31}$$

with:

σ'	Local solidity

it is possible to obtain expressions for the axial and angular induction factors, equating (3.11) with (3.28) and (3.18) with (3.29), respectively:

$$\frac{a}{(1 - a)} = \frac{\sigma' [C_L . cos(\phi) + C_D . sin(\phi)]}{4 . sin^2(\phi)} \tag{3.32}$$

$$\frac{a'}{(1 - a)} = \frac{\sigma' [C_L . sin(\phi) - C_D . cos(\phi)]}{4 . sin^2(\phi) . \lambda_r} \tag{3.33}$$

(According to some authors (Wilson and Lissaman, 1974), it is acceptable to set C_D as zero)

However, it is important to consider that this theory refers to an independence of each annular section of the blade to the adjacent ones. Although this does not correspond to reality, for normal operations tip speed ratios, the error is considered as acceptable. Beside this aspect, some corrections should be introduced to the BEM theory:

- According to equation (3.9), the axial induction factor has to be lower than 0.5, otherwise a reversal of the wake flow would be induced. Since this cannot occur, a different explanation is needed for this situation. In reality, for high values of λ (which lead to high values of a), the permeability of rotor is almost comparable to a disc. Some authors, such as Glauert (Glauert, 1926), proposed a correction for the axial induction factor curve (Figure 3.34);

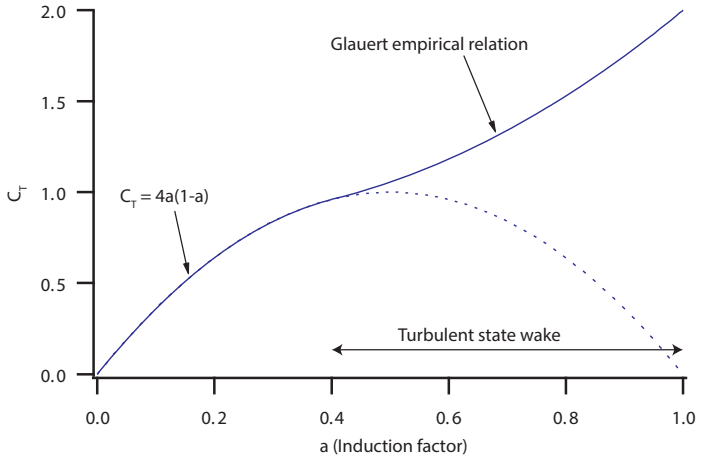

Figure 3.34 – Trend of thrust coefficients for high values of axial induction factor (adapted from (Manwell, McGowan et al., 2010))

- Another correction that should be taken into account is the loss of power production near the tip of the blades - called *tip-loss factor*. This is due to the discrete number and finite length of real blades, which is not accounted in the classical approach of the BEM theory. The most common approach to this problem is through the Prandtl's approximation.

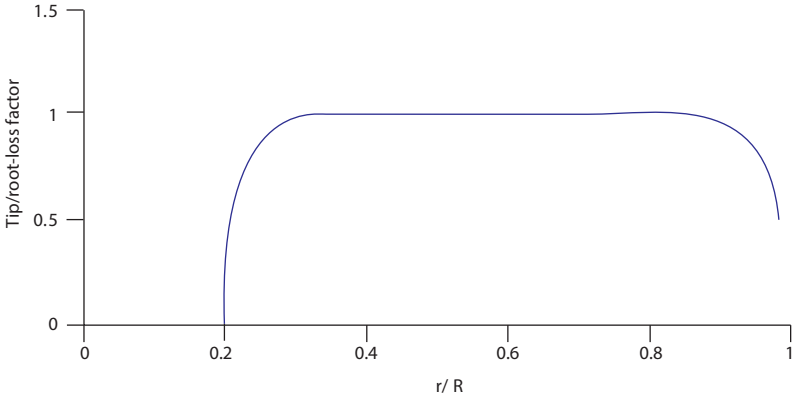

Figure 3.35 – Span-wise variation of combined tip/root-loss factor for a three-blade turbine optimized for a tip speed ratio of 6 and with a blade root at 20% span (Burton, Sharpe et al., 2001)

3.2.6 Control Strategies of Wind Turbines

At this point, the most important aspects of the theories explaining the performance of a wind turbine were introduced. Having those in mind, it is now possible to introduce some aspects related to control in the operation of the turbine. These control operations have an important influence in the dynamic behaviour of the overall structural system.

The performance of wind turbines requires some kind of control (passive or active) in order to adequately operate as expected. This is a crucial aspect mainly due to two reasons: to maximize the power production and to avoid excessive loads that could jeopardize the integrity of the structure.

In this subsection, three types of control will be briefly described: blades aerodynamic control (stall and pitch control) and rotor speed. The purpose of the description is to present the basic aspects related to control operations behind the different operating regimes of the wind turbines that will be later described in this work.

3.2.6.1 Stall Control

Stall control is a solution to control the aerodynamic loads acting on the rotor. This solution is based on the separation of the flow at the surface of the blades with increasing the wind speed for a constant tangential velocity of the rotor (without changing the blades pitch angle). This flow separation leads to a decrease of the lift force of the blade, limiting the aerodynamic power input.

Historically, stall control is a passive solution. As can be seen in Figure 3.36, with the increase of the wind speed, the angle of attack increases for a fixed blade pitch angle. The graph in the lower left corner of Figure 3.36 shows the evolution of the lift coefficient with the angle of attack for a common airfoil. With this graph, it is visible that the increase of the angle of attack beyond a certain limit leads to the creation of instability, dropping the lift force.

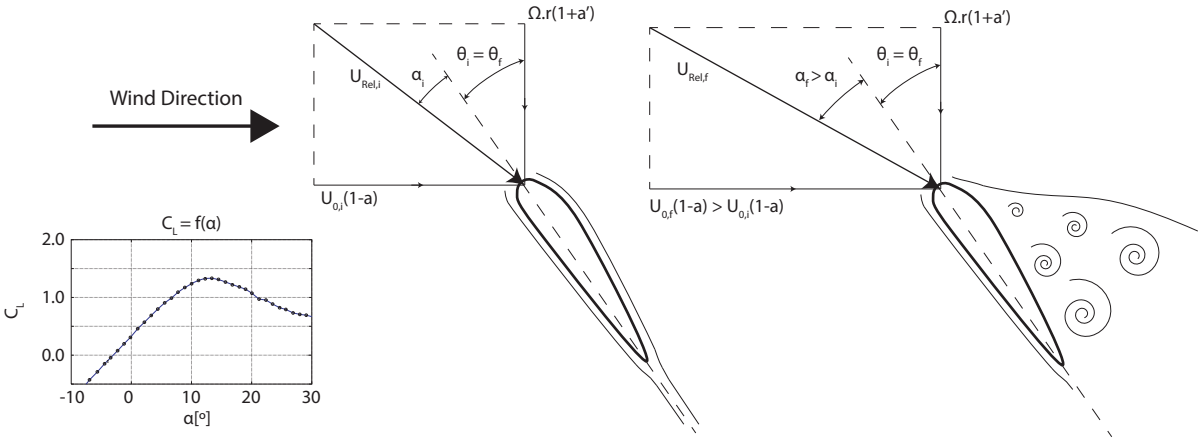

Figure 3.36 – Aerodynamic stall effect on a blade profile

Wind turbines with this design present a lower aerodynamic efficiency below rated regime than with a solution based on pitch control, since the rotor must operate closer to stall.

Although stall control seems to be a simple solution, it has some drawbacks, such as a less precise control of the power production and the inability to drop the thrust force of the rotor at high wind speeds (when compared to the pitch control solution) (Hau, 2006). For this reasons, the stall control is usually only used with turbines with a power output up to 1.5 MW.

With large wind turbines, the attempts to introduce this control technology have been made with a more complex construction, with the use of an active blade pitch angle adjustment. That is the case of the Izar Bonus 1.3MW/62 studied in Chapter 5.

3.2.6.2 Pitch Control

Pitch control of the blades is the nowadays standard solution in the wind industry. With this design, the blades are able to turn about their longitudinal axis with the help of actuators, allowing adjusting the angle of attack of the blade in order to regulate the rotor speed while keeping the load torque constant. Rotor blades are able to pitch until reach a feathered position (around 90º). This mechanism is illustrated in Figure 3.37.

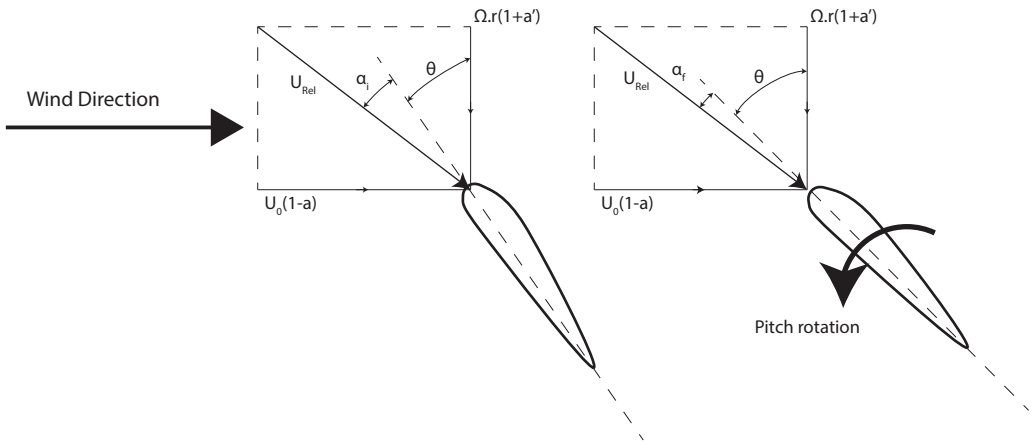

Figure 3.37 – Pitch control mechanism

Pitch control of the blades allows a better control of the rotor speed, resulting in a more constant power output. In Figure 3.38, the power curves of two wind turbines with stall and pitch control are shown. As can be seen, the last part of the curve (after the rated speed), is considerably more flat with pitch control. This is the solution implemented in both the Vestas V90-3.0 MW and Senvion MM82 studied in Chapters 5 and 7.

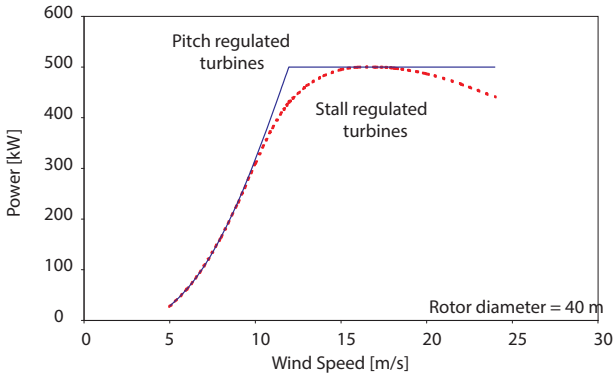

Figure 3.38 – Power curve of a 500 kW wind turbine with rotor regulation by active pitch and passive stall (adapted from (Burton, Sharpe et al., 2001))

3.2.6.3 Rotor Speed Control

In the case of variable-speed generators, it is possible to control, under a certain range, the speed of the rotor (or generator). As previously referred, this is an important advantage since the optimum production efficiency is achieved at the optimum tip speed ratio. Thus, a (theoretically) continuous adjustment of the rotor speed would be required to keep up with the variation of the wind speed (according to equation (3.20)). According to equations (3.10) and (3.20), the power output can be defined by:

$$P = \frac{1}{2}.\rho.\pi.R^5.\frac{C_P}{\lambda^3}.\Omega^3 \tag{3.34}$$

The maximum aerodynamic power is defined by introducing the optimum tip speed ratio (λ_{opt}) and the maximum power coefficient ($C_{P(max)}$) in equation (3.34), while the rotor speed is optimum (Ω_{opt}). Equation (3.34) can then be rewritten as:

$$P = K.\Omega^3 \tag{3.35}$$

where

$$K = \frac{1}{2}.\rho.\pi.R^5.\frac{C_P}{\lambda^3} \tag{3.36}$$

Equation (3.35) shows that the maximum aerodynamic efficiency is proportional to the cubic of the rotor speed. In the same sense, the torque is defined as proportional to the square of the rotor speed:

$$T = K.\Omega^2 \tag{3.37}$$

Considering these equations, it is concluded that, under steady state conditions (and assuming that the variables from equation (3.36) are at their optimum values), the maximum efficiency can be achieved by varying the rotor torque according to the squared value of the rotor speed. This is the control strategy for maximum efficiency. However, some restraints prevent the operation of the turbines following this strategy over the whole operating regimes.

Figure 3.39 illustrates the relationship between the torque and speed of the generator from a variable-speed wind turbine with pitch control. For this turbine, the referred strategy is followed between the operating points B and C. In this operating regime, the generator torque is proportional to the square of the generator speed, in order to be in line with the optimum power coefficient (red line in Figure 3.39). This means that, (theoretically) optimal power extraction occurs within this operating zone.

Due to aerodynamic noise, loads and other design constraints, it is not possible to follow the optimum C_P curve for all wind speed regimes, being the maximum allowable rotor speed achieved at a relatively low wind speed (Burton, Sharpe et al., 2001). For that reason, when reaching the operating point C, a different control strategy is followed. At this point, the increase of power production (with the increase of wind speed) is obtained by increasing the torque, while the rotor speed is kept at its rated value (line CE). When the rated generator rotor torque value is achieved, the power production is maintained at the same level by adjusting the pitch angle of the blades, which allows controlling the input torque generated by higher wind speeds (point E).

It should be noted that the described chain of operating regimes are referred to a situation in which no limitations are present for control. In reality, some constraints are present in the definition of the control algorithms, leading to the need of transitional regimes. Thus, the dashed line A'B'C'D'E' defines a chain of operating conditions more in line with the operation of wind turbines in real conditions.

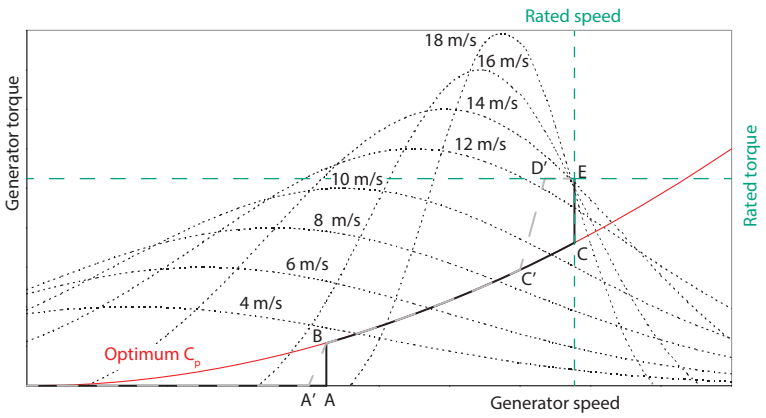

Figure 3.39 – Illustration of the torque-speed curve for a variable-speed wind turbine with pitch control (adapted from (Burton, Sharpe et al., 2001))

3.3 FINAL CONSIDERATIONS

This chapter starts with the description of the main structural elements of wind turbines. A special focus is given to the support structure (tower and foundation – in onshore models; tower, transition piece and foundation – in offshore models). This element conditions, in a large extent, the modal properties and, consequently, the dynamic behaviour of wind turbines.

The chapter continues with a depiction of the main costs related to a wind farm project for onshore and jacket-based offshore models. A high relative cost is found for the support structure and blades. Specially in the case of offshore installations, the foundation represents an important share of the overall cost.

Also the reliability of the various elements of wind turbines is analysed. It is seen that accumulated experience demonstrated that the support structure in onshore wind turbines is not a commonly problematic element. However, the increase of the wind turbine dimensions, together with the installation of turbines in offshore harsh environments, is expected to introduce new problems. The evaluation of the reliability of the wind turbine components is a key aspect on the definition of the maintenance procedures, including new strategies based on data collected by installed monitoring systems.

Lastly, a brief description of the wind turbine performance based on the axial momentum and blade element theories is introduced. This theoretical background represents a helpful insight for the comprehension and definition of the various operational conditions of a wind turbine. The variation of the conditions requires the definition of control strategies for the proper operation of the turbine. In that sense, simplified aerodynamic and rotor torque control strategies are included in this chapter. As will be seen in the following chapters, the variations imposed by the various regimes of operation of a wind turbine influence its modal properties.

4
STRUCTURAL BEHAVIOUR OF WIND TURBINES

4.1 Structural Dynamics

Wind turbine structures are highly dynamic systems. As illustrated in Figure 4.1, the normal operation of a wind turbine is a process in which different types of dynamic excitation take place. However, two main sources of excitation are evident: environmental conditions (wind loading and offshore conditions, if applicable) and the rotating machinery during operation, mainly the rotor.

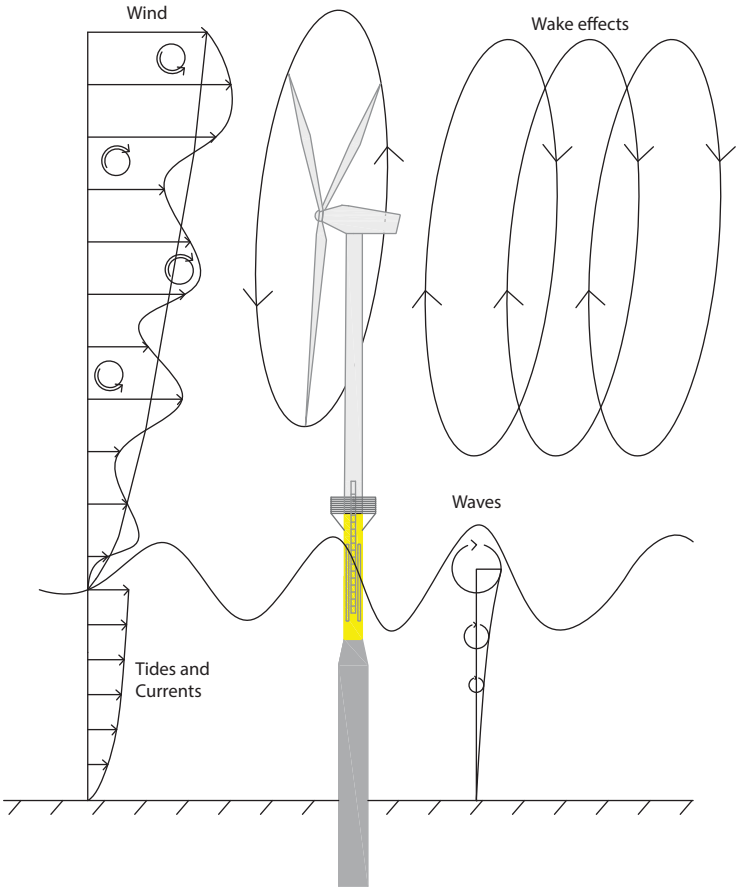

Figure 4.1 – Sources of dynamic excitations of an offshore wind turbine (for onshore turbines, tides, currents and waves are, obviously, not applicable)

Thus, an accurate description of the dynamic behaviour is extremely important in this context, otherwise resonance phenomena are very likely to occur due to several sources.

A complete wind turbine structure can be idealized as an assembly of coupled multi degree-of-freedom mass-spring-damper systems. With this in mind, the structure is defined according to its mass, damping and stiffness properties (Clough and Penzien, 1995):

$$M.\ddot{Y} + C_1.\dot{Y} + K.Y = F(t) \tag{4.1}$$

with:

M	Mass matrix
C_1	Damping matrix
K	Stiffness matrix
Y	Displacement vector
$F(t)$	Excitation force

Although the complete characterization of a wind turbine might be complex, simplifications for some components can be made for initial considerations. Within the scope of this thesis, the most important aspects related with the dynamic characterization of the tower, blades and the tower-blades coupling are presented.

4.1.1 Dynamic Characterization of the Tower

The tower structure of a wind turbine is a component for which a rigorous dynamic characterization is essential. However, simple geometric sections are usually used (namely, tubular sections) and a sufficiently accurate characterization of the material is also often achievable with simple methods (mainly for steel structures). Furthermore, the rotation of the rotor introduces small influence on the first natural frequency of the tower, which enables its calculation with the rotor at stand-still position with sufficient rigorous results. Taking this into account, a simple cantilevered column with distributed mass and a concentrated mass at the top (Figure 4.2) can be used for initial assessment of the natural frequency of the first tower bending mode.

Figure 4.2 – Simplified structure for calculation of the natural frequency of the tower bending mode

With this configuration, approximate values of the tower first natural frequency can be obtained through:

$$f_1 = \frac{c_{f,1}}{2.\pi}\sqrt{\frac{E_{Tower}.I_{Tower}}{m_{Top}.L_{Tower}^3 + c_{f,2}.m_{Tower}.L_{Tower}^4}} \tag{4.2}$$

with:

f_1	Tower first natural frequency
$c_{f,1}$	Constant value: 1.732 (Young and Buynas, 2002) or 1.7436 (Vugts, 2000), depending on literature sources
$c_{f,2}$	Constant value: 0.236 (Young and Buynas, 2002) or 0.227 (Vugts, 2000), depending on literature sources
E_{Tower}	Tower elastic modulus
I_{Tower}	Tower section inertia
m_{Top}	Tower top mass (including nacelle, all the equipment in it and the rotor)
m_{Tower}	Tower mass per unit length
L_{Tower}	Tower height

Figure 4.3 presents an illustration with the mode shape configuration of the first vibration mode for the fore-aft (1 FA) and side-side (1 SS) directions.

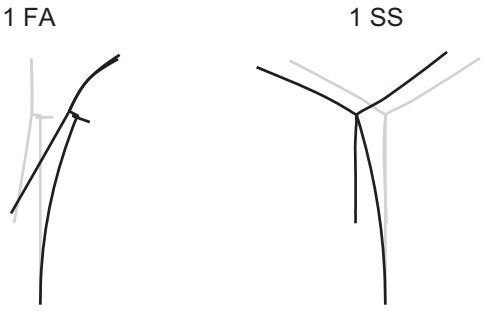

Figure 4.3 – First tower vibration mode for fore-aft and side-side directions: undeformed (grey) and deformed (black) structure (adapted from (Skjoldan, 2011))

4.1.2 Dynamic Characterization of the Rotor

The definition of the dynamic properties of the rotor blades presents a more complex nature than for the tower structure. Besides the material composition and geometry of the blades, it is important to realize that the dynamic behaviour of the rotor acts as a whole, which means that the stiffness of the shaft supporting bearings has a direct influence on the vibration modes. It is also important to understand that, when the wind turbine is operating (and the rotor is spinning), two particular effects take place which affect the dynamic behaviour of the structural system: gyroscopic and centrifugal stiffening effects.

The rotor modes of wind turbines can be divided into two groups: flapwise and edgewise (see Figure 3.2). For each order of these modes, three "sub-modes" need to be considered, namely, one symmetric and two asymmetric modes in each direction. These modes are presented in Figure 4.4. The symmetric mode is characterized by the deflection of the three blades in the same direction:

- Flapwise modes: the blades deflect in the rotor out-of-plane direction (1 FS);
- Edgewise modes: the blades deflect in the rotor plane direction (1 ES).

On the other hand, the two asymmetric modes are defined accordingly to the direction of the motion of the blades:

- Flapwise modes: tilt (1 FT) and yaw mode (1 FY);
- Edgewise modes: horizontal (1 EH) and vertical mode (1 EV).

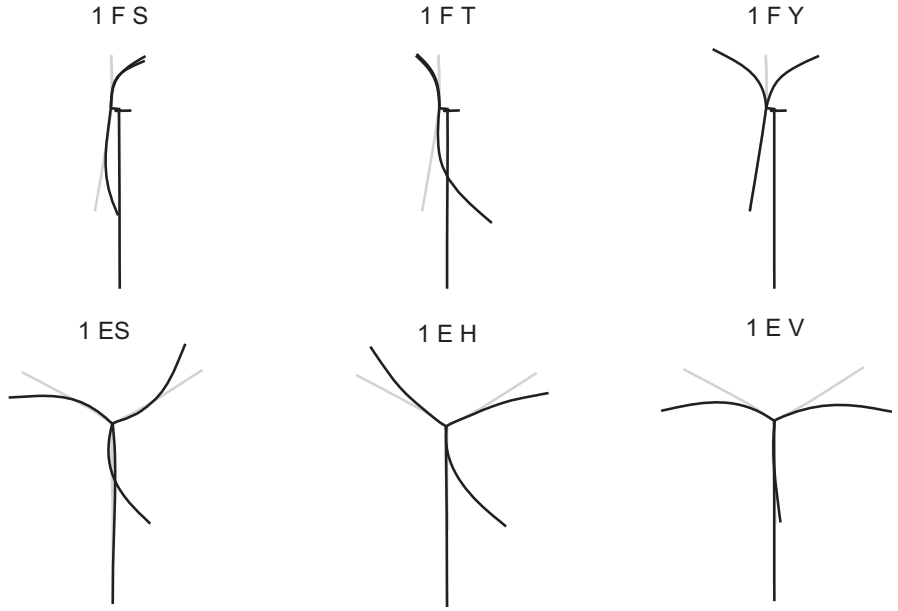

Figure 4.4 – First order rotor modes (for low values of pitch angle): undeformed (grey) and deformed (black) structure (adapted from (Skjoldan, 2011))

These asymmetric modes are associated with translation and rotation of the rotor. This is the reason why the stiffness of the supporting elements of the rotor has an important role in these modes.

When the wind turbine is under operation and the rotor is spinning, two particular effects need to be accounted for: gyroscope effects and centrifugal stiffening. These effects should be considered in the equation of motion (equation (4.1)) of the rotor as:

$$M.\ddot{X} + (C_1 + G)\dot{X} + +(K + K_C)X = F(t) \tag{4.3}$$

with:

G	Gyroscopic matrix
K_C	Geometric stiffness matrix

Gyroscope Effect

The rotation of the rotor introduces a well-known characteristic in the context of rotor dynamics: the gyroscopic effect. This effect is due to the flexibility of supporting bearings of the rotor which leads to deviation of the rotating axis from the bearing centre line (Yoon, Lin et al., 2013). Essentially, when the rotor is rotating at the shaft axis, the motion in the two orthogonal axes is coupled. This is evident by the skew-symmetric nature of the gyroscopic matrix (Ewins, 2000; Yoon, Lin et al., 2013). Thus, under rotation, the rotor suffers two rotational movements: the rotation of the shaft itself; and a whirl rotation due to gyroscopic effects. There are two types of whirl rotation, namely, forward (when the rotation is in the same direction of the shaft) and backward (when the rotation is in the opposite direction). Figure 4.5 illustrates these two phenomena for two different situations: one where the rotor/ stator system is symmetric and another where the system is non-symmetric.

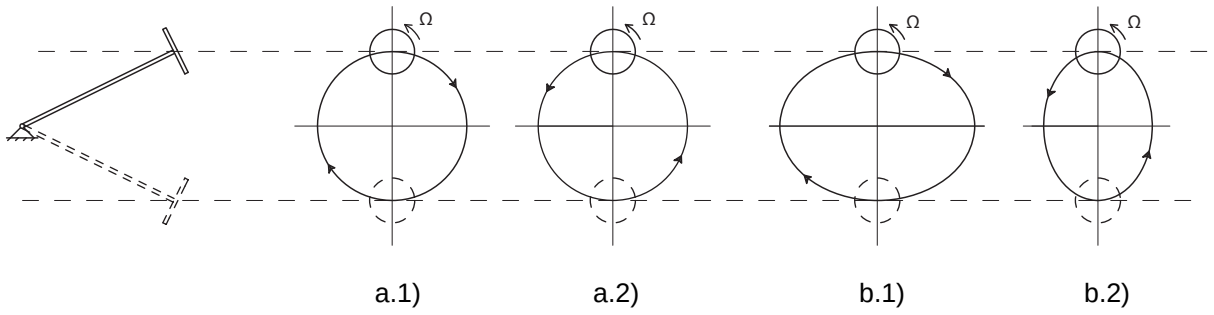

Figure 4.5 – Motion of the rotor system (for a fixed reference) including the gyroscopic effect (the smaller trajectory represents the rotation of the shaft around itself, while the larger path indicates the whirl motion): a) represents a symmetric rotor system; b) represents a non-symmetric system; .1 represents the backward whirl mode; .2 represents the forward whirl movement (adapted from (Ewins, 2000))

The dynamic behaviour of wind turbine rotors is similar to what was described above. With the rotation of the rotor, the two asymmetric modes couple (the tilt with the yaw flapwise mode; and the horizontal with the vertical edgewise mode), resulting in the development of the whirl modes. The frequency of these whirl modes (backward – BW - and forward - FW) drift, from a fixed-frame reference, due to the rotor rotation. This situation is illustrated in Figure 4.6. As exposed in Figure 4.5, the forward and backward definition of the whirl modes refers to the rotation of the rotor centre of mass in the same or against the rotor direction, respectively (Skjoldan, 2011).

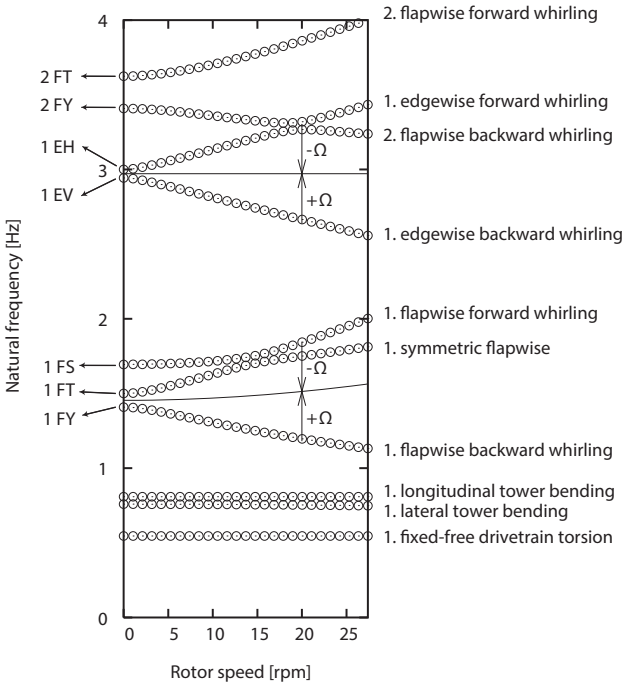

Figure 4.6 – Campbell diagram of fixed-frame natural frequencies (O) for the first 10 structural modes of a 600 kW three-bladed wind turbine. Lines denote the centre frequencies of the rotor whirling modes given $\pm\Omega$ added to the fixed-frame natural frequencies (adapted from (Hansen, 2007))

Figure 4.6 illustrates some important phenomena that should be considered when studying the dynamic behaviour of wind turbine rotors.

When the rotor is stopped, modes 4 and 5 (first flapwise yaw and flapwise tilt modes) are very close. The difference between them is due to different elastic supports in the corresponding directions. Usually, the yaw mode is lower than the tilt mode because towers are stiffer in tilt than in yaw direction (Hansen, 2003). The 6th mode, the flapwise symmetric mode, is slightly higher than the asymmetric ones. This is justified by the fact that this mode, in which all the blades vibrate simultaneous in-phase, beholds also some fore-aft motion of the tower in out-of-phase (Hansen, 2003). When the rotor starts to operate, a change in the frequency value of the modes is evident. As highlighted in Figure 4.6, the pair of asymmetric modes starts to couple and became pairs of whirling modes. Thus, FW and BW modes start to drift, increasing and decreasing their frequency values, respectively, in an amount equal to the rotor speed ($\pm\Omega$). This splitting phenomenon, identified considering a fixed reference of observation, is due to the gyroscopic effect.

Modes 7 and 8 have a similar behaviour as the described for the 4th and 5th mode. These frequencies are also slightly different when the rotor is stopped due to different flexibilities of the rotor supports. When the rotor starts to spin, a similar splitting effect is noticeable.

In the last two modes (2 flapwise FW and BW modes), the difference at parked situation of these two frequencies indicates an even greater difference in the requested flexibility of the support in both directions. Although the behaviour of these two modes is very similar to modes 4 and 5, it is important to refer that it is less pronounced due to the lower contribution of the gyroscopic reaction forces (Hansen, 2007).

The evolution of the frequencies with the rotor speed usually leads to situations where two different modes stay very close to each other. In the presented situation, the 1st flapwise FW with the 1st symmetric mode and the 1st edgewise FW with the 2nd flapwise BW feature very close frequencies. In these situations, the vibrations modes interact with each other, presenting a mode shape with a mixed configuration.

One last aspect should also be mentioned. If Figure 4.6 is observed carefully, it is possible to verify that the frequency of the 1 FS mode, which does not contain any gyroscopic effect, also increases with the rotor speed. This situation is also noticeable for the centre lines of the whirl modes (solid line) which imply that another effect is present that increases the value of the frequencies too. This phenomenon is called centrifugal stiffening.

Centrifugal Stiffening Effect

As introduced in the previous section, the centrifugal stiffening effect is responsible for the increase of the rotor modes frequencies with the rotor speed. As referred, this effect is very pronounced in the flapwise modes, being the responsible by the curved path of these frequencies in the Campbell diagram (Figure 4.6).

This effect is justified by an increase in stiffness due to centrifugal forces acting on the rotating blades. This centrifugal stiffening is then defined by the additional tensile forces installed on the blades for a r position along the blade (Naguleswaran, 1994):

$$F_C(r) = \int_r^{L_{Blade}} \rho_{Blade} . A_{Blade} . \Omega^2 (R_{Hub} + r)\, \mathrm{d}r \tag{4.4}$$

with:

F_c	Centrifugal force
ρ_{Blade}	Density of the blade
A_{Blade}	Cross section area of the blade
Ω	Rotational frequency of the rotor
L_{Blade}	Blade length
R_{Hub}	Rotor hub radius
r	Position of the blade under consideration

Alongside with the tensile force presented in the blade due to the centrifugal forces, the influence of the gravity (self-weight) can also be introduced. This effect, which is reflected by an axial force acting on the blade, depends on the position of the blade (Murtagh, Basu et al., 2005). Thus, the effect of the self-weight of the blade should be added or subtracted to its stiffness, either it is a tensile or a compressive force, respectively. However, it is referenced that this gravity effect is negligible when compared to the effect of the centrifugal stiffening (Arrigan, Pakrashi et al., 2011).

Several authors, among which (Naguleswaran, 1994) and (Yoo and Shin, 1998), studied the problem of determination of natural frequencies of simple beams rotating on a hub taking into account the centrifugal stiffening. However these studies focused on simple beams, with constant parameters along the length of the beams, which diverge substantially from a common wind turbine blade. More complex studies were developed for the specific case of the blades, e.g (Hansen, 2003), however they are outside the scope of this work. Nevertheless, a rough estimation of the increase of the natural frequency of a blade due to centrifugal stiffening is presented (Putter and Manor, 1978):

$$\omega_{Blade,R}^2 = \omega_{Blade}^2 + c_{Shoutwell} . \Omega^2 \tag{4.5}$$

with:

$\omega_{Blade,R}$	Angular frequency of a rotating blade
ω_{Blade}	Angular frequency of a blade at stand-still position
$c_{Shoutwell}$	Southwell coefficient: 1.73 (Madsen, Frandsen et al., 1984)

Although this effect is important and should be considered when studying the dynamic behaviour of the rotor vibration modes, it is not very noticeable in edgewise modes. This is justified by the softening effect that is also introduced by the centrifugal forces on the linear stiffness of deflection in the rotor plane that almost cancels the stiffening effect (Hansen, 2007).

4.2 FOUNDATION SOIL STIFFNESS

The consideration of the soil stiffness is an important aspect when trying to accurately simulate the behaviour of tall, slender structures. Thus, wind turbines are no exception. As an example, the guidelines of the Danish standard (Det Norske Veritas (DNV), 2002) refer a reduction between 0 % and 5 % up to a maximum of 20 %, when comparing a model with fixed boundary conditions and another with the consideration of the soil stiffness. A larger variation is presented by Hau (Hau, 2006) for an onshore wind turbine with a slab foundation (Figure 4.7).

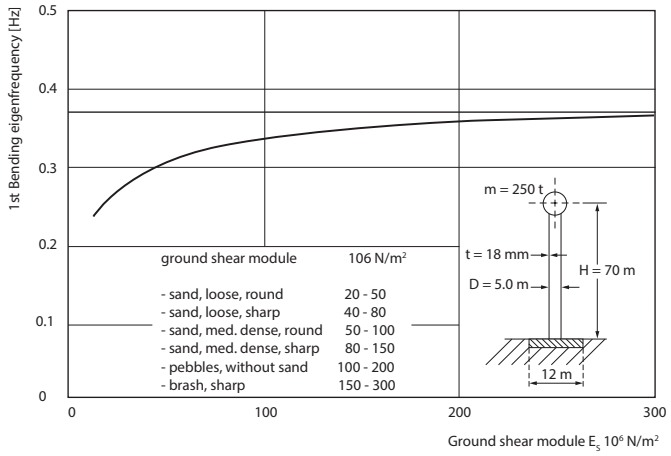

Figure 4.7 – Influence of the soil stiffness on the first natural bending frequency of a wind turbine tower (Hau, 2006)

For the modelling of the soil stiffness, the recommendations defined in the DNV guidelines (Det Norske Veritas (DNV), 2002) are then presented. In order to introduce the effect of the soil, four foundation springs must be included:

- Vertical spring stiffness - K_V;
- Horizontal spring stiffness - K_H;
- Rotational (rocking) spring stiffness - K_R;
- Torsional spring stiffness - K_T.

It is important to note that soil behaves in a non-linear manner. But instead of using non-linear springs, it is common to model the springs according to the strain level of the soil and then using springs with linear behaviour. DNV (Det Norske Veritas (DNV), 2002) suggests three different levels of dynamic loading (and corresponding shear strains γ):

- From earthquakes: large shear strains up to 10^{-2} to 10^{-1};
- From wind and ocean waves: moderate shear strains up to 10^{-2}, typically 10^{-3};
- From rotating machines: small shear strains, usually less than 10^{-5}.

After deciding which load case is of interest, it is necessary to compute the shear modulus G of the soil. This is usually accomplished through the use of the plot presented in Figure 4.8 together with the initial shear modulus G_0. The value of G_0 can be obtained according to the empirical expression:

$$G_0 = A\frac{(3-e)^2}{1+e}\sqrt{\sigma_0'}(OCR)^k \tag{4.6}$$

with:

G_0	Initial shear modulus (in kPa)
A	Coefficient depending on material (size, angularity of grains, …) - $A \approx 3000 \pm 1000$
e	Void ratio
σ_0'	Effective stress (in kPa)
OCR	Over consolidated ratio for clay soil (equal to 1.0 for sand)
k	Coefficient depending on the plasticity index I_p (according to Table 4.1)

Once the shear modulus of the soil is obtained, the Young modulus of soil is calculated according to:

$$E = 2.G(1+\upsilon) \tag{4.7}$$

with:

E	Young modulus
υ	Poisson's ration (according to Table 4.3)

Table 4.1 – Coefficient k

Plasticity Index (I_p)	k
0	0
20	0.18
40	0.30
60	0.41
80	0.48
> 100	0.50

Table 4.2 – Coefficient K

Type of soil	K
Loose sand	8
Dense sand	12
Very dense sand	16
Very dense sand and gravel	30 - 40

Table 4.3 – Poisson ratio

Type of soil	ν
Dense sands	0.25 – 0.30
Loose sands, stiff clays	0.35 – 0.45
Saturated clays	≃ 0.50

Two simpler alternative expressions for the determination of G_0 can be used for sand:

$$G_0 = 1000.K.\sqrt{\sigma_0'} \tag{4.8}$$

with:

K	Coefficient depending in the type of soil (according to Table 4.2)

and for clay:

$$G_0 = 2600.s_u \tag{4.9}$$

with:

s_u	Undrained shear strength

After computing the value of the initial shear modulus, the value of shear modulus (G) and damping (ξ) of the soil can be obtained with the help of Figure 4.8. Once these values are calculated, the stiffness of the foundation springs for circular slab footing are given by the equations presented in Table 4.4.

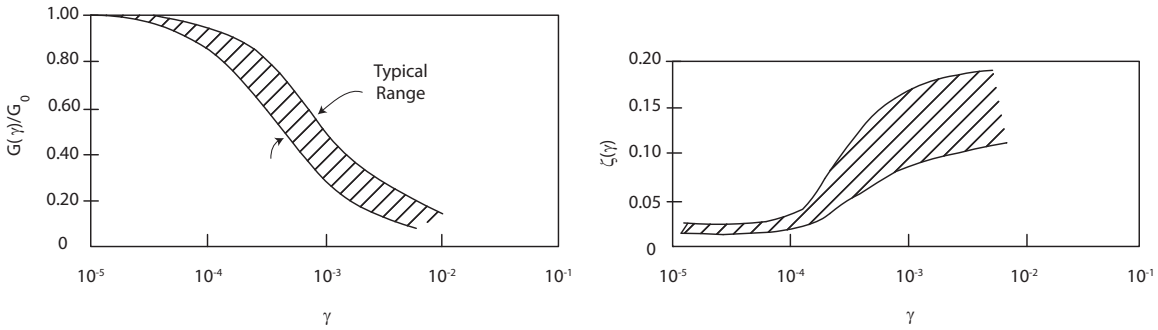

Figure 4.8 – Shear modulus and damping ratio according to strain level (adapted from (Det Norske Veritas (DNV), 2002))

It is important to refer that the values obtained from these tables are related to static stiffness (for excitation frequencies approaching zero). This assumption is correct for majority of the dynamic loading acting on wind turbines, although may introduce some errors for high frequency excitations.

After the foundation stiffness is calculated, springs should be introduced in the wind turbine model according to Figure 4.9 in order to more accurately reproduce the boundary conditions between structure and soil.

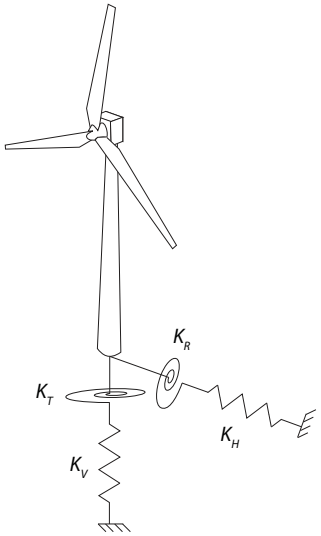

Figure 4.9 – Illustration of the foundation springs

Table 4.4 – Stiffness of foundation springs for circular footing on different substratum conditions (adapted from (Det Norske Veritas (DNV), 2002))

Foundation spring	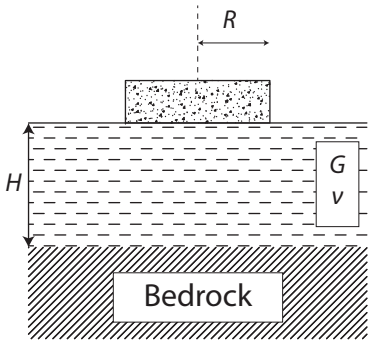	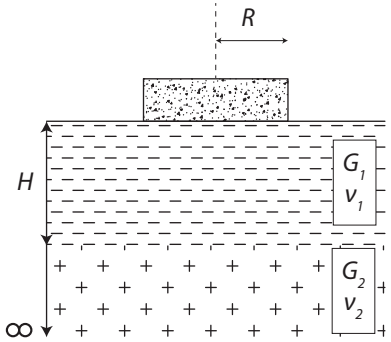 $0 \le G_1/G_2 \le 1$		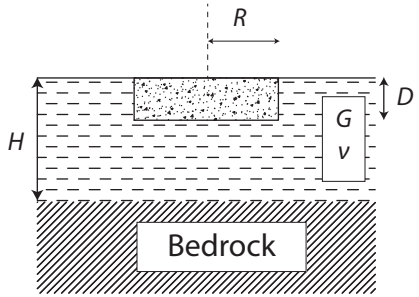 $D/R < 2$ $D/H < 1/2$
Vertical	$K_V = \frac{4.G.R}{1-\nu}\left(1 + 1.28\frac{R}{H}\right)$	$K_V = \frac{4.G_1.R}{1-\nu_1}.\frac{1+1.28.\frac{R}{H}}{1+1.28.\frac{R}{H}.\frac{G_1}{G_2}}$	$; 1 \le H/R \le 5$	$K_V = \frac{4.G.R}{1-\nu}\left(1 + 1.28.\frac{R}{H}\right)\left(1 + \frac{D}{2.R}\right)\left[1 + \left(0.85 - 0.28.\frac{D}{R}\right)\frac{D/H}{1-D/H}\right]$
Horizontal	$K_H = \frac{4.G.R}{1-\nu}\left(1 + 1.28\frac{R}{H}\right)$	$K_H = \frac{8.G_1.R}{1-\nu_1}.\frac{1+\frac{R}{2.H}}{1+\frac{R}{2.H}.\frac{G_1}{G_2}}$	$; 1 \le H/R \le 4$	$K_H = \frac{8.G.R}{1-\nu}\left(1 + \frac{R}{2.H}\right)\left(1 + \frac{2.D}{3.R}\right)\left(1 + \frac{5.D}{4.H}\right)$
Rotation	$K_R = \frac{8.G.R^3}{3(1-\nu)}\left(1 + \frac{R}{6.H}\right)$	$K_R = \frac{8.G_1.R^3}{3(1-\nu_1)}.\frac{1+\frac{R}{6.H}}{1+\frac{R}{6.H}.\frac{G_1}{G_2}}$	$;0.75 \le H/R \le 2$	$K_R = \frac{8.G.R^3}{3(1-\nu)}\left(1 + \frac{R}{6.H}\right)\left(1 + 2.\frac{D}{R}\right)\left(1 + 0.7.\frac{D}{H}\right)$
Torsion	$K_T = \frac{16.G.R^3}{3}$	-		$K_T = \frac{16.G.R^3}{3}\left(1 + \frac{8.D}{3.R}\right)$

4.3 TOWER-ROTOR DYNAMIC COUPLING

The previous characterization of the tower and rotor components (see sections 4.1.1 and 4.1.2) permits to analyse possible situations of dynamic coupling between these components. This analysis is of high importance since towers are becoming increasingly flexible.

Under operation, blades suffer with the action of the wind, besides cyclic gravitational forces. The resultant forces of the blades are then transmitted to the tower. However, when the forces "reach" the tower, they were already "filtered". In other words, considering only the wind loading, the spectral content of the wind changes when passing through the rotor. It is changed, in a larger extent, by the rotation of the blades, and, in a smaller fraction, by the dynamic properties of the blades.

In a situation of a rotor diameter sufficiently larger than the gusts size, the distribution of the wind energy spectrum when experienced by a rotating blade can differ significantly from the spectrum of the same wind observed by a fixed object (Connel, 1980). This alteration is reflected on a shifting of energy from lower frequencies to higher frequencies of the spectrum, with peaks located at integer multiples of the rotational frequency of the rotor (Figure 4.10) (Murtagh, Basu et al., 2005). This situation is explained by the fact that when the blades are spinning, they pass through a gust once per rotor revolution (if the gust is large enough) and, consequently, suffer a load peak with a frequency value of Ω. For the support structure (like the tower), the excitation will thus be $N_B.\Omega$ (3Ω for the common three-bladed wind turbine) since, within the period of 1/Ω, the same gust will be transversed N_B times.

This "changed" wind turbulence spectrum will act on the rotor blades and, subsequently, will be detected on the response of the tower (see section 4.6).

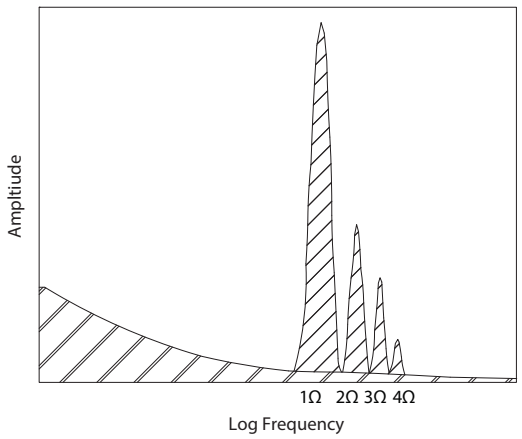

Figure 4.10 – Illustration of the spectral energy distribution for rotationally sampled spectrum. The peaks refer to integers of the rotor frequency of rotation (adapted from (Murtagh, Basu et al., 2005))

4.4 DEFINITION OF TOWER STIFFNESS

In Chapter 2, during the introduction about the historic developments of the wind turbine technology, reference was made about the different design concepts of the tower. In fact, the tower stiffness is a major consideration in the overall design of a wind turbine. In a wind turbine system, it is imperative to avoid a match of the natural frequency of the tower with the frequency of rotor rotation in order to prevent resonant problems. Thus, it would be desirable to have very stiff towers. In this situation, resonant situations would be avoided, since the frequency of rotation of the rotor (and its harmonics) would be considerable lower than the tower natural frequency. This was the strategy followed in the MOD-0 and WTS-75 models in the past (Hau, 2006). However, the increase of the size of the rotors and the need to reduce costs led to the need of reduction of the tower weight. Thus, a progressive increase in the tower flexibility led to the usually defined "soft-soft" towers. These soft-soft towers are characterized by a natural frequency lower than the rotor rotational frequency. This was the design strategy followed for the MOD-2 and WTS wind turbines. There is also an intermediate solution (named as "soft-stiff"), where the tower natural frequency is tuned in order to be placed between the rotational frequency (1Ω) and its first integer multiple (2Ω or 3Ω, for, respectively, two- or three-bladed wind turbines). In Figure 4.11 a simple scheme is presented with these three configurations.

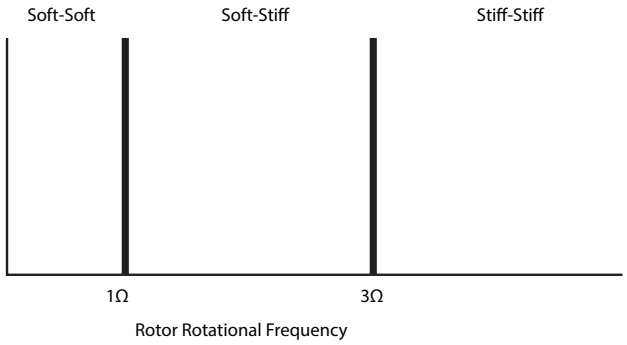

Figure 4.11 – Frequency intervals for tower stiffness for a fixed rotational speed wind turbine

Figure 4.11 refers to a situation of a fixed-speed wind turbine. For these cases, since there is only one operational rotational speed, the range of possible values for the tower natural frequency is wider. However, in the case of variable-speed wind turbines, further considerations had to be taken into account. In these situations, the range for the tower natural frequency becomes much narrower. With the purpose of a clearer explanation, a Campbell diagram of a 1.5 MW three-bladed variable-speed wind turbine is presented in Figure 4.12. In it, the natural frequencies of several components of the wind turbine are plotted against the rotational speed. The range of operation of the rotor is also shown. As can be seen, the first natural frequency of the tower remains above the rotational speed (1Ω) and below the integer multiple 3Ω. Thus, this is considered a soft-stiff tower.

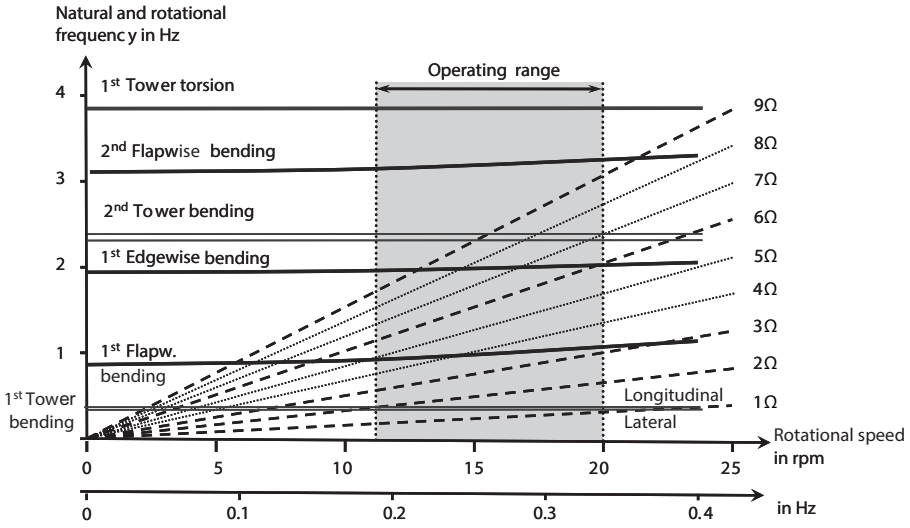

Figure 4.12 – Campbell diagram of a 1.5 MW three-bladed rotor, variable-speed wind turbine (adapted from (Gasch and Twele, 2012))

4.5 DAMPING

In the dynamic characterization of the wind turbine system, other important parameters that need to be determined, besides the value of the natural frequencies, are the damping coefficients. With the aim of illustrate the importance of these parameters on the supporting structure, a simple single degree of freedom (SDOF) structure, defined by its mass M, stiffness K and damping C_1, is presented in Figure 4.13 a). Its dynamic amplification factor (DAF – which represents the magnification the structure response suffers with the application of a dynamic load relative to the response to a static force) is defined by (Clough and Penzien, 1995):

$$DAF = \frac{1}{\sqrt{\left[1-\left(\frac{f_{Load}}{f}\right)^2\right]^2 + \left(2.\zeta.\frac{f_{Load}}{f}\right)^2}} \tag{4.10}$$

with:

f_{Load}	Applied load frequency
f	Natural frequency of the structure
ξ	Damping ratio of the structure

In Figure 4.13 b), the DAF for a simple SDOF structure was calculated for two different values of damping ratios. As can be observed, the DAF value is highly dependent on the damping value. The value of the structural response in resonance is considerably higher for a structure with a damping ratio of 0.2 % (a common value for a wind turbine in an idling or parked situation) than for a structure with ξ = 4 % (a conservative value for a wind turbine under production). For this reason, it is easy to understand that, for structures subjected to dynamic excitations (such as wind turbines), their damping value is a key-factor to handle with the problem of fatigue.

The damping of a wind turbine can be considered as linear sum of different damping sources: structural, aerodynamic, from devices, soil and hydrodynamic. From their nature, the last two are only referred to offshore wind turbines.

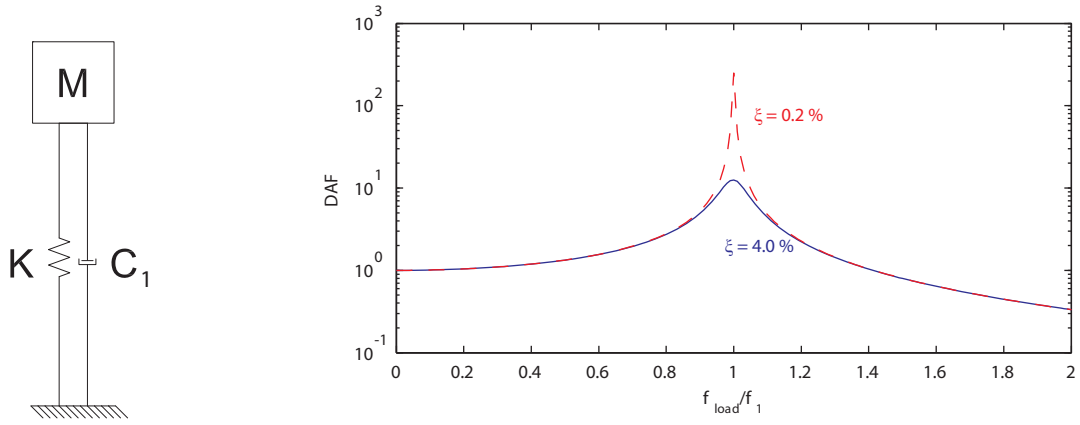

a) b)

Figure 4.13 – a) SDOF structure. b) DAF values for different damping ratios

4.5.1 Structural Damping

Structural damping is referred to the portion of damping that is intrinsic to the structure. It is due to the absorption of vibrations by internal friction and conversion into heat.

Structural damping depends on the type of material (e.g. concrete or steel) and on the type of contacting surfaces (e.g. types of connections in the structure). Also, offshore wind turbines usually present a higher damping value than onshore models, mainly due to the grouted connection (Tarp-Johansen, Andersen et al., 2009) or higher complexity of the foundation. Thus, different tower concepts and connections lead to different damping values.

Typical values of structural damping ratios are in the order of 0.2 % to 0.8 % (Det Norske Veritas (DNV), 2002; Tarp-Johansen, Andersen et al., 2009).

4.5.2 Aerodynamic Damping

One of the most important components of damping is the aerodynamic contribution. Aerodynamic damping has its origin in the wind load acting on the rotor or, more accurately, in the interaction between the wind flow and the motion of the structure. This phenomenon, which occurs for flexible structures, can be a source of instability under certain situations. However, for the along-wind direction, it is favourable and should be accounted for during the design stage and the evaluation of structure integrity along its lifetime. This interaction between wind flow and wind turbines can be explained through the simple description presented in (Kuhn, 2001):

"*A motion of the tower top in the wind direction (…) results in a smaller angle of attack at the rotor blades* [see Figure 3.33] *because the apparent out-of-plane velocity component* [$U_0(1 - a)$] *is reduced by the tower top velocity. A smaller angle of attack corresponds, for attached flow conditions, to lower aerodynamic lift and drag forces* [equations (3.24) and (3.25)] *and to a reduction of the thrust force (…). Likewise a movement of the nacelle against the wind direction increases both the angle of attack and the thrust force. In both situations the alternation of the thrust is oriented opposite to the disturbing tower top motion and is experienced as aerodynamic damping. (…)*

For higher angles of attack, stall occurs and the dynamic damping is lower or may even become negative because the slope of the lift curve is reduced. Under such conditions aero-elastic instability can occur if insufficient damping exists."

For the purpose of illustration, Figure 4.14 presents the experimental results for lift and drag coefficients for the NACA 63-415 airfoil obtained in a wind tunnel by Bak *et al* (Bak, Fuglsang et al., 2000). As can be seen, the lift coefficient has an almost linear increase for the initial range of angle of attack. Then, the slope of the curve starts to decrease until a peak is reached. After this point, the variation of the lift coefficient with the angle of attack becomes negative. The values of drag coefficients for angle of attack of around 15º are considerable low.

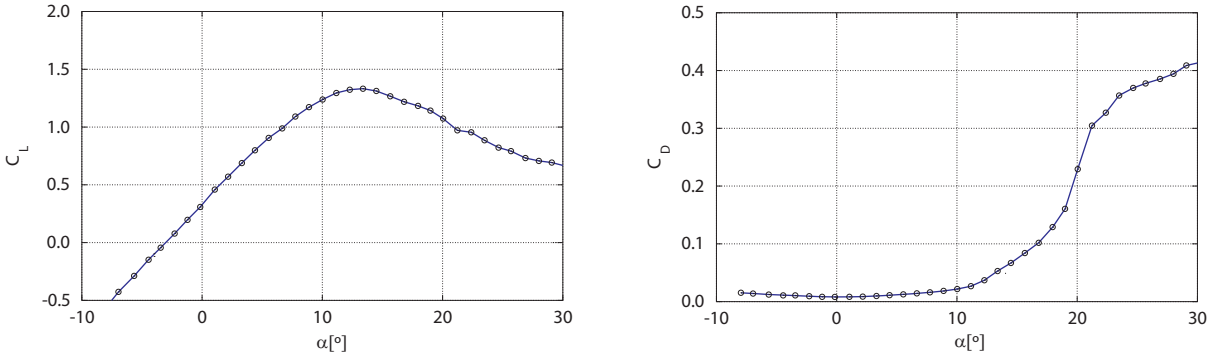

Figure 4.14 – Variation of lift (C_L) and drag (C_D) coefficients with the angle of attack (adapted from (Bak, Fuglsang et al., 2000))

Garrad (Kuhn, 2001) presented a simple equation (4.11) for the calculation of the aerodynamic damping for a wind turbine support structure. It assumes that the wind turbine is operating under stationary rotor dynamics at a high tip speed ratio, where the inflow angle (ϕ) is small and the drag forces are negligible compared to lift forces (Freris, 1990; Salzman and Tempel, 2005).

$$\xi_a \approx \frac{N_B . \rho_{air} . \Omega}{8 . \pi . f_{FA\,1} . M_{FA\,1}} \int_0^{L_{Blade}} \frac{\mathrm{d}C_L}{\mathrm{d}\alpha} . c(r) . r \, \mathrm{d}r \tag{4.11}$$

with:

$f_{FA\,1}$	Frequency of the first fore-aft vibration mode
$M_{FA\,1}$	Modal mass of the first fore-aft mode
L_{Blade}	Length of the blade
c	Airfoil chord

From the previous equation, some important aspects should be highlighted. The aerodynamic damping is inversely proportional to the natural frequency (and modal mass of the structure). This mean that structures with different philosophies of tower stiffness design (as presented in section 4.4) will lead to very different values of aerodynamic damping. On the other hand, the increase of the rotational speed of rotor increases the value of this additional portion of damping.

Some other important aspects should be also mentioned:

- The aerodynamic damping is specially noted for the first bending mode of the tower in the rotor out-of-plane direction (the first fore-aft vibration mode). This is expected since the aerodynamic forces act mainly in this direction;
- In the rotor plane direction (the side-side direction) the effect of the aerodynamic damping is expected to be negligible since there is a very low level of aerodynamic forces in this direction;
- In idling or parked situations, the effect of aerodynamic damping is expected to vanish for both orthogonal directions. This situation is due to the fact that, in these situations, the blades are usually in a feathered position (with high angles of attack). Nevertheless, some effect could

be noted for the side-side direction due to the opposition of the blade to the wind flow in this direction;

- Variable and fix rotor speed turbines present different values for aerodynamic damping (Salzman and Tempel, 2005). Fix speed turbines operate at high tip speed ratios in low wind speeds and lower tip speed ratios at high wind speeds (due to the constant rotor speed). For these reasons, in low wind speed the angle of attack is small and, consequently, the flow is attached to the blade. When the wind speed is higher, the angle of attack increases which lead to higher angles of attack and some separation of the flow at the blade. In the case of variable speed rotors, since they operate with their blades close to stall under rated wind speed, there is some flow separation which leads to an aerodynamic damping below the optimal value. For the higher wind speed, the flow stays attached to the blade and the damping is higher.

4.5.3 TOWER DAMPERS

One artificial method for additional introduction of damping in the support structure can be achieved with the installation of special devices, typically in the form of a mass pendulum. This technique is a widely implemented solution in tall structures. Ideally, it consists in the attachment of an additional mass, linked to the structure through a spring and a damper (Figure 4.15). The damper system is tuned according to the vibration mode which response is desired to be attenuated. Commonly, solutions consisting in a pendulum immersed in high viscous oil (Damgaard, Ibsen et al., 2013a), a tuned mass damper (Shirzadeh, Devriendt et al., 2013) or a liquid damper (Tarp-Johansen, Andersen et al., 2009) are used in wind turbines, usually installed offshore.

The damping value introduced by these devices depends on the implemented damper system and on the tuning accuracy. In (Colwell and Basu, 2009), a numerical study about the efficiency of a tuned liquid column damper in an offshore monopile wind turbine is presented.

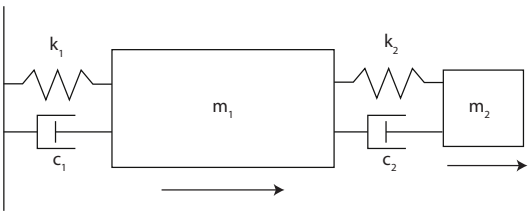

Figure 4.15 – Idealized structural system with the damper system (index 2) attached to the main system (index 1)

4.5.4 SOIL DAMPING

The operation of a wind turbine introduces vibrations at the ground level, causing cyclic motion of the surrounding foundation soil. In offshore wind turbine, the effect of the soil in the introduction of damping should be analysed. It is considered one of the most complex components of damping to be determined (Germanischer Lloyd (GL), 2005). Soil damping is formed by a combination of two parts: geometrical dissipation and material damping. Geometrical dissipation is due to wave propagation into the soil. However, it is referred that this effect is insignificant at frequencies below 1 Hz (Andersen, 2010). On the other hand, material damping is due to the internal friction of soil grains and should be accounted for.

The damping introduced by the soil is dependent on the type of soil and also, to some extent, on the type of foundation. Along with the inherent complexity of this phenomenon, it is comprehensible that there is a quite wide range of values between published works. Damping ratio values between 0.23 % and 1.00 % for monopile foundations are referred in (Tarp-Johansen, Andersen et al., 2009; Versteijlen, Metrikine et al., 2011; Damgaard, Ibsen et al., 2013a). Damgaard *et al* (Damgaard, Ibsen et al., 2013b) also studied the influence of soil damping in an offshore prototype wind turbine with a bucket foundation and found a value of 0.16 % for the damping ratio during power production.

4.5.5 HYDRODYNAMIC DAMPING

In offshore wind turbines, there is also another component of damping, the hydrodynamic damping. This component is essentially constituted by two terms: one due to wave radiation and another due to hydrodynamic drag. In order to assess the relative importance of each term, the value of the Keulegan-Carpenter number is usually analysed:

$$KC = \frac{u_a . T}{D} \tag{4.12}$$

with:

u_a	Flow velocity amplitude
T	Wave period
D	Characteristic length (diameter of cylinder section for a pile)

For small values of KC (below 2 (Naess and Moan, 2012)), the radiation damping is dominant; while for high value of KC, the drag component prevails. Thus, the contribution of each damping term depends on the type and size of the foundation solution (and also on the sea conditions).

Some authors refer the larger contribution of the radiation damping with respect to the viscous drag component for monopile wind turbine foundations (Tarp-Johansen, Andersen et al., 2009; Shirzadeh, Devriendt et al., 2013). Some typical values for the wave radiation component of the hydrodynamic damping are present in published works. Leblanc and Tarp Johansen (LeBlanc and Tarp-Johansen, 2011) present a value of 0.12 % for the damping ratio of an offshore wind turbine with a pile diameter of 4.7 m, with a water depth of 20 m and a natural frequency value of 0.3 Hz. Also in (Germanischer Lloyd (GL), 2005), the value of 0.11 % for damping ratio of a monopole wind turbine is presented. Likewise, Tarp-Johansen *et al* (Tarp-Johansen, Andersen et al., 2009) present a value of 0.22 %, following a numerical procedure.

Besides the hydrodynamic effect of the pile, the presence of mooring lines in floating wind turbines also represents an important contribution to the damping of the system (Hall, Buckham et al., 2013).

4.6 Cyclic Vibration Loads

As mentioned earlier, wind turbines are subjected to a large variety of dynamic loads (Manwell, McGowan et al., 2010). In this section, a special reference is made to cyclic loads. These loads hold a large importance when studying the response of the structure. With a dynamic monitoring system, it is expected to capture the resonance peaks of the structure in order to identify its natural frequencies. However, as cyclic loads are acting on the structure, some peaks will be present in the records that do not correspond to the dynamic properties of the structure. For this reason, there is the need for previous identification of these peaks. There are mainly three sources of this kind of loads: aerodynamic forces, mass unbalance or wave forces.

In Figure 4.16, the frequency domain spectrum response (acceleration) at the top of a three-bladed, fixed-speed wind turbine (obtained in a numerical analysis) is presented. This turbine was subjected to a three-dimensional turbulent wind field. As can be seen, several peaks spaced by 3Ω (highlighted by the red dashed line) are easily detected.

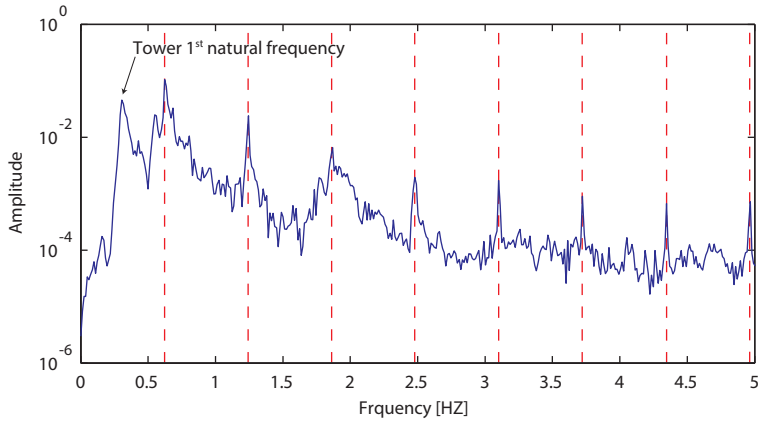

Figure 4.16 – Frequency domain spectrum of the acceleration of the top of the tower of a wind turbine due to turbulent wind inflow

In the situation of the Figure 4.16, the cyclic loads are only due to aerodynamic forces of three types:

- Rotational sampled turbulence spectrum: As already explained in section 4.3, for each revolution, each blade passes through a gust once. This will lead to an excitation of 1Ω for the blades and of $N_B.\Omega$ for the structures that support the rotor (3Ω in the case of Figure 4.16);
- Tower shadow: For an up-wind rotor, the presence of the tower disturbs the wind flow, retarding the wind speed. The decrease in the wind speed leads to a decrease of the force on the blade every time it passes in front of the tower, causing a cyclic excitation on the blade (and, consequently, on the tower). For down-wind rotors, the effect of the tower is more severe. The retardation of the flow is felt at larger distances and lead to strong excitations;
- Vertical wind shear: The mean wind velocity increases with height (Figure 4.17). With today's large rotor diameters, blades are long enough to experience a reasonable variation of wind speed from top to bottom position. Thus, blades will complete a cycle from the maximum to the minimum mean wind load in each rotor revolution.

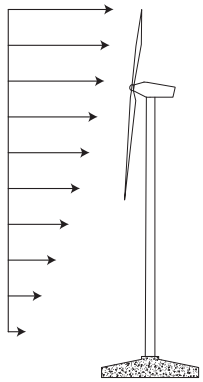

Figure 4.17 – Vertical wind shear

Unbalanced rotors represent another source of cyclic loads. It leads to a rotating force that can excite lateral vibrations of the nacelle and tower (Gasch and Twele, 2012). As examples of causes of unbalanced rotors, manufacturing defects and accumulation of ice can be pointed out. In Figure 4.18, a comparison of the response between an unbalanced mass rotor and a balanced rotor is shown. The time history was obtained through a numerical analysis, where the unbalanced rotor was defined by an abnormal mass at the tip of one of the blades with the purpose of evidence the described phenomenon. As can be observed, the unbalance presented in the rotor introduced an excitation with a frequency of 1Ω in the support structure.

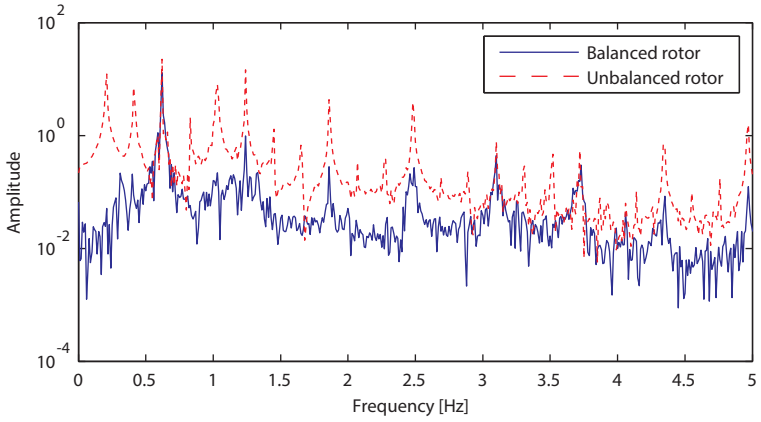

Figure 4.18 – Time history of the tower top accelerations for a balance and unbalance mass rotor

For offshore wind turbines, another source of excitation forces needs to be accounted for. Wave excitation acts on support structures in a wide range of frequencies, usually bellow the tower natural frequency (Tempel, 2006). Thus, time histories of the motion of an offshore tower will likely record these excitations, which need to be analysed and discharged when a dynamic continuous monitoring system is installed in a wind turbine. The usual wave excitation range of frequency is illustrated in Figure 4.19. As can be seen, the frequencies of excitation are not very well defined as are for aerodynamic forces.

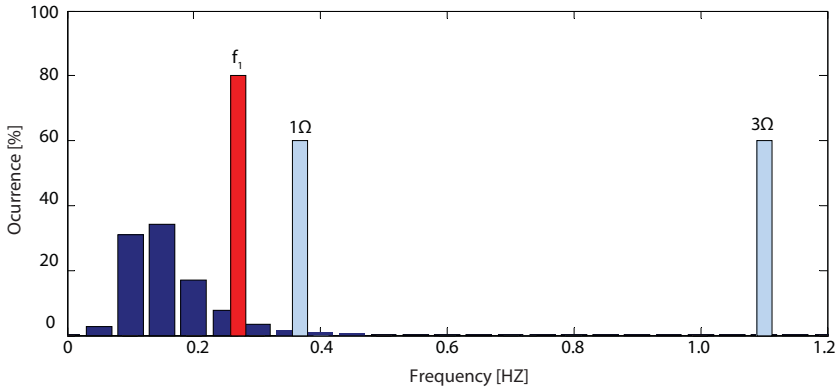

Figure 4.19 – Range of frequencies of wave excitation on an offshore wind turbine (Tempel, 2006)

4.7 NUMERICAL MODEL OF A WIND TURBINE

A numerical model of a wind turbine was developed with the HAWC2 software (Larsen and Hansen, 2007) in order to illustrate some of the methods presented throughout this thesis. HAWC2 is an aeroelastic code developed at Risø DTU and intended to calculate wind turbine response in the time domain. It uses a multibody formulation to model the wind turbine structure through beam elements, allowing to model each component of the wind turbine as an independent body. Each body is implemented in the model according to the finite-element theory.

HAWC2 code allows simulating the structural response of wind turbines at onshore and offshore environments, subjected to hydrodynamic and aerodynamic loading. Since the main case study of this work is an onshore wind turbine, only aerodynamic loads were considered. The aerodynamic model implemented in the HAWC2 code is based on the blade element theory (briefly introduced in Chapter 3). The implemented model is extended to account for the dynamic and skew inflow, wind shear effect, the effect due to large deflections of the blades, tip loss effect and dynamic stall. In addition, the tower shadow effect, referred in section 4.6, is also included.

The developed numerical model of the onshore wind turbine is based on the NREL 5MW reference wind turbine (Jonkman, Butterfield et al., 2009), which is available on (HAWC2 web site, 2013). This model was used as a basis for the numerical model described in the case study of the section 7.3.

The NREL 5MW reference wind turbine is a conceptual model of a representative utility-scale wind turbine. It is a three-bladed, upwind rotor with a variable-speed turbine and with pitch control mechanism. The power curve and the relationship between the wind speed and the rotor speed of the NREL 5MW wind turbine is presented in Figure 4.20.

The main dimensions of the model are presented in Figure 4.21, alongside with the position of the sensors considered to collect the accelerations of the structure.

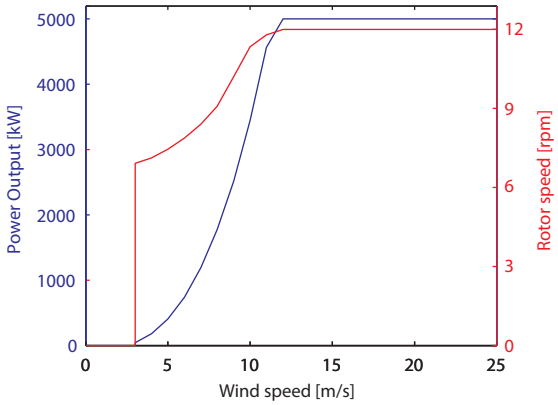

Figure 4.20 – Power curve (in blue) and relationship between rotor speed and wind speed (in red) of the NREL 5MW

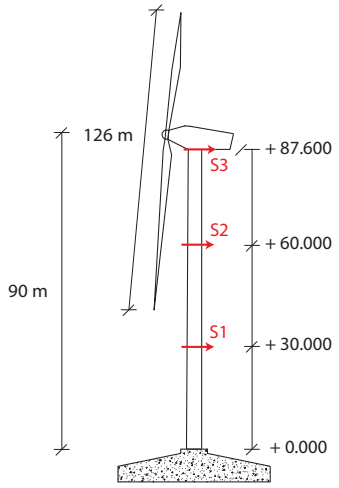

Figure 4.21 – Illustration of the numerical model of the NREL 5MW and position of the accelerometers

The aeroelastic analysis was performed for a time length of 700 s, with a time step of 0.02 s. The first 100 s were disregarded to avoid transient responses from the start of operation of the turbine.

During the analysis, the wind turbine was subjected to artificially generated wind speed time series with a mean wind speed of 15 m/s (Figure 4.22). The turbine was operating at the rated power output conditions. At this regime, the pitch angle is used to control the rotor speed and, for that reason, it varies along the analysed 600 s. The rotor mean speed is 12.1 rpm. The evolution of the rotor speed and of the blades pitch angle throughout the analysis is shown in Figures 4.23 and 4.24.

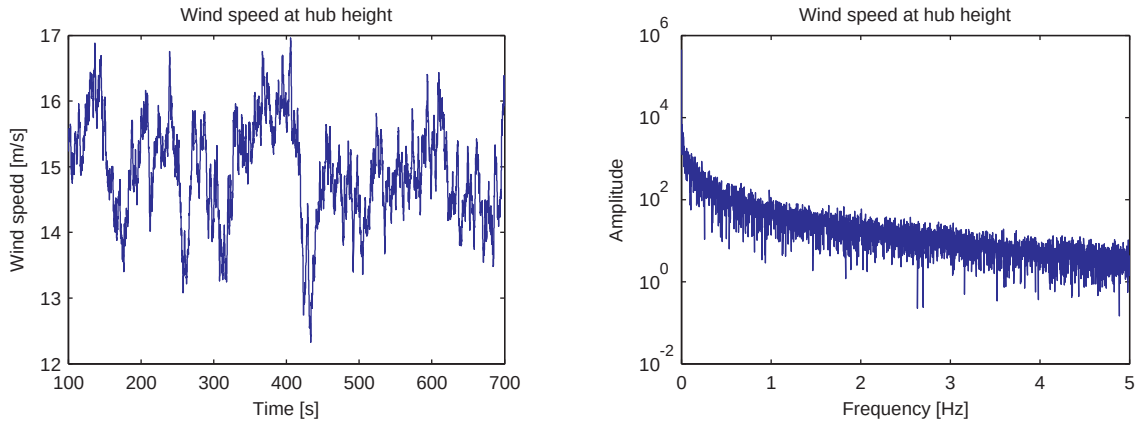

Figure 4.22 – Generated wind speed at the hub height (time and frequency domain)

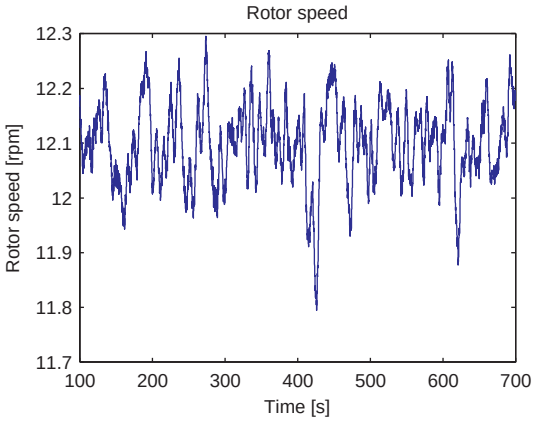

Figure 4.23 – Rotor speed

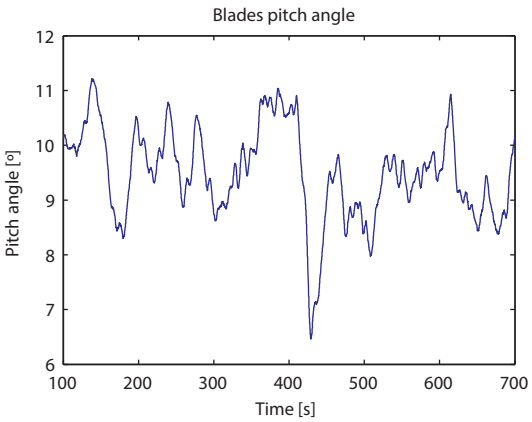

Figure 4.24 – Blade pitch angle

The acceleration time series obtained from the analysis of the considered sensors are presented in Figure 4.25, in both time and frequency domain. In this figure, only the considered 600 s are shown. It is interesting to note that the vibration levels recorded by sensor S2 (height + 60.000) are the highest from the three sensors.

In the frequency domain plots, the frequencies of the 3Ω, 6Ω, …, 24Ω harmonics are indicated with vertical dashed lines. The influence of the first 5 harmonics in the structural response of the wind turbine is clearly visible.

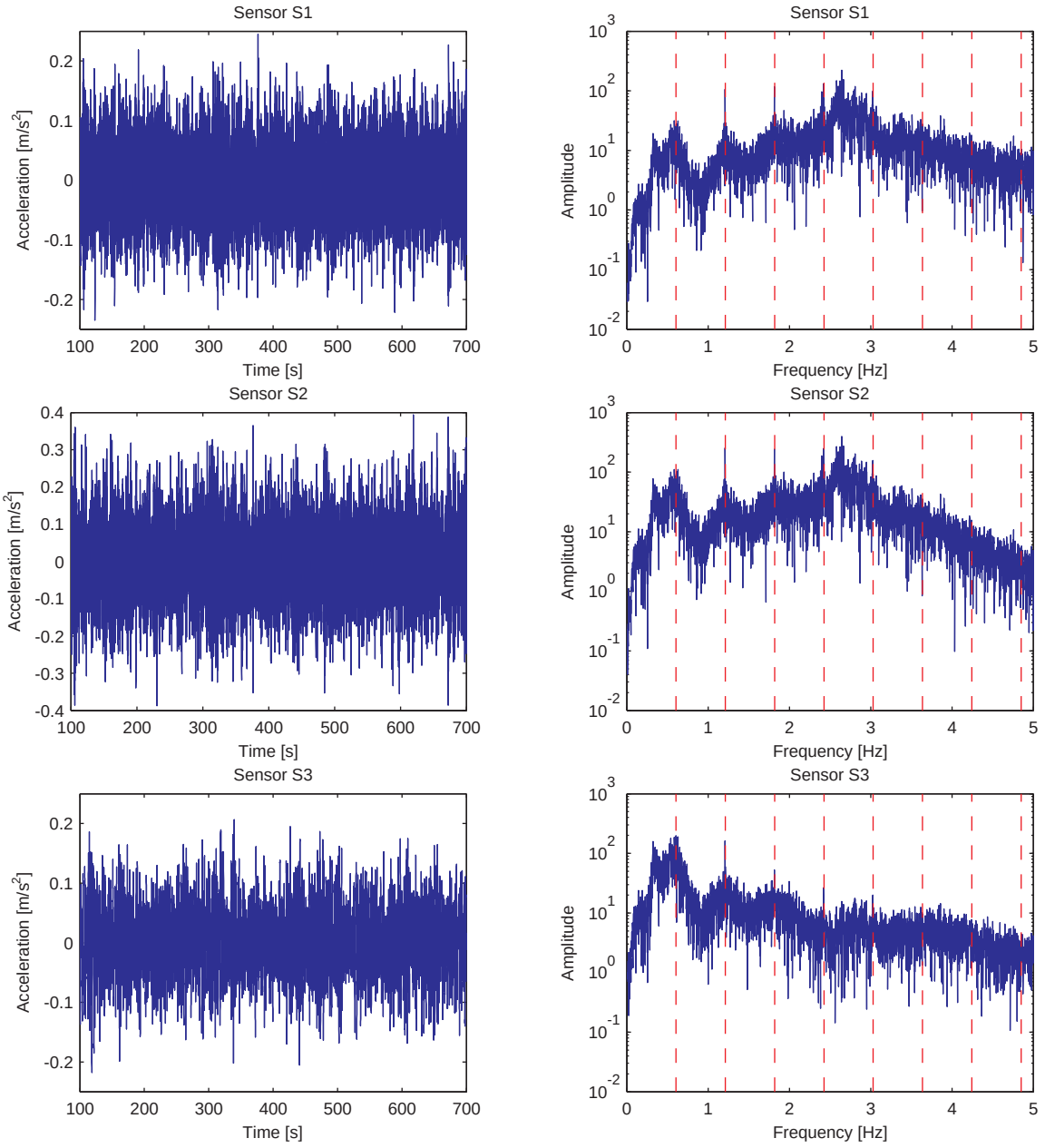

Figure 4.25 – Wind turbine acceleration captured by the sensors (time and frequency domain)

In order to ease the comprehension of some procedures presented throughout this thesis, only the two first tower vibration modes were considered. The dynamic properties of the wind turbine were obtained through an eigensolver implemented in the HAWC2 code. The natural frequency and the modal damping ratio of these two modes are presented in Table 4.5. It is important to note that the damping values presented are only referred to the structural component of damping and, for that reason, do not necessary reflect the effective damping of the modes during the analysis since the aerodynamic damping is not considered in the eigensolver and, consequently, in the values of shown in Table 4.5.

Table 4.5 – Modal properties of the HAWC2 model

Mode	Natural frequency [Hz]	Damping ratio [%]
1st tower bending mode (1 FA)	0.333	0.24
2nd tower bending mode (2 FA)	2.686	1.91

The configuration of the considered vibration modes is illustrated in Figure 4.26. The 1st tower bending mode is clearly a pure tower bending mode, with a first order configuration of the tower motion (Figure 4.26 a)). On the other hand, the 2nd tower bending mode beholds, besides the tower, an important contribution of the rotor to the global motion of the mode (Figure 4.26 b)).

a) d)

Figure 4.26 – Illustration of the considered vibration modes: a) 1 FA; b) 1 FS and c) 2 FA

4.8 FINAL CONSIDERATIONS

In this chapter, a dynamic characterization of the wind turbine structural system is developed. It starts with a description of the tower and rotor blades dynamic behaviour, including the commonly identified vibration modes. In addition, the importance of the soil condition to the dynamic properties of the structure is also highlighted. These properties of the support structure are usually used to define the type of wind turbine based on its stiffness. It can be defined as "soft-soft", "soft-stiff" and "stiff-stiff", depending on the relationship between the frequency of the first natural frequency of the tower and the rotor speed. This analysis is fundamental to avoid resonance phenomena in the wind turbine structural systems.

Afterwards, a characterization of the damping in wind turbines is performed. This is a property of utmost importance in the dynamic analysis of these structures since it is directly involved in the wear caused by fatigue loading. The several components of the damping that might be present in a wind turbine are referred, namely structural, aerodynamic, from external devices, soil and hydrodynamic.

The influence of the rotor blades rotation and rotor unbalances in the load spectrum of the support structure is also described. These two phenomena modify the wind loading spectrum, imposing well-defined excitations around the rotation harmonic frequencies of the rotor. The influence of these imposed loading on the identification of the modal properties of wind turbines is addressed in the next chapter.

Finally, a numerical model of the NREL 5MW used in the context of this thesis is described. A numerical simulation subjecting the model to an artificially generated wind speed time series is presented. The response obtained with the analysis will be used, in the following chapters, to illustrate some concepts introduced in this thesis.

5
OPERATIONAL MODAL ANALYSIS OF WIND TURBINES

5.1 INTRODUCTION TO OPERATIONAL MODAL ANALYSIS

The experimental identification of modal properties of structures is a subject of study with a long tradition. It was initially applied to small structures of mechanical engineering (most of the times in laboratory environment), in order to estimate modal frequencies, damping ratios and mode shapes. In these tests, an input force was applied to the structure that reacts with a particular response (output). In this type of traditional Experimental Modal Analysis (EMA), both the input and the output were measured in order to identify the modal properties of the structure. For this reason, this type of modal identification procedure is usually named as input-output method.

Later, EMA techniques were applied to larger civil engineering structures, like bridges, dams and buildings (Magalhães and Cunha, 2011). However, the transposition from small to large structures introduced critical difficulties regarding the excitation of the structure. Heavy and expensive means are often necessary to perform shaker, impact or pullback tests used for this kind of procedure (Felber, 1993). Some examples of application of EMA on large structures are presented in (Cunha and Caetano, 2006).

In the early 1990's, a remarkable evolution in the field of experimental identification gained great attention (Zhang, Brincker et al., 2005). With the technological developments of sensors and A/D converters, it became possible to measure lower levels of vibration alongside with lower levels of noise. Thus, sources of operational (like traffic) and ambient (like wind) excitation became sufficient to analyse the dynamic response of the structure. For this reason, new identification methods requiring only the measurement of the structure response were developed. These were named output-only methods. Compared to EMA, this new philosophy of experimental identification, usually also called Operational Modal Analysis (OMA) or Ambient Vibration Test, presents several advantages (Zhang, Brincker et al., 2005):

- OMA is cheaper and faster to conduct, avoiding the necessity of large masses or heavy excitation devices;
- Dynamic characteristics of the complete system under real loading conditions can be obtained;
- OMA can be used not only for dynamic design and structural control but also for vibration-based health monitoring and damage detection.

Nevertheless, OMA presents some disadvantages inherent to its concept (Magalhães and Cunha, 2011):

- Although the excitation is assumed to be of broad band nature, the frequency content may not cover the whole spectrum of interest, mainly in the case of structures with high natural frequencies. Also, if the excitation does not correspond to a flat distribution of energy along the frequency spectrum, some misidentification might occur;
- The modal mass is not estimated.

OMA has been widely used in the last years in several engineering domains. In civil engineering, this technique has been applied in diverse structures. Bridges (Cunha, Caetano et al., 2001), (Caetano, Magalhães et al., 2007), (Brownjohn, Magalhães et al., 2010), dams (Rodrigues, 2004)) and buildings ((Ventura, Finn et al., 2003), (Shi, Shan et al., 2012), (Gentile and Saisi, 2007) are among the most commons examples of structures tested with OMA methodology. In mechanical engineering, OMA is also applied in different structures, such as helicopters (Peeters, Cornelius et al., 2007), (Ameri, Grappasonni et al., 2013), aircrafts (Mevel, Benveniste et al., 2006), (Hermans and Auweraer, 1999) or vehicles (Goursat, Döhler et al., 2010), (Hermans and Auweraer, 1999).

5.2 APPLICATION OF OMA TO WIND TURBINES

The dynamic behaviour of wind turbines is a major concern, as exposed in the previous chapters. Thus, an experimental dynamic characterization of the system became a required tool in order to prevent possible resonance effects.

Wind turbine presents three important particularities that highlight the importance of application of OMA in these structures:

- Considering the typology and size of wind turbines, it is easy to understand the difficulty in providing means to adequately excite these structures;
- Wind turbines are located in windy locations. Thus, wind can be used as an ambient source of excitation (with a broadband spectrum);
- It is important to adequately identify the modal characteristics of the structural system, both in parked and in real operation conditions, since rotor operation can introduce important variations in these properties.

Therefore, it is not surprising that modal identification of wind turbines played an important role in the development of OMA.

The first formalized modal testing of blades and turbines began in the late 1970s (Carne and James Iii, 2010). In 1982, (Carne, Lobitz et al., 1982) developed a finite element procedure to be applied to vertical-axis wind turbines. In order to validate the procedure, an input-output test was performed in a 2 m height, research vertical axis wind turbine at parked condition and at different operating speeds. In the parked test, the excitation was achieved through a traditional impact hammer and accelerometers were used as sensors. For the tests realized under operation, it is referred that there were some difficulties in exciting the structure (Carne and James Iii, 2010). The solution adopted consisted on a pretensioned cable attached between the tower and one blade. When the cable was suddenly released, it created a broad-brand step-relaxation excitation (Carne and Nord, 1983). In this test, accelerometers were also used, alongside with strain gauges. The identified modal parameters consisted in frequency values, damping ratios and mode shapes, and the correlation obtained between numerical and experimental results was very good. However, the procedure for the step-relaxation technique was very time-consuming because, every time a new test was performed, the turbine had to be brought to parked condition.

Later in 1986, Carne *et al* performed a modal test of the 110 m height Éole VAWT in parked conditions (machine introduced in Chapter 2) (Carne, Lauffer et al., 1988). Since it was extraordinary higher than the 2 m height VAWT previously tested, a different approach was followed in this test: a traditional input-output test, where the excitation consisted in two forces of 45 kN and 135 kN applied on one blade and on the tower, respectively; and a second test in which the wind turbine was only subjected to wind loading and only the structural response was recorded. The later consisted in one of the first ambient vibration tests in which a full modal analysis was performed, including mode shapes, frequencies, and damping values (Carne and James Iii, 2010). In this test, four separate setups of response measurements were recorded, with four reference channels repeated in every setup. Then, auto- and cross-spectral densities were computed in order to extract the modal properties of the Éole turbine. The obtained results showed a very good correlation between the two experimental tests

(Carne, Lauffer et al., 1988), evidencing the advantages of ambient vibration tests (considerably faster and more practical) with regard to forced vibration tests.

The success achieved with the previous application led to the development of a new identification method named Natural Excitation Technique (NExT) (James, Carne et al., 1993). This technique was further validated and used in numerical (FloWind Corporation 19 m VAWT) and experimental tests, both in parked - FloWind Corporation 19 m VAWT - and in operation – DOE/ Sandia 34 m VAWT - situations (James, Carne et al., 1993). Reference should also be made to the application of NExT to a rotating 100 kW horizontal axis wind turbine (James, 1994).

After these initial tests, other authors have also performed some modal identification analysis on wind turbine structures. Molenaar (Molenaar, 2003) performed an experimental modal test on a 750 kW horizontal axis wind turbine, under parked conditions, in order to compare the results with a numerical model. For the test, the wind turbine was excited through the step-relaxation technique by applying a static load on the tower top and the structural response was measured with 19 accelerometers mounted both on tower and blades.

In (Osgood, Bir et al., 2010), continuing earlier works (Osgood, 2001), a parked 600 kW three-bladed horizontal axis wind turbine was experimentally tested following both forced and ambient vibration test procedures. For the forced vibration test, two independent hydraulic actuators were used, which excited the structure at the top in both orthogonal directions. The turbine was heavily instrumented with accelerometers, totalling 75 channels distributed in the tower, rotor and drive train. A very good correlation was obtained with the two tests (although it was possible to detect additional modes in the forced vibration test).

(Hansen, Thomsen et al., 2006) explored different excitation techniques for wind turbine testing. Experimental results obtained with two different types of harmonic excitation were confronted with the results from an ambient vibration test. The harmonic excitation was induced by blade pitch angle variation and by electrical torque variation. However, it was concluded that the excitation of wind turbines with these techniques presents some problems, namely:

- The excitation of high-frequency and highly damped modes is not technically possible due to limitation of the blade pitch actuators;
- The excited structure vibrations are not pure modal vibrations and the estimated damping is therefore not the actual modal damping. Since it is not possible to isolate the desired modes, the estimation of damping for modes with close frequencies will result in considerable errors.

In the opposite way, the authors (Hansen, Thomsen et al., 2006) concluded that the results obtained with the adopted output-only tool confirmed its suitability for identifying closely-spaced modes.

Griffith *et al* (Griffith, Mayes et al., 2010) conducted a modal identification test on a small 60 kW VAWT under parked conditions. As in the above references, an ambient vibration and forced vibration (excitation from an impact force, from step-relaxation and from human random excitation) were performed and both accelerometers and strain gauges were used. The results revealed good agreement between all the tests.

Chauhan *et al* (Chauhan, Tcherniak et al., 2011) and Carcangiu *et al* (Carcangiu, Tcherniak et al., 2012) experimentally studied a 3 MW, 100 m diameter wind turbine. In this work, OMA techniques were applied in order to extract the main vibration modes of the tower and rotor. For that purpose,

several accelerometers were placed on the tower, nacelle, gearbox and generator. Several vibration modes were identified and presented for different rotor speed regimes. A numerical aeroelastic model was also developed and the results obtained were correlated with the experimental ones.

Ozbek *et al* (Ozbek, Rixen et al., 2010; Ozbek and Rixen, 2012) monitored the dynamic response of a 2.5 MW HAWT using conventional instrumentation (strain gauges) and optical measurement systems (laser interferometry and photogrammetry). The wind turbine was tested under parked (both with strain gauges and laser interferometry) and rotating (both with strain gauges and photogrammetry) conditions. Although good results were achieved, two important drawbacks associated with the use of optical measurement systems are referred: laser interferometry is not suitable for rotating conditions testing; and the available camera systems used for the photogrammetry testing had a reduced memory, allowing to record only small measurement segments.

Also Marinone *et al* (Marinone, Cloutier et al., 2014) performed both experimental and operational modal analysis on two 225 kW wind turbines, in parked condition. A very complete instrumentation was used, with 80 accelerometers installed on the blades, hub, nacelle and tower and 6 seismic accelerometers installed at the foundation. The authors of the study were able to identify 18 vibration modes in the 0 – 15 Hz frequency range and the correlation between the results from the EMA and OMA was very good.

Apart from the entire wind turbine structure testing, blades properties are important features that need to be identified (Yang and Sun, 2013). (Thomsen, Petersen et al., 2000) tried to identify damping of edgewise blade modes of a 600 kW wind turbine under operation. For that purpose, the authors installed eccentric rotating masses in the nacelle to excite the desired modes. Modal identification tests are also often conducted under laboratory conditions (Griffith, Smith et al., 2006; Griffith and Carne, 2010; White, Adams et al., 2010).

Yang and Allen (Yang and Allen, 2012) also performed a modal analysis on a small wind turbine blade based on a laser scanning technique. The test was performed under parked conditions and the authors accomplished to identify some vibration modes (frequencies and mode shapes).

Another important field of application of OMA techniques on wind turbines is in offshore situations, since different foundation designs lead to different structural behaviours (section 3.1.1.5). Moreover, the contribution of the different types of damping is also difficult to predict (see section 4.5). Thus, the extraction of the modal parameters under operating conditions reveals as an essential tool for the correct comprehension of the dynamic behaviour of these structures.

Some work in this area has already been published. In (Devriendt, Magalhães et al., 2014), the modal identification of a 3.0 MW offshore wind turbine with monopile foundation is introduced. This study analyses the acceleration data recorded during 2 weeks (under non-operating conditions). The modal results obtained were then confronted with collected environmental data, such as tidal level and wind speed. This wind turbine is also study in section 5.9 of the present work.

In (Shirzadeh, Devriendt et al., 2013), the same wind turbine is experimentally tested. The main goal of the test was to calculate the damping value of the fundamental fore-aft (FA) vibration mode. For this purpose, both ambient and rotor-stop tests were performed. Rotor-stop tests (sometimes named "overspeed stop tests") are a type of forced vibration test, in which the turbine is operating at a normal situation until a sudden pitch-out of the blades (Figure 5.1). In this procedure the wind turbine is highly excited by the sudden absence of aerodynamic loads on the blades. Furthermore, the

aerodynamic damping contribution from the rotor almost does not interfere in the decay response of the structure, since the blades are pitched-out. The authors were able to identify the first pair of vibration modes (in FA and SS directions) and the obtained value of the damping in the FA direction was similar in both ambient and forced vibration tests. An aeroelastic model was also developed, in which the two tests were simulated with good results.

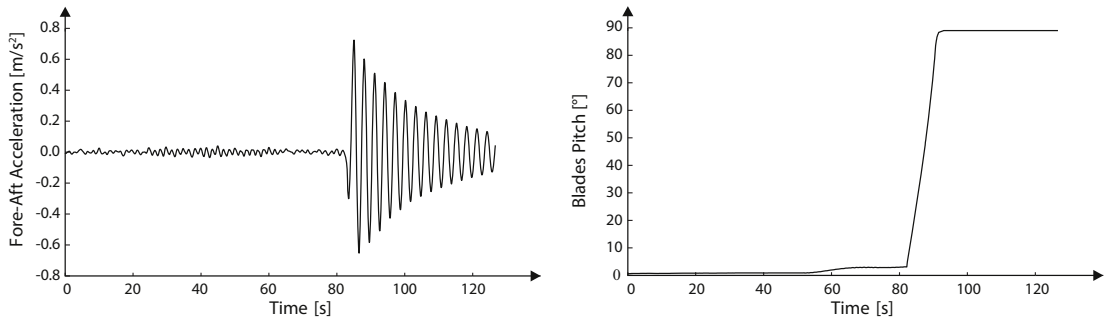

a) b)

Figure 5.1 – Example of fore-aft acceleration a) and blade pitch variation b) on a rotor-stop test (adapted from (Damgaard, Ibsen et al., 2013))

In (Damgaard, Ibsen et al., 2013) the dynamic characteristics of offshore wind turbines with monopile foundations are also studied. In this study, the value of damping of the fundamental mode for the side-side direction was investigated. Once again, ambient vibration and rotor stop tests were performed with the aim of extracting frequency and damping values for this vibration mode. In the analysis of the results, some considerations are also made concerning the damping introduced by the soil.

Like the previous authors, (Versteijlen, Metrikine et al., 2011) studied the damping effect present in an offshore wind turbine located in the Burbo Banks wind farm. 12 rotor stop tests were realized in order to assess the influence of the soil.

In (Ibsen and Liingaard, 2006), a different type of offshore wind turbine is studied. A 3 MW wind turbine with a prototype suction caisson foundation is tested in three different conditions: idling; without blades; and without blades and nacelle. For the test, 15 accelerometers were installed along the tower, and the structure was subjected to ambient excitation. The experimental results were compared with a numerical model of the structure.

5.3 PARTICULARITIES OF OMA APPLICATION TO WIND TURBINES

In the previous section, the main modal identification tests performed on wind turbines were presented. Although some refer to wind turbines under operation, there is an important part that only discusses the modal properties of the structure under parked or idling condition. This might seems a contradiction to one of the main advantages of OMA techniques – the ability to extract the modal characteristics under real operating conditions - but there is one main reason for that: the application of OMA to wind turbines under operation violates some of its basic assumptions (Tcherniak, Chauhan et al., 2010a; Ozbek, Meng et al., 2013).

There are mainly four assumptions for the applicability of OMA (Tcherniak, Chauhan et al., 2010a):

- The structure does not vary in time;
- The forces should have broadband frequency spectra;
- The forces have to be uncorrelated;
- The forces have to be distributed over the entire structure.

When in operation, wind turbines can be idealized as a set of connected substructures with rotations with respect to each other: the tower is fixed, the nacelle rotates on the top of the tower and the rotor spins relative to the nacelle. This is an obvious case of violation of the time invariance assumption of the structure.

Addressing the previous assumptions related to the input force, it is correct to assume that the wind, as exciting force, would validate all the conditions listed. This is the reason why OMA works in a straightforward way for wind turbines under parked situations: the structure is fixed (there is no relative movement between substructures) and the acting wind is the only excitation force. However, when the rotor is operating, the spectrum of the forces acting on the rotor changes from a flat spectrum to one with several peaks (as explained in Chapter 4).

Tcherniak *et al* (Tcherniak, Chauhan et al., 2010a) presents an analytical study in which evidences the violation of the temporal and spatial randomly distributed nature of the excitation forces, due to the effect of the operating rotor. The authors studied the temporal auto-correlation at different blade radius. The main results are presented in Figure 5.2.

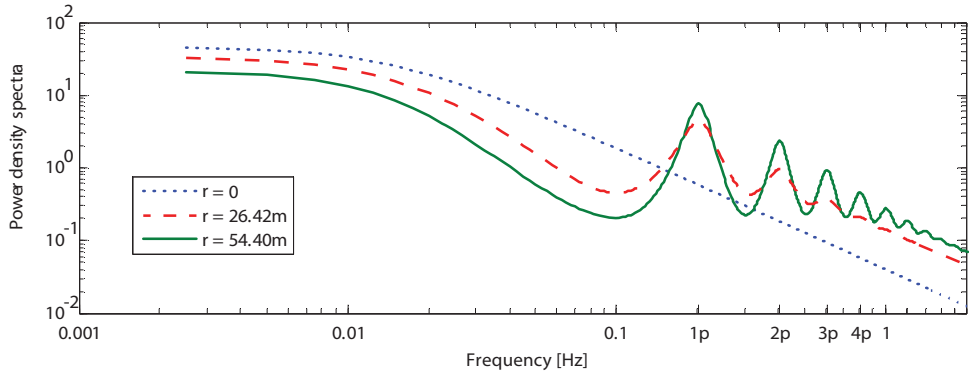

Figure 5.2 – Normalized power spectral density of the temporal auto-correlation functions computed for points on the same blade (for different radii cases) (adapted from (Tcherniak, Chauhan et al., 2010a))

As can be seen, the power spectral density functions (for radii higher than 0) are not flat as in a common wind spectrum (Kármán, 1948). Moving from the centre of the rotor to the blade tip, peaks with a frequency equal to the frequency of rotation of the rotor (and its harmonics) become more pronounced. This is motivated by the same phenomena exposed in Chapter 4:

- Every time a blade passes through a region with a determined wind speed (gust), the action on the blade is somehow "similar" to the prior passage (considering the gust is long enough) – this fact justifies the existence of the peaks;
- With the increase of radius of the point on the blade, the ratio between tangential speed of the point and the mean wind speed increases – this fact justifies the increase of the peaks with the increase of the radius of the point.

This is the reason why the second assumption presented earlier is violated. On the other hand, the results obtained for the point with $r = 0$, since it is stationary, do not present any peak. This is the reason why this assumption is not violated under parked conditions.

The third assumption of OMA (spatial non-correlation of the input excitation) was also investigated in (Tcherniak, Chauhan et al., 2010a). For this study, the authors computed the coherence (${\gamma_{AB}}^2$) between the wind speed fluctuations at different points (A and B) on the same and different blades:

$$\gamma_{AB}^2 = \frac{|S_u^{AB}(\omega)|^2}{S_u^{AA}(\omega).S_u^{BB}(\omega)} \tag{5.1}$$

with:

γ_{AB}^2	Coherence
S_u^{ij}	Auto- or cross-spectrum of wind turbulence at points *i* and *j* (respectively, if i = j and i ≠ j)

The results presented in (Tcherniak, Chauhan et al., 2010a) for points with different radii are shown in Figure 5.3. It is once again evident that several peaks are presented at rotor frequency (and its harmonics), leading to the violation of the third OMA assumption.

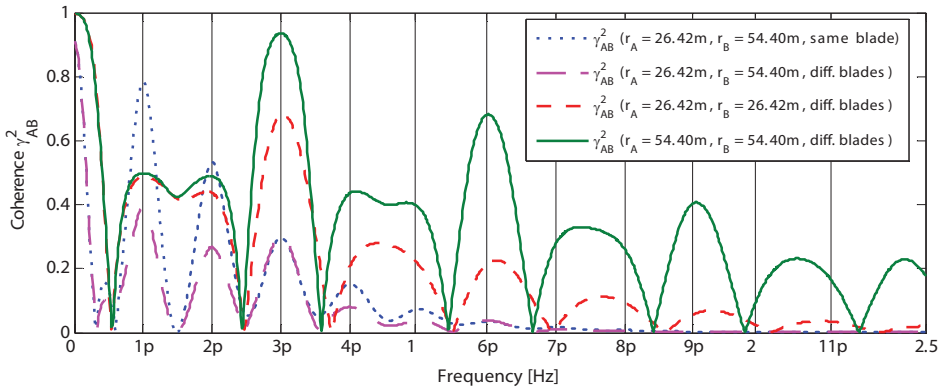

Figure 5.3 – Coherence functions for 2 points under different study scenarios (adapted from (Tcherniak, Chauhan et al., 2010a))

One important observation that should be noted is the wide shape of the peaks in Figure 5.3 (and also noted in Figure 5.2). This situation, in which the peaks have "thick tails", leads to the spread of the assumption violation for a quite wide frequency band around the harmonics. Contrary to a situation with narrow peaks, in which the signal is only "polluted" in a very narrow band of frequency around the harmonic, Figure 5.3 highlights the fact that the band between harmonics in which the coherence is approximately 0 is very narrow. This fact may increase the difficulty in applying OMA to wind turbines.

The last assumption, in which is referred that the forces have to be distributed over the entire structure, is almost fully fulfilled. Although the top of the supporting structure is subjected to a considerable higher loading when in operation (due to the rotor), the remaining part is also excited by the wind. Hence, this assumption does not introduce any additional concern in the modal analysis of wind turbines.

In spite of these difficulties, it is still possible to apply OMA to operating wind turbines. Section 5.4 describes the modal identification algorithms used in this work. Some possible solutions to overcome the problem of the assumptions violation are presented in section 5.6.

5.4 OUTPUT-ONLY STOCHASTIC IDENTIFICATION METHODS

In this section, an overview of the output-only algorithms implemented in Matlab (MathWorks, 2012) and used in this work is presented.

5.4.1 ALGORITHMS BASED ON IDENTIFICATION OF STATE-SPACE MODELS

This section introduces two different time-domain, parametric modal identification algorithms: the SSI-COV and the SSI-DATA. They both aim to identify a state-space model of the structural system from the measured signals (in this case, accelerations). For a better understanding of the methods, some considerations about state-space models and Kalman filters are also presented in this section.

5.4.1.1 State-Space model

A stochastic state-space model is an alternative time domain formulation of a dynamic system. In its discrete version, a stochastic state-space model is characterized by (Juang, 1994):

$$\begin{aligned} x_{k+1} &= A.x_k + B.u_k + w_k \\ y_k &= C.x_k + D.u_k + v_k \end{aligned} \tag{5.2}$$

with:

x	State vector (which contains the displacement and velocity vectors of the system)
y	Output vector (which contains the measured output values)
u	Input vector
A	State matrix
B	Input matrix
C	Output matrix
D	Direct transmission matrix
w	Vector containing noise due to disturbances and modelling inaccuracies
v	Vectors containing noise due to sensor inaccuracy

Among all the elements previously presented, a special reference should be made to the A matrix since it characterizes the structural system (it is possible to extract the modal properties of the system from its eigenvalues and eigenvectors). This is the reason why the main goal of these algorithms is to estimate this matrix.

In situations in which the inputs are unknown, as is the case of OMA, the terms related to u_k can be grouped together with the noise terms. In this situation, equation (5.2) can be rewritten as:

$$\begin{aligned} x_{k+1} &= A.x_k + w_k \\ y_k &= C.x_k + v_k \end{aligned} \tag{5.3}$$

The state-space model from equation (5.2) can also be defined in a modal basis. Considering a special case of similarity transformation:

$$x_k = \Psi.x_{m,k} \tag{5.4}$$

with:

Ψ	Matrix with eigenvectors of A in each column
$x_{m,k}$	Modal state vector at k instant

it is possible to define the modal state-space model:

$$\begin{aligned} x_{m,k+1} &= \Lambda.x_{m,k} + \Psi^{-1}.w_k \\ y_k &= V.x_{m,k} + v_k \end{aligned} \tag{5.5}$$

with:

Λ	Modal state matrix ($\Lambda_d = \Psi^{-1}.A.\Psi$)
V	Modal output matrix ($V = C.\Psi$)

One important property of the modal state-space model is that, due to the diagonal structure of the Λ matrix, it is possible to decouple the contribution of each vibration mode to the response of the structure. In the same way, the V matrix contains the observable components of the mode shapes in each column, in accordance with the eigenvalues from the Λ matrix.

Due to these characteristics, it is possible to reduce the order of the state-space model in order to consider only the desired modes. This property will be applied and discussed in section 5.5.2.3.

5.4.1.2 SSI-COV algorithm

The COVariance driven Stochastic Subspace Identification method is a time-domain, parametric method that identifies a stochastic state-space model from the output covariance matrix (or correlation, since the mean value of the signals is assumed to be zero). The algorithm presented in this work was developed and described in (Peeters, 2000).

The algorithm is based on the principal assumption that the correlation functions of the response of a structure excited by white noise are defined by a sum of sinusoids with exponential decrement. Since these sinusoids are related with the impulsive structural response, the dynamic characteristics of the structure can be then extracted from these functions.

The method starts with the computation of estimates of the output correlation matrix for 2.i-1 lags, being i an input of the method to be tuned by the analyst.

These correlation matrices are organized in a Toeplitz matrix:

$$T_{1|i}^{ref} = \begin{bmatrix} R_i^{ref} & R_{i-1}^{ref} & \dots & R_1^{ref} \\ R_{i+1}^{ref} & R_i^{ref} & \dots & R_2^{ref} \\ \dots & \dots & \dots & \dots \\ R_{2.i-1}^{ref} & R_{2.i-2}^{ref} & \dots & R_i^{ref} \end{bmatrix} \tag{5.6}$$

with:

$*^{ref}$	Refers to the reference sensors. Reference sensors are a subset of sensors that should present relevant modal ordinates of the modes to be identified. All sensors might be assumed as reference sensors.
$R_i{}^{ref}$	Correlation matrix evaluated at time lag i, between all sensors and reference sensors

Considering that the inputs are idealized as realizations of white noise processes and that the state vector can be characterized by a stationary stochastic process with zero mean, each correlation matrix R_i can be factorized according to (Overschee and Moor, 1996):

$$R_i = C.A^{i-1}.G \tag{5.7}$$

with:

G	Next-state output correlation matrix

Considering the application of the property presented in equation (5.7) to the Toeplitz matrix, one obtains:

$$T_{1|i}^{ref} = \begin{bmatrix} C \\ C.A \\ \dots \\ C.A^{i-1} \end{bmatrix} . \begin{bmatrix} A^{i-1}.G^{ref} & \dots & A.G^{ref} & G^{ref} \end{bmatrix} = O_i.\Gamma_i^{ref} \tag{5.8}$$

with:

O	Extended observability matrix
Γ	Reversed extended stochastic controllability matrix

Computing the singular value decomposition of the same Toeplitz matrix, the following factorization is obtained:

$$T_{1|i}^{ref} = U.S.V^T = [U_1 \quad U_2].\begin{bmatrix} S_1 & 0 \\ 0 & 0 \end{bmatrix}.\begin{bmatrix} V_1^T \\ V_2^T \end{bmatrix} = U_1.S_1.V_1^T \tag{5.9}$$

Comparing now equations (5.8) and (5.9), it is possible to define O and Γ matrices in a different way:

$$O_i = U_1.S_1^{1/2} \tag{5.10}$$

$$\Gamma_i^{ref} = S_1^{1/2}.V_1^T \tag{5.11}$$

Considering that matrix A characterizes the dynamic behaviour of the structural system, and observing equation (5.8), it is possible to state that, with the equalities from equations (5.10) and (5.11), the identification problem is solved. Since it is known that the C matrix is defined by the first l rows of the matrix O (l represents the number of measured outputs), the A matrix can be obtained through several ways. In this work, the following formulation was implemented:

$$\begin{bmatrix} C \\ C.A \\ \dots \\ C.A^{i-2} \end{bmatrix}.A = \begin{bmatrix} C.A \\ C.A^2 \\ \dots \\ C.A^{i-1} \end{bmatrix} \Leftrightarrow A = \begin{bmatrix} C \\ C.A \\ \dots \\ C.A^{i-2} \end{bmatrix}^{\dagger}.\begin{bmatrix} C.A \\ C.A^2 \\ \dots \\ C.A^{i-1} \end{bmatrix} \tag{5.12}$$

with:

$*^{\dagger}$	Moore-Penrose pseudo-inverse

Computing the eigenvalues (μ_n) and eigenvectors decomposition of matrix A, the results in discrete time are obtained:

$$\Lambda = \Psi.\Lambda.\Psi^{-1} \tag{5.13}$$

with:

Ψ	Matrix with eigenvectors in each column
Λ	Matrix with eigenvalues (μ) in the diagonal

The natural frequency values and modal damping ratios for each vibration mode are then obtained taking into account the conversion of the eigenvalues from discrete time to continuous time model:

$$f_n = \frac{Abs\left(\ln(\mu_n)/\Delta t\right)}{2.\pi} \tag{5.14}$$

$$\xi_n = -\frac{Re\left(\ln(\mu_n)/\Delta t\right)}{Abs\left(\ln(\mu_n)/\Delta t\right)} \tag{5.15}$$

with:

f_n	Frequency value of the n^{th} vibration mode
ξ_n	Damping ratio of the n^{th} vibration mode
Δt	Sampling interval of the outputs
$Abs(*)$	Absolute value of *
$Re(*)$	Real part of *

With the values of the frequency and damping identified, the only missing result is the mode shape of each vibration mode. The observable components of each mode shape are thus obtained with:

$$\phi = C.\Psi \tag{5.16}$$

with:

ϕ	Matrix with the mode shape configurations at the measured degrees of freedom

Some further considerations should be mentioned concerning the application of the SSI-COV algorithm to real structures. Considering the system identification of theoretical structures, the application of the Singular Value Decomposition to the Toeplitz matrix, leads to singular values equal (or very close) to zero after a certain order (see equation (5.9)). In other words, there should be a clear gap between singular values that defines the order of the model. However, in real structures, due to the noise contained in the signals and due to the fact that the used correlation functions are estimates, there is not a clear gap between singular values. Thus, it is common to calculate the results for different orders of the matrices A and C. With this method, a group of modal results is obtained for each order. Then, these results are compared with the results from the previous model order by analysing the variation between the estimated modal parameters. If the variation is within a previously defined limit, the result (or pole) is considered stable. The results obtained for different orders are usually presented in a stabilization diagrams as illustrated in Figure 5.5.

Example

The SSI-COV algorithm was applied to the acceleration time series obtained with the numerical model of the NREL 5MW wind turbine introduced in section 4.7. For this analysis, the three sensors were defined

as reference and 257 points were considered for calculation of the correlation functions (2.i -1 = 257). The obtained correlation functions are presented in Figure 5.4.

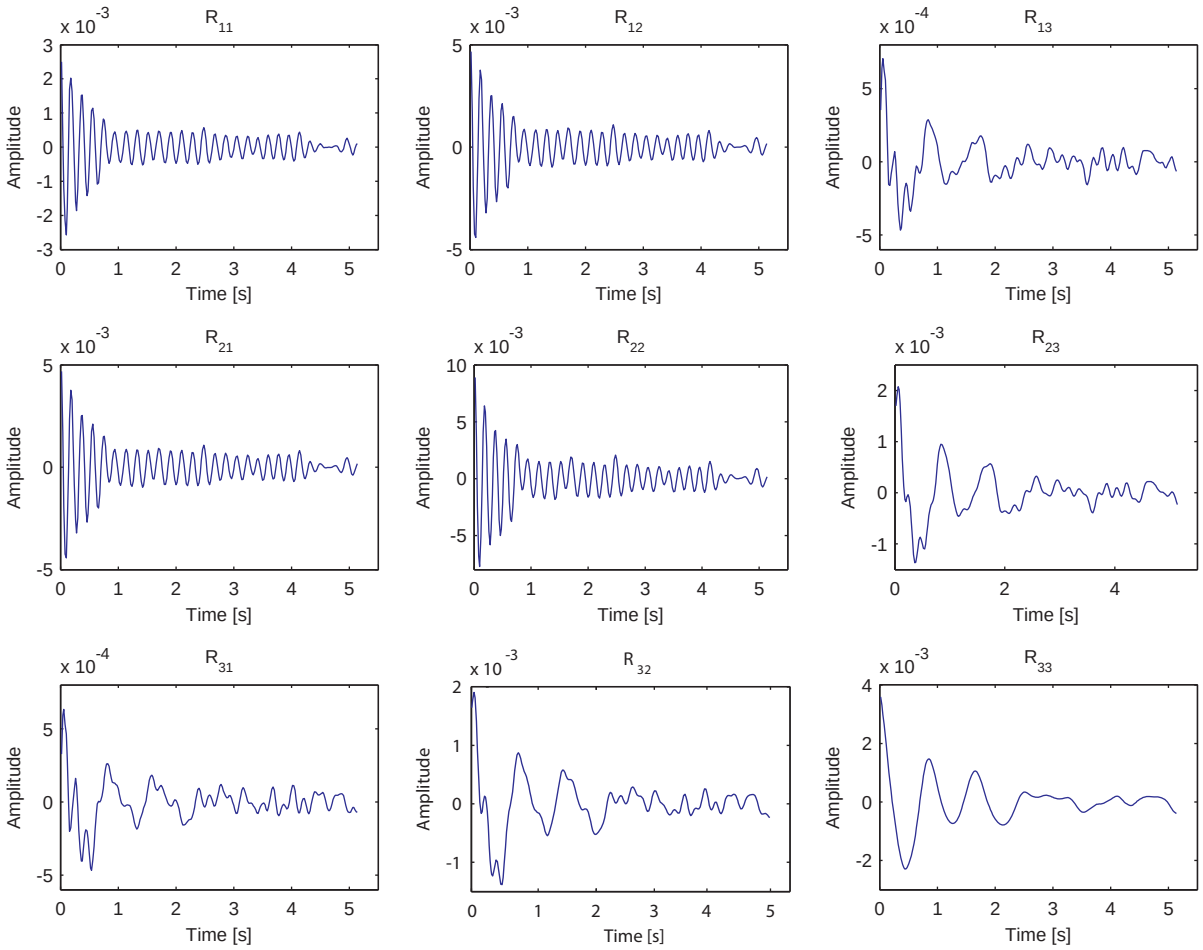

Figure 5.4 – Correlation functions

Considering the following stabilization criteria:

- Maximum variation of natural frequency (Δf): ≤ 1 %;
- Maximum variation of damping ratio ($\Delta \xi$): ≤ 5 %;
- Minimum MAC value (MAC): 0.99;
- Maximum damping ration value (ξ_{MAX}): 10 %.

a stabilization diagram considering results from models with orders between 1 and 50 was obtained (Figure 5.5). As can be seen, there are several clear alignments of stable poles. The alignments referred to the two first tower bending modes are well identified and are highlighted by red boxes.

In addition, other stable alignments are also noticed. Some of them coincide with frequency values corresponding to rotor rotation harmonics (3Ω to 12Ω). These alignments are identified at the top of the plot. As shown in Figure 5.5, these harmonics are misidentified by the algorithm as regular vibration modes. The remaining stable alignments are related to vibration modes from the rotor, which are not analysed in this example.

The modal damping of the stable poles is shown in Figure 5.6. In this figure, the poles related with the two considered vibration modes are also highlighted by red boxes.

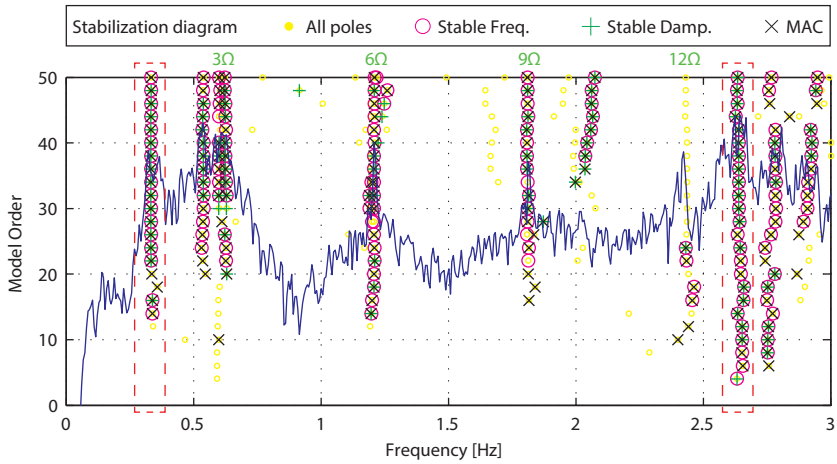

Figure 5.5 – Stabilization diagram obtained with the SSI-COV method (average spectra at the background)

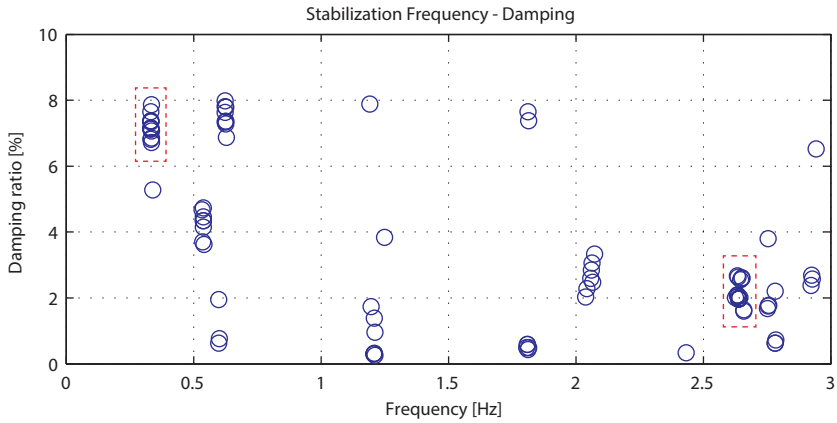

Figure 5.6 – Modal damping ratio estimates for the stable poles

The identified modal properties from the two vibration modes are shown in Table 5.1.

Table 5.1 – Modal properties: SSI-COV results vs reference results

Mode	SSI-COV results		Reference results	
	Natural frequency [Hz]	Damping ratio [%]	Natural frequency [Hz]	Damping ratio [%]
1	0.332	7.15	0.333	0.24
2	2.639	2.08	2.686	1.91

The results obtained for the natural frequency are in a good agreement with the reference values. On the other hand, the identified damping ratio for the 1st vibration mode is considerably higher than the value obtained with the HAWC2 eigensolver. This discrepancy is due to the fact that the identified damping is related to the effective damping of the mode during the 600 s. Thus, besides the structural damping, the identified value also includes the aerodynamic component of the damping. The results obtained with the SSI-COV algorithm clearly show the influence of the aerodynamic damping on the 1st vibration mode of the tower. This effect is not relevant for the 2nd vibration mode of the tower.

5.4.1.3 Kalman filter

The Kalman filter is an important aspect of the SSI-DATA algorithm. In that sense, a brief introduction to the non-steady-state Kalman filter is presented. A more detailed description can be found in (Juang, 1994).

The main goal of the Kalman filter is to compute an optimal estimation of the state vector at the instant k ($\hat{x}_k$) based on the observations up to $k-1$ and on the system matrices. Considering an initial state estimate $\hat{x}_0$ and the initial covariance of the state estimate $P_0 = E[\hat{x}_0.\hat{x}_0^T]$, the non-steady-state Kalman filter estimates $\hat{x}_k$ are obtained with the recursive utilization of the equations:

$$\hat{x}_k = A.\hat{x}_{k-1} + K_{k-1}(y_{k-1} - C.\hat{x}_{k-1}) \tag{5.17}$$

$$K_{k-1} = (G - A.P_{k-1}.C^T)(R_0 - C.P_{k-1}.C^T)^{-1} \tag{5.18}$$

$$P_k = A.P_{k-1}.A^T + (G - A.P_{k-1}.C^T)(R_0 - C.P_{k-1}.C^T)^{-1}(G - A.P_{k-1}.C^T)^T \tag{5.19}$$

with:

K_k	Kalman filter gain at instant k
P_k	Kalman error covariance matrix
R_0	Correlation matrix of the outputs (with zero time lag)

The Kalman filter state sequence organizes the Kalman filter state estimates obtained with equations (5.17) to (5.19):

$$\hat{X}_i = [\hat{x}_i \quad \hat{x}_{i+1} \quad \dots \quad \hat{x}_{i+N-1}] \tag{5.20}$$

5.4.1.4 SSI-DATA algorithm

The DATA-driven Stochastic Subspace Identification algorithm is another time-domain, parametric algorithm. Just like the SSI-COV algorithm, it aims to identify a state-space model in order to compute the modal properties of the system. However, instead of using the covariance between signals, SSI-DATA uses the projection of row space of future output into the row space of the past reference sensors. The concept behind this operation is the retention of all past information that is important to predict the future.

The version of SSI-DATA algorithm implemented in this work is presented in (Peeters, 2000), which in turn is based on (Overschee and Moor, 1996).

The SSI-DATA algorithm starts with the organization of the data in an Hankel matrix:

$$H^{ref} = \frac{1}{\sqrt{N}} \begin{bmatrix} y_0^{ref} & y_1^{ref} & \dots & y_{N-1}^{ref} \\ y_1^{ref} & y_2^{ref} & \dots & y_N^{ref} \\ \dots & \dots & \dots & \dots \\ y_{i-1}^{ref} & y_i^{ref} & \dots & y_{i+N-2}^{ref} \\ y_i & y_{i+1} & \dots & y_{i+N-1} \\ y_{i+1} & y_{i+2} & \dots & y_{i+N} \\ \dots & \dots & \dots & \dots \\ y_{2.i-1} & y_{2.i} & \dots & y_{2.i+N-2} \end{bmatrix} = \begin{bmatrix} Y_{0|i-1}^{ref} \\ Y_{i|2.i-1} \end{bmatrix} = \begin{bmatrix} Y_p^{ref} \\ Y_f \end{bmatrix} \begin{matrix} \updownarrow n_r.i & "past" \\ \updownarrow l.i & "future" \end{matrix} \tag{5.21}$$

with:

$2.i + N - 1$	Total number of data points (per channel)
l	Number of outputs sensors
n_r	Number of reference outputs
i	Parameters of the method to be defined by the analyst

It is common to divide the Hankel matrix into a past reference and a future part, the upper and lower part of the matrix, respectively. Considering this division, the projection operation can then be defined as:

$$P_i^{ref} = Y_f \,/\, Y_p^{ref} = Y_f \left(Y_p^{ref}\right)^T \left(Y_p^{ref} \left(Y_p^{ref}\right)^T\right)^{\dagger} Y_p^{ref} \tag{5.22}$$

The definition of the P_i^{ref} is a very important aspect of the algorithm. In fact, the SSI-DATA algorithm relies on fact that the P_i^{ref} can be factorized as product of the extended observability matrix O_i and the Kalman filter state sequence $\hat{X}_i$:

$$P_i^{ref} = O_i . \hat{X}_i = \begin{bmatrix} C \\ C.A \\ \dots \\ C.A^{i-1} \end{bmatrix} . [\hat{X}_i \quad \hat{X}_{i+1} \quad \dots \quad \hat{X}_{i+N-1}] \tag{5.23}$$

The most computational efficiency way to calculate P_i^{ref} is through the application of the RQ[1] factorization to the Hankel matrix:

$$H^{ref} = \begin{bmatrix} Y_p^{ref} \\ Y_f \end{bmatrix} = R . Q^T \tag{5.24}$$

[1] In a RQ factorization, the Q is an orthonormal matrix ($Q^T . Q = Q . Q^T = I_N$) and R is a lower triangular matrix.

Omitting the columns filled only with zeros in the R matrix, the R and Q matrices can be organized as follow:

$$H^{ref} = \begin{matrix} r.i \\ r \\ l-r \\ l(i-1) \end{matrix} \begin{matrix} \updownarrow \\ \updownarrow \\ \updownarrow \\ \updownarrow \end{matrix} \begin{bmatrix} R_{11} & 0 & 0 & 0 \\ R_{21} & R_{22} & 0 & 0 \\ R_{31} & R_{32} & R_{33} & 0 \\ R_{41} & R_{42} & R_{43} & R_{44} \end{bmatrix} \cdot \begin{bmatrix} Q_1^T \\ Q_2^T \\ Q_3^T \\ Q_4^T \end{bmatrix} \begin{matrix} \updownarrow \\ \updownarrow \\ \updownarrow \\ \updownarrow \end{matrix} \begin{matrix} n_r.i \\ n_r \\ l-n_r \\ l(i-1) \end{matrix}$$

$$\begin{matrix} n_r.i & n_r & l-n_r & l(i-1) & N \\ \leftrightarrow & \leftrightarrow & \leftrightarrow & \leftrightarrow & \leftrightarrow \end{matrix} \tag{5.25}$$

Computing the singular value decomposition of P_i^{ref}, the following factorization is obtained:

$$P_i^{ref} = U.S.V^T = [U_1 \quad U_2].\begin{bmatrix} S_1 & 0 \\ 0 & 0 \end{bmatrix}.\begin{bmatrix} V_1^T \\ V_2^T \end{bmatrix} = U_1.S_1.V_1^T \tag{5.26}$$

From the factorization process, O_i and $\hat{X}_i$ can be calculated according to:

$$O_i = U_1.S_1^{1/2} \tag{5.27}$$

$$\hat{X}_i = O_i^{\dagger}.P_i^{ref} \tag{5.28}$$

On the other hand, the projection of future row spaces into past row spaces can be expressed with the help of the R and Q submatrices:

$$P_i^{ref} = \begin{bmatrix} R_{21} \\ R_{31} \\ R_{41} \end{bmatrix}.Q_1^T \tag{5.29}$$

After the estimation of $\hat{X}_i$, it is necessary to compute the state sequence $\hat{X}_{i+1}$:

$$\hat{X}_{i+1} = O_{i-1}^{\dagger}.P_{i-1}^{ref} \tag{5.30}$$

The extended observability matrix O_{i-1} is obtained after deleting the last l rows of O_i, while P_{i-1}^{ref} is given by:

$$P_{i-1}^{ref} = [R_{41} \quad R_{42}].\begin{bmatrix} Q_1^T \\ Q_2^T \end{bmatrix} \tag{5.31}$$

At this point, the system matrices can be estimated through the application of the system of equations from the state-space model (see equation (5.3)):

$$\begin{bmatrix} X_{i+1} \\ Y_{i|i} \end{bmatrix} = \begin{bmatrix} A \\ C \end{bmatrix} . \hat{X}_i + \begin{bmatrix} W_i \\ V_i \end{bmatrix} \tag{5.32}$$

where the $Y_{i|i}$ matrix can be defined resorting, once again, to the R and Q submatrices:

$$Y_{i|i} = \begin{bmatrix} R_{21} & R_{22} & 0 \\ R_{31} & R_{32} & R_{33} \end{bmatrix} . \begin{bmatrix} Q_1^T \\ Q_2^T \\ Q_3^T \end{bmatrix} \tag{5.33}$$

Once all matrices all calculated, equation (5.32) can be used to estimate matrices A and C. Since it is an overdetermined problem, it can be solved through:

$$\begin{bmatrix} A \\ C \end{bmatrix} = \begin{bmatrix} \hat{X}_{i+1} \\ Y_{i|i} \end{bmatrix} . \hat{X}_i^{\dagger} \tag{5.34}$$

Once state-space matrices A and C are obtained, the modal properties of the structural system can be calculated with the already presented equations (5.13) to (5.16).

An important property of the SSI-DATA algorithm is that it allows to recover the noise covariance matrices Q, R and S from the state-space model equations:

$$\begin{bmatrix} Q & S \\ S^T & R \end{bmatrix} = \begin{bmatrix} W_i \\ V_i \end{bmatrix} . \begin{bmatrix} W_i^T & V_i^T \end{bmatrix} \tag{5.35}$$

Like in the case of the SSI-COV, it is common to calculate the state-state matrices (A and C) for different orders. Then a similar strategy is followed, where the results from the different orders are compared in order to identify the stable poles.

Example

The simulated acceleration time series from the NREL 5MW wind turbine were used to illustrate the SSI-DATA algorithm. For this analysis, three sensors were considered as reference and a value of i = 80 was used.

The stabilization criteria defined in the SSI-COV example were also used in this example. The obtained stabilization diagram is presented in Figure 5.7. The damping values of the stable poles are shown in Figure 5.8.

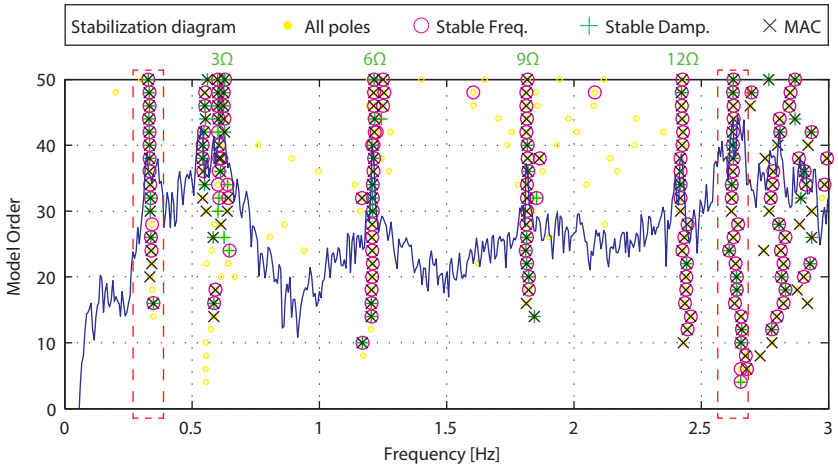

Figure 5.7 – Stabilization diagram obtained with the SSI-DATA method (average spectra at the background)

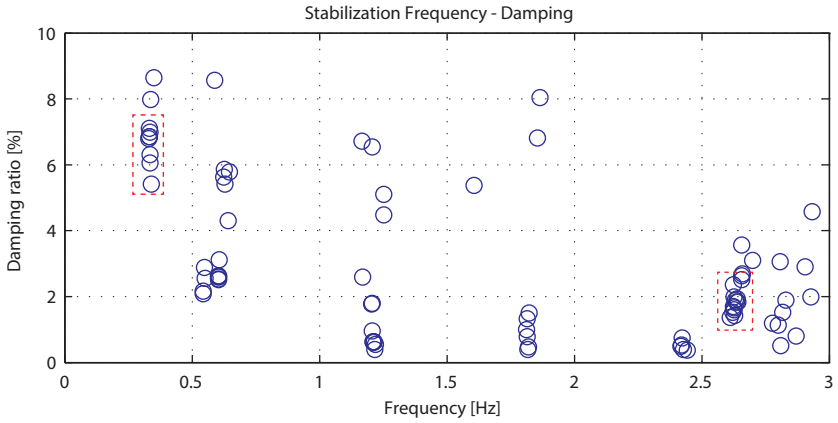

Figure 5.8 – Modal damping ratio estimates for the stable poles

The values of natural frequencies and damping ratios of the two founded vibration modes are shown in Table 5.2. The values are very similar to those previously obtained with the SSI-COV algorithm. Once again, the contribution of the aerodynamic damping is noticeable for the 1st vibration mode.

Table 5.2 – Modal properties: SSI-DATA results vs reference results

Mode	SSI-DATA results		Reference results	
	Natural frequency [Hz]	Damping ratio [%]	Natural frequency [Hz]	Damping ratio [%]
1	0.332	6.85	0.333	0.24
2	2.625	1.98	2.686	1.91

5.4.2 p-LSCF

The third and last identification method covered in this work is the poly-reference Least Squares Complex Frequency Domain method (p-LSCF), also known as Polymax. This is a parametric, frequency-domain method which was initially developed in order to identify the modal characteristics of a system from its frequency response functions (Guillaume, Verboven et al., 2003; Peeters, Auweraera et al., 2004). Later, the previously developed methodology was adapted by (Peeters and Auweraer, 2005) to work based on the output half-spectrum functions, an output-only version of this method. In this work, only this last version is presented.

5.4.2.1 Half-Spectrum

Prior to the application of the p-LSCF routine, the half spectrum matrix should be estimated.

Considering the input excitation as white noise, the input spectrum (S_{uu}) is constant and not dependent on frequency, and the output spectrum is obtained by:

$$S_{yy}(\omega) = H(\omega).S_{uu}.H^H(\omega) \tag{5.36}$$

Considering the modal decomposition of the frequency response function (Heylen, Lammens et al., 2007),

$$H(\omega) = \sum_{k=1}^{n} \frac{\phi_k.{l_k}^T}{i.\omega - \lambda_k} + \frac{{\phi_k}^*.{l_k}^H}{i.\omega - {\lambda_k}^*} \tag{5.37}$$

with:

n	Number of vibration modes in the frequency range under analysis
ϕ_k	Observable components of mode shape k
l_k	Modal participation factor of mode k
λ_k	System poles ($\lambda_k, {\lambda_k}^* = -\xi_k.\omega_k \pm i.\sqrt{1-{\xi_k}^2}.\omega_k$)

it is possible to define the output spectrum as a summation of the contribution of structural vibration modes (Peeters, 2000):

$$S_{yy}(\omega) = \sum_{k=1}^{n} \frac{\phi_k.{g_k}^T}{i.\omega - \lambda_k} + \frac{{\phi_k}^*.{g_k}^H}{i.\omega - {\lambda_k}^*} + \frac{g_k.{\phi_k}^T}{-i.\omega - \lambda_k} + \frac{{g_k}^*.{\phi_k}^H}{-i.\omega - {\lambda_k}^*} \tag{5.38}$$

with:

g_k	Operational reference vector of mode k

As can be observed, the previous equation has four poles for each mode which impose the use of models with twice the order of the system defined by equation (5.37). For this reason, the positive (or half) spectrum is usually used:

$$S_{yy}{}^{+}(w) = \sum_{k=1}^{n} \frac{\phi_k . g_k{}^{T}}{i.\omega - \lambda_k} + \frac{\phi_k{}^{*} . g_k{}^{H}}{i.\omega - \lambda_k{}^{*}} \tag{5.39}$$

Since the frequency response function (5.37) and the half spectrum (5.39) present similar modal decomposition, they both can be parameterized in exactly the same way (Peeters and Auweraer, 2005).

In this work, the Correlogram approach, restricted to the positive time lags of the correlation function, is used for the estimation of the half spectrum:

$$S_{yy}{}^{+}(\omega_j) = \frac{R_{yy}(0)}{2} + \sum_{k=1}^{j_m} R_{yy}(k.\Delta t) e^{-i.\omega_j . k.\Delta t} \tag{5.40}$$

with:

j_m	Number of time lags to analyse

With the Correlogram approach, an exponential window should be applied to the correlations before the use of equation (5.40). This window is important mainly for two reasons: to reduce the effect of leakage and to reduce the influence of the higher time lags, which have a larger variance (Peeters and Auweraer, 2005). The used exponential window follows the equation:

$$w_k = e^{-\beta . k . \Delta t}, \text{for } 1 \leq k \leq j_m \tag{5.41}$$

with:

β	Decay rate of the window

The application of the exponential window leads to biased values of damping for the computed poles. For this reason, the damping values should be corrected according to (Cauberghe, 2004):

$$\xi_{estimated} = \xi_{real} + \frac{\beta}{\omega} \tag{5.42}$$

5.4.2.2 Right Matrix-Fraction Description

The p-LSCF method uses a mathematical representation of the dynamic system called right matrix-fraction description (RMFD). The RMFD is used to model linear time-invariant systems,

parameterizing the transfer function as a right division of two polynomial matrices A^R and B^R (Reynders, 2009):

$$H(s) = B^R.(A^R)^{-1}$$
$$H(s) = \left[\sum_{r=0}^{p_b^R} B_r^R . s^r\right].\left[\sum_{r=0}^{p_a^R} A_r^R . s^r\right] \tag{5.43}$$

with:

A_r^R, B_r^R	Polynomial matrices
p_a^R, p_b^R	Model order of the A^R and B^R matrices, respectively
s	Complex variable

For the implemented version of the p-LSCF method, it is of great importance to refer the conversion from a RMRD model to a state-space model (Reynders, 2009). Assuming that matrices A^R and B^R have the same order (p) and that the degree of the polynomial with the determinant of $A^R(s)$ is equal to $p.l$ (where l refers to the number of structure inputs), the matrices A, B, C and D from the state-space model are obtained through (the subscript $*^R$ is dropped for simplification):

$$A = \begin{bmatrix} -{A_p}^{-1}.A_{p-1} & -{A_p}^{-1}.A_{p-2} & \dots & -{A_p}^{-1}.A_1 & -{A_p}^{-1}.A_0 \\ I & 0 & \dots & 0 & 0 \\ \vdots & \ddots & \dots & \vdots & \vdots \\ 0 & 0 & \dots & I & 0 \end{bmatrix}$$
$$B = \begin{bmatrix} {A_p}^{-1} \\ 0 \end{bmatrix} \tag{5.44}$$
$$C = \begin{bmatrix} B_{p-1} - B_p.{A_p}^{-1}.A_{p-1} & \dots & B_0 - B_p.{A_p}^{-1}.A_0 \end{bmatrix}$$
$$D = B_p.{A_p}^{-1}$$

with:

A_p	State matrix (of order p)
B_p	Input matrix (of order p)
I	Identity matrix

5.4.2.3 p-LSCF algorithm

The p-LSCF method models the half spectrum matrix using a right matrix-fraction description (RMFD) in the discrete-time frequency domain, the z-domain (Magalhães, 2010). This is achieved through the use of matrices A^R and B^R. Considering both matrices as polynomials of the same order p, they are defined as:

$$S_{yy}{}^{+}(\omega_j) = B^R.(A^R)^{-1} = \left[\sum_{r=0}^{p} B_r.\, e^{i.\omega_j.\Delta t.r}\right].\left[\sum_{r=0}^{p} A_r.\, e^{i.\omega_j.\Delta t.r}\right]^{-1} \tag{5.45}$$

Bearing in mind that these matrices contain the modal parameters of the dynamic system, the main goal of this method involves the calculation of A^R and B^R that reduce the approximation error associated to equation (5.45). The nonlinear least squares problem can be simplified to a linear problem according to (Guillaume, Verboven et al., 2003):

$$E^{LS}(\omega_j) = \left[\sum_{r=0}^{p} B_r.\, e^{i.\omega_j.\Delta t.r}\right] - S_{yy}{}^{+}(\omega_j).\left[\sum_{r=0}^{p} A_r.\, e^{i.\omega_j.\Delta t.r}\right] \tag{5.46}$$

Considering the polynomial basis functions evaluated at each frequency (ω_j) organized in one row with $(p+1)$ components:

$$\Omega(\omega_j) = \left[\Omega_0(\omega_j) \quad \Omega_1(\omega_j) \quad \dots \quad \Omega_p(\omega_j)\right] = \left[e^{i.\omega_j.\Delta t.0} \quad e^{i.\omega_j.\Delta t.1} \quad \dots \quad e^{i.\omega_j.\Delta t.p}\right] \tag{5.47}$$

equation (5.46) can be re-written as:

$$E_0{}^{LS} = \Omega(\omega_j).\begin{bmatrix} B_{0_o} \\ B_{1_o} \\ \vdots \\ B_{p_o} \end{bmatrix} + \left[\Omega_0(\omega_j).S_{yy}{}^{+}{}_o \quad \Omega_1(\omega_j).S_{yy}{}^{+}{}_o \quad \dots \quad \Omega_p(\omega_j).S_{yy}{}^{+}{}_o\right].\begin{bmatrix} A_0 \\ A_1 \\ \vdots \\ A_p \end{bmatrix} \tag{5.48}$$

with:

o	Line of the E, B_r or $S_{yy}{}^{+}$ matrix (which varies from 1 to the number of measured outputs - n_o)

Introducing the following definitions:

$$\alpha = \begin{bmatrix} A_0 \\ A_1 \\ \vdots \\ A_p \end{bmatrix} \tag{5.49}$$

$$\beta_0 = \begin{bmatrix} B_{0_o} \\ B_{1_o} \\ \vdots \\ B_{p_o} \end{bmatrix}, \text{with } o = 1, 2, \dots, n_o \tag{5.50}$$

equation (5.48) can be written in a more compact form:

$$E_0{}^{LS}(\beta_o, \alpha) = [X_o \quad Y_o].\begin{bmatrix} \beta_o \\ \alpha \end{bmatrix} \tag{5.51}$$

where:

$$X = \begin{bmatrix} \Omega(\omega_1) \\ \vdots \\ \Omega\left(\omega_{n_f}\right) \end{bmatrix} \tag{5.52}$$

$$Y_0 = \begin{bmatrix} \left(\Omega_0(\omega_1) \quad \dots \quad \Omega_p(\omega_1)\right) \otimes \hat{S}_{yy}{}^{+}{}_o(\omega_1) \\ \dots \\ \left(\Omega_0\left(\omega_{n_f}\right) \quad \dots \quad \Omega_p\left(\omega_{n_f}\right)\right) \otimes \hat{S}_{yy}{}^{+}{}_o\left(\omega_{n_f}\right) \end{bmatrix}, \text{with } o = 1, 2, \dots, n_o \tag{5.53}$$

with:

$\otimes$	Kronecker product operator
ω_1, ω_f	Limits of the frequency range under analysis

Expanding equation (5.51) with all the parameters from matrices α and β, one obtains:

$$E_0{}^{LS} = \begin{bmatrix} X_1 & 0 & \dots & 0 & Y_1 \\ 0 & X_2 & \dots & 0 & Y_2 \\ \vdots & \vdots & \ddots & \vdots & \vdots \\ 0 & 0 & \dots & X_{n_0} & Y_{n_0} \end{bmatrix} \cdot \begin{bmatrix} \beta_1 \\ \beta_2 \\ \vdots \\ \beta_{n_0} \\ \alpha \end{bmatrix} = J.\theta \tag{5.54}$$

The solution for the identification problem can be solved through $J.\theta = 0$. However, this is very computationally demanding. For this reason, a different approach is usually followed. It consists on determining the model parameters through a linear least squares cost function obtained by adding all the squared elements of the matrix ${E_0}^{LS}$ evaluated at each discretized frequency:

$$\epsilon = \sum_{o=1}^{n_o} \sum_{r=1}^{n_r} \sum_{j=1}^{n_f} E_{o,r}(\omega_j).E_{o,r}(\omega_j)^* \tag{5.55}$$

with:

n_r	Number of reference outputs

From equations (5.52) and (5.53), (5.55) can be written as:

$$\varepsilon = (\beta_o, \alpha) = \sum_{o=1}^{n_o} tr\{E_o(\beta_o, \alpha)^H.E_o(\beta_o, \alpha)\} = \sum_{o=1}^{n_o} tr\left\{\begin{bmatrix}{\beta_o}^T & \alpha^T\end{bmatrix}.\begin{bmatrix}R_o & S_o\\ {S_o}^T & T_o\end{bmatrix}.\begin{bmatrix}\beta_o\\ \alpha\end{bmatrix}\right\}$$
$$R_o = Re({X_o}^H.X_o); S_o = Re({X_o}^H.Y_o); T_o = Re({Y_o}^H.Y_o) \tag{5.56}$$

with:

$tr(*)$	Trace of the matrix *

Thus, the minimum of the cost function is obtained with:

$$\frac{\partial\varepsilon(\beta_o, \alpha)}{\partial\beta_o} = 2(R_o.\beta_o + S_o.\alpha) = 0 \tag{5.57}$$

$$\frac{\partial\varepsilon(\beta_o, \alpha)}{\partial\alpha} = 2\sum_{o=1}^{n_o}({S_o}^T.\beta_o + T_o.\alpha) = 0 \tag{5.58}$$

Eliminating the unknowns β_0, the size of the system of equations can be reduced:

$$2\sum_{o=1}^{n_o}(R_o.\beta_o + S_o.\alpha) = 0 \Leftrightarrow \beta_o = -{R_o}^{-1}.S_o.\alpha \tag{5.59}$$

Then, the α matrix is obtained through:

$$2\sum_{o=1}^{n_o}(T_o - {S_o}^T.{R_o}^{-1}.S_o)\alpha = 0 \Leftrightarrow M.\alpha = 0 \tag{5.60}$$

In order to avoid the trivial solution $\alpha = 0$, a constraint should be imposed on the parameters. In (Cauberghe, 2004), it is suggested to impose A_0 (from the α matrix) as an identity matrix. Bearing this in mind, α is obtained with:

$$M.\alpha = 0 \Leftrightarrow \overset{\begin{matrix} & n_r & p.n_r \end{matrix}}{\begin{matrix} n_r \\ p.n_r \end{matrix}\left[\begin{array}{c|c} M_{aa} & M_{ab} \\ \hline M_{ba} & M_{bb} \end{array}\right]}.\begin{bmatrix} I \\ - \\ A_1 \\ \vdots \\ A_p \end{bmatrix} = \begin{bmatrix} 0 \\ - \\ 0 \\ \vdots \\ 0 \end{bmatrix} \Leftrightarrow M_{bb}.\alpha_b = -M_{ba} \Leftrightarrow \tag{5.61}$$

$$\alpha_b = -{M_{bb}}^{-1}.M_{ba} \Rightarrow \alpha = \begin{bmatrix} I \\ -{M_{bb}}^{-1}.M_{ba} \end{bmatrix}$$

Once α is defined, it is possible to compute the β_r matrix using equation (5.59), which defines the RMFD model.

The next step in the algorithm is the definition of the companion matrix:

$$Co = \begin{bmatrix} -{A_p}^{-1}.A_{p-1} & -{A_p}^{-1}.A_{p-2} & \dots & -{A_p}^{-1}.A_1 & -{A_p}^{-1}.A_0 \\ I & 0 & \dots & 0 & 0 \\ \vdots & \ddots & \dots & \vdots & \vdots \\ 0 & 0 & \dots & I & 0 \end{bmatrix} \tag{5.62}$$

If matrix A from equation (5.44) is compared to matrix Co from equation (5.62) it is easily observed their similarity. Thus, Co represents the matrix A from the state-space model. The remaining matrices from the model can be computed through equation (5.44).

With the state-space model defined, the modal parameters of the dynamic system can be calculated using, once again, the equations (5.13) to (5.16).

As referred in the case of the SSI-COV algorithm, there is no prior knowledge about what model order (p) will produce the best results. For this reason, several orders are computed and the results are usually presented in a stabilization diagram.

Example

The application of the p-LSCF algorithm to the simulated acceleration signals obtained for 3 degrees of freedom of the NREL 5MW wind turbine model was performed from correlation functions with 256 points. Then, the half-spectrum functions were obtained for subsequent estimation of matrices A and B. These functions are shown in Figure 5.9.

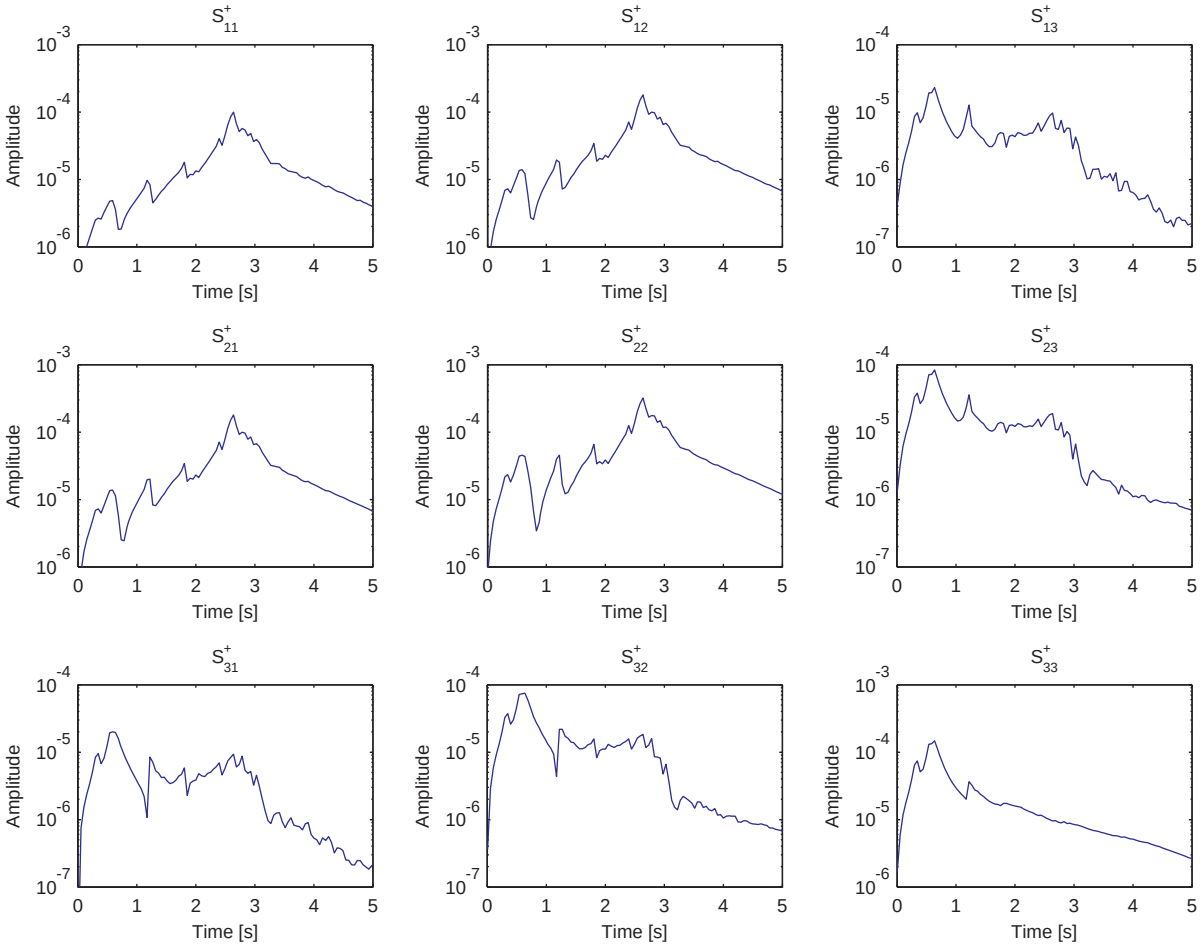

Figure 5.9 – Half-spectrum functions

The stabilization diagram for models with order between 2 and 35 was created considering the same stabilization criteria defined for the SSI-COV and SSI-DATA algorithms (Figure 5.10). The modal damping ratio results associated with the stable poles are shown in Figure 5.11.

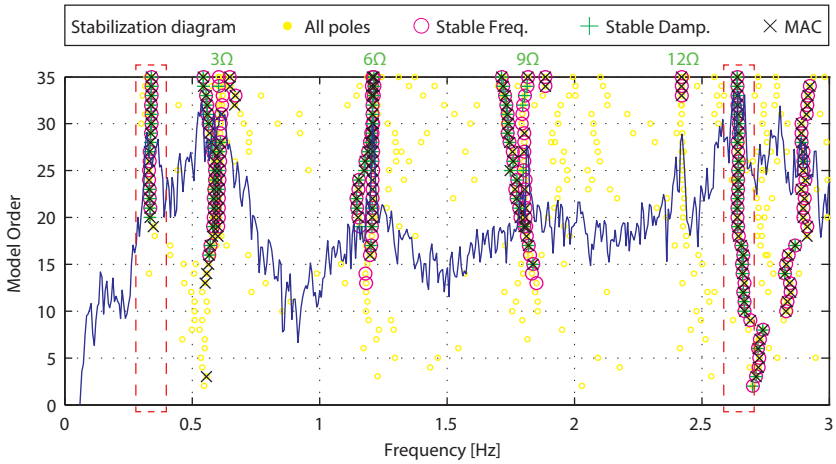

Figure 5.10 – Stabilization diagram obtained with the p-LSCF method (average spectra at the background)

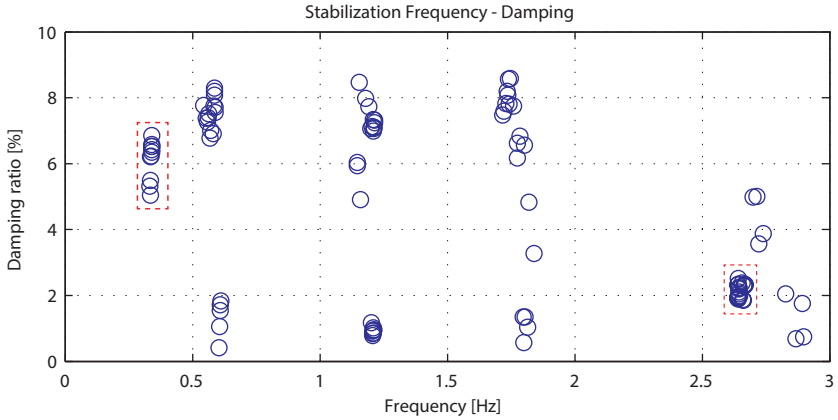

Figure 5.11 –Modal damping ratio estimates for the stable poles

The final results obtained with p-LSCF algorithm are presented in Table 5.3. The results are similar to those previously obtained with the other two identification algorithms.

Table 5.3 – Modal properties: p-LSCF results vs benchmark results

Mode	p-LSCF results		Benchmark results	
	Natural frequency [Hz]	Damping ratio [%]	Natural frequency [Hz]	Damping ratio [%]
1	0.339	6.791	0.333	0.24
2	2.641	1.99	2.686	1.91

5.5 MODAL RESPONSE ESTIMATION

One interesting post-processing methodology of the presented stochastic identification methods allows using the computed state-space matrices to reconstruct the measured acceleration signals as a sum of modal contributions. With this tool, the measured acceleration signals are splited into several modal responses. A modal response is defined as the acceleration response of a SDOF with the same modal properties of the considered mode.

This result is obtained with the definition of a forward innovation model from the state-space model matrices. This methodology is presented for the three parametric stochastic identification models: SSI-DATA, SSI-COV and p-LSCF.

5.5.1 FORWARD INNOVATION MODEL

The state-space model, presented in 5.4.1.1, can also be represented under different forms. One of these representations is the forward innovation model. This representation is obtained with the application of the Kalman filter to the stochastic state-space model (Overschee and Moor, 1996):

$$\begin{aligned} z_{k+1} &= A.z_k + K.e_k \\ y_k &= C.z_k + e_k \end{aligned} \tag{5.63}$$

with:

z_k	State vector
e_k	Innovation sequence

The innovation sequence e_k is a white noise vector, with the covariance matrix defined as:

$$E\left[e_p.e_q^T\right] = R_e.\delta_{pq} \tag{5.64}$$

The forward innovation model is thus defined with the matrices K and R_e, in addition to the state-space matrices A and C already defined. These matrices can be obtained through the solution of the discrete Riccati equation [(Peeters, 2000)]:

$$P = A.P.A^T + (G - A.P.C^T)(R_0 - C.P.C^T)^{-1}(G - A.P.C^T)^T \tag{5.65}$$

with:

P	Forward state covariance matrix ($P = E[z_k.z_k^T]$)
G	Next-state output correlation matrix
R_0	Correlation matrix of the outputs (with zero time lag)

After calculation of the forward state covariance matrix, the covariance matrix of the innovation sequence is obtained as:

$$R_e = R_0 - C.P.C^T \tag{5.66}$$

and, finally, the Kalman gain is computed according to:

$$K = (G - A.P.C^T)R_e^{-1} \tag{5.67}$$

5.5.2 Application to the Stochastic Identification Algorithms

The methodology herein presented for modal response estimation is applied to the three parametric identification algorithms.

Initially, the methodology for the SSI-DATA algorithm is introduced. It is based on the technique presented in (Peeters, 2000). Then, an adaptation of this methodology for the SSI-COV and p-LSCF is introduced. This constitutes one of the new developments included in the present work, with practical relevance in the context of the continuous dynamic monitoring (see Chapter 7).

5.5.2.1 Application to the SSI-DATA algorithm

The definition of the forward innovation model after the SSI-DATA algorithm (introduced in section 5.4.1.4) requires the computation of the next-state output correlation matrix G and the correlation matrix R_0. These matrices can be directly calculated once the noise covariance matrices R, Q and S from the state-space model are recovered (equation (5.35)).

Then, the Lyapunov equation is used to obtain Σ:

$$\Sigma = A.\Sigma.A^T + Q \tag{5.68}$$

Finally, the R_0 and G matrices can be computed as:

$$R_0 = C.\Sigma.C^T + R \tag{5.69}$$

$$G = A.\Sigma.C^T + S \tag{5.70}$$

Once these matrices are obtained, it is possible to define a forward innovation model (equation (5.63)) through the application of equation (5.65) to (5.67).

The forward innovation model from equation (5.63) can then be defined in the modal basis:

$$z_{m,k+1} = \Lambda_d . z_{m,k} + K_m . e_k$$
$$y_k = V . z_{m,k} + e_k \tag{5.71}$$

with:

$z_{m,k}$	Modal state vector ($z_{m,k} = \Psi^{-1} . z_k$)
K_m	Modal Kalman gain ($K_m = \Psi^{-1} . K$)

The advantage of using the model in a modal basis is that, since Λ_d is a diagonal matrix, $z_{m,k}$ represents the separate contribution of each vibration mode to the total response signal. Rearranging equation (5.71), it can be written as:

$$z_{m,k+1} = (\Lambda_d - K_m . V) z_{m,k} + K_m . y_k$$
$$e_k = -V . z_{m,k} + y_k \tag{5.72}$$

At this point, it is possible to use the system of equations (5.72) as a state-space model in order to estimate the modal state sequence $z_{m,k}$ and the innovation sequence e_k from the measured acceleration y_k. The measured acceleration can then be reconstructed as the sum of an estimated response part ($\hat{y}_k$) with an estimation error part (e_k):

$$y_k = \hat{y}_k + e_k = \left(V . z_{m,k}\right) + e_k \tag{5.73}$$

In the previous equation, $\hat{y}_k$ represents the estimated contribution to the response from the vibration modes, while e_k represents the estimation error, i.e., the part of the response that cannot be explained by the stochastic state-space model.

In addition, the acceleration signal estimation $\hat{y}_k$ can be also thought as a sum of contributions from n single vibration modes. The estimated modal response can be split in single modal responses as:

$$\hat{y}_k = \sum_{i=1}^{n} \hat{y}_{i_k} = \sum_{i=1}^{n} v_i . z_{m,k_i} \tag{5.74}$$

with:

y_{i_k}	Estimated modal response of the i-th vibration mode
v_i	Column vector with the observable components of the mode shape of the i-th vibration mode
z_{m,k_i}	Array vector from the modal state vector corresponding to the i-th vibration mode

Naturally, $\hat{y}_{i_k}$ is a complex modal response. However, if the complex modal response of the pair of complex-conjugated poles from the same vibration mode is combined, the real modal response is obtained.

5.5.2.2 Application to the SSI-COV algorithm

The methodology presented in 5.5.2.1 uses specific results obtained with the SSI-DATA algorithm to estimate the modal response. The adaptation of this methodology to the SSI-COV cannot be done directly since the noise covariance matrices (Q, R and S) from the state-space model are not obtained with this method.

Thus, a procedure to estimate the modal response from the identified state matrix A and output matrix C is introduced in this section. In its development, some steps from the SSI-DATA algorithm are used in order to estimate the noise covariance matrices from the state-space model.

The procedure starts with the computation of the Hankel matrix with the projection of row space of future output into the row space of the past reference sensors (equation (5.21). Then, the RQ factorization of the Hankel matrix is performed (equation (5.24) in order to compute the matrices $\hat{X}_i$, $\hat{X}_{i+1}$ and $Y_{i|i}$, respectively equations (5.28), (5.30) and (5.33).

Then, the residuals from the state-space model can be computed with the A and C matrices obtained with the SSI-COV algorithm and with the calculated matrices:

$$\begin{bmatrix} W_i \\ V_i \end{bmatrix} = \begin{bmatrix} \hat{X}_{i+1} \\ Y_{i|i} \end{bmatrix} - \begin{bmatrix} A \\ C \end{bmatrix} . \hat{X}_i \tag{5.75}$$

Finally, the noise covariance matrices are obtained with:

$$\begin{bmatrix} Q & S \\ S^T & R \end{bmatrix} = \begin{bmatrix} W_i \\ V_i \end{bmatrix} . [W_i^T \quad V_i^T] \tag{5.35}$$

At this point, it is now possible to use the methodology introduced in 5.5.2.1.

The validation of this procedure is illustrated through a simple example in the Appendix A.

5.5.2.3 Application to the p-LSCF algorithm

The procedure introduced in section 5.5.2.1 can also be used with the results from the p-LSCF, since it is possible to define a state-space model from a RMFD model (section 5.4.2.2). However, some additional challenges are present in its application.

The main restriction to the application of this procedure to the state-space matrices obtained with the p-LSCF algorithm is that the resolution of the Riccatti equation requires that all poles λ (see equation (5.37)) from the state matrix A are stable (Overschee and Moor, 1996).

In order to evaluate the stability of the poles and exclude the unstable poles (i.e. associated with negative modal damping ratios), the unit circle can be used. The unit circle limits the stable region of the poles in the z-domain. The radius of pole i in the unit circle is given by:

$$z_i = e^{-\xi_i.\omega_i.\Delta t} \tag{5.76}$$

with:

ω_i	Natural frequency (of the pole i)
Δt	Time sampling interval

The unit circle is illustrated in Figure 5.12.

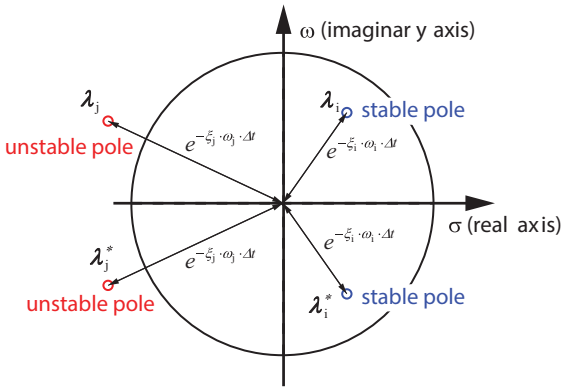

Figure 5.12 – Identification of a stable and unstable pole in the unit circle

Since it is desired to only account for the stable poles (and the respective vibration modes), it is necessary to eliminate the unstable poles from the A and C state-space model matrices.

In this work, a truncation based methodology of the modal state-space model is used. The identified A and C matrices are initially transformed into the modal basis:

$$\Lambda = \Psi^{-1}.A.\Psi \tag{5.77}$$

$$V = C.\Psi \tag{5.78}$$

As referred in section 5.4.1.1, the Λ is a diagonal matrix with the eigenvalues of the system and V is a matrix with the observable components of the vibration modes in the columns. After the transformation from equations (5.77) and (5.78), the eigenvalues corresponding to the unstable poles can now be removed, deleting the corresponding lines and columns from matrix Λ. Similarly, the columns from the V matrix can now be removed in accordance to the deleted eigenvalues. This truncation operation is illustrated in Figure 5.13.

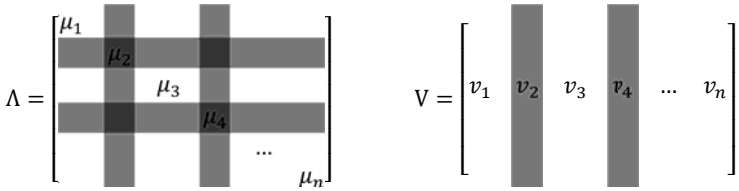

Figure 5.13 – Elimination of the unstable poles in the matrix Λ and V (truncation operation)

After the truncation is complete, the state-space model can be recovered from the modal basis through the inversion of the equations (5.77) and (5.78). After this step, it is possible to follow the procedure presented for the SSI-COV algorithm in section 5.5.2.2.

The validation of this procedure is illustrated through a simple example in the Appendix A.

Example

With the aim of illustrate the methodology presented to decompose the acceleration time series into modal responses, the procedure was applied to the acceleration time series numerically generated with the NREL 5MW wind turbine model. For that purpose, the results obtained with the application of the SSI-DATA algorithm (presented in the example of the section 5.4.1.4) were used as reference for the validation of the post-processing tool applied with the other identification algorithms.

A state-space model of order 50, obtained with the SSI-DATA, was used to define the forward innovation model. Since the resonance response of the wind turbine at the harmonics frequencies was identified as a regular vibration mode (Figure 5.7), it is also possible to estimate the response of the structure at these frequencies.

Figure 5.14 presents the modal responses of top sensor S3 for the two tracked vibration modes (1 FA and 2 FA) and the two first harmonics (3Ω and 6Ω). The responses obtained illustrate the importance of the 1st vibration mode (1 FA) and the 3Ω harmonic excitation to the motion at the top of the wind turbine tower.

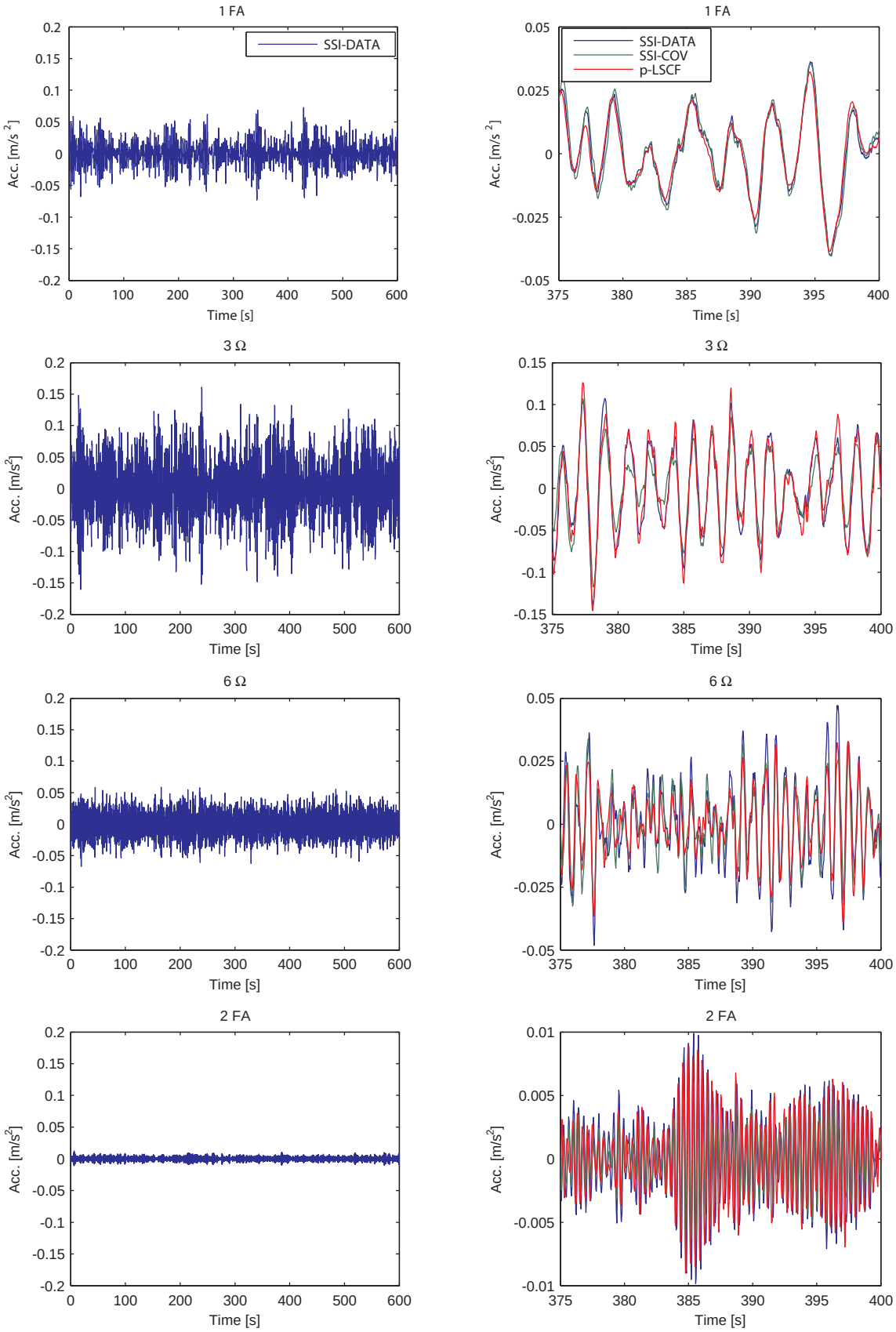

Figure 5.14 – Modal responses of the top sensor S3 (only the 1 FA and 2 FA modes and the 3Ω and 6Ω harmonics were considered)

5.5.3 Quantification of the Modal Contributions

An interesting outcome from the decomposition of the original signal into several modal acceleration responses is that the relative contribution from each of these modes can be quantified (Cara, Juan et al., 2013).

The procedure starts after the estimation of the modal acceleration response from each vibration mode and the associated error:

$$y = \hat{y} + e \tag{5.73}$$

with:

y	Time series of the original signal
$\hat{y}$	Time series of the estimated modal response
e	Time series of the innovations

Equation (5.73) can be also written as a sum of the estimated vibration mode acceleration:

$$y = \sum_{i=1}^{n} \hat{y}_i + e \tag{5.73}$$

with:

$\hat{y}_i$	Time series of the estimated modal response of the i-th vibration mode

Multiplying each element from the previous equation by the transpose of y and retaining only the diagonal elements of the matrices, the following is obtained:

$$\begin{gathered}(y.y^T)_D = \left(\sum_{i=1}^{n} \hat{y}_i . y^T\right)_D + (e.y^T)_D \Rightarrow \\ (y.y^T)_D = (\hat{y}_1.y^T)_D + (\hat{y}_2.y^T)_D + \cdots + (\hat{y}_n.y^T)_D + (e.y^T)_D\end{gathered} \tag{5.79}$$

with:

$(*)_D$	Diagonal elements of matrix *

In the previous equation, the diagonal elements of $\hat{y}_i.y^T$ and $e.y^T$ represent, respectively, the covariance between the estimated modal response from mode i and the original signal and the covariance between the estimation error and the original signal. Normalizing equation (5.79), one obtains:

$$\left[(y.y^T)_D{}^{-1}.(y.y^T)_D\right] = \left[(y.y^T)_D{}^{-1}.\left(\sum_{i=1}^{n}\hat{y}_i.y^T\right)_D\right] + \left[(y.y^T)_D{}^{-1}.(e.y^T)_D\right] \Rightarrow$$
$$[\underline{1}] = \Delta_m + \Delta_e \Rightarrow [\underline{1}] = \Delta_1 + \Delta_2 + \cdots + \Delta_n + \Delta_e \tag{5.80}$$

with:

$[\underline{1}]$	Vector filled with elements equal to one
Δ_i	Vector with the contribution of the estimated modal response of the i-th vibration mode
Δ_e	Vector with the contribution of the estimation error

The procedure presented so far is referred to an acceleration signal from a single sensor. Thus, the contribution of each vibration mode to the original signal is only referred to that single sensor. However, it is common to have more than one sensor installed on the structure. In that case, a global assessment of the modal contribution can be obtained with the mean value of the Δ_i and Δ_e vectors obtained from the l installed sensors:

$$\delta_i = \frac{1}{l}\sum_{n=1}^{l}\Delta_i(n) \tag{5.81}$$

$$\delta_e = \frac{1}{l}\sum_{n=1}^{l}\Delta_e(n) \tag{5.82}$$

with:

δ_i	Global contribution of the i-th vibration mode
δ_e	Global contribution of the estimation error

Example

The acceleration signals obtained with the NREL5 MW wind turbine model were once again used to illustrate the procedure presented in this section.

In that sense, the modal responses obtained with the forward innovation model defined with the state-space model of order 50 from the SSI-DATA algorithm was used to estimate the modal contribution to the recorded acceleration from the 3 sensors. Once again, only the 1 FA and 2 FA modes and the two first rotor harmonics were considered.

Figure 5.15 presents the contribution of each considered modes/ harmonic excitations for the three sensors, together with the estimated error (Δ_e). It should be noted that the sum of the presented

contributions (including error) is not equal to 1, since some residual contributions from the other modes/ harmonic excitations are not presented in the figure.

The acceleration time series recorded by the sensors S1 and S2 are clearly dominated by the 2 FA. It is an expected result because the mode shape of this mode presents higher modal amplitudes at the positions of these sensors than the 1 FA mode. On the other hand, the acceleration signal captured by the S3 sensor is dominated by the 3Ω harmonic excitation and, in a smaller scale, by the 1 FA mode. This is justified by the fact that motion configuration of this mode/ harmonic presents its higher modal amplitude at the top of the tower.

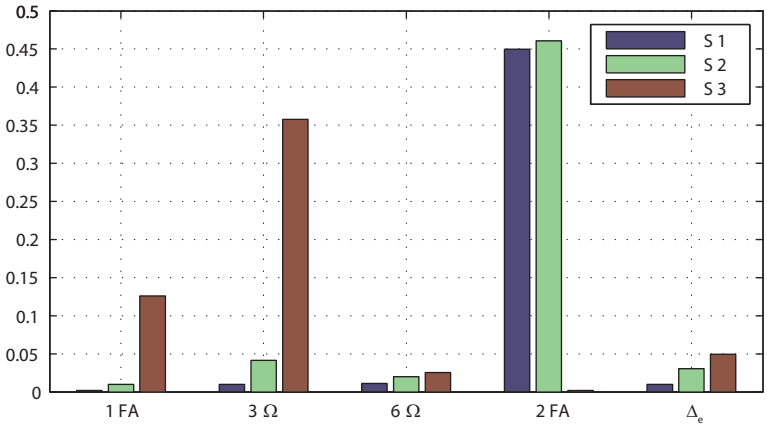

Figure 5.15 – Modal contributions from the 1 FA and 2 FA modes, 3Ω and 6Ω harmonics and error to the acceleration signals obtained for sensors S1, S2 and S3 with the NREL 5MW wind turbine model

5.6 AUXILIARY TOOLS TO OVERCOME OMA VIOLATIONS

In section 5.3, some violations of the OMA assumptions were presented and discussed. It was justified why, under operating conditions, OMA identification algorithms (such as the ones presented in section 5.4) cannot be directly applied to wind turbine signals in the same way as when under parked conditions. Thus, alongside with the application of the identification algorithms, some auxiliary tools may need to be used. Reference should be made that for some strategies presented below, some input information, usually obtained with the data collected by the SCADA system, is required.

5.6.1 COORDINATE TRANSFORMATION - NACELLE ROTATION

There are some alternative procedures to handle the problem of structure time-variance due to nacelle rotation. The choice between then should be made according to the quality of the data available from the SCADA system.

Considering sensors installed in the tower, framed into a global stationary reference, it is necessary to apply a coordinate transformation to the collected signals so that these will follow the nacelle orientation, defined by the fore-aft (FA) and side-side (SS) directions (moving reference). On the other hand, if sensors are installed in the nacelle, no transformation is required since they are framed into the moving reference.

Yaw angle data acquisition rate is high enough

When yaw angle data is available with an acquisition rate sufficiently high (equal to the acquisition rate of the sensors or high enough to track the nacelle rotation with a good precision), the raw data obtained from the sensors should suffer a coordinate transformation according to:

$$\begin{bmatrix} X'(t,\theta) \\ Y'(t,\theta) \end{bmatrix} = R(\theta).\begin{bmatrix} X(t) \\ Y(t) \end{bmatrix}$$
$$R(\theta) = \begin{bmatrix} cos(\theta) & sin(\theta) \\ -sin(\theta) & cos(\theta) \end{bmatrix} \quad (5.83)$$

with:

X', Y'	Nacelle (moving) reference coordinates
X, Y	Tower (stationary) reference coordinates
R	Rotation matrix
θ	Angle between the tower sensors referential and nacelle orientation (see Figure 5.16)

This transformation leads to the projection of the collected acceleration time series in the FA and SS directions (Figure 5.16).

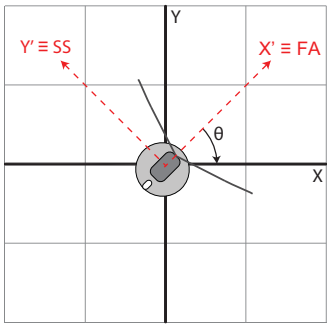

Figure 5.16 – Illustration of the angle between the sensors referential and nacelle orientation (θ)

Yaw angle data consists of time-averaged values

When the data from yaw angles is only available in the form of time-averaged values (e.g. 10 minutes mean values), there are two possible strategies to proceed with the coordinate transformation:

- The same rotation matrix (equation (5.83)) should be used for the entire raw data from that period;
- As an alternative, OMA algorithms can be applied directly to the raw data without any pre-processing. Then, the configuration of the mode shapes should be multiplied by the same rotation matrix of equation (5.83).

This approach only provides adequate results when the nacelle does not suffer important rotations during the adopted time interval.

5.6.2 Coordinate Transformation - Rotor Rotation

The spinning rotor, as referred earlier, is another source of violation of the structure time-invariance requirement. The rotation of the rotor with respect to the nacelle introduces time-dependence in the mass, stiffness and gyroscopic matrices (Ewins, 2000). In experimental testing, a coordinate transformation is required in situations where sensors are located in the rotating components of the rotor (such as blades), under operating conditions.

The referred violation can be faced through Multi-Blade Coordinate (MBC) transformation (also named as Coleman transformation) (Hansen, 2007; Bir, 2008). The MBC transformation helps integrate the dynamics of individual blades into the whole structural system, converting the motion of each blade in the rotating blade frame into the ground-fixed frame (the same of the tower coordinate system). With this transformation, the periodic terms in the equations of motion are eliminated (Hansen, 2007). The MBC transformation is defined, for the most common case (3-bladed rotor wind turbines), as (Bir, 2008):

$$a_0 = \frac{1}{3}\sum_{i=1}^{3} q_i$$
$$a_1 = \frac{2}{3}\sum_{i=1}^{3} q_i.\cos(\psi_i) \quad (5.84)$$
$$b_1 = \frac{2}{3}\sum_{i=1}^{3} q_i.\sin(\psi_i)$$

with:

a_0, a_1, b_1	Multi-blade coordinates (ground-fixed frame)
q_i	Deflection of the i-th blade (rotating frame)
ψ_i	Azimuth location of the i-th blade: $\psi_i \approx \Omega.t + (i-1).\frac{2\pi}{3}$ (it is assumed that for $\psi = 0$, the blade is vertically up)

The new degrees of freedom in the ground-fixed frame (a_0, a_1 and b_1) represent now a cumulative behaviour of all rotor blades, instead of each individual blade (q_i). Two examples of the physical meaning of the new coordinates is presented in (Hansen, 2007), for operating conditions with a low value of blades pitch angle:

If $q_i \rightarrow$ flapwise blade deflection shape (Figure 5.17)

$a_0 \rightarrow$ simultaneous flapwise motion of all blades

$a_1 \rightarrow$ tilt motions of the rotor

$b_1 \rightarrow$ yaw motions of the rotor

If $q_i \rightarrow$ edgewise blade deflection shape

$a_0 \rightarrow$ simultaneous edgewise motion of all blades

$a_1 \rightarrow$ horizontal motions of the rotor

$b_1 \rightarrow$ vertical motions of the rotor

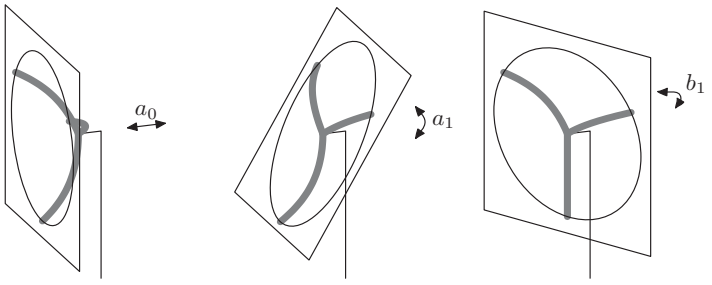

Figure 5.17 – Multi-blade coordinate when qi represents flapwise motion (Skjoldan, 2011)

The inverse transformation (from ground-fixed coordinates to the rotating frame) is given by:

$$q_i = a_0 + a_1.\cos(\psi_i) + b_1.\sin(\psi_i) \tag{5.85}$$

In (Tcherniak, Chauhan et al., 2010b), a routine for the application of MBC transformation to records from sensors located on the rotor is proposed:

1. The signals of points located on the blades and tower (and also other locations) and the azimuth angle are acquired as time histories;
2. The signals data from the rotating parts are subjected to MBC transformation using the azimuth data. The signals data from the non-rotating components (tower and nacelle) are not transformed;
3. The new signals obtained with MBC transformation and the signals from non-rotating components are the inputs to OMA identification algorithms;
4. The frequencies and damping values are determined;
5. The resulting mode shapes are subjected to inverse MBC transformation (5.85); the results can be directly animated overlaid by the rotor rotation.

Although MBC is an useful tool to eliminate the periodic effect of the rotor, there are some practical aspects that may complicate its application (Ozbek, Meng et al., 2013):

- If the measurements are only taken from one blade, the transformation cannot be applied;
- The measurements must be taken at equal radial locations for all the blades;
- The application of the MBC transformation requires the knowledge of the instantaneous position of the blade (azimuth angle).

Two last comments should be made about the use of MBC transformation to wind turbines. There is one fundamental assumption of this method (verified for almost all wind turbines): the rotor has to be isotropic, which means, the all the blades are identical, identically pitched and symmetrical mounted on the hub (Hansen, 2003). Another important aspect about the effects of utilization of this technique is that, although it removes the periodicity from the matrices, it does not eliminate the periodicity character of the excitation forces.

5.6.3 Periodic Nature of the Excitation Forces

The periodic nature of the excitation is probably the most difficulty OMA assumption violation to overcome. Since the structural response contains harmonic components due to rotor rotation, the modal identification process can be considerable hindered (or even become impossible). Thus, auxiliary processing tools may be important to remove the pollution in the signal due to the presence of harmonics. In that sense, three methodologies are introduced.

5.6.3.1 Kurtosis-based Methods

One alternative method associated to the detection of harmonics is based on the properties of kurtosis. Kurtosis is a statistical measure that can be used to estimate how peaked or flat a distribution is when compared to the normal distribution. It is defined as:

$$\beta_{2_{(x|\mu,\sigma)}} = \frac{E[(x-\bar{x})^4]}{\sigma^4} \tag{5.86}$$

with:

$E[\ \ ]$	Expectation value
$\bar{x}$	Mean value of the distribution
σ	Standard deviation of the distribution

where $\beta_2 > 3$, $\beta_2 = 3$ and $\beta_2 < 3$ define distributions as leptokurtic (distribution more peaked than normal distributions), mesokurtic (normal distribution) and platykurtic (more flat than normal distribution), respectively. It is common to express this measure in the form of excess kurtosis:

$$\beta^*_{2_{(x|\mu,\sigma)}} = \frac{E[(x-\bar{x})^4]}{\sigma^4} - 3 \tag{5.87}$$

With this designation, leptokurtic, mesokurtic and platykurtic distributions will be defined as $\beta_2{}^* > 0$, $\beta_2{}^* = 0$ and $\beta_2{}^* < 0$.

This kurtosis can also be used as an indicator of the presence of harmonic components (Brincker, Andersen et al., 2000):

- It is assumed from the central limit theorem that any linear combination of a large number of random variable tends to a normal distribution independently of the statistical properties of the variables. Thus, the stochastic structural response, due to loading from a sufficient large number of independent sources, will be approximately Gaussian (see Figure 5.18 for the Gaussian probability function). For this reason, the value of excess kurtosis will be $\beta_2{}^* = 0$ (mesokurtic distribution);
- In the case of a pure harmonic, the probability function presents a characteristic shape with two symmetric peaks approaching infinity (Figure 5.18). As result, it will present a value of excess kurtosis of $\beta_2{}^* = -1.5$.

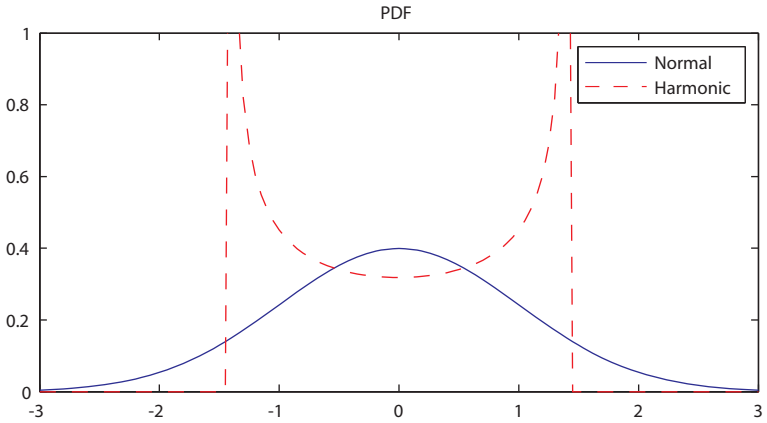

Figure 5.18 – Normalized probability density function of a pure structural mode (blue line) and pure harmonic component (red dashed line)

Based on these properties, some methodologies were proposed (Jacobsen, Andersen et al., 2006; Andersen, Brincker et al., 2007; Jacobsen, Andersen et al., 2008). However, some difficulties are expected regarding the application of these methods to the modal identification of wind turbines. In fact, it is referred that when the harmonic is located closed to the natural frequency of a structural mode, the results may deteriorate (Jacobsen, Andersen et al., 2008).

5.6.3.2 Cepstral Method

The Cepstral method is another methodology aiming to eliminate the effect of harmonics in a signal. The concept of cepstrum was initially introduced with the aim of detecting echoes in seismic analysis (Bogert, Healy et al., 1963). This method consists in editing the vibration signals in the cepstrum domain. The Cepstral method proposed in (Randall and Sawalhi, 2011) consists in editing the real cepstrum while keeping the original phase. The cepstrum can be obtained as:

$$C(t) = iFFT\left[\log\left(X(\omega)\right)\right] \tag{5.88}$$

where:

$$X(\omega) = FFT\left(x(t)\right) = |X(\omega)|.\, e^{i.angle\left(X(\omega)\right)} \tag{5.89}$$

with:

$\lvert X(\omega)\rvert$	Magnitude of the Fourier transformation of $x(t)$
$angle\left(X(\omega)\right)$	Phase angle of the Fourier transformation of $x(t)$

and, consequently:

$$\log\big(X(\omega)\big) = \ln(|X(\omega)|) + i.arg(\omega) \tag{5.90}$$

Equation (5.88) will result in the "complex cepstrum". On the other hand, if the phase of X is set to zero, "real cepstrum" is obtained.

The main steps of this methodology are presented in Figure 5.19. It consists on the combination of the edited "real cepstrum" (where influence of the harmonics is removed) with the unmodified phase information. The complex spectrum is then retrieved by exponentiation.

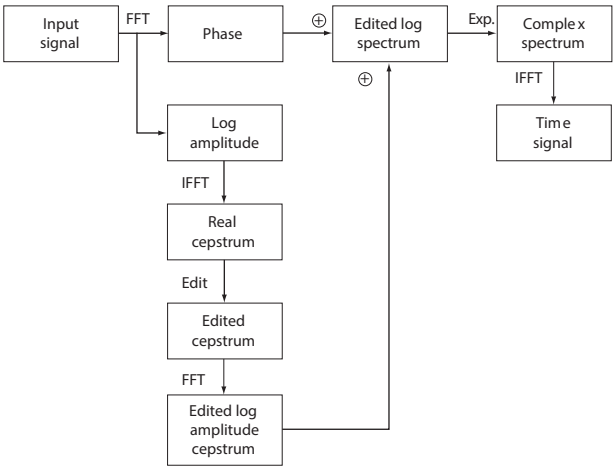

Figure 5.19 – Algorithm of the Cepstral method used to eliminate the effect of harmonics in signals (adapted from (Randall and Sawalhi, 2011))

The application of this methodology to vibration signals from wind turbine is described in the literature. The results indicated that the use of the cepstral method is still not a definite solution to solve this problem. In some cases (Manzato, White et al., 2013), the application of the cepstral method led to an improve of the results, while in other situations (Manzato, Devriendt et al., 2014), its application spoiled the modal identification.

5.6.3.3 Time Synchronous Averaging

The Time Synchronous Averaging (TSA) method aims to transform a signal containing time-varying frequency components (as varying rotor speed) into a constant frequency component. The main feature of this method is the digitally resample of the original signal (acquired with a constant time interval – time domain) to a constant angular spacing – angular domain. This resampling process is illustrated with the help of Figure 5.20. After this step, the "varying" harmonic, transformed into a "constant" frequency harmonic, should be eliminated with a filter.

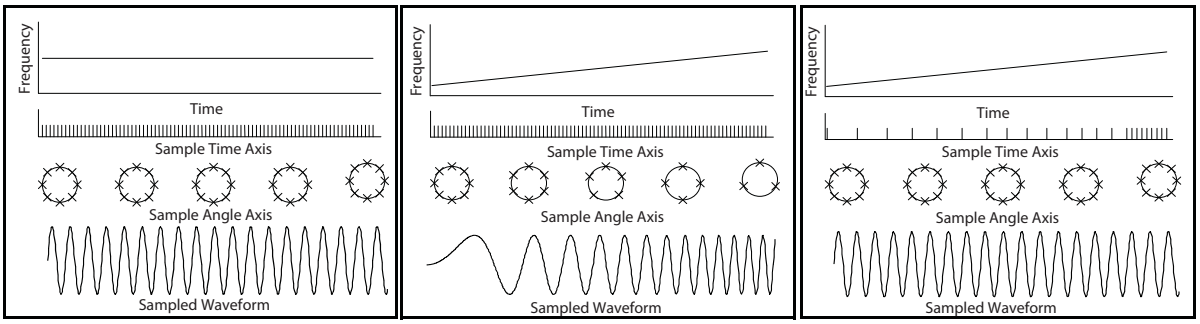

a) b) c)

Figure 5.20 – Graphical representation: a) sine with constant frequency; b) sine with increasing frequency with constant Δt; c) sine with increasing frequency and constant $\Delta\theta$ (adapted from (Blough, 2006))

Time synchronous averaging represents an useful tool to identify a varying frequency of excitation along time. As example, Peeters et al (Peeters, Cornelius et al., 2007) refers a successfully case study in which this technique was applied to an helicopter.

However, the application of this method for the analysis of vibration signals from wind turbines presents some drawbacks, including the need to know the position or frequency/ radial speed of the rotor with very good precision, which implies the installation of additional sensors at the turbine. Other important difficulties are also referred in literature regarding the application of TSA to wind turbines. Tcherniak et al (Tcherniak, Chauhan et al., 2010a) refers that it should not work properly since this method suits better in situations where the harmonics are identified as well-defined sharp peaks. As shown in section 5.3, the peaks obtained from the harmonic excitation present the previously introduced "thick tail" characteristic. This difficulty was experimentally confirmed in (Manzato, White et al., 2013).

Although different methodologies to identify and remove the effect of harmonics in vibration signals have been developed, their application to wind turbine signals have not revealed as a definite solution for this problem. In that sense, other types of strategies are usually employed, as shown in Chapter 7.

5.7 AUTOMATED OPERATIONAL MODAL ANALYSIS

In the implementation of a dynamic monitoring system, it is desirable to have the least possible human intervention. In that sense, an additional procedure has to be added to the output-only identification algorithms presented in section 5.4 to avoid the intervention of an experienced operator in the analysis of stabilization diagram. For this reason, an algorithm for automated extraction of the desired modal parameters from the stable poles on a stabilization diagram is necessary.

According to (Reynders, Houbrechts et al., 2012), three major types of strategies have been proposed to automate the identification process: histogram analysis, non-hierarchical and hierarchical clustering.

In histogram analysis, with the aim of identify vertical alignments of stable poles, the frequency axis is divided into a certain number of bins and the poles contained in each bin are counted. Scionti *et al* (Scionti, Lanslots et al., 2003) presented an algorithm based on this procedure.

Another approach to perform an automatic interpretation of stabilization diagrams is cluster analysis. Cluster analysis is a multivariate statistical analysis technique of classification, in which the objects (poles) are partitioned into a certain number of classes (Gordon, 1999). This partition of data into a set of disjoint classes (or clusters) leads to the integration (of similar objects) and separation (of unrelated objects) of the data. Concerning the actual problem presented in this work, clustering analysis is used as a tool to group physical poles that refer to the same vibration mode. This can be accomplished by considering poles as objects with quantitative parameters – the modal parameters. Clustering analysis can be divided in mainly two categories: hierarchical and non-hierarchical algorithms.

Non-hierarchical clustering procedures allocate data poles into a pre-specified number of clusters. Initial seeds are defined by the user among which the clusters will be created (Reynders, Houbrechts et al., 2012). The poles will be then assigned to the cluster in order to optimize the criterion of high internal homogeneity (within clusters) and high external heterogeneity (between clusters). A famous mathematical algorithm is the k-means method (Gordon, 1999). The major drawbacks of non-hierarchical algorithms are the need of a priory definition of the number of clusters (vibration modes) and the selection of the seeds (although the latter may be overcome by a random selection of the seeds (Magalhães, 2010)). An illustration of this algorithm is presented in Figure 5.21). Some examples of application of this algorithm for automated classification of poles on system identification are presented in (Verboven, Parloo et al., 2002; Scionti and Lanslots, 2005).

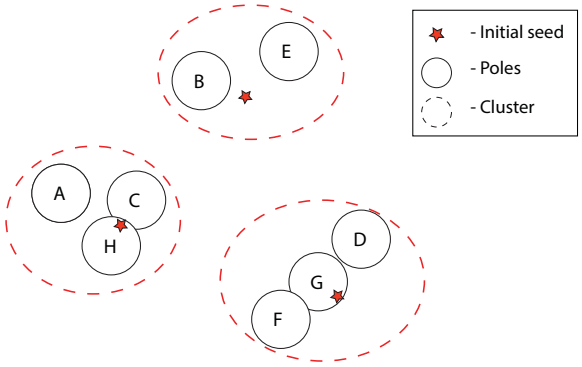

Figure 5.21 – Non-hierarchical clustering

The last described strategy is the hierarchical clustering analysis. With this strategy, each initial pole is considered a cluster. Then, and in each step, the closest poles are aggregated into the same cluster until all poles are combined in one large cluster (Figure 5.22). The algorithm of a hierarchical clustering methodology is as follows:

1. Definition of distance between poles. This property will measure the closeness between poles;
2. Calculation of similarity between every clusters. The criteria for similarity calculation has to be chosen (the more common are single link, complete link, group average link, Ward's method, centroid method and median (Gordon, 1999));
3. Linking of the clusters in an hierarchical tree;
4. Definition of a rule to cut the hierarchical tree. This rule will define the final number of clusters.

It should also be referred that, contrary to what can happens in non-hierarchical methods, a pair of poles grouped together at a certain step cannot be separated in subsequent steps. Pappa et al (Pappa, III et al., 1997) is said to be the first author to report the utilization of this kind of strategy for automatic system identification (Reynders, Houbrechts et al., 2012). Other descriptions are presented in (Verboven, Guillaume et al., 2003) and (Magalhães, Cunha et al., 2009) with examples of application with the LSCF and SSI-COV method, respectively.

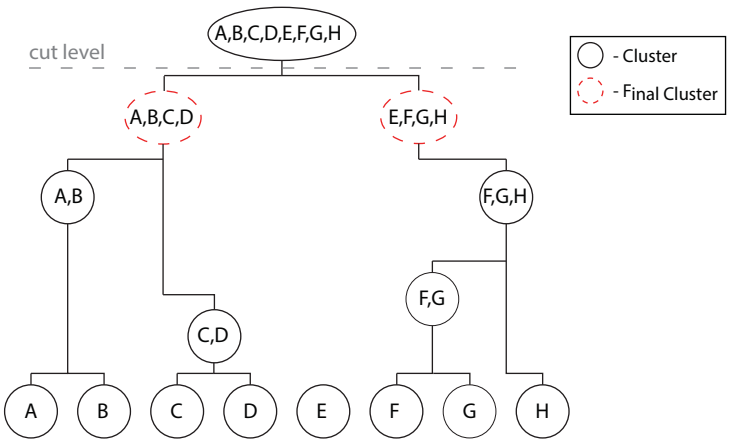

Figure 5.22 – Hierarchical clustering

5.7.1 Implemented Hierarchical Cluster Analysis

The strategy implemented in the monitoring system described in this work is based on a hierarchical clustering algorithm. The aim of application of this algorithm is to automatically separate spurious poles from the physical ones and to aggregate the latter in clusters according to the different vibration modes.

Taking into account the algorithm presented earlier, the initial step of the analysis comprises the computation of the distance between all pairs of poles. For this calculation, the modal properties of each pole should be used. However, the utilization of the modal damping usually presents two important drawbacks: different modes may present the same value of damping and the extracted values of damping ratios present high variance. For these reasons, the use of the modal damping as a

pole property for calculation of similarity between poles was dropped. Thus, the frequency value and the mode shape (more specifically, the MAC value) were the properties used for distance calculation between poles (Magalhães, Cunha et al., 2009):

$$d_{i-j} = \left|\frac{f_i - f_j}{f_j}\right| + \left(1 - MAC_{i,j}\right) \tag{5.91}$$

with:

$f_{i,j}$	Frequency value of pole i or j
$MAC_{i,j}$	Modal assurance criterion between mode shapes of pole i and j

The different parameters of equation (5.91) can be computed with weighting factors, which allows assigning different importance to each property. However, this possibility was not used in the monitoring system. As can be concluded from the observation of equation (5.91), the shorter the distance is, the greater the similarity between poles and the higher the probability that both are referred to the same vibration mode.

After the calculation of the distance between poles, it is necessary to decide a criterion to assess the similarity between clusters. In the implemented strategy, the single link was used. This criterion defines the distance between two clusters as the smallest distance between poles contained in different clusters. This distance is the same as defined in equation (5.91).

Once the hierarchical tree is constructed, it is necessary to define another criterion for the cut level. This decision cannot be based on a hard criterion, like a final number of clusters: it is not possible to know how many clusters will be formed containing spurious poles; besides, there are structural modes which will not be detected in every setup. These aspects introduce an uncertainty about the final number of physical and spurious clusters. Thus, the chosen criterion imposes a degree of homogeneity inside the cluster: a maximum distance between any point and its closest point in the same cluster. However, this maximum distance has to be carefully evaluated, since it can lead to the split of similar poles into different clusters (if the distance is too tight) and the aggregation of different poles into the same cluster (if the distance is too large).

After the application of the previous criterion, it is necessary to pick the final clusters containing physical poles. Considering that poles referring to physical modes are consistent along the different orders of the system identification algorithms, an initial cut-off criterion should be implemented to eliminate clusters with a reduced number of poles. Then, the modal properties of the remaining cluster can be compared with the reference properties of the vibration modes intended to be tracked. These reference properties can be defined during an initial training period.

Example

The results obtained with the application of the SSI-COV algorithm to the acceleration time series from the NREL 5MW wind turbine model were used to illustrate the implemented hierarchical cluster methodology. In this example, the maximum distance between poles was set to 0.02 and a minimum number of poles in a cluster in order to be considered was defined as 5. The results obtained with the

cluster analysis are presented in Figure 5.23, where the considered cut level of 5 poles is represented by the dashed red line).

The natural frequency and damping ratio of the poles found after the consideration of the cut level are shown in Figure 5.24. In this figure, the small circles represent the properties of the stable poles, while the large circles indicate the mean values of the poles inside each cluster.

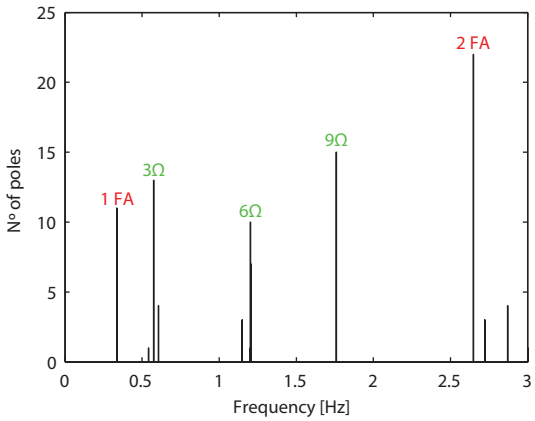

Figure 5.23 – Number of poles obtained for each cluster defined according to the implemented hierarchical cluster analysis (the red dashed line indicates the cut level)

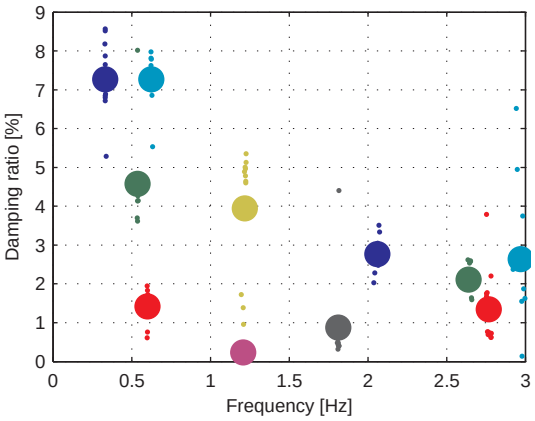

Figure 5.24 – Natural frequency and damping ratio of the selected clusters (the small circles represent the properties of the pole, while the large circles indicate the mean values of the poles inside each clusters

5.8 CASE STUDY – IZAR BONUS 1.3MW/62

5.8.1 INTRODUCTION

This section presents the most relevant results from the experimental identification of the dynamic properties of a Izar Bonus 1.3MW/62 wind turbine. This analysis is integrated in a project to upgrade the wind turbine with an extension of the blades, hereafter designated as Rotor Blade Extension (RBE). This project was led by Energiekontor Windpower Improvement GmbH and was developed in collaboration with the Institute of Science and Innovation in Mechanical and Industrial Engineering (INEGI).

In the scope of the RBE project, several tasks were developed in order to assess the feasibility of the rotor upgrade. Among them, the bending stress of the blades, the evaluation of debris in the gear box oil and the definition of the wind turbine power curve before and after the rotor extension were analysed. The Laboratory of Vibrations and Monitoring (ViBest) of FEUP was invited to perform dynamic tests of the wind turbine blades (Oliveira, Magalhães et al., 2014).

In the context of the project, the assessment of the blades dynamic properties before and after the extension allows to analyse three important aspects:

- Assessment of the natural frequency of the rotor blades modes – it is of the utmost importance to guarantee that the frequency values of the extended blades are not close the tower modes and to the frequency of rotation of the rotor;
- Assessment of the damping ratios from the rotor blades modes – it is important to assess if there is significant change in the structural damping of the blades after the extension;
- Independent assessment of the natural frequency of each blade – this analysis is intended to check if the RBE does not change the structural similarity between the blades.

Within the RBE project, data collected by two different measurement systems were used: one system based on fibre Bragg grating sensors and another based on accelerometers.

The results presented in this section are mainly focused on the assessment of the dynamic properties of the wind turbine blades before and after the rotor extension. However, it was given the opportunity to performed an ambient vibration test (before the implementation of the RBE), including simultaneous measurements at the tower and blades. In this context, a rotor-stop test was also performed in order to assess the damping ratio of the first and second tower bending modes in the FA direction.

5.8.2 DESCRIPTION OF THE WIND TURBINE

The Izar Bonus 1.3MW/62 wind turbine presents a traditional configuration, with a three-bladed upwind rotor with a diameter of 62 m (Figure 5.25). The tower is in steel and the hub is 68 m height. The wind turbine is part of the Penedo Ruivo wind farm, located in the northern part of Portugal, in a highly complex terrain. The turbine started operating in 2005.

Figure 5.25 – Photo of the Izar Bonus 1.3MW/62

The generator is of the fixed-speed type and presents two different rotational operating speeds: 13 and 20 rpm. It presents a rated-output power of 1.3 MW. The rotor blades have an active-stall control system.

The analysed data was collected during periods of time when the rotor was parked and the blades were pitched by an angle of about 97º. Under this situation, the blade motion in the flapwise direction occurs in the rotor plane while the motion in the edgewise direction is oriented to out of the plane of the rotor. This configuration is opposite to the one under operation. Figure 5.26 presents two photos illustrating both configurations.

a) b)

Figure 5.26 – Blade orientation: a) operating situation; b) parked situation

5.8.3 Measurement System

As previously referred, two distinct measurement systems were used in this analysis: one based on fibre Bragg grating sensors and another based on accelerometers.

5.8.3.1 Measurement System Based on Fibre Bragg Grating Sensors

The measurement system based on fibre Bragg grating sensors is a permanent system installed in the wind turbine. It is composed by strain and temperature sensors installed at each blade; all sensors are connected in the hub to an interrogation unit which processes the data and delivers it in a local industrial PC which stores the information.

The system is intended to measure strains at the blades root due to bending stresses. For each of the three blades, four sensors, referred here as A, C, E and K, were installed at their roots, measuring the strains at these positions. Sensors A and E are referred to the motion in the flapwise direction (bending around the weaker axis), while sensors C and K are related to the edgewise direction (bending around the stronger axis). Each pair of sensors measures the strains at opposite positions of the same direction. Figure 5.27 illustrates the position of the sensors on the blades.

The data was acquired with a sampling frequency of 100 Hz and then decimated to focus the analysis in the frequency range 0 – 5 Hz.

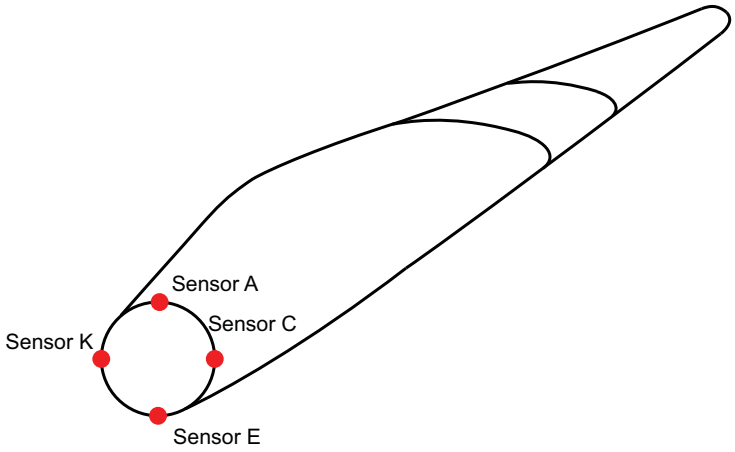

Figure 5.27 – Position of the sensors of the measurement system based on fibre Bragg grating sensors

5.8.3.2 Measurement System Based on Accelerometers

In the context of the RBE project, it was also possible to perform an ambient vibration test (including measurements at the tower and blades) and a rotor-stop test of the wind turbine (with measurements at the tower). This test took place only before the extension of the blades.

During the ambient vibration test, six tri-axial 24-bit strong motion recorders GeoSIG GSR-24 (with internal force balance accelerometers), synchronized by GPS, were used to collect acceleration time series at different position of the wind turbine. Three data sets of 16 minutes were recorded at a sampling frequency of 100 Hz and then decimated in order to focus the analysis in the frequency range of 0 – 5 Hz.

In each setup, a different wind turbine blade was monitored, alongside with the instrumentation installed at the tower. The test was conducted under low wind speed conditions and the nacelle presented a misalignment of around 110º to the wind direction. The elements monitored in each setup are identified in Table 5.4.

Table 5.4 – Measurement setups and corresponding instrumented structural elements during the ambient vibration test

Data set	Time length [min]	Sensors	Instrumented elements
1	16	S1 to S4 S5 and S6	Tower Blade A
2	16	S1 to S4 S5 and S6	Tower Blade B
3	16	S1 to S4 S5 and S6	Tower Blade C

Throughout the test, four accelerometers (S1 to S4), were kept fixed at tower positions at the platform levels 6, 8 and 10, as schematized in Figure 5.28. Both sensors S3 and S4 were placed at the top platform in order to identify possible torsion components of the vibration modes.

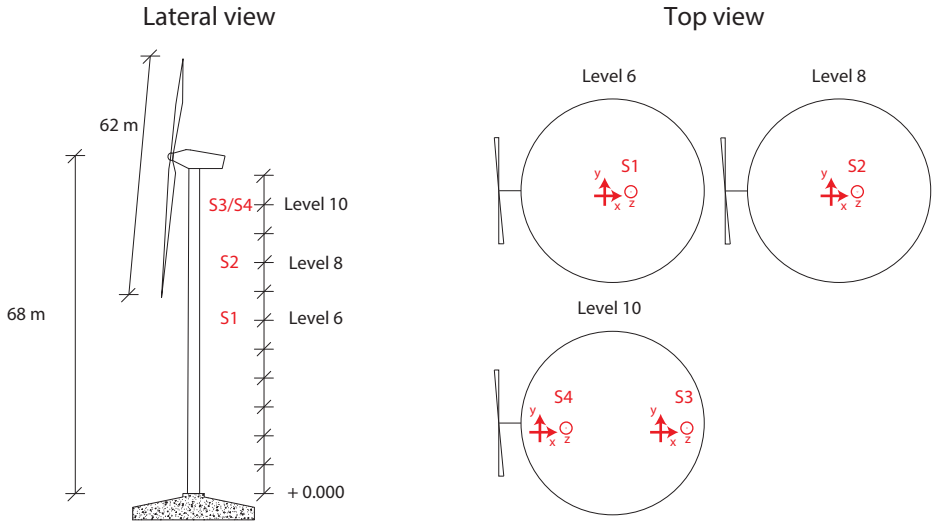

Figure 5.28 – Accelerometers position kept fixed at the tower during the three data sets

In each set, a different wind turbine blade was monitored with two accelerometers (S5 and S6). The blade to be instrumented was oriented in the horizontal position and the two accelerometers were placed inside the parked blade in the positions characterized in Figure 5.29 (the mechanical brake was activated and the blades were pitched with an angle of 97º). The position of the sensors at the blade for the three setups is presented in Figure 5.30.

a) b)

Figure 5.29 – Position of the instrumented blade during the recorded setups: a) position for the blade A and C (data sets 1 and 3); b) position of the blade B (data set 2)

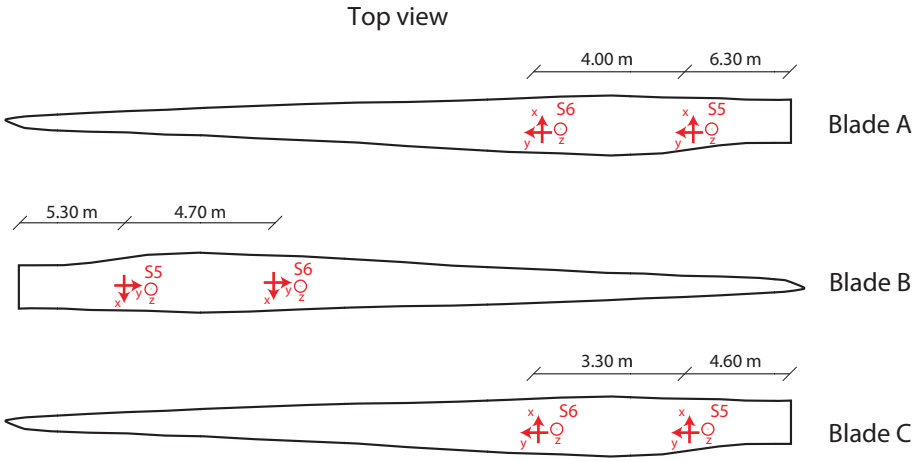

Figure 5.30 – Position of the sensors inside the different blades

Figure 5.31 presents an illustration of the monitored elements of the wind turbine. The blue line represents the instrumented tower, while the red line denotes the portion of the blade which was monitored. The crosses stand for the positions of the installed sensors. On the other hand, the black dashed lines represent the part of the wind turbine that was not instrumented.

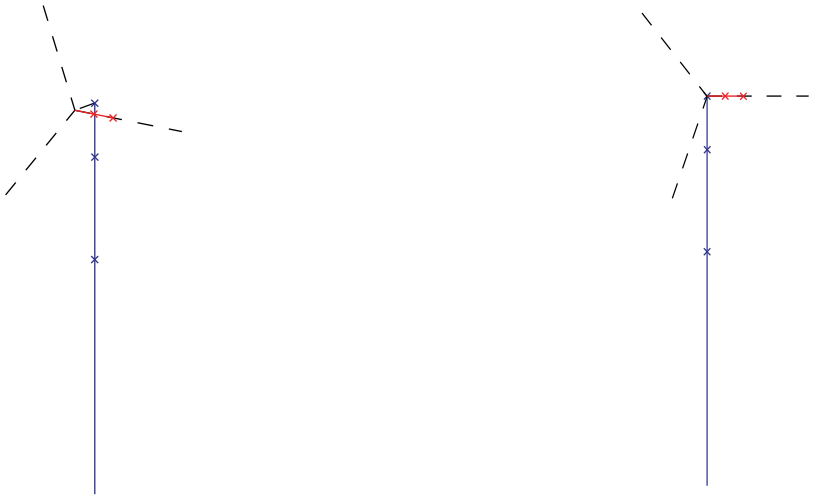

Figure 5.31 – Instrumented elements of the wind turbine: a) isometric view; b) front view

The performed rotor-stop test was conducted at the end of the day, when the wind speed was around 4.5 m/s. The test consisted in the sudden stop of the rotor, when the wind turbine was operating at normal conditions, with a rotor speed of 13 rpm. The stop was accomplished through the activation of the mechanical brake and the change of the blades pitch angle. With this operation, it was possible to create an impulse at the top of the wind turbine in the FA direction.

In the scope of the rotor-stop test, only the acceleration at the tower was recorded. For that reason, only the sensors S1 to S4 from Figure 5.28 were considered.

5.8.4 Analysis before the installation of the RBE

The identification of the dynamic properties of the wind turbine blades, prior to the installation of the RBE, was performed with data from the installed fibre Bragg grating sensors and data recorded by the accelerometers.

The signals collected with the fibre Bragg grating system were used as primary source of data, since the response of the three blades is recorded simultaneously. The test with accelerometers placed both at the tower and blades allowed to better understand the configuration of the vibration modes.

5.8.4.1 Analysis of fibre Bragg grating sensors measurements

The data collected by the measurement system based on fibre Bragg grating sensors corresponds to a setup of 18 min. It is referred to a period when the wind turbine was parked, with the mechanical brake activated and the blades pitched with an angle of 97º. The mean wind speed, during the 18 minutes was, roughly, 10 m/s.

In this analysis, the signal from the sensor E installed in blade C was not recorded and, for that reason, only 11 channels were considered. Figure 5.32 shows the recorded signals from the three blades during the considered period. As can be seen, for the considered period, the vibration amplitude in the flapwise direction is higher than in the edgewise direction.

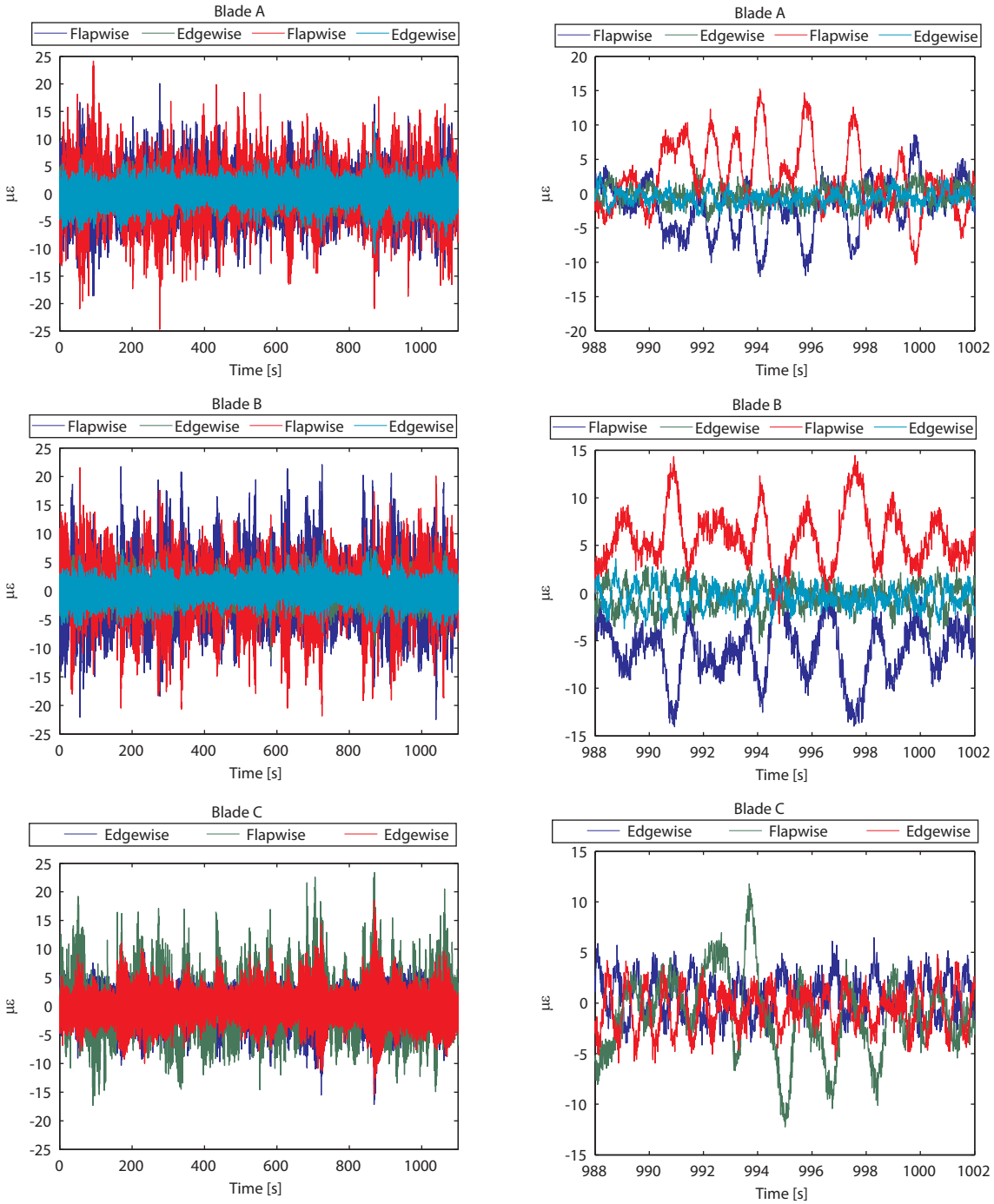

Figure 5.32 – Strain measured by the fibre Bragg grating sensors: a) complete time series; b) zoom of a period of 14 seconds

As preliminary analysis, the averaged normalized power spectrum density of the time series collected by each sensor of the three blades was computed. It is presented in Figure 5.33. It is visible how several resonance peaks can be identified in this figure.

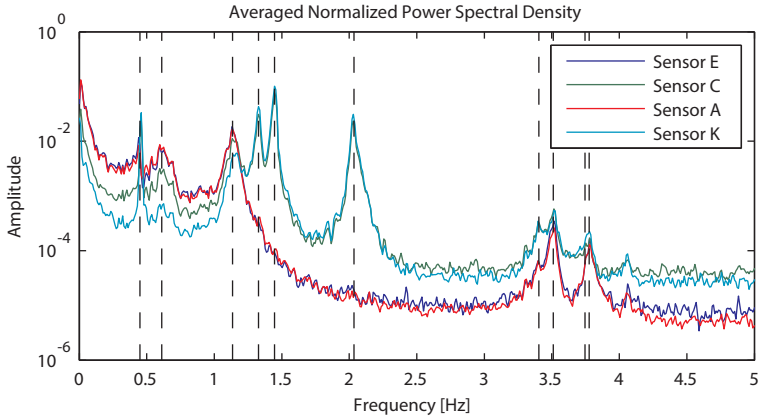

Figure 5.33 – Averaged normalized power spectrum density from each sensor (the dashed lines indicate the main peaks of the spectra)

The identification of the modal parameters was based on the application of two different parametric identification algorithms: the SSI-COV (see section 5.4.1.2) and p-LSCF (see section 5.4.2). In this analysis, the 11 collected signals were processed all together.

The results obtained with the two algorithms were very similar and in accordance with the spectra from Figure 5.33. The stabilization diagram obtained with the p-LSCF algorithm is presented in Figure 5.34.

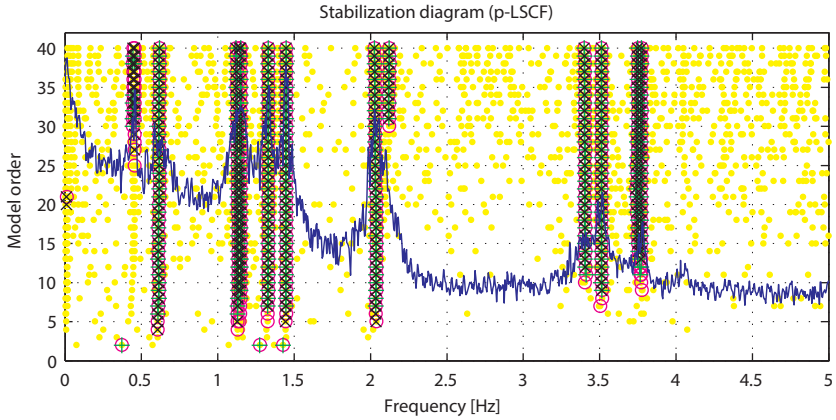

Figure 5.34 – Stabilization diagram obtained with the p-LSCF algorithm for the data obtained with the measurement system based on fibre Bragg grating sensors

From the analysis of the stabilization diagrams obtained with both methods, it was possible to estimate the modal parameters of the 13 vibration modes presented in Table 5.5, including three pairs of closely spaced modes (around 0.40 Hz, 1.14 Hz and 3.76 Hz). The results obtained with the two algorithms were very similar. Notwithstanding, the use of the p-LSCF algorithm allowed the identification of three additional vibration modes.

Table 5.5 – Comparison of results obtained with the SSI-COV and p-LSCF methods

Mode	SSI-COV		p-LSCF	
	Natural frequency [Hz]	Damping ratio [%]	Natural frequency [Hz]	Damping ratio [%]
1	-	-	0.441	0.38
2	-	-	0.456	0.17
3	0.610	7.22	0.610	8.51
4	1.136	2.44	1.129	1.93
5	1.146	3.05	1.146	2.51
6	1.328	0.76	1.329	0.59
7	1.447	0.60	1.449	0.47
8	2.035	0.71	2.039	0.54
9	-	-	2.108	1.00
10	3.404	1.61	3.399	1.14
11	3.512	0.55	3.512	0.55
12	3.745	1.44	3.745	1.31
13	3.776	0.47	3.776	0.42

Since the available layout of sensors only assessed the modal curvature at the blades root, a complete description of the mode shapes is not possible. Nevertheless, considering that the shape of the first modes of wind turbine rotors usually follows a typical configuration, an estimation of the first modes is presented. The modal curvatures at the blades root from each identified vibration mode, alongside with an illustration of the theoretical shapes of the first 8 modes, are presented in Figure 5.35. Since the data from channel E from blade C was not available, the symmetric value obtained for the sensor A of the same blade was used for purposes of illustration (identified with the white bar).

The mode shapes from the first two vibration modes do not resemble any typical rotor mode shape configuration. These two modes present natural frequency values in accordance with typical first tower bending modes in the FA and SS directions. Nevertheless, this fact was only confirmed with the analysis of the results obtained with the ambient vibration test (section 5.8.4.2).

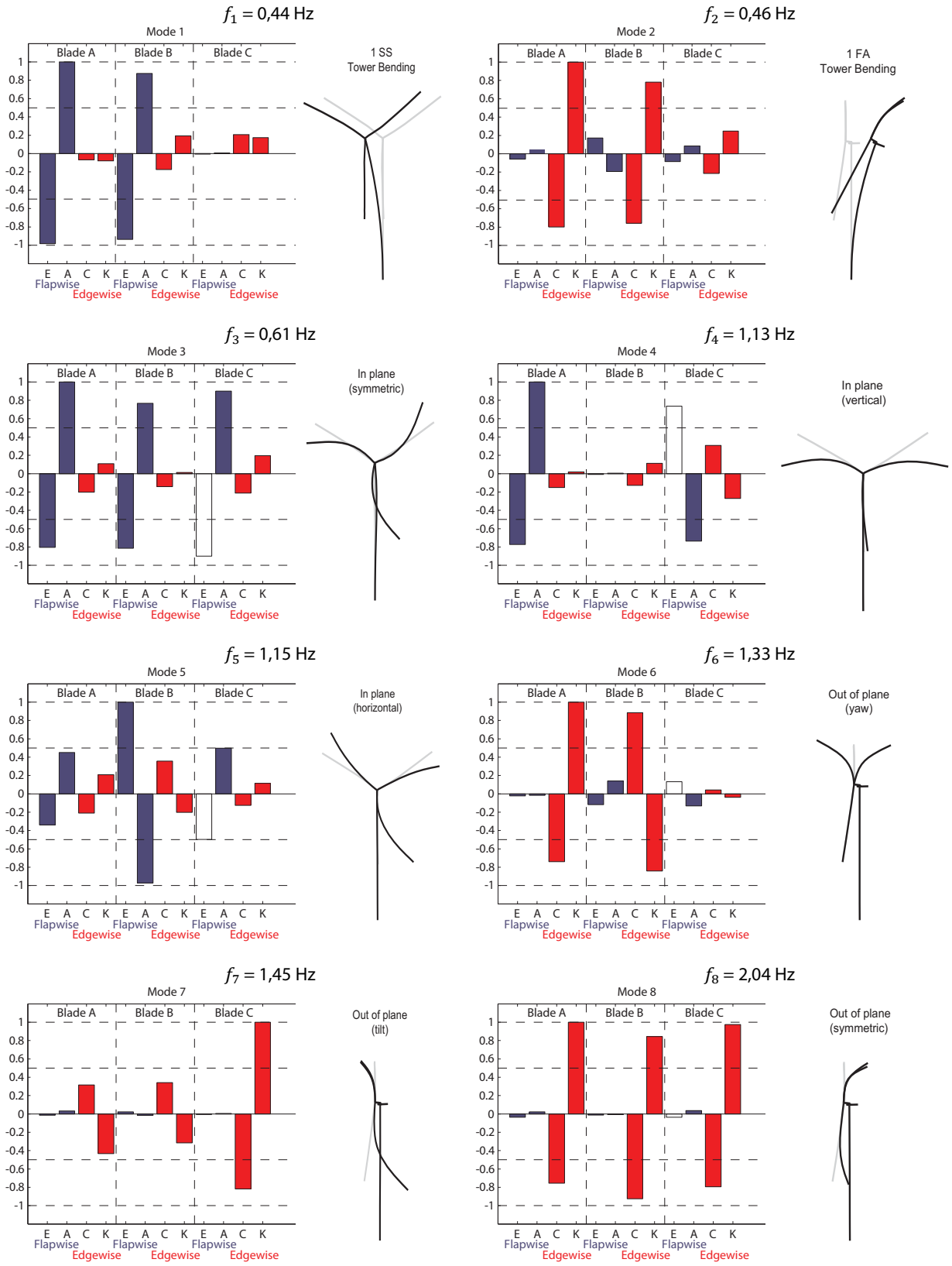

Figure 5.35 –Amplitude of the modal curvature obtained for the identified vibration modes and respective illustration (the rotor configuration during the measurement period may not exactly match the illustration)

It is noticed that the illustrations presented for the rotor vibration modes are referred to the wind turbine under parked condition. Under this condition, the flapwise motion occurs in the rotor plane, while the edgewise motion is related to motion out of plane of the rotor. This configuration is opposite to the one when the wind turbine is operating and, for that reason, these illustrations should not be extrapolated for that condition.

Furthermore, the third identified vibration mode (f = 0.61 Hz) is probably dominated by the drive train inertia and by the support condition of the rotor (the mechanical brake was activated).

5.8.4.2 Analysis of accelerometers measurements

In order to clarify the source of the resonance peaks around 0.4 Hz and 4.0 Hz, and to validate the previous results obtained with the fibre Bragg grating sensors , an ambient vibration test and a rotor-stop test were performed with a set of tri-axial accelerometers.

Ambient Vibration Test

Firstly, an independent analysis was performed for the data collected from the blades and from the tower.

The three data sets recorded during the ambient vibration test by the accelerometers located at the blades are shown in Figure 5.36, together with the normalized power spectra density. The analysis permitted to conclude that the spectra obtained for each blade are very similar. The shape of the spectrum obtained for blade A shows a larger difference for the range 2 – 4 Hz when compared with the other two data sets, though. This fact may be explained by the impulsive excitation on the blade A at around 400 s, which may have excited, in a larger extent, the modes in this frequency range. This impulsive excitation was due to a strong gust that occurred during the measurement period.

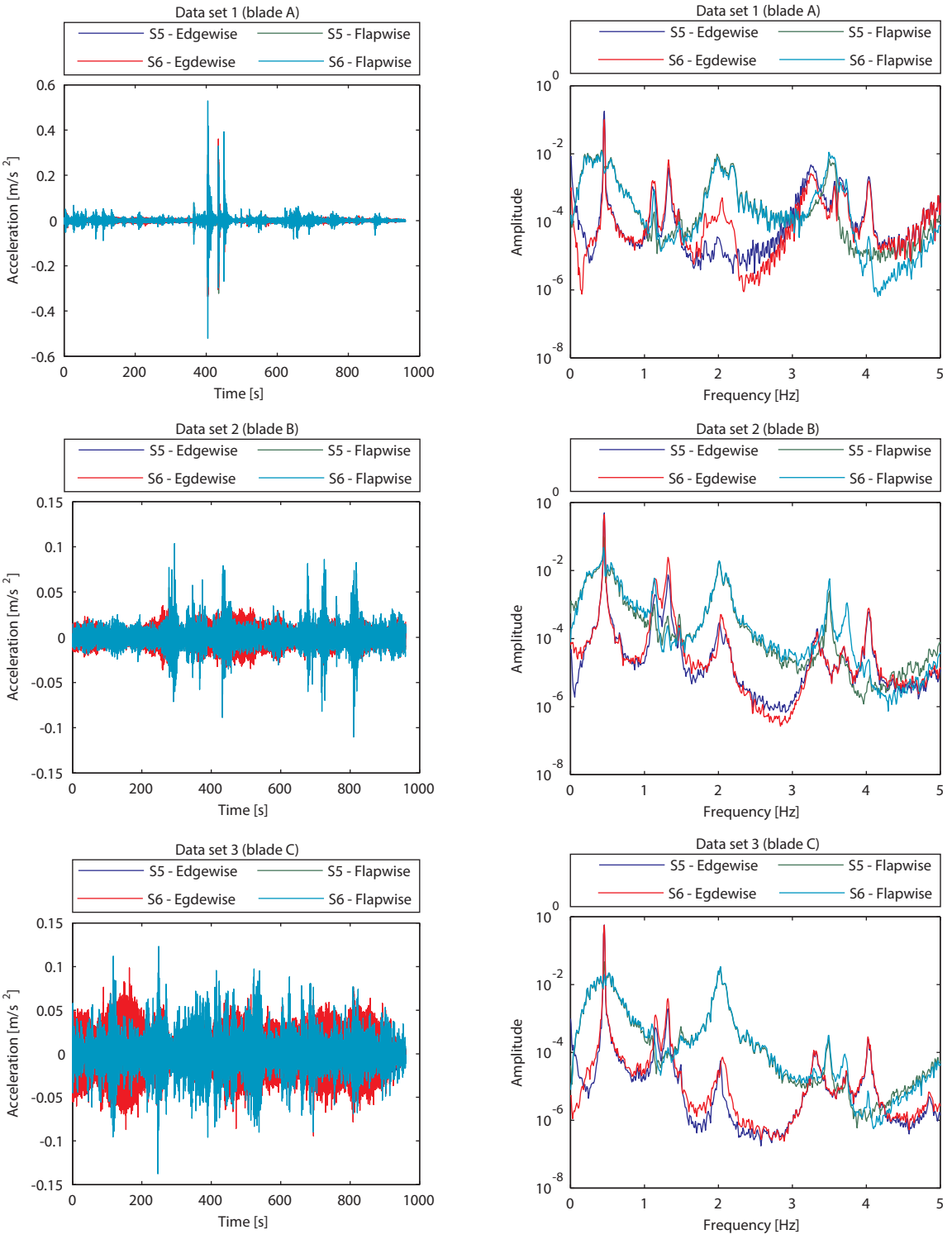

Figure 5.36 – Recorded data sets from the accelerometers placed at the blades, during the ambient vibration test: a) time domain; b) normalized power spectral density

The preliminary analysis of the data sets recorded with the sensors located at the tower was performed considering two different signals combination for the tower top sensors S3 and S4: half-sum and half-

difference of the horizontal accelerations. With this strategy, it is possible to identify modes with relevant bending (with the half-sum) and torsion (with the half-difference) components of the tower.

The averaged normalized power spectral density of the acceleration time series in the FA direction recorded by the sensors placed at the tower top is presented in Figure 5.37 a). On the other hand, the averaged normalized power spectral density of the accelerations in the SS direction is presented in Figure 5.37 b). Both spectra clearly evidence one important resonance peak around 0.4 Hz. In addition, the spectra referred to the SS direction evidence a second important peak around 4.0 Hz. It is also visible, for the half-difference signal combination in the SS direction, a resonance peak at 3.3 Hz that is not seen for the half-sum combination. Thus, this peak is probably due to a vibration mode with an important torsion component.

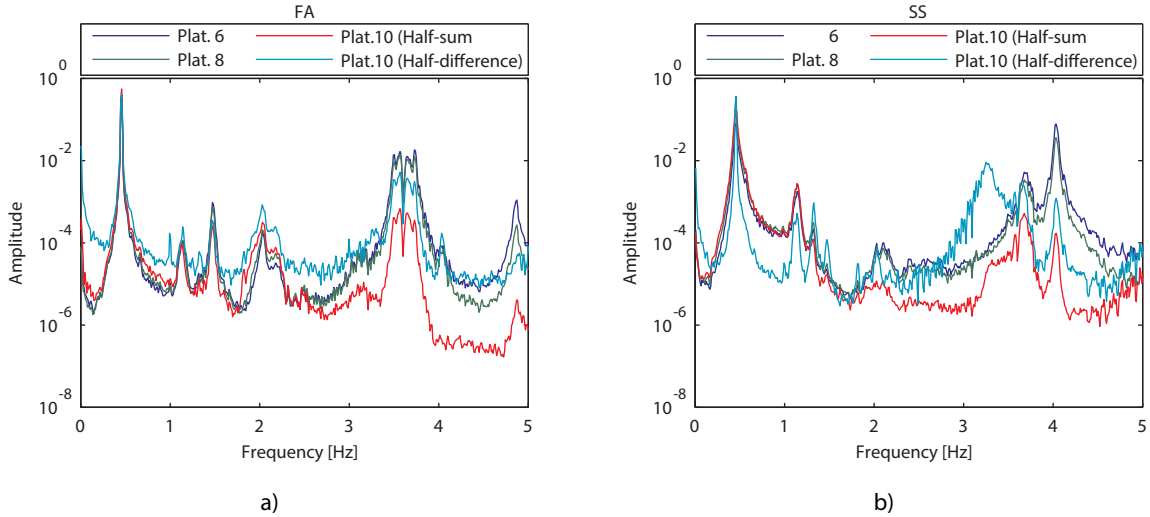

a) b)

Figure 5.37 – Averaged normalized power spectral density of the of the acceleration time series recorded by the sensors placed at the tower in the a) FA and b) SS direction

The identification of the modal parameters was also based on the application of the SSI-COV and p-LSCF algorithms. In this analysis, each data set was analysed separately and all signals from tower and blades were considered together. With the purpose of illustrating the obtained results, Figure 5.38 shows the stabilization diagram associated with the acceleration time series collected during setup 2.

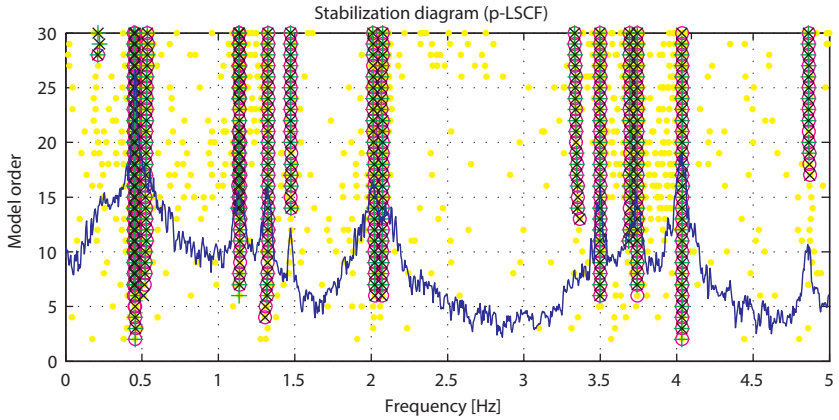

Figure 5.38 – Stabilization diagram obtained with the p-LSCF algorithm for the data collected with the measurement system based on accelerometers during setup 2

The analysis of the three data sets led to the identification of 16 vibration modes of the wind turbine. Table 5.6 summarizes the modal properties from these vibration modes identified with the p-LSCF algorithm. The obtained results present a good agreement for the different analysed data sets. It is observed that, apart from some modes, the majority of them simultaneously evidence motion of the rotor blades and tower. From the identified modes, only the 1st, 2nd, 15th and 16th mode presented a dominant tower motion (without important motion of the blades). For that reason, it was concluded that they represent the 1st and 2nd pair of tower bending modes.

The obtained results are in good agreement with the ones estimated with the measurement system based on fibre Bragg grating sensors. However, the modal properties of 3rd vibration mode present an important deviation between the two measurement systems. This may be due to a worst identification of this mode with the accelerometers since the resonance peak of this mode is almost not noticeable in Figure 5.36.

Table 5.6 – Natural frequencies (f) and modal damping ratios (ξ) of the identified vibration modes with the data recorded by the accelerometers and comparison with the results obtained with the fibre Bragg grating measurement system (F.B.G.) using the p-LSCF algorithm

Mode	Data set 1		Data set 2		Data set 3		F.B.G.		Description
	f [Hz]	ξ [%]	f [Hz]	ξ [%]	f [Hz]	ξ [%]	f [Hz]	ξ [%]	
1	0.452	2.51	0.445	1.93	0.455	1.89	0.441	0.38	Tower SS
2	0.456	0.13	0.459	0.22	0.456	0.17	0.456	0.17	Tower FA
3	0.520	10.95	0.530	10.30	0.542	9.41	0.610	8.51	Blade flapwise
4	1.128	0.28	1.134	0.54	1.120	0.47	1.13	1.93	Blade flapwise Tower SS
5	1.140	0.52	1.140	1.18	1.156	1.18	1.146	2.51	Blade flapwise Tower SS
6	1.326	0.76	1.324	0.89	1.318	0.64	1.329	0.59	Blade edgewise
7	-	-	1.474	0.41	1.492	0.61	1.447	0.47	Blade flap/edgewise Tower FA
8	1.994	1.56	2.016	0.79	2.020	0.91	2.029	0.54	Blade flap/edgewise
9	2.078	0.81	2.062	1.02	2.062	0.86	2.108	1.00	Blade flapwise
10	3.260	0.90	3.330	1.02	3.310	0.86	3.399	1.14	Blade edgewise Tower torsion
11	3.485	0.33	3.498	0.35	3.490	0.42	3.512	0.55	Blade flapwise Tower FA
12	3.735	0.29	3.742	0.36	3.738	0.38	3.776	0.42	Blade flap/edgewise Tower FA
13	4.038	0.35	4.034	0.33	4.034	0.36	-	-	Tower SS
14	4.874	0.32	4.862	0.37	4.8868	0.40	-	-	Tower FA

The mode shapes of some of the identified vibration modes are shown in Figure 5.39, following the illustration introduced in Figure 5.31 (only the instrumented elements are plotted). Although the measurement system based on accelerometers allows identifying two additional vibration modes (when compared to the fibre Bragg grating system), the interpretation of the mode shapes with important rotor motion presents greater difficulties.

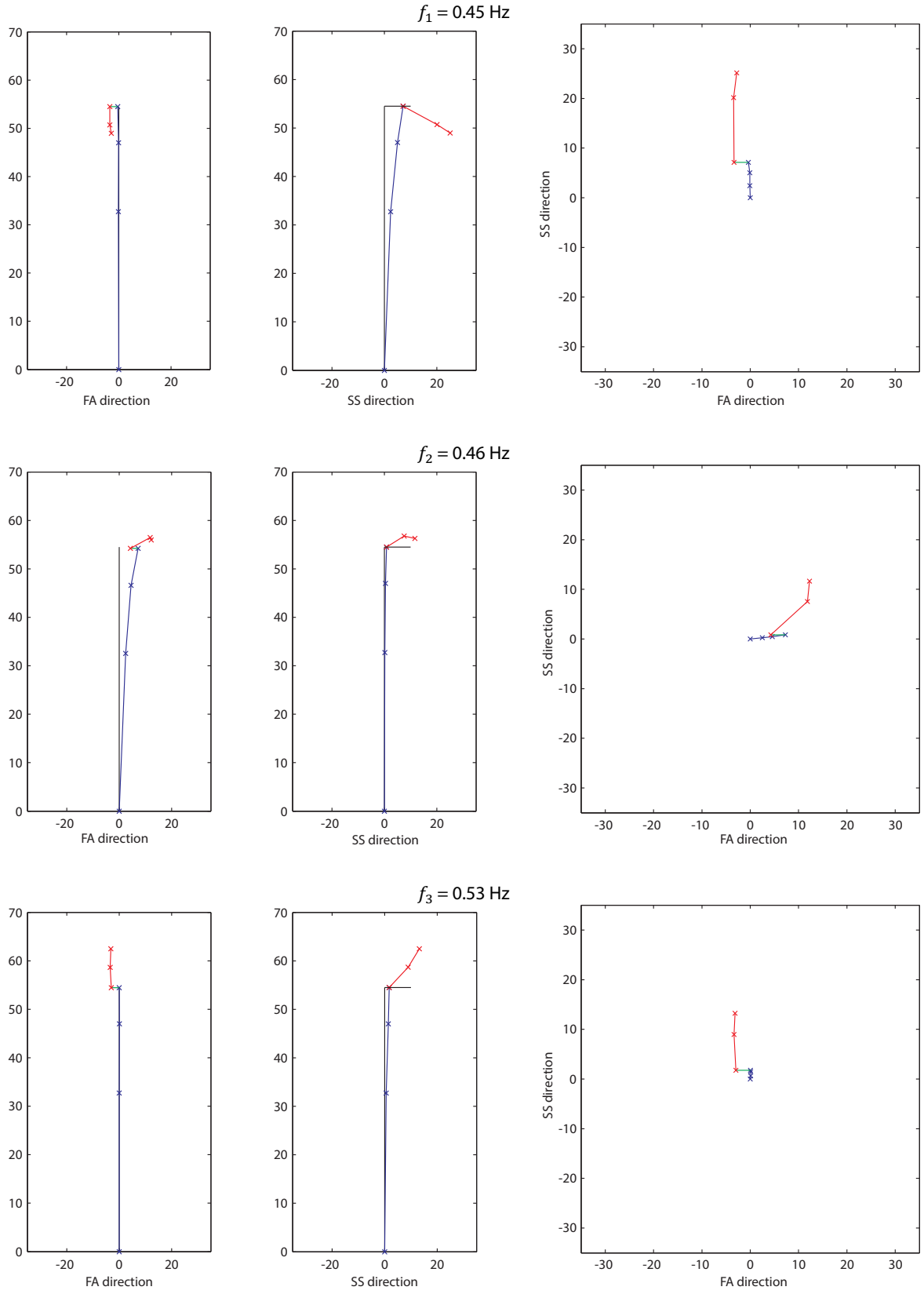

Figure 5.39 – Mode shapes of the first three vibration modes identified with the measurement system based on accelerometer

Rotor-stop Test

In addition to the ambient vibration test, a rotor-stop test was also performed with the aim of identifying the damping ratio of the first tower bending mode in the FA direction. The acceleration time history recorded by the sensors oriented in the FA direction is shown in Figure 5.40. A maximum value around 0.6 m/s^2 was achieved. The motion of the wind turbine after the sudden stop is mainly in the FA direction; however movement in the orthogonal direction is also noticed (Figure 5.40).

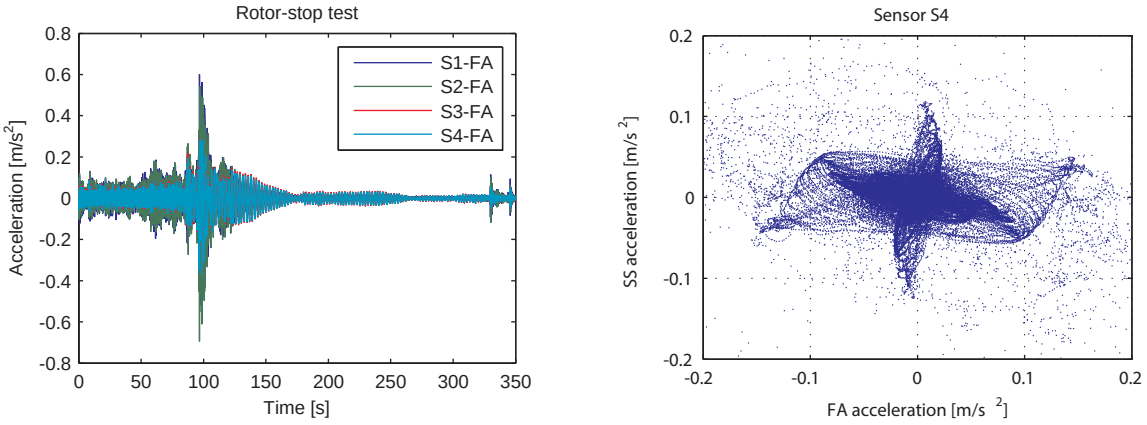

a) b)

Figure 5.40 – a) Time history from the recorded acceleration by the sensors oriented to the FA direction. b) Movement seen from above from the accelerations at S4 sensor (top sensor)

The main modes excited with the rotor-stop test are the 2nd vibration mode (1st tower FA mode) and the 8th vibration mode (the identified rotor symmetric out of plane mode) in Table 5.6. The spectra obtained with the recorded acceleration time series are presented in Figure 5.41, where the resonance peaks of the referred modes are evidenced.

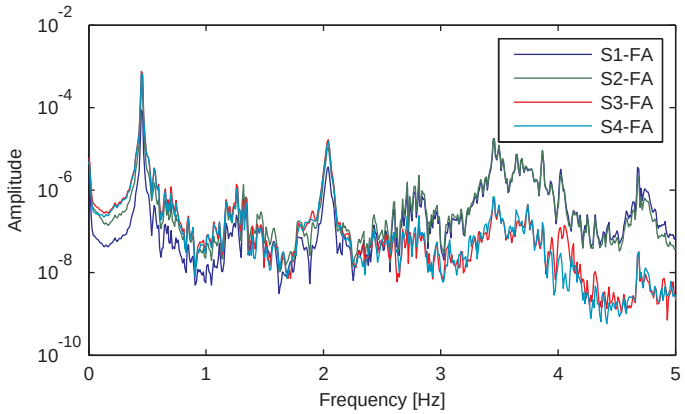

Figure 5.41 – Power spectral density from the acceleration time series recorded during the rotor-stop test

In order to determine the damping level of the 1st FA tower bending mode, the signals recorded by sensors were filtered and an exponential function was adjusted to the envelope of the free decay signal. The used exponential function is defined according to:

$$y(t) = A.e^{-\xi.2.\pi.f.t} \tag{5.92}$$

For this analysis, a low-pass band filter with a cut of frequency of 1 Hz was used. Considering that the filtered response does not present a perfect theoretical free decay response, three different amplitude ranges were considered to adjust an exponential window: the initial part, the last part and the whole decay. Figure 5.42 a) to c) presents the fittings performed to the acceleration time series recorded by sensor S4, considering the three signal ranges.

The fitting obtained with the exponential function considering the first part of the signal is clearly misfit. It is visible from Figure 5.42 a) that the function does not follow the progress of the signal. On the other hand, the other two fittings seems to properly envelope the free decay signal.

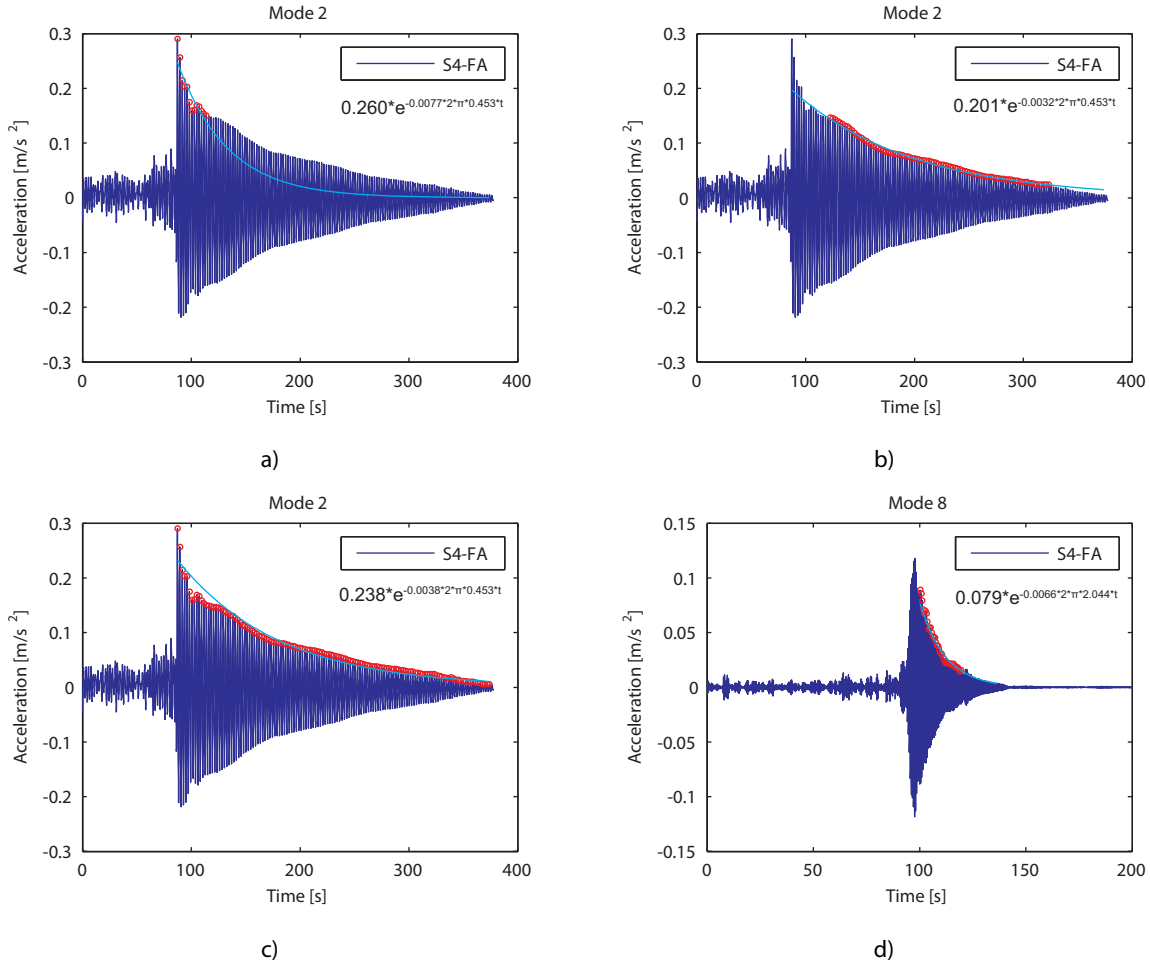

Figure 5.42 – Identification of the modal damping ratio of the 2nd and 8th vibration mode through filtering and fitting of an exponential function to the envelope of the free decay response

The same procedure was also applied to the 8th vibration mode. This mode is characterized by a symmetric in-phase bending of the three blades in the FA direction and, for that reason, was clearly excited during the test. For this mode, a band-pass filter for the frequency range 1.5 – 2.5 Hz was considered since the influence of other modes in this range seems negligible. The filtered response obtained for this mode presents an almost perfect free decay shape and, for that reason, only one adjustment was performed. Figure 5.42 shows the fitting operation performed for the 8th vibration mode.

In addition to the referred analysis, a second procedure was also used to estimate the damping value of the 2nd and 8th modes. This procedure is based on the application of the SSI-COV algorithm (introduced in section 5.4.1.2). This algorithm is adapted to consider the free decay signals as input of the method, instead of the correlation functions calculated from the ambient responses (Magalhães, Cunha et al., 2010). This procedure was applied to the same range of points previously presented for the two modes.

The results obtained with both procedures are shown in Table 5.7. For the 2nd vibration mode (1st FA mode), the fitting obtained with the initial part of the decay, associated with higher vibration levels, provided an higher value, which can be an indication that the damping may increase with the increasing of the vibration amplitude. The other two fittings performed for this mode represent a good estimation of the damping value for lower vibration amplitudes with a good agreement between the two used procedures. This value is considerable higher than the value obtained with the ambient vibration test, which is consistent with hypothesis of the damping dependency with the vibration amplitude

The damping value obtained for the 8th mode is coherent with the values obtained with the ambient vibration test.

It should be noted that damping values associated with operating condition can be considerable different, and generally higher, than these ones identified with parked conditions.

Table 5.7 – Natural frequencies (f) and modal damping ratios (ξ) of the 2nd and 8th vibration modes identified with the rotor-stop test with the filtering and fitting procedure and with the SSI-COV method

		Filtering and fitting		SSI-COV	
Mode	Considered range	Natural frequency [Hz]	Damping ratio [%]	Natural frequency [Hz]	Damping ratio [%]
2	Initial	0.453	0.77	0.452	0.68
2	Last	0.453	0.32	0.453	0.29
2	All	0.453	0.38	0.453	0.32
8	-	2.044	0.66	2.043	0.81

5.8.5 ANALYSIS AFTER THE INSTALLATION OF THE RBE

The RBE consists on a blade tip that is attached to the original blades in order to extend the rotor blades length. With the increase of the swept rotor area, this is a solution to improve the energy production on wind farms. An illustration of the RBE is presented in Figure 5.43.

The RBE installation consists on the overlapping of the original rotor blade tip by two half shells. These two shells are then fixed with adhesive resin. With this solution, the length of each blade is extended with 1.5 m length tips, increasing the swept area of the rotor in 8.6 %. Each blade tip weights 45 kg, which represents an increase of 1 % of the blade mass. The main properties of the RBE are summarized in Table 5.8.

For the analysis of the dynamic characteristics of the wind turbine blades after the RBE, only the data collected by the measurement system based on fibre Bragg grating system was considered.

Table 5.8 – Main characteristics of the RBE applied to the Izar Bonus 1.3MW/62

Length of RBE	3.0 m
Extension of the blade	1.5 m
Updated diameter	65 m
Increase swept rotor area	8.6 %
Weight of RBE (per blade)	45 kg
Variation of blade mass	+ 1 %

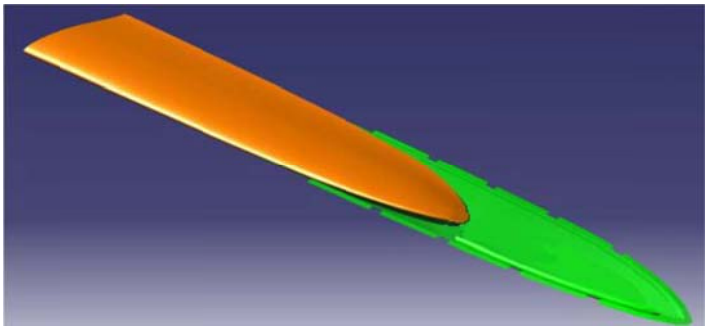

Figure 5.43 – Illustration of the RBE (Salavessa, 2014)

5.8.5.1 Analysis of the fibre Bragg grating sensors measurements

The data considered for the analysis corresponds to a setup of 18 minutes in which the rotor was parked. The mean wind speed observed during the setup was 7.5 m/s. In this data set, all the 12 sensors were available.

The averaged normalized power spectrum density of each sensor is presented in Figure 5.44. As can be seen, the spectra present a shape that is similar with the one shown in Figure 5.33 (related to data collected prior to the installation of the RBE). However, there is a decrease in the natural frequency values of the vibration modes.

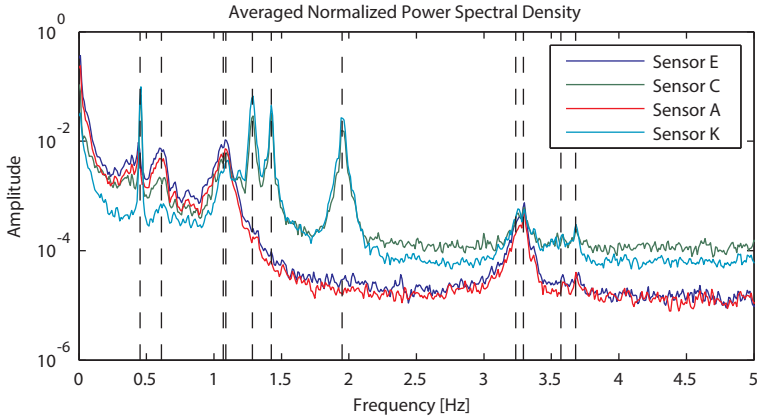

Figure 5.44 – Averaged normalized power spectrum density from each sensor (the dashed lines indicate the main peaks of the spectra)

The decrease in the natural frequency values is more evident when the signals collected before and after the RBE are confronted. Figure 5.45 shows the averaged normalized power spectrum density functions of the signals collected before and after the extension of the blades. Although, the global shape of the spectra is kept, there is an evident decrease of the frequency values of the resonance peaks.

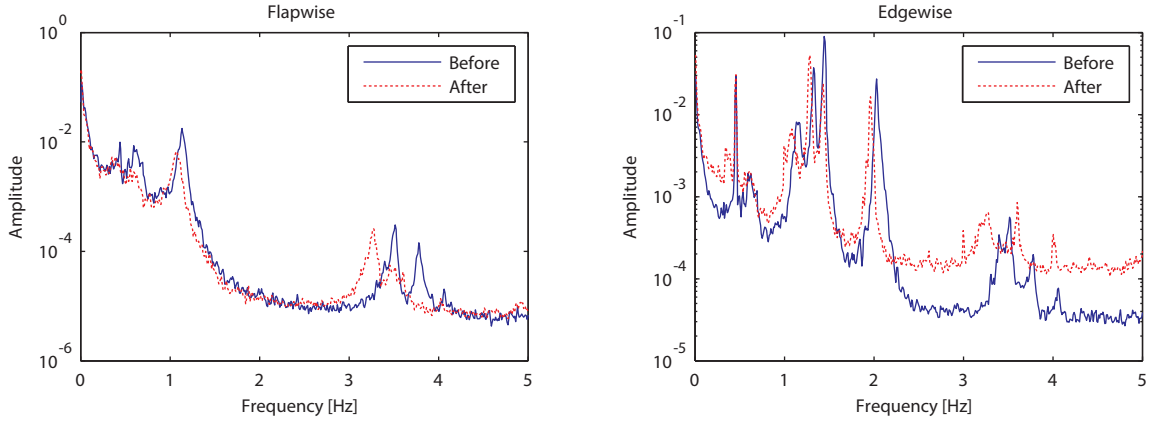

Figure 5.45 – Averaged normalized power spectrum density of the three blades before and after the RBE

The identification of the modal properties of the wind turbine after the RBE was performed with the same output-only algorithms. Once again, the results obtained with both algorithms were similar. In order to illustrate these results, the stabilization diagram obtained with the p-LSCF algorithm is presented in Figure 5.46.

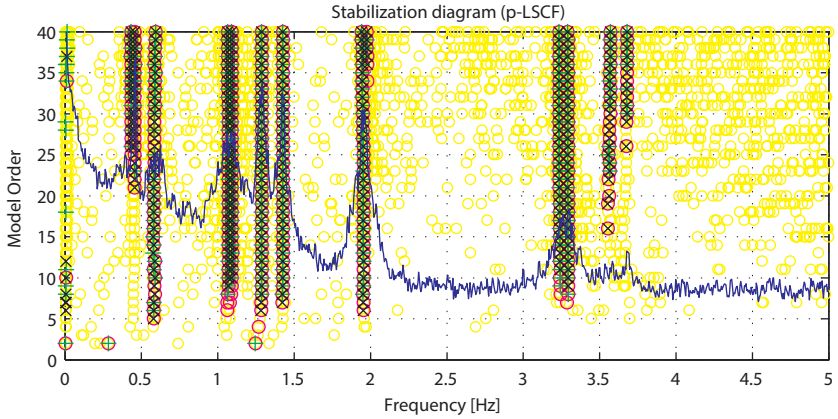

Figure 5.46 – Stabilization diagram obtained with the p-LSCF algorithm for the data obtained after the RBE

Several vibrations modes were again identified. However, due to the difficulty in the interpretation of their mode shapes, only the first 8 modes were considered. The results are presented in Table 5.9. The correspondence between the modes identified before and after the RBE was done considering the type of mode (in plane or out of plane) and the proximity between natural frequencies

From the results, it can be seen that the first two modes (tower bending modes) are only slightly affected by the RBE. However, the accuracy on the identification of these modes is lower than for the others since the main element of motion (the tower) is not instrumented.

The remaining modes, mainly related with motion of the rotor, present a consistent decrease on the value of the natural frequencies. It was noted that for modes 6 and 7 there is a change on the mode configuration (from yaw to tilt and vice versa). This might be motivated by a different position of the blades in the rotor plane during the two testing periods.

Table 5.9 – Natural frequencies (f) and modal damping ratios (ξ) from the first 8 identified vibration modes before and after the RBE (p-LSCF algorithm)

Mode	Before RBE			After RBE			Δf [%]
	f [Hz]	ξ [%]	Description	f [Hz]	ξ [%]	Description	
1	0.441	0.38	1st Tower SS	0.432	2.69	1st Tower SS	-2.0
2	0.456	0.17	1st Tower FA	0.456	0.10	1st Tower FA	0.0
3	0.610	8.51	In plane (symmetric) + drive train	0.589	6.39	In plane (symmetric) + drive train	-3.4
4	1.129	1.93	In plane (vertical)	1.068	2.96	In plane (vertical)	-5.4
5	1.146	2.51	In plane (horizontal)	1.095	2.98	In plane (horizontal)	-4.5
6	1.329	0.59	Out of plane (yaw)	1.286	0.75	Out of plane (tilt)	-3.2
7	1.449	0.47	Out of plane (tilt)	1.425	0.76	Out of plane (yaw)	-1.7
8	2.039	0.54	Out of plane (symmetric)	1.949	0.70	Out of plane (symmetric)	-4.4

5.8.6 CONCLUSIONS

This section presented the work carried out in the experimental identification of the dynamic properties of an Izar Bonus 1.3MW/62 wind turbine. In this study, different measurement systems were used to collect vibration signals from the tower (accelerometers) and blades (fibre Bragg grating sensors and accelerometers).

The analysis of the data allowed to identify 14 vibration modes, including the first two pairs of tower bending modes and the 6 first order rotor blades modes. The results obtained with both measurement systems revealed to be consistent.

After the installation of the Rotor Blade Extension, and the consequent increase of blades mass in 1 %, the decrease of the rotor modes natural frequencies was clearly identified, showing the ability of the used tools to identify small changes of the structural elements of the wind turbine.

A rotor-stop test was also performed, enabling the analysis of the modal damping ratio of the 1st tower bending mode in the FA direction and the 1st symmetric flapwise mode with greater precision. In that sense, two alternative procedures were used. A good coherence of results was obtained with both methods.

5.9 CASE STUDY – VESTAS V90-3.0MW

5.9.1 INTRODUCTION

This section presents the results obtained with the analysis of 80 acceleration data sets collected by a dynamic monitoring system installed at a Vestas V90-3.0MW offshore wind turbine. This study was developed with the aim of verifying the suitability of the developed tools when applied to offshore wind turbines.

The data used in this analysis was kindly provided by the Offshore Wind Infrastructure Application Lab (OWI-Lab - www.owi-lab.be/).

5.9.2 WIND TURBINE DESCRIPTION

The Vestas V90-3.0MW wind turbine is part of the Belwind wind farm, 46 km off the Belgian cost, on the Bligh Bank, North Sea (Figure 5.47). This offshore wind farm is composed by 55 Vestas V90-3.0MW turbines founded on monopiles, leading to a total power output capacity of 165 MW.

Figure 5.47 – Location of the Belwind wind farm (Belwind Offshore Energy, 2009)

The studied Vestas wind turbine is characterized by a 90 m diameter, upwind rotor, with a rated rotor speed of 16.1 rpm. The pitch angle of the three rotor blades is controlled by a pitch actuator. The power curve of the turbine is introduced in Figure 5.48.

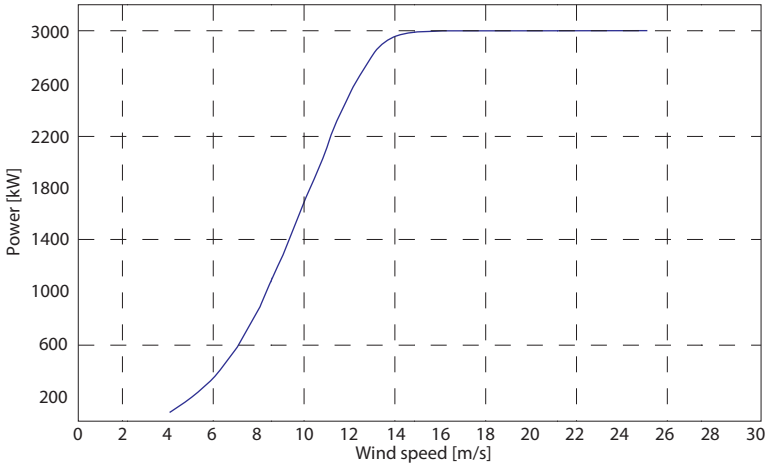

Figure 5.48 – Vestas V90-3MW power curve

The support structure of the wind turbine is a monopile with a diameter of 5 m. Its penetration depth is 20.6 m. The transition piece is 25 m high and the interface between the tower and the transition piece is 17 m above sea level. The water depth at the turbine location is 22.9 m and the hub height is, on average, 72 m above sea level. Figure 5.49 illustrates the main dimensions of the wind turbine. The soil at the location is considered stiff, mostly consisting of sand (Devriendt, Weijtjens et al., 2014).

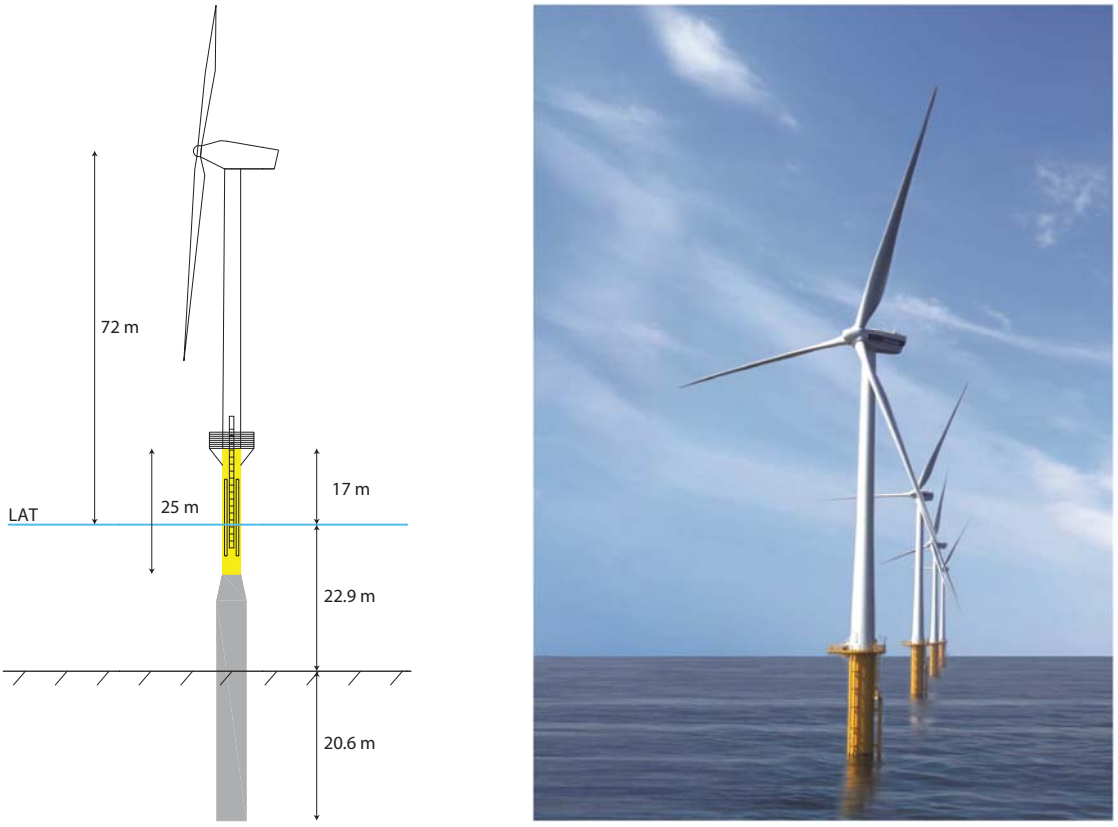

Figure 5.49 – Vestas V90-3.0MW wind turbine installed at the Belwind wind farm (Belwind Offshore Energy, 2009)

5.9.3 Monitoring System Description

The Vestas wind turbine is instrumented with several sensors, among which accelerometers, strain gauges, load cells and displacement sensors (Weijtjens, 2014). Alongside, a subset of the SCADA data was made available by the wind farm owner. In the scope of this study, only the accelerometer data, together with the respective SCADA data, was considered.

The accelerometers are installed at the tower and transition piece, using 10 sensors distributed along 4 levels of measurements (19 m, 27 m, 41 m and 69 m above sea level). At the 4 levels of measurement, 2 sensors record the horizontal motion in both orthogonal directions, while 2 additional accelerometers are installed at the top level to capture the torsional motion of the support structure (Devriendt, Magalhães et al., 2014). The measurement locations are illustrated in Figure 5.50.

The data acquisition system is mounted at the transition piece. The accelerometer data is acquired with a sampling rate of 5 kHz and then re-sampled with a sampling frequency of 12.5 Hz. Lastly, the coordinate transformation introduced in section 5.6.1 is performed to the recorded signals to orientate them according to the FA and SS directions.

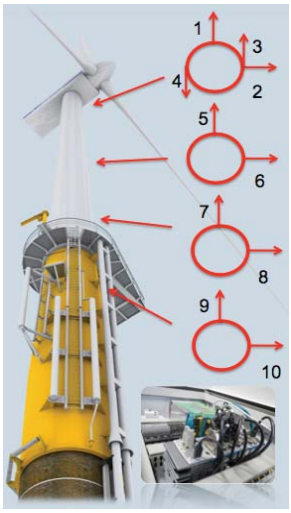

Figure 5.50 – Position of the accelerometers at the different levels of the wind turbine (Devriendt, Magalhães et al., 2014)

5.9.4 Acceleration Data Sets

The data analysed in this section is referred to 80 setups of 10 minutes, grouped into 4 different operation conditions.

Case 1 is referred to a situation in which the turbine is not operating. Figure 5.51 presents an example of a data set from this case. As can be seen in the SCADA data plotted in Figure 5.52, the wind turbine is idling with large values of blades pitch angle. Under these conditions, the wind turbine support structure mainly vibrates in the SS direction probably due to the larger opposition of the blades to the air flow in this direction (due to large pitch angle values) and to some possible misalignment of the rotor to the wind (due to the fact that the turbine is not operating). This is visible in the bottom plot of Figure 5.51, where the RMS values of the acceleration from each sensor are shown (sensors 3 and 4 were not considered in the plot).

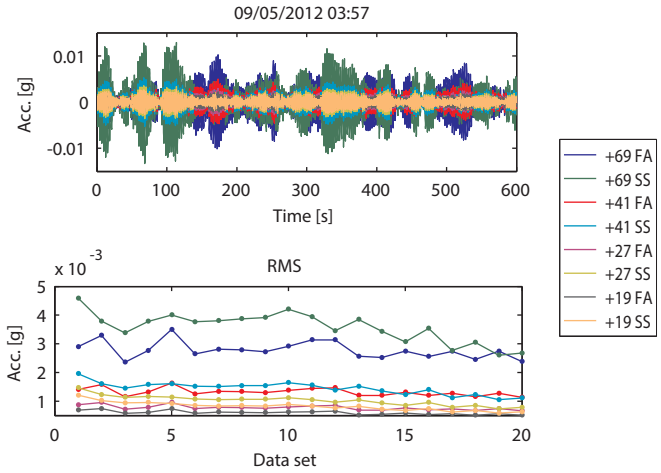

Figure 5.51 – Example of measured acceleration time series (top plot) and RMS values of the 20 data sets from Case 1 (bottom plot)

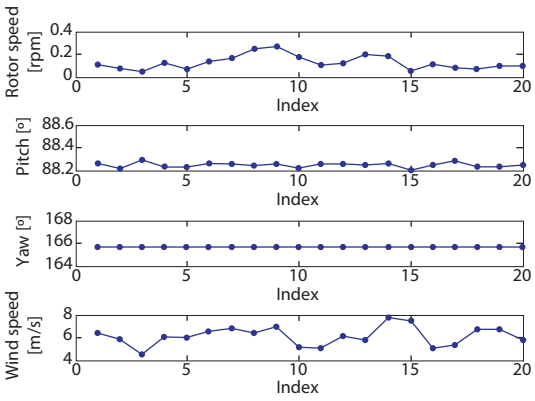

Figure 5.52 – SCADA data of the 20 data sets from Case 1

The remaining 3 cases are referred to production periods under different conditions. The data sets from Case 2 consist of acceleration time series during periods when the turbine is operating close to the rated wind speed, with the highest wind speed values from the 4 cases (Figure 5.54). The acceleration levels from the 20 data sets of this case present also the largest values (Figure 5.53). Under these conditions, with the rotor orientated to the main wind direction and the blades with low pitch angles, the turbine support structure vibrates mainly in the FA direction. It is also interesting to note that the measurement level with the highest vibration level is not the top level (+ 69 m) like in the data from Case 1, but the + 41 m level. In fact, it is observed that the top level present similar vibration levels to the +27 m level. This phenomenon is analysed in Chapter 7 in another case study.

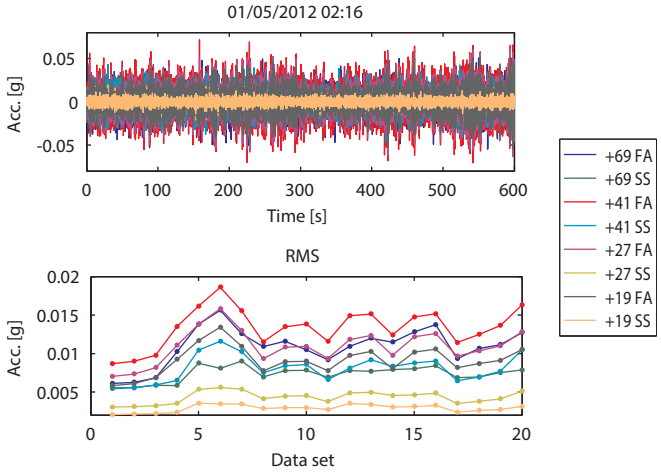

Figure 5.53 – Example of measured acceleration time series (top plot) and RMS values of the 20 data sets from case 2 (bottom plot)

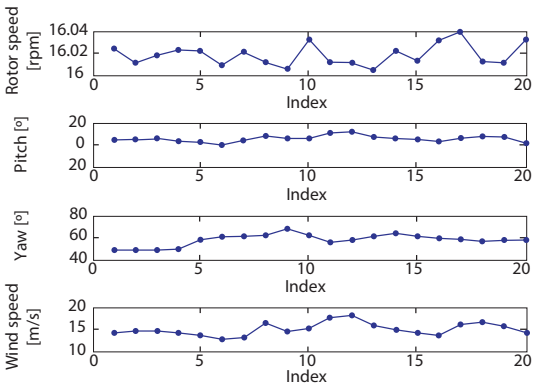

Figure 5.54 – SCADA data of the 20 data sets from case 2

Case 3 consists of data sets with varying rotor speeds (Figure 5.56). Similarly to case 2, the turbine also presents the highest acceleration levels of the support structure at +41 m level (Figure 5.55).

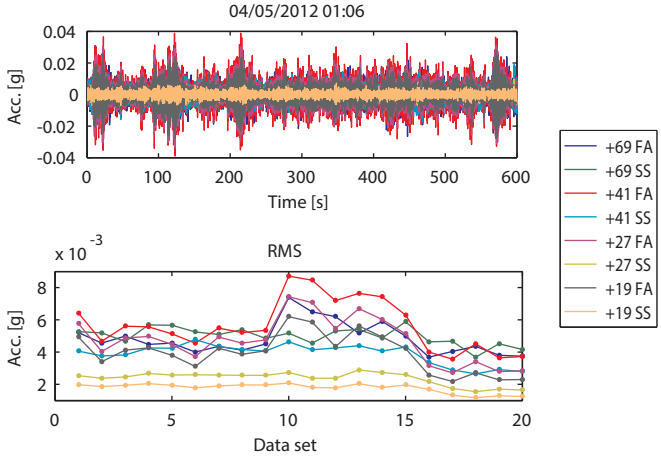

Figure 5.55 – Example of measured acceleration time series (top plot) and RMS values of the 20 data sets from case 3 (bottom plot)

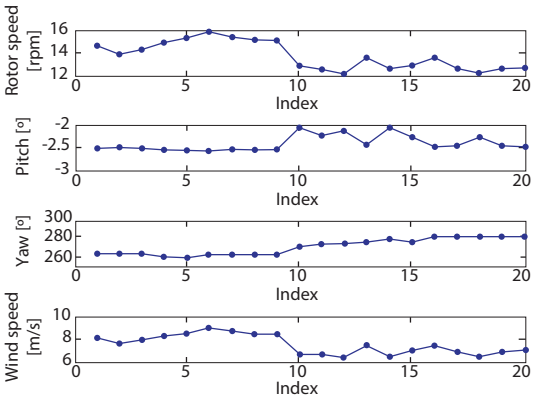

Figure 5.56 – SCADA data of the 20 data sets from case 3

Lastly, Case 4 comprises the time series under operating conditions with the lowest acceleration levels (Figure 5.57). This case is referred to data sets in which the turbine is operating with a nearly constant rotor speed of 10 rpm (Figure 5.58). The only exception is the 6th data set, where a stoppage of the operation seems to occur.

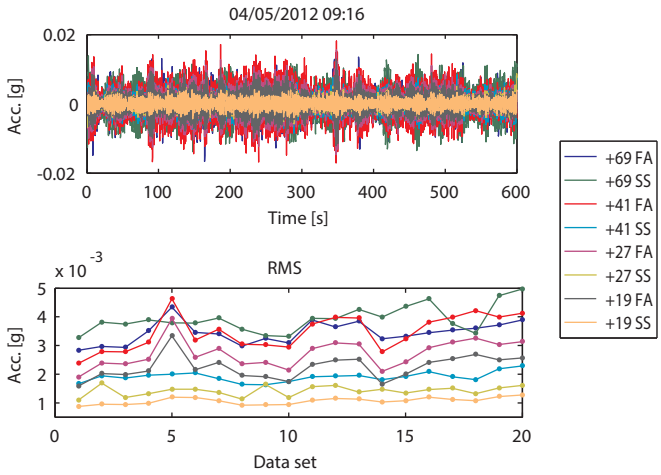

Figure 5.57 – Example of measured acceleration time series (top plot) and RMS values of the 20 data sets from case 4 (bottom plot)

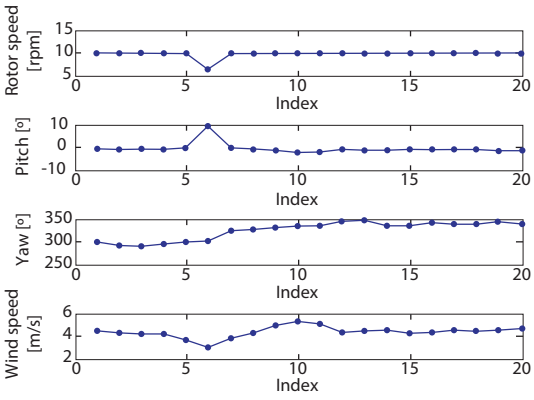

Figure 5.58 – SCADA data of the 20 data sets from case 4

The colour map shown in Figure 5.59 illustrates the distribution of energy in the analysed frequency range (0 – 4.5 Hz) using the first singular value spectra of the 80 acceleration data sets within the frequency range 0 - 4.5 Hz. The frequency values corresponding to the harmonics 3Ω to 24Ω are also represented by dashed lines. From an initial analysis of the figure, a vertical alignment with high energy around 0.36 Hz is immediately noticed throughout the 4 studied cases. This alignment is probably due to the 1st pair of support structure bending modes, since its value is within the common values of these modes. It is also interesting to observe the large scattering of energy around the frequency values below this alignment. This situation is probably due to the wave excitation. As

introduced in Chapter 4, the range of frequencies of wave excitation is usually spread along a relative wide range of frequencies below the 1st pair of bending modes.

The presented colour map also highlights an important aspect in the analysis of the data from this offshore wind turbine. The energy scattering of the 4 cases is very different from each other. The first 20 data sets (referred to Case 1), present a clean spread of energy, with three well-defined alignments around 1.20, 1.44 and 1.50 Hz and three additional not so well-defined alignments around 3.24, 3.60 and 3.90 Hz, besides the aforementioned alignment around 0.36 Hz. However, for the remaining 3 cases (corresponding to operating conditions), only the alignment around 0.36 Hz is clearly identified, due to the important influence of the rotor harmonics in the spectra. Notwithstanding, a frequency range of high energy is still seen around 1.50 Hz, although with a considerably higher dispersion than in Case 1. Alignments of high energy corresponding to the possible modes around 3.24, 3.60 and 3.90 Hz are also hard to identify in Figure 5.59 in these 3 operating cases.

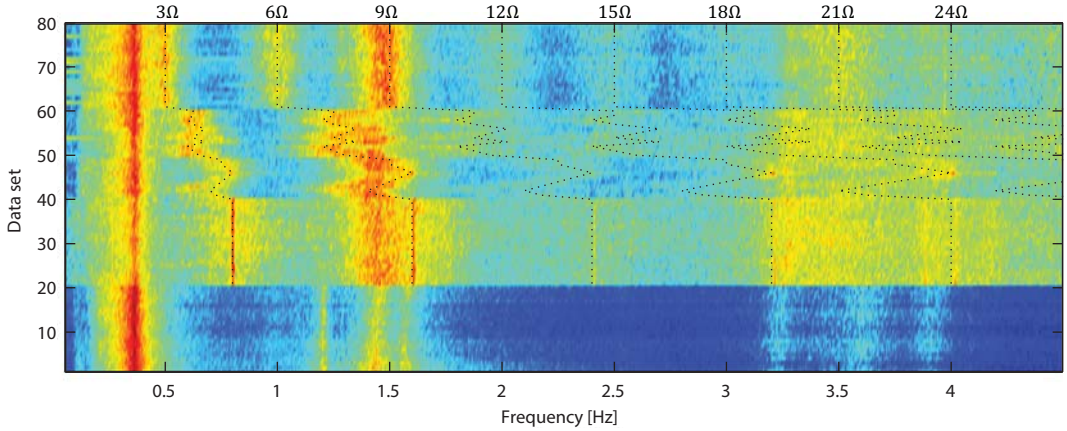

Figure 5.59 – Colour map with the 1st singular value spectra of the 80 data sets (the regions with the hotter colours represent the highest energy)

Figure 5.60 illustrates the difference in the spectra from operating and non-operating conditions. As expected, the presence of harmonics is clearly evident. The 3 alignments around 1.20, 1.44 and 1.50 Hz visible in Figure 5.59 are also easily identified in Figure 5.60 for non-operating conditions. Under operating conditions, the obtained spectrum is apparently changed in this frequency range. The peak corresponding to the vibration mode around 1.20 Hz is not present in this frequency. At the same time, a new (but smaller) peak with a slightly lower frequency value (around 1.17 Hz) is found for the turbine under operating conditions. This may be a sign that this mode corresponds to a rotor vibration mode, changing its frequency value according to the pitch angle of the blades. Two very close peaks around 1.42 Hz and 1.46 Hz are found in the spectra corresponding to operating conditions, while only the latter is identified in the spectra from non-operating conditions. In addition, the resonance peak around 1.50 Hz found under non-operating conditions is apparently not identified under operating conditions due to the interference of the 6Ω harmonic in this frequency range.

The three modes around 3.24, 3.60 and 3.90 Hz, identified in the colour map referred to the Case 1 are also identified in Figure 5.60 for both situations. However, it is expected that some harmonics may affect the quality of the identification process of these modes. It is interesting to note that these 3 modes do not present a well identified resonance peak as the other modes do. This is the reason why the energy alignments of these modes in Figure 5.59 are not as clear as the others.

Lastly, the spectra in Figure 5.60 also allow assessing the influence of the wave excitation in the dynamic response of the wind turbine support structure. This excitation is spread in small peaks with frequency values below the first resonance peak (around 0.36 Hz).

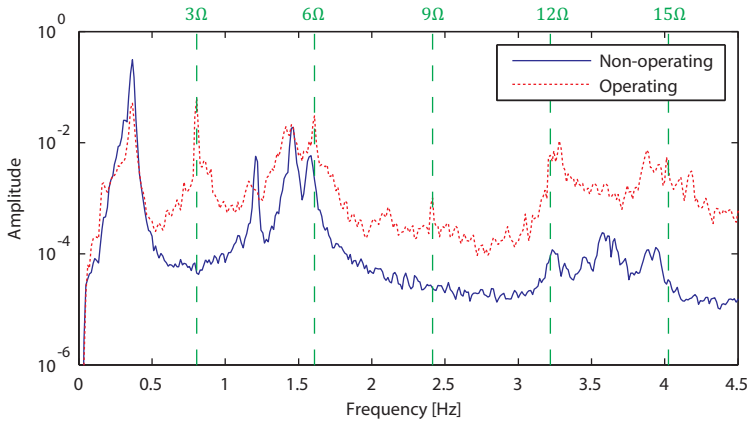

Figure 5.60 – ANPSD from two different setups: under non-operating conditions (rotor speed = 0 rpm; wind speed = 6 m/s) and operating conditions (rotor speed = 16.0 rpm; wind speed = 17 m/s). The vertical dashed lines indicate the frequency values of the rotor speed 3Ω and its harmonics

5.9.5 Modal Results

In the context of the analysis of the modal properties of the Vestas V90 offshore wind turbine, the SSI-COV and the p-LSCF modal identification algorithms were used. Figure 5.61 presents the stabilization diagrams obtained with the p-LSCF algorithms to a data set corresponding to non-operating conditions. From the figure, it is possible to clearly identify 8 alignments of stable poles. These alignments are in agreement with the previous considerations made for non-operating conditions. The right side of Figure 5.61 shows a zoom of the same stabilization diagram between 0.30 and 0.40 Hz, attesting the presence of two closely spaced alignments (corresponding to the first pair of support structure bending modes). Furthermore, it is also possible to observe the presence of some additional poles mainly due to the wave excitation.

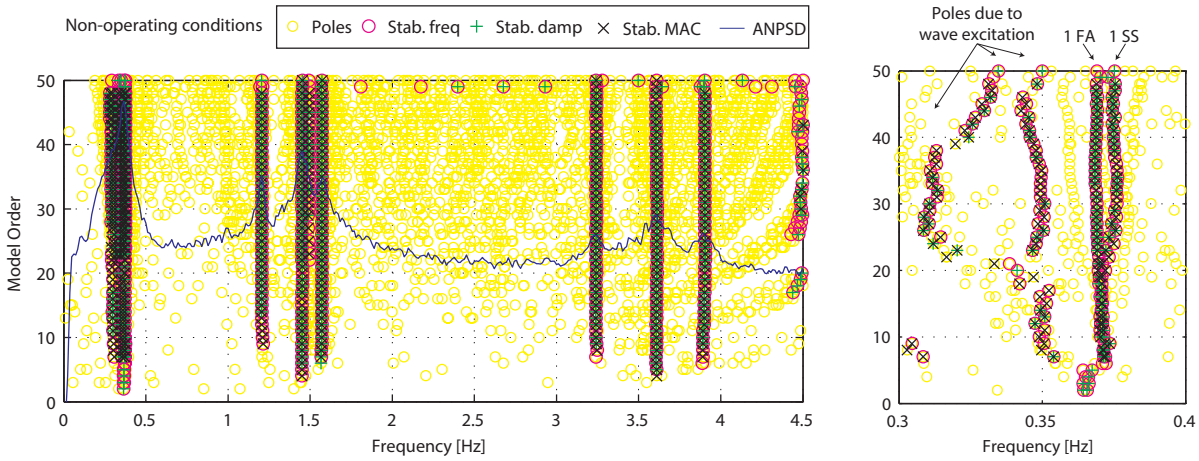

Figure 5.61 – Stabilization diagram obtained with the p-LSCF algorithm in a data set corresponding to non-operating conditions

Figure 5.62 introduces the stabilization diagram obtained for a data set recorded during operating conditions with the p-LSCF algorithm. From this figure, it is visible that the rotor harmonics are identified as alignments of stable poles, just like real vibration modes. Notwithstanding, both the first pair of bending modes and the modes around 3.24, 3.60 and 3.90 Hz have clear alignments of stable poles.

The right plot of Figure 5.62 shows a zoom of the stabilization diagram between 1.1 and 2.2 Hz. From this figure, it is possible to see the existence of stable alignments around 1.17, 1.75 and 2.10 Hz. While the former is close to a resonance peak identified during non-operating conditions (around 1.20 Hz), the last two are only identified when the turbine is operating. In addition, two close alignments of poles are also visible around 1.41 and 1.44 Hz. This situation is different from the one obtained with the turbine under parked/ idling conditions, where only one vibration mode was identified in this frequency range. As will be seen ahead, these two modes present a similar mode shape.

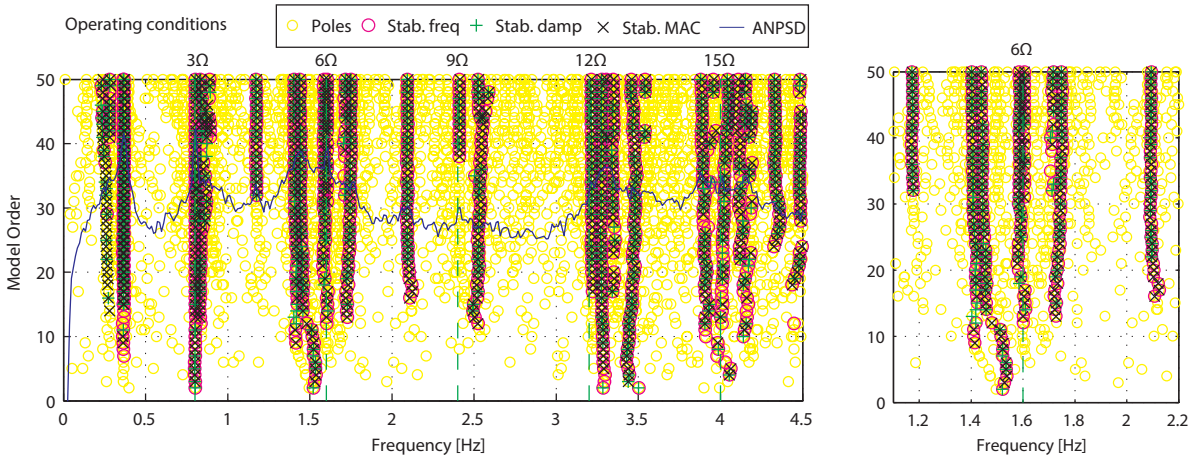

Figure 5.62 – Stabilization diagram obtained with the p-LSCF algorithm in a data set corresponding to operating conditions

Since only a limited number of data was analysed, it is not possible to clearly attest the nature of some vibration modes, as well as the correspondence of some modes between parked/ idling and operating conditions. Thus, it is not possible to elaborate a clarifying Campbell diagram, which could help to better interpret the identified vibration modes. If a proper Campbell diagram could be obtained, it would be possible to check which modes are related to the blades rotor motion as these modes are highly dependent on the rotor speed when fixed sensors are used, as explained in Chapter 4. Notwithstanding, some modes are clearly identified and their nature is indubitably understood. This is the case of the first pair of support structure bending modes, which natural frequencies are kept fairly constant during non-operating and operating conditions.

The mode shapes of the 8 vibration modes identified under non-operating conditions are presented in Figure 5.63. These modes are identified by the index "non" (from non-operating conditions). The two first modes are indubitably the first pair of bending modes (in FA and SS direction). The 3rd, 4th and 5th identified modes present a second-order configuration for their mode shapes in the FA, SS and FA direction, respectively. However, it is noticed that 3rd mode presents practically null displacement at the top sensor, while the other two show some motion at this level. The last three identified modes also present a similar configuration, potentially a 3rd order shape configuration. However, since the first

level of measurement is around + 19 m, it is not possible to accurately estimate the configuration of this mode in the lower part of the support structure.

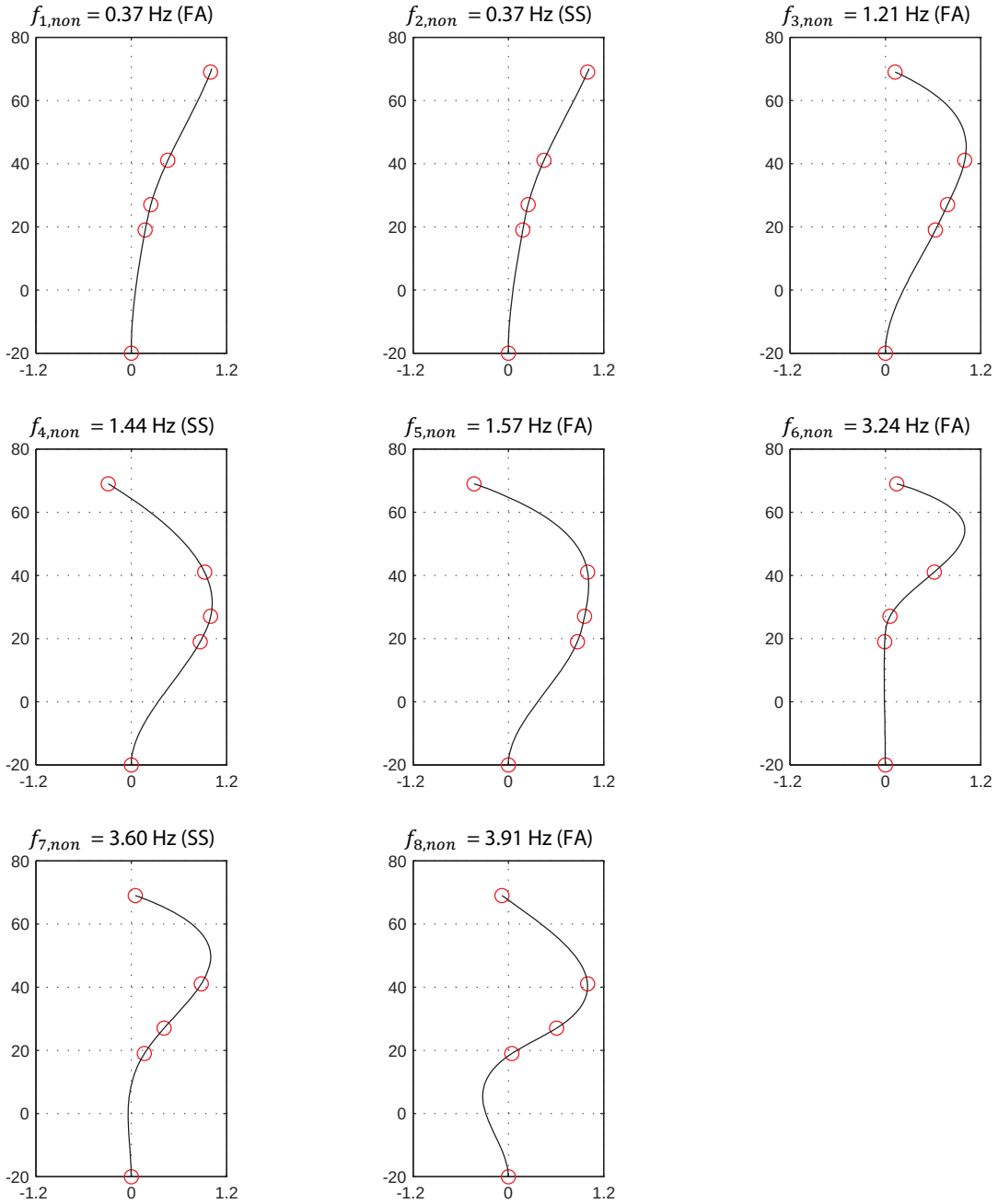

Figure 5.63 – Tower mode shapes of the identified vibration modes under non-operating conditions

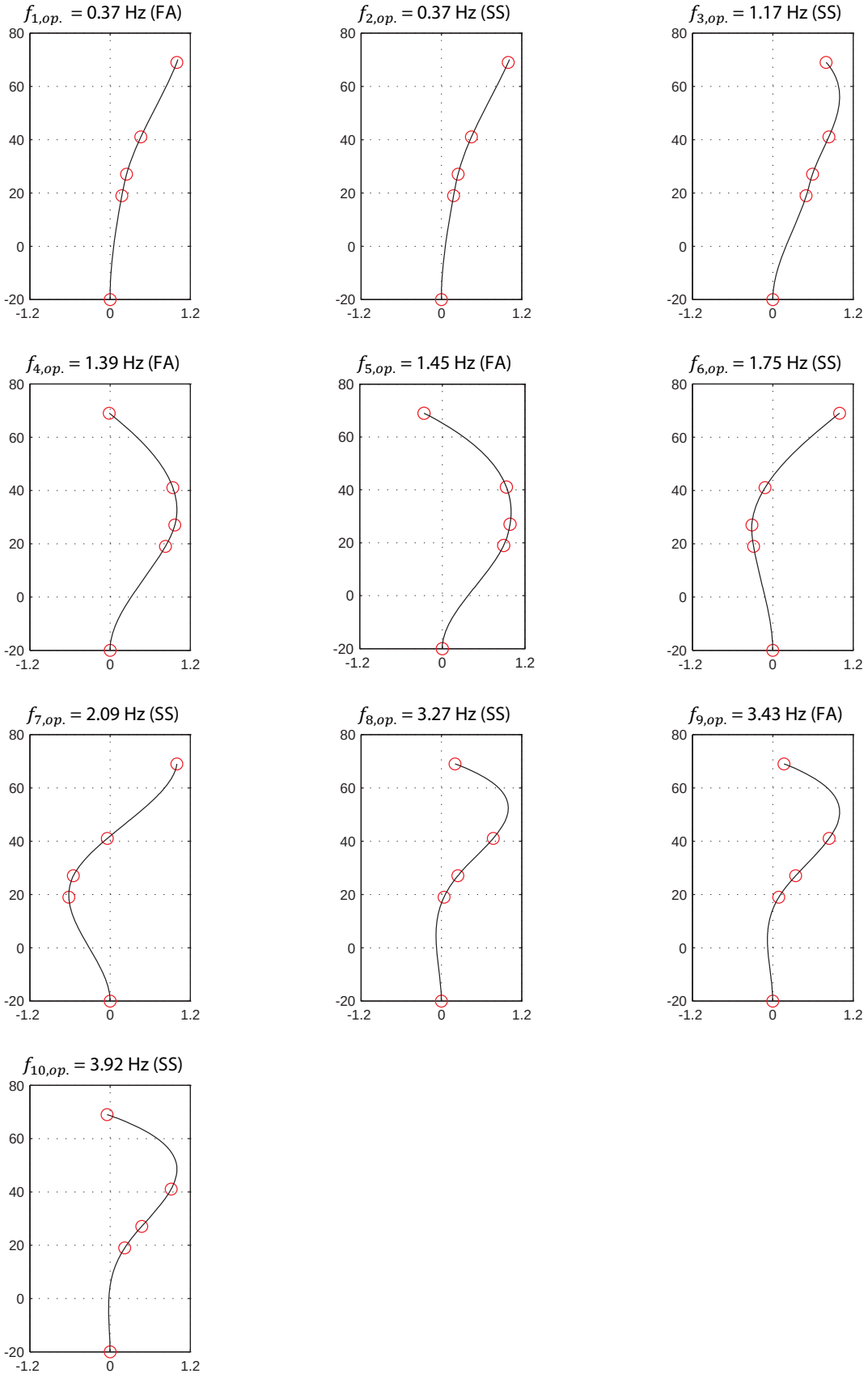

Figure 5.64 – Tower mode shapes of the identified vibration modes under operating conditions

Figure 5.64 introduces the mode shapes of the 10 identified vibration modes during operating conditions, identified with the index "op.". The two first modes are the 1st pair of support structure bending modes, also identified during non-operating conditions. The 3rd, 6th and 7th are modes vibrating in the SS direction that were not identified with the data corresponding to Case 1. Thus, these are modes potentially linked to asymmetric edgewise blades rotor motion, since this type of modes creates a reaction at the top of the tower in the SS direction, due to the configuration of the blades with low pitch angles (contrary to the configuration in standstill conditions, where the pitch angle is usually around 80º - 90º). On the other hand, the configurations of 4th and 5th modes (both in FA direction) resemble the ones from the 3rd and 5th modes under parked/ idling conditions. However, a mode with a configuration similar to the 4th mode (in the SS direction) was not identified in the analysed data sets, turning it difficult to assess the nature of these modes. Lastly, the 8th, 9th and 10th modes show a similar configuration to the 6th, 7th and 8th modes identified under non-operating conditions. However, it is interesting to note that all of them changed their direction of vibration. The reasons behind this phenomenon are probably related to the interference of the blades pitch angle in the motion of these modes. A more profound comprehension of these modes would require the analysis of a more extended period of data.

After the main vibration modes were preliminary analysed, all the data was automated processed in order to obtain the modal properties of the introduced modes. After the application of the output-only identification algorithms to the recorded acceleration time series, the cluster algorithm described in section 5.7.1 was applied to the obtained stable poles. A maximum distance of 0.02 was defined for the single linkage criterion. Figure 5.65 shows the computed clusters from the stabilization diagrams represented in Figures 5.61 and 5.62, quantifying the average frequency value of the poles included in each cluster and the number of poles of each cluster. In this analysis, it was decided to exclude the clusters with a number of poles lower than 6, as identified by the red dashed line.

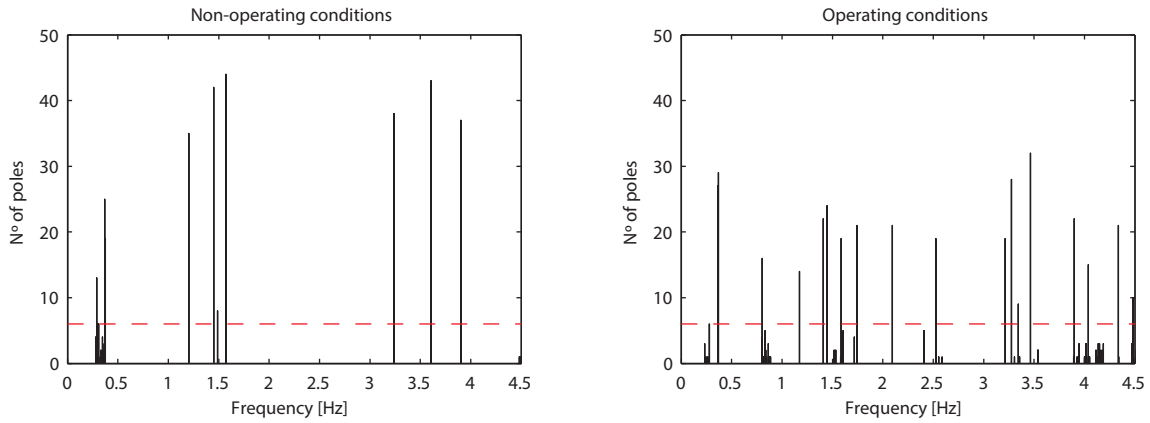

Figure 5.65 – Characterization of the clusters: average frequency and number of poles included in each cluster

A representative value of the modal properties from each cluster (frequency value, damping ratio and mode shape) was kept. Figure 5.66 shows the representative frequency value of the considered clusters for each data set. In this figure, each selected results was defined as FA or SS, according to the main direction of vibration of its mode shape. This figure is illustrative of the increased difficulty in the identification of the vibration modes under operating conditions. While in Case 1 the considered poles present a very stable and clear evolution of their frequency values, a part from some disturbance

around the 1st pair of bending modes due to the wave excitation, the same does not occur for the remaining cases. Under operating conditions, the appearance of relevant clusters due to the presence of the harmonics is evident. Besides the harmonics, this figure allows to confirm some previous referred considerations. For example, it is evident that the last 3 modes detected for both under parked/ idling and operating conditions inverted theirs main direction of vibration. Furthermore, both the $6, op.$ and $7, op.$ modes are clearly distinguished once the turbine is operating (although not in every case). Lastly, the two closely spaced modes $4, op.$ and $5, op.$ are also identifiable only in cases 2, 3 and 4.

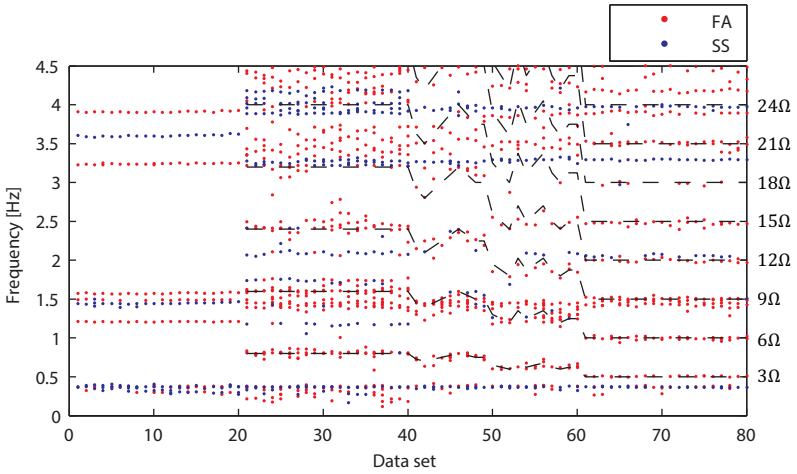

Figure 5.66 – Considered poles from each data set according to the main direction of vibration of the mode shape (the dashed lines refer to the frequency value of the harmonics of each data set)

In order to identify the selected reference vibration modes from the poles obtained with the identification algorithms, the modal properties presented in Figures 7.63 and 7.64 were used as reference properties of the modes. Thus, for each data set, the clusters with a frequency value close to a reference natural frequency value were selected. The frequency range adopted to consider a pole varied between 10 % (for the 1st pair of bending modes) and 20 % (for the others). Within the considered poles, the one with highest correlation with the reference mode shape (i.e. the highest value of MAC coefficient) is selected. Only modes with MAC values higher than 0.80 were considered.

This procedure was applied together with the p-LSCF and SSI-COV modal identification algorithms, as already stated. For the p-LSCF method, positive time lags of the correlation with 1024 points were used to calculate the spectra, together with an exponential window with a factor of 0.1. A maximum model order of 50 was considered. In order to assess the stability of a pole, the criteria exhibited in Table 5.10 were followed. These settings were already used for the results previously presented in this section.

Table 5.10 – Stable pole criteria for models of consecutive orders

Modal parameter	Maximum allowed variation
Frequency	$\Delta f \leq 1\,\%$
Damping	$\Delta \xi \leq 5\,\%$
Mode Shape	$MAC \geq 0.97$

Figure 5.67 presents the results obtained after the comparison of the selected cluster properties with the properties of the reference modes. From this figure, it can be seen that the modes were successfully identified throughout all the cases. Only the identification of the $3, op.$ mode shows a poor success rate, being only identified in case 2. In this figure, the colours selected for the tracked modes from Case 1 purposely does not match with the colours from the other Cases since it was not intended to link the identified vibration modes from non-operating conditions with the ones from operating conditions.

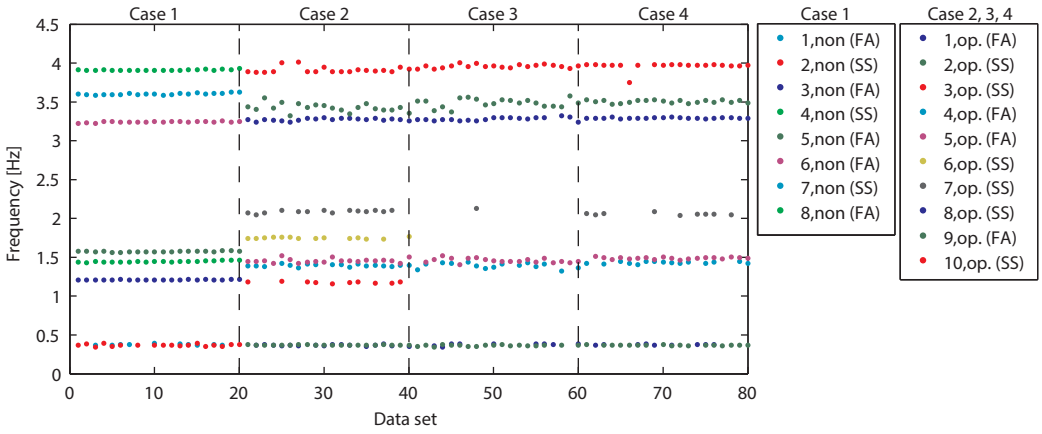

Figure 5.67 – Tracked vibration modes

The identified modal properties of the vibration modes with the p-LSCF algorithm throughout the 4 cases are summarized in Table 5.11. From these results, it is interesting to note that, under non-operating conditions, the 2nd mode (the 1st bending mode in the SS direction) presents higher damping values than its pair in the FA direction. However, under operating conditions, this situation is inverted, being the mode in the FA direction the one with the highest damping values. This situation is caused by a possible deviation of the rotor from the wind direction and to the high pitch value of the blades when the turbine is parked/ idling (Case 1). Under this configuration, the blades present a larger opposition to the air in the SS direction, leading to the appearance of some contribution of aerodynamic damping in this direction. When the turbine is operating (Case 2, 3 and 4), the rotor is oriented to the main wind direction and the blades present a low pitch angle. Under these circumstances, the main opposition to the air by the rotor is presented in the FA direction, vanishing the aerodynamic contribution in the SS direction. Since the aerodynamic damping component increases with the increase of the wind speed (assuming similar blades pitch angle), the damping values of the mode in the FA direction shows its highest values in Case 2, corresponding to the data sets with the highest wind speed.

Another interesting aspect of the results obtained is related with the damping values of the last 3 mode shapes of both parked/ idling and operating conditions. It is noted that for non-operating conditions, the SS vibration mode (7th mode) presents the highest damping values, while the other 2 modes vibrating in the FA direction present similar damping values. When the turbine is operating, the two SS modes present similar damping values (8th and 10th modes), while the 9th mode (in the FA direction) shows the highest damping ratio. This correspondence reinforces the idea of these modes found in Case 2, 3 and 4 may be linked to the last three modes found in 1 case.

Table 5.11 – Mean values of natural frequency and damping ratio obtained with the p-LSCF algorithm

	Case 1		Case 2		Case 3		Case 4	
Mode	f [Hz]	ξ [%]	f [Hz]	ξ [%]	f [Hz]	ξ [%]	f [Hz]	ξ [%]
1	0.374	1.77	0.364	4.68	0.375	2.16	0.373	2.87
2	0.366	2.23	0.368	1.66	0.361	1.56	0.365	1.40
3	1.207	0.65	1.174	0.77	-	-	-	-
4	1.444	1.20	1.393	1.39	1.390	1.52	1.428	0.88
5	1.571	1.01	1.453	1.00	1.457	1.30	1.487	0.89
6	3.239	0.56	1.746	1.10	-	-	-	-
7	3.600	1.70	2.085	1.09	2.126	0.80	2.054	1.16
8	3.907	0.89	3.269	0.67	3.278	0.93	3.290	0.79
9	-	-	3.423	1.19	3.484	1.49	3.503	1.65
10	-	-	3.910	0.49	3.958	1.07	3.960	0.52

The same strategy was also followed with the SSI-COV algorithm. For this method, 512 points of the correlation functions were used. The state-space models were defined with a maximum order of 100. Table 5.12 sums up the main results obtained with this algorithm. Although similar, the results attained with this algorithm were not as good as the ones obtained with the p-LSCF, for the analysed data. This is particularly relevant due to non-identification of 3rd and 7th vibration mode during operating conditions.

Table 5.12 – Mean values of natural frequency and damping ratio obtained with the SSI-COV algorithm

	Case 1		Case 2		Case 3		Case 4	
Mode	f [Hz]	ξ [%]	f [Hz]	ξ [%]	f [Hz]	ξ [%]	f [Hz]	ξ [%]
1	0.366	1.66	0.365	6.78	0.370	5.19	0.366	4.23
2	0.366	2.01	0.369	2.07	0.365	2.40	0.364	1.91
3	1.207	0.57	-	-	-	-	-	-
4	1.444	1.29	1.397	1.23	1.399	1.24	1.413	0.90
5	1.573	1.12	1.444	1.60	1.457	0.79	1.473	1.19
6	3.236	0.72	1.741	0.95	-	-	-	-
7	3.591	1.51	-	-	-	-	-	-
8	3.902	1.02	3.273	0.57	3.281	0.61	3.288	0.61
9	-	-	3.458	1.93	3.494	2.01	3.483	1.13
10	-	-	3.923	0.56	3.935	0.72	3.978	0.21

5.9.6 Conclusions

This section presented the results obtained with the analysis of vibration data collected during a short period of time from a Vestas V90-3.0MW offshore wind turbine. In this analysis, four different scenarios of operation were studied, including idling and power production conditions.

The analysis undertaken permitted to identify 8 vibration modes during non-operating conditions and 10 modes during power production conditions. It was noticed that the dynamic properties of the wind turbine are considerably different depending if the system is operating or not.

An automated procedure was successfully applied to the data to automatically track the modal properties of the identified vibration modes throughout the different cases. The results obtained gave a good indication about the possibility of development of a generic dynamic monitoring system to be installed in both onshore and offshore, as exposed in (Oliveira, Weijtjens et al., 2014).

Due to the restricted period of analysis, it was not possible to attest the accuracy of the monitoring system to detect small damages on the support structure of the wind turbine. Notwithstanding, work developed on the same wind turbine using a long period of data revealed a good accuracy in the detection of structural changes in the foundation (Weijtjens, Verbelen et al., 2015).

6
FATIGUE ASSESSMENT OF WIND TURBINES

6.1 INTRODUCTION TO FATIGUE PROBLEMS IN WIND TURBINES

Wind turbines are structures predominantly subjected to dynamic loads. During a life period of 20 years, long and flexible blades from a large rotating component (the rotor) suffer from both the turbulent wind and the gradient wind shear. This rotating equipment is placed at the top of a slender structure (prone to resonance problems), suffering from a cyclic wind flow disturbance (the tower shadow effect). This scenario illustrates the harsh environment that the wind turbine structure has to withstand.

From a fatigue point of view, the design of a wind turbine is a very complex task. Wind turbines are composed by large structural components designed with several materials, leading to different properties and assessment procedures (Sutherland, 2000). Also, the definition of the loading scenarios is a difficult and extensive task (especially for offshore turbines). Apart from quasi-static loads (such as sea current), environmental loads acting on the wind turbines show a dynamic, non-deterministic nature, leading to a considerable uncertainty in their quantification and frequency of occurrence.

Some published studies refer the complexity and uncertainty associated with the fatigue assessment of wind turbines support structures. In (Tempel, 2006), the fatigue assessment of the monopile support structure was performed using a numerical frequency-domain approach. In this work, a large number of environmental conditions were analysed, aiming to reproduce the wind and sea states.

The study present in (Dong, Moan et al., 2012) shows a different approach for fatigue analysis of welded connections on offshore jacked support structures for wind turbines. In this work, the uncertainties associated with several design aspects, such as loading scenarios, dynamic behaviour of the structure and corrosion, are taken into account to perform a fatigue reliability analysis.

The numerical assessment of the fatigue damage in a floating wind turbine is described in (Kvittem and Moan, 2015). In this work, the need for a correct tuning of the dynamic properties is said to be very important to avoid a rapid increase of fatigue damage at the support structure.

The work described in (Weijtjens, Iliopoulos et al., 2015) presents the initial results obtained with the installation of fibre Bragg gratings strain sensors at the tower and transition piece of the Vestas V90-3.0 MW introduced earlier in Chapter 5. In the present research, a clear relationship between fatigue damage rate and wind turbulence intensity is evidenced.

In this work, the fatigue assessment is focused on the tower of the wind turbine.

6.2 Fatigue Design Loads

Wind turbines are subjected to a large variety of dynamic loads contributing to the fatigue wear of the structure. There are mainly three sources of fatigue loads for wind turbines:

- Wind;
- Rotor operation (and all the consequences of its rotation, such as the tower shadow effect);
- Waves.

Wind loading is the primary external source of excitation of wind turbines. In Chapter 3, a brief theoretical explanation about the rotor thrust force introduced by the wind was already developed. In the context of fatigue analysis, it is also of interest to understand how it dynamically affects the wind turbine structure.

Time varying wind speed time series are usually assumed as the sum of two components: a mean wind speed U and a turbulent component u. Considering the HAWC2 example introduced in Chapter 4, the two aforementioned components of the wind speed at the hub height are illustrated in Figure 6.1.

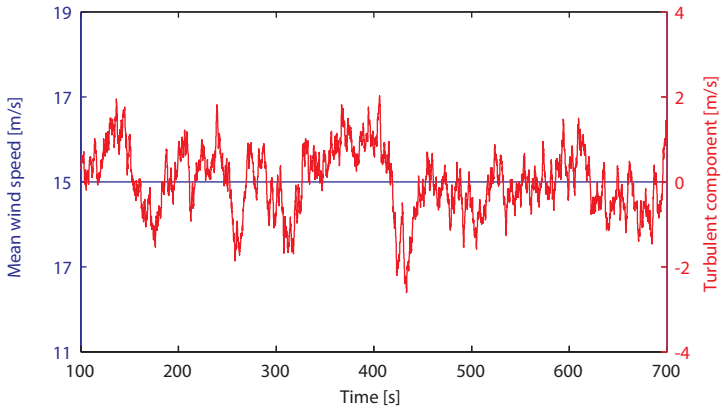

Figure 6.1 – Mean wind speed and turbulent component of the wind speed at the hub height (simulated in the context of the NREL 5MW wind turbine example)

The turbulent component of the wind can thus be seen as the component responsible for the dynamic excitation of the wind turbine. It is considered a non-deterministic variable and, for that reason, it is usually defined by statistical means. A common way to define the turbulence intensity of the wind I_w in the flow direction is through the ratio between the standard-deviation of the wind speed and its mean value:

$$I_w = \frac{\sigma_w}{U} \tag{6.1}$$

In addition to the turbulence in the mean wind direction, also the lateral and vertical turbulence are defined similarly.

The turbulence is usually represented in the spectral form. This representation allows understanding the frequency regions with higher excitation energy. The most commonly used turbulence spectra

models are the von Kármán and the Kaimal spectra (Burton, Sharpe et al., 2001). Figure 6.2 presents the von Kármán turbulence autospectral density function for several mean wind speeds. As can be seen, the energy is essentially concentrated at the very low frequency values.

For common wind turbine structures, whose lowest vibration mode is usually around 0.30 – 0.40 Hz, the energy from the lowest part of the spectrum is mainly responsible for the quasi-static response of the structure, i. e., with high amplitude displacement cycles with large periods of occurrence. On the other hand, the remaining frequency range of the spectrum is responsible for the resonance driven motion of the wind turbine. This means that, in this frequency range, the motion of the wind turbine is commanded by resonance of the main support structure vibration modes.

The mean component of the wind may be also important for fatigue analysis of some structural details. For example, the assessment of fatigue damage of some materials (such as composite or concrete) or elements (such as prestressed bolted connections) is dependent on the mean value of the stress cycles. Notwithstanding, other elements (such as steel towers) do not require any consideration about the mean stress level for fatigue analysis according to the main standards/ guidelines (section 6.3.2).

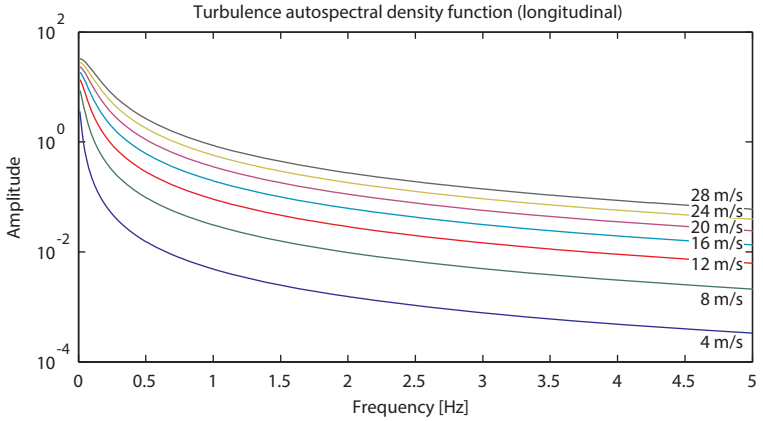

Figure 6.2 – Von Kármán longitudinal turbulent spectra for various mean wind speeds (I_w= 10 %)

The rotor operation is another source of excitation of wind turbines. As stated in section 4.6, the rotation of the rotor introduces cyclic loads at integer multiples of the rotor speed. For the wind turbine support structure, the energy of this excitation will be mainly located at the frequency of 3Ω and its integer multiples. For a common variable-speed wind turbine (with a rotor operating regime between 8 and 20 rpm), the 3Ω harmonic excitation presents a frequency between 0.4 Hz and 1.0 Hz.

Figure 6.3 illustrates the change introduced in the aerodynamic rotor thrust by the rotor rotation using data from the NREL 5MW wind turbine example. In this figure, the (theoretical) aerodynamic force that would be obtained if the harmonic effect is vanished ("aerodynamic force") is compared with the actual aerodynamic rotor thrust calculated by the HAWC2 code ("aerodynamic rotor thrust"). These forces represent the load transmitted by the rotor blades to the support structure of the wind turbine. The effect introduced by the rotor rotation is clearly visible, with well-defined peaks at the harmonic frequencies. It is thus concluded that, during operating periods, the wind load really applied on the support structure does not follow a turbulence spectrum like the one from Figure 6.2 but one similar to the presented in Figure 6.3.

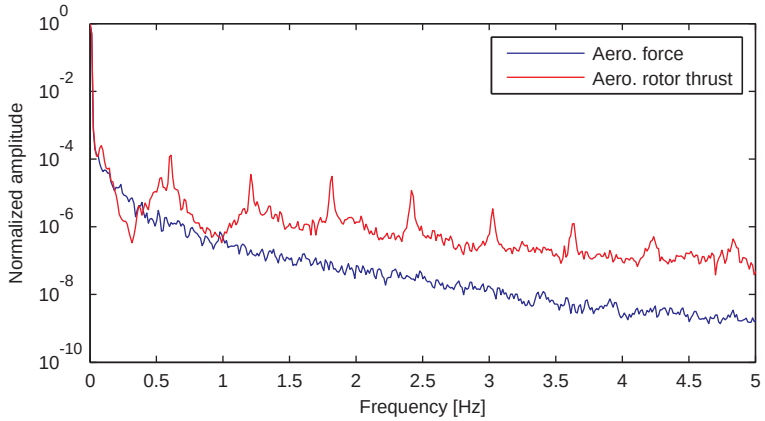

Figure 6.3 – Averaged normalized spectrum of the aerodynamic force and aerodynamic rotor thrust

At offshore conditions, wave excitation is another important source of dynamic loading of the wind turbine support structure. Waves are mainly originated as result of the wind action along the surface of the sea. Thus, just like the wind, waves also present an apparent random behaviour (wave loading is considered a non-deterministic process too).

The formation of waves can be seen as a combination of several regular waves, defining the sea surface. It is thus helpful to define the energy distribution in the frequency domain. In that sense, two important statistical properties should be referred: the significant wave height (H_s) and the peak period (T_p). The significant wave height is related to the magnitude of the waves. It is approximately four times the standard deviation of the sea surface height (Manwell, McGowan et al., 2010). The peak period is the wave period associated with the most energetic waves (which can be also defined in terms of frequency - f_p).

The wave spectrum is an essential tool to assess the loading environment to which the wind turbine will be subjected. The two most commonly used wave spectra are the Pierson-Moskowitz and the JONSWAP spectra.

The shape of the Pierson-Moskowitz wave spectrum was fitted to measurements from the Atlantic Ocean during long periods of constant environment conditions (Pierson and Moskowitz, 1964). This spectrum only considers the wind speed as input. Later, this spectrum was updated to consider H_s and T_p as input.

The JONSWAP spectrum corresponds to a modified version of the Pierson-Moskowitz spectrum (Hasselmann, Barnett et al., 1973). It is based on measurements performed in the North Sea. The JONSWAP spectrum is characterized by a higher and narrower peak (when compared to the Pierson-Moskowitz spectrum). For that reason, the JONSWAP spectrum is often used for extreme event analysis (Manwell, McGowan et al., 2010).

Figure 6.4 presents the 22 representative sea state conditions for the 20 m water depth Offshore Wind farm Egmond aan Zee (OWEZ), located in the Dutch North Sea (Tempel, 2006). For this figure, the Pierson-Moskowitz wave spectrum was used. It is seen that the highest energy is related to low frequency values, below the common values of natural frequency of the 1st support structure bending mode. Notwithstanding, it is also visible that, although the peak may present a wide spread of energy

for low values of wave height, the energy is almost zero for very low frequencies. This is an indication that the wave loading may not induce a quasi-static response of the wind turbine.

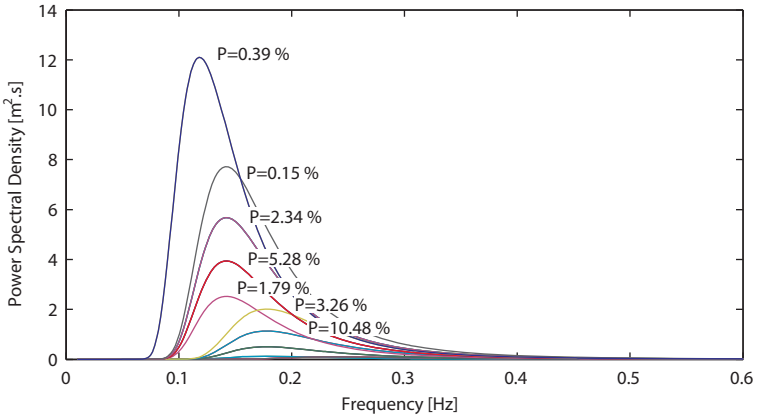

Figure 6.4 – Wave spectra from the OWEZ site (the probability of occurrence of the first 7 states with higher wave height is shown)

6.3 Application to Wind Turbine Support Structures

6.3.1 Main Structural Details

Wind turbine structures, due to their geometry and assembly process, have several details that need to be verified against fatigue. Considering only the tower structure, there are mainly three spots of interest: the flanged connection between tower segments (including bolts), the welded connection between the cylindrical sheet and the flange; and the stress concentration due to the door opening at the bottom of the tower.

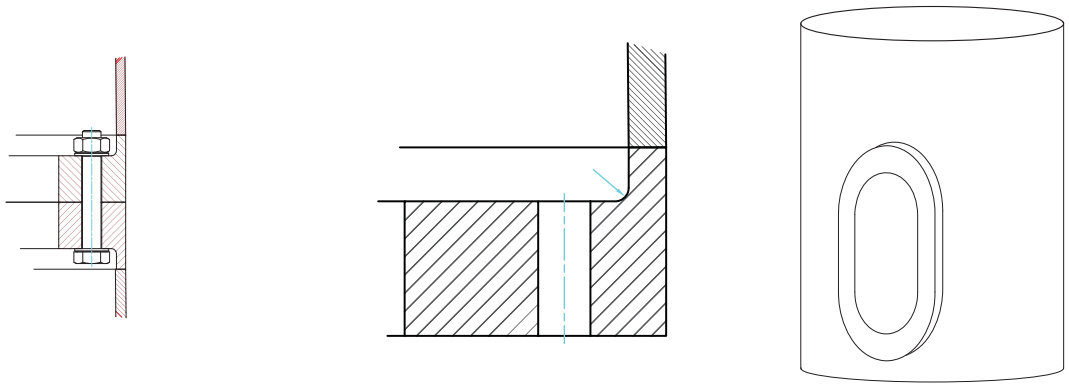

a) b) c)

Figure 6.5 – a) Bolted connection between flanges. b) Welded connection between cylindrical sheet and the flange. c) Door opening at the bottom of the tower

The connection between the tower and the foundation is also another sensitive location for fatigue (Currie, Saafi et al., 2015). Considering onshore wind turbines, the constant vibration of the structural system can lead to cracking of the concrete around the ring imbibed in the foundation (see Figure 6.6). The problem of fatigue is even more severe in offshore wind turbines. The grouted connection of the transition piece is a very delicate location for fatigue and is subjected to very high stresses (see Figure 3.9). In addition, also some offshore foundation models (such as the tripod and jacket foundations) need an accurate analysis of fatigue efforts, due to their complicate geometry and high number of joints.

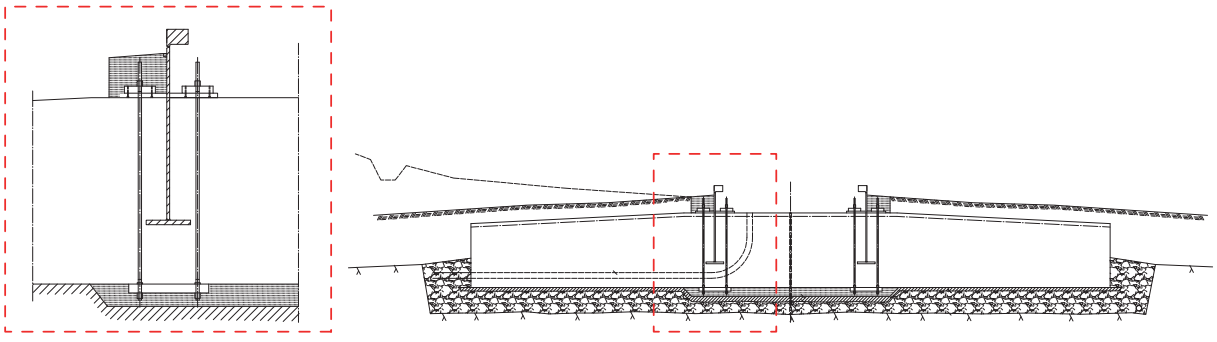

Figure 6.6 – Detail of the connection between the insert ring and the slab foundation

6.3.2 FATIGUE ANALYSIS ACCORDING TO STANDARDS/ GUIDELINES

The main standards/ guidelines of wind turbines, including (International Electrotechnical Commission (IEC), 2009; International Electrotechnical Commission (IEC), 2014), (Det Norske Veritas (DNV), 2011) and (Germanischer Lloyd (GL), 2010; Germanischer Lloyd (GL), 2012), suggest the application of the linear accumulation of damage for fatigue assessment of elements of the support structure. These standards refer the use of a S-N curve according to the detail under analysis, together with the Rainflow Counting method for determination of the histogram with the stress cycles.

For the design of steel support structures, all the standards/ guidelines define similar S-N curve equations for fatigue analysis. As example, (Germanischer Lloyd (GL), 2010) defines the same S-N curve as the EC 3 but disregards the threshold value of the fatigue strength. The S-N curve defined in EC 3 and GL for a particular detail is presented in Figure 6.7.

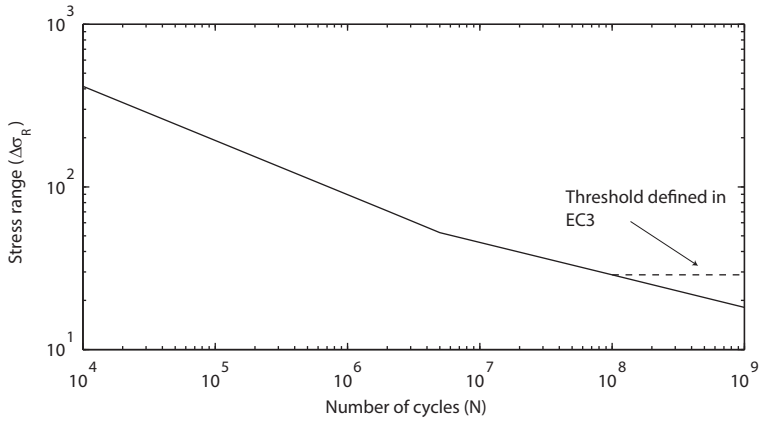

Figure 6.7 – S-N curve defined in GL and EC 3 (detail 71)

In addition, corrections to the S-N curves are proposed in some standards/ guidelines, considering thickness, corrosion and material effects, among others.

The consideration of the mean stress in fatigue analysis is also referred in the standards/ guidelines, since different structural details required different approaches:

- The fatigue analysis of concrete elements, such foundations and grouted joints, requires the knowledge of the mean stress;
- The study of fatigue state of the pre-loaded bolted joints also requires the consideration of the mean stress level. This is due to the non-linear relation between the stress state of the tower and the forces in the bolts (Sørensen and Sørensen, 2011);
- For the analysis of steel elements from the support structure, the mean value of the stress cycles is usually disregarded. Some standards/ guidelines present a correction coefficient to consider the mean stress effect. However, this consideration only introduces a positive effect when a portion (or the whole range) of the stress range is in the compression side. Thus, in this context, the disregarding of this coefficient (and consequently, of the mean stress effect) is conservative.

These documents also define partial safety factors to account for the uncertainties about material, loads and consequences of failure (although some documents do not define each value separately).

Both IEC, GL and EC 3 consider the safety factors that increase the loads. On the other hand, DNV defines a safety factor (named Design Fatigue Factor - DFF) which is considered as a magnification factor of the accumulated damage D. As example, the safety factors defined in the referred documents for the steel elements of an onshore tower are summarized in Table 6.1.

Table 6.1 – Partial safety factors defined in standards/ guidelines

Standard/ Guideline	Load	Material	Consequences of failure	Total
GL	1.0	-	1.15	1.15
EC 3	1.0	1.15	-	1.15
IEC*	1.0	1.1	1.15	1.265
DNV*	-	-	-	2.00

* These documents are referred to offshore wind turbines

6.4 FATIGUE ASSESSMENT USING ACCELEROMETERS

The structural response due to fatigue loading is usually monitored using strain gauges. The use of strain gauges requires the installation of sensors in each section under study. This usually requires scrapping the point of the structure, which is not well regarded by the wind farm owners. Other important drawback about using strain gauges is their sensitivity to harsh environment. Thus, it is difficult and expensive to estimate the stress condition of structural details of offshore wind turbine under the water level with these sensors. This represents an important issue, since the inspection of these elements is only possible using underwater equipment.

In that sense, a method enabling the analysis of the fatigue condition along the entire wind turbine support structure would represent a useful tool for the management of a wind farm. This would be especially important for offshore turbines, since it would allow estimating the condition of underwater structural details.

One important aspect of the wind turbines structures is that they are highly dynamic systems, subjected to important dynamic loading excitations, as referred in section 6.2. Consequently, the use of a sensor capable of recording this dynamic motion would likely be an important source of information for fatigue analysis. Thus, it seems legitimate to use accelerometers to evaluate the dynamic response of wind turbine support structures and then perform the fatigue analysis with this input.

Displacements (and, consequently, stresses) can theoretically be computed from acceleration data. Considering the acceleration function given by $\ddot{y}$, the velocity and displacement functions are given, in the time domain, by the single and double integration of $\ddot{y}(t)$, respectively:

$$\begin{aligned} \dot{y}(t) &= \int_0^t \ddot{y}(t)\, dt + \dot{y}_0 \\ y(t) &= \int_0^t \dot{y}(t)\, dt + y_0 \end{aligned} \tag{6.2}$$

with:

$y(t), \dot{y}(t), \ddot{y}(t)$	Displacement, velocity and acceleration functions (in time domain)
$\dot{y}_0$	Initial velocity
y_0	Initial displacement

Nonetheless, the computation of displacements from accelerations cannot be performed directly, as it may lead to considerable errors. Observing the previous equation, it is immediately noted that the two initial conditions (y_0 and $\dot{y}_0$) are not known and, if they are not null, they will introduce errors in the double integration process. These errors are illustrated in Figure 6.8. Both illustrated displacement functions departed from the same acceleration function but with different initial conditions. As can be seen, there is an initial offset (due to y_0) and a drift along the function (due to $\dot{y}_0$) that leads to a considerable lag between the two functions.

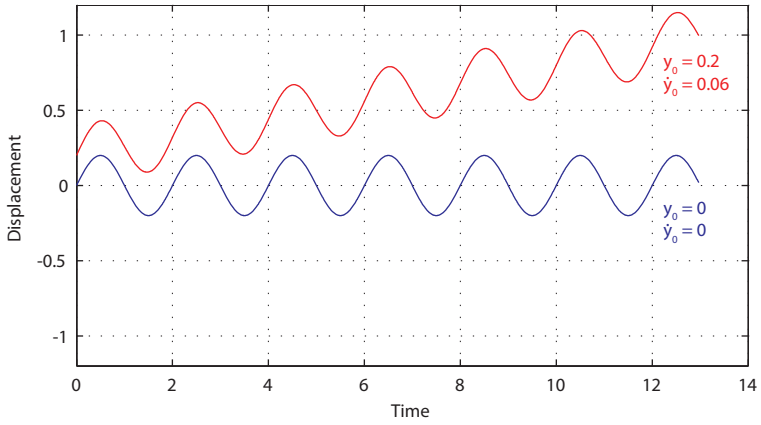

Figure 6.8 – Results from double integration of acceleration functions with different initial conditions

Notwithstanding, there are some methodologies published regarding the estimation of the stress time history from accelerometers. However, they are focused on the dynamic component of the displacements, i. e., the quasi-static displacements, which depend on the initial conditions and on the static loads, are disregarded.

In (Hjelm, Brincker et al., 2005) and (Aenlle, Skafte et al., 2013), an interesting methodology is presented. This procedure uses the measured accelerations to estimate the dynamic properties of the structure. Alongside, the measured accelerations are integrated twice to obtain an estimation of the displacements. Using the estimated displacements and the experimentally identified vibration modes, the modal coordinates can be estimated according to:

$$y(t) = \sum_{i=1}^{n} \phi_{exp,i} \cdot q_{exp,i}(t) \tag{6.3}$$

with:

y	Estimated displacements
$\phi_{exp,i}$	Mode shapes experimentally obtained
$q_{exp,i}$	Modal coordinates
n	Number of considered vibration modes

Equation (6.3) can be solved directly if the number of mode shapes equals the measured degrees of freedom. If the measured degrees of freedom exceed the number of vibration modes considered, the equation can be solved with the least square method.

Once the dynamic characteristics are known, a finite-element model of the structure is developed, which is calibrated and updated based on the experimental results. With the numerically obtained mode shapes, it is possible to estimate the displacements at any point of the structure through:

$$y(t) = \sum_{i=1}^{n} \phi_{FEM,i} . q_{exp,i}(t) \tag{6.4}$$

with:

$\phi_{FEM,i}$	Mode shapes obtained from the finite-element model
$q_{exp,i}$	Modal coordinates obtained from equation (6.3)

Considering that the relationship between bending moment and curvature at a given section of the structure is defined by:

$$M = E.I.\frac{d^2y}{dz^2} \tag{6.5}$$

with:

E	Young modulus of the material
I	Second moment of inertia of the cross section

and that the bending stress is given by:

$$\sigma = \frac{M}{I}h \tag{6.6}$$

with:

σ	Bending stress
M	Bending moment
h	Distance from neutral axis to the point of interest of the section

the bending stress at any point along the height of the structure (z axis) is then calculated according to the combination of equations (6.5) and (6.6):

$$\sigma(z,t) = E\frac{d^2y(z,t)}{dz^2}h = \sum_{i=1}^{n} E\frac{d^2\phi_i(z)}{dz^2}q_i(t).h \tag{6.7}$$

with:

ϕ_i	Mode shape from i-th vibration mode
$q_i(t)$	Modal coordinate from i-th vibration mode

This formulation implies that the function describing each vibration mode has to be derived twice (in order to the height) to obtain the stress at any point of the structure. An example of application of the methodology to a reduced two story building model is presented in (Aenlle, Hermanns et al., 2013).

The described procedure is developed with the support of a finite-element model. However, its application to wind turbines presents some important drawbacks. Firstly, the need of a properly calibrated finite-element model of a wind turbine can be an obstacle, since geometrical and material characteristics of the nacelle and rotor are usually not provided by the manufacturer. In addition, the direct use of the experimentally obtained mode shapes in equation (6.7), avoiding the need of a finite-element model, may lead to important errors in the double derivative operation. Lastly, the quasi-static component of the displacements, mostly due to wind action, is not considered.

In order to overcome these obstacles, a procedure to assess the stress condition at any location of a wind turbine support structure is presented in next section.

6.4.1 Proposed Procedure for Fatigue Assessment

The procedure for fatigue assessment at any location of the wind turbine support structure is proposed in this section. The procedure is inspired on the one presented in the previous section, albeit with some modifications.

The procedure is based on the estimation of the acceleration modal responses at any point of the wind turbine support structure. These (modal) acceleration time series are later integrated into displacements, which are used to estimate the stress condition of the support structure.

The procedure starts after the estimation of the modal properties of the wind turbine (with application of the algorithms presented in section 5.4). The estimated state-space matrices A and C are then used to define a forward innovation model to estimate the modal acceleration responses at the sensors position, as explained in section 5.5.

Once the modal acceleration responses are computed, the modal displacements can be estimated through a double integration process. In this work, the acceleration time series are transformed into the frequency domain and thereafter double integrated. The modal displacement of the structure motivated by the i-th vibration mode at one of the sensors position is thus defined as:

$$Y_i(\omega) = -\frac{\ddot{Y}_i(\omega)}{\omega^2} \tag{6.8}$$

with:

Y	Displacement (in the frequency domain)
$\ddot{Y}$	Acceleration (in the frequency domain)

The obtained displacements are then transformed back to the time domain.

After the displacement field for each vibration mode is achieved, it is possible to compute equivalent forces imposing the same (modal) deformation. The equivalent forces acting along the height of the support structure at the k time step from the i-th vibration mode are obtained according to:

$$F_{i_k} = K.y_{i_k} \tag{6.9}$$

with:

F_i	Equivalent forces from the i-th vibration mode
K	Stiffness matrix of the support structure of the wind turbine
y_i	Vector with displacements regarding the i-th vibration mode
k	Time step

Equation (6.9) requires the definition of the stiffness matrix of the wind turbine support structure. Contrary to the nacelle and rotor, the support structure can be defined through very simple models. The tower structure can be assumed as a simple cantilevered beam, once the material and structural characteristics (variation of the bending stiffness along the height) are known.

The total equivalent forces acting along the height of the support structure at the k time step are obtained as a sum of the contribution from the n identified vibration modes:

$$F_k = \sum_{i=1}^{n} F_{i_k} \tag{6.10}$$

Equation (6.9) defines equivalent loads at the measurements points (where the modal amplitudes of the mode shapes are known) imposing the same modal deformation of mode i. Thus, if the mode shape is defined by a limited number of points (as is usual the case, since the number of accelerometers placed along the structure is reduced), equation (6.9) will conduct to large concentrated loads at few

points of the structure. In this case, the stress condition obtained for the support structure will not correspond to reality.

In order to overcome this problem, an interpolation of the experimentally found mode shapes is used (e.g. spline interpolation) to obtain a more detailed estimation of the modal amplitudes of the mode along the height of the support structure. As referred in section 5.5, the information about the mode shapes is contained in the V matrix from the forward innovation model (see equation (5.71)). When the mode shapes are interpolated, a new V matrix is defined, named V_{Interp}, which can be used to estimate the accelerations at the interpolation points:

$$\hat{y}_k = V_{Interp}.z_{m,k} \tag{6.11}$$

Once the acceleration time series at the interpolation points are obtained, the presented procedure can be used to estimate equivalent loads at these points. Considering that a fine resolution is used in the interpolating operation, the loads will resemble a distributed load, leading to a stress field in accordance with the reality.

The interpolating operation has the advantage of avoiding the need of a well calibrated finite-element model. However, the suitability of the interpolation must be carefully analysed. In situations where the number of sensors is limited and vibration modes with high order modal configurations are important for the displacement response, this operation may introduce important errors. In the case of support structures of wind turbines, the displacement response is mainly conditioned by the first bending mode and low order harmonics. These mode shapes (and operating deflection shapes) present smooth configurations. Thus, a large number of sensors is not required for their correct definition.

Figure 6.9 illustrates the application of the presented methodology to a wind turbine support structure, using three levels of measurement. In this figure, the red circles represent the identified modal amplitudes from the considered mode shapes, which are used to obtain the interpolation presented by the thick line. The stress at any point of the structure is then obtained as a sum of the stress contribution from each vibration mode. However, it is important to refer that the equivalent forces computed with equation (6.9) should not be confused as real loads acting on the structure, since they are just a gimmick used to recreate the deformed structure.

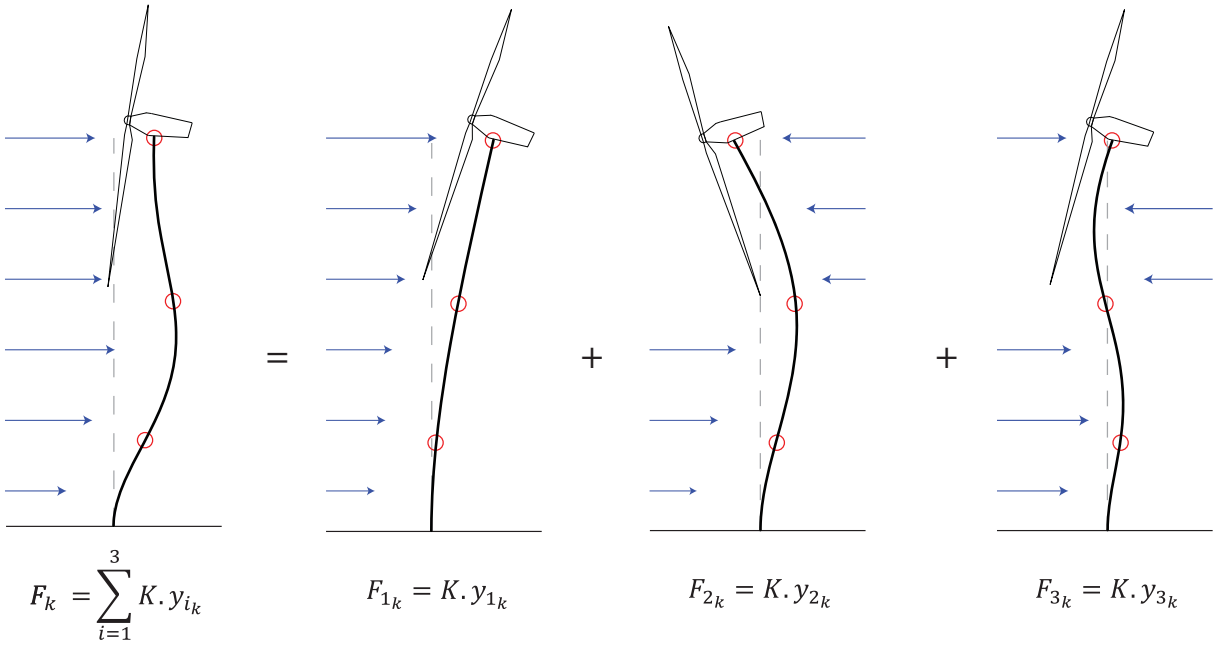

Figure 6.9 – Illustration of the proposed methodology to estimate the equivalent forces along the tower height

One critical step when using accelerometers for fatigue assessment of structures is the double integration operation. From equation (6.8), it is noticed that the result is prone to errors for frequency values close to zero. Figure 6.10 illustrates a typical result obtained with the double integration of acceleration time series from wind turbines support structures. It presents the estimation of the displacement at the top position (computed according to equation (6.8)) from a simulated acceleration (sensor S3) of the HAWC2 example. The displacement directly obtained with the numerical analysis, from which the mean value was subtracted, is also presented. The comparison between the two signals evidences a clear distortion of the estimated signal in the time domain. The estimated displacement is governed by an erroneous large period cycle, masking the real displacement time series. This illustrates the difficulty in estimating displacements from accelerations.

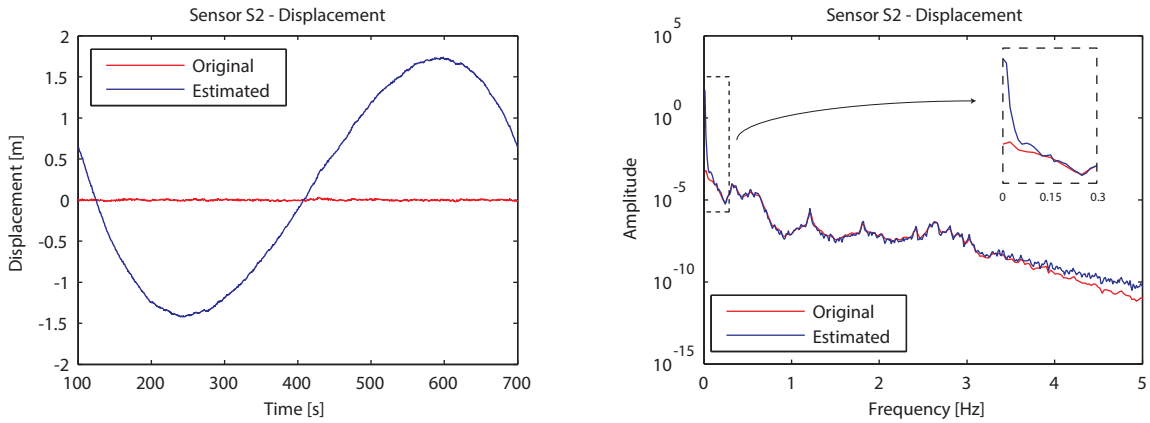

Figure 6.10 – Time and frequency representation of the displacement (from which the mean value was subtracted) obtained with the HAWC2 model (original) and estimated displacement computed through the double integration process without any filtering window

It is thus comprehensible that this procedure is not capable of estimating the stress associated with the very low frequency range of the spectrum. This part of the response spectrum, usually related to the quasi-static component of the wind loading, will be referred in this work as "quasi-static" component of the stress.

On the other hand, the described procedure is adequate to estimate the stress condition associated with the remaining part of the spectrum, which includes the contribution of the vibration modes and sinusoidal excitations (such as waves and rotor rotation driven harmonics). This component will be referred as the "dynamic" component of the stress.

A complementary approach is thus required to estimate the quasi-static component of the stress. This approach takes advantage of the fact that most of the wind action is applied on the support structure as a thrust force at the hub level. Thus, it can be assumed that the quasi-static deformation of the structure is similar to a cantilevered beam with a concentrated load at the top (Figure 6.11). The stiffness matrix defined for the estimation of the dynamic component of the stress can then be used to estimate this deformation.

Once this deformation shape is known, the knowledge of the quasi-static condition of a reference point along the support structure is enough to estimate the stress condition along the entire structure. This reference quasi-static condition can be the stress (measured with strain gauges), the displacement (measured with GPS antenna) or the curvature (measured with inclinometers) evolution along time at an adequate section of the support structure.

The use of a single measurement point to estimate the condition of the whole support structure is illustrated in Figure 6.11. Assuming the deformed shape of the structure and a known reference condition, the bending moment from the quasi-static component (and, consequently, the bending stress) can be extrapolated for the rest of the structure.

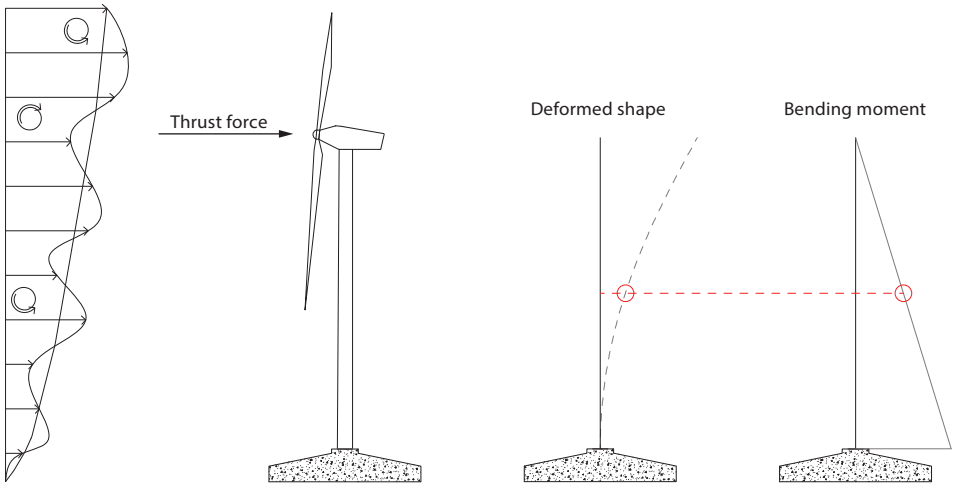

Figure 6.11 – Thrust force applied to the wind turbine and illustration of the equivalent deformation and bending moment of the support structure due to the quasi-static component of the loading

6.4.1.1 Estimation of the Quasi-Static and Dynamic Stresses Contributions to Fatigue

During the proposed procedure for fatigue assessment of wind turbine support structures, the contribution for fatigue damage of the quasi-static and dynamic components of stress are splitted. Each component is analysed by different methodologies in order to estimate the bending stresses along the structure. It is thus necessary to define which parts of the response spectrum correspond to the quasi-static and dynamic components and how the response should be separated.

As previously referred, the main problem associated with the integration of accelerations is related to the lowest range of frequencies of the spectrum. When performing the double integration operation with equation (6.8), the estimation of the displacement corresponding to this range loses accuracy.

In that sense, the separation of the structural response in the two components should eliminate this problem. The dynamic component should then be defined only for frequency values in which these errors are not present. This can be achieved by applying a high-pass filter to the response acceleration signal. At the same time, this frequency range should include all the contributions from vibration modes and external dynamic loading excitations. On the other hand, a low-pass filter should be applied to the measured reference quasi-static signals in order to contain only the frequency content associated to the quasi-static component of the wind loading.

Based on these requirements, two window filters were designed. The high-pass window was design to despise the frequency content below the frequency cut f_{c1}. From this point, a cosine taper window is defined between f_{c1} and f_{c2}. From f_{c2}, the signal is kept unaffected. The filter is intended to be used with the acceleration signal, in the frequency domain, before the double integration process introduced with equation (6.8). On the other hand, the low-pass filter is designed as the complementary of the high-pass, in such a way that no energy is lost during the process. Both filter windows are shown in Figure 6.12.

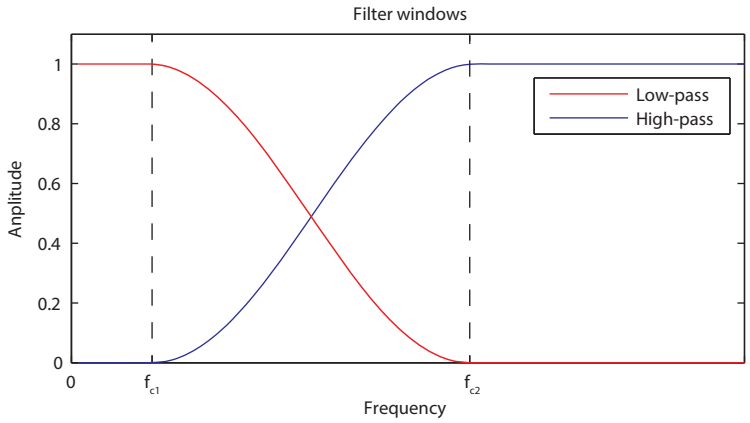

Figure 6.12 – Low-pass and high-pass filter window

The filter parameters (f_{c1} and f_{c2}) should be adjusted according to each situation. The main constraints to define the parameters are the lowest natural frequency of the wind turbine, the first detected harmonic excitation, the wave loading spectrum (if the turbine is located offshore) and the eventual frequency limits for the linear behaviour of the accelerometers. The filter should then be defined in order to consider these effects in the dynamic component of the displacements.

The main steps of the proposed procedure for fatigue assessment of the wind turbine support structure are summarized in Figure 6.13. As previously described, the procedure starts with the computation of the low-pass filtered quasi-static signal from the quasi-static input data (stress, displacement or curvature). Similarly, the dynamic acceleration data is obtained with the application of the referred high-pass filter to the collected acceleration signals. From this point, two independent procedures are applied in order to compute the two contributions to fatigue.

The quasi-static contribution to fatigue is obtained assuming the applied forces acting solely on the rotor blades (and then transmitted to the tower through the hub). Since the deformed shape of a cantilever beam with a concentrated force at the top is known, the stress condition along the support structure can be estimated based on the quasi-static condition of a reference point (installed sensor).

The procedure to estimate the dynamic contribution to fatigue requires a more complex methodology. It starts with the decomposition of the "dynamic" acceleration data into modal (and harmonic, if the turbine is operating) responses. These acceleration time series are integrated to obtain modal (or harmonic) displacement responses. Then, the modal (or harmonic) displacement responses are estimated at non measured locations through an interpolation of the experimentally found mode shapes. Lastly, equivalent forces are obtain, for each vibration mode (or harmonic), imposing the same (modal) deformation.

Once the quasi-static and dynamic contributions to stress are estimated, the fatigue condition at an arbitrary position of the wind turbine support structure can be obtained by summing these two components.

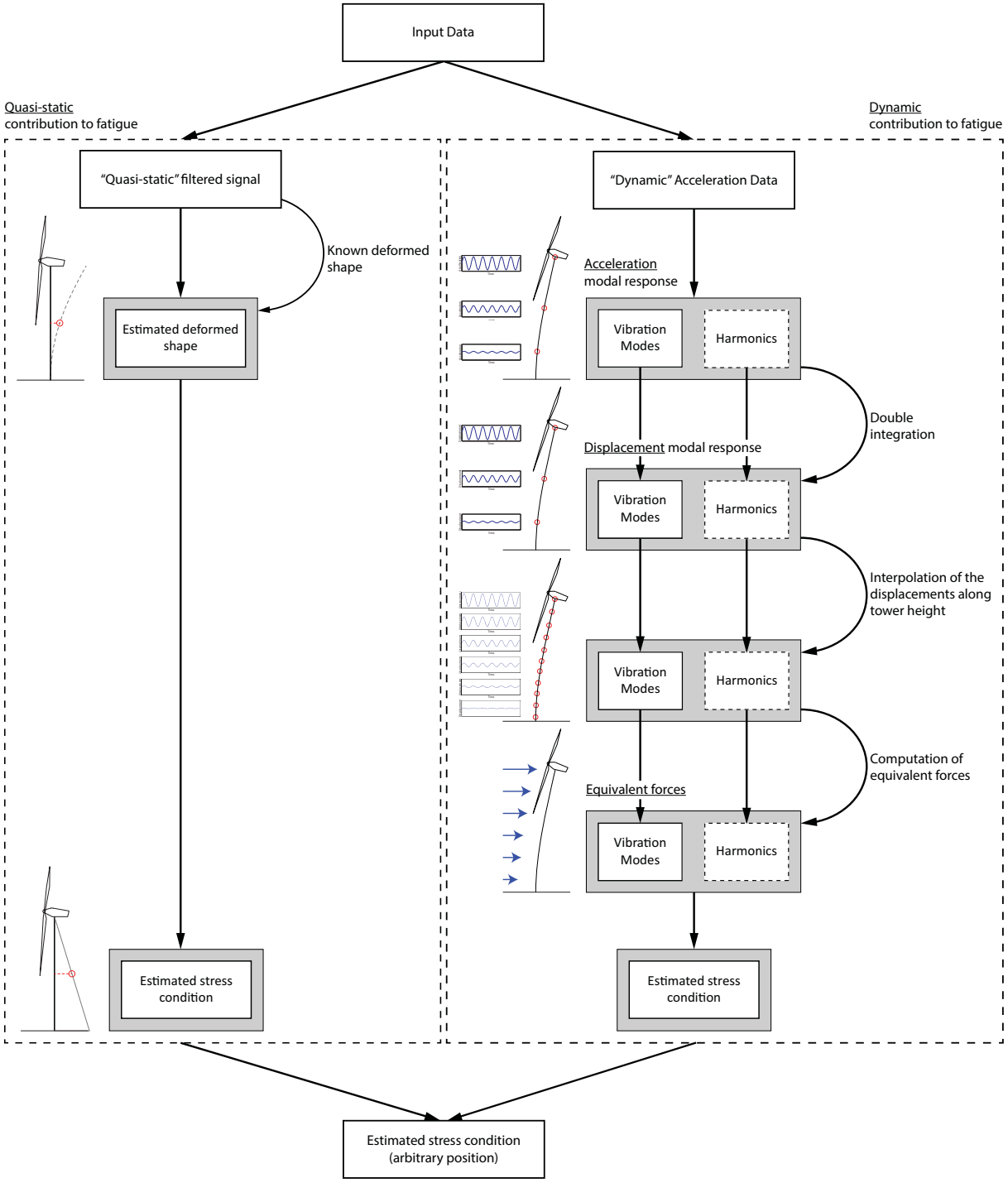

Figure 6.13 – Chain of events included in the proposed procedure for fatigue assessment at any position of the wind turbine support structure

Example

In order to illustrate the proposed methodology, an additional sensor was introduced in the equipment layout shown in Figure 4.21. This sensor is required to obtain the reference quasi-static condition. It is assumed that the displacement at the position of sensor S1 is known.

For the analysis, the filter parameters f_{c1} and f_{c2}were defined as 0.10 Hz and 0.15 Hz, respectively. The measured displacement and the signal obtained after the application of the low-pass filter are presented in Figure 6.14.

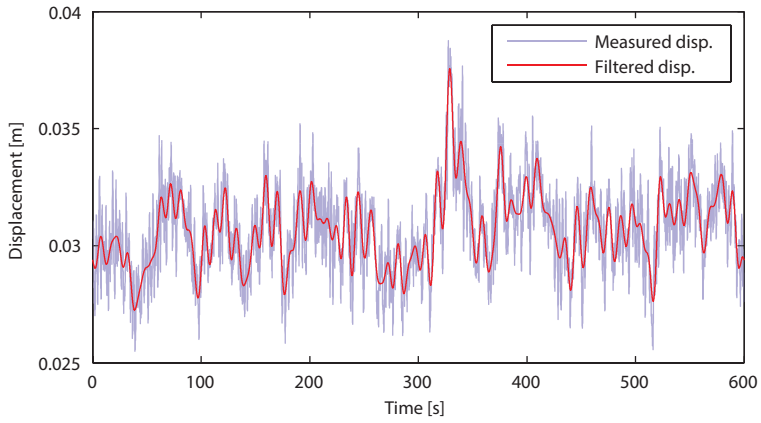

Figure 6.14 – Measured displacement and low-pass filtered displacement time series at S1 sensor position

Once the displacement at the S1 position is known, it is possible to estimate the quasi-static condition at any position along the support structure. Figure 6.15 shows the comparison between the real ("original" - which was filtered with the same low-pass window), and estimated quasi-static displacements at the S2 and S3 sensors position. As expected, the agreement between the signals is very good.

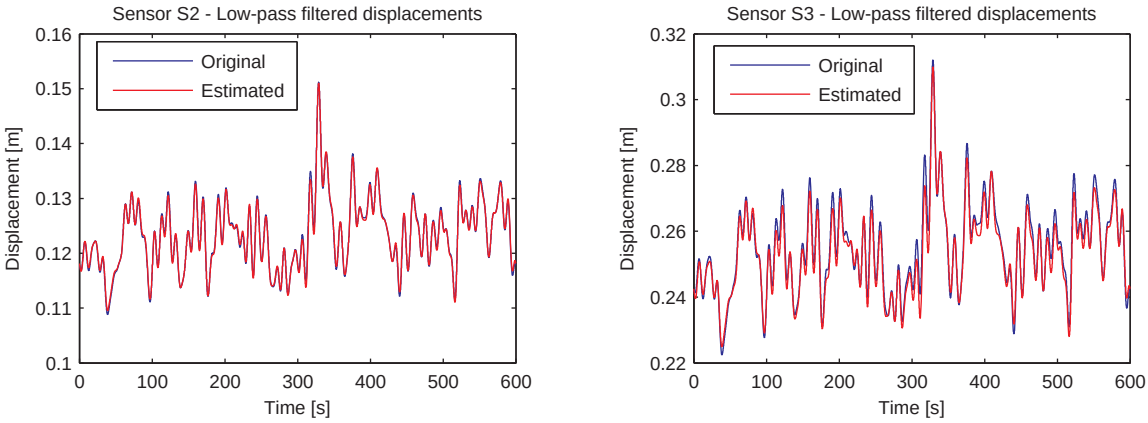

Figure 6.15 – Original and estimated low-pass filtered displacements at S2 and S3 sensors position

Together with the stiffness matrix, the low-pass filtered signal of the measured displacements at S1 position is used to estimate quasi-static component of the bending moment at the foundation level. The obtained results are shown in Figure 6.16. An almost perfect correlation is observed between the estimated and the original quasi-static base bending moment.

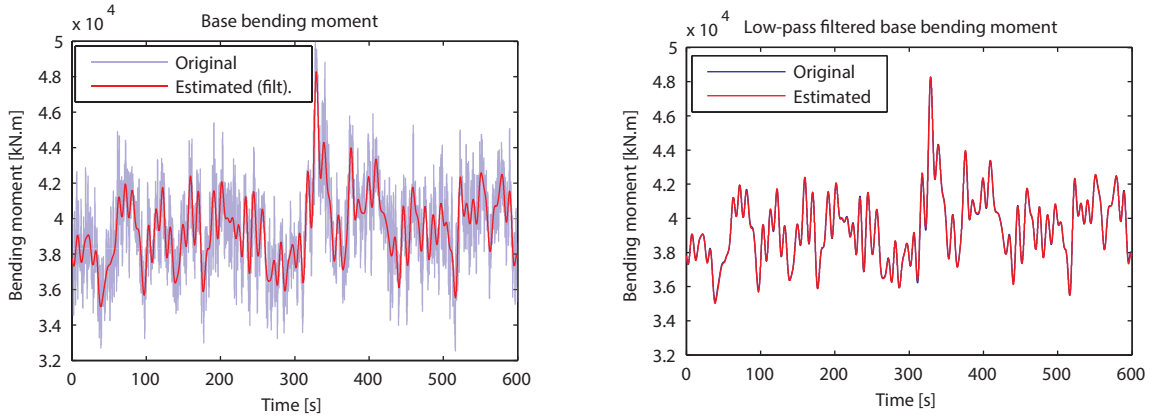

a) b)

Figure 6.16 – Comparison of the estimated quasi-static component of the base bending moment with: a) original bending moment; b) low-pass filtered bending moment

After the estimation of the quasi-static component, it is necessary to compute the dynamic component of the bending moment. In this example, the SSI-COV modal identification algorithm was used. Using the modal acceleration responses estimated with the algorithm presented in section 5.5, the dynamic component of the displacements at the sensors position was computed. The results were then compared to the displacements obtained with the HAWC2 simulation after application of the high-pass filter. Figure 6.17 shows the very good agreement between both results.

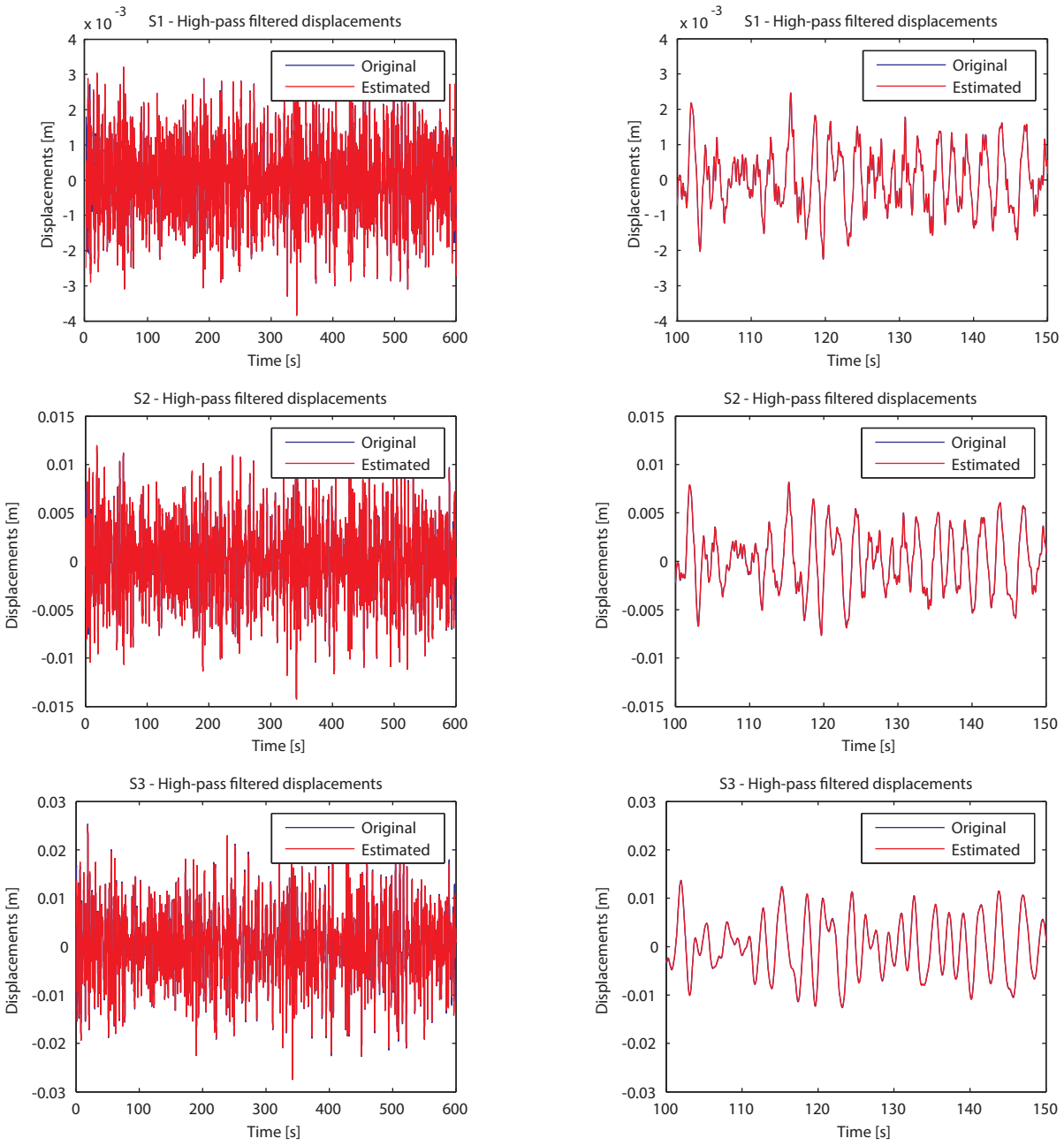

Figure 6.17 – Original and estimated high-pass filtered displacements at the sensors position (the right hand plots are a zoom of the left hand figures)

During the integration process in the frequency domain, numerical errors are introduced in the displacement signal due to the application of the filter window over the acceleration time series. In order to minimize these errors, a window is applied to the acceleration signal (in time domain) to attenuate the amplitude of the signal in the beginning and end, prior to the integration. Figure 6.18 compares the dynamic displacement obtained without and with the application of the attenuate window. It is visible that, if the window is not used (Figure 6.18 a)), an error is present in the signal. Although the use of the window may distort even further the initial and last part of the signal, it allows to confidently control the length of these erroneous segments. With this strategy, it is thus possible to disregard these two time segments when computing the bending stress for fatigue analysis purposes.

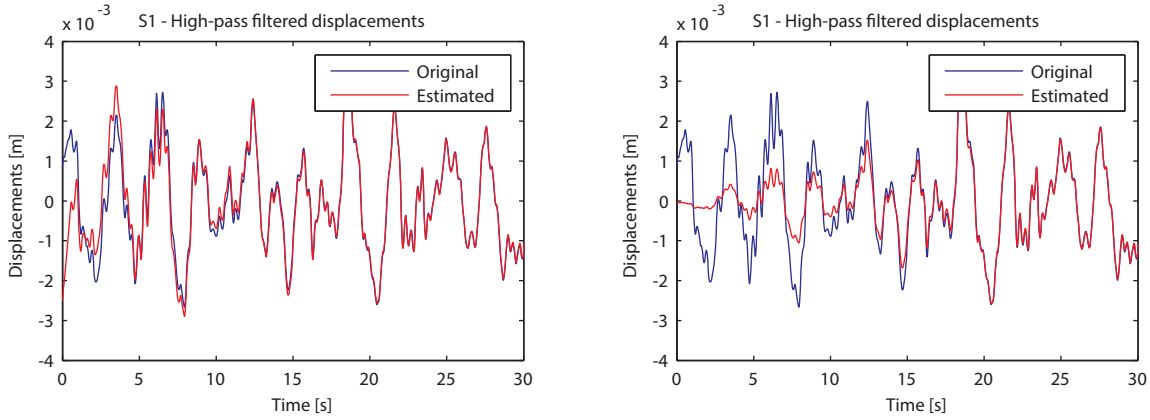

Figure 6.18 – Estimated dynamic displacements at sensor S1: a) without using the attenuate window; b) using the attenuate window

The estimated dynamic displacements are then used to compute the dynamic component of the bending moment at any position of the support structure. In this example, the foundation level was chosen. Through the procedure introduced in section 6.4.1, the dynamic component of the bending moment at the foundation level was estimated. The result is presented in Figure 6.19 alongside with the high-pass filtered bending moment obtained as results of the numerical analysis. In this figure, the effect of the applied attenuating window is seen in the beginning and end of the estimated time series. These two segments should then be disregarded.

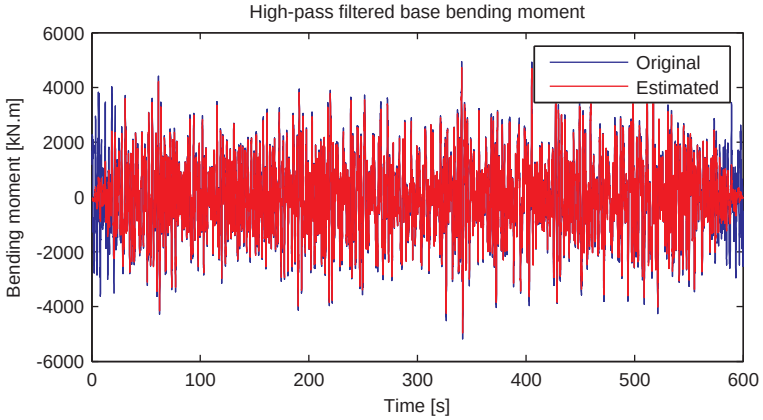

Figure 6.19 – Comparison of the estimated dynamic component of the base bending moment with the original high-pass filtered bending moment

With both quasi-static and dynamic components estimated, the total bending moment can be obtained with a sum between the two components. The total bending stress at the foundation level is shown in Figure 6.20, where the initial and last transient segments were already eliminated.

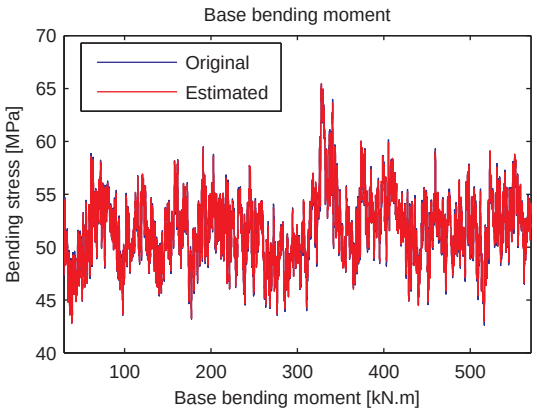

Figure 6.20 – Comparison between the original and estimated base bending stress

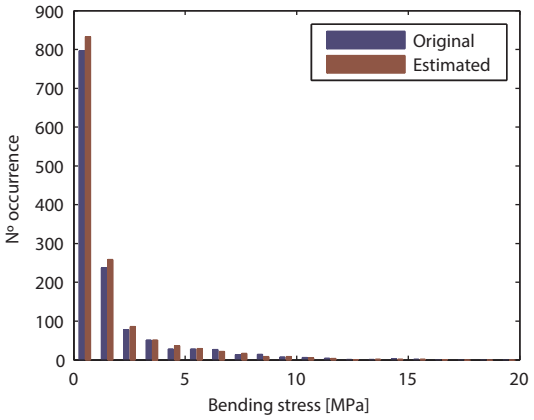

Figure 6.21 –Histogram with the number of cycles from the original and estimated bending stress at the foundation level

At this point, the histogram of the loading cycles can be computed. This histogram is compared with the one corresponding to the original bending moment in Figure 6.21 (from which the same initial and last parts were also not considered).

It would be interesting to characterize the relative contribution of each component (quasi-static and dynamic) to the total fatigue condition of a wind turbine. In that sense, numerical analyses were performed to assess each contribution for different wind conditions. However, it was noticed that the contributions are dependent on the control system (mainly, on the pitch control) and, for that reason, they are not generalizable to any wind turbine.

6.4.2 Virtual Sensors

The methodology presented in the previous section requires the installation of a certain number of accelerometers along the wind turbine support structure. Nevertheless, nowadays wind turbines are usually equipped with a bi-directional accelerometer at the top as part of their SCADA system. Thus, the use of this single sensor for dynamic monitoring of the wind turbines would avoid the need of installing additional sensors (and, consequently, reduce the cost of the monitoring system).

The use of a top sensor as the only measurement sensor of the monitoring system introduces an important limitation, concerning the fatigue assessment of the wind turbine support structures. Since it is only possible to obtain a single modal amplitude per direction, it is not possible to accurately estimate (and, later, interpolate) the configuration of vibration modes along the height of the structure.

In order to overcome this problem, two solutions may be regarded: the use of a calibrated finite-element model; or the characterization of the mode shapes during a training period.

The use of a calibrated finite-element model can be used to obtain the configuration of the vibration modes. The contribution of each mode to the response can then be scaled according to the modal amplitude obtained with the single accelerometer. Then, the procedure presented in section 6.4.1 can be used. Notwithstanding, the development of a finite-element model of a wind turbine presents important challenges as previously referred.

The characterization of the mode shapes during a training period was used in this work. With this approach, a suitable number of temporary sensors is installed at the wind turbine support structure during a short period of time (e.g. between two scheduled maintenance operations). Throughout this period, the modal tracking of the wind turbine modes is accomplished with all the sensors (permanent plus temporary), allowing to characterize the modal amplitudes at the measurement positions, under different operating conditions. In addition, the characterization of the operational deflection shapes of the wind turbine vibrating at harmonics frequencies along the operating regime of the turbine is also necessary. The number of installed sensors during this period has to be sufficient to obtain a satisfactory characterization of these vibration configurations.

After the training period, the mode shapes (and operational deflection shapes) are well characterized at the positions of the permanent and temporary sensors. At this point, the continuous monitoring of the wind turbine is performed with the single sensor. As result, the identified modes shapes are characterized by a single modal amplitude per direction (at the permanent sensor position). These modal amplitudes are used to scale the contribution of mode shapes (and operational deflection shapes) characterized during the training period. With this step, a new V matrix is defined and the estimated acceleration time series at the unmeasured locations are obtained with:

$$\hat{y}_k = V.z_{m,k} \tag{6.12}$$

Example

The methodology based on virtual sensors was applied to the numerical NREL 5MW wind turbine example. In this example, the recorded acceleration time series from one sensor was used to predict the acceleration at the location of the other two sensors. The mode shapes obtained with the analysis in which all sensors were considered were adopted to define the V matrix, simulating the results from a training period.

Three different analyses were then performed, considering in each one a different single sensor. Initially, the single acceleration time series was used as input for the output-only modal identification algorithm. For this example, the SSI-COV algorithm was selected. From the identification results, a suitable model order was considered to define the state-space model.

Considering the selected state-space model, the forward innovation model was obtained as introduced in section 5.5.2. Then, the acceleration time series at the location of the non-considered sensors were estimated through equation (6.12).

Figure 6.22 illustrates the results obtained with this analysis. In this figure, each column is referred to an analysis where a single sensor was used to estimate the acceleration from the other two. For example, the first column is referred to the analysis where the S1 sensor was used as single sensor. The predicted acceleration to the considered single sensor is also presented in each column to show the error associated with application of the model (see equation (5.73)).

The results presented in this figure show a good agreement between the predicted and original time series at the unmeasured places. However, it is noticed that the consideration of the top sensor S3 as single sensor produces the worst results. This situation is due to the fact that the acceleration response at the S1 and S2 location is mainly dominated by vibration modes with reduced modal amplitude at the tower top.

Consequently, the identification of these modes will be worse when a sensor at the tower top is considered as single sensor, leading to a poorer agreement between the predicted and the real acceleration signal.

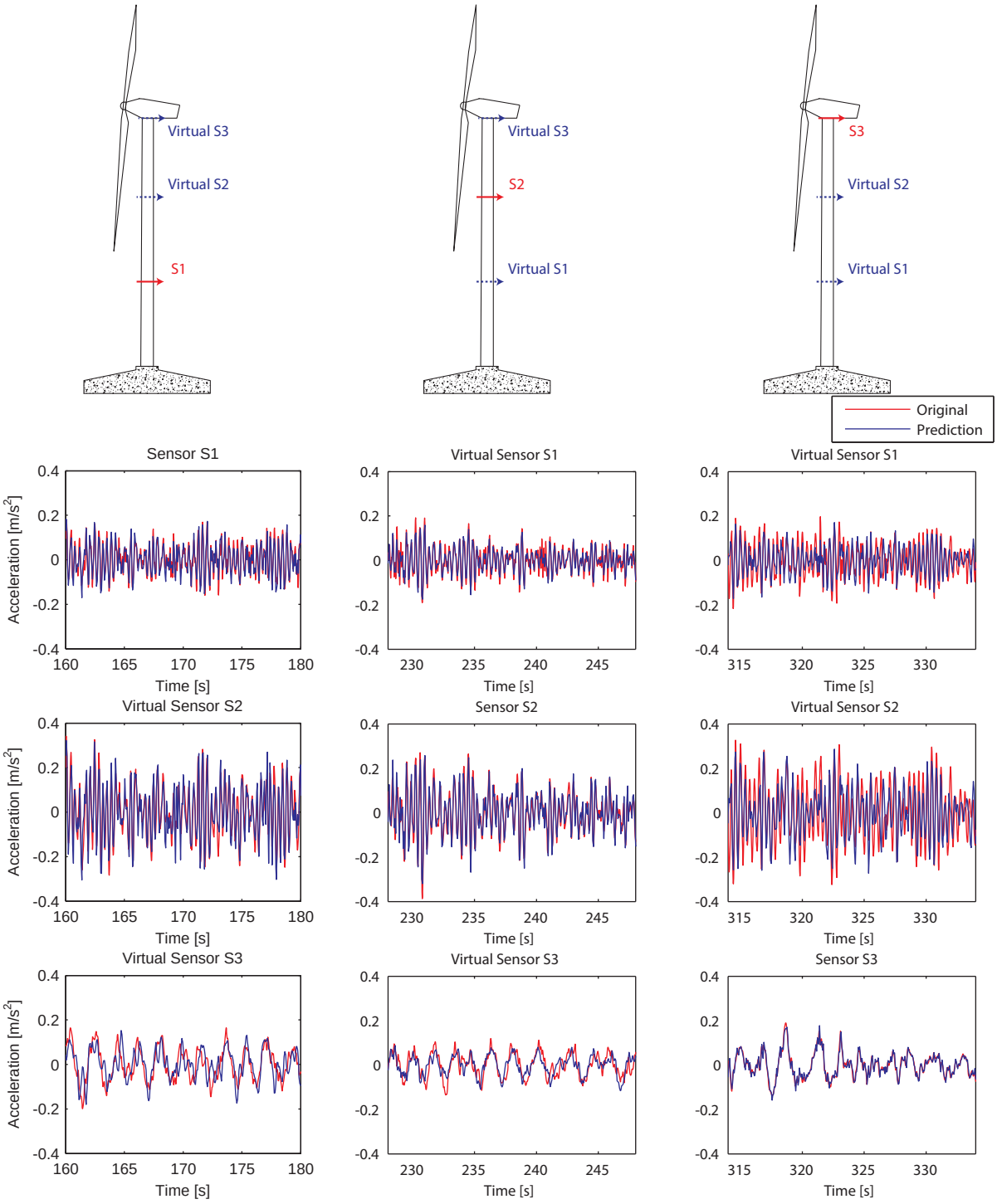

Figure 6.22 – Comparison between the recorded and estimated acceleration at the sensors position when a single sensor is used to estimate the time series of the other two sensors. Each column is referred to the results obtained with the consideration of a different single sensor

6.5 FINAL CONSIDERATIONS

The fatigue assessment of wind turbine structures is an important indicator for the evaluation of their structural integrity. Due to the highly dynamic nature of the loads, the structure is almost continuously subjected to cyclic excitations, requiring a special attention to guarantee a proper operation throughout its life.

In that sense, this chapter introduced the main aspects related to the fatigue assessment of the wind turbine support structure. The main loads acting on the support structure were described for both onshore and offshore wind turbines. Also, a survey covering the main standards and guidelines about the design method for fatigue assessment of the support structure was developed.

A methodology for estimation of the fatigue state at any point of the wind turbine support structure was proposed in this chapter. The method is based on the independent estimation of the quasi-static (using sensors measuring strains, displacements or curvatures) and dynamic (using accelerometers) contributions to fatigue. This procedure was illustrated using the results obtained with the NREL 5MW numerical example.

Lastly, the possibility of using a single level of measurement of acceleration to estimate the dynamic contribution to fatigue was addressed. It was noticed that the sensor usually installed in the nacelle is not enough to accurately estimate the acceleration at other positions of the support structure. Two alternative positions for installation of a single level of measurement were tested, which provided better results.

The proposed methodology to estimate the fatigue condition at any point of the wind turbine support structure is further exploited in the next chapter, where experimental data is used to test the accuracy of the method. In the same way, the ability to reduce the number of sensors and, at the same time, maintain the level of accuracy is also addressed in the next chapter.

7
STRUCTURAL MONITORING OF WIND TURBINES

7.1 INTRODUCTION TO STRUCTURAL MONITORING OF WIND TURBINES

The assessment of the integrity of wind turbines and their components is a field of study with a high level of interest. As exposed in section 3.1.3, some mechanical and electronic components present relative high rate of failures and consequent downtime. This non-production time (together with the cost of repair/ replacement of the components) considerable increases the revenue losses, both for onshore and offshore locations. This is even more critical for high power rated turbines. It should also be highlighted that the specificity of offshore environment introduces some new variables in the cost function:

- Offshore turbines are expected to become considerably larger than onshore ones (in dimension and rated power). This situation introduces two important variables: downtime corresponds to a greater loss of income; and the components to be replaced are heavier and larger, which makes their transportation and installation more difficult;
- The need of adequate weather conditions to reach the structure at offshore locations, leads to longer downtimes.

Considering the reasons presented above, the continuous monitoring of the condition of the support structure (foundation, tower and, in some situations, transition piece) can introduce some important advantages. Firstly, it should be noticed that if the support structure fails and collapse, the entire investment is lost. Thus, a system able to anticipate such dramatic damage at the tower is very important since it allows earlier reparation, preventing the failure of the entire system. Besides this, three important aspects should also be considered for the installation of a monitoring system at the support structure:

- The qualitative and quantitative assessment of vibration levels might lead to the identification of high-vibrational events and/ or periods of time corresponding to reduced turbine performance;
- If the natural frequency of the tower is close to the rotational frequency of the rotor (or its multiples), Germanischer Lloyd Guidelines (Germanischer Lloyd (GL), 2010; Germanischer Lloyd (GL), 2012) refer the need of a continuous monitoring vibration system. With this system, it is possible to track the value of the natural frequency along the life of the wind turbine and evaluate possible resonance problems;

- The continuous assessment of the structural condition and operation of the support structure might give a good support to decide about the extension of operation after the initial predefined period of life or, in the other hand, if the structure should be dismantled (or reinforced) before the expected period of life due to unforeseen loads and/ or degradation.

Considering specifically offshore wind turbines, the installation of a monitoring system at the support structure is even more advantageous. Being this type of structures fairly recent, the degree of knowledge is not as mature as for onshore systems. Mainly for this reason, some additional motivations should be considered for the installation of a monitoring system:

- The effects of the sea acting at the structure (mainly waves) are still not mastered. For this reason, there is some uncertainty when dealing with the fatigue life of these structures. Furthermore, some structural aspects, like foundations and the grouted joint in the transition piece (Rücker, 2007), are prone to rapid wear, which may require specific structural health assessment procedures;
- One specific problem of offshore wind turbines is scour around the foundation piles. This problem increases the flexibility of the entire structure and leads to reduction of the support structure natural frequency (Zaaijer, Tempel et al., 2002; Prendergast, Gavin et al., 2015). This situation may lead to resonance problems if the natural frequencies of important support structure vibration modes are reduced to values close to the harmonics of the rotor speed. Figure 7.1 shows the evolution of the 1st and 2nd natural frequency values of a monopile support structure. It is seen that these modes (especially the 2nd mode) are very sensitive to this problem;
- Conversely, the increasing of the foundation stiffness might also represent a problem when the correspondent increase of the frequency values brings them close to harmonics. This is the case of soft-stiff solutions. A real case study in which a progressive increase of the modes frequency values was noted is presented in (Weijtjens, Verbelen et al., 2015). It is referred that this phenomenon may be related to soil stiffening due to cyclic loading.

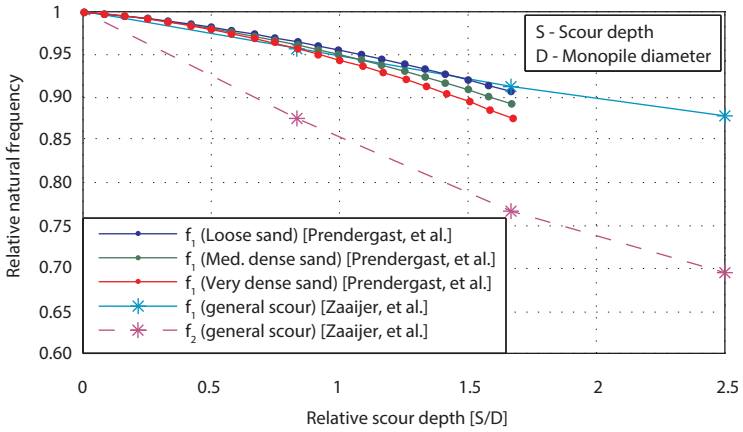

Figure 7.1 – Variation of natural frequencies of offshore wind turbines with scour (adapted from (Zaaijer, Tempel et al., 2002) and (Prendergast, Gavin et al., 2015))

Thus, the implementation of a monitoring system in wind turbines allowing the assessment of the actual condition of the components and support structure would introduce considerable

improvements in the definition of an Operation and Maintenance (O&M) strategy, following a predictive maintenance (see section 3.1.3). With this kind of maintenance, a continuous assessment of the condition of the components is available, which permits to detect damages at an early stage. At this stage, different strategies can be considered, such as derating of the turbine (Griffith, Yoder et al., 2013) with the goal of operating with minimal increase of the damage and of preventing the damage of one component from spreading to others (Hyers, McGowan et al., 2006) (e.g. if the pitch of one blade is not working properly, the aerodynamic asymmetry created will introduce additional loads on the drive train which may damage this component). Besides this, with the early damage detection, it is possible to order replacement components and schedule maintenance in a timely manner with minimum downtime (Adams, White et al., 2011) and avoid the abrupt shutdown of the plant.

Considering the potential benefits of the introduction of monitoring systems in wind turbines, it is comprehensible the interest of all industry agents involved, including insurers. Insurers play an important role in the wind energy business, since a significant portion of O&M are due to insurance costs (Morthorst and Jacobsen, 2004). Thus, the acceptance by insurer institutions that monitoring systems have an important role in maintenance management could contribute for better conditions for wind turbine owners. Receptivity to this change by insurers started around 2002, when some German insurers introduced a review clause in which it was required that all roller bearings in a drive train have to be replaced after either 40 000 operating hours or five years (whichever is earlier) unless an appropriate Condition Monitoring System had been installed (Becker and Poste, 2006). Gothaer (Wind Power Monthly, 2003), GCube (Appleyard, 2013) and Allianz (Gellermann, 2012) also refer monitoring system as a need for proactive maintenance measures. The latter also highlights the importance of monitoring of other components, such as blades, tower and foundation (Gellermann, 2012).

Alongside with the insurances perspectives, another key aspect is the economic benefit of the installation of a monitoring system. McMillan and Ault (McMillan and Ault, 2007) studied this subject for a predictive maintenance strategy (with the introduction of a condition monitoring system for the generator, gearbox, blades and power electronics system) against the more common periodic maintenance for a 5 MW offshore wind turbine. They concluded that the predictive strategy introduces economic benefits, if the monitoring system provides accurate diagnosis, of around 60 % to 80 %.

The CONMOW project also studied the costs of preventive and corrective maintenance for offshore wind turbines (Wiggelinkhuizen, Watson et al., 2007). It was concluded that the costs of corrective maintenance are a factor of 2 higher than for preventive maintenance.

The monitoring of the condition of wind turbine components can be performed by various techniques, in particular Condition Monitoring (CM) and Structural Health Monitoring (SHM). Conceptually, these two techniques refer to different fields of operation: CM is oriented to the machinery, mainly rotating components (such as drive trains), whilst SHM deals with major structural components (such as foundations, tower and blades). This is the guidance that will be used throughout this work. Nonetheless, the scope of application of the two concepts is not universal (Carden and Fanning, 2009) and there seems to be a unification of the monitoring systems around the name Condition Monitoring (e.g. GL guidelines (Germanischer Lloyd (GL), 2003) encompasses the monitoring system for every components of a wind turbine, such as gear boxes and towers, under the CM definition).

7.1.1 CONDITION MONITORING OF WIND TURBINES

Condition monitoring is referred as "*the process of monitoring a parameter of condition in machinery, such that a significant change is indicative of development failure*" (Wiggelinkhuizen, Watson et al., 2007). It is a technique used to assess the condition and detect early damages and/ or malfunctions in components machinery. Condition monitoring is widely used in other fields of industry (Şeker, Ayaz et al., 2003; Fast and Palmé, 2010).

As referred previously, Condition Monitoring has been steadily gaining some support from the industry, especially due to the considerably high rates of failure from some components. A sign of confidence in the application of monitoring systems in wind turbines is the requirement, by some guidelines/ standards, of their installation in offshore turbines. For example, GL guidelines (Germanischer Lloyd (GL), 2003) define as mandatory, as minimum components to be monitored, main bearings, gearbox and generator.

Condition Monitoring can be applied to a large variety of components. However, the components of major concern are usually rotors, pitch mechanisms, drive trains (including gearboxes and bearings) and generators (Hyers, McGowan et al., 2006). For this, various techniques have been developed to detect problems related to these components, which stand, among others:

- Vibration-based analysis;
- Acoustic emission;
- Ultrasonic testing techniques;
- Oil analysis;
- Strain measurements;
- Electrical effects;
- Thermography;
- Performance monitoring.

A more complete list of techniques and processing tools can be accessed in (Hameed, Hong et al., 2009; Liu, Tang et al., 2010; García Márquez, Tobias et al., 2012; Yang, Tavner et al., 2014; Liu, Tang et al., 2015). Although currently there is a long list of CM techniques in the context of wind turbines, Germanischer Lloyd Guidelines (Germanischer Lloyd (GL), 2003) states that, to be within its certification standards, the monitoring system should be defined by a vibration-based analysis. This requirement is justified by the fact that this technique allows an earlier detection (Figure 7.2).

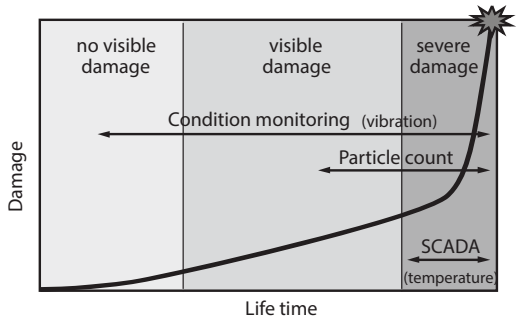

Figure 7.2 – Detection of damage by different systems defined by GL Guidelines (Germanischer Lloyd (GL), 2003)

7.1.2 SHM OF WIND TURBINES

A possible definition of the Structural Health Monitoring concept is presented in (Boller, Chang et al., 2009): *"SHM is the integration of sensing and possibly also actuation devices to allow the loading and damaging conditions of a structure to be recorded, analysed, localized, and predicted in a way that nondestructive testing becomes an integral part of the structure."*. Thus SHM methods deal with the problem of assessing the structure integrity through the installation of sensors with the aim of detecting early damage. This kind of monitoring concept dates back from earlier the 1980s (Boller, Chang et al., 2009). Over the time, the knowledge in this field increased at a very high rate, mainly due to the easier and cheaper access to various sensors. Some theoretical definitions were developed (see, for example, the fundamental principles of SHM presented in (Worden, Farrar et al., 2007)). One important idea presented by Rytter (Rytter, 1993) is referred to the different levels in damage detection (Figure 7.3).

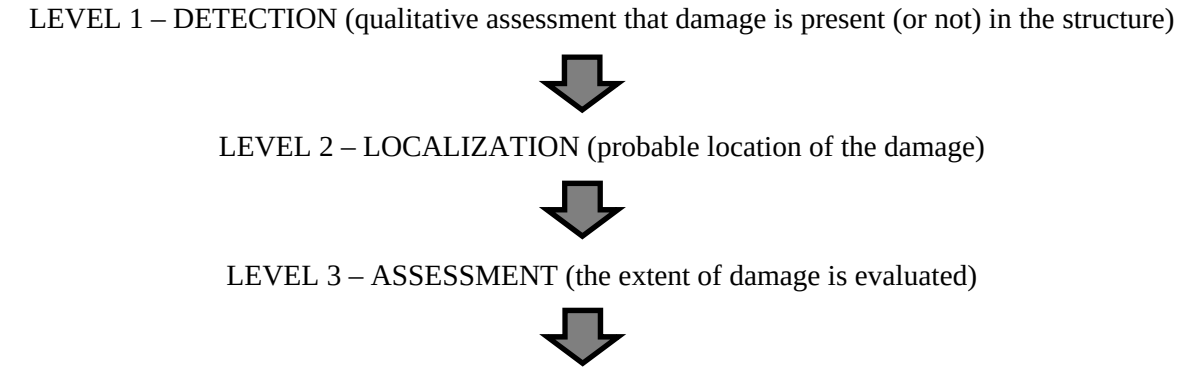

Figure 7.3 – Levels in damage assessment

SHM systems have been applied for years in different types of civil engineering structures. Magalhães *et al* (Magalhães, Cunha et al., 2009) implemented a monitoring system in concrete arch bridge. Hu *et al* (Hu, Moutinho et al., 2012) implemented a similar SHM system in a footbridge. Brownjohn (Brownjohn, 2007) presents several examples of SHM applications in a variety of structures, among which dams, offshore installations, nuclear installations and tunnels. Some examples of very complete SHM systems installed in bridges are presented in (Boller, Chang et al., 2009).

Lately, the application of SHM to wind turbines has been one of the main topics of study. Blades have been the preferred substructure of study due to their high propensity for failures. However, recently also the support structure (tower and foundation) have focused some attention concerning safety issues. This is mainly due to the increasingly higher dimensions of the tower, alongside with larger loads and masses at the top, due to larger rotor diameters, and due to the lack of knowledge of the environmental situations at sea and greater wear of structures in offshore installations.

Several methods of SHM for application in wind turbines have already been developed. An exhaustive list of methods (referred to blades) is introduced in (Boller, Chang et al., 2009) and (Ciang, Lee et al., 2008). Also in (Wymore, Van Dam et al., 2015), a general overview of the state of development of health monitoring systems is presented. When considering SHM for support structures, essentially two

methods are used: vibration-based and strain measurement. The present work deals with the application of SHM to the support structure of wind turbines through the application of vibration-based methods.

Some numerical studies about the feasibility of using the frequency values of the vibration modes to identify structural damage in wind turbines are present in the literature. Adams *et al* (Adams, White et al., 2011) simulated three different types of damage in different locations in a numerical model: blade root section, low-speed shaft and yaw joint. Through a sensitivity analysis, the variations of the first 14 natural frequencies were calculated for each damage scenario. Also, some developments have been made in order to assess the evolution of the frequency values of the support structure with scour (Zaaijer, Tempel et al., 2002; Sørensen and Ibsen, 2013; Prendergast, Gavin et al., 2015).

A good example of the use of vibration-based methodologies for damage detection on the support structure is given in (Pelayo, López-Aenlle et al., 2011). In this work, high levels of vibration, together with cracks at the foundation, were detected in two wind turbines. For diagnosing the cause of this anomaly, operational modal tests were performed in these two turbines, alongside with a similar but healthy wind turbine. For these tests, accelerometers were placed on the foundation and on the lower part of the tower. The results showed that both damaged wind turbines presented lower values of natural frequencies than the healthy turbine (around 7 % to 3 %). After this assessment, the foundations of the two wind turbines were reinforced. Then, the tests were once again performed and the results indicated an increase in the natural frequencies (in line with the healthy wind turbine). Also, in (Currie, Saafi et al., 2015), problems related to high levels of vibration at the foundation level of onshore wind turbines, due to damage around the bottom flange of the embedded ring, were described.

In the experimental field, some cases of implementation of vibration-based monitoring systems are described in literature. During the HISTWIN project (Veljkovic, Heistermann et al., 2012), a monitoring system was implemented on a wind turbine for almost one year. For the instrumentation, accelerometers, strain measurements, temperature sensors and inclinometers were used, together with some SCADA data. During this period, the modal identification of the tower was performed, as well as the fatigue assessment of the tower and bolts from the flanged connections between segments.

A different approach for a monitoring system is described by Braam *et al* (Braam, Obdam et al., 2012). In this work, a strategy of monitoring an entire wind farm with the installation of additional sensors in just a few reference turbines is presented. On the reference turbines, fibre optic sensors were installed on the blades with the aim of measure strains (load indicators) and evaluate the fatigue state of these turbines. The relations between these load indicators and the parameters measured by the SCADA system (present in every turbine of the wind farm) were then established, in order to extrapolate the load accumulation of the non-reference turbines. This methodology allows defining a maintenance strategy considering the most mechanically loaded wind turbines. In (Guo and Infield, 2012), also a more economical SHM system is presented, since it only uses built-in SCADA parameters. It consists in the processing of data from the SCADA system, mainly 10 min. averaged values of the tower top and drive train accelerometers. This data is then correlated with other SCADA data and analysed in the context of the different operational regimes of the rotor.

Also in (Hu, Thöns et al., 2015b; Hu, Thöns et al., 2015a), a study about the implementation of a vibration-based monitoring system at a prototype 5 MW wind turbine with tripod foundation installed onshore is described in two parts. For this system, 8 accelerometers distributed along the support

structure were used. In the first part, the main results concerning the dynamic characterization of the wind turbine are presented. Then, in the second part, the modal results obtained during a period of 2 years were used to assess the detection of damage at the tower and foundation.

The offshore Vestas V90-3.0 MW, introduced in section 5.9, is also used in the context of a project aiming to develop monitoring systems based on the dynamic properties of wind turbines. The results obtained up to date are described in (Weijtjens, Verbelen et al., 2015).

The assessment of the variation of natural frequencies in order to detect blade damage is also a field of current study. The majority of published works, both in the experimental (Wang, Liang et al., 2014; Ulriksen, Tcherniak et al., 2015) and numerical domain (Hoell and Omenzetter, 2014), refer the small sensitivity of the frequency values of the first order blades vibration modes to common small damages. Notwithstanding, in (Marulo, Petrone et al., 2015), an experimental study of the sensitivity of the dynamic properties of a small-scale blade to a very severe damage is described. The blade was tested to buckling and its modal properties were analysed before and after the buckling. In this case, the variation was notorious, exposing that the application of this kind of monitoring technique may be only effective for detection of heavy damages.

7.2 VIBRATION-BASED SHM SYSTEM

The structural health monitoring system presented in this work is developed based on a vibration-based methodology. The system is composed by two modules, aiming to present a solution for two important problems within the scope of structural condition assessment of the support structure of wind turbines: detection of damage at an early stage and fatigue life estimation.

One of its components (damage detection), follows a modal approach (Fritzen, 2005). In this system, the modal parameters of the wind turbine structure (natural frequencies, damping ratios and mode shapes) are continuously extracted and tracked over time. Thus, anomalous variations of modal parameters, which may be caused by the occurrence of damage, are detected. As damages are normally associated with stiffness reduction, and assuming a negligible variation of mass (which is perfectly admissible on wind turbines), abnormal reductions of the natural frequencies are assumed as presence of damage. Thus, natural frequencies are considered a prime indicator for damage detection in wind turbines, as already exposed in previous sections. Some examples of similar monitoring system implemented on civil engineering structures are presented in (Peeters, 2000; Magalhães, 2010; Hu, 2011).

The second module of the monitoring system is referred to the estimation of the fatigue life condition of the support structures of wind turbines. This component is based on the procedure introduced in Chapter 6. Once a continuous estimation of the loading cycles of the structure is obtained, an on-line evaluation of the increment of damage in virtually every structural detail can be achieved. Then, it is possible to perform some estimation regarding the real fatigue life of the support structure.

7.2.1 DAMAGE DETECTION

The damage detection module of the monitoring system aims to detect abnormal structural changes at an early stage. In that sense, the monitored frequency values of the vibration modes are used as damage indicators. In this section, the procedures implemented to reduce the variability of the tracked frequency values and to identify possible situations of damage are introduced.

7.2.1.1 Removing of Environmental and Operational Effects on Natural Frequencies

Wind turbines are subjected to a large variability of environmental effects, such as ambient temperature, wind, boundary conditions, among others (Sohn, 2007). Alongside, the operation of wind turbines also introduce important modifications on their structural condition, such as variation of pitch and yaw angle, varying rotor speed, among others (see section 3.2.6). These effects are an important source of variability of the modal properties of the support structures, often introducing variations with greater amplitude than the damage itself. Consequently, if it is desirable to detect small scale damage at an early stage, the influence of external factors has to be "cleaned" from the modal properties. Usually, only the natural frequencies are used.

Some practical cases studied are also presented in the literature. Magalhães *et al* (Magalhães, Cunha et al., 2012) studied the variation of natural frequencies due to temperature in a concrete arch bridge, while Hu *et al* (Hu, Caetano et al.) and Moser and Moaveni (Moser and Moaveni, 2011) performed a similar work in footbridges. For its turn, interesting correlations between the modal properties of the offshore Vestas V90-3.0 MW and the tidal level are presented in (Devriendt, Magalhães et al., 2014).

In order to understand and remove the influence of environmental and operational effects on the modal properties of the structure, three different types of approaches can be followed: physical models, models whose environmental effects are used as input and models which do not consider these inputs.

The last two models were tested in the context of the dynamic monitoring system described in this work. These methods are considerable easier and quicker to implement and operate, however they required a period of training in which a representative variation of the environmental and operational effects should be included.

The methods considering the measurement of the environmental and operational effects in the conception of the model are defined as input-output methods. The application of these methods for removal of the external influences in the context of wind turbines seems, from a conceptual point of view, very suitable. Since the SCADA system collects a variety of operational and environmental data related to the wind turbine in which it is installed, the access to these records is easier and do not require the installation of any additional sensor. In this approach, two methodologies are described based on Multivariate Linear Regression Models and Dynamic Regression Models.

On the other hand, the approach not requiring the measurement of the operational/ environmental effects is referred as output-only methods. In the context of wind turbines, output-only methods can be also used in association with the previously presented input-output methodologies with the aim of achieving a "cleaner" time evolution of the natural frequencies. This can be obtained since there may be external factors not recorded by the SCADA system that also influence the modal properties. Within this scope, the approach based on the Principal Component Analysis was tested (Johnson and Wichern, 2002). However, it was observed that the application of this method did not improve the results obtained with the linear regression models. For that reason, this method was not considered in the context of the monitoring system described in this work.

Multivariate Linear Regression Models

Multivariate Linear Regression Models deal with the problem of predicting values of response (dependent) variables from a collection of predictor (independent) variable values (Johnson and Wichern, 2002). These models can also be used to assess the effects of the predictor variables on the responses. In order to expose a clearer explanation, these models will initially be address to the situation of just one dependent variable and, at the end, the generalization for multiple response variables is introduced.

For the present case of study, the natural frequency values of one vibration mode is considered the response variable, while the predictor variables are represented by the operational/ environmental effects. Initially, the degree of influence in the variation of the response is assessed and quantified for each environmental effect (predictors). Then, the defined model is ready to predict response values from a particular moment according to known predictors of the same moment. Finally, real and predicted response values can be compared and the magnitude of the deviation evaluated.

The mathematical definition of a Multivariate Linear Regression Model is provided by (Johnson and Wichern, 2002):

$$y = Z.\beta + \varepsilon \tag{7.1}$$

with:

y	Vector with n observations of the dependent variable
Z	Matrix with the n values of the p predictors variables (for p operational/ environmental effects)
β	Vector with weight parameters of the p predictor variables
ε	Vector with the values of the random error

The vector ε, which represents the random error due to measurement issues and due to the existence of variables not explicitly considered in model, presents the following properties (Johnson and Wichern, 2002):

$$\begin{gathered} E[\varepsilon] = 0 \\ Cov[\varepsilon] = E[\varepsilon.\varepsilon^T] = {\sigma_\varepsilon}^2.I \end{gathered} \tag{7.2}$$

with:

$E[*]$	Expected value operator
$*^T$	Transpose operator
σ_*	Standard deviation
I	Identity matrix

When defining the matrices from equation (7.1), some considerations are employed. The first column of Z is filled by ones, so this matrix contains $(p+1)$ columns. Also, the values of Z are usually normalized, being each element subtracted from the mean values and then divided by the standard deviation of the variable:

$${Z_i}' = \frac{Z_i - E[Z_i]}{\sigma_{Z_i}} \tag{7.3}$$

with:

Z'	Normalized value of Z

With this configuration, the first element of the vector β contains the mean value of the observed variable.

Before the definition of the model, it is needed to assess which predictors influence the response variable. For this step, the predictors with high correlations with the response variable and low correlations with the other predictors should be selected (Magalhães, 2010). A suitable tool for the evaluation of the correlation between two variables x and y is the Pearson's product-moment correlation coefficient (Johnson and Wichern, 2002):

$$r_{xy} = \frac{Cov(x,y)}{\sigma_x . \sigma_y} \tag{7.4}$$

where values close to zero represent a low linear correlation, while values close to one (in absolute value) might indicate a good correlation. It should be noted that this tool only considers linear correlations. Thus, if a zero value is obtained, it does not imply that a non-linear relation is also not present.

Once the choice of the relevant predictors is complete, the vector β should be estimated. This vector (named as $\hat{\beta}$) is obtained through application of the least squares method and defined in (Johnson and Wichern, 2002):

$$\hat{\beta} = (Z^T . Z)^{-1} . Z^T . y \tag{7.5}$$

Since the weight factors of the predictor variables are already defined, the vector ε should then be evaluated. In that sense, an estimation of the residual random errors is given by the difference between the real and estimated response variable (Johnson and Wichern, 2002):

$$\hat{\varepsilon} = y - \hat{y} = (I - Z . (Z^T . Z)^{-1} . Z^T) . y \tag{7.6}$$

Two ways for assessing the quality of the model adjustment can be used. The first one is through the computation of the estimation of variance of $\hat{\varepsilon}$:

$$\hat{\sigma}_\varepsilon{}^2 = \frac{1}{n} . \sum_{k=1}^{n} \varepsilon_k{}^2 \tag{7.7}$$

However, this indicator has the disadvantage of being dependent of the absolute values of y variable. To solve this problem, a coefficient is presented in (Johnson and Wichern, 2002) that avoids this inconvenience:

$$R^2 = 1 - \frac{\sum_{k=1}^{n} \varepsilon_k{}^2}{\sum_{k=1}^{n} (y_k - \bar{y})^2} = \frac{\sum_{k=1}^{n} (\hat{y}_k - \bar{y})^2}{\sum_{k=1}^{n} (y_k - \bar{y})^2} \tag{7.8}$$

The coefficient R^2 is a ratio of variances that aims to quantify the proportion of variance of y "explained" by the selected predictor variables (it varies from 1 to 0, where 1 holds to situations where the adjust passes through all data points – a "perfect adjust" -, while 0 corresponds to a total independence between response and predictor variables).

After the assessment of the residual errors is complete and the results are accepted, the model is ready to predict future values of the response variable ($\hat{y}_0$) based only on the predictors not considered for its definition (z_0):

$$\hat{y}_0 = z_0.\hat{\beta} \tag{7.9}$$

At this point, the model is capable of predicting natural frequencies (the response variable), based on the environmental effects (the predictor variables) from the same period. Thus, observed and forecasted values can be compared. Since errors (ε) from this difference are inevitable, the definition of a range in which the errors are acceptable is required. In that sense, if the errors ε are considered as normally distributed, a confidence interval of $100(1-\alpha)$ % is given by (Johnson and Wichern, 2002):

$$\hat{y}_0 \pm t_{n-p-1}\left(\frac{\alpha}{2}\right).\sqrt{\hat{\sigma}_\varepsilon[1 + {z_0}^T(Z^T.Z)^{-1}.z_0]} = \hat{y}_0 \pm I(z_0) \tag{7.10}$$

with:

$t_{n-p-1}\left(\frac{\alpha}{2}\right)$	The upper $100(1-\alpha)^{\text{th}}$ percentile of a t-distribution with *n-p-1* degrees

The previous equation set a range $]\hat{y}_0 - I(z_0);\ \hat{y}_0 + I(z_0)[$ with a defined confidence level in which the new values of response variable should lay in. If the previously referred considerations about the construction of the matrix Z are met (first column of Z is filled with ones and the elements of the other columns are normalized), the confidence interval can be written as (Magalhães, 2010):

$$\bar{y} - I(z_0) < \tilde{y}_0 - \sum_{j=2}^{p} \beta_j.z_{0j} < \bar{y} + I(z_0) \tag{7.11}$$

with:

$\tilde{y}_0$	New response variable value (which was not considered for the definition of β)

The previous equation can be interpreted in the context of the monitoring situation under study. Once the training period for the definition of matrix $\hat{\beta}$ is complete, predictions of the frequency values ($\bar{y}$) from the subsequent periods can be computed. These predictions will be formulated considering the entire set of environmental effects covered during the training period. For this reason, predicted frequencies will present variations that are interpreted as normal, i.e., this variations do not refer to any kind of damage since the training period is assumed to have occurred during a healthy stage of the structure. When comparing the predicted and real values of the natural frequencies from the

subsequent periods, their difference should be evaluated. If it is abnormally high (i.e., the value is outside the confidence interval defined in equation (7.11)), the variation cannot be explained by the environmental effects considered during the training period, and an abnormal condition affecting the structure, such as damage, may be present.

The generalization of the presented method is easily performed for several dependent variables (frequency values of several vibration modes). This can be achieved by formulating the previous methodology as many times as response variables or through the matrix equation:

$$Y = Z.B + E \tag{7.12}$$

with:

Y	Matrix with n observations of the m dependent variables
Z	Matrix with the n values of the p predictors variables (p environmental effects)
B	Matrix with weight parameters of the p predictor variables
E	Matrix with the values of the random error

One last property from these models should also be referred: Multivariate Linear Regression Models are not valid for extrapolations. For that reason, a period of training with a wide range of values from the environmental effects should be used.

Dynamic Regression Models

An extension of the previous approach is given by the Dynamic Regression Models. In the previous section, it was shown that a Multivariate Regression Model, in order to predict a response value at a time instant k, uses the observations of the predictor variables at the same k time instant – it is then considered a static model. On the other hand, a Dynamic Regression Model considers that observations of predictor variables at previous time instants also influence the foreseen of the dependent variables. This consideration is very useful when dealing with response variables with a large inertia to variations of predictors.

The implementation of Dynamic Regression Models follows the same procedure as the Multivariate Models. The only change in the methodology is the introduction of additional predictors consisting of "past" observations of the independent variables.

7.2.1.2 Damage detection

The described statistical techniques allow estimating a variable (the residual error) which can be used as an indicator of abnormal conditions (usually damage) of a monitored wind turbine structure. However, since it is desired that the monitoring system operates in an autonomous way, an automatic procedure to identify situations of damage is required.

A general procedure to control the residual error from the frequency values of several vibration modes is obtained with the application of control charts. Control charts, one of the simplest techniques of

statistical process control, are used to evaluate if one or more variables are kept within predefined limits, which indicates that the process is occurring without abnormalities. For this reason, control charts are a very suitable technique to monitor possible frequency deviations due to damage.

A typical control chart is presented in Figure 7.4. It consists of a graphical display, with horizontal development (usually associated with time), in which observations are plotted. There are also some control parameters: a centre line, which represents the average value of the quality characteristic under study; an upper (UCL) and lower control line (LCL) defining an interval in which the observations are considered "in-control". If an observation has a value considered as abnormal, it falls outside this interval and is considered as "out-of-control".

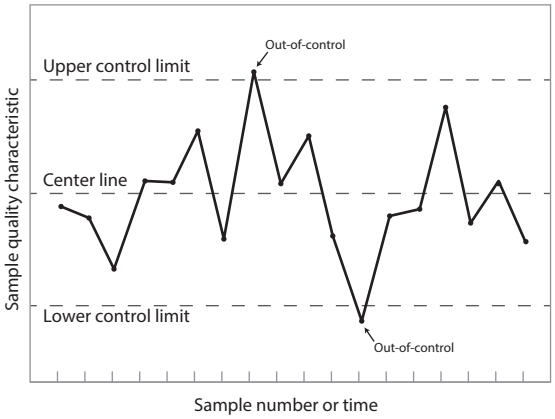

Figure 7.4 – Control chart

A common control chart to assess the evolution of a single variable is the Shewhart $\bar{X}$-chart. In the process control, the points (in the plot) under control represent a single observation or the mean of a group of observation (subsample). For a $\bar{X}$-chart, the definition of the upper and lower control lines is given by (Montgomery, 2009):

$$UCL = \bar{\bar{x}} + R.\sigma$$
$$LCL = \bar{\bar{x}} - R.\sigma \tag{7.13}$$

with:

$\bar{\bar{x}}$	Mean value from all observations
σ	Standard deviation. When each point represent one single observation, σ is the standard deviation from all observations; if each point represents the mean of a subsample with r elements, σ is given by the quotient between the standard deviation from all observations and $\sqrt{r}$
R	"Distance" between the control lines and the centre line. If $R = 3$ is defined in a distribution considered as normal, the control limits correspond to a confidence level of 99.7 %

When dealing with a situation with more than one variable (like m vibration modes), it is required a slightly evolution from a univariate technique (such as the $\bar{X}$-chart) to a multivariate technique. A similar technique of the Shewhart $\bar{X}$-chart for monitoring more than one parameter is the T^2 control

chart. The T^2 control chart is a simple tool to detect deviations in the characteristics under evaluation. Although very similar to $\bar{X}$-charts, T^2 control charts present two distinct characteristics: the vertical axis does not represent the quality characteristic under evaluation, but a statistic test named T^2; and the LCL is always zero.

This multivariate statistical parameter control can be also applied to individual observations or subgrouped data (subsamples). When every observation is checked (i.e. each point of the plot represents one observation), the T^2- statistic and the UCL are computed according to (Montgomery, 2009):

$$T^2 = \frac{n}{n+1}.(x-\bar{\bar{x}})^T.S^{-1}.(x-\bar{\bar{x}})$$
$$UCL = \frac{(n-1).m}{n-3}.F_{m,n-m}(\alpha) \tag{7.14}$$

with:

n	Number of observations collected during the reference period
x	Individual observation (vector with m components)
S	Covariance matrix
$F_{m,n-m}(\alpha)$	α percentage point of the F distribution with m and $n-m$ degrees of freedom

If, instead of checking all the observations, subsamples with r observations are verified, the T^2-statistic and the UCL are computed according to (Montgomery, 2009):

$$T^2 = r.(\bar{x}-\bar{\bar{x}})^T.S^{-1}.(\bar{x}-\bar{\bar{x}})$$
$$UCL = \frac{m.(s+1).(r-1)}{s.r-s-m+1}.F_{m,s.r-s-m+1}(\alpha) \tag{7.15}$$

with:

$\bar{x}$	Subgroup average
$\bar{\bar{x}}$	Process average
s	Number of groups collected during the reference period

7.2.2 Fatigue Monitoring

Wind turbines are structures predominantly subjected to dynamic loads throughout their period of life. In that sense, the continuous assessment of the fatigue condition of structural components can anticipate a fatal damage. Although failures from fatigue damage are also not expected to occur (if the structural design is correct), there is a large uncertainty about the real loading condition that the wind turbines will face. Thereby, the conditions considered during the design stage might not correctly recreate the actual conditions, leading to an over or underestimation of the components life. For these reasons, the implementation of a fatigue monitoring system can be an important advantage for the management of wind farms.

Support structures, as seen in Chapter 3, are a fundamental component of wind turbines that cannot fail at any circumstance, otherwise the whole system is jeopardized. Furthermore, their design is usually very conservative with respect to fatigue, which may lead to real fatigue life considerably higher than 20 years (the usually considered expected fatigue lifetime). Thus, the implementation of a fatigue monitoring system for assessment of the real solicitation of the support structure can introduce several advantages. If the monitoring system indicates that damage is not present in the structure, the fatigue monitoring system can be extremely useful in the following aspects:

- Estimation of the evolution of real fatigue condition of the support structure and its suitability with the expected lifetime (usually 20 years);
- Since an estimation of the real condition of fatigue damage is known, the results of the fatigue monitoring system could be an essential element for a decision about extending the lifespan of the structure, leading to a higher profitability of the investment;
- Possibility of repowering or overpowering of the system, while keeping the support structure. If the fatigue monitoring system indicates a considerable margin of safety at the end of the period of life initially stipulated, together with a situation of non-damage detection by the dynamic monitoring system, one of these two options could be considered. For that purpose, a careful inspection of the structure would have to be carried out on-site. However, the results obtained with both components of the monitoring system, could provide a factual evidence of the overall good condition and low level of structural loading during the first period of life. The decision about repowering and overpowering could greatly reduce the cost of tower + foundation portion, which contributes with 18 % and 23 % of the capital cost for onshore and offshore installations, respectively (see section 3.1.2).

The description of fatigue monitoring systems and publication of results from long periods of data acquisition is not very common in literature. In the context of the HISTWIN project (Veljkovic, Heistermann et al., 2012), a 2.1 MW wind turbine tower was monitored with strain rosettes, among other sensors. Results from two periods of 139 and 159 days for the most unfavourable structural detail lead to the conclusion of a considerable overdesign of the fatigue strength.

Another work considering the problem of fatigue in the support structure of a wind turbine is reported in (Pollino and Huckelbridge, 2012). A 100 kW wind turbine was monitored with strain gauges during approximately one year. The authors studied the principal structural details of the tower and also concluded that the fatigue life of these elements were significantly higher than 20 years.

An interesting study is described by Thies *et al* (Thies, Johanning et al., 2014) about the fatigue damage assessment of the mooring lines of an offshore floating marine energy converter. This equipment, that also comprises a 1.2 m diameter wind turbine, was monitored with load cells to measure the tension forces in the mooring system.

Outside the scope of wind turbine support structures, there is a greater range of studies about the assessment of fatigue and prediction of the remaining period of life on steel structures. As an example, Ye *et al* (Ye, Ni et al., 2012) presented a study about a long-term monitoring data of dynamic strain on a steel bridge (the Tsing Ma Bridge).

7.2.2.1 Estimation of the Remaining Lifetime

The results of fatigue damage of the support structure obtained during a representative time period may be used to estimate the remaining fatigue life of the structure. A direct way of doing this is considering the monitored period as representative of the whole period of life. In that case, the estimated accumulated damage at the end of the design fatigue life of the structural detail is obtained as:

$$E[D] = \frac{T_{lifetime}}{T_{monitored}} . D_{monitored} \tag{7.16}$$

with:

$T_{lifetime}$	Design fatigue life (usually 20 years)
$T_{monitored}$	Period of time which was considered for fatigue monitoring
$D_{monitored}$	Accumulated damage throughout the monitored period

However, this extrapolation assumes that the monitored period is representative of the loading scenarios from the whole period of operation of the wind turbine. Considering that the monitored period may not be representative of the environmental loading along the estimated period of life, a more complex approach should be followed.

An alternative approach can be obtained if the information about the environmental data is recorded. In that case, loading scenarios should be defined according to the simultaneous occurrence of the various environmental parameters. Important parameters such as mean wind speed, turbulence intensity and wind direction should be considered. Also, the significant wave height and peak period should be included for offshore installations. The variability of the parameters is usually reduced into bins with a representative magnitude in order to ease the computation of probability. Figure 7.5 shows part of the scatter diagram from the OWEZ site, where the probability of occurrence of loading scenarios with a mean wind speed of 10 m/s combined with various wave conditions is shown. In this figure, the wave loading condition is defined by the significant wave height H_s (introduced in section 6.2) and the mean zero-crossing period T_z (instead of the peak period T_p). This period is referred to the mean value of the zero up-crossings of a point at the sea surface (Tempel, 2006).

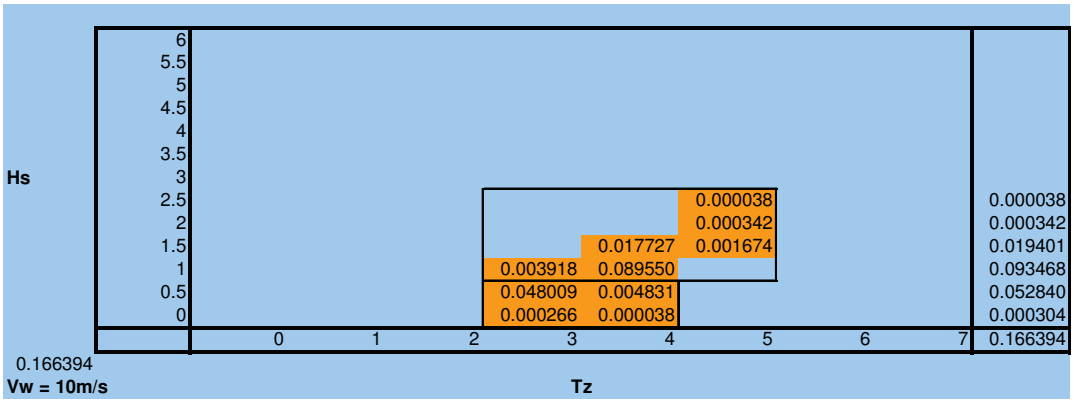

Figure 7.5 – Part of scatter diagram corresponding to the mean wind speed of 10 m/s (the values represent the probability of occurrence of the loading scenarios) (Tempel, 2006)

Once a representative probability of occurrence of the environmental loading scenarios is obtained, the accumulated damage at the end of the design fatigue life of the structural detail can be estimated according to:

$$E[D] = \frac{T_{lifetime}}{T_{monitored}} . \sum_{i=1}^{m} P_i(U, I_w, \dots) . D_i \tag{7.17}$$

with:

$T_{lifetime}$	Design fatigue life (usually 20 years)
$T_{monitored}$	Period of time which was considered for fatigue monitoring
P_i	Probability of occurrence of the load scenario i
D_i	Accumulated damage of load scenario i during the monitoring period ($T_{monitored}$)

The monitoring period of the structure (which might be much shorter than the monitoring period of the loading conditions) should include all the important load conditions for the quantification of D_i.

7.2.3 Overview of the Dynamic Monitoring System Main Steps

At this point, all the important aspects of the dynamic monitoring system were already introduced. This section briefly summarizes the chain of processes throughout the developed system.

The chart with the chain of procedures is presented in Figure 7.6. The processing starts with the acquisition of the 10 min. acceleration time series and data from environmental and operational conditions. Initially, the acceleration signals are decimated and a coordinate transformation is applied to these signals according to the yaw angle recorded by the SCADA system, in order to orientate the signals according to the FA and SS direction.

After this preprocessing, the module related to structural damage detection starts with the automated modal analysis. The first step is referred to the application of the output-only identification algorithms

(SSI-COV, SSI-DATA and p-LSCF) to the acceleration signals. These algorithms were introduced in section 5.4. The results obtained are then analysed through a cluster analysis (section 5.7.1), in which the poles with similar modal properties are gathered into the same clusters. Lastly, these clusters are compared with reference modal properties (frequency values and mode shapes) of the vibration modes intended to be tracked in order to separate the clusters referred to these modes from the other ones. These reference properties are defined during a training period prior to the automated processing. Once they are defined, these properties are saved in a database, being used in every processing cycle.

From the moment the modal tracking is complete, it is necessary to remove the influence of the operational and environmental effects on the frequency values of the identified modes. In that sense, multivariate linear regression models have to be defined during a representative period (again, prior to the automated process). Once these models are set, they are applied to the identified frequency values in order to reduce their variability. This process was presented in section 7.2.1.1.

The last step of the module is referred to the assessment of important deviations of the frequency values (damage detection). The implemented procedure, based on control charts, was introduced in section 7.2.1.2. A caveat should be made at this level that, if subsamples with more than one observation are used, the damage detection step is only processed after the required number of observations is achieved.

The module related to the fatigue assessment of the wind turbine support structure starts after the application of the output-only identification algorithms to the acceleration signals. At this point, it is necessary to select an order of the state-space model. This selection should take into consideration the order with the highest number of identified modes with important contribution to the support structure motion. For that reason, the results from the modal tracking represent an important information. Furthermore, the selected order should contain poles related to the low order harmonics (when the turbine is operating). Thus, the data from the SCADA system is also important at this point.

Once the state-space model order is selected, it is possible to define the forward-innovation model. With the transformation of the model into the modal basis, it is thus possible to obtain the modal state vector, essential information to estimate the acceleration at unmeasured locations (this procedure was presented in section 5.5). At this point, a detailed estimation of the mode shapes along the height of the support structure is required to estimate the acceleration time series at every location. Two options are available:

- If the number of installed sensors at the structure is enough to estimate the mode shapes of the most important modes along the height of the support structure, an interpolation of the experimentally found mode shapes can be used. This methodology was referred in section 6.4.1;
- On the other hand, if a reduced number of sensors is used, reference support structure mode shapes of the important modes should be used. In addition, operational deflection shapes of the harmonics should also be used for situations under operation. Both mode shapes and operational deflection shapes must be defined after a period of training and should consider the different operating conditions of the wind turbine. This procedure was described in section 6.4.2.

With the possibility of estimate the acceleration time series at every position of the wind turbine support structure, the fatigue damage of the structure is assessed with the procedure proposed in section 6.4.1. During this process, the stiffness matrix of the support structure is required and should be previously calculated according to the mechanical properties of the support structure.

Lastly, the fatigue damage estimations from the 10 min. time series should be continuously summed in order to obtain a cumulative damage of the support structure. Once representative damage accumulation events from the various environmental loading scenarios are recorded, it is possible to perform an estimation of the damage condition at the end of the designed fatigue life and, thus, predict the real lifetime of the structure. This procedure was introduced in section 7.2.2.1.

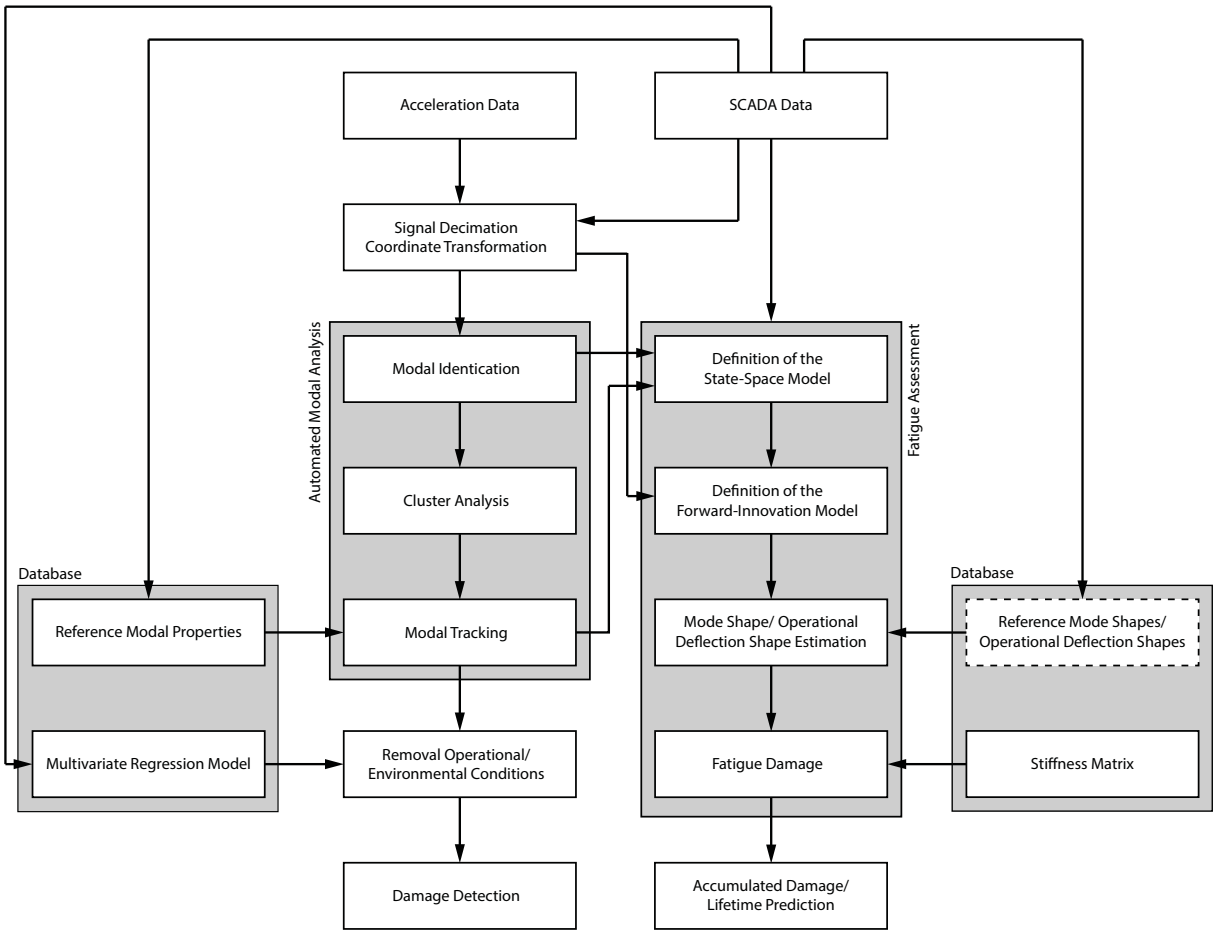

Figure 7.6 – Chain of events included in the dynamic monitoring system (the dashed box is only referred to situations in which a reduced number of sensors is used)

7.3 CASE STUDY – SENVION MM82

7.3.1 INTRODUCTION

This section introduces the main results obtained with the application of the vibration-based structural health monitoring methodology to a 2.0 MW Senvion MM82 wind turbine. In that sense, a long-term study was performed for this wind turbine.

The goal of this study was to demonstrate the suitability of dynamic monitoring systems to be installed at wind turbines. The work contemplated several steps:

- Installation of the monitoring equipment;
- Implementation of the structural health monitoring tools in an automated way;
- Full comprehension of the dynamic behaviour of the wind turbine in different operating and environmental conditions;
- Identification of the main vibration modes;
- Assessment of the capability of the implemented dynamic monitoring system to detect small damages;
- Fatigue assessment of the wind turbine support structure;
- Study about the feasibility of the implementation of monitoring systems with a smaller number of sensors.

7.3.2 WIND TURBINE DESCRIPTION AND NUMERICAL MODELS

The Senvion MM82 is a 2.0 MW onshore wind turbine. This wind turbine started operating in 2007 at the Torrão wind farm, in the north of Portugal (Figure 7.7).

Figure 7.7 – Location of the Torrão wind farm

This wind turbine is characterized by 82 m diameter, up-wind rotor with variable speed operation, with three pitch controlled blades. The generator of this model is of the asynchronous type and the hub is located at 80 m high.

Figure 7.8 – Senvion MM82 wind turbine installed at the Torrão wind farm

The support structure comprises a reinforced concrete slab foundation and a steel tubular tower. The tower is composed by three segments, totalizing 76 m in height. These segments are connected by bolted flanged connections. The main technical characteristics of the wind turbine are summarized in Table 7.1.

Table 7.1 – Main technical characteristics of the Senvion MM82

Model	Senvion MM 82
General	
Rated-power [MW]	2.0
Cut-in wind speed [m/s]	3.0
Rated Wind speed [m/s]	13.0
Cut-out wind speed [m/s]	25.0
IEC class	IIa
Rotor	
Nº blades	3
Rotor orientation	Horizontal axis Up-wind rotor
Rotor speed range [rpm]	8.5 – 17.1 (±16 %)
Rotor diameter [m]	82.0 (Blade length: 40 m)
Control systems	Pitch and rotor speed control
Machinery	
Generator type	Variable-speed asynchronous generator
Gearbox	3 stage Planetary/ helical gear (ratio: 105.4)
Yaw system	Active system with disc brake
Tower	
Type	Steel tubular
Hub height [m]	80
Base diameter [m]	4.300
Top diameter [m]	2.955

Aiming to obtain an initial approach of the modal properties of the Senvion MM82 wind turbine, two numerical models were developed. Initially, the structural behaviour of the tower was modelled with the ANSYS software (Ansys Inc., 2011), according to technical drawings made available by the manufacturer. Four-node shell elements with six degrees of freedom at each node were used to model the shell components of the tower, while the flanged bolt connections were simulated with beam elements. For the nacelle and rotor blades components, a point element with a representative concentrated mass was employed on their centre of gravity. The connection between tower and foundation was defined as fixed. Figure 7.9 presents a global view and a detail from the door opening of the finite element model.

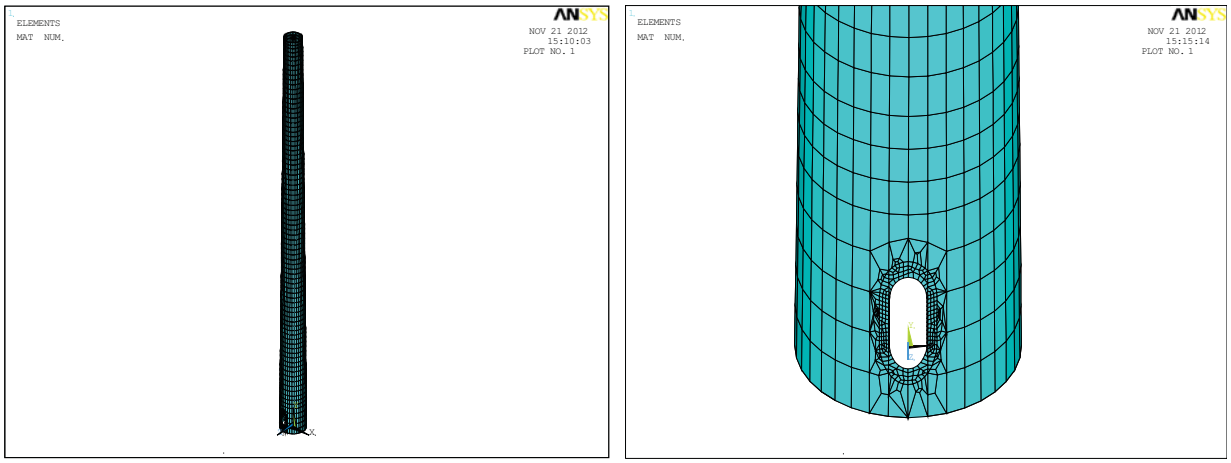

Figure 7.9 – Global view and detail of the door opening of the Senvion MM82 finite element model

The second numerical model of the Senvion MM82 wind turbine was developed using the HAWC2 aeroelastic code (Larsen and Hansen, 2007). For this model, an improvement on the previous model developed using ANSYS was introduced. In addition to modelling the tower structure according to technical drawings, the nacelle and rotor blades were also modelled. Since the characteristics of these elements were not provided, the characteristics from the NREL 5MW reference wind turbine (Jonkman, Butterfield et al., 2009) were scaled down to meet the characteristics of the Senvion MM82 wind turbine. The connection between tower and foundation was also defined as fixed.

The results obtained after the modal analysis of both models for the frequency values of the first 2 pairs of tower bending modes are shown in Table 7.2. It is observed that the results achieved with both models are coherent, giving a good indication about the expected frequency values of these modes.

Table 7.2 – Natural frequency values of the first 2 pairs of tower bending modes obtained with the numerical models developed using ANSYS and HAWC2

	Natural frequency [Hz]	
Modes	ANSYS	HAWC2
1 SS	0.378	0.366
1 FA	0.378	0.361
2 FA	2.963	2.771
2 SS	2.967	2.830

The mode shapes of the referred modes are illustrated in Figure 7.10. It is seen that second pair of bending modes includes an important participation of rotor blades motion, while this contribution is imperceptible in first pair.

1 SS

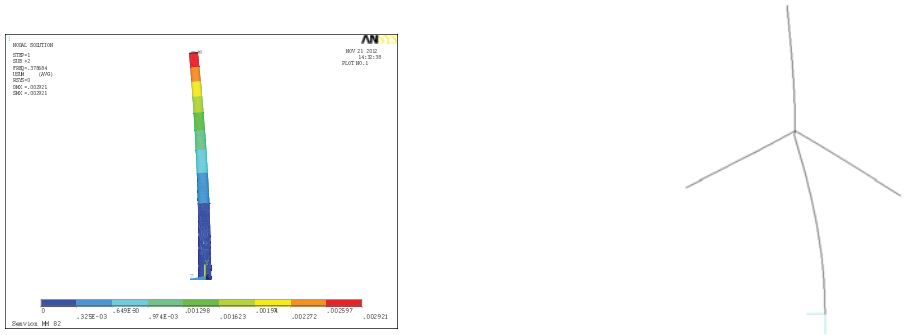

1 FA

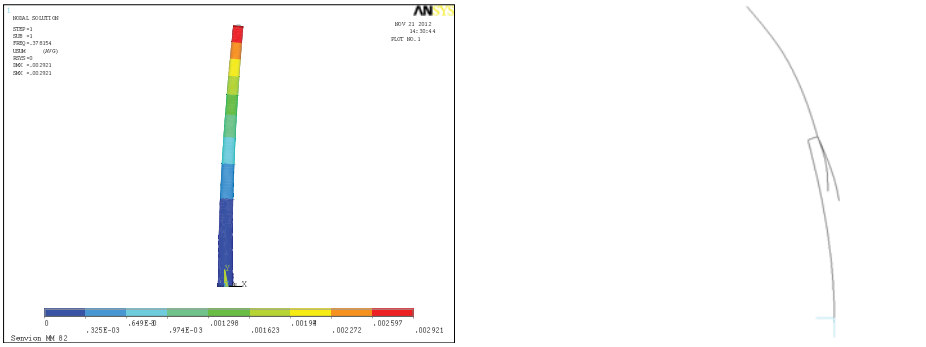

2 FA

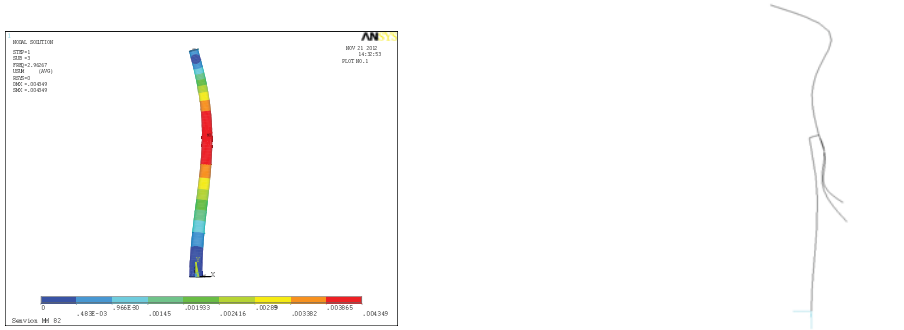

2 SS

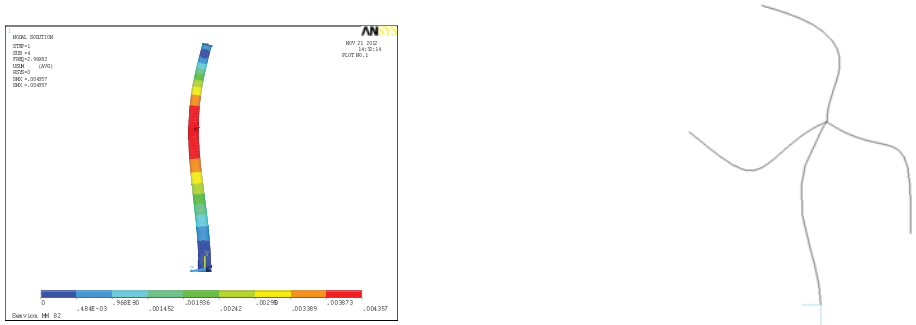

Figure 7.10 – Mode shapes of the first 2 pairs of tower bending modes obtained with the numerical models (left column: ANSYS; right column: HAWC2)

7.3.3 Operating Conditions

The Senvion MM82 operates within a wind speed regime between 3 and 25 m/s, reaching its rated power at a wind speed of 13 m/s. This power production condition is expressed in the power curve of the turbine (Figure 7.11).

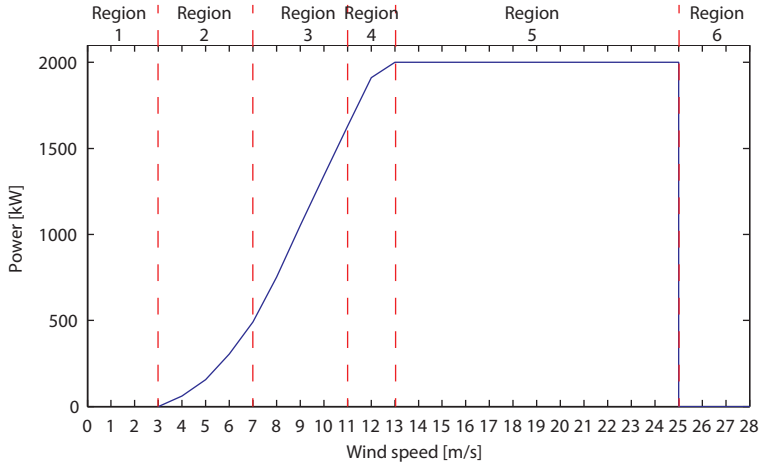

Figure 7.11 – Senvion MM82 power curve

Figure 7.11 also indicates the various operating conditions of the wind turbine. The first region is upper-limited by the cut-in speed of the turbine and is characterized by very low wind speeds. In this region, the wind speed is not enough to create a consistent rotor torque and, thus, the turbine does not operate and the rotor is usually parked or idling. While in this region, the control strategy of the turbine involves the analysis of the wind condition in order to evaluate a feasible start of the turbine operation.

When the wind speed is higher than the cut-in value, the turbine enters in Region 2. In this region, the wind turbine starts the power production regime in which the rotor operates close to an optimal tip-speed ratio. This regions corresponds to line BC' in Figure 3.39 and characterized by an important variation of rotor speed.

Once the Region 3 is achieved, the wind turbine enters in a regime defined by line C'D' in Figure 3.39. This is a transition condition in which the rotor torque achieves its rated value while the rotor speed slightly increases. During both Regimes 2 and 3, the pitch angle of the blades is kept constant on its minimum value and the system acts on the yaw actuator to keep the rotor orientated to the main direction of the wind.

Region 4 is defined by the start of operation of the blades pitch actuator. In this region, the rotor reaches its rated speed and the blade pitch angle is adjusted to keep the rotor speed under defined values.

Once the turbine is operating at its rated power, the Region 5 is reached. In this region, the main goal of the control system is to keep constant this production level. For that goal, the blade pitch angle is controlled over this region, increasing its value with the increase of the wind speed. The actuation of the control system over the blade pitch permits to control the rotor speed, keeping the production constant, as well as to avoid exceeding electrical and mechanical load limits.

The last region of Figure 7.11 is referred for wind speeds higher than the cut-out value. At this point, the wind load acting on the system is excessive and the production is stopped. In order to avoid extreme loads, the turbine is shutdown, the blades are pitched out of the wind.

These six regions define, in a simplistic way, the control system of a wind turbine for different wind speed conditions. Thus, if it is desired to track the modal properties of the wind turbine over its period of life, the variations occurring within each region need to be considered. For that reason, the data recorded by the SCADA system has an important role in the monitoring system.

The different operating regions are also evident in the evolution of the rotor speed with the wind speed (Figure 7.12). In this figure, the rotor speed range from the variable-speed generator system is evident. During the period in analysis, Region 6 was not detected.

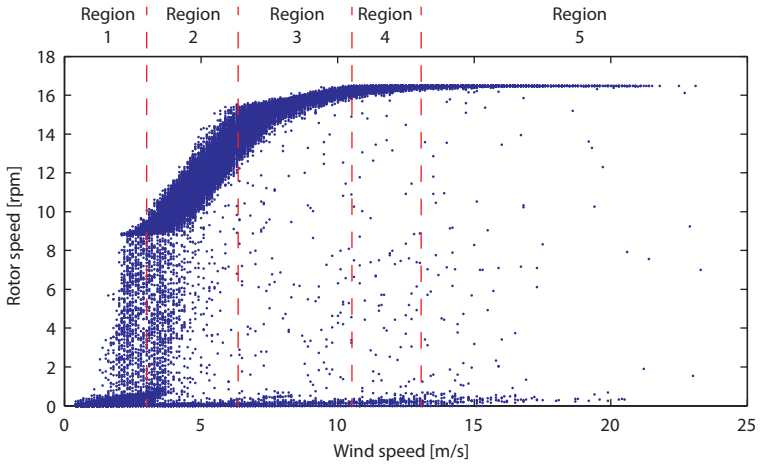

Figure 7.12 – Rotor speed vs wind speed

The behaviour of the pitch angle with the rotor speed is depicted in Figure 7.13. In this figure, the different operating conditions of the wind turbine system are also visible. Up to the wind cut-in speed, the pitch angle is kept with high values (around 70º to 90º). Under this condition, the blades are only able to slowly rotate, which is desire since the wind speed is too low for production. From the moment the wind speed is higher than the cut-in speed, the pitch decreases and the generator starts operating (from around 8.8 rpm). The pitch angle is kept low until the Region 4 is reached. Since the pitch actuator acts practically at the rated rotor speed, the increase of the pitch angle in Region 4 and 5 is not completely perceptible in the plots of Figure 7.13.

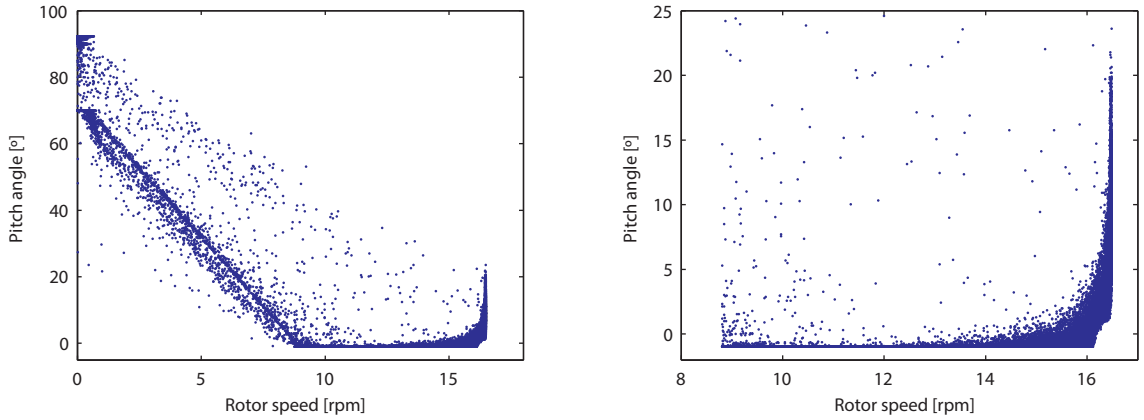

a) b)

Figure 7.13 – Pitch angle vs rotor speed: a) all regimes; b) only operating regimes

The illustration of evolution of the blades pitch angle actuator with the wind speed (Figure 7.14) is helpful to understand the pitch mechanism in Region 4 and 5. In this figure, the start of the actuator around 11 m/s is clearly visible. From the observation of Figure 7.14 b), it is also possible to attest that the increase rate of the pitch angle with the wind speed is lower in Region 5 than in Region 4.

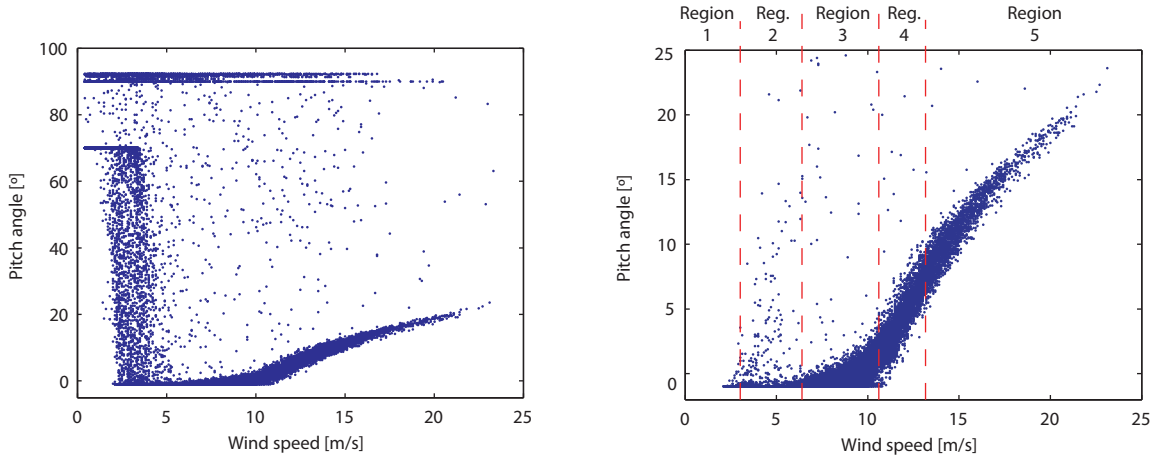

a) b)

Figure 7.14 – Pitch angle vs wind speed: a) all regimes; b) only operating regimes

The analysis of the recorded SCADA data also permitted to conclude that the main wind incidence direction is around 110º. It is concluded, from the wind rose of Figure 7.15, that the higher wind speed regimes are also obtained for this direction.

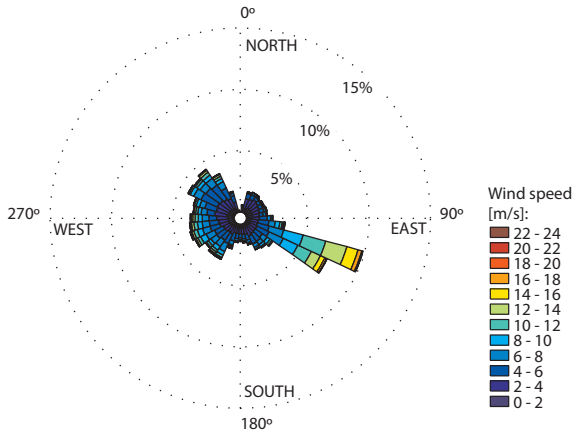

Figure 7.15 – Wind rose histogram of mean wind speed

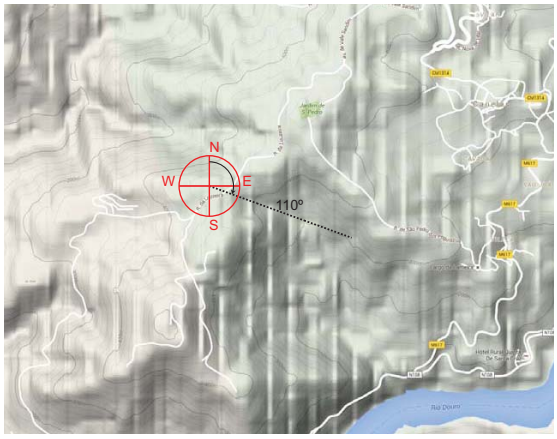

Figure 7.16 – Local orography on the wind turbine site

The local orography at the wind turbine site is represented in simplified form in Figure 7.16. In this figure, the origin of the referential represents the wind turbine location. It is interesting to note that at the direction of 110º, the terrain presents an apparent depression.

7.3.4 Monitoring System Description

The implemented monitoring system is based on a central acquisition system to which all sensors are connected. It is composed by 9 uni-axial accelerometers distributed along the tower height and at the foundation level, according to the scheme presented in Figure 7.17. All the accelerometers were fixed to the tower through fixing clamps on the tower flanges. The central acquisition system is located at the first platform, around +20.000 m. All the equipment is placed inside the wind turbine.

With the considered instrumentation layout, the acceleration on both horizontal directions at three different tower sections is measured. In addition, the pair of sensors S5 and S7 enables the characterization of motion associated with torsion modes.

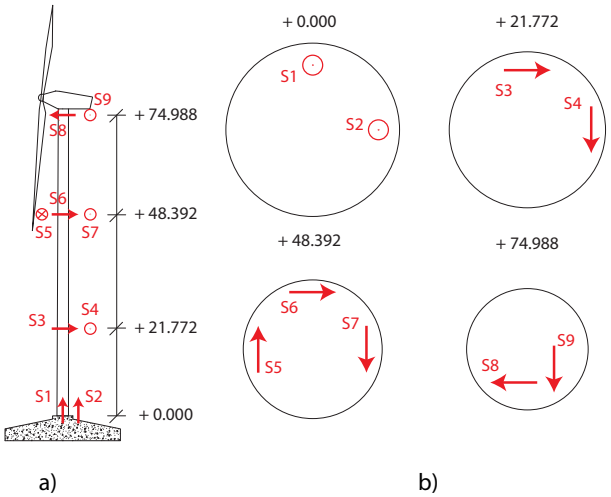

Figure 7.17 – Position of the accelerometers at the different levels of the wind turbine: a) front view; b) top view of the instrumented sections

The installed sensors are force balance accelerometers, model CMG-5S from Guralp (Figure 7.18). This accelerometer presents a dynamic range of 140 dB, with a frequency band from DC to 100 Hz. The measuring range varies from $\pm$0.1g to 4.0g.

The central acquisition system is composed by a CR-5P unit from GeoSIG (Figure 7.18). This unit is composed by a digitizer (CR-5PAD24) and an internal computer (CR-5PRHDx). The digitizer allows the connection of up to 9 uni-axial accelerometers and is equipped with a 24-bit analog-to-digital converter. The internal computer controls the recording operations.

The CR-5P unit was configured to record 10 min. acceleration time series with a frequency sampling of 50 Hz. The length of the time series was decided in order to match the 10 min. period used by the SCADA system to compute the mean values of the monitored parameters.

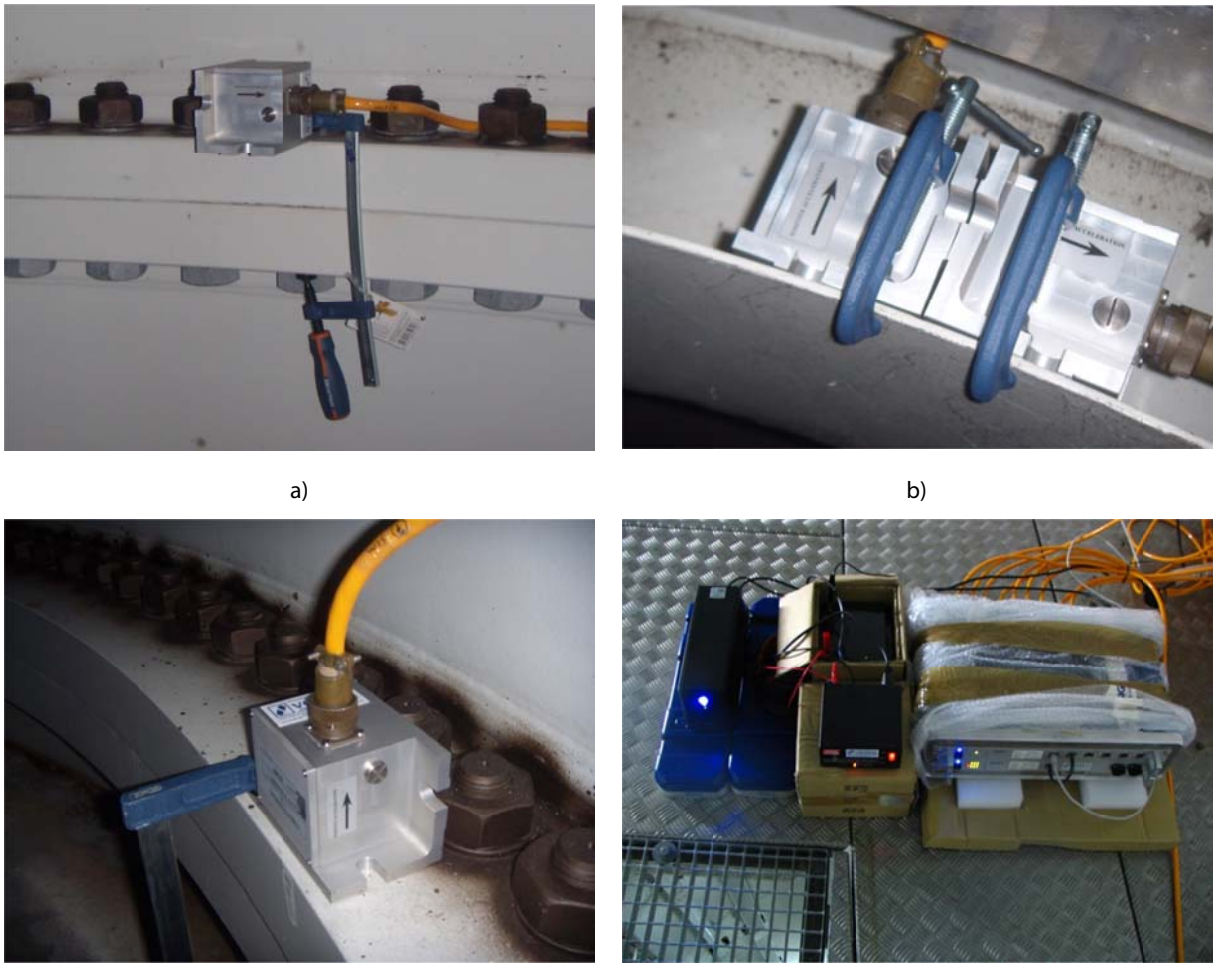

a) b) c) d)

Figure 7.18 – Accelerometers installed at: a) tower flange; b) top tower flange; and c) foundation flange. d) Central acquisition system with the CR-5P unit

The dynamic monitoring system is complemented by the SCADA system of the wind turbine. This system records the mean, maximum and minimum value from 10 min. period of several operational and environmental parameters. Among them, some were important for the context of this structural health monitoring project:

- Wind speed and direction;
- Rotor speed;
- Yaw angle;
- Blades pitch angle;
- Outdoor temperature.

Since it was not possible to connect the central acquisition system to an external GPS antenna, the data recorded by the CR-5P was manually synchronized to the SCADA data. This operation was tuned using the date information of startup and shut-down events of the turbine recorded by the SCADA data, which were correlated to events of sudden increase or decrease of the tower vibration levels.

The dynamic monitoring system was installed at the wind turbine on the 22th of July of 2013. Unfortunately, problems related to electrical power supply of the central acquisition system prevented a continuous operation. Moreover, it was only possible to have access to the equipment during maintenance periods, which annulled the possibility to make rapid interventions once the problems were noticed. For that reason, it was not possible to avoid some periods with a low rate of recorded setups (or even inactivity of the system). A total number of 37 685 data sets were collected during this period. The percentage of recorded setups for each month between 22/07/2013 and 21/07/2014 is evidenced in Table 7.3.

Table 7.3 – Percentage of recorded setups between 22/07/2013 and 21/07/2014

Year	2013						2014						
Month	7	8	9	10	11	12	1	2	3	4	5	6	7
Recorded Setups [%]	100	100	63	0	23	89	89	100	100	94	67	59	53

7.3.5 PRELIMINARY RESULTS

The processing of the continuously collected data comprehends an initial task of filtering and resampling to reduce the sampling frequency to 25 Hz. After this step, a coordinate transformation is applied to the acceleration time series measured at the tower in order to obtain signals that are always aligned with the FA and SS directions.

Examples of the different excitation conditions that the wind turbine is subjected to are illustrated in Figures 7.19 to 7.21. Figure 7.19 shows the acceleration time series of the recorded setup with the highest observed mean wind speed (23.3 m/s). On the other hand, Figures 7.20 and 7.21 present two situations of sudden increase and decrease of the vibration level related to a situation of startup and shutdown of the rotor, respectively.

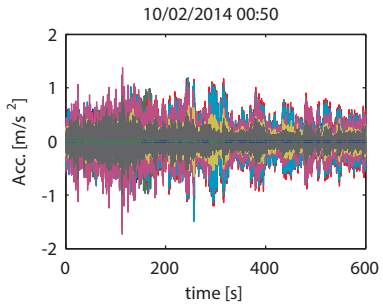

Figure 7.19 – Acceleration time series from a setup with the highest observed mean wind speed (23.3 m/s)

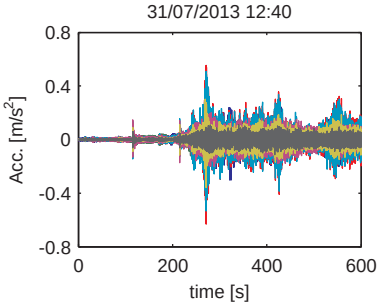

Figure 7.20 – Acceleration time series during a startup event

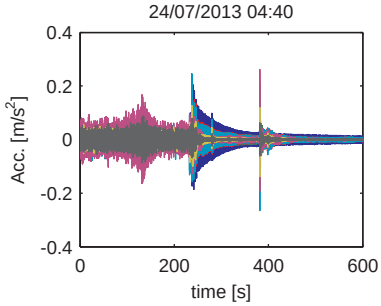

Figure 7.21 – Acceleration time series during a shutdown event

The variation of the vibration levels during the monitored period is shown in Figures 7.22 and 7.23 for, respectively, the RMS and maxima values from each recorded 10 min. time series. The maximum acceleration recorded in FA direction was 3.73 m/s^2 while in the SS direction was 3.10 m/s^2. As expected, the vibration levels at the foundation are considerably lower than in the tower.

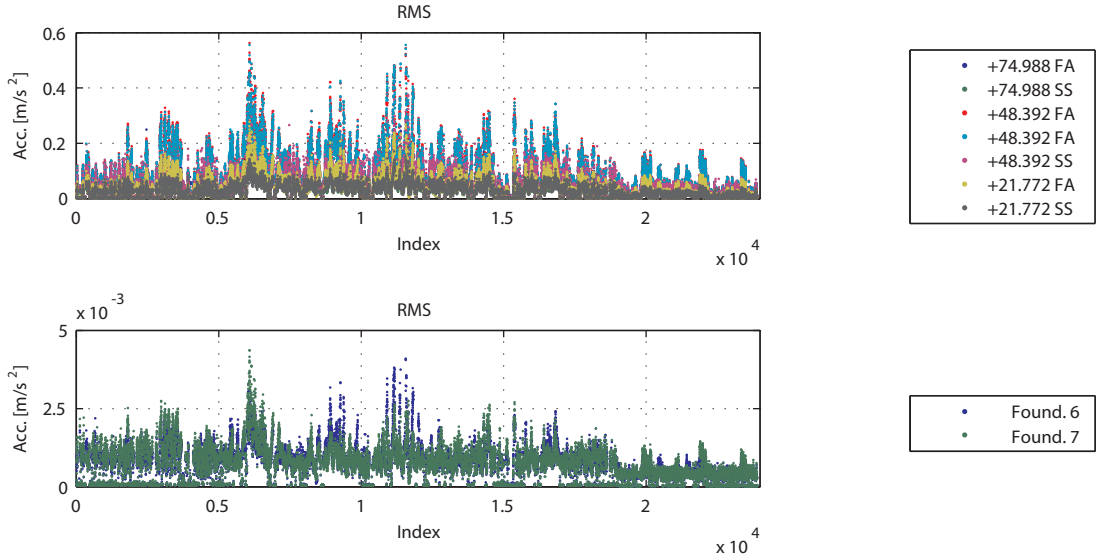

Figure 7.22 – Time evolution of the RMS values of the acceleration time series collected during the monitored period

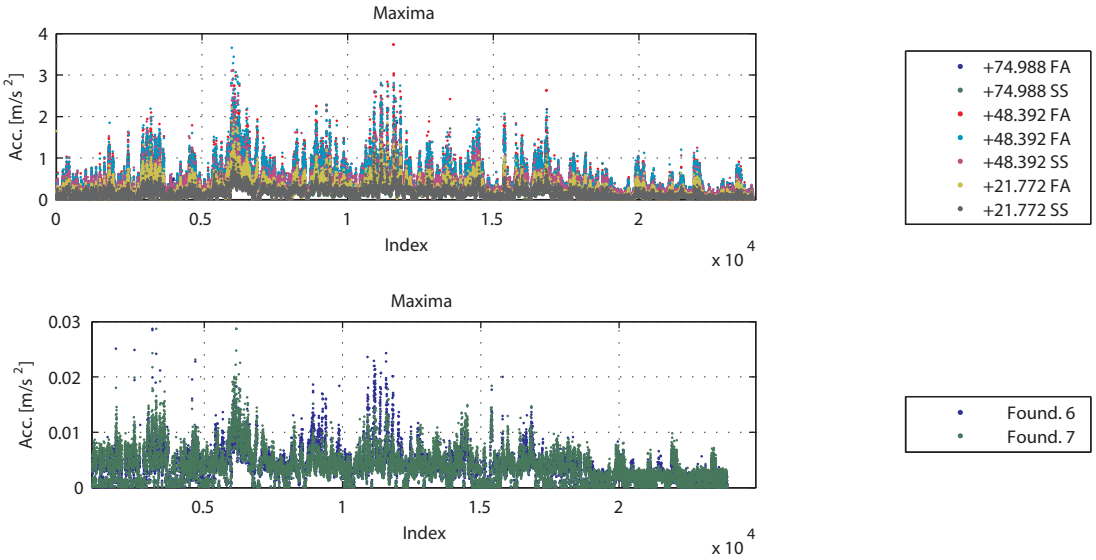

Figure 7.23 – Time evolution of the maxima values of the acceleration time series collected during the monitored period

It is interesting to observe that the higher values of acceleration do not occur at the tower top but at +48.392 m level. This is a common situation when the turbine is operating (the majority of the time). However, when the turbine is parked or idling, the highest vibration levels were recorded by the top sensors (+ 74.988 m). This behaviour was also noticed in the analysis of the offshore Vestas V90 wind turbine (section 5.9).

Figure 7.24 shows the RMS values of acceleration in the FA direction for operating and non-operating situations. It can be seen that, when the turbine is operating, the acceleration level at the +48.392 m height is clearly higher than at the other two levels. Indeed, the vibration levels at the top (+ 74.988 m) and +21.772 m are similar. On the other hand, when the turbine is not operating, the level of vibration usually increases from the lowest part to the top of the tower structure. Nevertheless, the vibration at the +48.392 m sometimes exceeds the value from the top sensor. The causes for this behaviour will be further analysed in section 7.3.6.4.

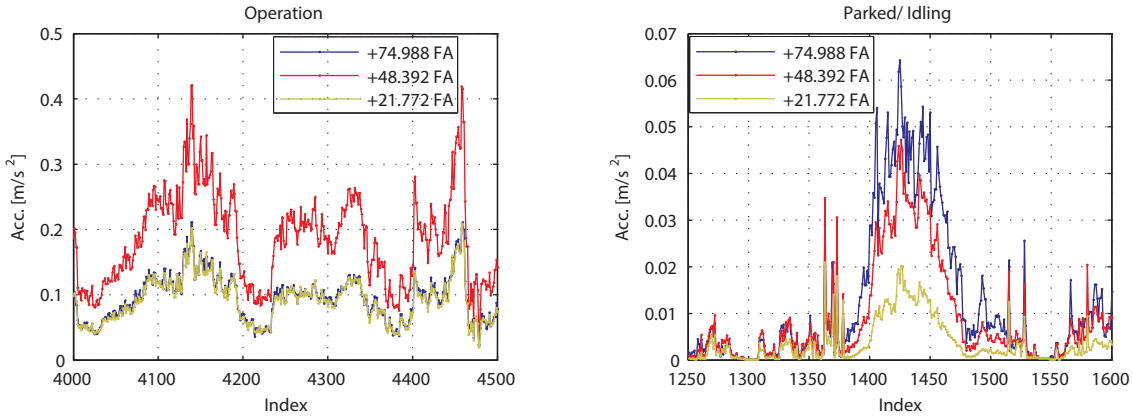

a) b)

Figure 7.24 – Time evolution of the RMS values of the acceleration time series during: a) operating conditions and; b) parked or idling conditions

The wind excitation is, naturally, the main driver of wind turbine vibration. Figure 7.25 presents the time evolution of the RMS values at the +74.988 m level in the FA direction and of the wind speed. As expected, there is a clear coherence between acceleration level and wind speed.

The relationship between the RMS values of acceleration and the wind speed is also illustrated in Figure 7.26. From the figure, it seems that the acceleration continuous increases with the increase of the wind speed.

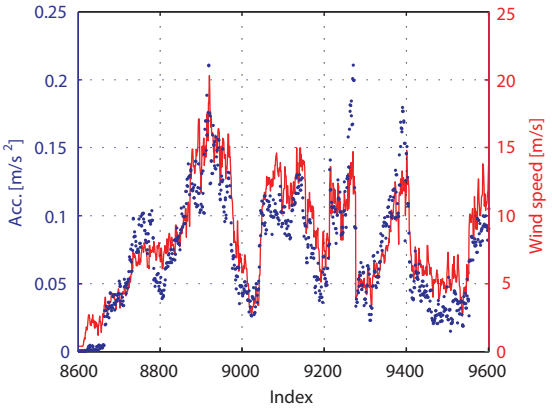

Figure 7.25 – RMS values of acceleration of the +74.988 m sensor in the FA direction vs the wind speed

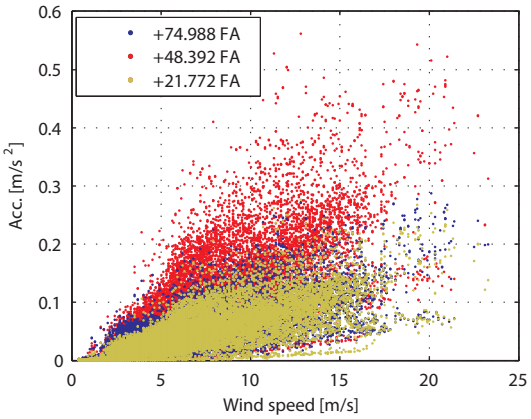

Figure 7.26 – Correlation of the RMS values of the sensors in the FA direction with the wind speed

The variation of the vibration amplitude with the yaw angle is an important analysis to check the directions with greater wear of the support structure. As expected, the vibration level is highly dependent on the rotor orientation (which is conditioned by the wind direction). Figure 7.27 presents the RMS values of the acceleration in FA direction according to the yaw angle. As can be seen, this figure is coherent with the main wind directions illustrated in the wind rose of Figure 7.15.

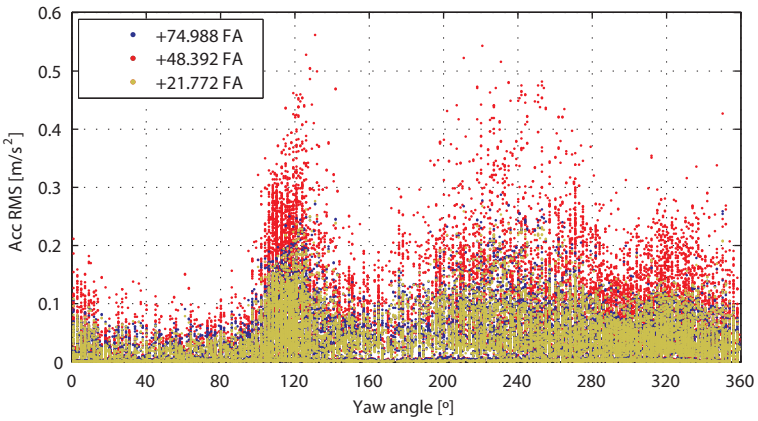

Figure 7.27 – RMS values of the acceleration in the FA direction according to the yaw angle

Figure 7.27 clearly indicates the directions according to which the structure vibrates with the highest levels. However, as the wind speed is not evenly distributed across all the directions (as shown in Figure 7.15), it is not possible to make any consideration about the heterogeneity of the support structure just with this observation.

In order to compare the vibration amplitude for different angles of nacelle orientation, only the recorded setups from a narrow range of wind speeds, under operating conditions, were selected. With this consideration, it can be assumed that the wind excitation is roughly similar across all directions. Still, differences can exist in terms of wind turbulence.

Figure 7.28 presents the box plots obtained for the RMS values of acceleration in the FA direction for the top sensor considering only setups when the turbine was operating and the wind speed was between 6 and 7 m/s. For the analysis, the yaw angles were grouped in 18 ranges of 20º, from 0º to 360º. In this figure, the line connects the median value of each group, while the edges of the box represent the 25th and 75th percentiles. The whiskers were extended to the most extreme points not considered as outliers. In the background, the data considered for the analysis is plotted in light grey. This figure clearly indicates that, for roughly similar wind conditions, the structure presents higher vibration levels for the ranges 100º – 140º and 180º – 240º than for remain directions. The first range coincides with the main direction of the wind.

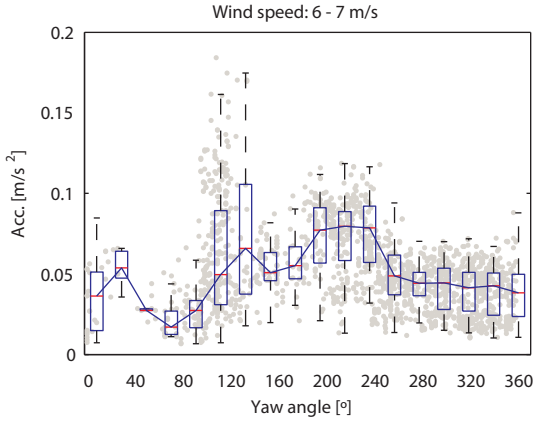

Figure 7.28 – Box plots of the RMS values of acceleration of the top sensor in the FA direction according to the yaw angle, considering setups when the turbine was operating and the wind speed was in the 6 – 7 m/s range

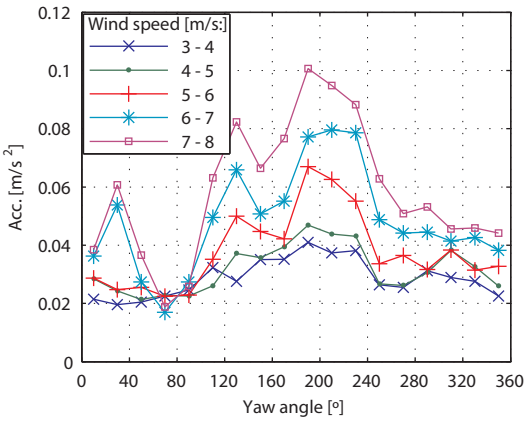

Figure 7.29 – Median values of the RMS values of acceleration of the top sensor in the FA direction according to the yaw angle, considering setups when the turbine was operating and several wind speed ranges

This analysis is further extended to ranges of wind speed whose number of recorded setups is representative of all yaw sectors. For that reason, ranges with the largest wind speeds were not considered since they mainly occur in a few yaw sectors. Figure 7.29 presents the results obtained with this analysis, considering wind speed ranges between 3 and 8 m/s. In this figure, only the median values are shown. The results obtained are in line with the conclusion already introduced for Figure 7.28. It is interesting to note that, for example, the highest values obtained with the wind speed range 4 – 5 m/s are similar to the values obtained for the 7 - 8 m/s in the 300º - 360º region. From this analysis, it seems that the foundation is less stiff along the directions that are more excited by the wind. However, it should be noticed that this analysis should have taken into account the turbulence of the wind flow, which also influences the dynamic excitation of the support structure. Since this information is not provided by the SCADA system, it is not possible to confirm the presented considerations.

It is also interesting to assess the evolution of RMS values of acceleration with the rotor speed (Figure 7.30). As expected, the vibration levels tend to increase with the increase of the rotor speed.

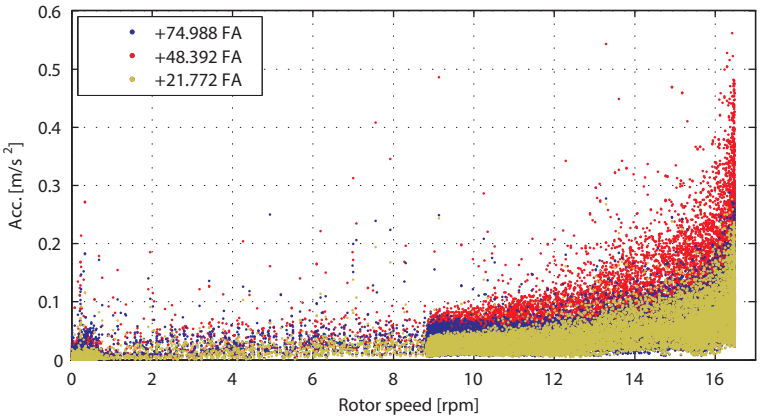

Figure 7.30 – RMS values of acceleration vs the rotor speed

The colour map presented in Figure 7.31 illustrates the frequency content of the acceleration signals during a period of one month. This figure is a top view of the first singular value spectra of the spectrum matrices obtained from each recorded setup. The regions with the hotter colours represent the highest energy. Two vertical alignments with high energy are clearly visible around 0.35 Hz and 2.80 Hz (indicated by arrows). These frequency values are coherent with the results obtained for the first and second pairs of tower bending modes of the numerical models described in section 7.3.2. Albeit with less energy, two additional alignments are also visible around 1.30 Hz and 1.80 Hz (also indicated by arrows).

In the same figure, the rotor speed frequencies from the 1Ω, 3Ω and 6Ω harmonics are represented by dashed lines. As expected, the excitation introduced by the rotor rotation is visible, mainly for the 3Ω harmonic. In a small scale, the 6Ω harmonic is also detected and seems to cross the 1.30 Hz alignment several times. The 1Ω harmonic alignment is very tenuous and is only visible in a few setups.

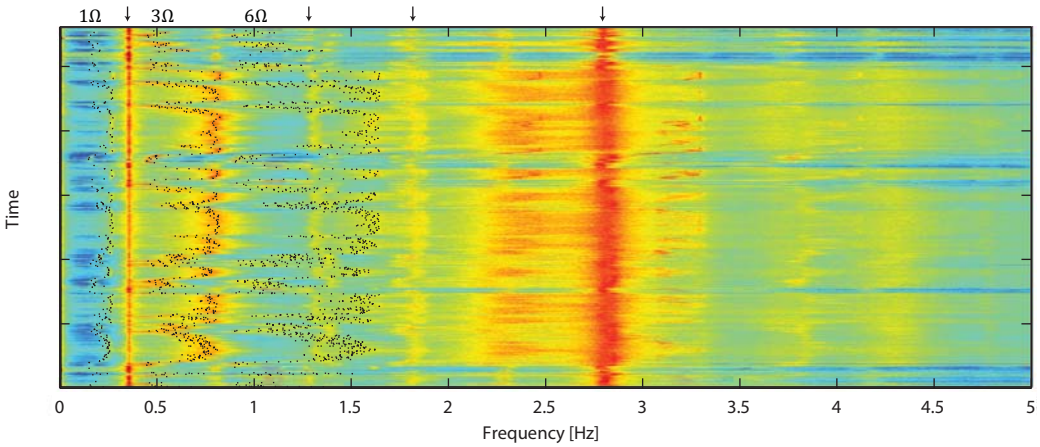

Figure 7.31 – Colour map with the variation of the signals frequency content during the 15/02/2014 and 15/03/2014

7.3.6 CONTINUOUS CHARACTERIZATION OF THE DYNAMIC PROPERTIES

The design of a dynamic monitoring system requires the previous knowledge of the wind turbine modal properties. In that sense, the results obtained with an ambient vibration test (Oliveira, Magalhães et al., 2013) and with the analysis of initial recorded data were used to characterize the dynamic properties of the wind turbine. This initial characterization was used to tune the dynamic monitoring system to detect possible damage situations.

7.3.6.1 Dynamic Characterization of the Wind turbine

As presented in section 7.3.3, wind turbines are time-varying structures subjected to different operating conditions. As example, Figure 7.32 presents the averaged normalized power spectrum density of two different setups, one referring to a non-operating situation and another referred to an operating condition. The shape of the spectra are considerable distinct. The most distinguished feature is the appearance of peaks at the harmonics frequencies in the operating setup. These peaks are due to the external excitation caused by the tower shadow effect. From the figure, it is also visible a small peak around 1Ω. As expected, this peak is considerable smaller than the ones associated with other harmonics.

Besides the harmonic peaks, other interesting characteristics are also evident. The two peaks around 1.10 Hz and the peak at 2.30 Hz, clearly identified under non-operating conditions, are practically not visible in the operating setup. Furthermore, the peaks from the non-operating conditions spectrum at 1.30 and 1.80 Hz seem to move to slightly higher frequency values.

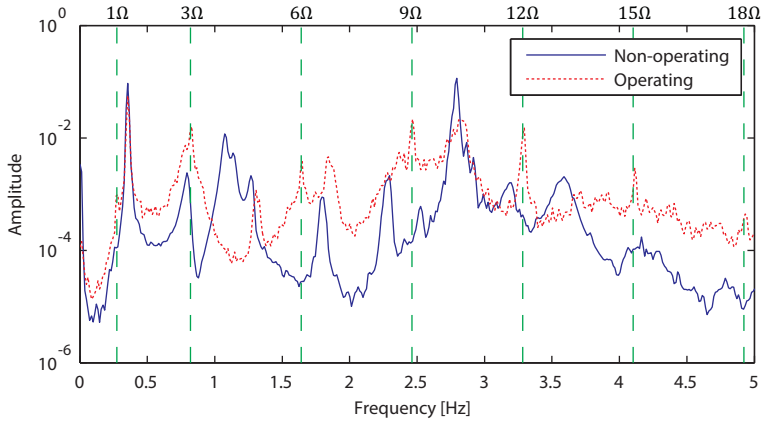

Figure 7.32 – ANPSD of two different setups: under non-operating conditions (rotor speed = 0 rpm; wind speed = 1.9 m/s) and operating conditions (rotor speed = 16.4 rpm; wind speed = 10.7 m/s). The vertical dashed lines indicate the frequency values of the rotor speed and its harmonics

It is thus important to perform a preliminary analysis of the properties of the most relevant vibration modes and their variation throughout the various operating conditions. In that sense, the recorded setups were initially processed with the modal identification algorithms introduced in section 5.4. Then, an automatic interpretation of the produced stabilization diagrams was performed by the algorithm based on the hierarchical clustering presented in section 5.7.1. The same datasets used to plot the ANPSD in Figure 7.32 are used to illustrate this preliminary analysis. The methodology is similar to the one described in section 5.9 for the case study related to the Vestas V90.

Figure 7.33 shows the stabilization diagrams associated with the selected datasets provided by the SSI - COV algorithm, including an averaged spectrum at the background. As expected, the spectrum and the stabilization diagram associated with the parked condition are clearer. Still, in the other stabilization diagram several vertical alignments of stable poles can be easily identified.

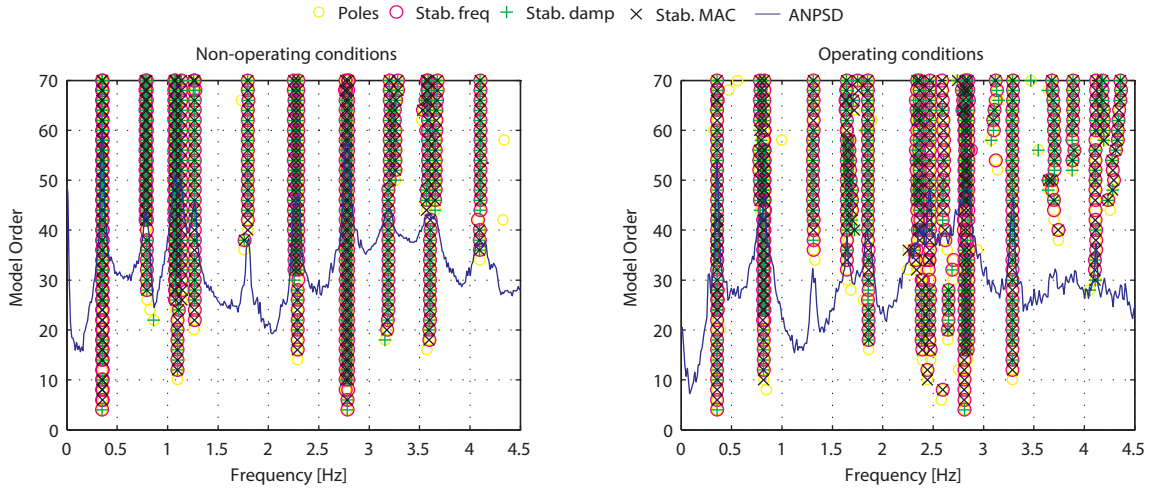

Figure 7.33 – Stabilization diagrams obtained with the SSI-COV algorithm for operating and non-operating conditions

The automatic processing of the stabilization diagrams generated by the identification algorithms (the three tested methods produce similar stabilization diagrams) is then obtained with the cluster algorithm. Figure 7.34 characterizes the obtained clusters by the average frequency of the poles included in each cluster and by the number of poles. At this preliminary stage, it was decided to exclude just the clusters with a very low number of poles (less than 6, as marked by the red dashed line).

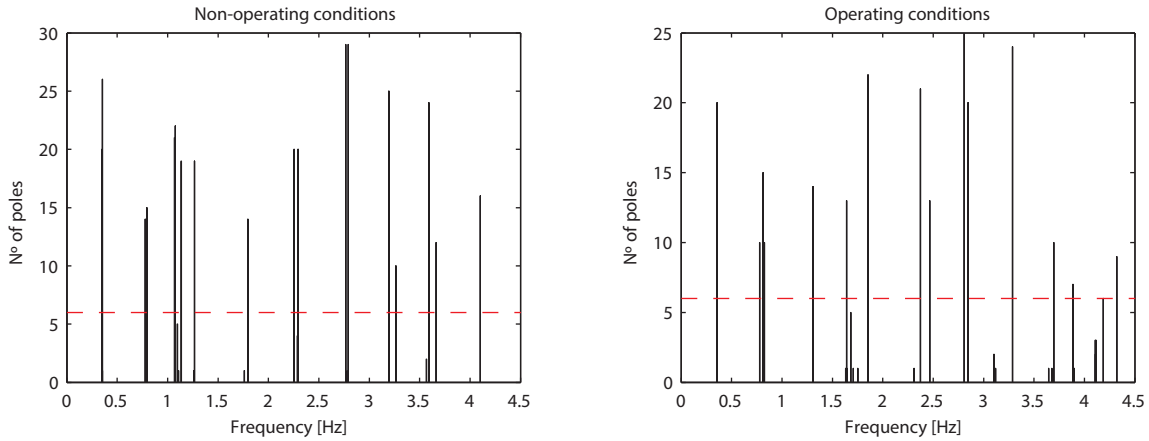

Figure 7.34 – Characterization of the clusters: average frequency and number of poles included in each cluster

For each considered cluster, a representative value of frequency, damping and mode shape was retained. Each cluster was then classified as FA or SS, according to the direction of its representative mode shape. After this preliminary analysis, it is possible to plot all the considered clusters in a Campbell diagram, considering the main direction of vibration (Figure 7.35). In this figure, several

alignments of clusters are clearly identified, corresponding to vibration modes. However, it also shows some clusters located around the diagonal dashed lines (corresponding to the harmonics associated with the rotor rotation). These clusters, are only present when the turbine is in operation (rotor speed higher than 8.7 rpm), corresponding to poles motivated by the harmonic excitation.

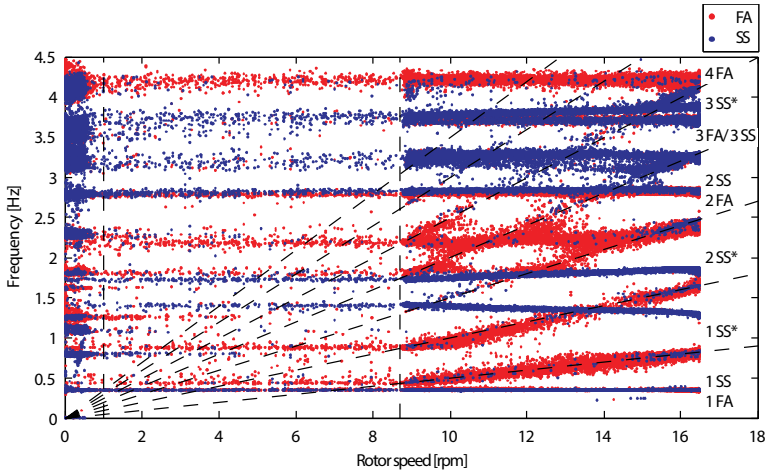

Figure 7.35 – Campbell diagram of considered clusters of stable poles. The vertical dashed lines separate the non-production situation, a transition state and the operating regimes of the wind turbine. The diagonal dashed lines represent the harmonic frequencies associated with the rotor rotation (multiples of 3Ω)

From this figure, some initial considerations should be highlighted. The two well defined vertical alignments around 0.35 Hz and 2.80 Hz in Figure 7.31 are clearly visible in the Campbell diagram along the whole rotor speed regimes. In fact, they both correspond to two pairs of closely spaced vibration modes in the FA and SS directions, as initially indicated by the numerical models. For the pair of cluster around 2.80 Hz it is interesting to note that for high values of rotor speed (higher than 15 rpm), the number of SS clusters of this pair tend to decrease. On the other hand, FA poles appear in the same alignment of the SS poles. This phenomenon is clearly visible in Figure 7.36, where the clusters are compared with the wind speed. Apparently, after a certain point of operation (Figure 7.37), the mode vibrating in the SS direction tends to change its main direction of vibration to FA (although not perfectly aligned to the FA direction as its FA clusters pair). Looking at Figures 7.13 and 7.14, it can be attested that this point of operation coincides with the start of the blades pitch actuation.

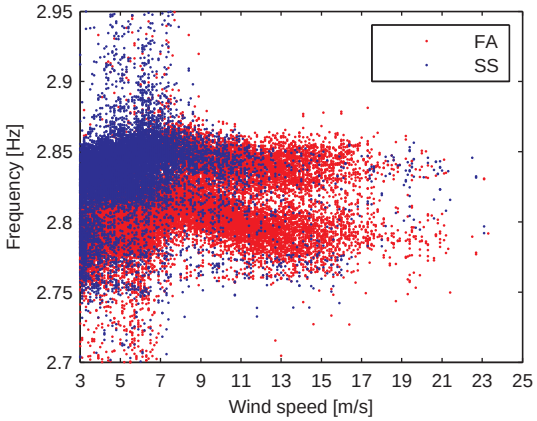

Figure 7.36 – Zoom of the clusters around 2.70 Hz and 2.95 Hz vs. wind speed

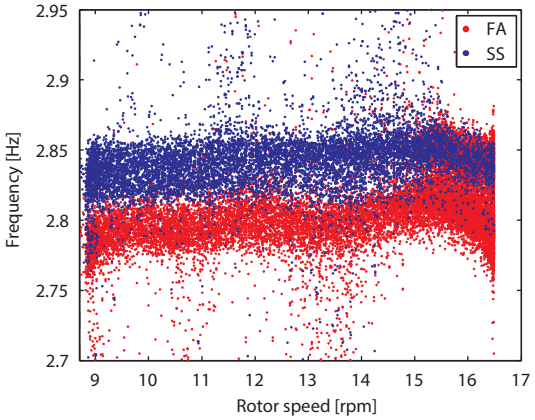

Figure 7.37 – Zoom of Campbell diagram around 2.70 Hz and 2.95 Hz

In addition, the other two referred alignments (1.30 Hz and 1.80 Hz) are also distinguished as SS clusters in all operating conditions. It is interesting to note that the frequency value of these two modes seems to decrease and increase, respectively, with the increase of the rotor speed (Figure 7.38). As referred in section 4.1.2, this is an expected behaviour of rotor whirling modes when considering a fixed reference (as is the case of the implemented monitoring system with sensors at the tower). Nonetheless, this figure also evidences that, with the start of the blades pitch actuation, both modes tend to decrease their natural frequency, changing their behaviour. It is also interesting to note that these two modes do not seem to be affected by the rotor harmonics, even when their frequency value is close (or coincident) with the one from the harmonic.

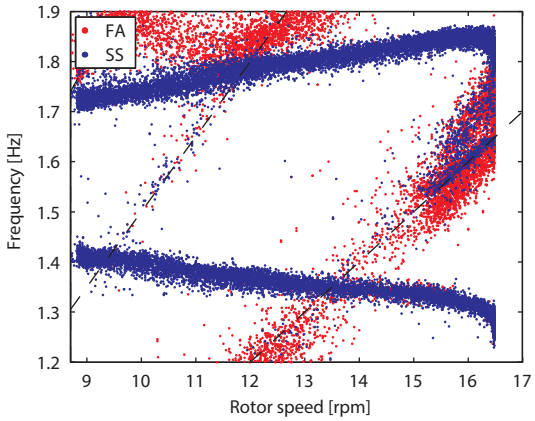

Figure 7.38 – Zoom of Campbell diagram around 1.20 Hz and 1.90 Hz

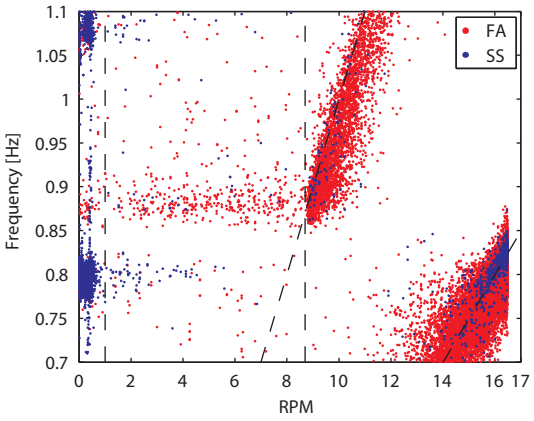

Figure 7.39 – Zoom of Campbell diagram around 0.70 Hz and 1.10 Hz

The alignment of clusters around 3.70 Hz is composed by FA and SS clusters (although it is not clearly visible in Figure 7.35). A detailed analysis of this alignment shows that it is referred to only one mode, since the FA and SS cluster do not appear at the same time. This phenomenon is analysed in more detail in the next section.

The analysis of Figure 7.35 is also important to assess the influence of the rotor excitation on the detection of the vibration modes throughout the operating regimes. It is observed that some stable

horizontal alignments of cluster are only visible until the start of the turbine operation. The alignment of FA clusters around 0.80 Hz is an example of this phenomenon (Figure 7.39). This alignment may be related to vibration modes whose influence on the tower motion is too low to be noticed when the rotor starts spinning. Another example of the harmonic effect is illustrated with the horizontal alignment of FA clusters around 2.30 Hz. From the rotor speed of 8.7 rpm, it is noticed that this alignment tend to fluctuate according to the harmonics that cross it.

Considering this initial analysis, 9 modes were decided to be followed in the scope of the dynamic monitoring system. This decision was made based on the importance of the mode to the wind turbine motion and on influence of the harmonics over the mode.

A nomenclature is also given for the monitored modes. It is referred to the number of the order of the mode and to the main direction of vibration. In addition, when the evolution of the identified frequency value of a mode is clearly dependent on the rotor speed, an "*" is added to the name since it may be referred to a rotor mode. The vibration mode with frequency value around 3.70 Hz is labelled as 3 FA/ 3 SS, since, as referred, it seems to vibrate either way.

Considering the results obtained with this preliminary analysis, 6 operating regimes were adopted to define the reference properties of the monitored vibration modes. For each regime, reference values of frequency value and mode shape of the 9 considered modes were kept. These regimes are characterized in Table 7.4.

Table 7.4 – Regimes considered for reference modal properties of the vibration modes

Operating regime	Wind turbine condition
1	Parked or idling (with high pitch angle values higher than 72º)
2	Parked or idling (with pitch angle value lower than 72º)
3	Transition regime from non-operation to operation (rotor speed between 0 and 8.7 rpm)
4	Operating regime, defined by the lowest operating rotor speed and the point where the pitch angle starts to increase to avoid excessive rotor torque values (around mean wind speed of 10 m/s)
5	Operating regime, between regime 4 and the highest operating rotor speed
6	Wind speed higher than cut-out speed

Regime 1 is referred to setups when the pitch angle of the blades is at its maximum level. As introduced in Figure 7.14, under certain non-operating conditions, the pitch angle of the blades is set to values around 90º. Regime 2 is also referred to non-operating situations, but the pitch angle is defined to values of around 70º.

The region defined as a transition state in Figure 7.35, related to setups where the turbine starts operating, is named as Regime 3. Since the SCADA system records 10 min. mean values, the rotor speed values of this regime are between 0 and the lowest operating rotor speed (8.7 rpm).

Regime 4 is regarded to setups in which the rotor speed is higher than 8.7 rpm and the pitch angle is kept at its lower level, i.e., before the pitch actuator is actively varying the angle of attack of the blades.

Once the pitch angle starts increasing in order to avoid excessive rotor speed values, it is considered as Regime 5. This Regime extends to the limit operating conditions of the turbine.

Lastly, Regime 6 is referred to situations when the wind speed is higher than the turbine cut-out wind speed. However, this regime was not identified during the monitoring period.

With the aim of illustrating the 9 considered vibration modes, the reference mode shapes from Regime 4 are presented Figure 7.40. At the bottom of each mode shape, a polar plot shows the magnitude and phase angle of the modal amplitude of the sensors orientated to the main direction of vibration. It can be seen that some are not perfect real modes, since some amplitudes present phase angles slightly different from 0º or 180º.

From the illustrations of Figure 7.40, it is possible to conclude that the two pairs of closely-spaced modes around 0.35 Hz (modes 1 SS and 1 FA) and 2.80 Hz (2 FA and 2 SS) are, respectively, the first and second pairs of tower bending modes, which is in accordance with the results of the numerical models described in section 7.3.2 (Oliveira, Magalhães et al., 2013).

The remaining modes are certainly related to motion from other structural elements besides the tower, such as the rotor blades. This fact is in line with the behaviour observed in the Campbell diagram for the modes 1 SS*, 2 SS* and 3 SS*.

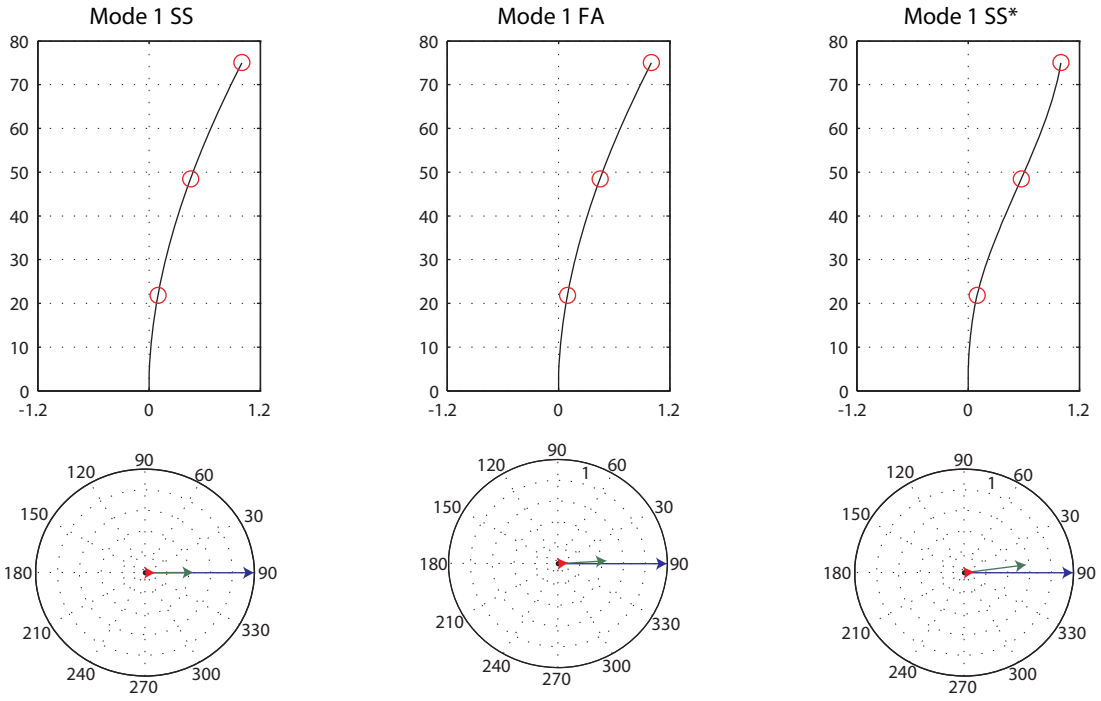

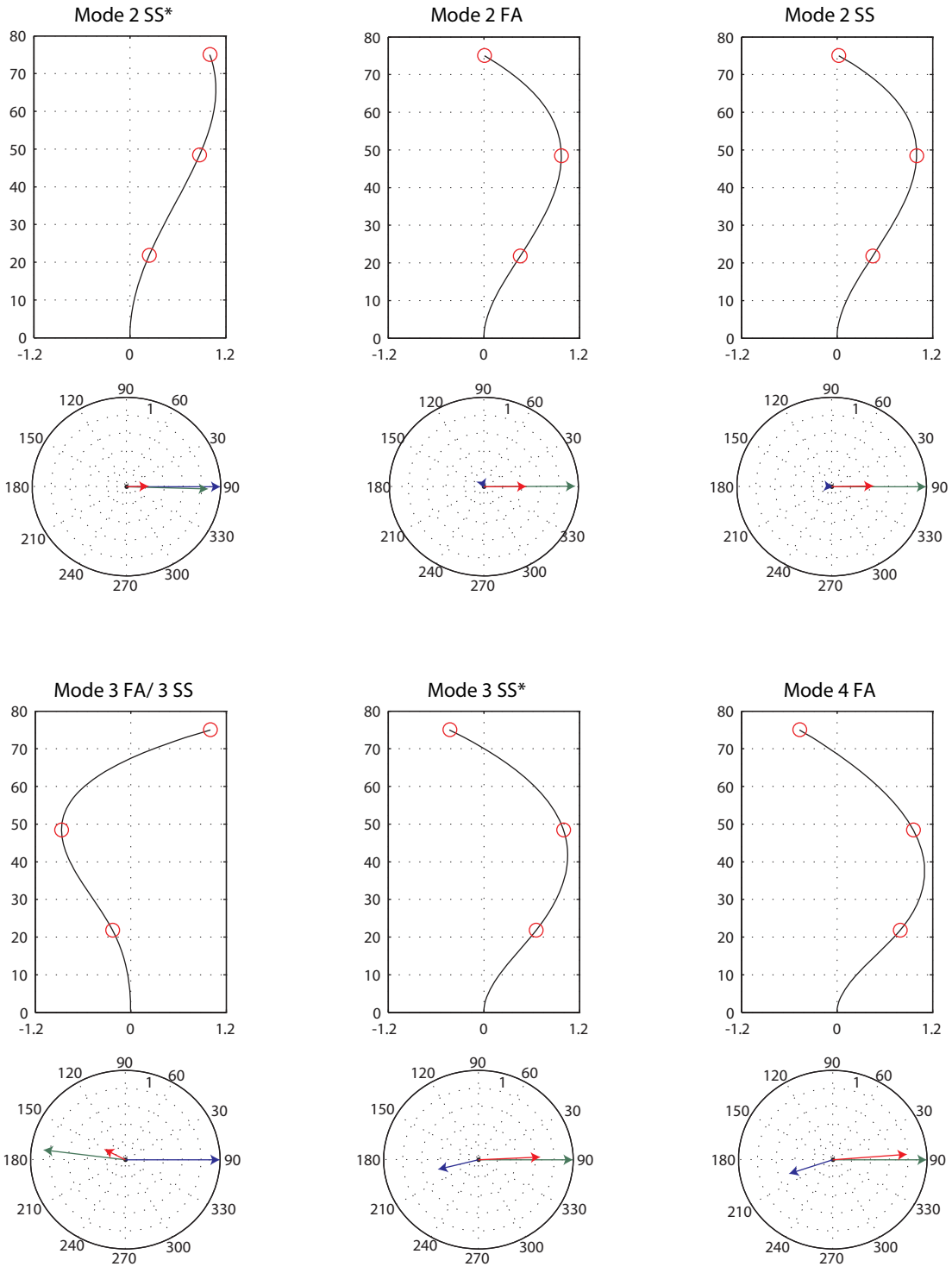

Figure 7.40 – Tower mode shapes of the tracked vibration modes

7.3.6.2 Automated Identification of the Modal Parameters

Three output-only modal identification algorithms were used to perform an automated analysis of the modal parameters of the wind turbine: SSI-COV, SSI-DATA and p-LSCF. Once the reference modal properties of the vibration modes intended to be tracked were defined, it was possible to perform the identification in a completely automated way.

The strategy introduced in previous sections was followed. For each identification algorithm, a pole is classified as stable in a stabilization diagram if it respects the limits presented in Table 7.5 for variations between models of consecutive orders. Once the stable poles are identified, the hierarchical cluster algorithm is applied. For this process, a maximum distance of 0.02 was defined for a single linkage criterion.

Table 7.5 – Stable pole criteria for models of consecutive orders

Modal parameter	Maximum allowed variation
Frequency	$\Delta f \leq 1\ \%$
Damping	$\Delta \xi \leq 5\ \%$
Mode Shape	$\mathrm{MAC} \geq 0.97$

From the obtained clusters, only the ones with a number of poles higher than 6 were considered. Then, for each reference mode, the clusters presenting an average natural frequency that did not differ more than a predefined percentage value (10 % to 20 % depending on the mode type) from the reference natural frequency value were selected. From those, it is selected the one that presents the average mode shape with the highest correlation with the reference mode shape (evaluated with the MAC coefficient). Modes with MACs lower than 0.80 are not considered.

The stated parameters were tried on several initial datasets and proved to deliver good and coherent results. Figure 7.41 shows the Campbell diagram after the tracking (comparison of the cluster properties with the reference properties of the vibration modes intended to be monitored). It can be seen that, in this particular application, this simple tracking procedure was adequate to eliminate the influence of the harmonics in the modes under analysis. For that reason, it was not necessary to use the methods presented in section 5.6.3.

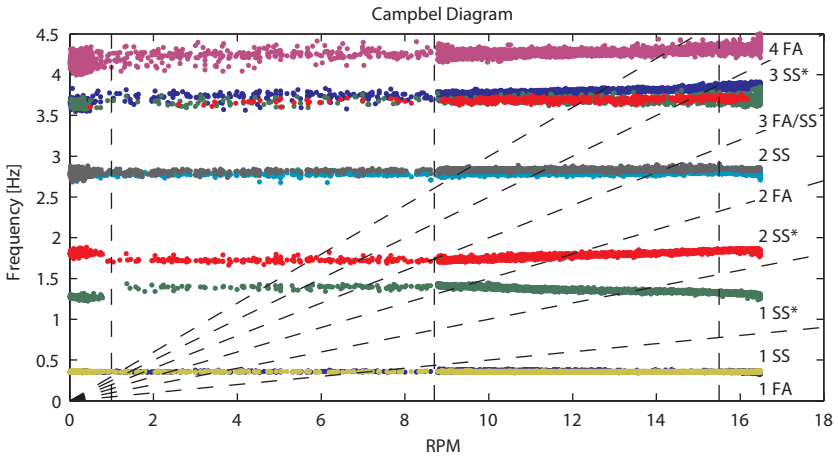

Figure 7.41 – Campbell diagram with the tracked vibration modes (p-LSCF algorithm)

Naturally, it was also necessary to define the input parameters for each modal identification algorithm. Initial datasets were used to tune these parameters.

The SSI-COV algorithm requires two input parameters: the i number of points of the correlation function and the maximum order of the model. It was decided to adopt correlation functions of 128 points and a maximum order of 70.

Table 7.6 presents the main statistics related to the performance of this algorithm in the automated identification of the 9 considered vibration modes. A success rate above 60 % is consistently obtained, except for the 3 FA/3 SS, 3 SS* and 4 FA modes. Also, the 1 FA mode shows a considerably lower success rate than its pair. This fact is probably due to the high values of damping of this mode which hinders the identification of this mode by the algorithms. For the 3 FA/3 SS mode, the low success rate is explained by the fact that this mode presents an unusual behaviour, which tends to change its main direction of vibration according to the nacelle orientation. Thus, since a minimum MAC value for the modal tracking was defined, only a small portion of the clusters identified in the frequency range of this mode were considered. On the other hand, the low value obtained for the identification of the 3 SS* and 4 FA modes are mainly related to non-operating conditions (Regimes 1 and 2) and to the Regime 5. In these three regimes, the success rate was considerably low.

From the analysis of Table 7.6, it is interesting to check that within the first pair of tower bending modes, the 1 SS mode presents a much smaller dispersion of its natural frequency than the 1 FA mode. Again, the high values of damping of the 1 FA mode may have influenced the quality of the detection of this mode.

Table 7.6 – Statistics related to the results obtained with the SSI-COV algorithm

Mode	Success Rate [%]	f_{mean} [Hz]	f_{std} [Hz]	$f_{coef.\ var.}$
1 SS	81.2	0.354	0.002	0.005
1 FA	67.4	0.355	0.007	0.020
1 SS*	63.4	1.325	0.051	0.039
2 SS*	78.3	1.791	0.060	0.034
2 FA	75.8	2.792	0.024	0.009
2 SS	83.7	2.828	0.030	0.011
3 FA/ 3SS	9.1	3.673	0.042	0.011
3 SS*	29.5	3.782	0.043	0.011
4 FA	38.3	4.236	0.072	0.017

The second time domain identification algorithm used was the SSI-DATA. For this algorithm, two parameters were defined: the number of i blocks of the Hankel matrix and the maximum order of the model. After initial tuning, it was concluded that i = 70 blocks, together with a maximum model order of 70 led to the best results.

The main statistics about the automated modal identification with the SSI-DATA are introduced in Table 7.7. The results are in line with the ones obtained with the SSI-COV. On the identification of the 4 FA mode, a considerably increase was obtained.

Table 7.7 – Statistics related to the results obtained with the SSI-Data algorithm

Mode	Success Rate [%]	f_{mean} [Hz]	f_{std} [Hz]	$f_{coef.\ var.}$
1 SS	84.7	0.355	0.002	0.006
1 FA	67.4	0.358	0.008	0.022
1 SS*	84.9	1.330	0.050	0.038
2 SS*	89.8	1.793	0.057	0.032
2 FA	74.0	2.789	0.024	0.009
2 SS	60.2	2.829	0.030	0.011
3 FA/ 3SS	14.9	3.690	0.039	0.011
3 SS*	44.9	3.789	0.047	0.012
4 FA	82.3	4.266	0.079	0.019

The last identification algorithm used in the dynamic monitoring system was the p-LSCF. Positive time lags of the correlation with 1024 points were used to calculate the spectra. An exponential window with a factor of 0.1 was also used. A maximum model order of 40 was considered. The obtained results show that this algorithm provided much higher success rates for the modes not so successfully identified with the other two algorithms.

Table 7.8 – Statistics related to the results obtained with the p-LSCF algorithm

Mode	Success Rate [%]	f_{mean} [Hz]	f_{std} [Hz]	$f_{coef.\ var.}$
1 SS	80.8	0.354	0.002	0.006
1 FA	64.7	0.354	0.007	0.019
1 SS*	87.4	1.330	0.049	0.037
2 SS*	85.5	1.793	0.058	0.032
2 FA	80.1	2.796	0.017	0.006
2 SS	85.5	2.831	0.026	0.009
3 FA/ 3SS	43.2	3.700	0.030	0.008
3 SS*	67.8	3.809	0.058	0.015
4 FA	95.1	4.276	0.081	0.019

Once the modal parameters are identified, it is possible to analyse the variation of the parameters with the operational and environmental factors. Figure 7.42 characterizes the evolution of the natural frequencies of the 9 monitored vibration modes along the monitoring period. The variability of the frequency values is evident.

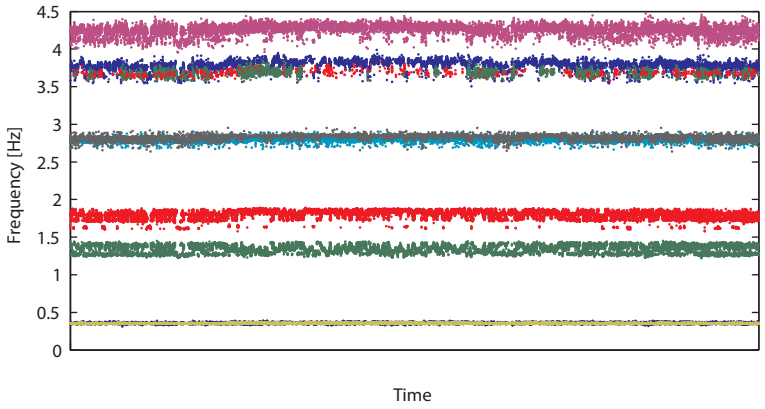

Figure 7.42 – Variation of the of the monitored natural frequencies

Figure 7.43 a) shows a zoom of the frequency variation of 1 FA and 1 SS vibration modes along the recorded setups. It is visible that the variability of the 1 FA mode is much higher than of the 1 SS, which is in agreement with the results presented in Tables 7.6 to 7.8. Figure 7.43 b) evidences the variation of the natural frequencies of the 1 SS* and 2 SS* modes, mainly due to their dependence on the rotor speed.

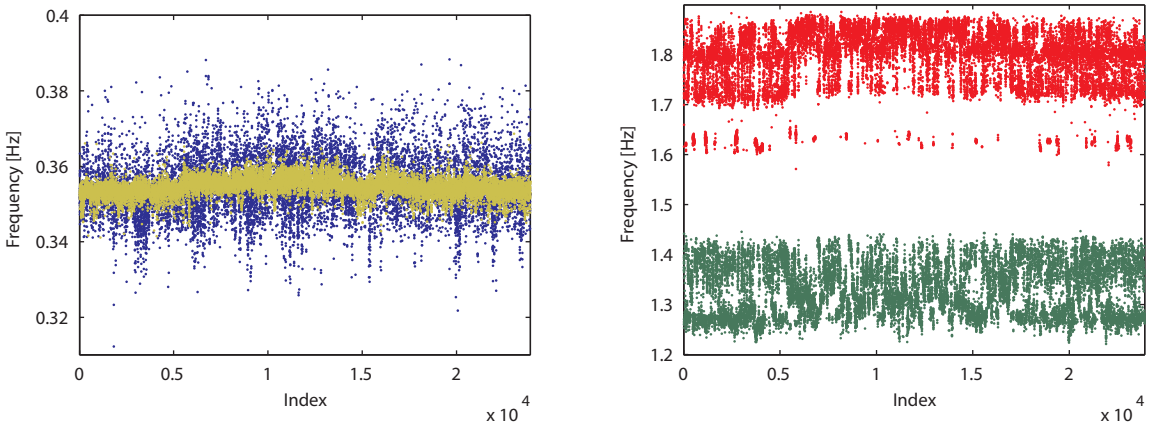

Figure 7.43 – Zoom of the natural frequencies along the recorded setups: a) 1 FA and 1 SS; b) 1 SS* and 2 SS*

In order to better understand the behaviour of the modal parameters of the 9 tracked modes, Figure 7.44 shows the variation of the natural frequencies for each operating regime. This graphic evidences the suitability of defining different Regimes for modal tracking. For example, the variation of the frequency values of the modes 1 SS* and 2 SS* is notorious. Apart from these modes, also the 2nd pair of tower bending modes shows a different behaviour when the turbine starts operating, with a better separation of the two modes.

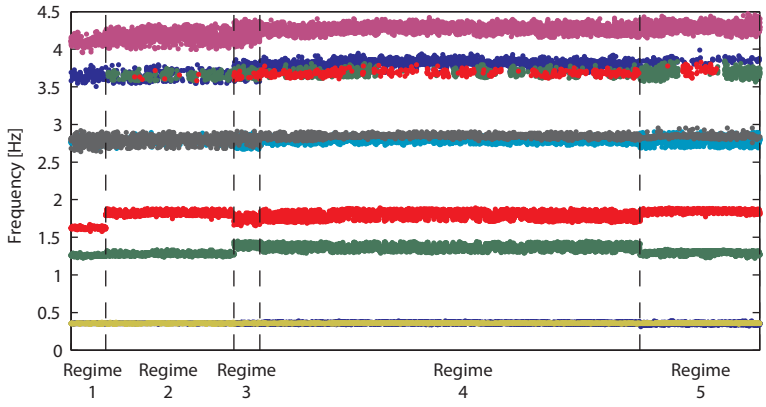

Figure 7.44 – Variation of the natural frequency, for each operating regime, of the monitored vibration modes

Figure 7.45 a) presents a closer look of the first pair of tower bending modes. It is interesting to note that the variability of the 1 FA mode is smaller than the 1 SS mode for non-operating conditions. Once the turbine starts operating, the dispersion of the frequency values from this mode greatly increases. On the other hand, the variability of the 1 SS mode is kept almost constant throughout the different operating regimes. These facts reinforce the idea that the high values of damping of the 1 FA mode, during operating conditions, may have influenced the accuracy of the detection of this mode. Figure 7.45 b) evidences the better separation of the 2nd pair of tower bending modes under operating conditions.

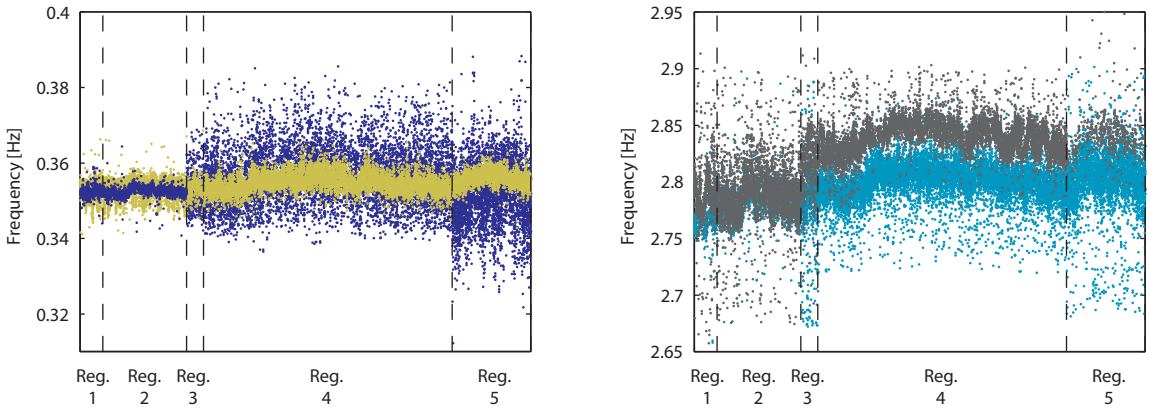

a) b)

Figure 7.45 – Variation of the natural frequency, for each operating regime, of: a) 1 FA and 1 SS; 2 FA and 2 SS

The results obtained with the identification of the natural frequencies and damping ratios of 9 monitored vibration modes with the p-LSCF algorithm are shown in Tables 7.9 and 7.10 for each regime.

Table 7.9 – Results obtained for each operating regime: natural frequencies

Mode	1		2		3		4		5	
	f_{mean} [Hz]	f_{std} [Hz]	f_{mean} [Hz]	f_{std} [Hz]	f_{mean} [Hz]	f_{std} [Hz]	f_{mean} [Hz]	f_{std} [Hz]	f_{mean} [Hz]	f_{std} [Hz]
1 SS	0.353	0.003	0.353	0.003	0.354	0.002	0.355	0.001	0.355	0.002
1 FA	0.352	0.001	0.352	0.001	0.355	0.004	0.357	0.006	0.349	0.006
1 SS*	1.258	0.011	1.277	0.011	1.400	0.020	1.362	0.033	1.294	0.018
2 SS*	1.625	0.011	1.812	0.017	1.729	0.025	1.793	0.045	1.844	0.013
2 FA	2.767	0.012	2.784	0.013	2.781	0.022	2.799	0.015	2.796	0.014
2 SS	2.792	0.020	2.790	0.021	2.819	0.022	2.842	0.016	2.841	0.012
3 FA/ 3SS	-	-	3.659	0.042	3.664	0.038	3.702	0.028	3.702	0.026
3 SS*	3.668	0.050	3.683	0.055	3.748	0.053	3.812	0.036	3.870	0.018
4 FA	4.107	0.033	4.167	0.046	4.253	0.068	4.301	0.040	4.349	0.048

Table 7.10 – Results obtained for each operating regime: damping ratios

Mode	1		2		3		4		5	
	ξ_{mean} [%]	ξ_{std} [Hz]	ξ_{mean} [%]	ξ_{std} [Hz]	ξ_{mean} [%]	ξ_{std} [Hz]	ξ_{mean} [%]	ξ_{std} [Hz]	ξ_{mean} [%]	ξ_{std} [Hz]
1 SS	0.974	0.631	0.733	0.438	0.707	0.590	0.630	0.394	1.096	0.548
1 FA	0.351	0.482	0.213	0.356	1.490	1.128	3.659	1.390	7.868	2.169
1 SS*	0.502	0.207	0.646	0.316	0.845	0.232	0.932	0.236	0.860	0.152
2 SS*	0.543	0.261	0.746	0.297	0.746	0.271	0.916	0.247	1.113	0.211
2 FA	0.175	0.100	0.195	0.120	0.624	0.231	0.884	0.320	1.291	0.284
2 SS	0.301	0.127	0.254	0.167	0.344	0.162	0.451	0.225	0.662	0.181
3 FA/ 3SS	-	-	0.778	0.275	1.013	0.350	1.395	0.427	1.820	0.407
3 SS*	0.572	0.230	0.551	0.228	0.660	0.224	0.719	0.149	0.888	0.232
4 FA	0.476	0.170	0.457	0.178	1.079	0.433	1.598	0.374	1.566	0.467

The evolution of the 1 SS* and 2 SS* modes with the rotor speed is illustrated in Figure 7.46. This figure resembles the typical behaviour the of rotor whirling modes. It is visible that, when the turbine is consistently rotating (for rotor speed higher than 8.7 rpm), the 1 SS* and 2 SS* modes have a similar behaviour with, respectively, a backward and a forward whirling mode. Considering that, when in operation, these modes are detected by tower motion in the SS direction, i. e., in the direction of the rotor plane, these two modes are most likely related to edgewise vibration modes. From the three configurations of first order edgewise modes shown in Figure 4.4, only asymmetrical modes create a reaction force at the rotor and, thus, are capable of inducing a detectable tower motion. For these reasons, it expected that 1 SS* and 2 SS* modes are in fact the first backward and forward edgewise modes, respectively.

A regression model for each vibration mode is also presented in Figure 7.46 in dashed lines. These regression models were adjusted to the frequency values obtained for the two modes during events regarding Regime 4. Regime 5 was not considered for the definition of the models because this regime implies the variation of the blades pitch angle which introduces changes in the behaviour. The intercept of the regression models with the origin (rpm=0) gives an approximation of the frequency values of these two modes under parked conditions and with a pitch angle around 0º. Values of 1.526 Hz and 1.558 Hz were obtained for, respectively, the backward and forward mode. However, this configuration does not occur in the monitored wind turbine. When under parked conditions, the blades are usually oriented with a pitch angle between 72º and 90º, changing the direction of vibration of the edgewise modes from in-plane rotor motion (when in operation) to out-of-plane (when in non-operation conditions). Consequently, the support conditions of the blades are also changed with this transition. Due to these reasons, modes vibrating at the referred frequencies were not detected. It was then investigated if, during events from Regime 1 and 2, there were modes with natural frequencies next to these frequencies and with a tower mode shape similar to the ones from the 1 SS* and 2 SS* modes but vibrating in the FA direction (as referred, during non-operating conditions, the edgewise modes vibrate out of the plane rotor). The cluster referred to the found vibration modes during Regime 1 and 2 are shown in Figure 7.46 in lighter colours. It is seen that, while for the 1 SS* mode, the identified modes have natural frequencies close to each other during Regime 1 and 2 ($f \approx 1.26$ Hz), the same does not happen for the 2 SS* ($f = 1.63$ Hz and $f = 1.81$ Hz for, respectively, Regime 1 and 2). In

fact, the identified clusters for the 2 SS* mode present a considerably change in the natural frequency between Regime 1 and 2. Unfortunately, this situation could only be deeper investigated if instrumentation at the blades would be available. Even though, the referred clusters for Regime 1 and 2 were considered for monitoring purposes.

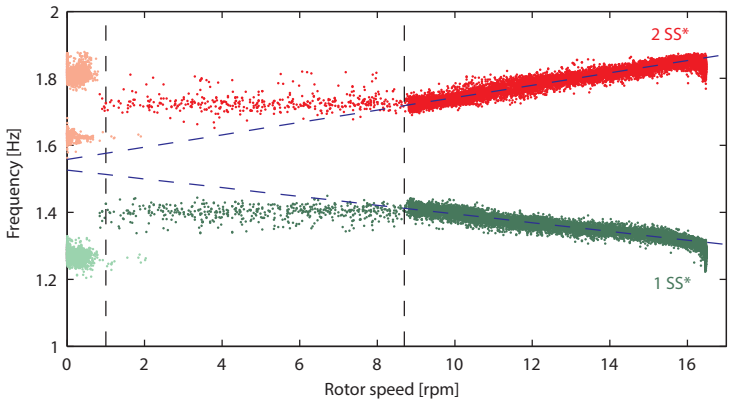

Figure 7.46 – Evolution of the frequency values of the 1 SS* and 2 SS* with the rotor speed

Likewise, although on a smaller scale, the natural frequencies of the second pair of tower bending modes (2 FA and 2 SS) also shows an increasing trend with the operating regimes. On the other hand, the 1 FA and 2 SS modes do not have a very distinct trend over the regimes, as shown in Figure 7.47

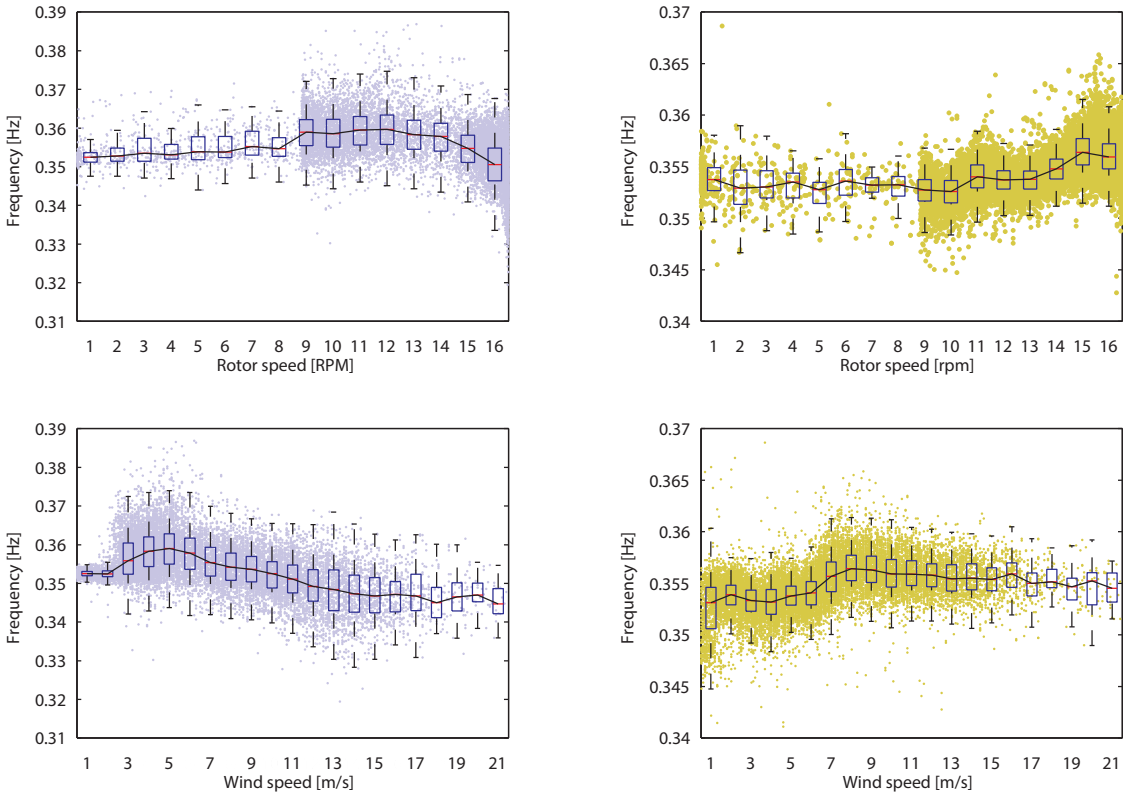

a) b)

Figure 7.47 – Median (and box plots) of the frequency values: a) 1 FA mode; b) 1 SS mode

Globally, the damping ratio of the FA modes increases with the increase of the wind speed (which usually implies a higher rotor speed). This is mostly due to the contribution of the aerodynamic component of damping. As expected, this increase of the damping values is not notorious in the SS modes due to the lower opposition to the wind flow in this direction. It is however noticed that the damping of SS modes increases in Regime 5. This is probably due to the aerodynamic change introduced by the increase of the blades pitch angle.

The analysis of the evolution of the damping of the two pairs of bending modes illustrates the complex dynamics of a wind turbine. For non-operating conditions (Regimes 1 and 2), the damping values of the SS modes are higher than for the FA modes. This situation is due to the deviation of the rotor from the main wind direction and to the high pitch value of the blades. Under these conditions, the blades present a larger opposition to the wind flow in the SS direction, leading to the appearance of aerodynamic damping in this direction.

Once the turbine starts operating, the rotor is orientated to the main wind direction and the blades pitch angle is set to its minimum value. These conditions, together with the higher wind speed, lead to the increase of the aerodynamic damping in the FA modes and the almost vanishing of this contribution in the SS modes. Since the aerodynamic damping component increases with the increase of the wind speed, the damping values of the 1 FA and 2 FA modes are consistently growing over the operating regimes. This effect is more noticeable for modes with large modal amplitude at the tower top, where the wind force is higher. For this reason, the 1 FA mode presents higher values than the 2 FA (whose modal amplitude at the top is very small).

The top plots of Figure 7.48 illustrate the evolution of the damping ratio of the 1 FA and 1 SS vibration modes with the rotor speed. The increase of the damping values of the 1 FA mode when the turbine starts operating is evident. It is also noted that the damping increases when reaching the final part of the rotor speed range. Notwithstanding, these figures only shows the evolution of damping until the wind rated speed is achieved (around 13 m/s). For that reason, the lower graphic of Figure 7.48 presents the evolution of the damping of the 1 FA mode with the wind speed. The shape of the adjusted line clearly shows a drop in the damping value around 15 – 17 m/s. This situation is consequence of the increase of the pitch angle in Regime 5 which reduces the thrust force at the tower top and, consequently, reduces the rotor blades opposition to the wind flow in the FA direction.

On the other hand, the adjusted line for the damping values of the 1 SS mode only shows small variations over the different operating conditions, with a reduction when the turbine starts operating and an increasing when reaching its rated speed.

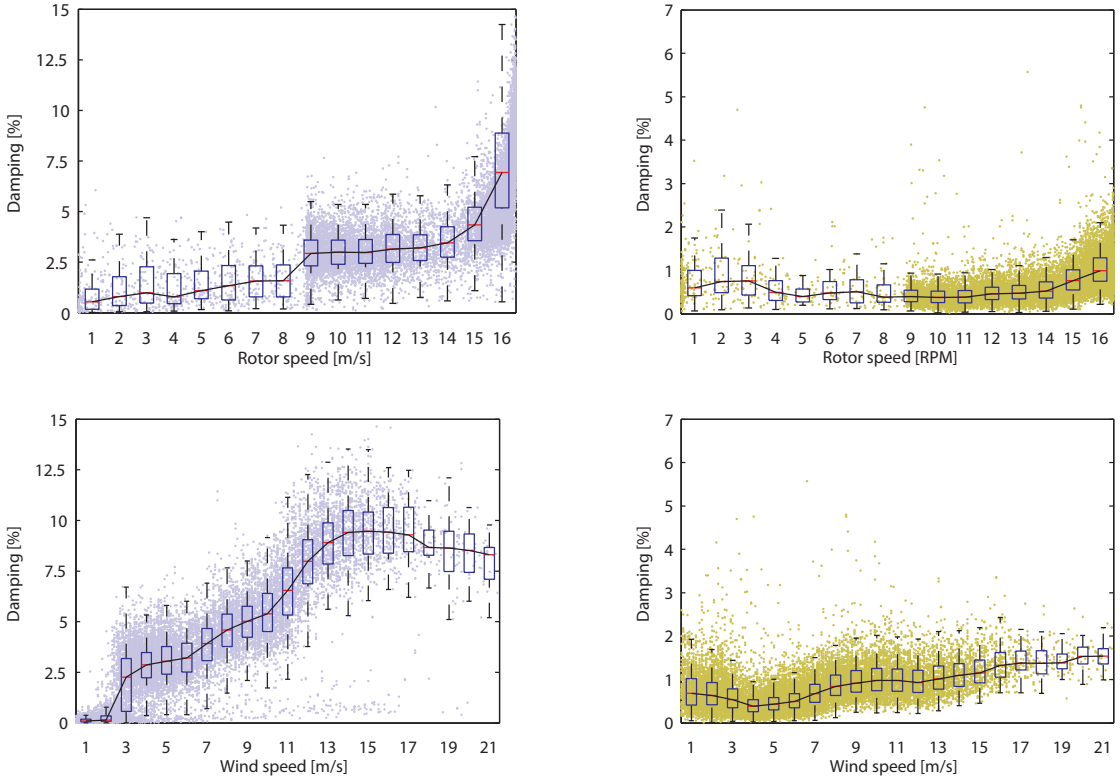

Figure 7.48 – Median (and box plots) of the damping ratios: a) 1 FA mode; b) 1 SS mode

The situation illustrated in Figures 7.36 and 7.37, about the possible change of mode shape orientation of the 2 SS mode for high wind speed conditions, was further investigated during the modal tracking. In that sense, an additional reference "mode" named 2 SS(/FA), based on the 2 SS mode but with an orientation between the FA and the SS direction, was considered. As results, it was possible to confirm that this "mode" was identified on setups in which the 2 SS was missing. Considering the number of setups in which the 2 SS(/FA) "mode" was tracked, the success rate of the 2 SS increases from 67.1 % to 85.5 % (with the p-LSCF algorithm).

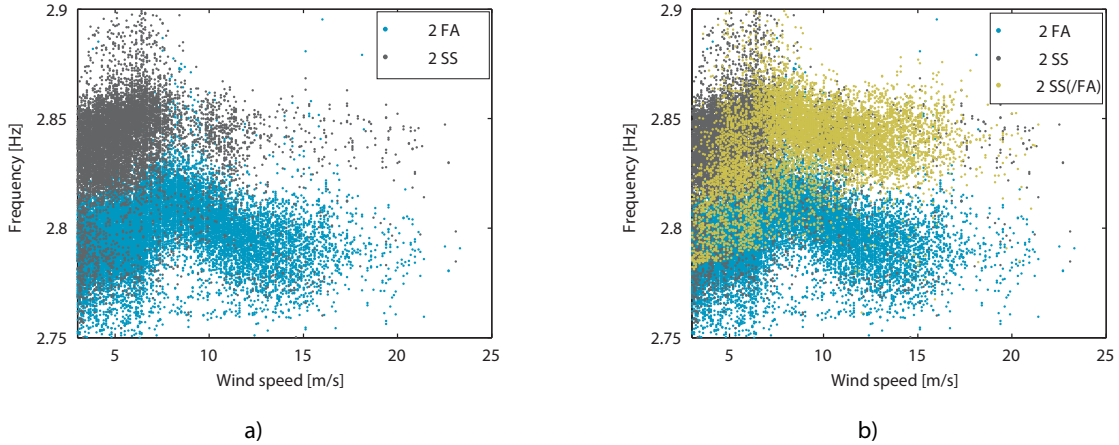

Figure 7.49 – a) Evolution of the 2 FA and 2 SS modes with the wind speed. b) Evolution of the 2 FA, 2 SS and the 2 SS/(FA)

7.3.6.3 Damping Estimation from Free Decay Responses

The previous section showed the evolution and characterization of the modal properties of the wind turbine main vibration modes under different operating conditions. One of the most important features obtained with this analysis is the characterization of the modal damping, mainly the damping of the first tower bending (1 FA) mode. This is a crucial property with strong influence on the fatigue lifetime of the support structure of a wind turbine.

During the monitored period, several recorded events related to shutdown situations were detected. These are events in which the wind turbine is initially operating and, at a certain point, the wind turbine cease power production, stopping the rotor. The reasons behind these events are usually associated to situations when there is a wind speed reduction to values below the cut-in or to very high wind speed (above the cut-out speed) and it is accomplished through the increase of the blades pitch angle to values close to 90º.

Under these circumstances, when the blades pitch angle is changed, an instantaneous impulse acts at the top of the tower, imposing a free decay response of the structure. This decay can then be used to accurately estimate the damping of the vibration modes. This methodology usually provides more accurate estimates of the damping than with the ambient vibration response [(Magalhães, Cunha et al., 2010)].

Taking advantage of the information provided by the SCADA system, the acceleration events with a maximum and minimum rotor speed values, respectively, above and below the minimum rotor speed were initially selected. From these, the ones regarded to start up events were dismissed. The remaining ones were then visually inspected to assess the quality of the free decay response. Only the acceleration time series containing a clean exponential decay shape of the acceleration response were kept. Figure 7.50 a) illustrates an example of a considered free decay response, where the referred exponential decay shape can be observed. On the other hand, Figure 7.50 b) shows an example of a disregarded shutdown event. As can be seen, the decay response does not resemble the referred decay shape. This fact may be due to the lack of a sudden absence of the thrust force at the top of the tower.

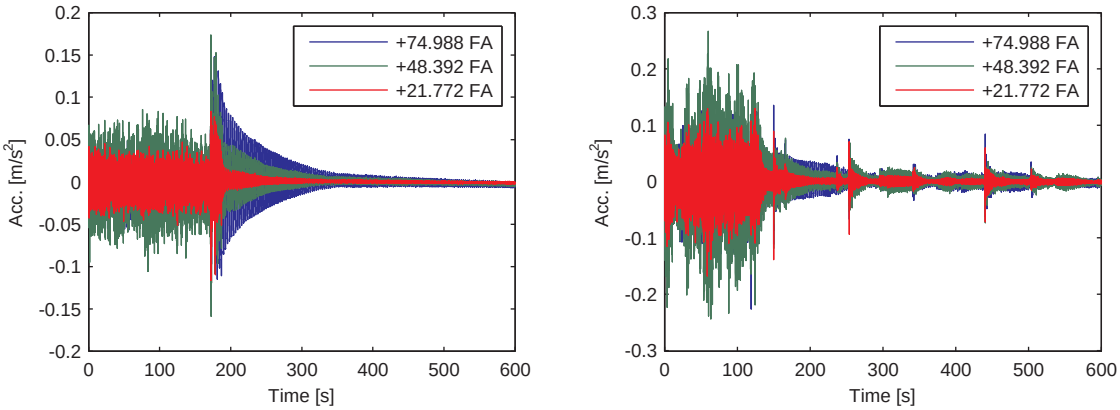

Figure 7.50 – Events in which a shutdown was detected: a) structural response following an exponential decay; b) example of structural response not following the common exponential decay

From the initially pre-selected events, 51 were chosen to be analysed. The majority of the events are referred to situations in which the wind speed dropped to values below the cut-in. In addition, 7 events were detected whose measured maximum wind speed was above the rated speed and the minimum wind speed as also above the cut-in value. However, in none of these events, the maximum wind speed is above the cut-out value. Figure 7.51 illustrates the minimum and maximum wind speed measured by the SCADA system for the selected events.

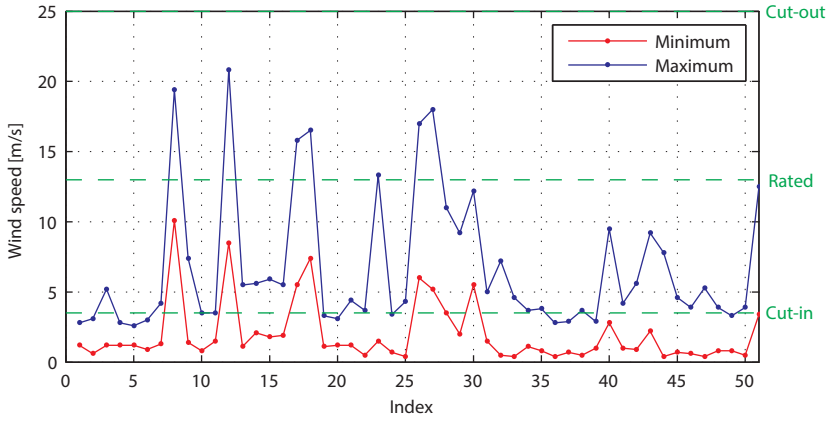

Figure 7.51 – Measured maximum and minimum wind speed occurred in the selected 10 min. events containing a free decay response

Figure 7.52 illustrates the diversity of the acceleration levels observed within the selected free decay responses. Figure 7.52 a) shows the decay response from an event whose maximum and minimum wind speed was, respectively, 19.4 m/s and 10.1 m/s. On the other hand, Figure 7.52 b) presents the acceleration time series of a decay response from a period in which the wind speed varied between 4.2 m/s and 1.0 m/s, which means that the turbine stopped because the wind speed was too low for power production. Comparing both figures, the difference in the level of acceleration is notorious.

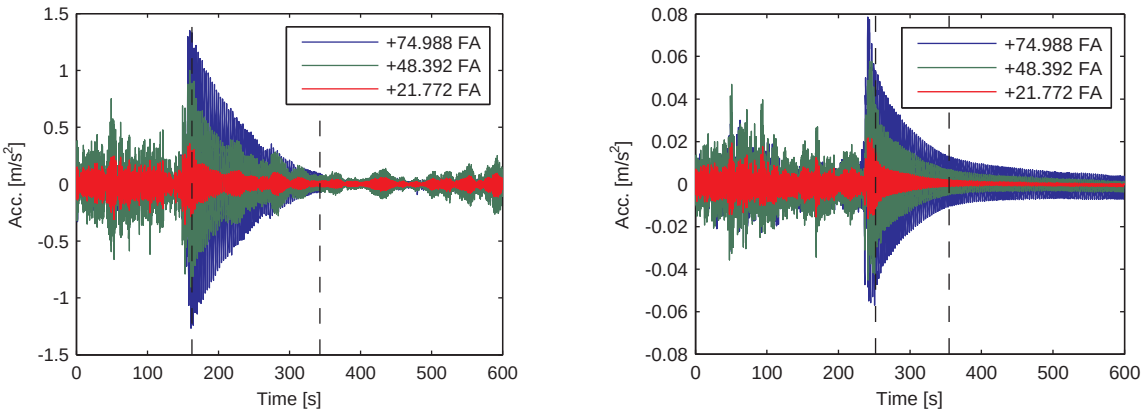

Figure 7.52 – Free decay response from: a) a high wind speed event; b) a low wind speed event

During the free decay events, the motion of the tower is mainly in the FA direction. Figure 7.53 shows the evolution of the FA and SS acceleration at the tower top of the decay responses represented in Figure 7.52 for the time segments enclosed by the vertical dashed lines. In this figure, corresponding to

a top view of the tower motion, the hotter colours correspond to the beginning of the time segment while the cold colours correspond to the final instants of the analysed period.

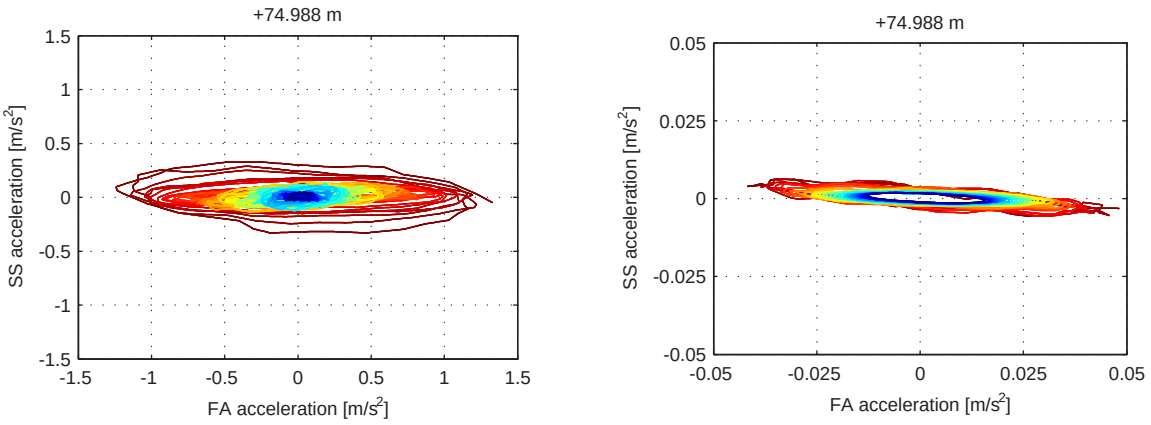

a) b)

Figure 7.53 – Evolution of the FA and SS acceleration (top view) from: a) a high wind speed event; b) a low wind speed event (the hotter colors correspond to the beginning of the time segment while the cold colors are referred to the final instants)

Initially, the two events introduced in Figure 7.52 were analysed by fitting an exponential function to the free decay envelope, in the same manner as in section 5.8.4.2 for the rotor-stop tests performed for the Izar Bonus 1.3MW/62 wind turbine. A low-pass filter with a frequency cut of 0.5 Hz was applied to both signals. The exponential function was then fitted to the local maxima points of the filtered signals, as illustrated in Figure 7.54. The results obtained for the frequency value and damping ratio of the 1 FA mode are presented in Table 7.11.

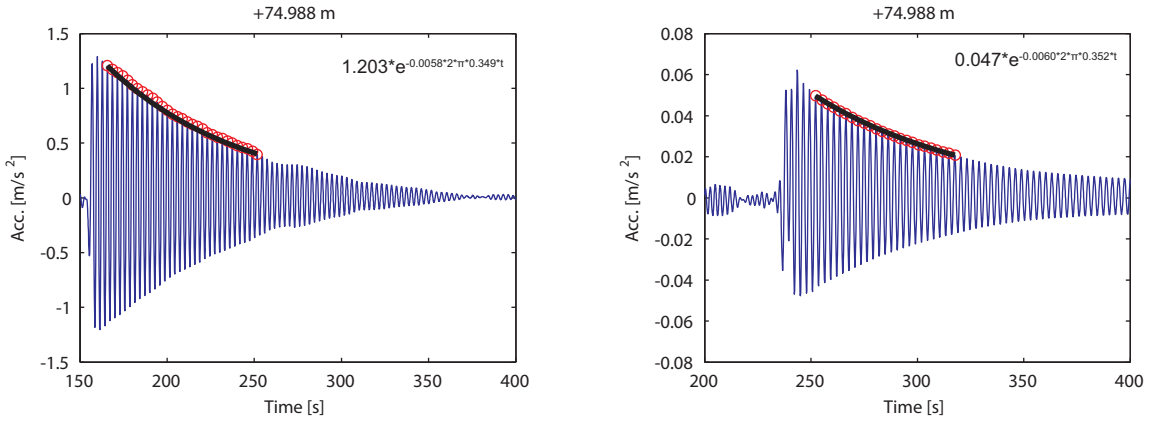

a) b)

Figure 7.54 – Identification of the modal damping ratio of the 1 FA vibration mode through filtering and fitting of an exponential function to the envelope of the free decay response from: a) a high wind speed event; b) a low wind speed event

The two free decay responses were also analysed through the application of the SSI-COV algorithm adapted to consider the measured free decays as input. This method was also used in section 5.8.4.2 to study the structural response of the Izar Bonus 1.3MW/62 wind turbine to the rotor-stop test. The

time segments defined to fit the exponential function in Figure 7.54 were used as inputs of the algorithm. The obtained stabilization diagrams are shown in Figure 7.55. Besides the one referred to the 1 FA mode, other vertical stable alignments are also evident. The results obtained for the 1 FA mode are summarized in Table 7.11.

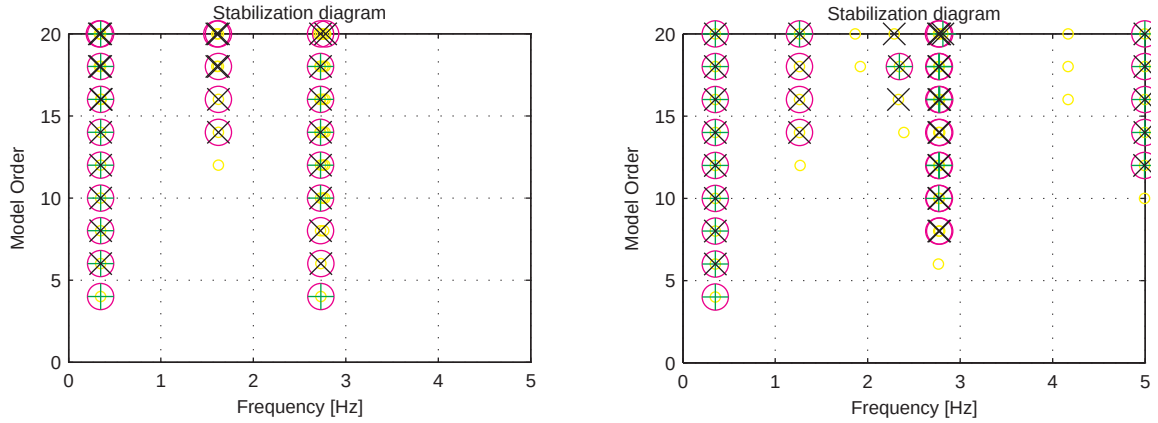

a) b)

Figure 7.55 – Stabilization diagram obtained with the application of the SSI-COV algorithm

The results obtained with the two procedures presented very similar values for frequency and damping ratio. It is also visible that there is no apparent influence of the wind speed on the damping values of the mode. It should be noted that in both free decays, due to change of orientation of the blades (from low angles of pitch to values to close to 90º), the contribution of the aerodynamic damping for the FA mode is not relevant.

Table 7.11 – Natural frequency (f) and modal damping ratio (ξ) of the 1 FA vibration mode identified with the filtering and fitting procedure and the SSI-COV method

	Exponential window		SSI-COV	
	f [Hz]	ξ [%]	f [Hz]	ξ [%]
high wind speed event	0.349	0.58	0.349	0.59
low wind speed event	0.351	0.60	0.352	0.62

The described analysis was then extended to all the selected free decay events. For the procedure based on filtering and fitting, a routine was developed to find the best exponential function to fit the decay response of the wind turbine. The results obtained were then visually analysed in order to validate the results. The obtained results are presented in Figure 7.56.

The segment of the acceleration time series used for the filtering and fitting procedure was also considered as input for the SSI-COV algorithm. In order to automate the procedure based on this method, a cluster analysis was performed after each run of the algorithm. With this processing solution, the procedure becomes similar to the one described for the continuous modal identification in section 7.3.6.1. The results obtained are also shown in Figure 7.56.

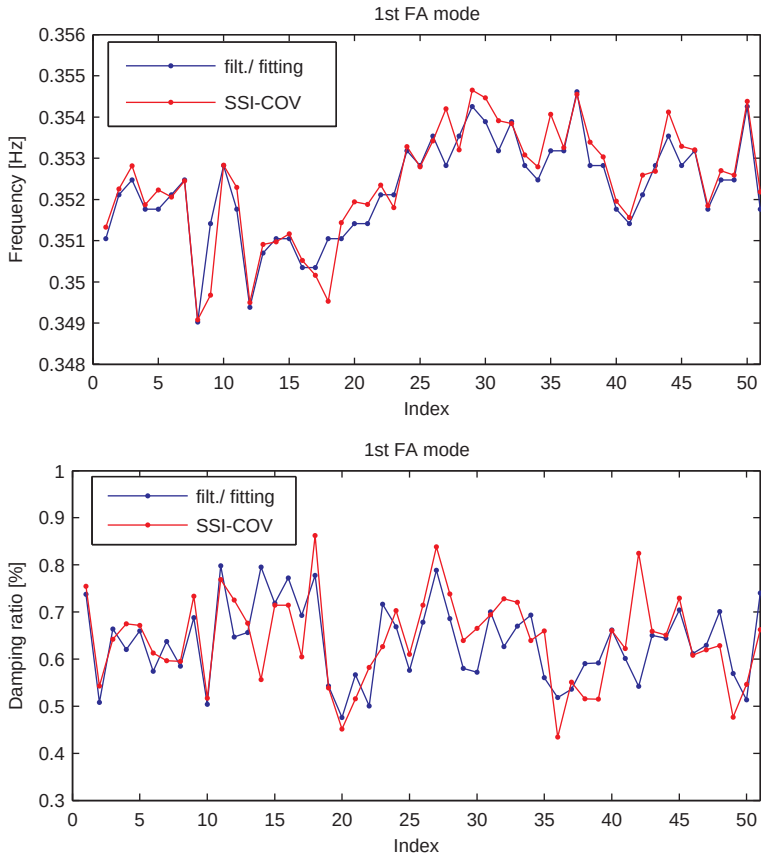

Figure 7.56 – Results obtained for the 1st FA mode with the filtering and fitting procedure and SSI-COV algorithm for frequency value (top plot) and damping ratio (bottom plot)

The results obtained show a good agreement between the two methods. Some variability in the results is noticed though. It was thus decided to assess if the operational and environmental parameters could explain this variance. Figure 7.57 illustrates the evolution of the modal properties identified with the SSI-COV methodology with maximum absolute values (MAX) of the selected segments of the acceleration decay responses. From these figures, it is visible that the majority of the decays is related to events with values smaller than 0.4 m/s^2 which difficulties the identification of a clear trend. Notwithstanding, there is an apparent decrease of the frequency values of the 1 FA mode with the acceleration. However, the number of events with MAX values higher than 0.4 is too low to confirm this trend.

On the other hand, the identified values of modal damping do not present a distinct dependency on the acceleration level. This conclusion is contrary to what usual occurs in common civil structure, where the damping tends to increase with the acceleration level.

Theoretically, the study of the free decay events could allow the study of the structural damping of the wind turbine. However, comparing the damping values identified with the free decay events with the results from the automated modal tracking, it is visible that they are considerably higher than the ones from the non-operating Regime 1 (in which the blades orientation is equal to the observed in the free decay events after the impulse) and lower than the ones observed in Regime 3 (in which the wind conditions are similar to the free decay events).

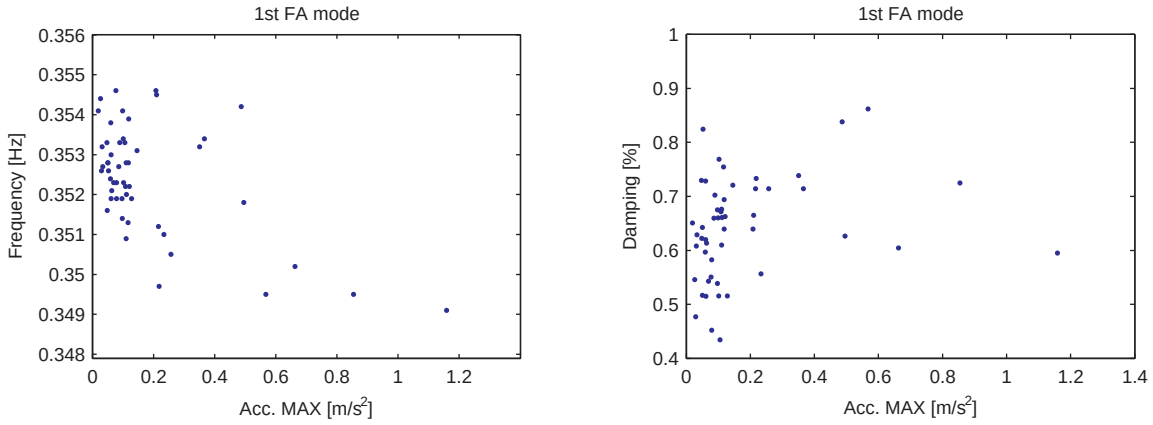

a) b)

Figure 7.57 – Evolution of the frequency value (a)) and damping ratio (b)) of the 1st FA mode with the maximum absolute values of acceleration

Although the study of the frequency values indicates some possible relations with the vibration level, it is not sufficient to explain the variation detected along the 51 decay events. This variation is mostly related to the temperature dependency of this modal property. This relation is shown in Figure 7.59, where a clear trend is visible. In this figure, some points (enclosed in a red circle) are visible with frequency values lower than what the trend suggests. These points are referred to events with high acceleration amplitudes, suggesting that, in fact, the vibration level may interfere in the frequency values of this mode.

With regard to the damping, it cannot be identified the source of the observed scatter.

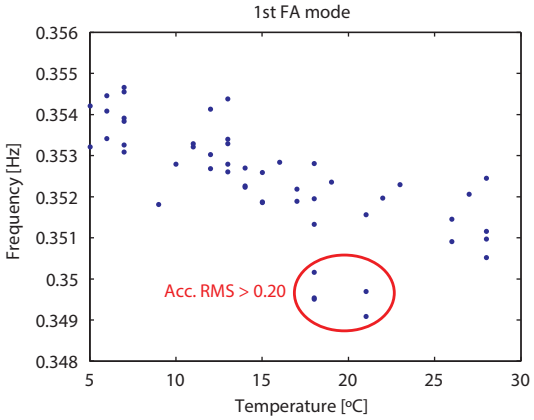

Figure 7.58 – Evolution of the frequency value of the 1st FA mode with temperature

7.3.6.4 Participation of the Vibration Modes/ Harmonics to the Measured Dynamic Response

The methodology presented in section 5.5 to decompose the measured acceleration time series into several modal and stationary responses (due to harmonics) was implemented in the developed dynamic monitoring system.

In the application of the modal response estimation, it is required the selection of a representative model order. The state-space matrices computed for that model order will then be used to define the

forward innovation model. While in the example of section 5.5, a manual selection was performed based on the observation of the stabilization diagram, an automated strategy for choosing the best model order is required as part of a monitoring system. The implemented strategy is thus based on the selection of the order with the highest number of stable poles whose clusters were chosen during the tracking procedure. When the turbine is operating (Regimes 4 and 5), cluster referred to the harmonics were also considered in the selection of the model order. For a cluster to be considered as representative of the stationary response due the harmonic excitation, its frequency value has to be within a range of ± 10 % of the multiples of the mean rotor speed from the setup under analysis. In cases in which there is more than one cluster meeting this condition, the cluster containing the higher number of poles is chosen. If this cluster has more poles than a pre-defined minimum number, it is defined as representative of the wind turbine response due to the harmonic excitation. In this application, a minimum number of 6 poles was defined. The 1Ω, 3Ω and 6Ω harmonics were considered in this analysis, although the first was only identified in 5.6 % of the operating setups.

Figure 7.59 characterizes the RMS values of the modal contributions associated with the modes vibrating in the FA direction, alongside with the harmonics, at the +74.988 m level. It is visible that the dynamic motion is dominated mainly by the 3Ω harmonic and the 1 FA mode. As expected, the acceleration response in 1Ω harmonic frequency represents a very low level. It is also interesting to note that the 1 FA mode (and also the 6Ω harmonic) present a different behaviour from the other responses, do not continuously increasing with the increase of the rotor speed (or wind speed). It is observable that, when the turbine starts operating, there is a steep increase on the values from the 1 FA mode, which tend to disappear when the turbine reaches the 10 rpm. This increase in the modal acceleration response of the 1 FA is probably due to the excitation of this mode by the 3Ω harmonic. Considering Figure 7.35, it is possible to attest that the 3Ω harmonic is close to the 1 FA mode at rotor speeds between 8.7 and 10 rpm which can lead to the excitation of this mode and, consequently, to the increase of the vibration amplitudes. A similar situation seems to occur with 6Ω harmonic response. For wind speed around 3 m/s (corresponding to the start of the turbine), an increase of the acceleration levels is also visible in Figure 7.59 b). This situation is probably justified by the interaction between this harmonic and the non-tracked FA mode with a frequency around 0.80 Hz (Figure 7.35).

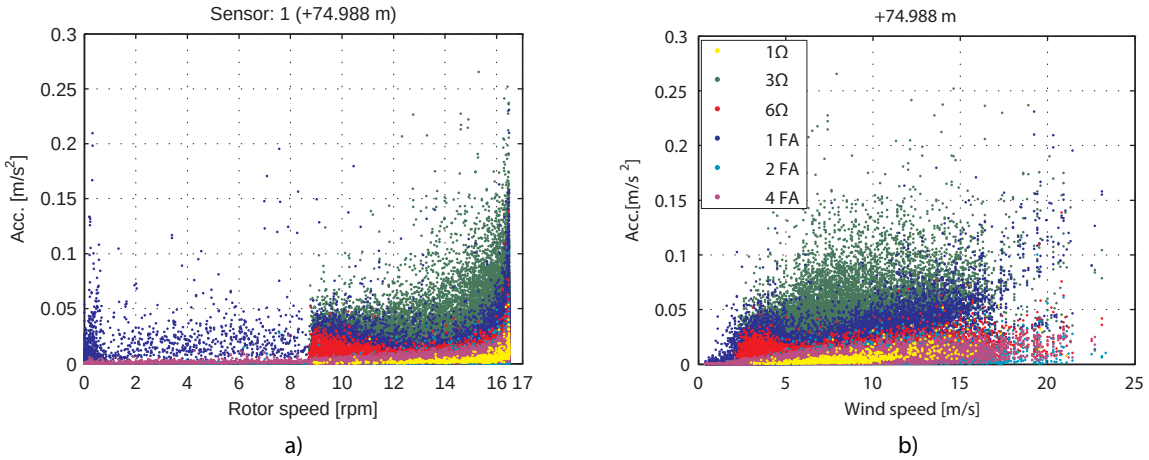

a) b)

Figure 7.59 – RMS values from the modal and stationary responses in the FA direction at level +74.988 m with: a) rotor speed; b) wind speed

Once the recorded acceleration time series are decomposed into modal (and stationary) responses, it is possible to use the procedure introduced in section 5.5.3 to quantify the relative contribution of each responses to the measured signal. Likewise in the example from section 5.5.3, the acceleration responses due to the harmonic excitation were also considered in this analysis. This analysis is helpful to better understand the changes in the dynamic behaviour of the wind turbine structure over the different conditions.

Figure 7.60 shows the evolution of the relative modal contribution of the FA modes and 1Ω, 3Ω and 6Ω harmonics to the measured acceleration at the tower top sensor with the wind speed. The median values (from each range of 0.5 m/s of wind speed) from the biggest contributors responses (1 FA mode, 3Ω and 6Ω harmonics) are represented by the lines in light colour. For low wind speed conditions (non-operating scenarios), the dynamic behaviour at the tower top is clearly dominated by the 1 FA mode, with participations of almost 100 % in certain setups. Once the turbine starts operating, the response is partially dominated by the 3Ω harmonic and by the 1 FA mode, whose participation is still representative mainly due to the excitation of this mode by the 3Ω harmonic, as previously explained. From the moment this effect vanishes, it is observed that the acceleration is practically dominated by the 3Ω harmonic. From this point, the participation of this harmonic and the 1 FA mode tend to converge to a participation of 30 % each with the increase of the wind speed. The participation of the 6Ω harmonic is only relevant when the turbine starts its operation, decreasing from this point to participation levels below 5 % with the increase of the wind speed.

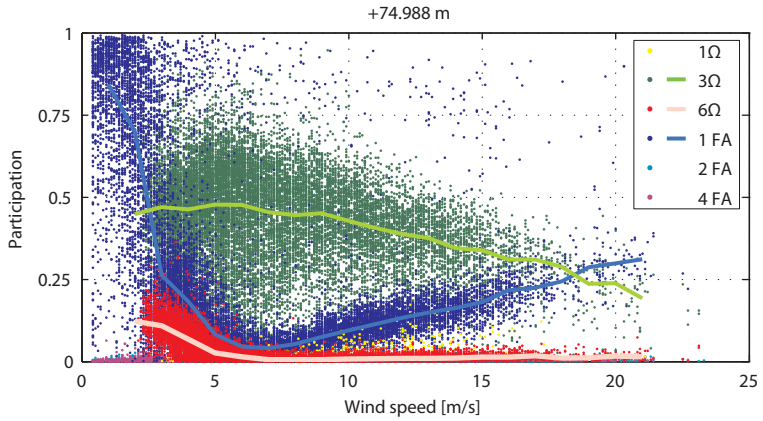

Figure 7.60 – Variation of the participation of the modal and stationary responses in the measured acceleration in the FA direction at level +74.988 m with wind speed

The analysis presented to the sensor at the tower top was also performed at the +48.392 m level in the FA direction. The results are presented in Figure 7.61. The acceleration, in the FA direction, is dominated by the 2 FA mode with RMS values clearly higher than the ones presented in Figure 7.59 for the 1 FA mode. This result is probably justified by the excitation introduced by the blade rotation (due to the tower shadow effect) at the level +48.392 m, corresponding to the maximum modal amplitude of the 2 FA mode. Anyway, the dynamic displacements would be expected to be higher at the tower top than at +48.392 m due to the lowest natural frequency of the 1 FA when compared to the 2 FA mode. This is confirmed later in section 7.3.7.

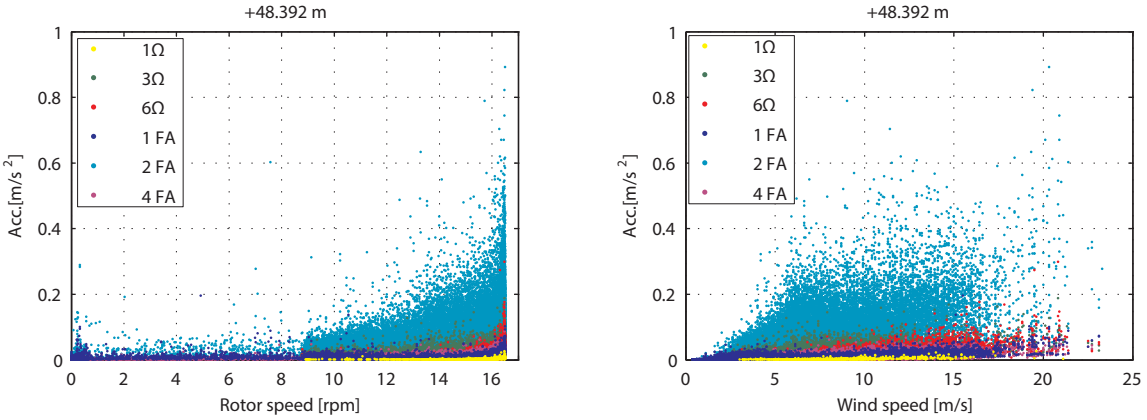

Figure 7.61 – RMS values from the modal and stationary responses in the FA direction at level +48.392 m with: a) rotor speed; b) wind speed

The quantification of the contribution of the modal and stationary responses to the measured acceleration time series was also assessed. The results are shown in Figure 7.62. In this figure, besides the modes considered in Figure 7.60, the stationary response due to the 9Ω harmonic was also included. However, it is important to note that around a rotor speed of 14 rpm, this harmonic crosses the potential untracked FA vibration mode, identified with a frequency of around 2.30 Hz (Figure 7.35). Since this potential mode was not considered during the tracking procedure, the automated algorithm developed to identify clusters related to the harmonics cannot distinguish, for this region of the Campbell diagram, a cluster representative of the 9Ω harmonic from one representative of this mode. Thus, it is possible that clusters referred in Figure 7.62 as due to the 9Ω harmonic are actually representative of this potential mode.

The results presented in Figure 7.62 clearly show that, under low wind speed conditions (non-operating regimes), the acceleration is dominated by the 1 FA mode. Some sparse points from the 1 FA with high modal contribution are also visible for high wind speeds but these are referred to setups with no power production. When the rotor starts operating, the contribution of the 1 FA drops drastically, keeping low for every wind speed condition. As expected, the acceleration is dominated by the 2 FA mode while the remaining the modes and harmonics are kept low during all operating conditions. Notwithstanding, it is observed that, for wind speeds around 7 and 13 m/s, the relative contribution of the 2 FA decreases slightly. This region coincides with the increase of the contribution of the 9Ω harmonic. This increase is due to the cross of this harmonic with the referred potential vibration mode with frequency of 2.30 Hz, leading to a possible interaction or resonance of this mode. For wind speeds higher than 13 m/s, the relative contribution of the 2 FA increases to levels similar to the ones obtained to winds speed below 7 m/s and the contribution of the 9Ω harmonic drops, meaning that this effect was reduced.

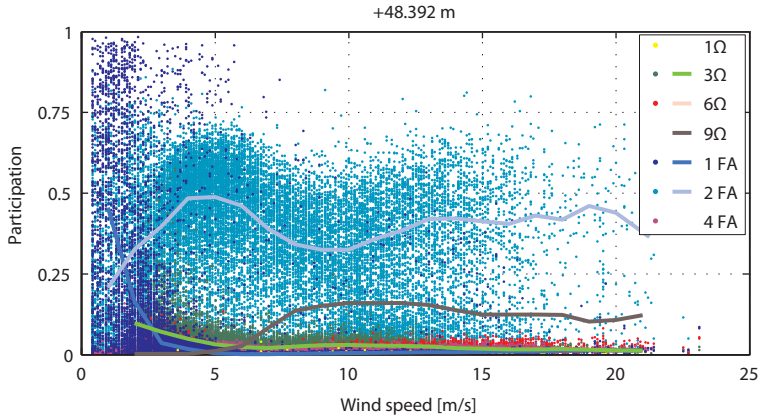

Figure 7.62 – Variation of the participation of the modal and stationary responses in the measured acceleration in the FA direction at level +48.392 m with wind speed

7.3.6.5 Removal of Operational and Environmental Effects

The characterization of the influence of the operational and environmental factors on the modal properties of the tracked vibration modes is an important step to remove a significant part of their variability. As these effects may introduce variations on the modal parameters with higher amplitudes than the damage itself, the removal of the influence of these effects is crucial to detect small damages at an early stage.

Wind turbines are equipped with sensors measuring several operational and environmental conditions. This data is usually accessed through the SCADA system, as is the case of the Senvion MM82 wind turbine. Some of the results obtained with this data were used to illustrate the operating conditions of the turbine in section 7.3.3. For that reason, the application of methods to remove the influence of the effects that take into account measurements of the predictors (input-output methods) represents a suitable option to be applied to wind turbines.

The definition of the regression models is usually performed considering a period of data large enough to include all the important variations of the predictors. In that sense, a period of one year is usually used to define the regression model (Magalhães, Cunha et al., 2012). This model is then used to evaluate the possible occurrence of damage in the following years. Since it was only possible to acquire acceleration data corresponding to a period of about one year, a slightly different strategy was followed in this work. Thus, the whole data was split into two different periods, consisting each one in data from intercalary days. With this strategy, both periods contain results within a period of one year, but from different days. Period 1 was then used to define a suitable multivariate regression model, while Period 2 was used to assess the existence of damage.

The influence of some operational factors on the modal properties was already presented throughout section 7.3.6.2. As example, the effect of the rotor speed on the frequency values of the modes, namely for the 1 SS* and 2 SS*, was shown. The changes on the behaviour of the natural frequencies with the different operating regimes were also presented in Figure 7.44. The variability shown between regimes evidences the effect that different factors have on the wind turbine. For that reason, a different multivariate linear regression model was established for each operating regime, reflecting the different

conditions. The operational and environmental factors recorded by the SCADA system and considered in this analysis were:

- Wind speed (w. s.);
- Outdoor temperature (temp.);
- Rotor speed (r. s.);
- Blade pitch angle (pitch).

The operating regime 1 is characterized by values of blades pitch angle (around 90º) with small variations, during non-production setups. Thus, the considered predictors influencing the most the variability of the frequency values are the temperature and, in a small scale, the wind speed. These expected results are confirmed by the obtained correlation coefficients (computed according to equation (7.4)) and presented in Table 7.12. This coefficient permits to highlight the modes whose natural frequencies are more (linearly) influenced by the factors under study. Figures 7.65 and 7.66 show two examples of the correlation between natural frequency and the wind speed and temperature for two different modes, respectively.

Table 7.12 – Correlation coefficients between natural frequencies and operational/ environmental factors (Regime 1)

	w. s.	temp.	r. s.	pitch
1 SS	0.12	-0.23	0.08	0.08
1 FA	0.38	-0.28	0.34	-0.03
1 SS*	-0.49	-0.36	-0.44	0.09
2 SS*	0.19	-0.57	0.01	0.46
2 FA	0.25	-0.64	0.15	-0.02
2 SS	-0.13	-0.43	-0.13	-0.08
3 SS*	0.29	-0.70	0.21	-0.11
4 FA	-0.36	-0.49	-0.35	-0.01

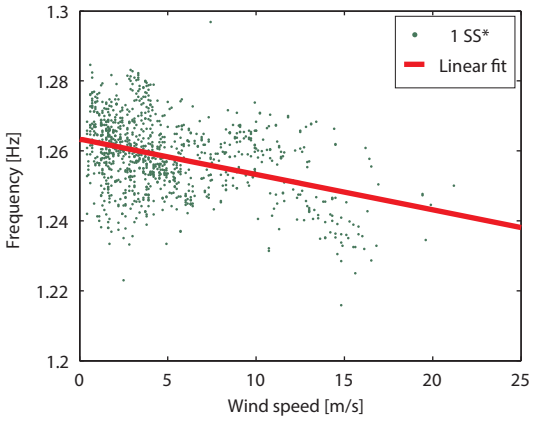

Figure 7.63 – Natural frequency of 1 SS* mode (Regime 1) vs wind speed

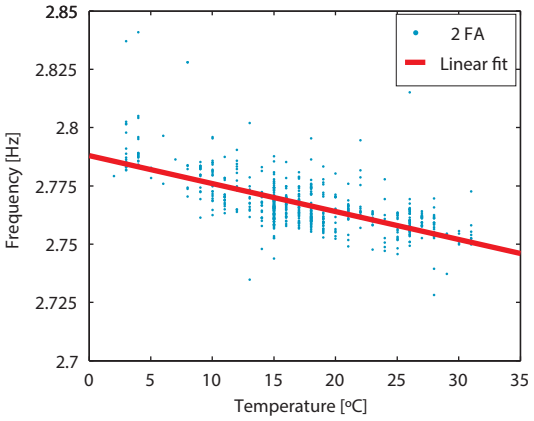

Figure 7.64 – Natural frequency of 2 FA mode (Regime 1) vs temperature

Regime 2 is similar to Regime 1 to the extent that they are both referred to non-production setups, in which the blades pitch angles is kept almost constant (although at lower values in Regime 2). Thus, it is comprehensible that the predictors with the highest correlation with the natural frequencies are again the wind speed and the temperature, as seen in the results of Table 7.13.

Table 7.13 – Correlation coefficients between natural frequencies and operational/ environmental factors (Regime 2)

	w. s.	temp.	r. s.	pitch
1 SS	0.27	-0.28	0.33	-0.06
1 FA	-0.11	-0.64	0.01	0.03
1 SS*	-0.45	-0.36	-0.39	0.06
2 SS*	-0.19	-0.39	-0.13	-0.03
2 FA	-0.06	-0.57	0.03	0.03
2 SS	-0.18	-0.36	-0.09	-0.05
3 SS*	-0.12	-0.35	0.04	-0.12
4 FA	-0.07	-0.31	-0.01	-0.15

The correlation coefficients obtained between natural frequencies from Regime 3 and operational/ environmental factors are shown in Table 7.14. Operating regime 3 corresponds to transition situation in which the turbine changes from parked/ idling configuration to operating conditions, or vice-versa. For that reason, both the rotor speed and pitch angle show important changes during these setups. However, apart from some modes (such as 1 SS*, 2 SS* and 4 FA modes), these changes do not seem to have an important influence on the frequency values.

Table 7.14 – Correlation coefficients between natural frequencies and operational/ environmental factors (Regime 3)

	w. s.	temp.	r. s.	pitch
1 SS	-0.09	-0.33	-0.08	-0.01
1 FA	0.03	-0.19	0.22	-0.23
1 SS*	-0.70	-0.37	0.09	-0.23
2 SS*	0.56	-0.26	-0.01	0.19
2 FA	0.02	-0.38	-0.02	0.00
2 SS	-0.03	-0.31	0.25	-0.22
3 SS*	0.25	-0.12	0.05	0.02
4 FA	0.17	-0.20	0.32	-0.23

The number of identified setups regarded to Regime 4 is considerably higher than for the first 3 regimes. This fact permitted to obtain a better characterization of the variations of the natural frequencies for this regime. The results obtain for the correlation analysis are presented in Table 7.15.

Table 7.15 – Correlation coefficients between natural frequencies and operational/ environmental factors (Regime 4)

	w. s.	temp.	r. s.	pitch
1 SS	0.22	-0.50	0.27	0.08
1 FA	-0.40	0.02	-0.39	-0.14
1 SS*	-0.93	0.15	-0.95	-0.26
2 SS*	0.91	-0.42	0.97	0.15
2 FA	0.44	-0.51	0.51	0.05
2 SS	0.23	-0.54	0.34	-0.05
3 SS*	0.84	-0.53	0.88	0.15
4 FA	0.41	-0.55	0.48	0.10

Both the rotor speed and wind speed (which are themselves correlated) present interesting high values of correlation with the frequencies. As expected, the pitch angle does not represent an interesting source for explanation of the frequencies variability, since its value is practically constant during this Regime. On the other hand, the temperature presents important linear relationship with the frequencies, which are confirmed by visual observation of the results. The evolution of the frequency values of the 2 FA mode with the temperature is illustrated in Figure 7.65.

The highest correlation values are obtained with the rotor speed. Due to the nature of the whirl modes, this fact is especially important for the 1 SS* and 2 SS* modes. This phenomenon is illustrated for the 2 SS* mode in Figure 7.66.

Although slightly lower than with the rotor speed, the correlation coefficients obtained with the wind speed are also relevant. However, this fact is mainly related to the relation between the wind speed and the rotor speed than to physical relations between the wind and the natural frequencies.

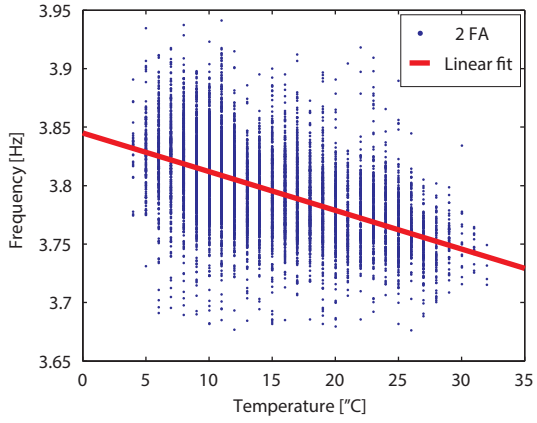

Figure 7.65 – Natural frequency of 3 SS* mode (Regime 4) vs temperature

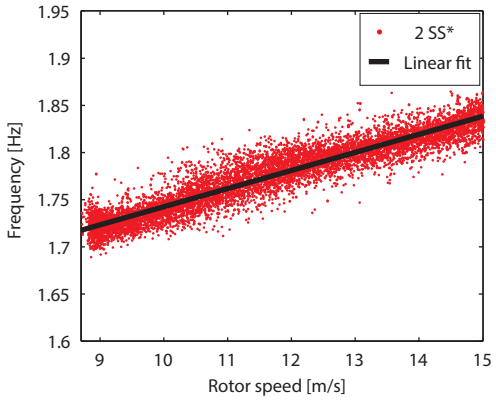

Figure 7.66 – Natural frequency of 2 SS* mode (Regime 4) vs rotor speed

Finally, Regime 5 is related to production setups with the strongest wind speed conditions. It is characterized by an increase of the blades pitch angle with the wind speed in order to control the rotor speed. This Regime is then commanded by the pitch angle, which in turn is defined according to the wind speed. The relation between the pitch angle and the wind speed was already introduced in Figure 7.14. Again, the 1 SS* and 2 SS* present a large variability of their frequency values due to operational

factors. The variation introduced by the pitch angle in the frequency values of the 1 SS* mode is shown in Figure 7.67. Also the temperature seems to be an important predictor of the natural frequency of the 1 SS mode. This relationship is illustrated in Figure 7.68.

Table 7.16 – Correlation coefficients between natural frequencies and operational/ environmental factors (Regime 5)

	w. s.	temp.	r. s.	pitch
1 SS	-0.02	-0.47	0.00	-0.01
1 FA	-0.31	-0.27	-0.34	-0.34
1 SS*	-0.91	-0.19	-0.68	-0.92
2 SS*	-0.68	-0.32	-0.42	-0.67
2 FA	-0.22	-0.56	-0.26	-0.22
2 SS	-0.06	-0.57	-0.05	-0.04
3 SS*	-0.22	-0.47	-0.01	-0.19
4 FA	0.42	-0.11	0.33	0.43

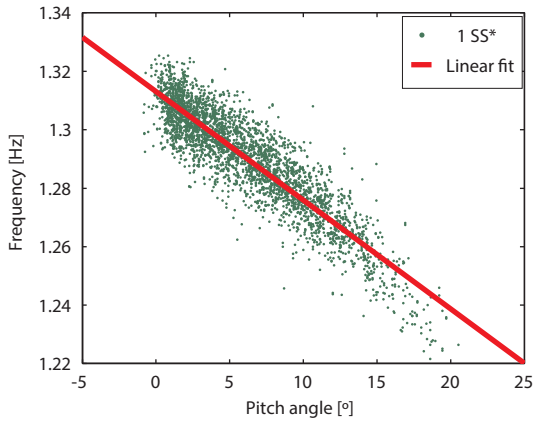

Figure 7.67 – Natural frequency of 1 SS* mode (Regime 5) vs blades pitch angle

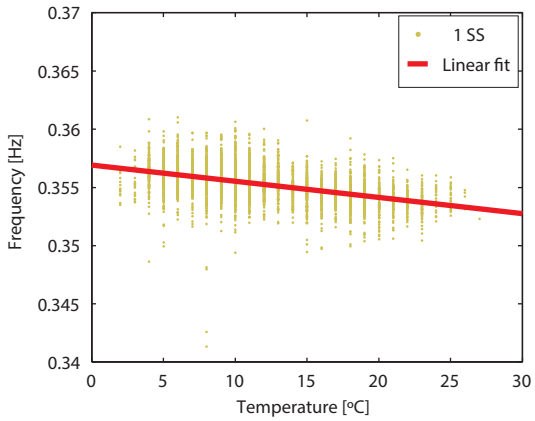

Figure 7.68 – Natural frequency of 1 SS* mode (Regime 5) vs temperature

Once the influence of the predictors was analysed for each regime, two alternative regression models were considered: SM1 and SM2.

SM1 only considers the predictors with important physical relations with the natural frequencies. For that reason, even predictors with high correlation coefficients (such as wind speed in Regime 4 and 5) were not considered, since the coefficient value is not related to a physical relation with this predictor but to a correlation between other predictors, as previously referred. The predictors considered for this model are presented in Table 7.17. On the other hand, the SM2 model considers all predictors, aiming to define a general regression model with potential application without any previous analysis (Table 7.17).

Table 7.17 – Considered predictors for regression models SM1 and SM2

SM 1	Regime				
Predictors	1	2	3	4	5
w. s.	x	x	x		
temp.	x	x	x	x	x
r. s.				x	
pitch					x

SM 2	Regime				
Predictors	1	2	3	4	5
w. s.	x	x	x	x	x
temp.	x	x	x	x	x
r. s.	x	x	x	x	x
pitch	x	x	x	x	x

The suitability of both models to produce forecasts was quantified through the computation of the coefficient of determination R^2_{for}, presented in equation (7.8). For its calculation, the Period 2 of data was used to assess the quality of the forecasts (as previously referred, this period of data was not considered in the construction of the regression models). The results obtained for the two models are very similar (Table 7.18). In that sense, the SM 2 was chosen since it considers all predictors, making its use more general to be implemented in any wind turbine in any regime.

It is observed from Table 7.18 that the modes related to rotor motion (1 SS*, 2 SS* and 3 SS*) present the highest values of R^2_{for}. The good quality of the predictions of these modes is justified by the fact that the variability of these modes is mostly driven by the rotor speed, which is a known predictor. On the other hand, the 1st tower bending modes (1 SS and 1 FA) presents the lower coefficients of determination of all modes, showing that their variability is less dependent on the considered operational/ environmental effects. One possible cause to the low coefficients obtained for some modes might be related to the potential influence of asymmetric soil conditions on the natural frequency values, which could be considered by using the yaw angle as predictor in the regression model. However, it was decided not to use this predictor in order to assess the accuracy of the monitoring system to detect foundation asymmetries (see section 7.3.6.6). Notwithstanding, in situations in which the installation of the monitoring system is performed at an early stage of the turbine operation, the consideration of the yaw angle in the model would increase the accuracy of the system to detect abnormal structural changes.

Table 7.18 – Coefficients of determination obtained with the regression models

Modes	SM 1	SM 2
1 SS	0.295	0.297
1 FA	0.377	0.391
1 SS*	0.965	0.967
2 SS*	0.950	0.952
2 FA	0.458	0.458
2 SS	0.706	0.719
3 SS*	0.860	0.864
4 FA	0.777	0.780

Although steel structures do not usually present a significant thermal inertia, concrete structures do. Considering the importance of the support conditions (i. e. concrete foundation) in the definition of the dynamic properties of wind turbines, alternative dynamic models were also analysed in order to assess the influence of temperature records from previous time instants on the structure (see section 7.2.1.1). In that sense, 5 dynamic models were considered. These models consider all the predictors from the SM 2 model (including the temperature at the instant under consideration), along with the temperature records referred to different time delays of 3, 6, 12, 18 and 24 hours. For each dynamic model referred to a temperature measurement from a previous time instant, the temperatures from the more recent time instants were also considered. This means that, for a dynamic model considering temperature record with a delay of 12 hours, the temperature measurements from the current time instant and from time delays of 3, 6 and 12 hours were considered. The results obtained are shown in Table 7.19. In this table, the dynamic models are identified by the largest time delay considered. It can be seen that, although some improvements are noticed for the 1 FA and 3 SS* modes, smaller values were obtained for the 2nd pair of tower bending modes. Since the 2 FA and 2 SS modes are very sensitive to structural changes in the foundation condition and, consequently, represent important features to assess the existence of damage, the static model SM 2 was considered to be adequate to eliminate the environmental and operational effects on the frequency values.

Table 7.19 – Coefficients of determination obtained with the dynamic models (the largest time delay considered for each model is indicated within parenthesis)

Modes	DM 1 (3 hours)	DM 2 (6 hours)	DM 3 (12 hours)	DM 4 (18 hours)	DM 5 (24 hours)
1 SS	0.296	0.293	0.292	0.284	0.299
1 FA	0.396	0.399	0.392	0.388	0.391
1 SS*	0.966	0.967	0.966	0.964	0.965
2 SS*	0.949	0.949	0.951	0.947	0.947
2 FA	0.450	0.445	0.436	0.440	0.428
2 SS	0.716	0.713	0.721	0.707	0.710
3 SS*	0.866	0.866	0.864	0.871	0.875
4 FA	0.775	0.774	0.771	0.767	0.770

In order to illustrate the quality of the SM 2 model, Figure 7.69 presents the predicted values of natural frequency of the 1 SS* and 4 FA modes for some data sets from Period 2, alongside with the identified values of these modes with the monitoring system. The accuracy of the prediction obtained with this model is clearly visible in this figure.

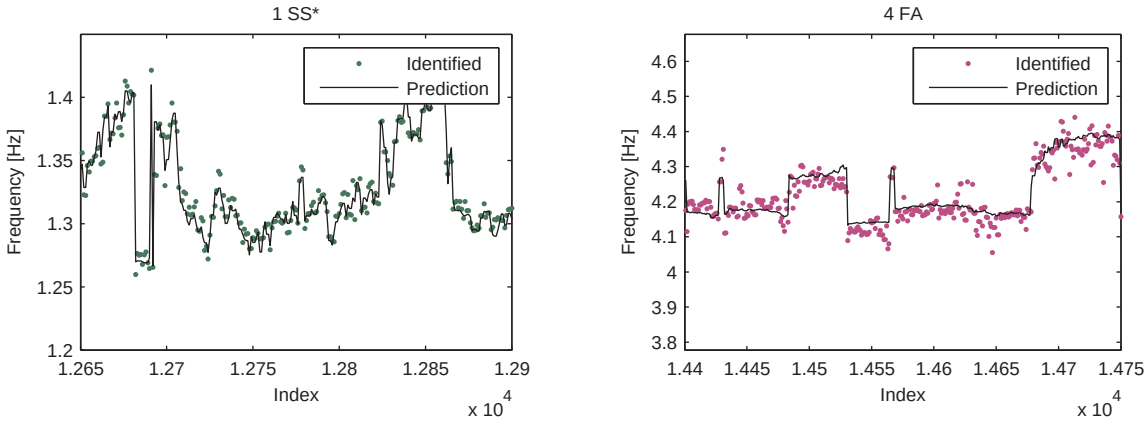

Figure 7.69 – Identified and predicted frequency value of the 1 SS* and 4 FA using the SM 2 mode during (data corresponding to Period 2)

Using the regression model SM2, the effect of operational and environmental effects on the natural frequencies of the modes can be then minimized. Figure 7.70 shows the time evolution of the frequency values of the 1 SS* mode before and after the removal of these effects during period 2. These effects (mainly the rotor speed) have a large influence on the variation of the frequency values of this mode. Notwithstanding, the SM2 model is capable of mitigating the influence of these effects, as seen in the bottom figure.

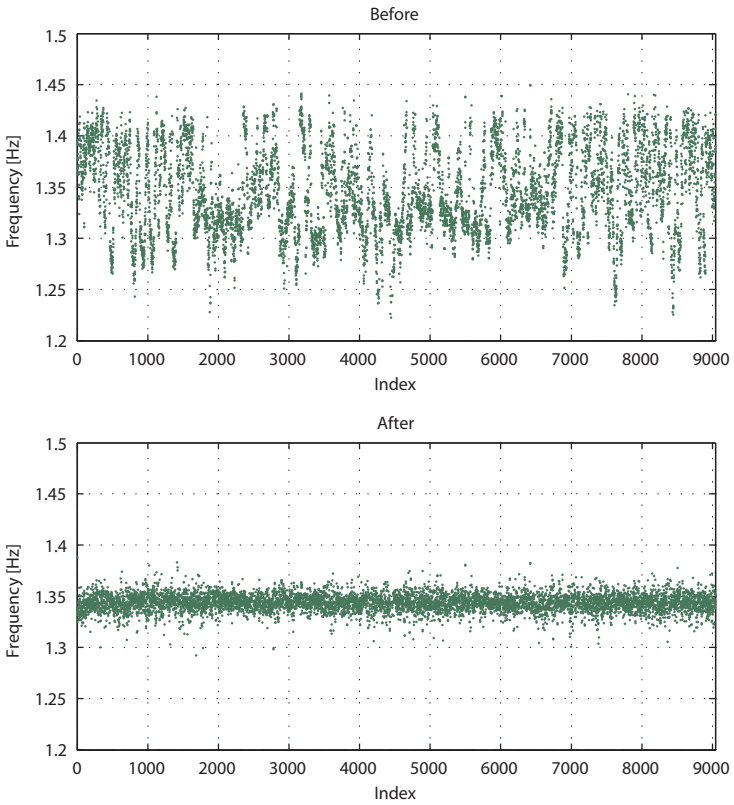

Figure 7.70 – Time evolution of the frequency values of the 1 SS* mode before (top) and after (bottom) the removal of the operational and environmental effects during period 2

Figure 7.71 presents the frequency values of the 2 FA vibration mode along the time. Although this mode does not present a variability as high as the 1 SS* mode, it is also possible to attest its reduction after the correction of the frequency values with the regression model SM 2.

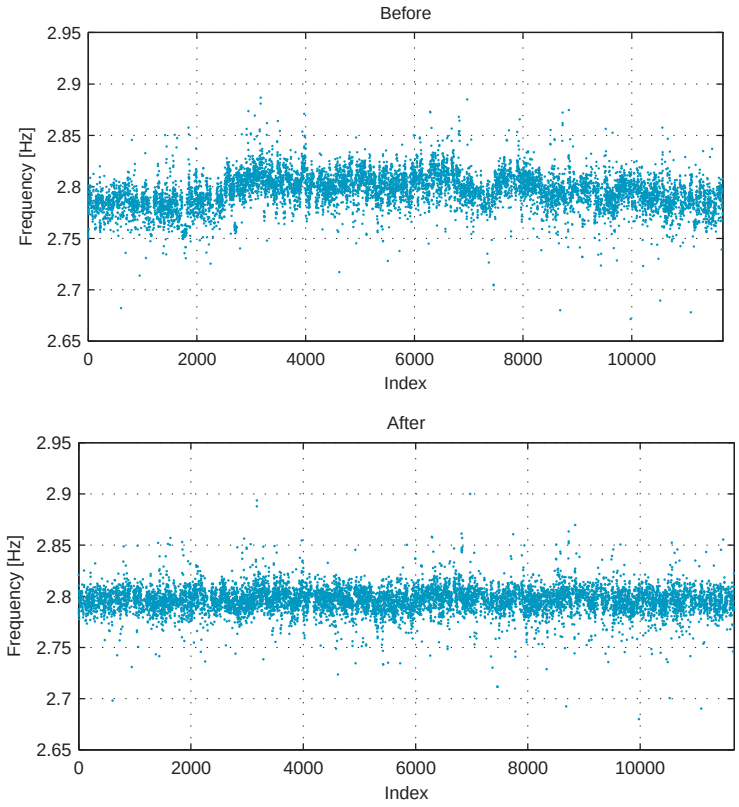

Figure 7.71 – Time evolution of the frequency values of the 2 FA mode before (top) and after (bottom) the removal of the operational and environmental effects during period 2

The reduction of variability of the frequency values of the vibration modes is also evident in the histograms of Figure 7.72. As can be seen, the 1st tower bending mode in the SS direction presents the lowest reduction in its variability from the three considered modes. This result is in accordance with the results from Table 7.18. The reduction obtained with the correction of the frequency values of the 2 FA mode is notorious in the histogram, where the corrected frequencies are concentrated in a narrower range. Lastly, the histogram of the 1 SS* mode illustrates the large reduction of variability obtained with the regression model. It is also interesting to note the considerable different shape of the histogram of this mode before the correction, illustrating the different nature of these rotor modes in comparison with tower modes.

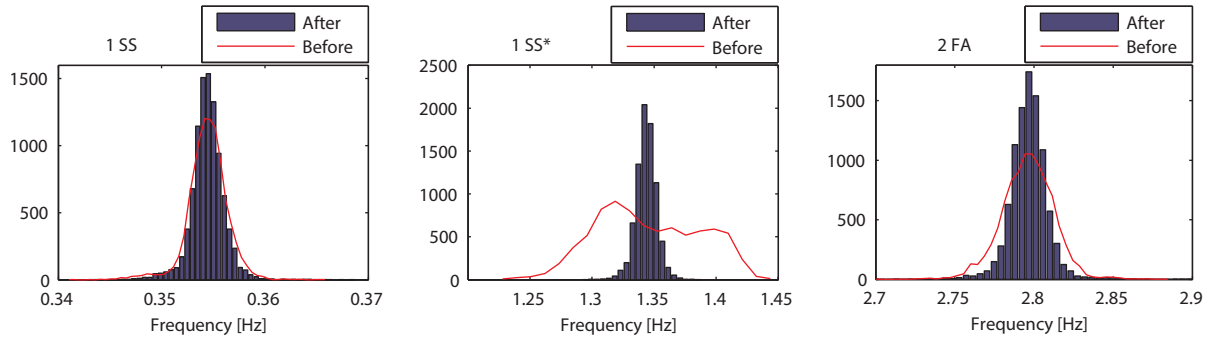

Figure 7.72 – Histograms of the natural frequencies of the 1 SS, 1 SS* and 2 FA modes before and after the removal of operational and environmental effects

7.3.6.6 Damage Detection

The definition of the static regression model in the previous section and the subsequent removal of the influence of the operational and environmental effects allowed reducing the variability of the frequency values of the tracked vibration modes. Thus, it is now possible to assess the variations of these values in order to detect the occurrence of small structural changes.

One important issue related to structural changes in wind turbines is the possible reduction of the foundation stiffness along time. Although this problem is more related to offshore turbines, due to scour, it is also relevant in onshore since problems in the connection of the tower with the foundation have already been observed in several towers. Therefore, it is interesting to assess if a variation of frequency is noticed in the monitored Senvion wind turbine. As referred in section 7.1, the 2nd pair of tower bending mode is one of the most sensitive modes to changes in the stiffness of the foundation. In that sense, the frequency values of the 2 FA and 2 SS modes from periods 1 and 2 were corrected according to the model SM 2 and plotted against the yaw angle. The results obtained are presented in Figure 7.73. In these figures, also the median values and the box plots corresponding to the 25th and 75th percentile are shown. It is seen that, although small, both plots present coherent fluctuations. The mode in the FA direction presents the highest values of frequency at 150º and at 330º (= 150º + 180º). On the other hand, the smallest values are found for yaw angles of 70º and 240º (≈ 70º + 180º). It is interesting to note that the highest values of frequency of the 2 SS mode are obtained for the directions of the smallest values of 2 FA mode and vice-versa. This means that it is very likely that the foundation or the connection of the tower to the foundation is not structurally homogeneous, with the stiffest direction in the 150º - 330º direction and a (practically) orthogonal softest direction in the 70º-240º direction.

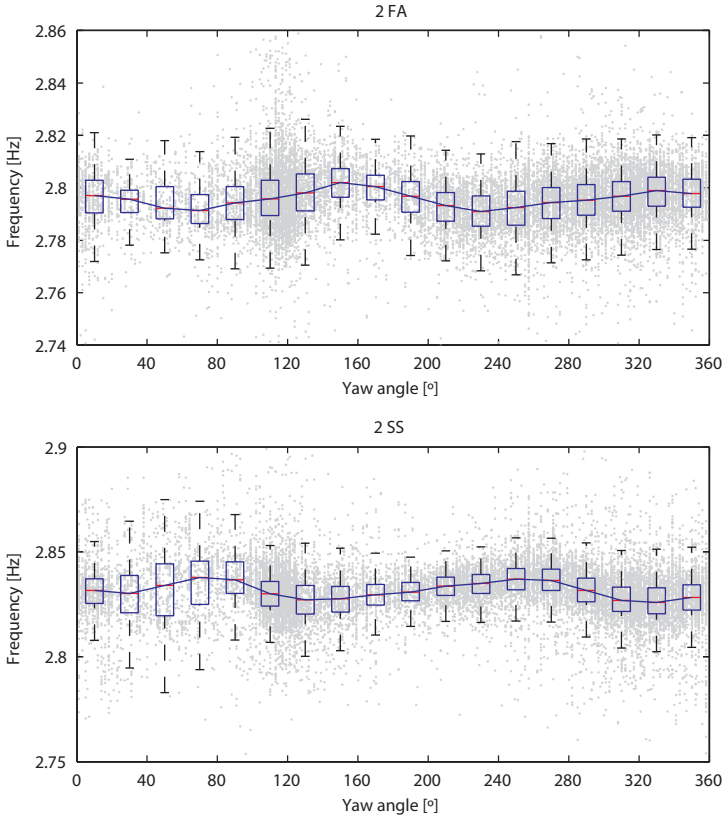

Figure 7.73 – Corrected frequency values of the 2 FA (top) and 2 SS (bottom) from Period 1 and 2 vs yaw angle

Although in a smaller scale, it is also possible to identify the same variation of the frequency value of the 1 SS vibration mode with the yaw angle (Figure 7.74). This variation is similar to the one presented by the 2 SS, which reinforces the idea of a possible asymmetry of the foundation stiffness. The 1 FA mode do not evidences a noticeable variation, probably due to its larger variability which probably hinders possible fluctuations due to asymmetric foundation conditions.

Nevertheless, it is not possible to say, at this moment, that these conclusions attest the existence of damage in the foundation or, more likely, in the tower-foundation connection. It is possible that this non-homogeneity of the foundation is already present since the beginning of operation of the turbine and that is related to slightly different soil conditions under the large foundation of the support structure. In that sense, the installation of a continuous dynamic monitoring at the initial stage of the turbine operation would lead to conclusive results, permitting to identify if this non-homogeneity is a consequence of structural changes occurred throughout its period of life or if it just represents the stiffness of the foundation conditions.

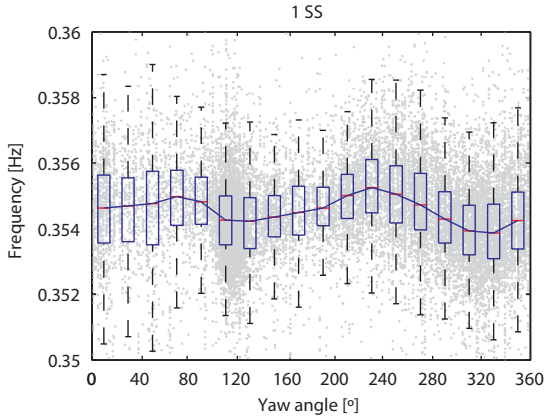

Figure 7.74 – Corrected frequency values of the 1 SS from Period 1 and 2 vs yaw angle

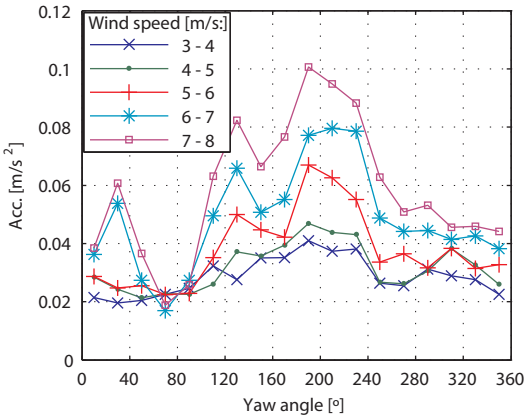

Figure 7.75 – Median values of the RMS values of acceleration of the top sensor in the FA direction according to the yaw angle, considering setups when the turbine was operating and several wind speed ranges

In the previously presented Figure 7.29, the variation of RMS values of acceleration from narrow ranges of wind speeds with the yaw angle was analysed. This plot is again presented in Figure 7.75. It is interesting to see that the direction with the highest acceleration RMS values (around 180º - 240º) coincides with the softest direction. Still, the acceleration levels around 70º are very low, which may seems a contradiction. However, the number of recorded operating events with the nacelle oriented to the yaw sector between 0º and 70º is smaller than for the other sectors, which may not be representative and, thus, hinder the effect of the softest foundation when the turbine is oriented to this sector.

The yaw sector between 110º and 140º is also a sector with high acceleration RMS values. This is the direction of the main wind incidence, as shown in Figure 7.15. This sector is located in a transition location between the stiffest and softest directions of the foundation. For that reason, the high acceleration levels detected might be also related to the wind action itself (higher levels of turbulence) than just motivated by a possible loss of stiffness of the foundation.

As previously referred, damage in wind turbine support structures is usually related to foundation problems. For offshore turbines, scour problems are likely to occur, decreasing the strength of the foundation and potentially decreasing the expected fatigue life of the structure (Sørensen and Ibsen, 2013). Although in a small scale, some problems of excessive levels of vibrations were also detected due to damage in the interface connection between tower and foundation (Pelayo, López-Aenlle et al., 2011; Currie, Saafi et al., 2015).

Apart from foundation problems, rotor blades are also elements prone to damage and with a costly replacement, as shown in section 3.1.3. In that sense, it would be interesting to assess the sensitivity of the identified rotor vibration modes to small structural damages of the blades.

In order to evaluate the ability of the dynamic monitoring system to detect the presence of small damage in the previously referred elements of a wind turbine, a strategy based on the introduction of artificial damage was followed. For the assessment of damage at the foundation, two scenarios were studied. The damage scenario D1 is related to scour problems in offshore wind turbines. In that sense, the evolution of the first natural frequency of the support structure with the scour depth presented in

(Prendergast, Gavin et al., 2015) was considered (see Figure 7.1). A small scour depth of around 0.075 times the base diameter of the monopile is considered. For the case of the Senvion MM82, with a tower base diameter of 4.300 m, this damage corresponds to a scour depth of around 0.32 m, while for the offshore Vestas V90 wind turbine represents a depth of 0.38 m. This damage is said to correspond to a decrease of the first tower bending mode of around 0.2 %. However this study only considers the evolution of the first natural frequency, while nothing is said about the second mode of the support structure. To overcome this situation, results of the studies introduced in (Sørensen and Ibsen, 2013) and (Zaaijer, Tempel et al., 2002) were considered. These studies present a ratio between the decrease of the second tower bending mode relative to the first tower bending mode of 2.1 times to 2.6 times, respectively, for monopile foundations. Following these results, a conservative value of 2.0 was used in this damage scenario. Since it is not expected that rotor blades modes are influenced by this damage, their frequency values is not changed.

The second case of foundation damage (scenario D2) reproduces the frequency variation detected in (Pelayo, López-Aenlle et al., 2011). This study describes the dynamic tests performed in three wind turbines, from which two of them presented anomalous vibration levels. It was also found that these turbines presented cracks at the foundation. The test indicated that the frequency values of the identified vibration modes from these two turbines were consistently lower than the ones from the third healthy turbine. Initially, the frequency deviations of the first and second tower bending modes presented by the turbine with the smallest amplitude of variations were considered in this scenario. However, since this damage scenario was clearly identified, a smaller variation was studied. Thus, a variation 5 times smaller than the variation reported in the study was used for this damage scenario. Due to the difficulty in the comparison between the 4 FA mode and the vibration modes presented in this study, this mode was also not considered. Again, the frequency value of the rotor blades modes was not changed for this scenario.

The last damage scenario (D3) is related to blade damage. As referred in section 7.1.2, the majority of published studies refer the small sensitivity of the natural frequencies of the blade modes to small, common damages. In that sense, the model of the Senvion MM82 developed in the HAWC2 code (introduced in section 7.3.2) was used to assess the sensitivity of the 1 SS* and 2 SS* modes to structural damage at the blades. Considering that the eigenvalue analysis performed by the HAWC2 code is related to the turbine with the blades according to an operating configuration but under parked conditions, the expected frequency value of these two modes, introduced in section 7.3.6.2, was used to tune the stiffness of the blades. Due to the high uncertainties in modelling the structural elements located inside the nacelle, as well as the rotor blades, the estimation of the frequency value of the 3 SS* mode was not possible. The comparison between the frequency values obtained with the numerical model and with the monitoring system is introduced in Table 7.20.

Table 7.20 – Comparison between the expected frequency values of the 1 SS* and 2 SS* modes during the monitored period (non-operating conditions) with the results obtained with the HAWC2 model

	Natural frequency [Hz]	
Modes	Monitoring	HAWC2
1 SS*	1.526	1.530
2 SS*	1.558	1.556

The presence of damage at just one (or two) blades leads to an anisotropic rotor. In that sense, the identification of such damage would be more easily detected through the identification of the 1Ω harmonic (as illustrated in Figure 4.18) or through the identification of phenomena such as the ones described in (Ramírez, Tcherniak et al., 2015), where a clear distinction in the singular values spectrum of the structure is identified between an isotropic and an anisotropic rotor.

Therefore, the damage scenario D3 is referred to a similar deterioration of three blades, which may be caused by continuous wear of the blades due to operation. The stiffness of the three blades was decreased in 15 % over a length of 2 m, corresponding to 5 % of the total length of the blade. The damage was located at around 33 % in chord length from the blade root, which is said to be the location more prone to damage (Ciang, Lee et al., 2008). The imposed variation of stiffness led to a decrease of -0.65 % of the 1 SS* and 2 SS* rotor vibration modes. It was also noticed that the imposed stiffness variation was not significantly reflected in the other modes. For that reason, only the rotor modes 1 SS* and 2 SS* were used to detect this damage scenario.

The variation of the natural frequencies of the vibration modes with the considered damage scenarios is resumed in Table 7.21. It is considered that the damage from each scenario occurred at the middle of Period 2. The artificial damage is thus introduced in the detected frequencies from the second part of Period 2 by reducing their values according to the values presented in Table 7.21.

Table 7.21 – Variation of the natural frequencies of the modes associated with the damage scenarios

	Δf [%]		
Modes	D1	D2	D3
1 SS	-0.20	-0.50	0.00
1 FA	-0.20	-0.50	0.00
1 SS*	0.00	0.00	-0.65
2 SS*	0.00	0.00	-0.65
2 FA	-0.40	-0.24	0.00
2 SS	-0.40	-0.24	0.00
3 SS*	0.00	0.00	-
4 FA	-	-	-

The methodology followed to assess the presence of damage in the wind turbine is based on the use of T^2 control charts, already introduced in section 7.2.2. This multivariate technique allows assessing the evolution of several vibration modes in the same chart. For the construction of these control charts, the residual error was used. As referred, the residual error is the difference between the identified frequency value of a vibration mode and its predicted value according to the defined SM 2 regression model, as illustrated in Figure 7.69.

The control charts obtained for an undamaged situation and the three damage scenarios are presented in Figure 7.76. In their construction, groups with 36 observations were considered (corresponding to a quarter of a day). It is seen that the damages are clearly detected in all situations. However, a different upper limit control of the chart from the one defined in equation (7.15) was used due to the large number of false alarms obtained with this limit. This situation is most likely due to the fact that

features considered do not respect all the assumptions adopted for the definition of the limits (Magalhães, Cunha et al., 2012). To overcome this limitation, a different limit was imposed. This limit is defined by considering that 95 % of the values from the training period are considered within the safety region.

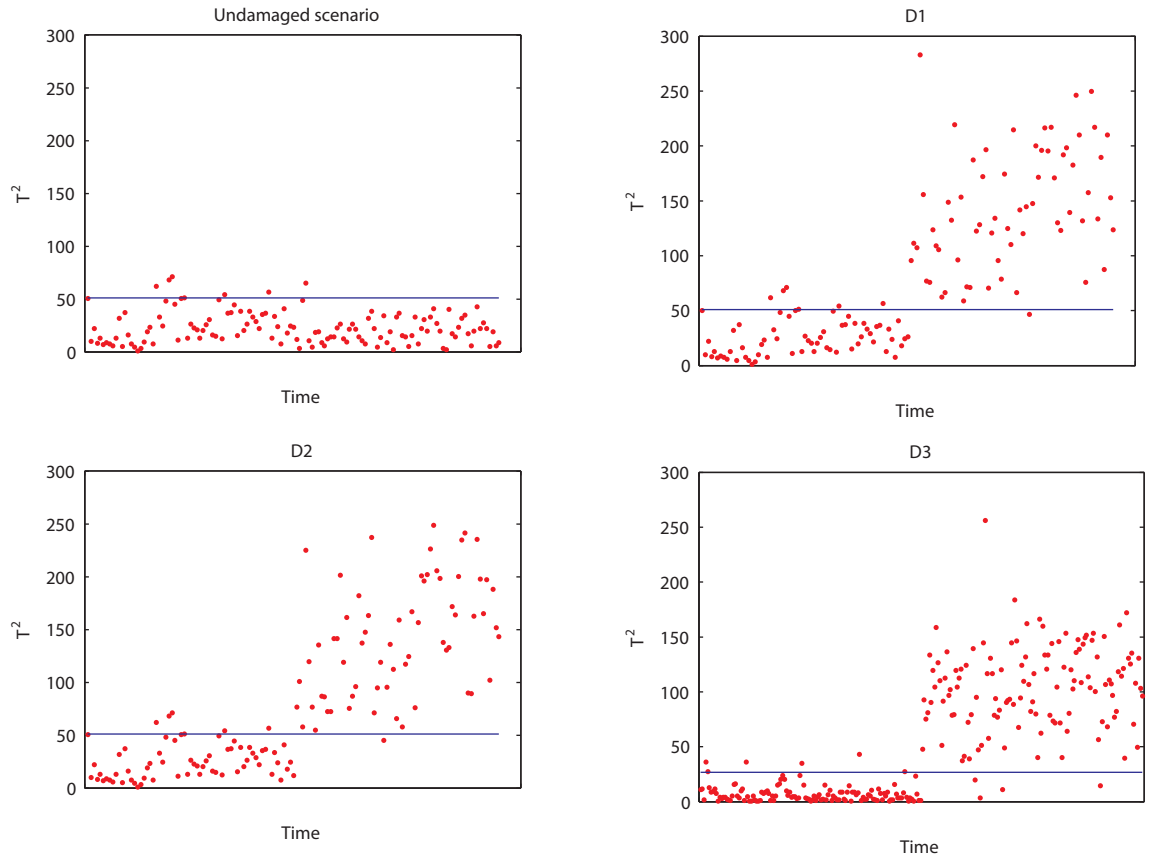

Figure 7.76 – T^2 control charts associated with a scenario where no damage is present and with the three defined damage scenarios

This is a very relevant result, since it demonstrates that quite small damages in the foundation (and, although with less accuracy, in the blades) can be detected with the developed monitoring methodology. In the case of scenario D1, it is relevant to note that the identified damage (0.075 $D_{Monopile}$) is considerably smaller than the recommended design value of 1.30 $D_{Monopile}$ (Det Norske Veritas (DNV), 2011).

It should be further referred that a longer monitoring period would even permit the detection of smaller frequency variations due to a better and more complete regression model and due to the possibility of using more observations to compute the T^2 control chart, leading to more robust results.

7.3.7 FATIGUE ASSESSMENT RESULTS

The characterization of the fatigue condition of the wind turbine support structure was performed according to the procedure introduced in section 6.4.1. Unfortunately, it was not possible to install, during the period of this thesis, additional sensors to quantify the quasi-static motion of the tower. Consequently, this work is only focused on the estimation of the dynamic component of fatigue damage.

The procedure is illustrated with 10 min. acceleration time series recorded during a period of strong wind conditions, with a mean wind speed of 20.9 m/s and maximum (instantaneous) speed of 35.9 m/s. During this period, the turbine operated at its rated rotor speed (around 16.5 rpm) and the blades pitch angle varied between 11.1º and 27.9º, in order to control the rotor torque. The acceleration time series collected by the dynamic monitoring system in the FA direction are presented in Figure 7.77.

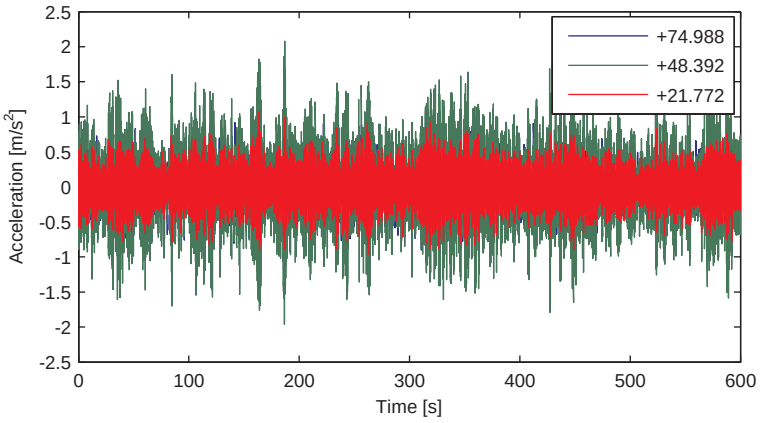

Figure 7.77 – Acceleration time series in the FA direction

Prior to the integration process, the acceleration time series were multiplied by a time window with the aim of softening the start and end of the time series as discussed in section 6.4.1.1. These initial and last parts are then disregarded in the integrated displacement time series. After an initial analysis of several setups, it was considered that the disregarded of the initial and last 30 seconds would guarantee a safety margin to avoid transient errors.

For the double integration process, the filter introduced in section 6.4.1.1 (Figure 6.12) was used. The constants of the filter (f_{c1} and f_{c2}) were set to only consider the dynamic component of the displacements.

A good solution to tune these two parameters would be possible with the temporary use of instrumentation to measure the stress condition of the tower at an arbitrary condition. Since it is possible to estimate the stress condition at any position of the support structure with the presented methodology, the results obtained with the temporary instrumentation would be compared with the ones estimated with the accelerometers in order to tune the parameters. Since it was not possible to install this instrumentation, a compromise between the amplification of possible low frequency errors and the loss of relevant dynamic component information was studied with the help of numerical tests performed with the HAWC2 code (Larsen and Hansen, 2007). As result, the constants f_{c1} and f_{c2} were defined as, respectively, 0.10 Hz and 0.15 Hz. In that sense, the analysis described in this section regarding the fatigue assessment of the Senvion MM82 wind turbine is focused on the validation of the

developed procedure considering only the dynamic component of the fatigue, and not on the estimation of the real fatigue condition of the structure.

Figure 7.78 shows the obtained displacements at the measurement levels in the FA direction. As expected, the displacements are higher at the top, in opposition to what was obtained with the acceleration time series (Figure 7.77). This result was expected since the displacements are mainly driven by the 1st pair of tower bending modes. In this figure, the transient initial and last parts are indicated by the vertical dashed lines and correspond to the referred 30 seconds in each part.

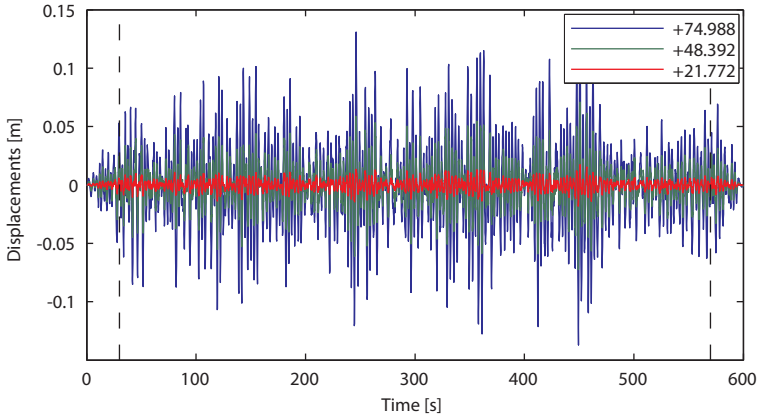

Figure 7.78 – Dynamic displacement time series in FA direction (the vertical dashed lines indicate the disregarded initial and last part)

Once the dynamic displacements along the turbine support structure are obtained, it is possible to estimate the dynamic component of the stress condition at any level of the tower. As an example, the bending stress at one point of the tower section at the foundation level was computed using the procedure based on the SSI-DATA identification algorithm described in section 6.4.1.1. The result is presented in Figure 7.79.

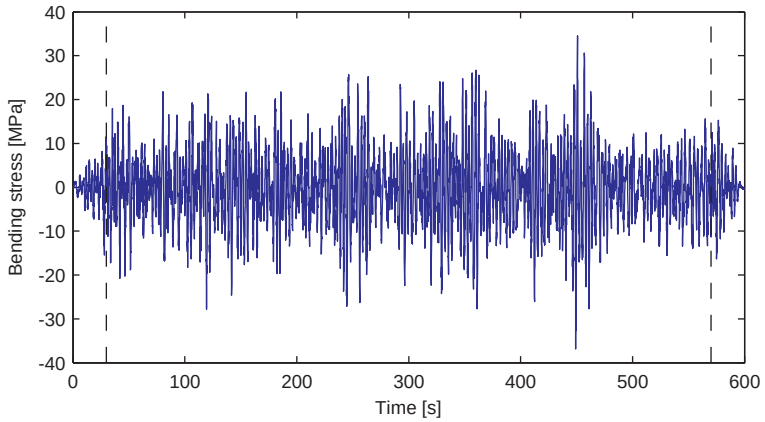

Figure 7.79 – Estimated dynamic bending stress at the foundation level due to motion in the FA direction (the vertical dashed lines indicate the disregarded initial and last part)

Lastly, the load cycles are counted with the Rainflow algorithm. The histogram with the number of bending stress cycles associated with different stress amplitudes is shown in Figure 7.80. The damage due to fatigue can then be assessed with the S-N curve defined for the detail under analysis.

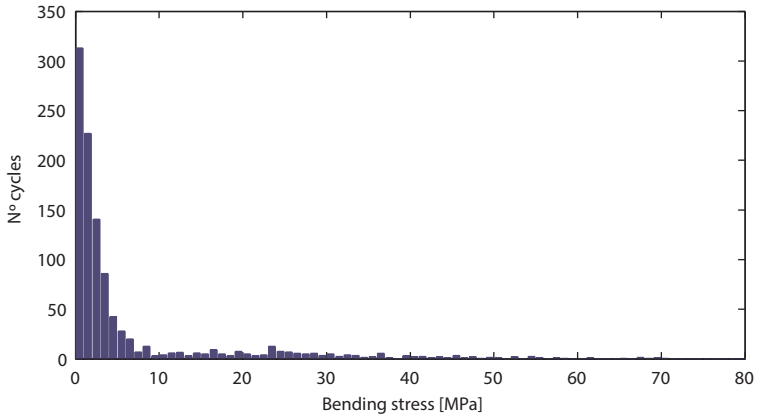

Figure 7.80 – Histogram with the number of bending stress cycles

Considering that sensors installed at the tower structure are capable of detecting the motion in both orthogonal directions, the stress due to bending in the SS direction can also be computed with this methodology. With the stress condition computed in both FA and SS directions, it is thus possible to estimate the bending stress condition at any point of the tower cross section. Initially, the bending moment vectors in the FA and SS directions are reoriented according to the original SCADA referential (N-S, E-W). This coordinate rotation, illustrated in Figure 7.81, depends on the yaw angle.

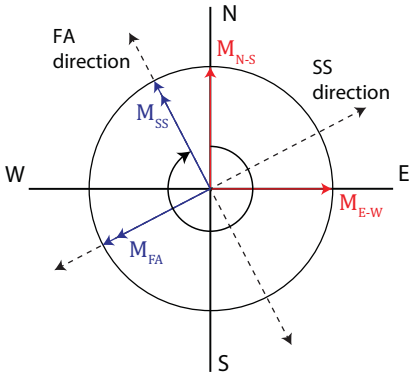

Figure 7.81 – Coordinate rotation from FA-SS referential to NS-EW referential

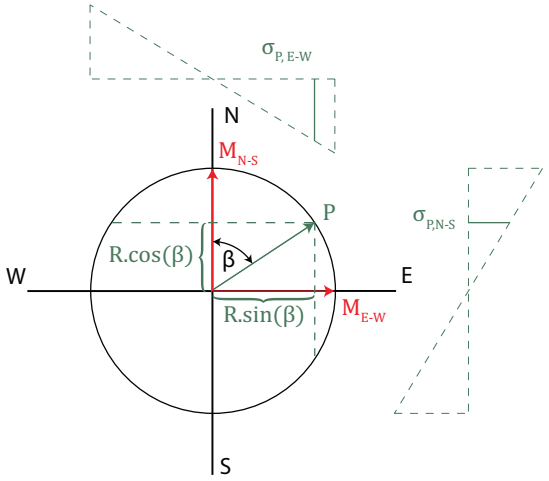

Figure 7.82 – Calculation of the bending stress at a generic point P

After defining the moment vectors in the original SCADA referential, it is then possible to estimate the stress condition at any point of the support structure cross section. This operation is illustrated in Figure 7.82 for a generic point P. The stress condition at the point P is then defined according to:

$$\sigma_P = \frac{M_{N-S}[R.\sin(\beta)]}{I} + \frac{M_{E-W}[R.\cos(\beta)]}{I} \tag{7.18}$$

with:

I	Area moment of inertia of the cross section
R	Radius of the cross section

A discretization of the cross section in 18 sectors was considered in order to assess the fatigue condition at the foundation level. The detail 71 from Eurocode 3 (European Comitee for Standardization (CEN), 2005) was used to study the welding-on flange connection between the tower and the foundation (Sørensen and Sørensen, 2011). The S-N curve corresponding to this detail was already introduced in Figure 6.7.

Alongside with the bending stress estimation, it is also of utmost importance to have confidence on the obtained results. Since the procedure estimates the acceleration time series as a sum of vibration modes/ harmonics, it is necessary to evaluate if the estimations do not underestimate the motion of the structure (due to a badly defined state-space model) or, on the other hand, overestimate the importance of some frequency content (due to numerical residues). In that sense, the residual error Δ_e from the forward innovation model (equation (5.80)) can be used to assess the quality of the estimated acceleration time series. However, in the context of stress estimation, in which a double integration is performed to estimate the displacement time series, the use of residual error as the only quality control parameter is not sufficient.

Figure 7.83 shows an example of an estimated acceleration time series obtained from the forward innovation model, using all the 7 installed sensors. The residual error Δ_e obtained is low (2 %), indicating that the estimation is good. The good agreement between the two signals is visually verified.

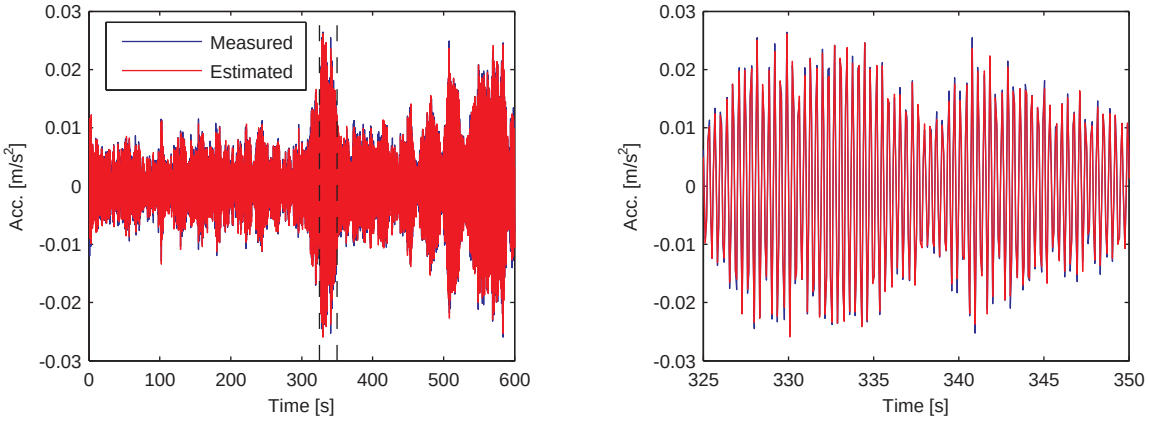

Figure 7.83 – Measured and estimated acceleration time series at the level +21.772 in the SS direction, considering all sensors as input for the forward innovation model (the right hand side figure shows a zoom of the time segment identified in the left hand side figure by the dashed lines)

However, looking at these results in the frequency domain, important errors in the lowest part of the frequency range are observed. Figure 7.84 shows the power spectral density of the measured and estimated acceleration time series illustrated in Figure 7.83 (the spectrum is averaged with segments of 1024 points in order to facilitate the explaination). From this figure, it is possible to attest that, although a good estimation is obtained around important resonance peaks (namely the 1st and 2nd tower bending modes, as well as the 3Ω and 6Ω harmonics), there is an erroneous increase of the amplitude of several peaks in the low part of the spectrum. Since the response is clearly dominated by the 2nd bending mode, these errors are almost imperceptible in time domain, as evidenced in Figure 7.83. This is the reason why the error Δ_e is low.

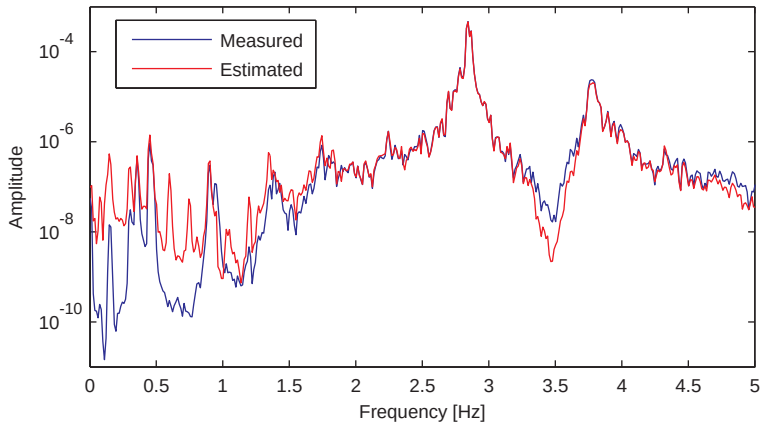

Figure 7.84 – Measured and estimated acceleration time series (in frequency domain) at the level +21.772 in the SS direction, considering all sensors as input for the forward innovation model

The main problem related to the bad estimation of the lower part of the spectrum occurs during the integration process to estimate the displacement time series. As referred in section 6.4.1.1, during this operation, the amplitude of vibrations related to the low frequencies is increased. Consequently, the displacement time series obtained from the measured and estimated acceleration will lead to considerably different results. Figure 7.85 illustrates the displacement time series obtained from the

measured and estimated acceleration signals represented in Figure 7.83. The erroneous majoration of the displacements obtained from the estimated signals is evident. Under these circunstancies, the estimation of the stress condition would naturally lead to erroneous results.

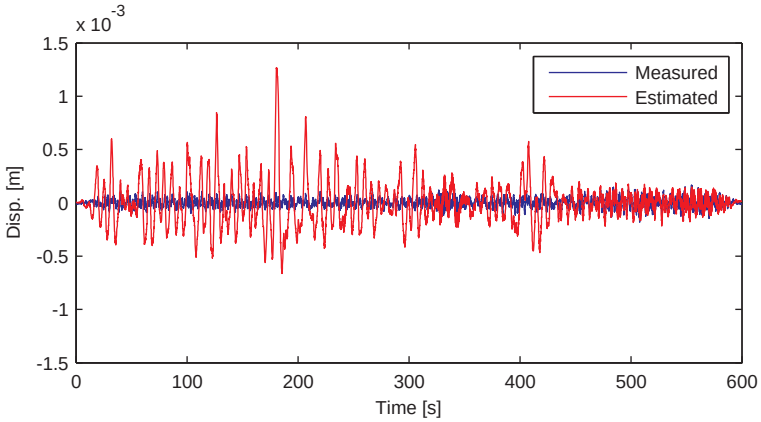

Figure 7.85 – Displacement time series obtained with the double integration process based on the measured and estimated acceleration signals

Due to possible occurrence of situations such as the one described, an additional quality index of the estimation is required to assess the adjustment in the lowest part of the spectrum. An index Δ_{freq} based on the relative difference of the energy countained in the lowest part of the frequency range of the estimated and measured acceleration signals was chosen. This index is defined as the ratio between the area defined by the difference of the spectra of the estimated and measured acceleration and the area defined by the spectrum of the measured acceleration signal (dark grey area in Figure 7.86). Only the frequency range between f_1 and f_2 is considered to compute this index. In the present work, these values were defined as 0.10 Hz (equal to f_{c1}) and 0.35 Hz, in order to evaluate the adjustment of the signal for the frequency range below the 1st tower bending mode.

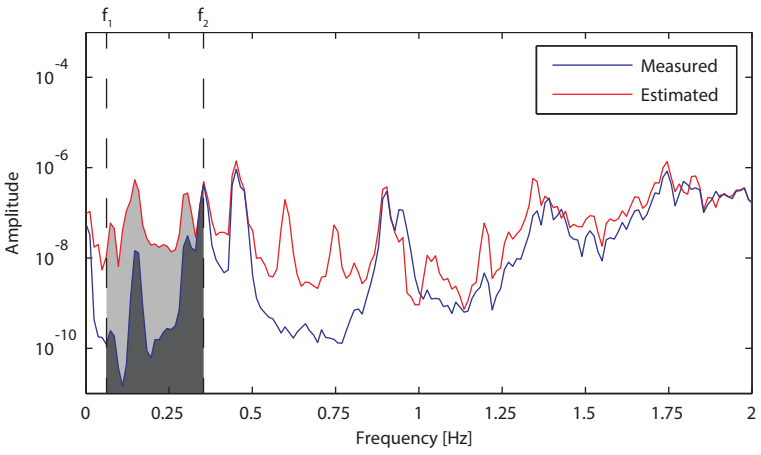

Figure 7.86 – Definition of the area between the spectra of the estimated and measured acceleration signals and the area from the measured signal

The results obtained for the quality indices using data sets collected during one year of monitoring were initially assessed. It was observed that the quality index Δ_e is not very restrictive. Figure 7.87 a)

shows the evolution of percentage of selected 10 min. time series events with the value adopted for Δ_e considering the results obtained with the three tested modal identification algorithms. It is seen that for the method based on the SSI-DATA algorithm almost all events are considered for an admissible level of 0.15. For the other algorithms, it is visible that the estimations are apparently not so good.

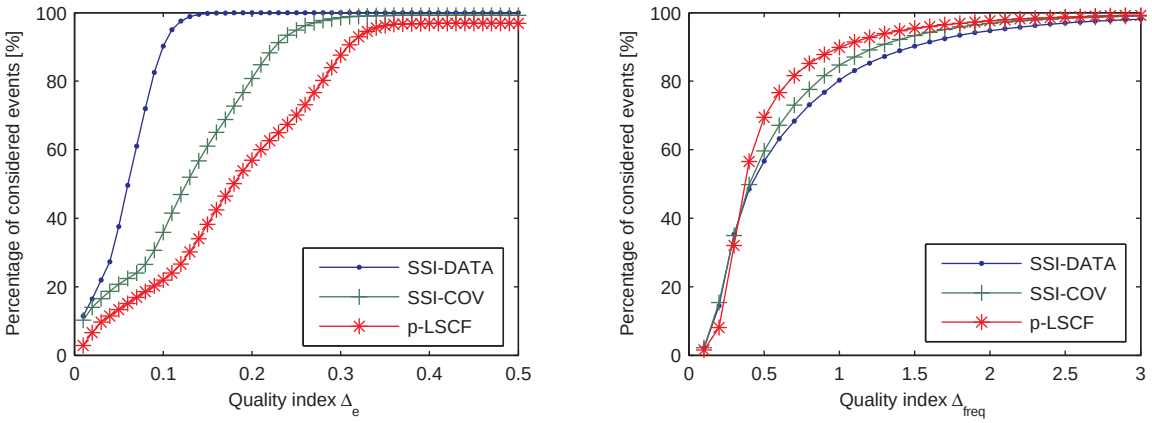

a) b)

Figure 7.87 – Percentage of considered events with the evolution of: a) Δ_e index; b) Δ_{freq} index

The values computed for the second quality index Δ_{freq}, referred to the quality of the adjust on the lowest frequency range of the spectrum, were also initially assessed. The percentage of events considered with the evolution of the Δ_{freq} index is presented in Figure 7.87 b). It was concluded that most results contain an increase of the energy in the frequency range considered for this index (0.1 – 0.35 Hz). It was thus noticed that the biggest problem associated with the bad estimation of this part of the spectrum is related to the unrealistic increase of the computed stress levels of the structure. It is interesting to note that the quality of the results provided by the alternative identification methods is inverse to the quantified by the index Δ_e. Nevertheless the difference is not very large.

Based on this preliminary analysis of the quality indices, a strategy was defined to accurately disregard bad estimations of the fatigue damage. In that sense, it was decided to use the Δ_e index to identify and dismiss events in which the defined forward innovation model was clearly not capable to estimate the acceleration time series as a sum of contributions of vibration modes/ harmonics. A value of Δ_e = 0.20 was thus chosen, since it considers almost all events and, at the same time, imposes a limit that guarantees the quality of the estimates. The maximum admissible value of the Δ_{freq} was defined to admit a maximum error Δ_{freq} = 0.90. With this value, a rate of considered events of more than 90 % was achieved when the combination of the best estimations obtained from the three algorithms is computed.

At this point, the fatigue damage estimation from the recorded acceleration time series can be computed. Figure 7.88 shows the evolution of accumulated damage calculated with the SSI-DATA algorithm at the welding-on flanged connection between the tower and the foundation using the S-N curve from the GL standard. From this figure, two periods of time with a rapid increase of damage are noticed. The first period corresponds to events occurred during November 2013, while the second occurs in February 2014. It is interesting to note that these two periods correspond to two long periods of consecutive data sets with high mean wind speeds.

It is also interesting to confirm that the most damaged sectors are the 100º-120º (and its symmetric 280º-300º) which is in accordance with the main wind direction of the wind (around 110º, see Figure 7.15).

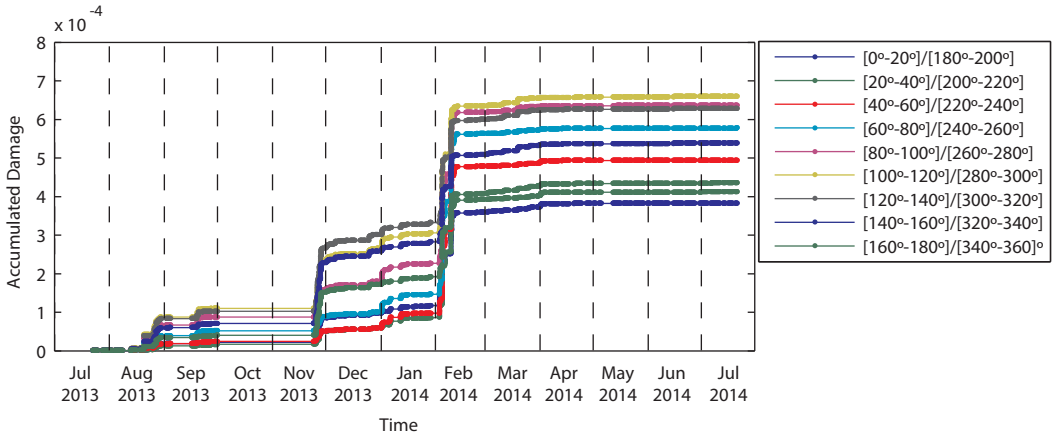

Figure 7.88 – Time history of the accumulated damage at the foundation level (with S/N curve from GL standard) using the methodology based on the SSI-DATA algorithm

A direct extrapolation of the accumulated damage to the expected life of the wind turbine (20 years) can be performed according to equation (7.16). The results obtained with the three methods are presented in Table 7.22. As expected, the values obtained with the S-N curve from the EC3 code are slightly lower due to the consideration of the threshold referred in section 6.3.2 (Figure 6.7).

Table 7.22 – Direct extrapolated accumulated damage at the end of the design life

	SSI-DATA	SSI-COV	p-LSCF
GL	0.0420	0.0422	0.0213
EC3	0.0319	0.0339	0.0195
Success rate [%]	76.8	64.0	46.7

The results obtained present very low values of accumulated damage. Nevertheless, some important aspects should be highlighted. Firstly, it should be noted that the estimated damage is only referred to the dynamic component of the bending stress. Large loading cycles from the quasi-static frequency regime, which might have important contributions to the fatigue damage of the structure are not considered in these results. Two additional causes for this low accumulated damage should be also referred. The location of the Senvion MM82 wind turbine is considered a low-turbulence site, which means that high amplitude stress variations are not expected to occur frequently. This aspect has a direct impact on the estimation of the fatigue life of the analysed structural detail, since it only depends on the measured amplitude of the stress cycles and not on the mean stress level. In addition, technical problems occurred at the beginning of October, preventing the operation of the dynamic monitoring system during this month and almost the entire month of November. Thus, considering the detected high rate of damage during the end of November, it is very likely the occurrence of important events

during this period that were not measured, which may have masked the real value of accumulated damage at the end of the monitoring period.

Considering the confidentiality usually associated with projects related to the measurement of real fatigue damage values, it is not easy to frame the obtained results. Nevertheless, the work presented in (Loraux and Brühwiler, 2015), related to the fatigue analysis of a wind turbine tower using strain gauges, highlights the conservatism of the current codes, based on a preliminary assessment of experimentally obtained accumulated fatigue damage. Although the results are not comparable, it is interesting to note that, even when the static, quasi-static and dynamic responses are taken into account, a considerably higher fatigue lifetime than the design value of 20 years is expected.

The direct extrapolated estimation of total accumulated damage due to the dynamic component of the bending stress shows a considerably variation, with values between 0.0420 and 0.0213 (using the S-N curve from the GL standard) and 0.0319 and 0.0195 (using the S-N curve from the EC3 standard). This discrepancy is mainly related to the different acceleration time series considered in each algorithm for fatigue estimation (due to the quality indices restrictions), leading to different results at the end. This situation is partially shown by the different success rate presented at the last line of the table. The methodology using the SSI-DATA presents a higher rate. These values are comprehensible since the original methodology is based on the SSI-DATA, while the other two are adaptations of the method. The methodology based on the p-LSCF presents the worst success rate probably because it requires the manipulation of the state-space matrices to remove the unstable poles.

One consequence of using different acceleration events to extrapolate the accumulated damage at the end of the expected fatigue life of the structure is that different wind loading conditions are considered. Figure 7.89 a) shows the number of events for each mean wind speed in the sector 100º - 120º (corresponding to the main wind incidence direction) during one year using the data recorded by the SCADA system. Alongside, Figure 7.89 b) presents the probability density function (PDF) of the same data. In the same figures, the distribution of the events considered in the fatigue estimation with each algorithm is also shown. It is seen that, while the events considered for the SSI-DATA algorithm seems to follow the wind speed distribution, the other two methods diverge considerably. The SSI-COV shows an increase in the occurrence of events in the low (lower than 7 m/s) and high wind speeds (higher than 15 m/s), while there is a notorious lack of events in the range 7 - 15 m/s. On the other hand, the events considered with the p-LSCF algorithm focus on the low wind speed region. These facts contribute to the discrepancy in the results presented in Table 7.22.

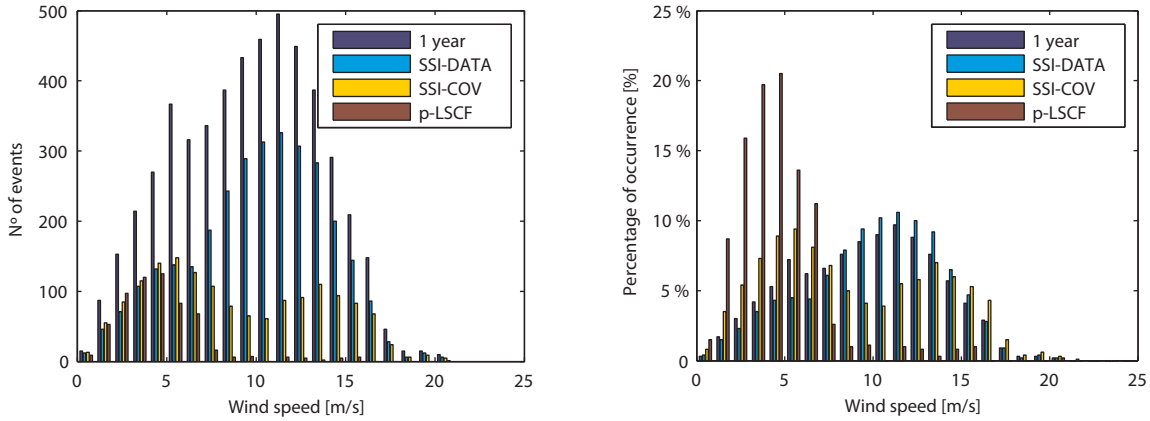

a) b)

Figure 7.89 – Histogram a) and probability density function b) of mean wind speed (in the sector 100º-120º) during one year according to the data recorded by the SCADA system and to the data considered for fatigue estimation with the three algorithms

A simple way to attest the quality of the results obtained with the three algorithms is the computation and comparison of damage estimated from the same acceleration time series events. In that sense, the results obtained with the SSI-DATA were considered as reference, since they consider more data sets, and only the events that were both considered for the other algorithms and the SSI-DATA were used to compute the estimated damage. The accumulated damage obtained with SSI-COV and p-LSCF algorithm is directly compared to the one computed with the SSI-DATA since they are related to the same acceleration events. Table 7.23 shows the results obtained with this study, presenting the deviation obtained relative to the reference method (SSI-DATA algorithm). As can be seen, the agreement is now much better, especially for the estimation based on the SSI-COV where an error lower than 8 % was achieved.

Table 7.23 – Deviation of accumulated damage of coincident events relative to the methodology based on SSI-DATA algorithm

	SSI-DATA	SSI-COV	p-LSCF
GL	-	+ 7.5 %	- 19.8 %
EC3	-	+ 7.8 %	- 20.6 %

The advantage of using different algorithms to estimate the fatigue damage for the same period of time is the ability to choose the best estimations obtained with each method for each acceleration time series event according to the quality indices. The results obtained for the direct extrapolated damage (according to the S-N curve from the GL and EC3 standards) using the best estimations from the three algorithms are shown in Table 7.24. It is visible the increase of the success rate to 91.0 %.

Table 7.24 – Estimation of accumulated damage at the end of design life considering a direct extrapolation and an adjusted extrapolation according to the PDF of the wind speed using the best estimations from the three algorithms

	Direct extrapolation	Adjusted to wind speed PDF
GL	0.0371	0.0357
EC3	0.0283	0.0271
Success rate [%]	91.0	

Another advantage of using different algorithms to estimate the fatigue damage for the same period of time is the possibility of consider more loading scenarios and, consequently, approximate the considered wind conditions to the actual distribution of wind conditions. This advantage is illustrated in Figure 7.90, where the PDF of the mean wind speed in sector 100º - 120º obtained with the data considered when the best estimations from the three algorithms were used is compared with the PDF defined with the data recorded by the SCADA system during one year. Both PDFs seem to be similar enough to allow an adjustment of the results obtained with the best estimations to follow the "real" distribution of wind speed (as introduced in section 7.2.2.1). In this case, it was only possible to quantify the damage accumulation associated with the mean wind speed of 10 min. period. The results of accumulated damage at the end of the design life after adjusting the loading scenarios according to the PDF of the mean wind speed are shown in Table 7.24.

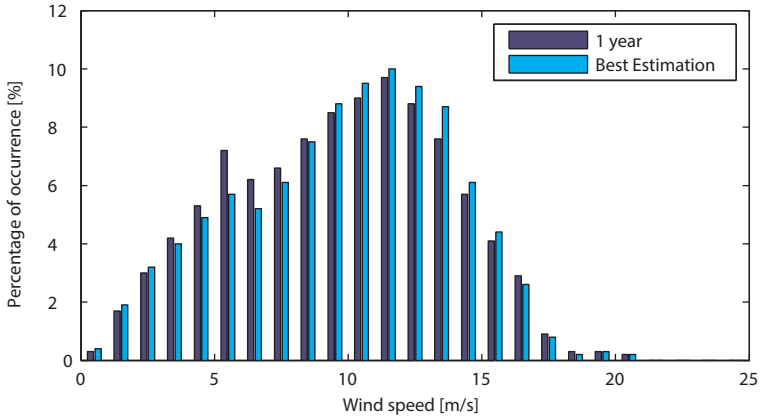

Figure 7.90 – Probability density function of mean wind speed (in the sector 100º-120º) during one year of data recorded by the SCADA system (1 year) and the events included in the best estimation obtained with the three algorithms

Naturally, the estimation of damage due to the dynamic component of fatigue would improve if more data from the monitoring system was available or, in case it is not possible, if a characterization of the wind conditions over a longer period was known.

7.3.8 Optimization of the Monitoring System

The installation of the dynamic monitoring system is desirable if it adds value to the investment. As referred in section 6.4.2, nowadays wind turbines are already equipped with a bi-directional accelerometer at the nacelle level as part of its own control system. Thus, it would be interesting to assess the level of accuracy that can be achieved with a dynamic monitoring system with a reduced

number of sensors, both for modal tracking and fatigue assessment. At the most extreme solution, it would be interesting to only use the top sensor as part of the monitoring system.

This section introduces the results obtained with the two modules of the monitoring system using three different solutions of sensors layout. The first solution uses only one biaxial sensor at the top level (+74.988 m) to perform both modal tracking (for damage detection) and fatigue analysis. This represents the aforementioned most interesting solution from the economic point of view. The second proposed solution uses only one biaxial sensor at the +48.392 m level of measurement (around 2/3 of the tower height). Lastly, the third solution is based on the use of two biaxial sensor placed at +74.988 m and at +48.392 m levels.

7.3.8.1 Layout 1 (+74.988 m level)

The option based on the use of only the top level of measurement (sensors S8 and S9) is the most interesting solution. Since wind turbines are nowadays equipped with a bi-directional accelerometer sensor at this position, the use of this sensor for damage detection and fatigue assessment of the support structure would represent an important benefit without any relevant investment.

Although interesting from an optimization point of view, this solution presents an important drawback: due to the very low modal amplitude of the 2nd pair of support structure bending modes at this level (2 FA and 2 SS modes from Figure 7.40), it is not possible to accurately identify and track these two modes. This handicap has consequences for both modules of the dynamic monitoring system. In the context of damage detection, this optimization solution prevents the tracking of the most interesting indicators of foundation damage. This situation will necessarily influence the degree of precision in the detection of small damages at the foundation level. Moreover, it is not possible to consider these two modes for fatigue assessment, since it is very difficult (or even impossible) to use a very small modal amplitude as a reference value to scale a mode shape.

Modal Tracking and Damage Detection

The acceleration data recorded by the sensors at the top level was used to perform the tracking of the vibration modes. The strategy presented in section 7.3.6.2 was followed to process to the recorded data during the monitored period. The same input parameters for the three modal identification algorithms were used and the same criteria to assess the stability of the poles (Table 7.5) were followed. However, instead of a minimum MAC value of 0.80 in order to consider a cluster of poles to the tracking procedure, a minimum value of 0.50 was defined. This value was chosen due to the poor definition that is achieved with only one bi-directional sensor (representing only one modal amplitude per direction) and corresponds to a differentiation between modes in the FA and SS direction.

Figure 7.91 illustrates the Campbell diagram obtained after the tracking procedure. From this figure, it is visible that, as expected, the 2 FA and 2 SS modes are badly estimated and, for that reason, should be disregarded. On the other hand, it is interesting to note that the influence of the harmonics is still disregarded after the tracking procedure. This fact is due to the complex nature of the operational deflection shape exhibited by poles referred to the harmonics, in contrast to the more real nature of the vibration modes.

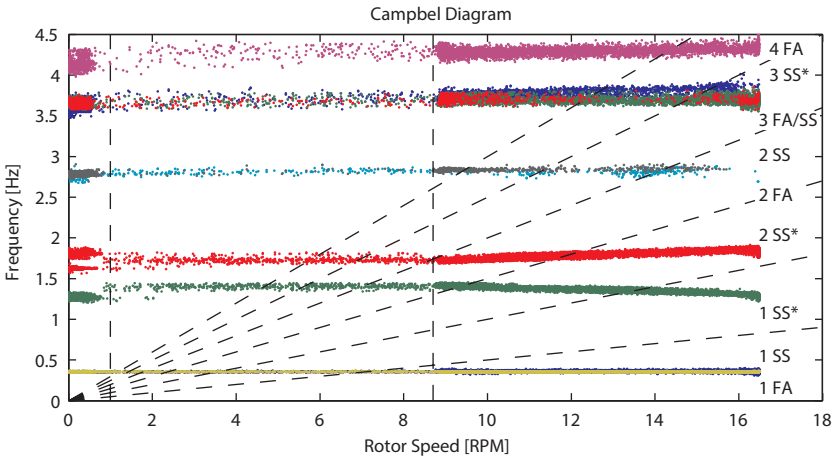

Figure 7.91 – Campbell diagram with the tracked vibration modes with Layout 1 (SSI-COV algorithm)

The statistics related to the success in the identification of the 9 vibration modes are introduced in Table 7.25. Comparing these results with the ones obtained when all sensors are used (Tables 7.6 to 7.8), it is concluded that the success rate of the first 4 modes have increased when only the top sensors are considered. Although this might seem a contradiction, it is explained by the lower MAC condition imposed to consider a cluster of poles. With this MAC condition, it is only possible to distinguish between FA and SS modes which are, in fact, the only information that can be extracted from the mode shapes with this sensors layout. The coefficient of variation of the frequency values of these modes does not present an important increase relative to the solution using all sensors, which is a good indicator for their use in damage assessment.

As regards the last 3 modes, the success in their identification was rather low and, for that reason, these modes were not considered for damage detection.

Table 7.25 – Success rate and coefficient of variation obtained with the identification algorithms (with Layout 1)

Mode	SSI-COV		SSI-DATA		p-LSCF	
	Success Rate [%]	$f_{coef.\ var.}$	Success Rate [%]	$f_{coef.\ var.}$	Success Rate [%]	$f_{coef.\ var.}$
1 SS	93.8	0.005	95.5	0.005	86.3	0.005
1 FA	86.6	0.022	87.3	0.019	43.3	0.018
1 SS*	90.5	0.037	92.0	0.037	56.5	0.035
2 SS*	96.9	0.031	96.9	0.031	93.6	0.029
2 FA	-	-	-	-	-	-
2 SS	-	-	-	-	-	-
3 FA/ 3SS	31.7	0.012	39.7	0.018	42.8	0.012
3 SS*	19.3	0.022	29.6	0.019	30.6	0.019
4 FA	27.5	0.017	56.7	0.019	84.8	0.019

The ability of the dynamic monitoring system to detect damage was then assessed using the first pair of bending modes (1 FA and 1 SS) and the rotor blades modes 1 SS* and 2 SS*. Initially, the same

damage scenarios shown in Table 7.21 (for a sensor layout with all sensors) were tested. It was verified that the damage scenario D1, related to the scour problems in an offshore wind turbine, was not properly detected. This scenario is especially relevant to the second pair of bending modes which are not detected with this solution. For that reason, a new scenario D1* related to scour damage was defined, reflecting the minimum detectable frequency variation of the first pair of modes. It was concluded that, in order to be detectable, the scenario D1* would have to imply a frequency variation of -0.50 % of the first pair of support structure bending modes (an increase of 2.5 times when compared to the original D1 scenario). In terms of scour damage, the new damage scenario D1* represents a depth of 0.162 times the base diameter of the monopile, i. e., a depth of 0.70 m and 0.82 m if the Senvion MM82 tower base and the Vestas V90 monopile are used as reference, respectively. Although this value is more than twice the value achieved when all sensors are used, it still represents a very early state of damage, being considerably lower than the recommended design value of 1.30.*D* (Det Norske Veritas (DNV), 2011).

The second damage scenario D2, reproducing a frequency variation 5 times smaller than the one described in a test of damaged onshore wind turbines (Pelayo, López-Aenlle et al., 2011), was also analysed and it was concluded that, even with this layout solution, it would be detected. In fact, the variation imposed by this damage scenario for the first pair of tower bending modes is similar to the one observed in the scenario D1*.

The last damage scenario (D3) is related to blade damage. It was concluded that, for the same imposed stiffness variation described in section 7.3.6.6, the damage is still detected with this layout solution.

Table 7.26 – Variation of the natural frequencies of the tracked modes associated with the damage scenarios

	Δf [%]		
Modes	D1*	D2	D3
1 SS	-0.50	-0.50	0.00
1 FA	-0.50	-0.50	0.00
1 SS*	0.00	0.00	-0.65
2 SS*	0.00	0.00	-0.65
2 FA	-	-	-
2 SS	-	-	-
3 SS*	-	-	-
4 FA	-	-	-

Figure 7.92 introduces the control charts obtained for the referred damage scenarios with Layout 1. As can be seen, the damage is easily detected which attest the feasibility of this solution. Although some accuracy was lost in the damage scenario D1, it is seen that it provides a good solution for detection of damage at an early stage.

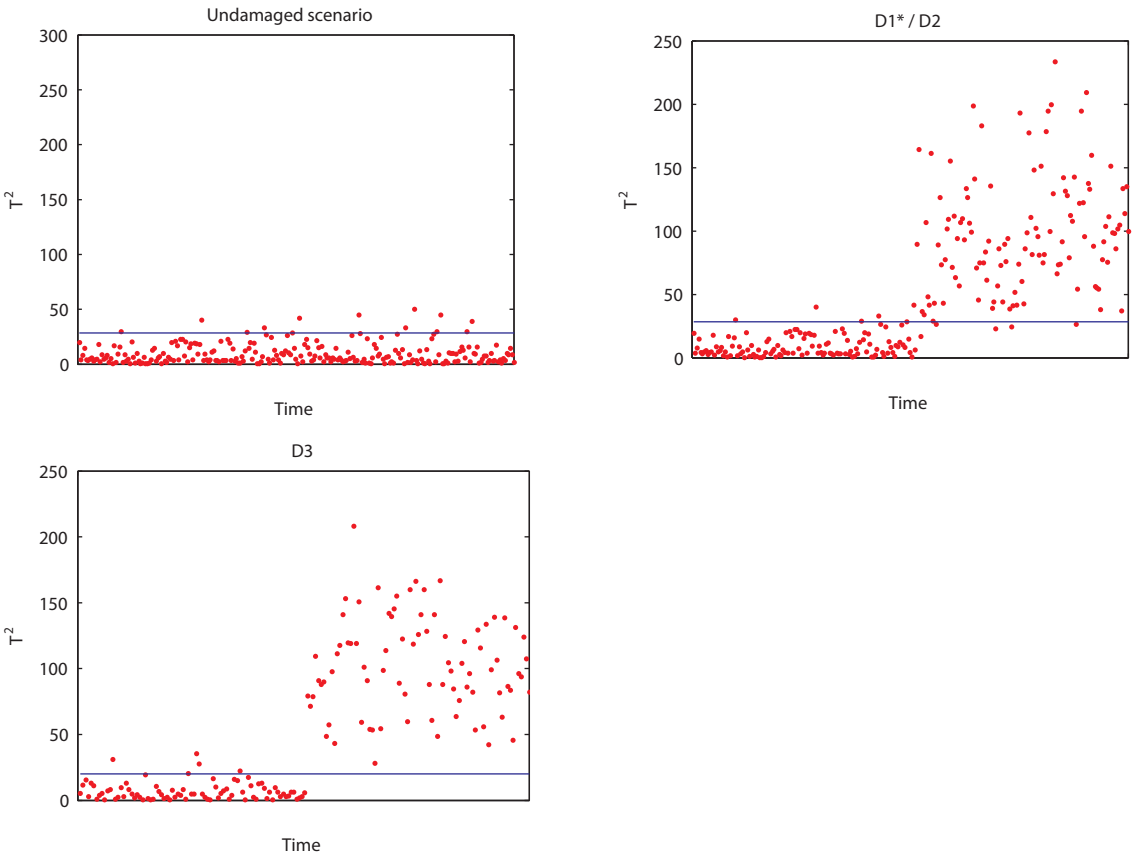

Figure 7.92 – T^2 control charts associated with a scenario where no damage is present and with the three defined damage scenarios (Layout 1)

Fatigue Results

The estimation of fatigue damage using a single level of measurement is an interesting application for the methodology introduced with the virtual sensors in section 6.4.2. With this methodology, it is possible to estimate the response of the wind turbine support structure at any point of the structure, using only a ("well positioned") single reference measurement point. In the case of the Layout 1, this reference point is the top measurement level. However, as was previously referred, this measurement position cannot be considered as "well positioned" since it coincides with a level of very low modal amplitude of an important vibration mode. Thus, it is not possible to accurately estimate the mode shape of this mode. In that sense, it was decided to despise all vibration modes and harmonics with a frequency value higher than 2 Hz. With this imposition, not only the second pair of bending modes is disregarded, but also some integer multiples of the harmonics are avoided since their operational deflection shapes also present a very low modal amplitude at the top of the tower.

The importance of the second pair of tower bending modes in the context of the dynamic behaviour of the wind turbine structure was already described in section 7.3.6.4. It is thus expected that, using this sensor layout, the estimation of the acceleration at the middle and lower part of the tower will be underestimated. Figure 7.93 illustrates this problem, using the acceleration time series collected by the S8 and S9 sensors during a production period (rotor speed = 12.4 rpm). The acceleration signals were then processed by the methodology based on the p-LSCF algorithm. The top figures compare the

original signal recorded by the sensor in the FA direction with the estimated signal as a sum of modes/ harmonics at the measured level in time and frequency domain. On the other hand, the plots at the middle and bottom of Figure 7.93 are referred to the estimations of the acceleration at unmeasured levels. Taking advantage of the non-used sensors (at levels +21.722 m and +48.392 m), the estimated acceleration time series at unmeasured locations are compared with the real measured time series.

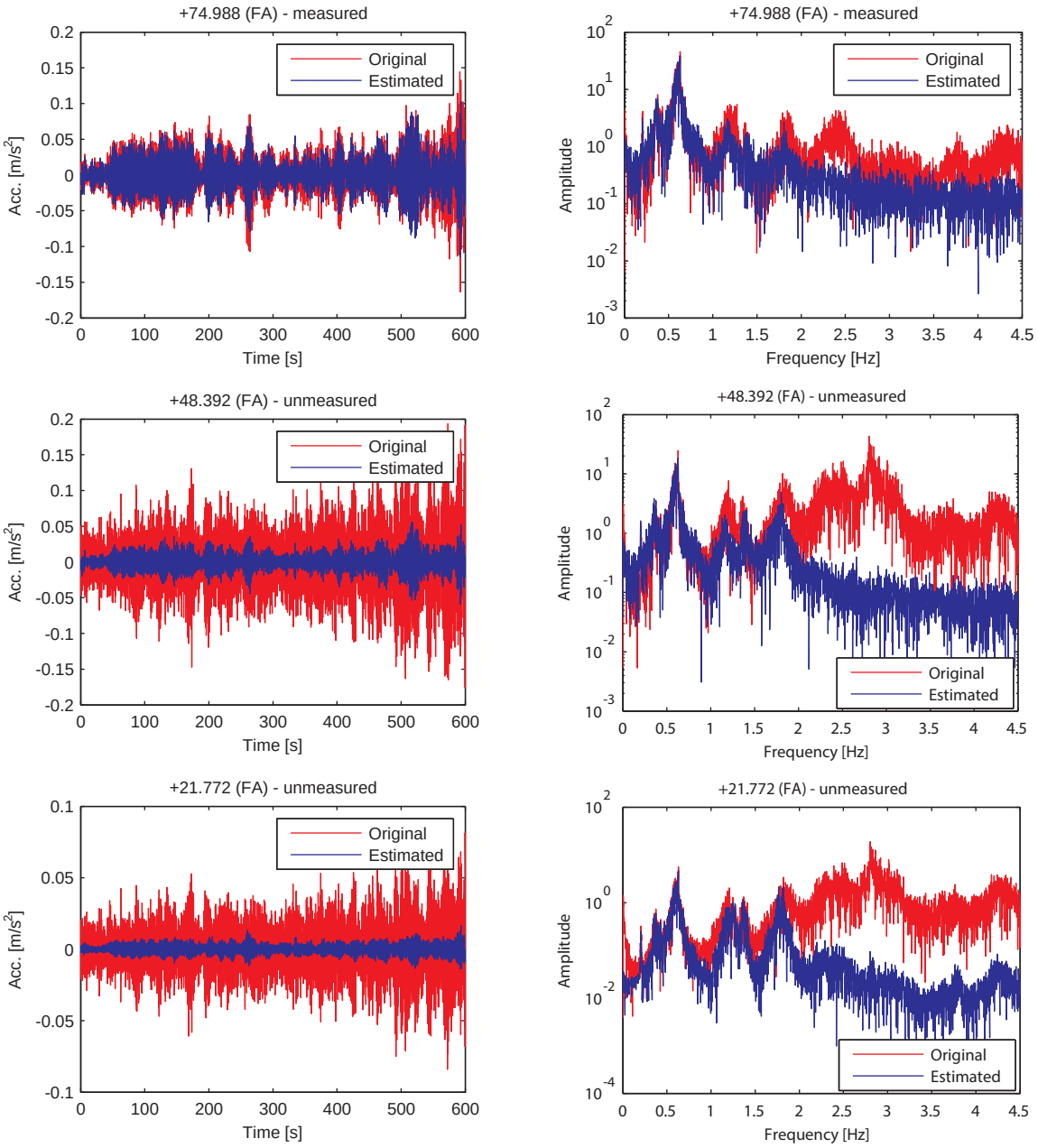

Figure 7.93 – Original and estimated acceleration time series at the measured level (+74.988 m) and unmeasured levels (+48.392 m and +21.772 m) in the FA direction

The observation of the plots in Figure 7.93 clearly shows that, as expected, the disregard of the energy contribution from the spectrum for frequency values higher than 2 Hz leads to an important underestimation of the acceleration at the lowest 2/3 of the tower. Nevertheless, it is seen that, for the

considered frequency range, the agreement between the estimated and the real acceleration signal is quite good. Even the contribution of the 3Ω harmonic (represented by the large peak around 0.62 Hz), which requires the estimation of its operational deflection shape, shows a good agreement.

The processing for fatigue damage estimation was then applied to the estimated acceleration signals. In order to illustrate the quality of the results obtained with this layout configuration, the dynamic component of the bending stress from a 10 min. period acceleration event at the foundation level was computed. The results were compared with the stress estimation obtained with the methodology based on the SSI-DATA considering the three levels of measurement, since it is considered the most accurate of the implemented procedures. The bending stress computed with the two procedures is shown in Figure 7.94. It is visible that the bending stress is underestimated mostly due to the non-consideration of the energy of the spectrum for frequency values higher than 2 Hz. Computing the damage associated with the two estimations (using the S-N curve from the GL standard), it is concluded that the value obtained with the procedure based on the p-LSCF with Layout 1 is 3.2 times lower than the value achieved with the SSI-DATA methodology using all sensors.

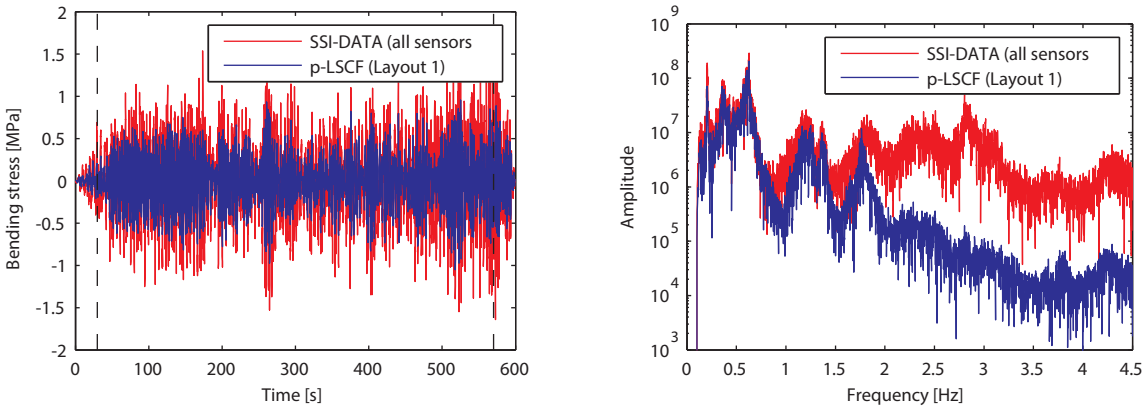

Figure 7.94 – Estimated dynamic bending stress at the foundation level due to motion in the FA direction (the vertical dashed lines indicate the disregarded initial and last part)

The same quality indices introduced in section 7.3.7 (Δ_e and Δ_{freq}) were used to despise erroneous estimations of fatigue damage. Naturally, these indices are only referred to the results associated with the considered S8 and S9 sensors. Figure 7.95 illustrates the evolution of percentage of acceleration events with the increase of the indices. Comparing these results with the ones presented in Figure 7.87, it is visible with the index Δ_e that the errors associated with the quality of estimation of the acceleration time series are higher. Qualitatively, it is seen that the procedure based on the SSI-DATA algorithm shows the best results, followed by the SSI-COV and, lastly, the p-LSCF, just like when all sensors were used. In relation to the index Δ_{freq}, the p-LSCF algorithm shows, again, the best results. However, with this sensor layout solution, the difference to the other methods is higher than when all sensors are used.

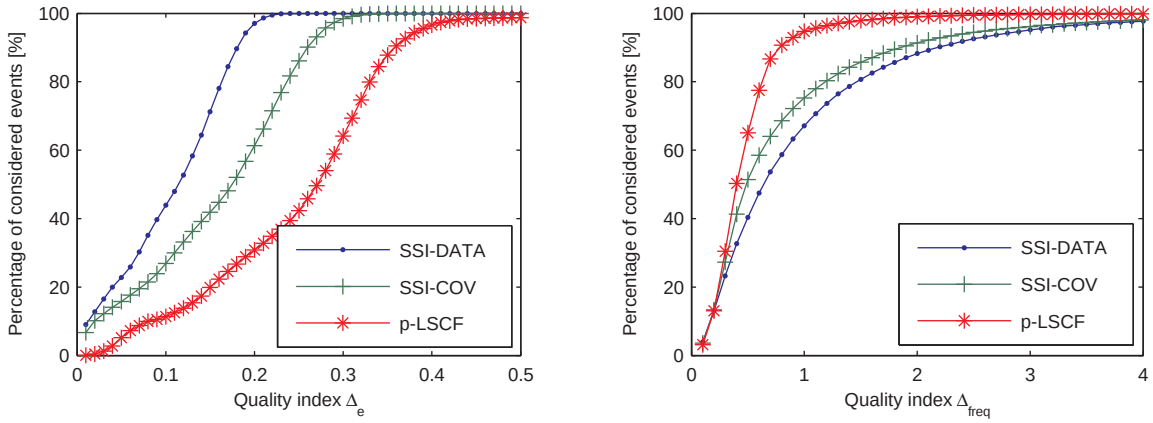

a) b)

Figure 7.95 – Percentage of considered events with Layout 1 with the evolution of: a) Δ_e index; b) Δ_{freq} index

As referred in section 7.3.7, the comparison of the direct extrapolated damage obtained with each methodology does not lead to a correct estimation of the quality of the results since it compares estimations of damage from different events. It is visible in the probability density function of Figure 7.96 a) that the considered events for each methodology differ considerably from each other.

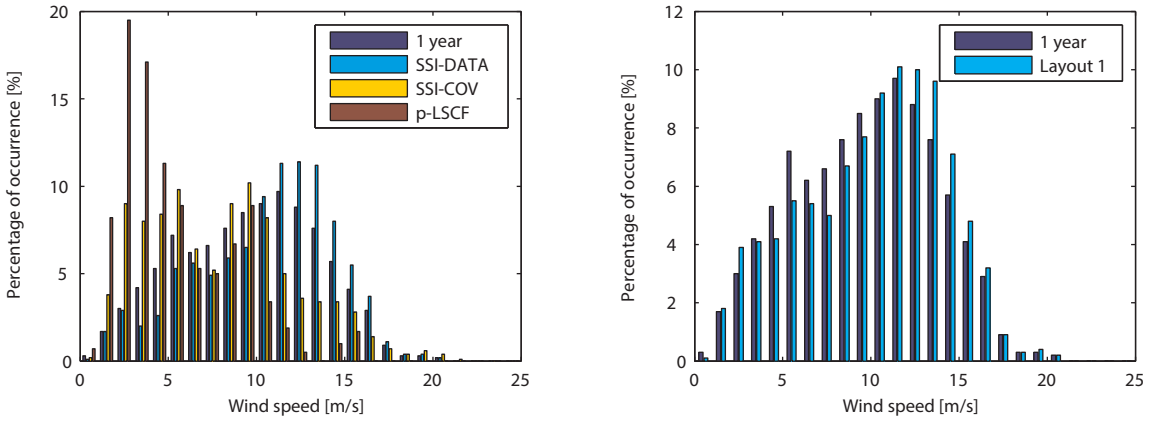

a) b)

Figure 7.96 – Probability density function of wind speed (in the sector 100º-120º) recorded by the SCADA system and from the data considered for fatigue estimation with Layout 1 with: a) the thee algorithms; b) best estimations from the thee algorithms

Thus, the estimated damage obtained with each methodology was compared with the damage estimated with the SSI-DATA using all sensors (considered the reference methodology) for the same events. The deviations obtained with the three methodologies are presented in Table 7.27.

Table 7.27 – Deviation of accumulated damage of coincident events between results with Layout 1 and the methodology based on SSI-DATA algorithm using all sensors

	SSI-DATA (All sensors)	SSI-DATA	SSI-COV	p-LSCF
GL	-	-67.4 %	-69.3	-41.2 %
EC3	-	-68.9 %	-71.1	-42.0 %
Success rate [%]	76.8	60.7	37.4	26.7

From the results, it is evident that the damage estimations with Layout 1 were not very good. The damage obtained with the three methodologies is clearly underestimated. Also the success rate achieved is low, with only one methodology (based on the SSI-DATA) showing a rate higher than 50 %.

Lastly, the fatigue damage using the best estimations from the three algorithms was computed. With this estimation, the distribution of considered wind speed events is close to the distribution obtained with the SCADA data (Figure 7.96 b)). The results are introduced in Table 7.28, where they are compared to the ones obtained with the best estimation using all sensors. Again, the values are considerably underestimated.

Table 7.28 – Estimation of accumulated damage at the end of design life considering an adjusted extrapolation according to the PDF of the wind speed using the best estimations from the three algorithms

	All sensors	Layout 1	Error
GL	0.0371	0.015	-57.8 %
EC3	0.0283	0.013	-52.4 %
Success rate [%]	91.0	79.4	-

7.3.8.2 Layout 2 (+48.392 m level)

Layout 2 represents an optimization of Layout 1. While the use of the top level as single level of measurement showed that it is not possible to consider the 2nd pair of bending modes, Layout 2 optimizes the selection of the single level of measurement. It was decided to use the measurement level at around 2/3 of the tower height (+48.392 m), since it (theoretically) enables the identification of all the important vibration modes. Looking to Figure 7.40, it is visible that none mode shape presents a reduced modal amplitude at this level.

Modal Tracking and Damage Detection

The same procedure described in section 7.3.6.2 was followed using the acceleration data collected by sensors S6 and S7 (at level +48.392 m). Just like in the case of Layout 1, a minimum MAC value of 0.50 was imposed during the modal tracking in order to distinguish between FA and SS modes. The Campbell diagram defined by the results obtained with the modal tracking procedure based on the p-LSCF algorithm is presented in Figure 7.97. From this figure, it is visible the good quality of the identification of the second pair of tower bending modes, confirming the suitability of the measurement location. On the other hand, it is visible that the 15Ω harmonic hinders the identification

of the 3 SS* mode. In fact, some clusters referred to this harmonic are misidentified as being from this mode. As for the other vibration modes, no further erroneous modal identifications were detected.

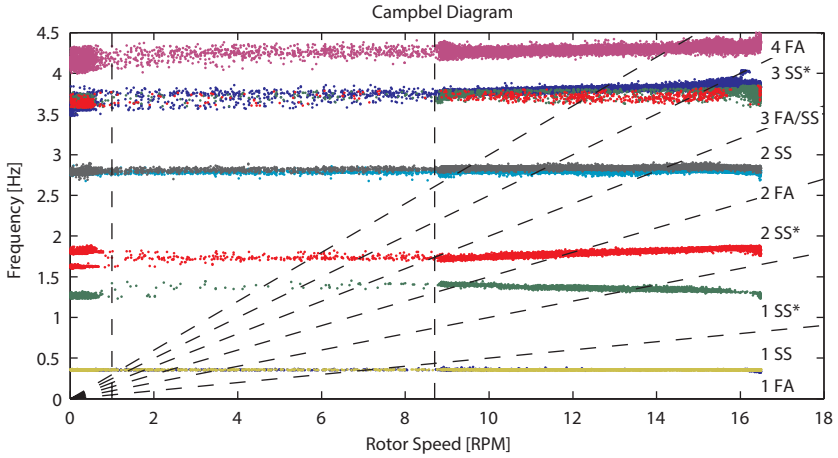

Figure 7.97 – Campbell diagram with the tracked vibration modes with Layout 2 (p-LSCF algorithm)

The success rate in the identification of the 9 vibration modes is summarized in Table 7.29. It is concluded that the results are good for the 1 SS, 1 SS*, 2 SS*, 2 FA and 2 SS modes, with high rates of success in the tracking process. On the other hand, the identification of the 1 FA presents a very low success rate, especially for the p-LSCF.

Table 7.29 – Success rate and coefficient of variation obtained with the identification algorithms (with Layout 2)

Mode	SSI-COV		SSI-DATA		p-LSCF	
	Success Rate [%]	$f_{coef.\ var.}$	Success Rate [%]	$f_{coef.\ var.}$	Success Rate [%]	$f_{coef.\ var.}$
1 SS	90.0	0.005	94.8	0.005	64.6	0.005
1 FA	46.0	0.018	61.0	0.019	18.6	0.016
1 SS*	48.7	0.040	84.7	0.037	29.6	0.034
2 SS*	84.6	0.031	93.4	0.031	72.5	0.029
2 FA	90.6	0.009	92.1	0.009	90.3	0.006
2 SS	73.5	0.012	83.3	0.011	72.8	0.010
3 FA/ 3SS	7.2	0.017	12.2	0.016	18.4	0.016
3 SS*	55.2	0.019	61.6	0.021	63.9	0.018
4 FA	30.6	0.018	76.2	0.018	96.2	0.018

After the modal tracking, the environmental and operational effects were removed from the frequency values, using a multivariate analysis (similar to the procedure described in section 7.3.6.5). Thus, using the frequency values as damage indicators, the three damage scenarios presented in section 7.3.6.6 (considering the dynamic monitoring system with three levels of measurement) were tested (see Table 7.21).

The control charts obtained are shown in Figure 7.98. It is evident that the three damage scenarios are well identified. Notwithstanding, the detection of damage referred to scenario D1 is not as clear as when all sensors are used.

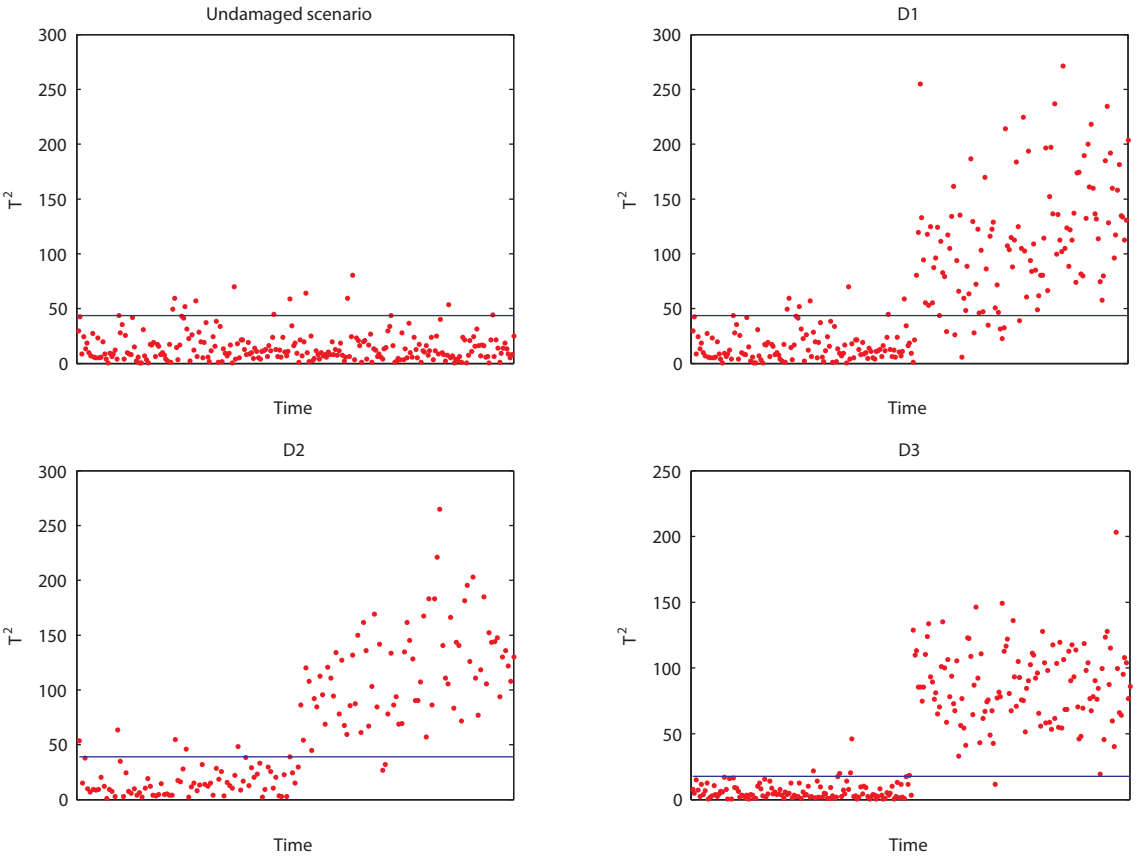

Figure 7.98 – T^2 control charts associated with a scenario where no damage is present and with the three defined damage scenarios (Layout 2)

Fatigue Results

Considering the position of the selected measurement level, it is expected that the problems noticed during the estimation of the acceleration time series with Layout 1 would disappear with this solution. In that sense, the frequency cut of 2 Hz defined with the Layout 1 was not imposed.

An example of the estimation of the acceleration time series obtained during production regimes (with a mean rotor speed of 11.7 RPM) in introduced in Figure 7.99. In this figure, the estimation of the acceleration at the measured level (+48.392 m) is presented alongside with the estimations at two unmeasured levels. Again, the +74.988 m and +21.772 m levels were selected in order to be possible to compare the estimations with the real acceleration time series. In this example, the methodology based on the SSI-COV algorithm was used. The very good agreement of the estimations at the unmeasured spots is notorious.

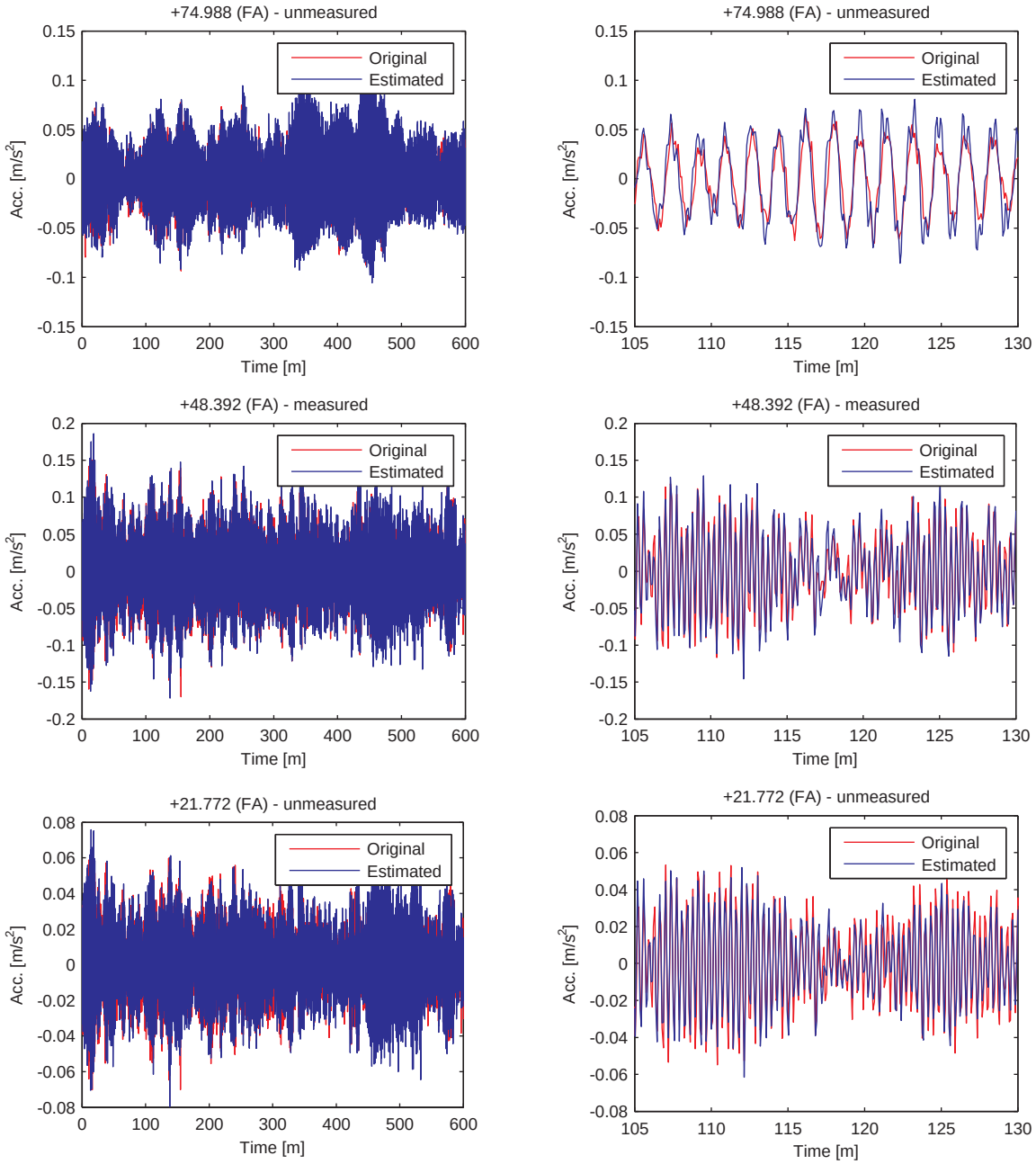

Figure 7.99 – Original and estimated acceleration time series at the measured level (+48.392 m) and unmeasured levels (+74.988 m and +21.772 m) in the FA direction

Naturally, the same quality indices were used to discharge erroneous estimations. It is noted that, qualitatively, the results are similar to the ones obtained with Layout 1. Nevertheless, there is an important improvement in the index Δ_{freq} for the methodology based on the SSI-COV algorithm.

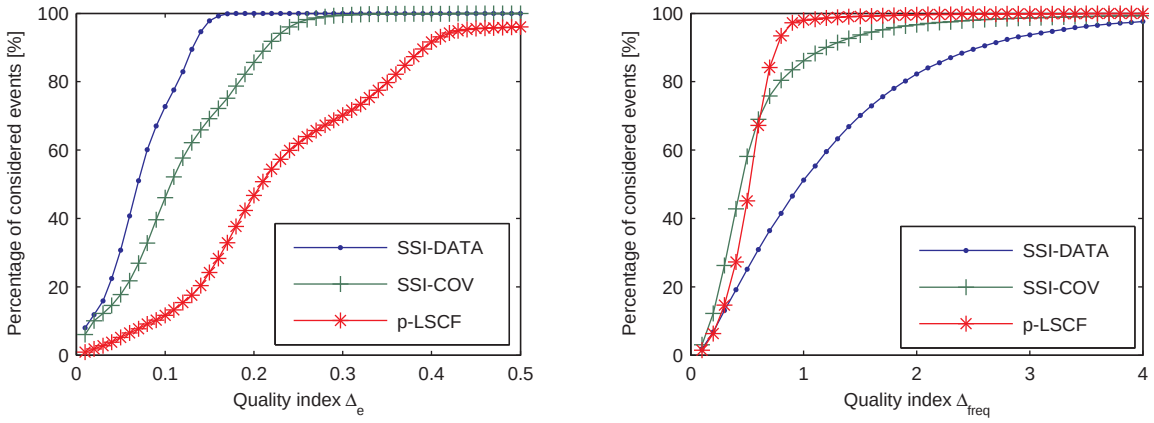

a) b)

Figure 7.100 – Percentage of considered events with Layout 2 with the evolution of: a) Δ_e index; b) Δ_{freq} index

The considered events for each methodology are again not enough to independently reproduce the density function of the wind speed, as seen in Figure 7.101 a). Thus, the same strategy previously followed to compare only the coincident events between the reference results (methodology based on SSI-DATA, using all sensors) and the various methods using Layout 2 was followed. The results are summarized in Table 7.30.

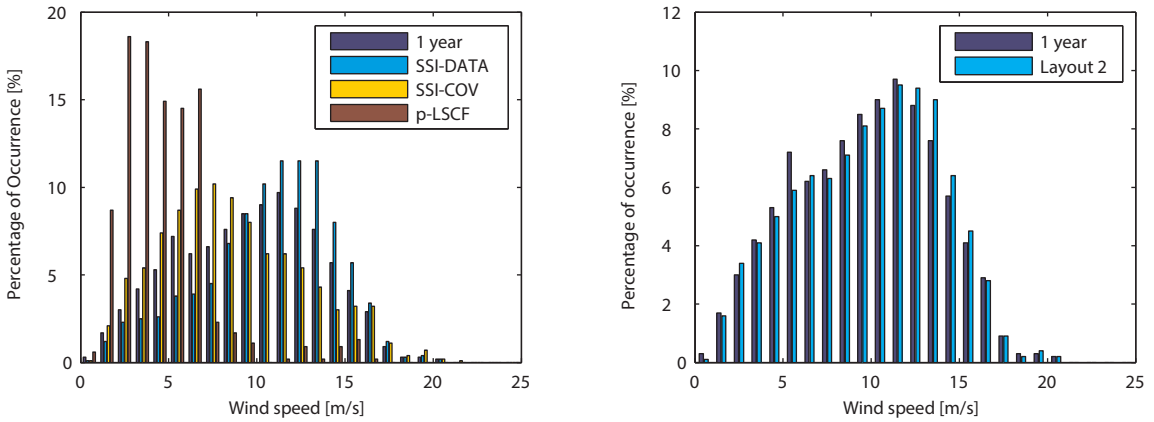

a) b)

Figure 7.101 – Probability density function of wind speed (in the sector 100º-120º) recorded by the SCADA system and from the data considered for fatigue estimation with Layout 2 with: a) the thee algorithms; b) best estimations from the thee algorithms

The results obtained confirm the good premise indicated by the quality of the estimations. Both the methodologies based on the SSI-DATA and SSI-COV show damage estimations very close to the ones obtained with the reference results. The success rate achieved with the SSI-COV algorithms should also be highlighted, which is considerably higher than the with SSI-DATA. This is an indication of the quality of the adaptation of the post-processing tools presented in section 5.5 (originally developed to the SSI-DATA) to the SSI-COV algorithm. Again, the p-LSCF presented the worst results, both for the success rate and damage estimation.

Table 7.30 – Deviation of accumulated damage of coincident events between results from Layout 2 the methodology based on SSI-DATA algorithm using all sensors

	SSI-DATA (All sensors)	SSI-DATA	SSI-COV	p-LSCF
GL	-	-8.1 %	-1.8 %	-47.8 %
EC3	-	-7.7 %	+2.3 %	-49.4 %
Success rate [%]	76.8	46.5	69.4	44.7

Lastly, the best estimations from the three algorithms were selected to estimate damage. With this consideration, the success rate increased to values similar to the ones obtained when the three levels of measurement are considered. At the same time, the distribution of the wind speed becomes similar to the one recorded by the SCADA system during one year (Figure 7.101 b)). Under these circumstances, the estimated damage is again close to the estimation using all sensors, with an error lower than 15 %. Considering the sensitivity of the S-N curve to small variations of the load cycles and the reduced number of recording channels used with this solution, this result has to be considered a very good approximation.

Table 7.31 – Estimation of accumulated damage at the end of design life considering an adjusted extrapolation according to the PDF of the wind speed using the best estimations from the three algorithms

	All sensors	Layout 2	Error
GL	0.0371	0.0305	-14.5 %
EC3	0.0283	0.0233	-14.1 %
Success rate [%]	91.0	91.0	-

7.3.8.3 Layout 3 (+74.988 m and +48.392 m levels)

Lastly, Layout 3 is a natural consequence of the two previous solutions. Layout 1 showed to be impractical for fatigue damage estimation, while Layout 2 demonstrated that it is a good choice for a single measurement level. However, opting for Layout 2 requires the installation of an additional level of measurement, while the top sensors are already installed. This means that the additional cost of using the Layout 2 or a solution based on the use of both levels of measurement is the same. For that reason, Layout 3 explores this possibility. It consists on the use of the two levels of measurement: at the top (+74.988 m) and around 2/3 of the tower height (+48.392 m).

Modal Tracking and Damage Detection

Again, the procedure previously described for the other solutions was applied to this case. The acceleration data recorded by sensors S6, S7 S8 and S9 was used as input for the monitoring system. The same input parameters described in section 7.3.6.2 were implemented. Also, since two levels of measurement enable a good level of detail of the mode shapes, a minimum MAC value of 0.80 was imposed to consider a cluster for the tracking procedure (the same value used when all sensors were considered).

The Campbell diagram obtained for the analysed period of data with this layout solution is shown in Figure 7.102. The results are in good agreement with the ones obtained when all sensors were used. However, it is noted a small influence of the 15Ω harmonic on the identification of the 3 SS* vibration mode, although in a smaller extent than in Layout 2.

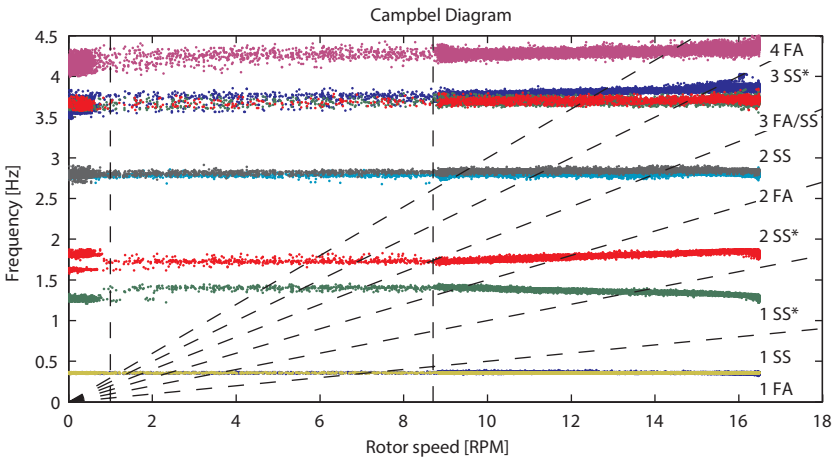

Figure 7.102 – Campbell diagram with the tracked vibration modes with Layout 3 (p-LSCF algorithm)

The statistics about the identification of the 9 vibration modes are summarized in Table 7.32. A significant improvement is clearly noticed in the success rate of the identification of almost all vibration modes. In fact, for some modes, the results are better than the ones obtained when all sensors are used. Nevertheless, the identification of the 1 FA mode by the p-LSCF algorithm is slightly lower than when all sensors are considered.

Table 7.32 – Success rate and coefficient of variation obtained with the identification algorithms (with Layout 3)

Mode	SSI-COV		SSI-DATA		p-LSCF	
	Success Rate [%]	$f_{coef.\ var.}$	Success Rate [%]	$f_{coef.\ var.}$	Success Rate [%]	$f_{coef.\ var.}$
1 SS	94.2	0.005	95.9	0.005	90.6	0.005
1 FA	82.7	0.021	80.2	0.019	59.7	0.020
1 SS*	80.7	0.038	89.3	0.037	85.9	0.037
2 SS*	93.9	0.031	95.4	0.030	93.3	0.030
2 FA	91.1	0.009	92.2	0.008	90.5	0.006
2 SS	74.1	0.012	82.3	0.011	69.4	0.010
3 FA/ 3SS	12.4	0.013	17.6	0.012	48.3	0.010
3 SS*	44.1	0.018	56.6	0.018	81.8	0.018
4 FA	19.3	0.019	56.8	0.020	97.0	0.019

Considering the quality of the results achieved, the same damage scenarios defined in section 7.3.6.6 were also tested for this layout solution (see Table 7.21).

The control charts obtained for the three damage scenarios are exposed in Figure 7.103. It is visible that the damage events are clearly identified, with results in line with the ones presented for a layout solution based on all sensors.

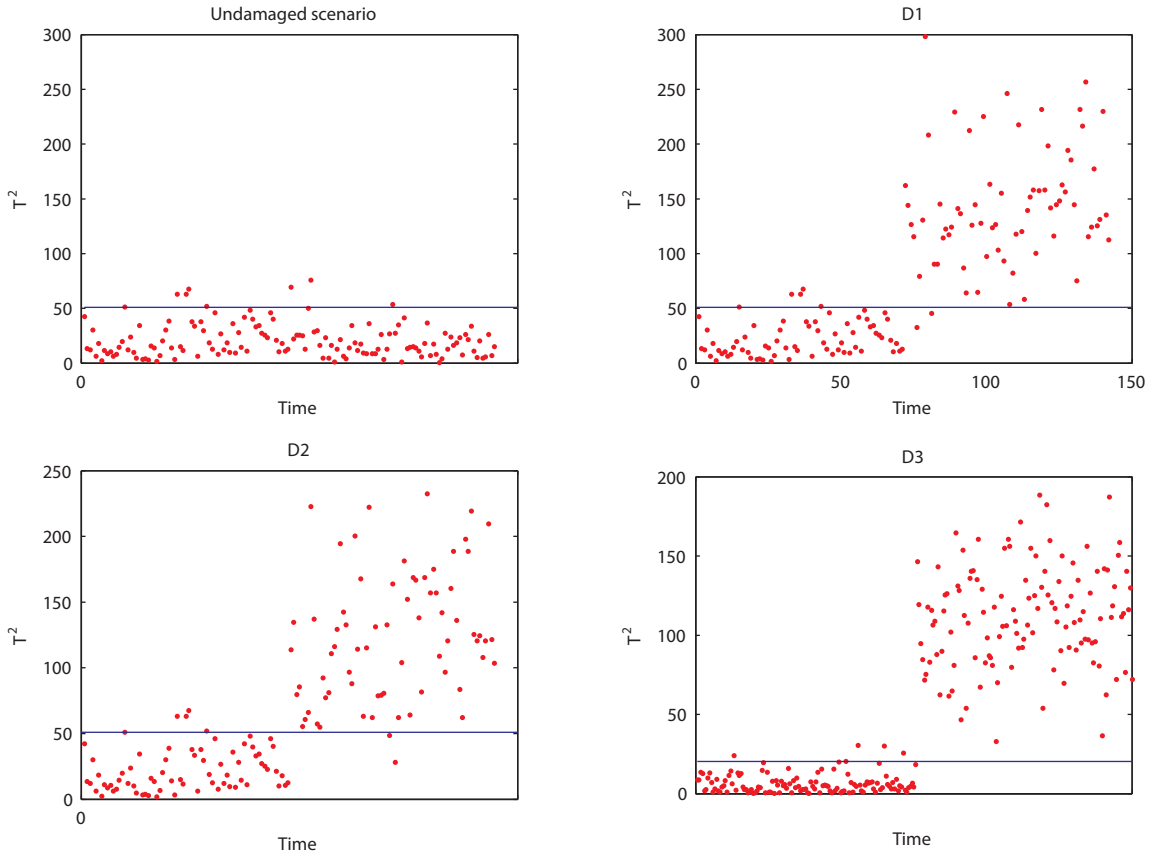

Figure 7.103 – T^2 control charts associated with a scenario where no damage is present and with the three defined damage scenarios (Layout 3)

Fatigue Results

Given the distribution of sensors in Layout 3 and the good results achieved with the modal tracking, it is expected that the estimation of the acceleration time series at unmeasured locations would be also good. Just like in the Layout 2, the frequency cut imposed for Layout 1 was not implemented in this solution.

The good estimation of the acceleration time series at unmeasured locations can be attested with Figure 7.104, referred to an event during a production period (with a mean rotor speed of 14.1 RPM). In this figure, the estimated accelerations at measured (+74.988 m and +48.392 m) and unmeasured (+21.772) positions in the FA direction are compared with the recorded time series by the sensors at the same positions. For this example, the methodology based on the SSI-DATA algorithm was used. It is visible that the estimated acceleration time series at the unmeasured position is very good.

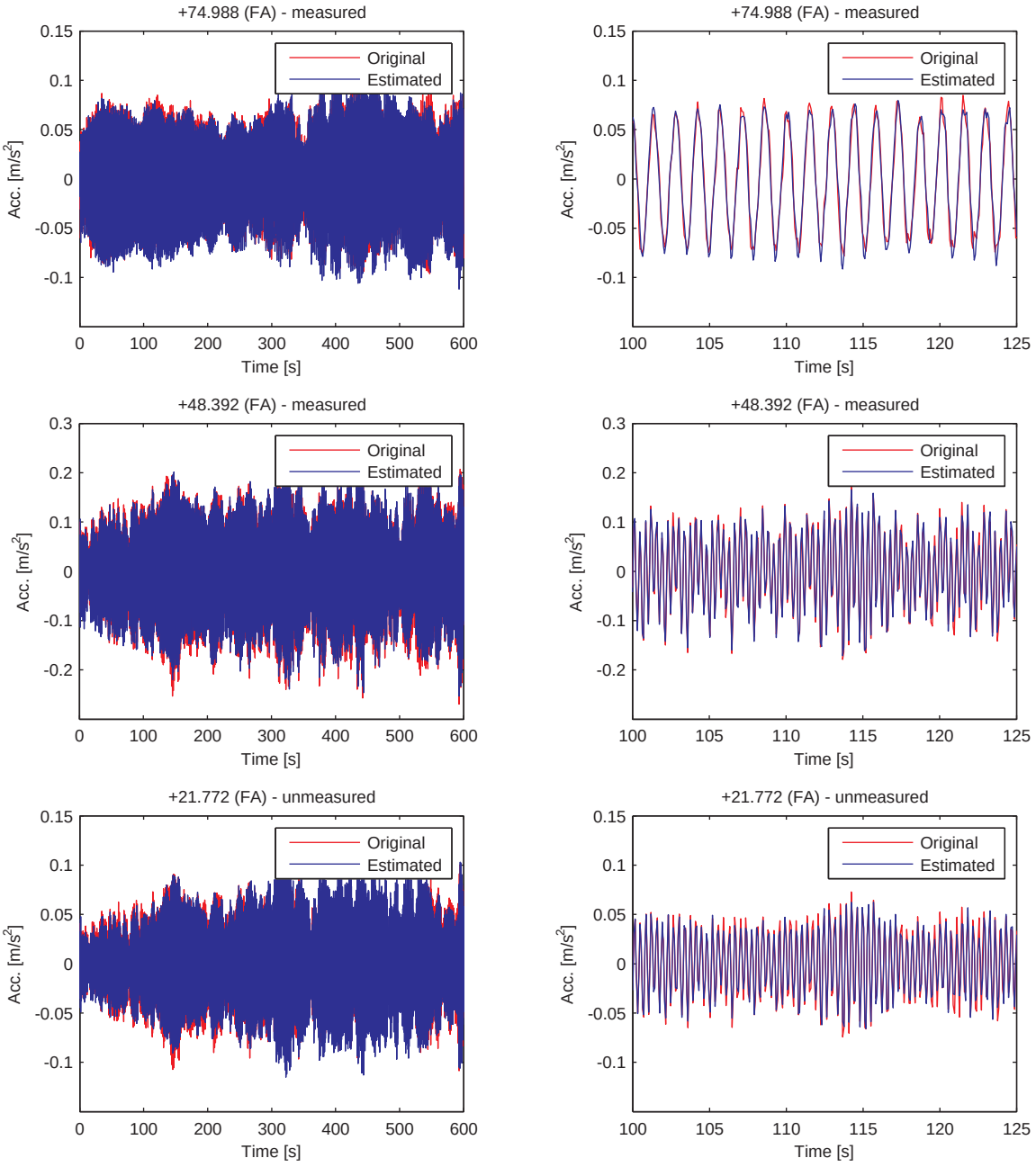

Figure 7.104 – Original and estimated acceleration time series at the measured levels (+74.988 m and +48.392 m) and unmeasured levels (+21.772 m)

Figure 7.105 evidences the evolution of the number of events with the increase of the two considered quality indices (Δ_e and Δ_{freq}) referred to the 4 used sensors. The results obtained with this layout solution are similar to the ones achieved with all sensors.

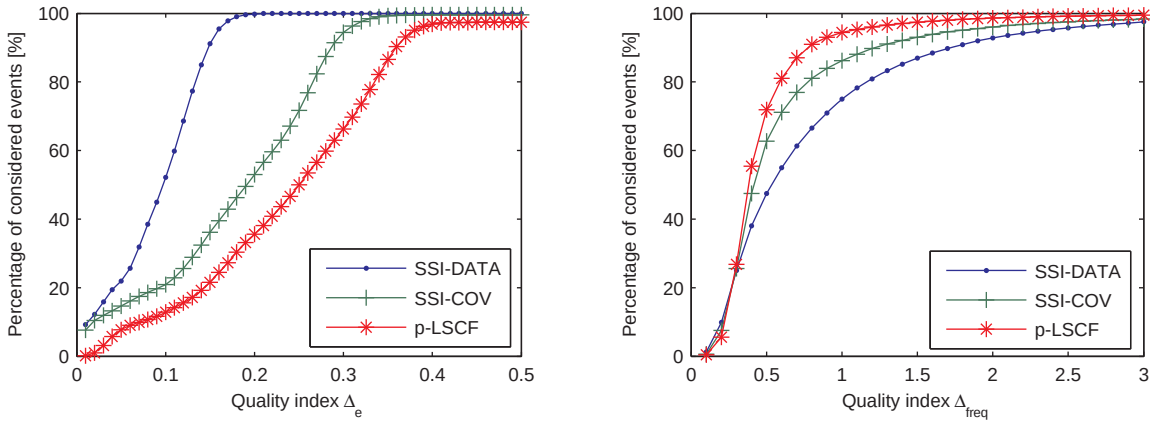

a) b)

Figure 7.105 – Percentage of considered events with Layout 3 with the evolution of: a) Δ_e index; b) Δ_{freq} index

The deviation associated with the direct comparison of the damage estimated with each methodology (using Layout 3) and the damage estimated with the reference methodology (SSI-DATA algorithm, using all sensors) for coincident events was again used to assess the quality of the results. The deviations are presented in Table 7.33. It is seen that results obtained with the SSI-DATA algorithm represent a very good agreement with the reference results, also showing a good success rate. Both the other two algorithms show lower success rates. Notwithstanding, they both show a good agreement of the damage estimation with the reference results, especially the methodology based on p-LSCF algorithm.

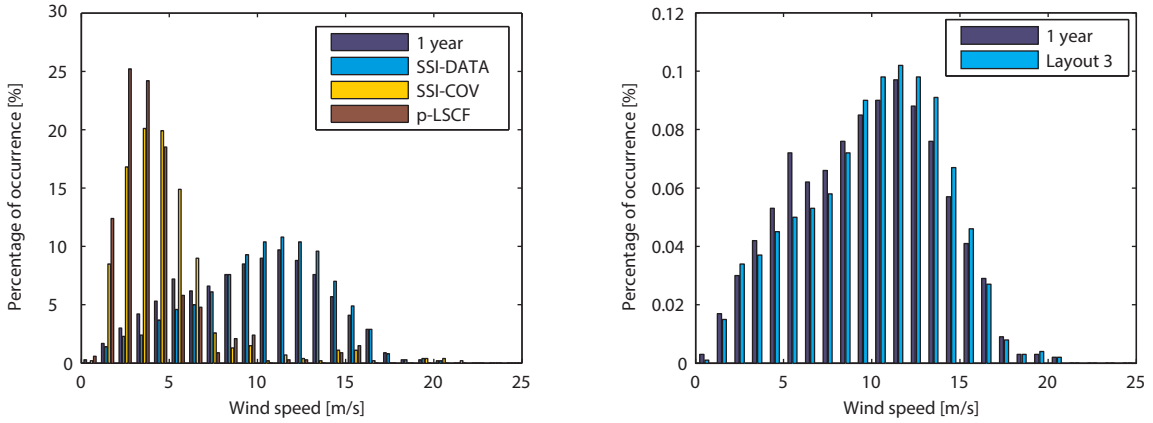

a) b)

Figure 7.106 – Probability density function of wind speed (in the sector 100º-120º) recorded by the SCADA system and from the data considered for fatigue estimation with Layout 3 with: a) the thee algorithms; b) best estimations from the thee algorithms

Table 7.33 – Deviation of accumulated damage of coincident events between results from Layout 3 the methodology based on SSI-DATA algorithm using all sensors

	SSI-DATA (All sensors)	SSI-DATA	SSI-COV	p-LSCF
GL	-	+7.9 %	-20.7	-13.3 %
EC3	-	+9.8 %	-20.7	-13.1 %
Success rate [%]	76.8	70.8	39.4	30.5

Using the best estimations provided by the three algorithms to increase the range of damage scenarios included in the analysis, it is possible to extrapolate the damage expected at the end of the design fatigue life according to the measured probability density function (PDF) of the mean wind speed. Figure 7.106 compares the PDF of the mean wind speed measured for the sector 100º-120º for the acceleration events considered when the best estimations from the three algorithms are used with the PDF obtained with the data recorded by the SCADA system during one year. The results obtained with the best estimation were then adjusted to follow the PDF of the mean wind speed obtained from the SCADA system. The results obtained are summarized in Table 7.34. It is visible that the estimation obtained with this layout solution is very similar to the estimated using all sensors (deviations smaller than 7 %), while a good success rate is also achieved.

Table 7.34 – Estimation of accumulated damage at the end of design life considering an adjusted extrapolation according to the PDF of the wind speed using the best estimations from the three algorithms

	All sensors	Layout 3	Error
GL	0.0371	0.0374	+4.93 %
EC3	0.0283	0.0289	+6.87 %
Success rate [%]	91.0	86.8	-

7.3.9 Conclusions

This section presented a complete analysis of the installation and implementation of a vibration-based structural health monitoring system in a 2.0 MW wind turbine. It starts with the presentation of the main characteristics of the wind turbine, together with a description of its operating conditions. Alongside, the modal results obtained with two developed finite element models are presented, serving for an initial assessment of the wind turbine vibration modes.

Then, the dynamic behaviour of the wind turbine structure under operational and parked conditions was analysed. The application of the implemented algorithms (SSI-COV, SSI-DATA and p-LSCF) for modal identification was successfully employed, allowing to identify 9 vibration modes, among tower and rotor blades modes. The continuous assessment of the wind turbine dynamic properties permitted to completely characterize its modal parameters throughout the different operating regimes. The developed methodology allowed to remove the influence of the harmonics in the identification of the most important vibration modes.

The analysis of the collected data during more than one year permitted to identify 51 data sets corresponding to free decay events. These acceleration events were analysed using two different

methodologies: one based on the adjustment of an exponential window and another based on the SSI-COV algorithm. The results obtained with both methods presented very coherent outcomes. Nevertheless, the values obtained for the damping of the 1 FA mode showed some variability which could not be fully explained.

An analysis about the relative contribution of the vibration modes and rotor harmonics to the measured acceleration was also performed following the procedure described in section 5.5. It was noticed that the participation of the modes/ harmonics on the measured signal is clearly dependent on the operating conditions and on the tower section under analysis.

After this, the identified natural frequency values of the tracked vibration modes were used to assess the influence of operational and environmental effects. In that sense, static and dynamic models were tested. Among these, the static model SM2 provided the best results, demonstrating the ability of the implemented methodology to minimize the influence of these external effects on the measured natural frequencies.

Using the outcomes obtained with the application of the regression model to the identified natural frequencies, the ability of the developed methodology to detect abnormal structural changes was tested. It was demonstrated the accuracy of the system to identify small variations of the tower bending modes along the yaw angle. This represents an important achievement since it allows to identify possible asymmetric conditions of the foundation stiffness. In addition, the methodology also proved being able to detect frequency variations associated with small damages on the foundation of onshore and offshore wind turbines and, although with a smaller precision, on the blades.

The fatigue condition of the wind turbine tower was also assessed following the procedure introduced in section 6.4.1.1. Due to the impossibility to install sensors to quantify the quasi-static motion of the tower, it was only possible to estimate the condition of the structure due to the dynamic component of fatigue. In that sense, the considerations made in this context only intended to validate the proposed methodology and did not aim to analyse the real fatigue condition of the structure. It was demonstrated that, for this scenario of study, the methodology based on the SSI-DATA and SSI-COV algorithms delivered the best results. A strategy based on the use of the best estimation from the three algorithms was also tested with good results.

Finally, an optimization of the dynamic monitoring system considering different sensors layout was proposed and tested. The first solution, based on a biaxial sensor at the tower top, revealed some deficiencies on the identification of some modes. Even though, it has proved successful in the identification of small damages (although without the precision of the solution based on all sensors). On the other hand, this layout performed very poorly for the fatigue assessment of the tower. Both layout solutions 2 and 3, based on one and two biaxial sensors, respectively, evidenced the good ability for detection of damage at an early stage and for fatigue assessment of wind turbine towers.

In short, this section proved the suitability of the developed vibration-based monitoring system to be implemented in wind turbines. The usefulness of the damage detection module was clearly demonstrated, while the component regarding the fatigue assessment of the tower is still at a development stage, requiring additional testing. Nevertheless, the results already obtained permit to anticipate the potential of this solution.

8
CONCLUSIONS AND FUTURE RESEARCH

8.1 CONCLUSIONS

This work explored the potential of using operational modal analysis in the monitoring of wind turbines. In this scope, several processing routines were developed and implemented to extract the maximum information that a monitoring system based on the dynamic response of wind turbines can deliver. The developed methodology was implemented into a vibration-based monitoring system, capable of operating continuously and in an automated way, that transforms the collected data into useful information for the wind farm owners.

The thesis starts with a global perspective of the wind energy industry. An overview of the main technical evolutions of wind turbines was presented, focusing on two crucial aspects that defined the success of some models: reliability and cost effectiveness. Then, a description of the main structural elements of wind turbines is made, with a special emphasis on their reliability and cost. A brief description of the main theories describing the performance of wind turbines is also introduced, aiming to facilitate the comprehension of the response of the turbine under different operating conditions.

Then, the focus of the thesis is orientated to the analysis and characterization of the dynamic behaviour of wind turbines. This characterization was helpful to study the applicability of the OMA techniques, used in the context of the work (SSI-DATA, SSI-COV and p-LSCF), to wind turbines. Several methodologies developed and implemented in the context of the dynamic monitoring system are also described:

- Automated procedure for operational modal analysis;
- Computation of the relative contribution of the vibration modes and harmonics to the measured acceleration response;
- Statistical tools for detection of damage;
- Fatigue assessment of the support structure using a reduced number of sensors.

The processing tools developed in this thesis were validated using three case studies. The first case study comprises the analysis of vibration data collected during two distinct periods on an Izar Bonus 1.3MW/62 wind turbine. With this study, some important achievements should be referred:

- The ability of the SSI-COV and p-LSCF algorithms to accurately identify the main tower and rotor blades vibration modes of the Izar Bonus 1.3MW/62 wind turbine using both accelerometers at the tower and fibre Bragg grating sensors at the blades was demonstrated;
- Analysis of the data collected before and after the Rotor Blade Extension was used to demonstrate the precision of the implemented modal identification algorithms to detect small variations of frequency, being able to detect the frequency shift associated with an increase of 1 % of the blades mass.

The second case study is an offshore Vestas V90-3.0MW wind turbine. For this study, a short period of data collected with a dynamic monitoring system was considered. The main conclusions regarding this analysis were:

- The potential of the SSI-COV and p-LSCF algorithms to identify the most important vibration modes of an offshore wind turbine was demonstrated for operating and non-operating conditions;
- The developed methodology for automated identification of the modal properties of the wind turbine was successfully employed, giving a good indication about the possibility of its application to generic onshore and offshore wind turbines.

Lastly, the third case is the most complete study of this thesis. It comprises the analysis of the acceleration data collected during a period of one year at a Senvion MM82 wind turbine. The major achievements obtained with this analysis are:

- The methodology developed for continuous assessment of the modal properties was successfully tested in the Senvion MM82 wind turbine. With this analysis, the suitability of this methodology for identification of the properties of the main vibration modes under several operating conditions was demonstrated;
- The analysis of the relative contribution of the vibration modes and harmonics for the acceleration response of the wind turbine showed the influence of the varying operating conditions on the dynamic behaviour of the turbine. Depending on the tower section under analysis and on the conditions of operation, the acceleration response may be dominated by the structural response due to the harmonic excitation 3Ω or by the 1 FA or 2 FA vibration modes;
- The use of a regression model demonstrated to be a suitable solution to minimize the operational and environmental effects. A model composed by individual static regression models for each operating regime proved to deliver the best results;
- The developed monitoring methodology showed its ability to detect small variations of the natural frequencies, associated with damages at a very early stage on foundation of onshore and offshore turbines. A lower precision was achieved in the detection of blades damage;

- The proposed procedure for assessment of the wind turbine tower due to the dynamic component of fatigue was validated. Additional testing is required to extract meaningful results from this methodology;
- An optimization of the dynamic monitoring system considering a reduction of the number of sensors was tested. It was concluded that significant results can be obtained for detection of damage using only one biaxial sensor at the tower top. However, in order to achieve results for both damage detection and fatigue assessment with a precision similar to the ones obtained when all sensors are considered, a solution based on one biaxial sensor installed on a convenient position or a solution based on two biaxial sensors are required. This last solution may, in fact, only require the installation of one additional sensor if the sensor incorporated in turbine control system can be used.

8.2 FUTURE RESEARCH

The work presented in this thesis contains useful contributions for the development of a vibration-based monitoring system to be implemented in wind turbines. Notwithstanding, some future research is still needed to benefit from all the potential that a dynamic monitoring system can provide. Some interesting topics are presented in the following paragraphs:

- By continuing the collection of data of the Senvion MM82 wind turbine, it would be possible to assess the increase in precision in the detection of damage using a more complete regression model (improving the mitigation of the external effects over the natural frequencies) and using more observations to compute the T^2 control chart (which would lead to more robust results);
- The installation of sensors in the rotor blades would permit to assess the increase in precision in the detection of damage in these structural elements, with regard to the accuracy obtained with the sensors installed at the tower. However, it is expected an additional difficulty in the analysis of the blades vibration data due to the influence of the rotor rotation. In that sense, effective tools to remove this effect need to be developed;
- The fatigue assessment of the wind turbine support structure requires further developments. In that sense, the installation of sensors for measuring the quasi-static motion of this structure is needed. Using this data, it would be possible to integrally apply the proposed procedure for fatigue assessment described in section 6.4.1;
- The accuracy of the estimated displacements obtained by integration of the acceleration time series requires an experimental validation. Thus, the installation of strain gauges in the wind turbine support structure would permit to study the precision obtained with this process (mainly for the lower frequency range of the spectrum);
- Alternative sensors to measure the dynamic response of wind turbines, such as MEMS sensors, should be also tested, in order to lower the installation costs. The precision obtained with this low-cost sensors should be then compared with the one obtained with more expensive sensors, such as the ones used in this work. With this information, a cost-benefit analysis would give an important insight about the possibility of making the system more accessible, allowing its installation on a larger number of turbines.

APPENDIX A

MODEL RESPONSE ESTIMATION - VALIDATION

A.1. INTRODUCTION

In order to validate the concepts introduced in section 5.5, related to the decomposition of the recorded acceleration signal into several modal (and harmonic) responses, a simple example is presented in this section. In that sense, a simple small-scale model of a two-floor frame structure is used. The analysis is conducted using only one direction, as shown in Figure A.1 a). The stiffness K, mass M and damping C_1 matrices of the structural system are introduced in Figure A.1 b).

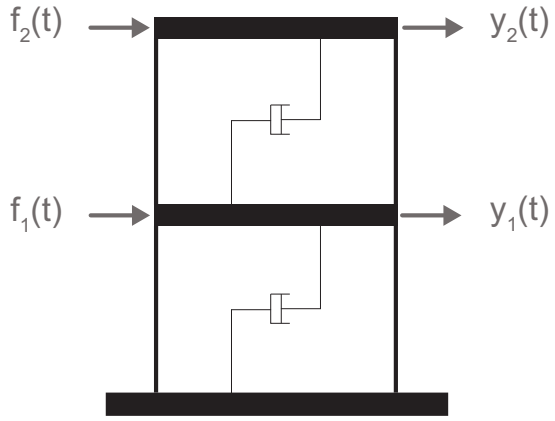

a)

$$K = \begin{bmatrix} 14.655 & -7.328 \\ -7.328 & 7.328 \end{bmatrix} (kN/m)$$

$$M = \begin{bmatrix} 0.0018 & 0 \\ 0 & 0.0018 \end{bmatrix} (ton)$$

$$C_1 = \begin{bmatrix} 0.0046 & -0.0023 \\ -0.0023 & 0.0023 \end{bmatrix} (KN.s/m)$$

b)

Figure A.1 – a) Illustration of the two-floor frame structure; b) Structural matrices of the model

With the previously introduced matrices, two vibration modes with well separated natural frequency values are obtained. The natural frequency and modal damping ratio values of the system as presented in Figure A.2, as well as illustrations of the mode shapes.

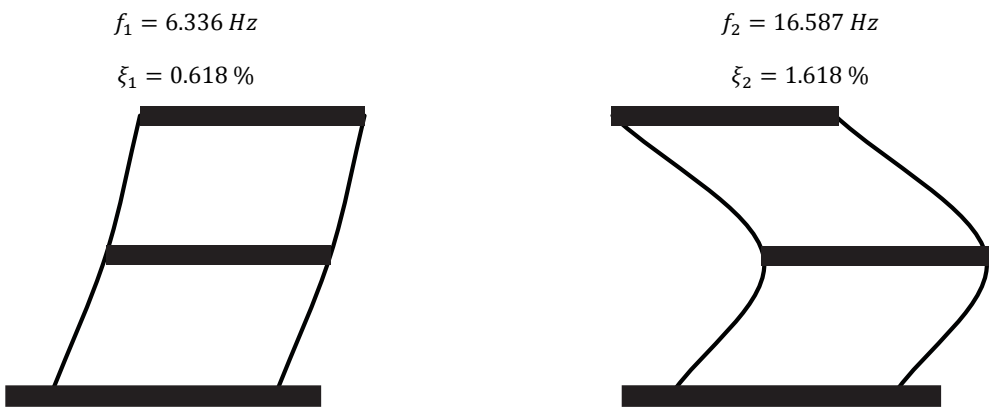

Figure A.2 – Modal characteristics of the two-floor frame structure

A.2. NUMERICAL SIMULATION

Using the introduced structural system, a numerical simulation was performed using the methodology presented in (Magalhães, 2010). Initially, a broadband excitation was artificially generated with normally distributed random numbers. This excitation was applied at the floor levels ($f_1(t)$ and $f_2(t)$).

The response of the structural system was obtained based on the discrete-time state-space model from the structural system, using a frequency sampling of 50 Hz. The considered time length of the simulation was 600 s. The simulated acceleration time series at the floor levels ($\mathrm{y}_1(\mathrm{t})$ and $\mathrm{y}_2(\mathrm{t})$) were computed as outputs.

Once the acceleration signals from the two floors were obtained, the methodology described in section 5.5 was applied using the three different modal identification algorithms. In that sense, it was required to tune the input parameters from each method. After an initial period of training, the parameters shown in Table A.1 were selected. The first line of the table ("Modal Identification") refers to the different input parameters required for each algorithm, while the second line ("Modal Response") denotes the values of the i parameter for the post-processing tool, according to section 5.5. Since the SSI-DATA algorithm uses the i parameter in the modal identification process, it is not necessary to define a new value for the post-processing step.

Table A.1 – Input parameters of the different algorithms used for modal identification and modal decomposition of the signal

	SSI-DATA		SSI-COV		p-LSCF	
Modal Identification	i	100	$2.i-1$	257	Nº of points of the Half-spectra	512
Modal Response	-	-	i	90	i	100

The results obtained with the application of the modal response post-processing tool to the output acceleration time series from the first floor are presented in Figure A.3. In this figure, the simulated acceleration is shown at the top, while the modal responses corresponding to the 1st and 2nd mode are illustrated in the middle and bottom plots. It is possible to attest that the estimated modal responses obtained with the different algorithms are almost coincident.

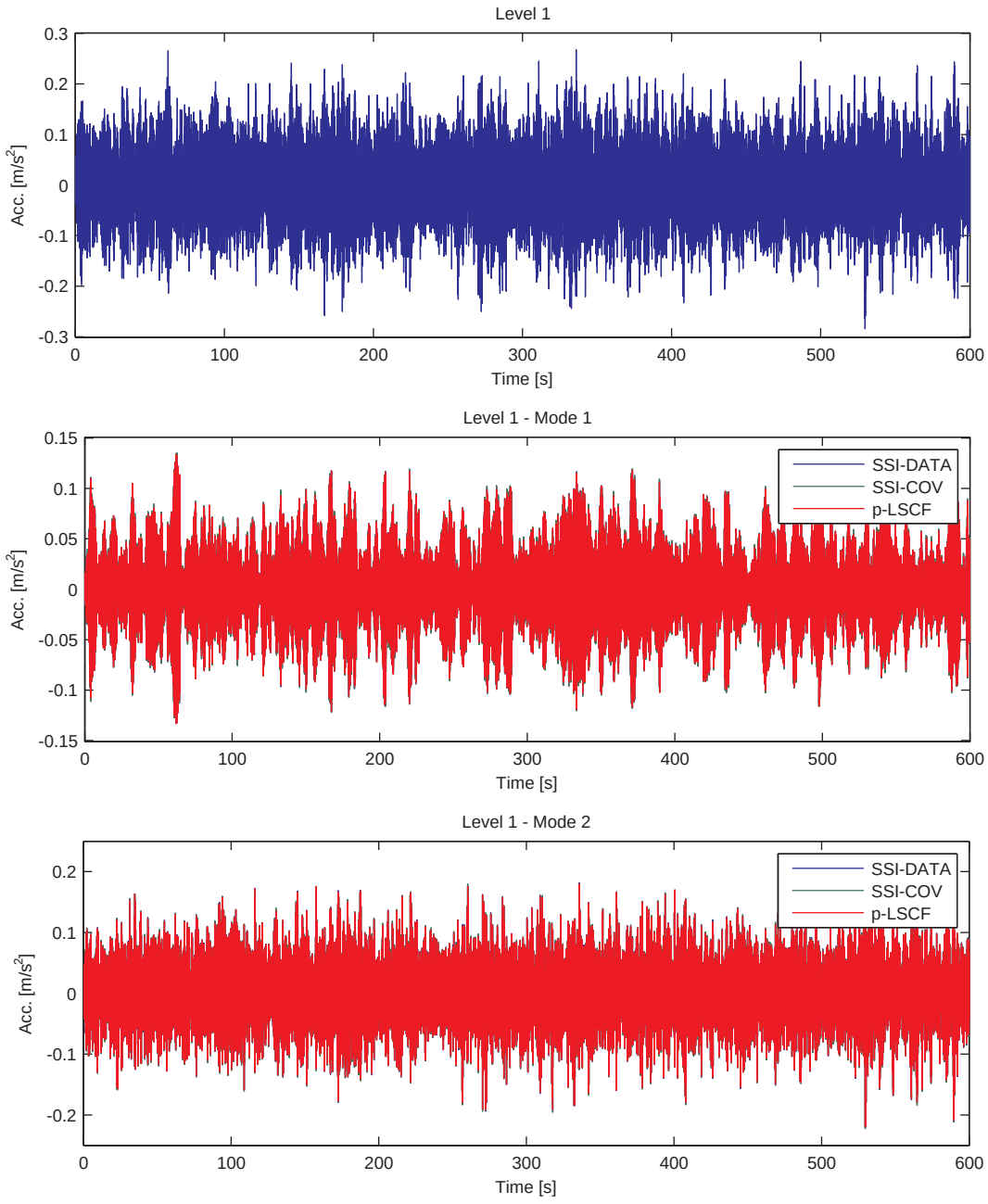

Figure A.3 – Output acceleration time series at level 1 (top) and estimated responses for the 1st and 2nd vibration modes obtained with the different algorithms during the whole period of simulation

Aiming to highlight the good initial impression given by Figure A.3, Figure A.4 presents the same results from the previous figure for a shorter time length (10 seconds). Again, the top plot refers to the numerically obtained acceleration, while the other two shows the modal responses from to the 1st and 2nd modes obtained with the different algorithms. In this figure, the very good agreement between the modal responses is evident.

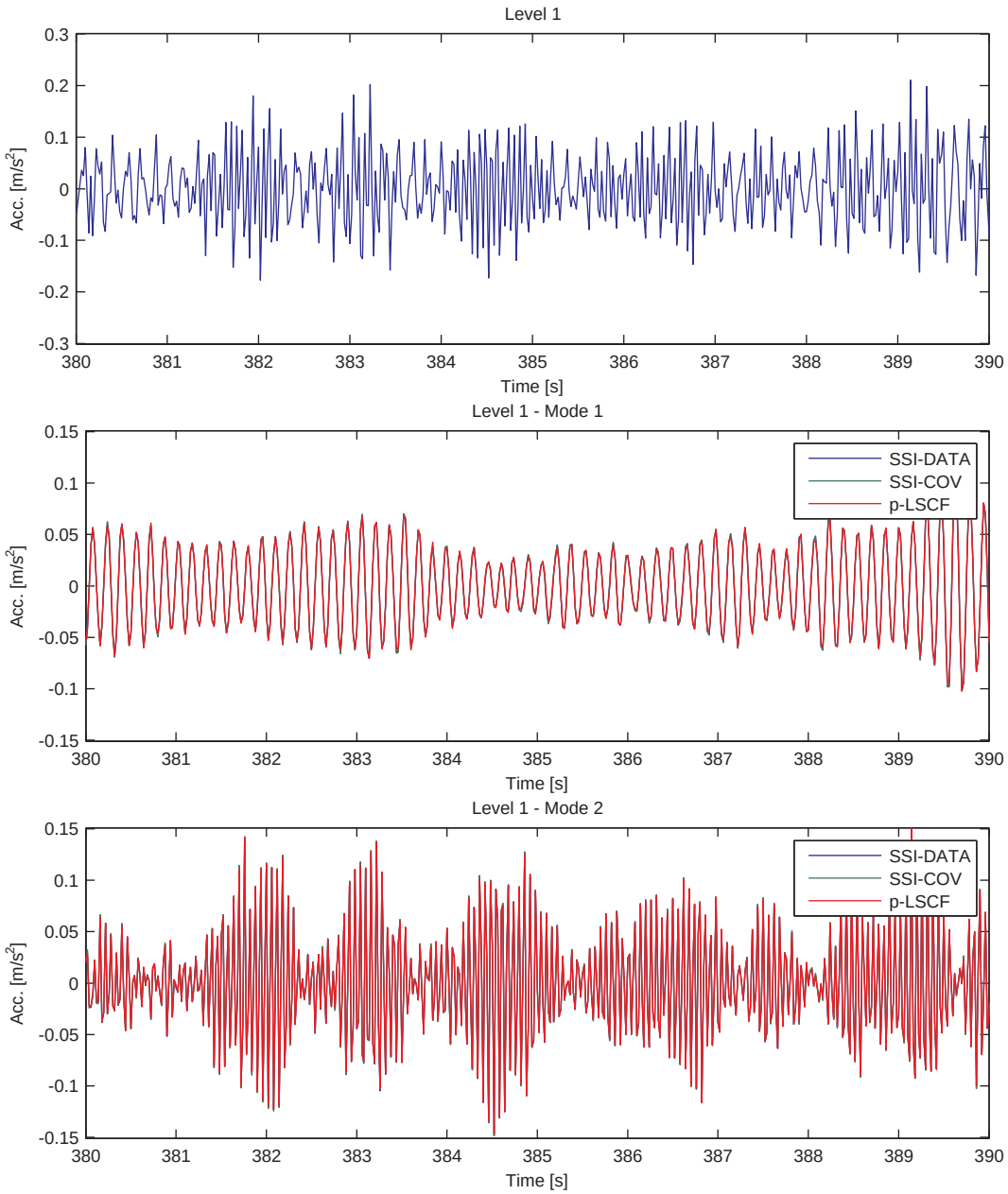

Figure A.4 – Output acceleration time series at level 1 (top) and estimated responses for the 1st and 2nd vibration modes obtained with the different algorithms during a period of 10 seconds

The analysis previously presented for the results achieved for the first floor of the structural system was also performed with the acceleration output of the second floor.

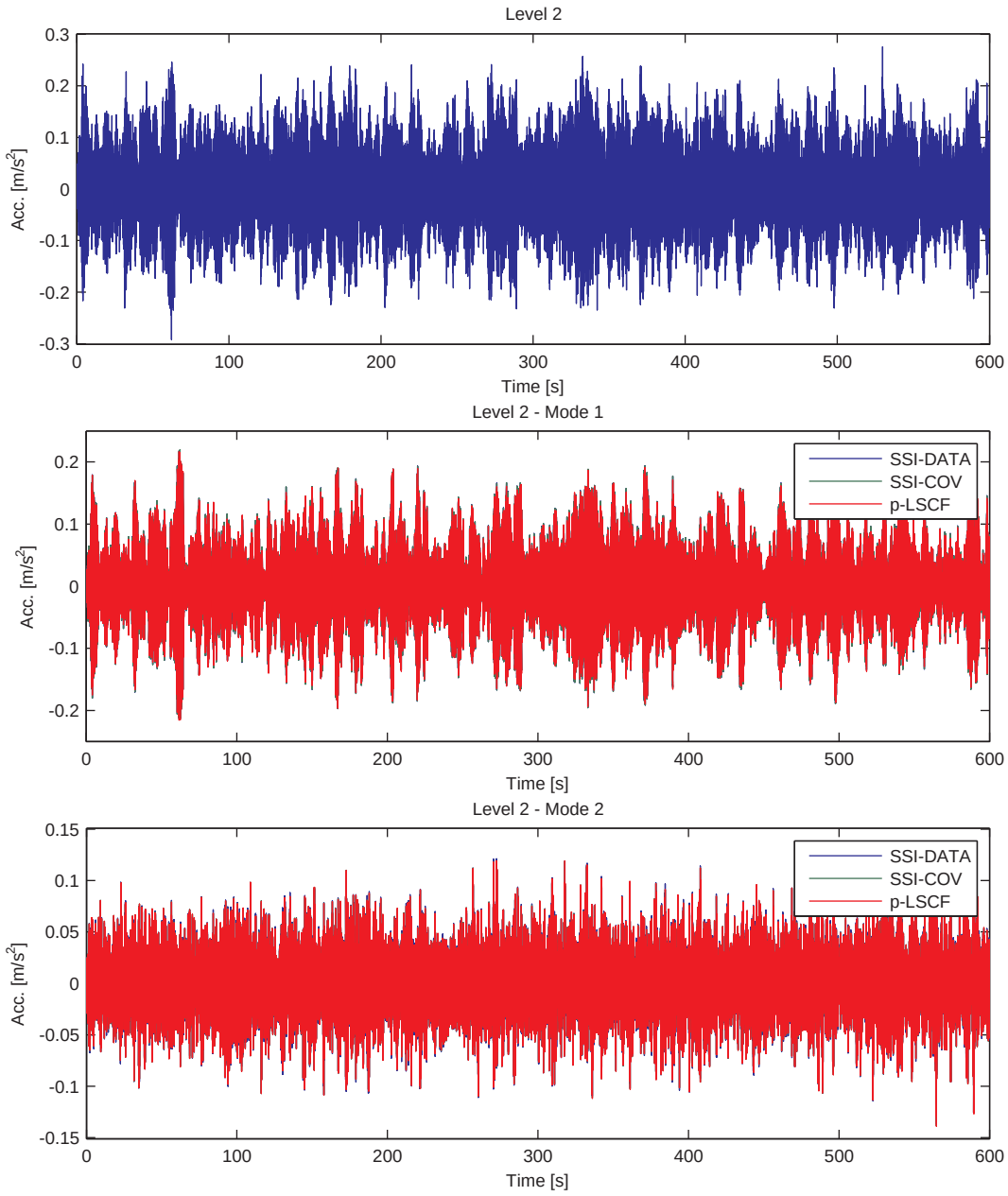

Figure A.5 – Output acceleration time series at level 2 (top) and estimated responses for the 1st and 2nd vibration modes obtained with the different algorithms during the whole period of simulation

A detailed representation of the results is introduced in Figure A.6. In this figure, the good agreement obtained for the modal responses is clearly noticed.

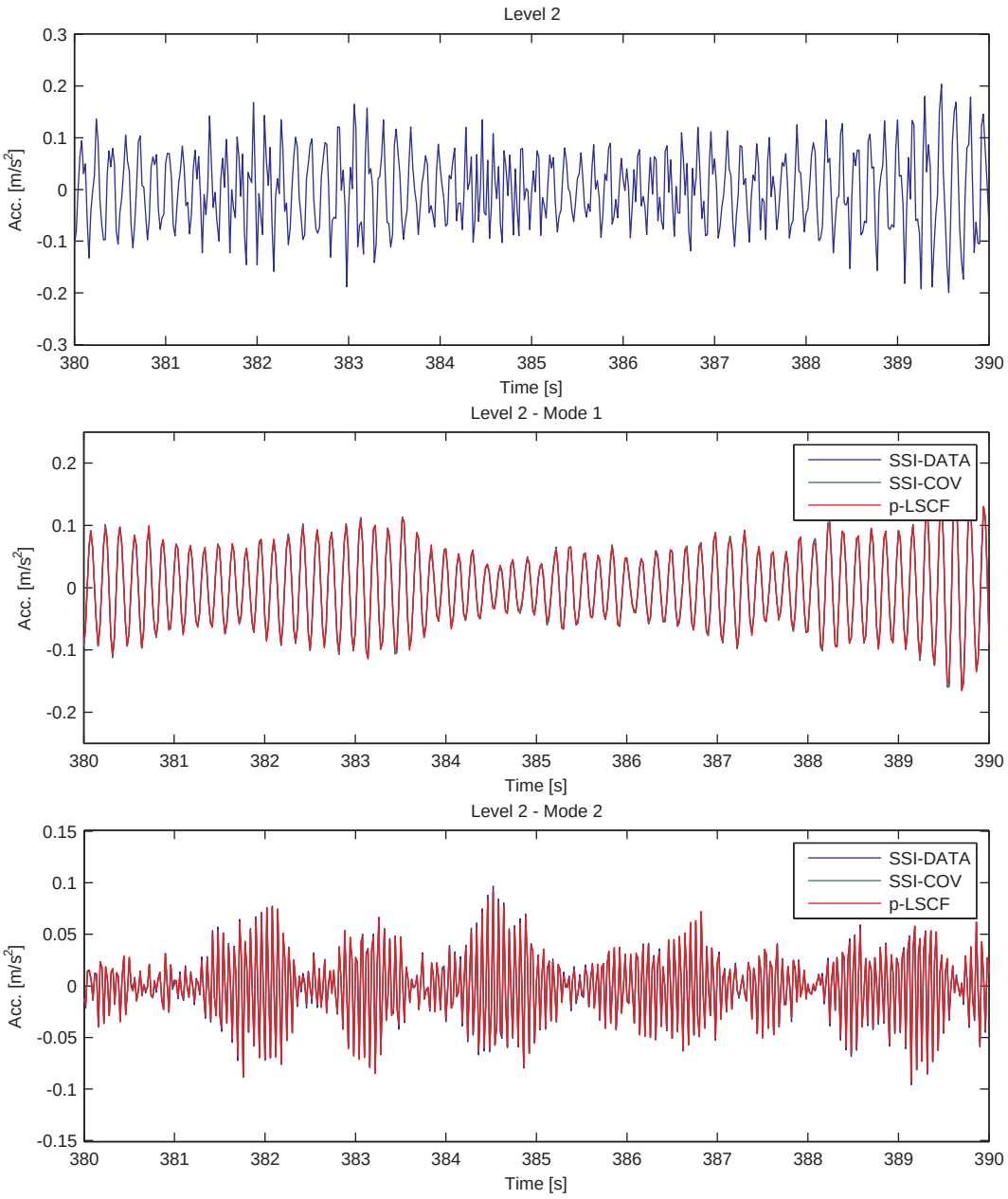

Figure A.6 – Output acceleration time series at level 2 (top) and estimated responses for the 1st and 2nd vibration modes obtained with the different algorithms during a period of 10 seconds

APPENDIX B

IZAR BONUS 1.3MW/62 WIND TURBINE – MODE SHAPES

B.1. INTRODUCTION

In this annex the mode shapes of the identified vibration modes of the Izar Bonus 1.3MW/62 wind turbine are presented.

B.2. ANALYSIS OF ACCELEROMETERS MEASUREMENTS

The mode shapes estimated from the acceleration measurements included ordinates at the instrumented blade and at the instrumented sections of the tower. For each mode, two lateral views (along the FA and SS direction) and one top view are presented in Figure B.1.

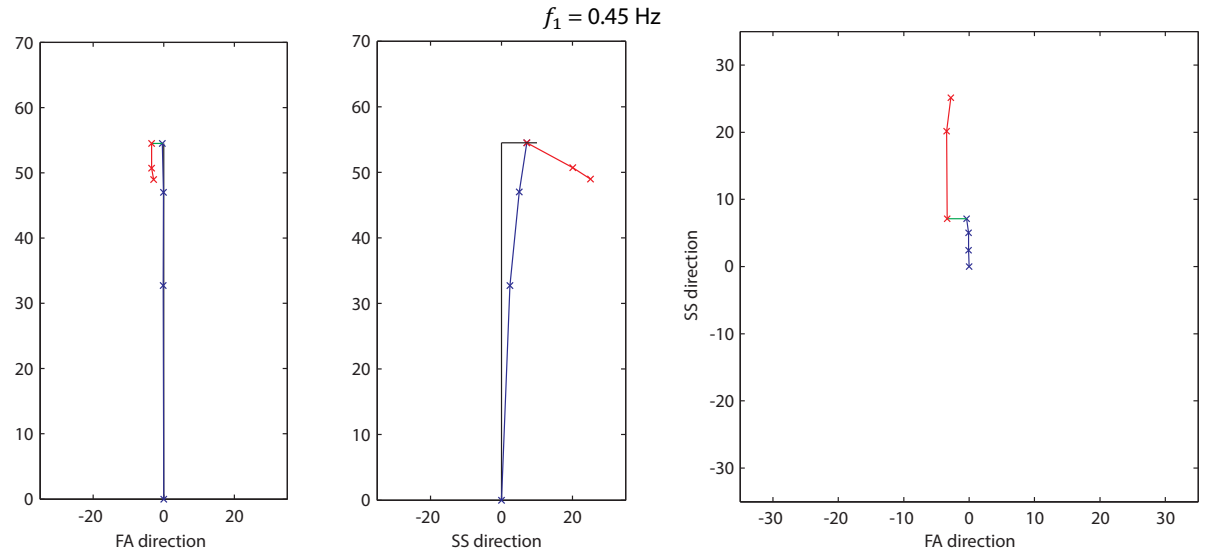

f_2 = 0.46 Hz

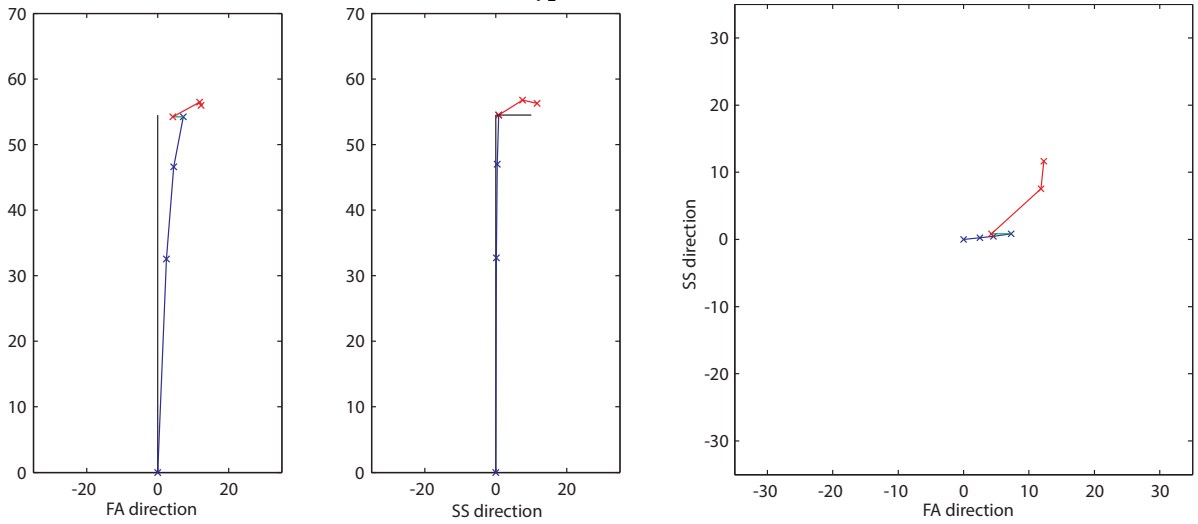

f_3 = 0.53 Hz

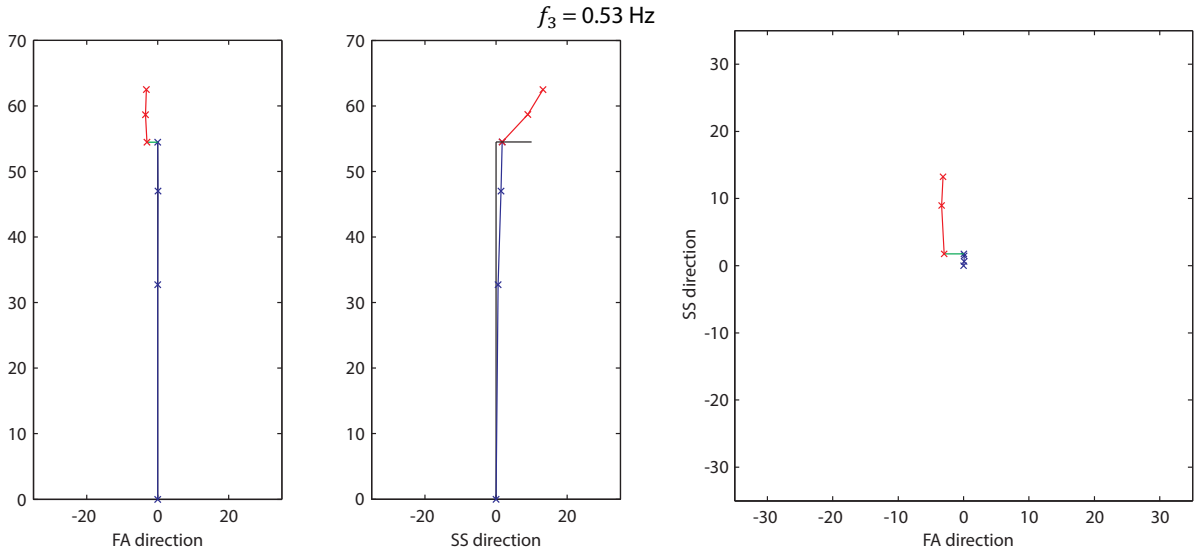

f_4 = 1.13 Hz

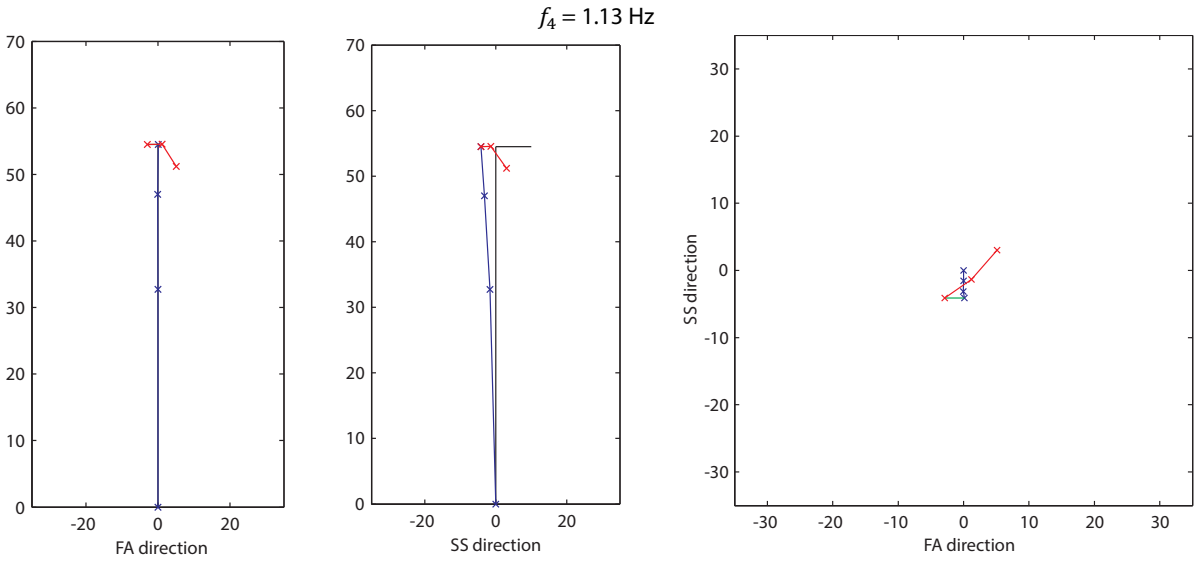

f_5 = 1.14 Hz

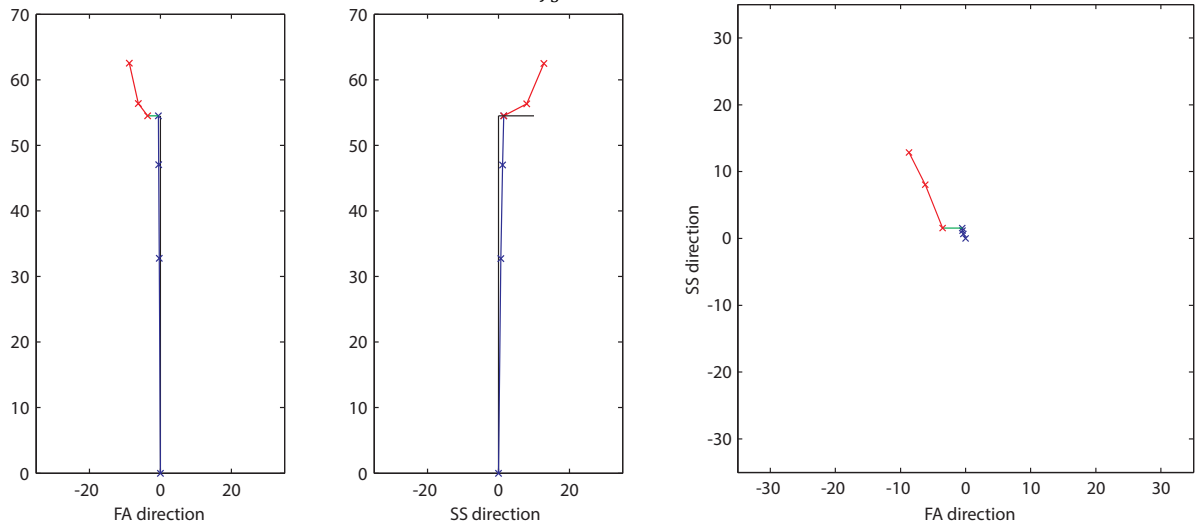

f_6 = 1.32 Hz

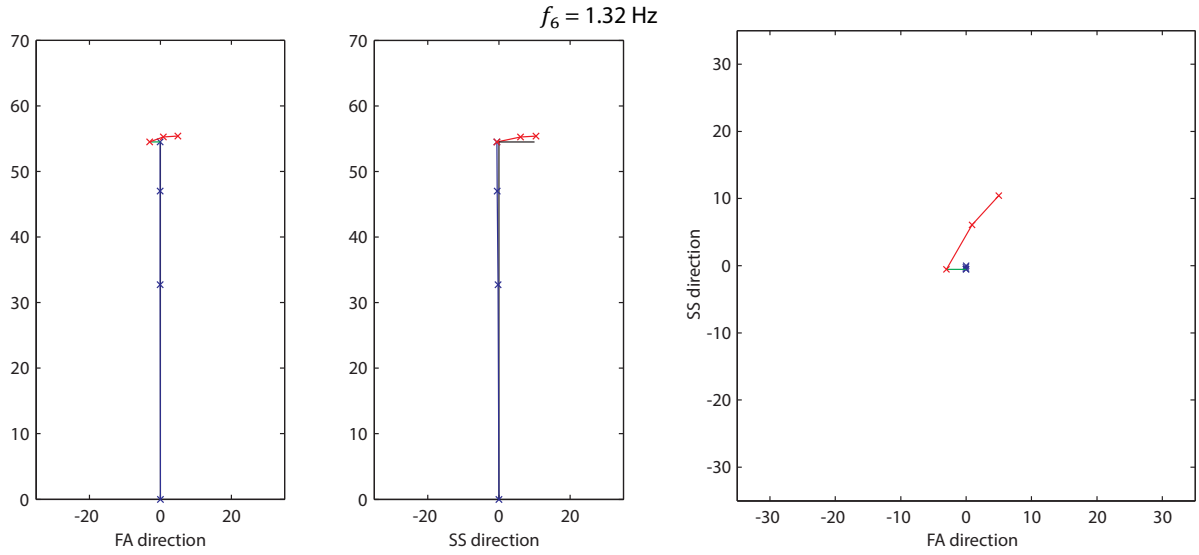

f_7 = 1.47 Hz

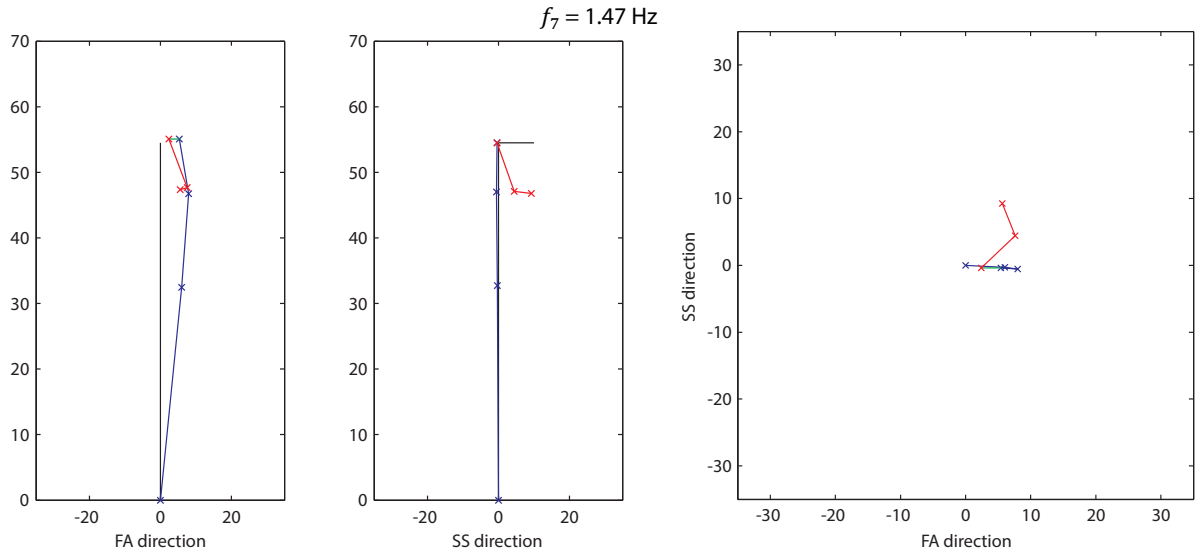

f_8 = 2.02 Hz

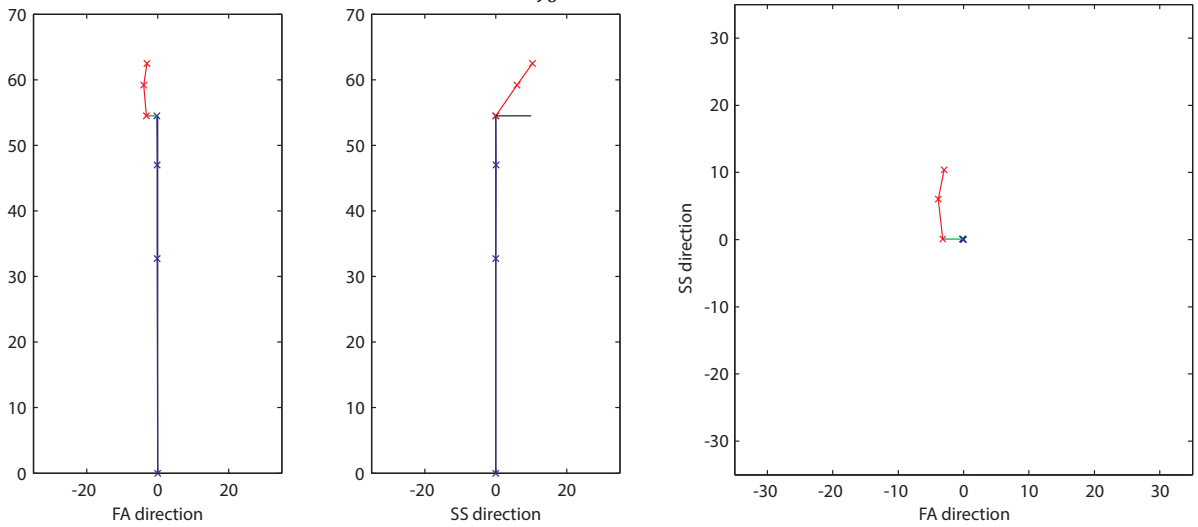

f_9 = 2.06 Hz

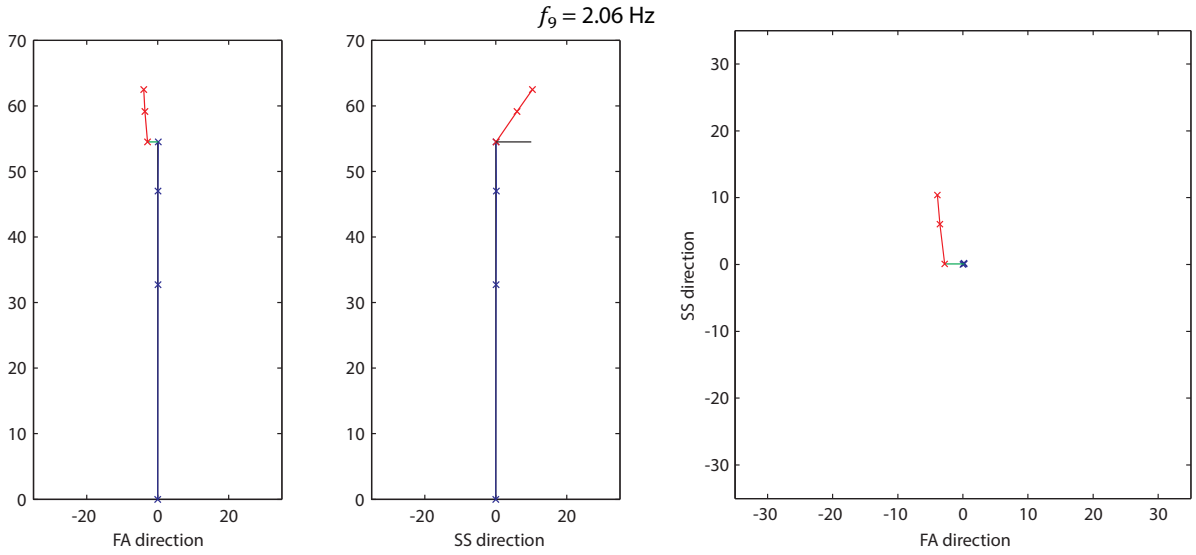

f_{10} = 3.33 Hz

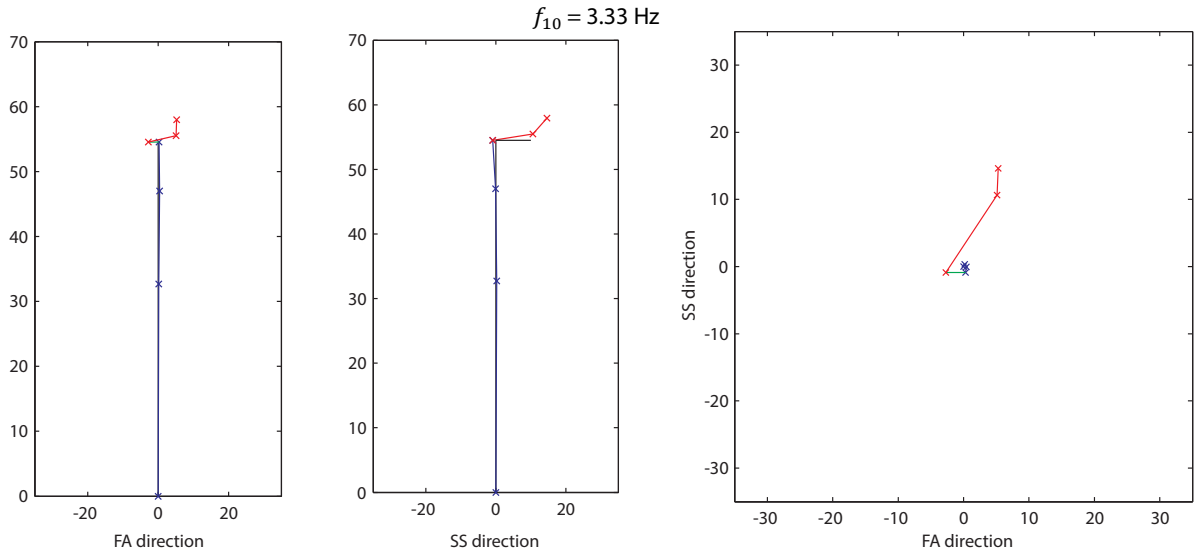

f_{11} = 3.45 Hz

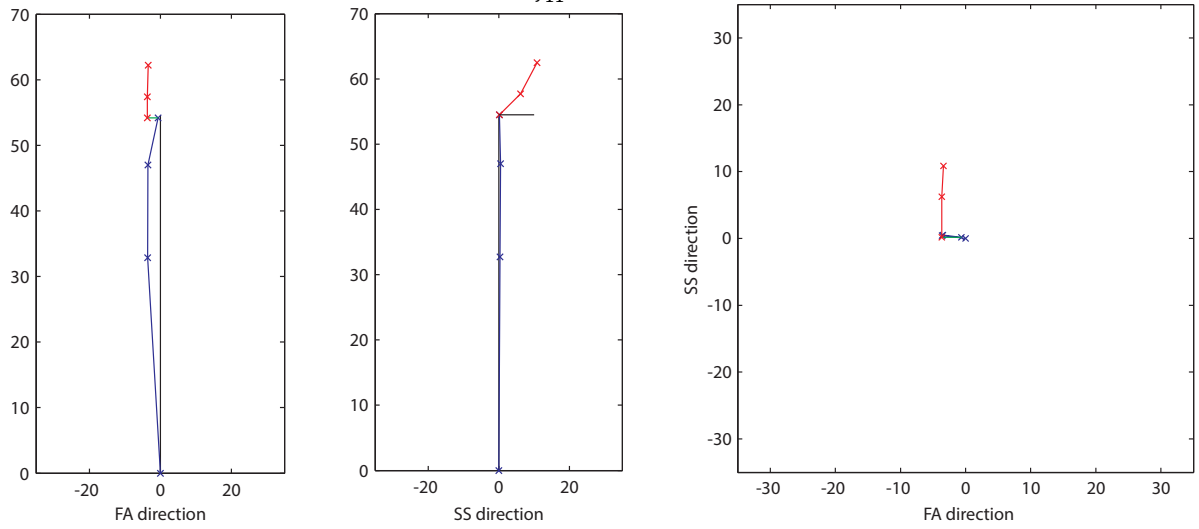

f_{12} = 3.74 Hz

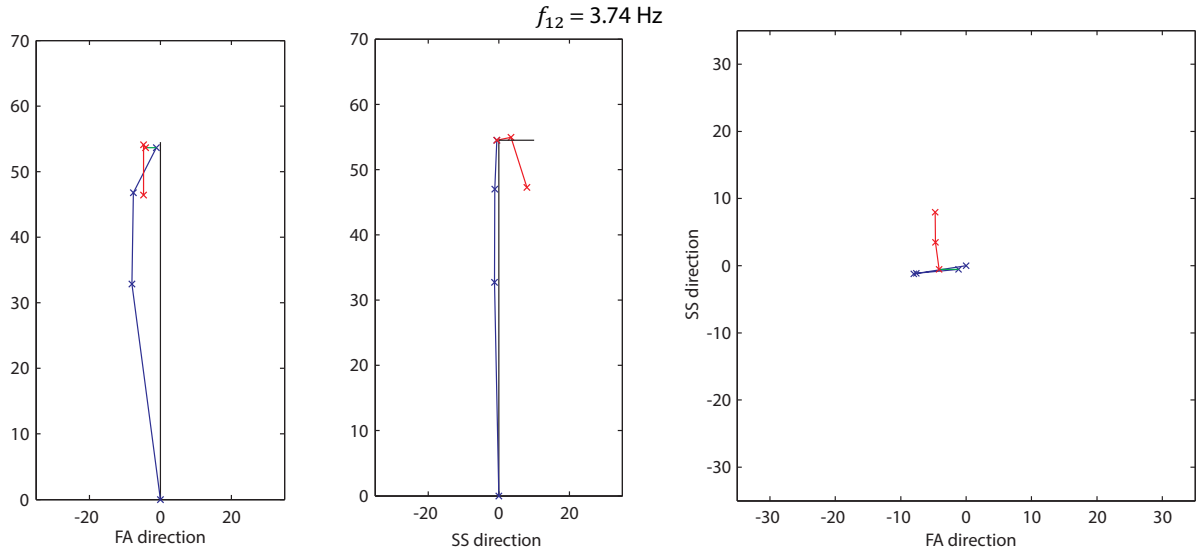

f_{13} = 4.03 Hz

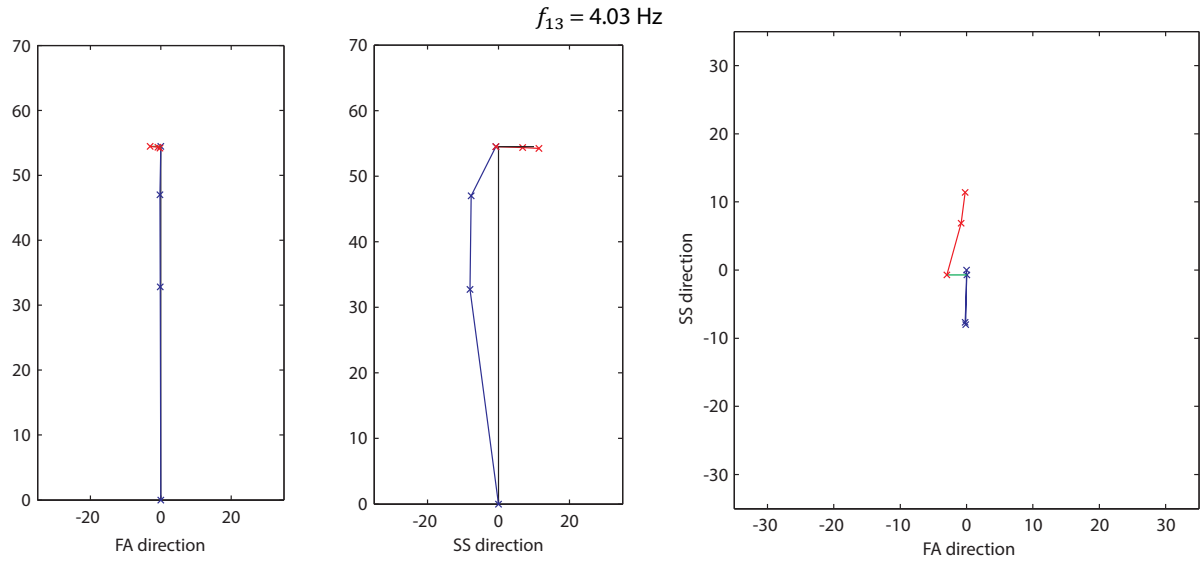

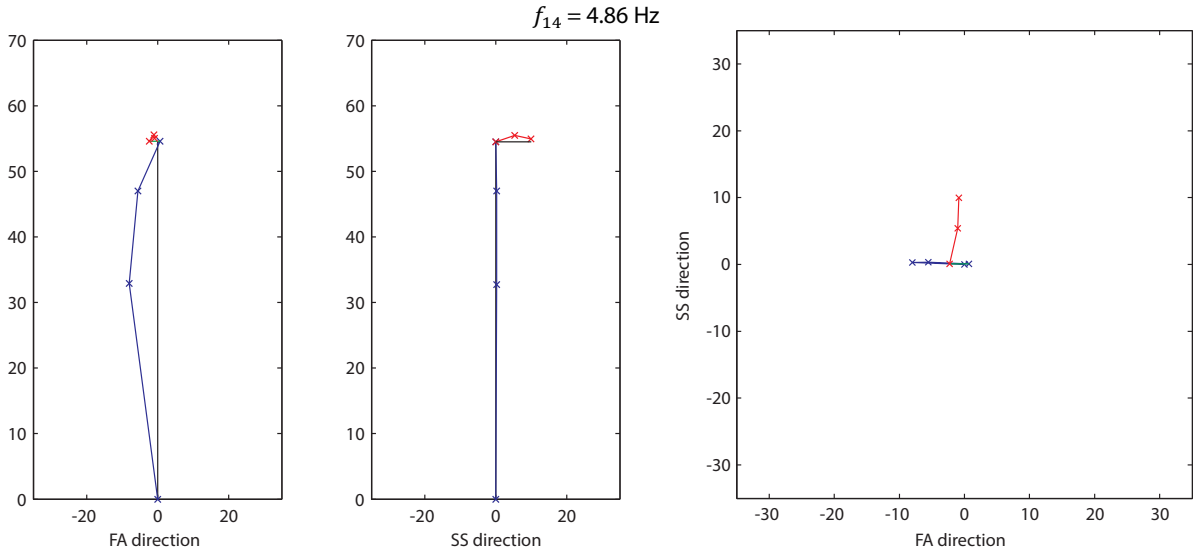

Figure B.1 – Mode shapes of the vibration modes identified with the measurement system based on accelerometers

B.3. Analysis of Fibre Bragg Grating Sensors Measurements (After RBE)

The amplitude of the modal curvatures from the first 6 rotor related vibration modes identified after the RBE are compared with correspondent modes identified before the RBE in Figure B.2. The modes related with tower motion are not presented since the influence of the installation of the RBE is more relevant in the rotor modes.

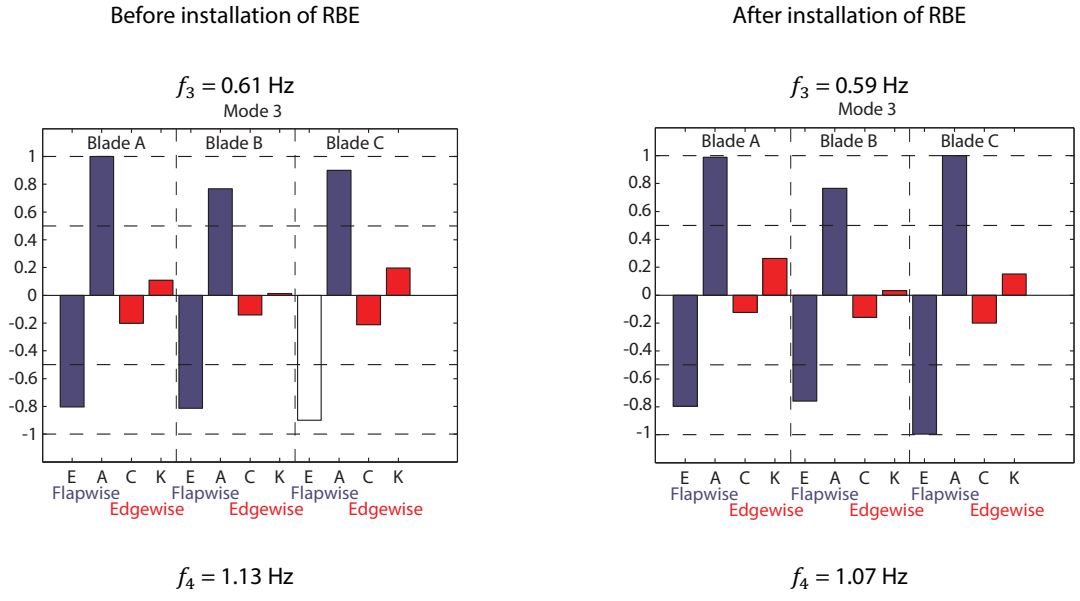

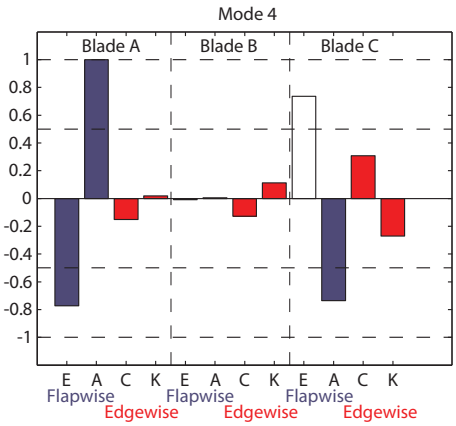

$f_5 = 1.15$ Hz

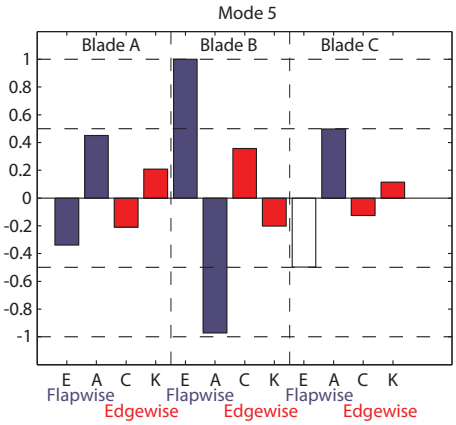

$f_6 = 1.33$ Hz

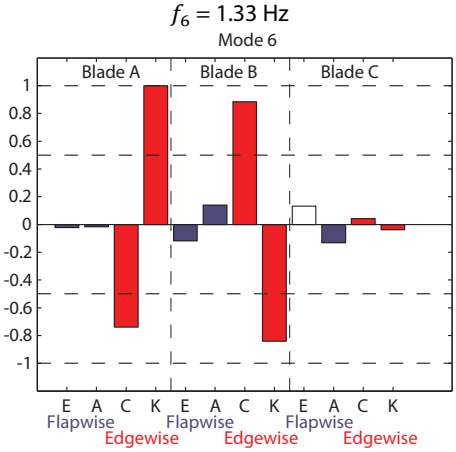

$f_7 = 1.45$ Hz

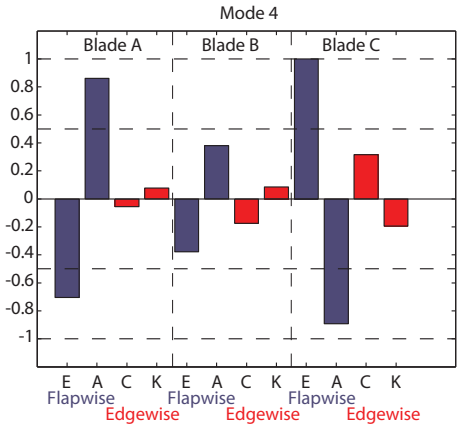

$f_5 = 1.10$ Hz

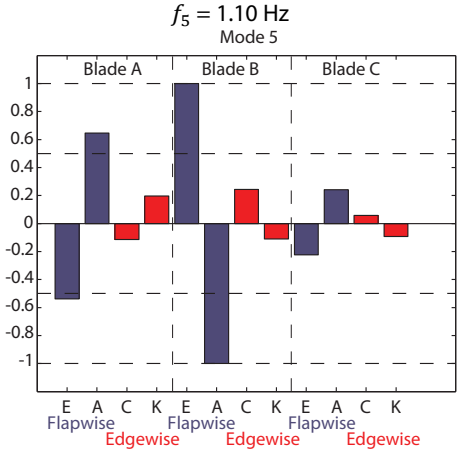

$f_6 = 1.29$ Hz

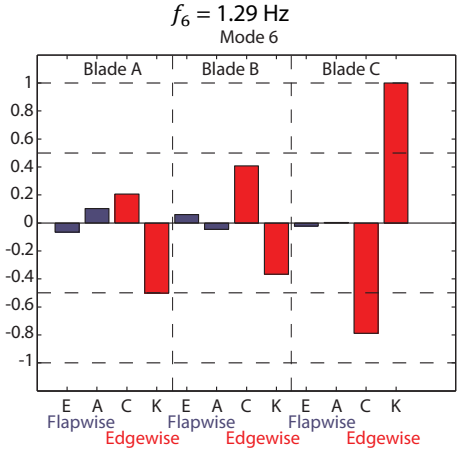

$f_7 = 1.43$ Hz

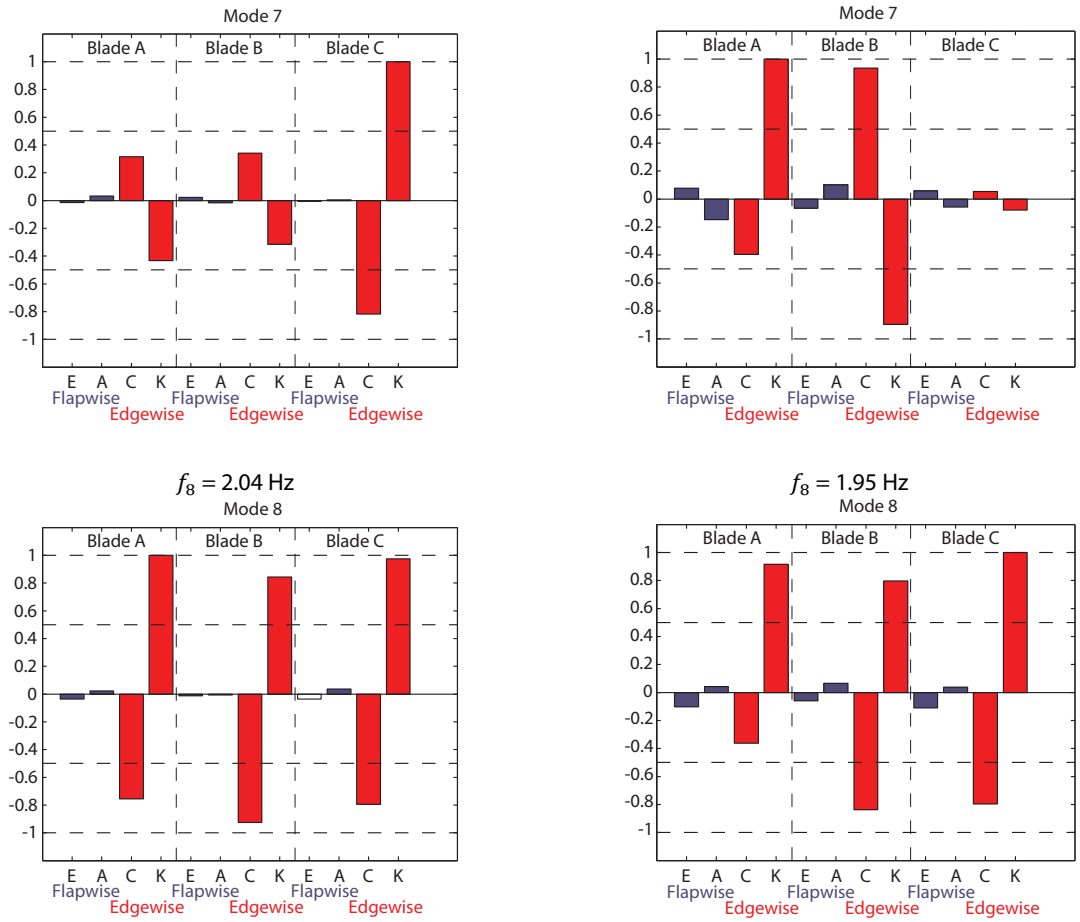

Figure B.2 – Comparison of the amplitude of the modal curvature of the first 6 identified rotor related modes before and after the RBE

REFERENCES

Ackermann, T. and L. Söder (2002). *An overview of wind energy-status 2002*. Renewable and Sustainable Energy Reviews **6**(1–2): 67-127.

Adams, D., J. White, M. Rumsey and C. Farrar (2011). *Structural health monitoring of wind turbines: method and application to a HAWT*. Wind Energy **14**.

Aenlle, M. L., L. Hermanns, P. Fernández and A. Fraile (2013). *Stress Estimation in a Scale Model of a Symmetric Two Story Building*. 5th International Operational Modal Analysis Conference (IOMAC). Guimarães, Portugal.

Aenlle, M. L., A. Skafte, P. Fernández and R. Brincker (2013). *Strain Estimation in a Glass Beam using Operational Modal Analysis*. XXXI International Modal Analysis Conference (IMAC). Florida, USA.

Ameri, N., C. Grappasonni, G. Coppotelli and D. J. Ewins (2013). *Ground vibration tests of a helicopter structure using OMA techniques*. Mechanical Systems and Signal Processing(35): 35-51.

Andersen, L. (2010). *Assessment of lumped-parameter models for rigid footings*. Computers & Structures **88**(23–24): 1333-1347.

Andersen, P., R. Brincker, C. Ventura and R. Cantieni (2007). *Estimating Modal Parameters of Civil Engineering Structures subject to Ambient and Harmonic Excitation*. Experimental Vibration Analysis for Civil Engineering Structures (EVACES). Porto, Portugal.

Anon (1890). *Mr. Brush's Windmill Dynamo*. Scientific American **Vol. LXIII**(No. 25): cover and p. 389.

Ansys Inc. (2011). *ANSYS Academic Research*. Release 14.0.

Appleyard, D. (2013). *Wind Insurance Claim Analysis Reveals Need for Monitoring*. 2013, from http://www.renewableenergyworld.com/rea/news/article/2013/08/wind-insurance-claim-analysis-reveals-monitoring-need.

Arántegui, R. L., T. Corsatea and K. Suomalainen (2013). *2012 JRC Wind Status Report*, European Commission. Joint Research Institute (JRC). Institute for Energy and Transport.

Arrigan, J., V. Pakrashi, B. Basu and S. Nagarajaiah (2011). *Control of flapwise vibrations in wind turbine blades using semi-active tuned mass dampers*. Structural Control and Health Monitoring **18**: 840-851.

Bak, C., P. Fuglsang, J. Johansen and I. Antoniou (2000). *Wind tunnel tests of the NACA 63-415 and a modified NACA 63-415 airfoil*. Technical Report Risø–R–1193. Roskilde, Denmark, Risø National Laboratory.

Baldwin, D. H. and J. Kennard (1985). *Development of Large, Horizontal-Axis Wind Turbines*. DOE/NASA/20320-62 NASA TM-86950

BARD Engineering GmbH. *BARD - Wind Offshore Projects*. 2013, from http://www.bard-offshore.de/en/projects.html.

Bartsch, C. (2012). *Fact-Sheet alpha ventus*. EWE, E-ON and Vattenfall.

Becker, E. and P. Poste (2006). *Keeping the blades turning: Condition monitoring of wind turbine gears*. Refocus **7**(2): 26-32.

Belwind Offshore Energy (2009). *Belwind - Wind farm in the North Sea (Press information)*.

Betz, A. (1920). *Das Maximum der theoretisch möglichen Ausnutzung des Windes durch Windmotoren (The maximum of the theoretically possible exploitation of the wind by wind motors)*. Zeitschrift f. d. gesamte Turbinenwesen **17**.

Betz, A. (1926). *Windenergie und Ihre Ausnutzung durch Windmühlen,*. Göttingen, Germany, Vandenhoeck.

Bir, G. (2008). *Multiblade Coordinate Transformation and Its Application to Wind Turbine Analysis*. ASME Wind Energy Symposium. Nevada, USA.

Blanco, M. I. (2009). *The economics of wind energy*. Renewable and Sustainable Energy Reviews **13**(6–7): 1372-1382.

Bloomberg New Energy Finance (2015). *Sustainable Energy in America: 2015 Factbook*. London, UK.

Blough, J. R. (2006). *Adaptive Resampling - Transforming From the Time to the Angle Domain*. XXIV International Modal Analysis Conference (IMAC). Missouri, USA.

Bogert, B. P., M. J. R. Healy and J. W. Tukey (1963). *The Quefrency Alanysis of Time Series for Echoes: Cepstrum, Pseudo-Autocovariance, Cross-Cepstrum, and Saphe Cracking*. Time Series Analysis(15): 209-243.

Boller, C., F.-K. Chang and Y. Fujino (2009). *Encyclopedia of Structural Health Monitoring*, John Wiley & Sons.

Braam, H., T. S. Obdam and T. W. Verbruggen (2012). *Low Cost Load Monitoring for Offshore Wind Farms*. International Conference on Noise and Vibration Engineering (ISMA). Leuven, Belgium.

Brincker, R., P. Andersen and N. Møller (2000). *Indicator for Separation of Structural and Harmonic Modes in Output-only Modal Testing*. XVIII International Modal Analysis Conference (IMAC). San Antonio, USA.

Brownjohn, J. M. W. (2007). *Structural health monitoring of civil infrastructure*. Philosophical Transactions of the Royal Society A: Mathematical, Physical and Engineering Sciences **365**(1851): 589-622.

Brownjohn, J. M. W., F. Magalhães, E. Caetano and Á. Cunha (2010). *Ambient vibration re-testing and operational modal analysis of the Humber Bridge*. Engineering Structures(32): 2003-2018.

Burton, T., D. Sharpe, N. Jenkins and E. Bossanyi (2001). *Wind Energy Handbook*, John Wiley & Sons.

Butterfield, C. P., W. Musial and J. Jonkman (2007). *Overview of Offshore Wind Technology*, National Renewable Energy Laboratory (NREL).

Butterfield, S., W. Musial and J. Jonkman (2005). *Engineering Challenges for Floating Offshore Wind Turbines*, National Renewable Energy Laboratory (NREL).

Byrne, B., G. Houlsby, C. Martin and P. Fish (2002). *Suction Caisson Foundations for Offshore Wind Turbines*. Wiind Engineering **26**(3): 145-155.

Caetano, E., F. Magalhães, Á. Cunha, O. Flamand and G. Grillaud (2007). *Comparison of Sochastic Identification Methods Applied to the Natural Response of Millau Viaduct*. Experimental Vibration Analysis for Civil Engineering Structures (EVACES). Porto, Portugal.

Cara, F. J., J. Juan, E. Alarcón, E. Reynders and G. De Roeck (2013). *Modal contribution and state space order selection in operational modal analysis*. Mechanical Systems and Signal Processing **38**(2): 276-298.

Carbon Trust. (2013). *Successful installation of first suction bucket foundation at Dogger Bank*. 2013, from http://www.carbontrust.com/news/2013/02/successful-installation-of-first-suction-bucket-foundation-at-dogger-bank.

Carcangiu, C. E., D. Tcherniak, S. Chauhan, J. Basurko and M. Rossetti (2012). *Numerical and Experimental Modal Characterization of a 3MW Wind Turbine*. EWEA 2012 Annual Event. Copenhagen, Denmark.

Carden, E. P. and P. Fanning (2009). *Vibration Based Condition Monitoring: A Review*. Structural Health Monitoring(4): 355-377.

Carne, T. G. and G. H. James Iii (2010). *The inception of OMA in the development of modal testing technology for wind turbines*. Mechanical Systems and Signal Processing **24**(5): 1213-1226.

Carne, T. G., J. P. Lauffer and A. J. Gomez (1988). *Modal Testing the EOLE*. New Mexico, USA, Sandia National Laboratories.

Carne, T. G., D. W. Lobitz, A. R. Nord and R. A. Watson (1982). *Finite Element Analysis and Modal Testing of a Rotating Wind Turbine*. New Mexico, USA, Sandia National Laboratories.

Carne, T. G. and A. R. Nord (1983). *Modal Testing of a Rotating Wind Turbine*. New Mexico, USA, Sandia National Laboratories.

Cauberghe, B. (2004). *Applied frequency-domain system identification in the field of experimental and operational modal analysis*. PhD thesis, V.U.Brussel.

Chauhan, S., D. Tcherniak, J. Basurko, O. Salgado, I. Urresti, C. E. Carcangiu and M. Rossetti (2011). *Operational Modal Analysis of Operating Wind Turbines: Application to Measured Data*. IXXX International Modal Analysis Conference (IMAC). Florida, USA.

Chou, J.-S. and W.-T. Tu (2011). *Failure analysis and risk management of a collapsed large wind turbine tower*. Engineering Failure Analysis **18**(1): 295-313.

Ciang, C. C., J.-R. Lee and H.-J. Bang (2008). *Structural health monitoring for a wind turbine system: a review of damage detection methods*. Measurement Science and Technology **19**: 1-20.

Clough, R. W. and J. Penzien (1995). *Dynamics of Structures*. Berkeley, USA, Computers & Structures, Inc.

Collins, J. L., R. K. Shaltens, R. H. Poor and R. S. Barton (1982). *Experience and Assessment of the DOE/NASA MOD-1 2000 kW Wind Turbine Generator at Boorne, North Carolina*.

Colwell, S. and B. Basu (2009). *Tuned liquid column dampers in offshore wind turbines for structural control*. Engineering Structures **31**(2): 358-368.

Commission of the European Communities (2008). *20 20 by 2020 - Europe's climate change opportunity*. t. C. Communication from the Commision to the European Parliament, the European Economic and Social Committee and the Committee of the Regions. Brussels, Switzerland.

Connel, J. R. (1980). *Turbulence spectrum observed by a fast-rotating wind turbine blade*, Battelle Pacific Northwest Laboratory.

Corrigan, R. D. and C. B. F. Ernsworth (1986). *Design and Initial Testing of a One Bladed 30-Meter Diameter Rotor on the NASA-DOE Mod-0 Wind Turbine*. DOE/NASA/20320-70 NASA TM-88810.

Cunha, Á. and E. Caetano (2006). *Experimental Modal Analysis of Civil Engineering Structures*. Sound and Vibration(40): 12-20.

Cunha, Á., E. Caetano and R. Delgado (2001). *Dynamic Tests on a Large Cable-Stayed Bridge. An Efficient Approach*. Journal of Bridge Engineering **6**(1): 54-62.

Currie, M., M. Saafi, C. Tachtatzis and F. Quail (2015). *Structural integrity monitoring of onshore wind turbine concrete foundations*. Renewable Energy **83**: 1131-1138.

Damgaard, M., L. B. Ibsen, L. V. Andersen and J. K. F. Andersen (2013a). *Cross-wind modal properties of offshore wind turbines identified by full scale testing*. Journal of Wind Engineering and Industrial Aerodynamics **116**: 94-108.

Damgaard, M., L. B. Ibsen, L. V. Andersen, P. Andersen and J. K. F. Andersen (2013b). *Damping Estimation of a Prototype Bucket Foundation for Offshore Wind Turbines Identified by Full Scale Testing*. 5th International Operational Modal Analysis Conference (IOMAC). Guimarães, Portugal.

Darrieus, G. J. (1931). *Turbine Having Its Rotating Shaft Transverse to the Flow of The Current*. U. S. P. Offcie.

Department of Energy & Climate Change (2010). *Value breakdown for the offshore wind sector*.

Det Norske Veritas (DNV) (2002). *Guidelines for Design of Wind Turbines*.

Det Norske Veritas (DNV) (2011). *DNV-OS-J101 - Design of Offshore Wind Turbine Structures*.

Devriendt, C., F. Magalhães, W. Weijtjens, G. De Sitter, Á. Cunha and P. Guillaume (2014). *Structural health monitoring of offshore wind turbines using automated operational modal analysis*. Structural Health Monitoring **13**(6): 644-659.

Devriendt, C., W. Weijtjens, M. El-Kafafy and G. D. Sitter (2014) *Monitoring resonant frequencies and damping values of an offshore wind turbine in parked conditions*. IET Renewable Power Generation **8**, 433-441.

Dong, W., T. Moan and Z. Gao (2012). *Fatigue reliability analysis of the jacket support structure for offshore wind turbine considering the effect of corrosion and inspection*. Reliability Engineering & System Safety **106**: 11-27.

Enercon GmbH (2005). *Installation of E-112 nearshore in Wilhelmshaven stopped*.

European Comitee for Standardization (CEN) (2005). *EN 1993-1-9 Eurocode 3: Design of steel structures - Part 1-9: Fatigue*.

European Commission (2011). *UpWind - Design limits and solutions for very large wind turbines*, The Sixth Framework Programme for Research and Development of the European Commission (FP6).

European Commission (2013). *EU energy in figures - Statistical Pocketbook 2013*. Luxembourg.

European Commission. (2015a). *2030 climate & energy framework*. from http://ec.europa.eu/clima/policies/strategies/2030/index_en.htm.

European Commission. (2015b). *2050 low-carbon economy*. from http://ec.europa.eu/clima/policies/strategies/2050/index_en.htm.

European Commission (2015c). *The European Union leading in renewables*. Brussels, Belgium.

European Wind Energy Association (EWEA) (2007). *Powering Change - EWEA 2006 Annual Report*. Brussels, Belgium.

European Wind Energy Association (EWEA) (2008). *Delivering Eenery and Climate Solutions - EWEA 2007 Annual Report*. Brussels, Belgium.

European Wind Energy Association (EWEA) (2009). *Winning with European Wind - EWEA 2008 annual report*. Brussels, Belgium.

European Wind Energy Association (EWEA) (2010). *Wind in Power - 2009 European statistics*. Brussels, Belgium.

European Wind Energy Association (EWEA) (2011a). *The European offshore wind industry key trends and statistics 2010*. Brussels, Belgium.

European Wind Energy Association (EWEA) (2011b). *Wind in Power - 2010 European statistics*. Brussels, Belgium.

European Wind Energy Association (EWEA) (2012a). *The European offshore wind industry key 2011 trends and statistics*. Brussels, Belgium.

European Wind Energy Association (EWEA) (2012b). *Wind in Power - 2011 European Statistics*. Brussels, Belgium.

European Wind Energy Association (EWEA) (2013a). *The European offshore wind industry - key trends and statistics 2012*. Brussels, Belgium.

European Wind Energy Association (EWEA) (2013b). *Wind in Power - 2012 European Statistics*. Brussels, Belgium.

European Wind Energy Association (EWEA) (2014a). *The European offshore wind industry - key trends and statistics 2013*. Brussels, Belgium.

European Wind Energy Association (EWEA) (2014b). *Wind in power - 2013 European statistics*. Brussels, Belgium.

European Wind Energy Association (EWEA) (2015a). *The European offshore wind industry - key trend and statistics 2014*.

European Wind Energy Association (EWEA) (2015b). *Wind in power - 2014 European statistics*. Brussels, Belgium.

Ewins, D. J. (2000). *Modal Testing: Theory, Practice and Application*. Baldock, England, Research Studies Press Ltd.

Fast, M. and T. Palmé (2010). *Application of artificial neural networks to the condition monitoring and diagnosis of a combined heat and power plant*. Energy **35**(2): 1114-1120.

Faulstich, S. (2010). *Component Reliabilty Ranking with Respect to WT Concept and External Environmental Conditions* Project UpWind.

Felber, A. J. (1993). *Development of a Hybrid Bridge Evaluation system*. PhD thesis, The University of British Columbia.

Freris, L. L. (1990). *Wind Energy Conversion System*. New York, USA, Prentice-Hall.

Fritzen, C.-P. (2005). *Vibration-Based Structural Health Monitoring – Concepts and Applications*. Key Engineering Materials **293** - **294**(3): 3 - 20.

García Márquez, F. P., A. M. Tobias, J. M. Pinar Pérez and M. Papaelias (2012). *Condition monitoring of wind turbines: Techniques and methods*. Renewable Energy **46**(0): 169-178.

Gasch, R. and J. Twele (2012). *Wind Power Plants - Fundamentals, Design, Construction and Operation*, Springer.

Gellermann, T. (2012). *Extension of the scope of Condition Monitoring Systems for multi-MW and offshore wind turbines1*. VDI-Conference Schwingungen von Windenergieanlagen 2012. Bremen, Germany.

Gentile, C. and A. Saisi (2007). *Ambient vibration testing of historic masonry towers for structural identification and damage assessment*. Construction and Building Materials(21): 1311-1321.

Germanischer Lloyd (GL) (2003). *Guideline for the Certification of Condition Monitoring Systems for Wind Turbines*. Rules and Guidelines - IV Industrial Services. Hamburg, Germany.

Germanischer Lloyd (GL) (2005). *Overall Damping for Piled Offshore Support Structures*. Note on Engineering Details.

Germanischer Lloyd (GL) (2010). *Guideline for the Certification of Wind Turbines*. Hamburg, Germany.

Germanischer Lloyd (GL) (2012). *Guideline for the Certification of Offshore Wind Turbines*. Hamburg, Germany.

Glauert, H. (1926). *The Analysis of Experimental Results in the Windmill Brake and Vortex Ring States of an Airscrew*. Aeronautical Research Committee Reports and Memoranda.

Global Wind Energy Council (GWEC) (2007). *Global Wind 2006 Report*. Brussels, Belgium.

Global Wind Energy Council (GWEC) (2008). *Global Wind 2007 Report*. Brussels, Belgium.

Global Wind Energy Council (GWEC) (2009). *Global Wind 2008 Report*. Brussels, Belgium.

Global Wind Energy Council (GWEC) (2010). *Global Wind 2009 Report*. Brussels, Belgium.

Global Wind Energy Council (GWEC) (2011). *Global Wind Report - Annual Market Update 2010*. Brussel, Belgium.

Global Wind Energy Council (GWEC) (2012). *Global Wind Report - Annual market update 2011*. Brussel, Belgium.

Global Wind Energy Council (GWEC) (2013). *Global Wind Report - Annual market update 2012*. Brussel, Belgium.

Global Wind Energy Council (GWEC) (2014). *Global Wind Report - Annual Market Update 2013*. Brussels, Belgium.

Global Wind Energy Council (GWEC) (2015). *Global Wind Report - Annual Market Update 2014*. Brussels, Belgium.

Gordon, A. D. (1999). *Classification*, Chapman and Hall/CRC.

Gordon, L. H., J. S. Andrews and D. K. Zimmerman (1983). *Mod-2 Wind Turbine Development*. DOE/NASN20305-9 NASATM-83460.

Goursat, M., M. Döhler, L. Mevel and P. Andersen (2010). *Crystal Clear SSI for Operational Modal Analysis of Aerospace Vehicles*. XXVIII International Modal Analysis Conference (IMAC). Florida, USA.

Government of Portugal (2015). *Green Growth Commitment*. Lisbon, Portugal, Ministry of Environment Spatial Planning and Energy,.

Gray, L. (2013). *Wind turbine collapses in high wind*. 2013, from http://www.telegraph.co.uk/earth/energy/windpower/9837026/Wind-turbine-collapses-in-high-wind.html.

Griffith, D. T. and T. G. Carne (2010). *Experimental Modal Analysis of 9-meter Research-sized Wind Turbine Blades*. XXVIII International Modal Analysis Conference (IMAC). Florida, USA.

Griffith, D. T., R. L. Mayes and P. S. Hunter (2010). *Excitation Methods for a 60 kW Vertical Axis Wind Turbine*. XXVIII International Modal Analysis Conference (IMAC), Florida, USA.

Griffith, D. T., G. Smith, M. Casias, S. Reese and T. W. Simmermacher (2006). *Modal Testing of the TX-100 Wind Turbine Blade*. New Mexico, USA, Sandia National Laboratories.

Griffith, D. T., N. C. Yoder, B. Resor, J. White and J. Paquette1 (2013). *Structural health and prognostics management for the enhancement of offshore wind turbine operations and maintenance strategies*. Wind Energy.

Guillaume, P., P. Verboven, S. Vanlanduit, H. V. d. Auweraer and B. Peeters (2003). *A Poly-Reference Implementation of the Least-Squares Complex Frequency-Domain Estimator*. XXII International Modal Analysis Conference (IMAC). Florida, USA.

Guo, P. and D. Infield (2012). *Wind Turbine Tower Vibration Modeling and Monitoring by the Nonlinear State Estimation Technique (NSET)*. Energies **5**: 5279-5293.

Hall, M., B. Buckham and C. Crawford (2013). *Evaluating the importance of mooring line model fidelity in floating offshore wind turbine simulations*. Wind Energy: n/a-n/a.

Hameed, Z., Y. S. Hong, Y. M. Cho, S. H. Ahn and C. K. Song (2009). *Condition monitoring and fault detection of wind turbines and related algorithms: A review*. Renewable and Sustainable Energy Reviews **13**(1): 1-39.

Hansen, M. H. (2003). *Improved Modal Dynamics of Wind Turbines to Avoid Stall-induced Vibrations*. Wind Energy **6**: 179-195.

Hansen, M. H. (2007). *Aeroelastic Instability Problems for Wind Turbines*. Wind Energy **10**(6): 551-577.

Hansen, M. H., K. Thomsen and P. Fuglsang (2006). *Two Methods for Estimating Aeroelastic Damping of Operational Wind Turbine Modes from Experiments*. Wind Energy(9): 179-191.

Harman, K., R. Walker and M. Wilkinson (2008). *Availability trends observed at operational wind farms*. European Wind Energy Conference (EWEC). Brussels, Belgium.

Hasselmann, K., T. P. Barnett, E. Bouws, H. Carlson, D. E. Cartwright, K. Enke, J. A. Ewing, H. Gienapp, D. E. Hasselmann, P. Kruseman, A. Meerburg, P. Müller, D. J. Olbers, K. Richter, W. Sell and H. Walden (1973). *Measurements of wind wave growth and swell decay during the Joint North Sea Wave Project (JONSWAP)*. Hamburg, Germany, Deutsches Hydrographisches Institut.

Hau, E. (2006). *Wind Turbines - Fundamentals, Technologies, Application, Economics*, Springer.

HAWC2 web site. (2013). *HAWC2 model - NREL 5-MW Reference Wind Turbine*. from http://www.hawc2.dk.

Henderson, A. R. (2003). *Support Structures for Floating Offshore*. Workshop on Deep Water Offshore Wind Energy Systems.

Henderson, A. R., C. Morgan, B. Smith, H. C. Sorensen, R. J. Barthelmie and B. Boesmans (2003). *Offshore Wind Energy in Europe - A Review of the State-of-the-Art*. Wind Energy **6**(doi: 10.1002/we.82): 35-52.

Hermans, L. and H. V. d. Auweraer (1999). *Modal Testing and Analysis of Structures Under Operational Conditions: Industrial Applications*. Mechanical Systems and Signal Processing **13**(2): 193-216.

Heylen, W., S. Lammens and P. Sas (2007). *Modal Analysis Theory and Testing*. Belgium, Katholieke Universiteit Leuven.

Hjelm, H. P., R. Brincker, J. Graugaard-Jensen and K. Munch (2005). *Determination of Stress Histories in Structures by Natural Input Modal Analysis*. XXIII International Modal Analysis Conference (IMAC). Florida, USA.

Hoell, S. and P. Omenzetter (2014). *Detection and localization of trailing edge disbond in a large wind turbine blade*. International Conference on Offshore Renewable Energy. Glasgow, UK.

Hu, W.-H. (2011). *Operational Modal Analysis and Continuous Dynamic Monitoring of Footbridges*. PhD thesis, Faculdade de Engenharia da Universidade do Porto.

Hu, W.-H., E. Caetano and Á. Cunha *Structural health monitoring of a stress-ribbon footbridge*. Engineering Structures **57**.

Hu, W.-H., C. Moutinho, E. Caetano, F. Magalhães and Á. Cunha (2012). *Continuous dynamic monitoring of a lively footbridge for serviceability assessment and damage detection*. Mechanical Systems and Signal Processing **33**: 38-55.

Hu, W.-H., S. Thöns, R. G. Rohrmann, S. Said and W. Rücker (2015a). *Vibration-based structural health monitoring of a wind turbine system Part II: Environmental/operational effects on dynamic properties*. Engineering Structures **89**: 273-290.

Hu, W.-H., S. Thöns, R. G. Rohrmann, S. Said and W. Rücker (2015b). *Vibration-based structural health monitoring of a wind turbine system. Part I: Resonance phenomenon*. Engineering Structures **89**: 260-272.

Hyers, R. W., J. G. McGowan, K. L. Sullivan, J. F. Manwell and B. C. Syrett (2006). *Condition monitoring and prognosis of utility scale wind turbines*. Energy Materials: Materials Science and Engineering for Energy Systems **1**(3): 187-203.

Ibsen, L. B. and M. Liingaard (2006). *Prototype bucket foundation for wind turbines - natural frequency estimation*. Aalborg, Denmark, Aalborg University - Department of Civil Engineering.

Ibsen, L. B., M. Liingaard and S. A. Nielsen (2005). *Bucket Foundation, a status*. Copenhagen Offshore Wind, Copenhagen, Denmark.

Institute of Mechanical Engineering and Industrial Management (INEGI) and Portuguese Renewable Energy Association (APREN) (2015). *Wind Farms in Portugal - December 2014*.

International Electrotechnical Commission (IEC) (2009). *IEC 61400-3 Wind turbines – Part 3: Design requirements for offshore wind turbines*.

International Electrotechnical Commission (IEC) (2014). *IEC 61400-1 Wind turbines –Part 1: Design requirements*.

International Energy Agency (IEA) (1984). *International Energy Agency - Co-operation in the Development of Large-Scale Wind Energy Systems (Annual Report of 1983)*, IEA LS WECS Executive Commitee.

International Energy Agency (IEA) (1989). *IEA Large-Scale Wind Energy - Annual Report 1988*, IEA LS WECS Execuiive Committee.

Jacobsen, N.-J., P. Andersen and R. Brincker (2006). *Using Enhanced Frequency Domain Decomposition as a Robust Technique to Harmonic Excitation in Operational Modal Analysis*. International Conference on Noise & Vibration Engineering 2006 (ISMA). Lueven, Belgium.

Jacobsen, N.-J., P. Andersen and R. Brincker (2008). *Applications of Frequency Domain Curve-fitting in the EFDD Technique*. XXVI International Modal Analysis Conference (IMAC). Florida, USA.

James, G. H. (1994). *Extraction of modal parameters from an operating HAWT using the Natural Excitation Technique (NExT)*. 13th Energy-Sources Technology Conference and Exhibition (ETCE) on Wind Energy. Los Angeles, USA.

James, G. H., T. G. Carne and J. P. Lauffer (1993). *The Natural Excitation Technique (NExT) for Modal Parameter Extraction From Operating Wind Turbines*. New Mexico, USA, Sandia National Laboratories.

Johnson, G. L. (2001). *Wind Energy Systems*, Prentice Hall.

Johnson, R. A. and D. W. Wichern (2002). *Applied multivariate statistical analysis*. New Jersey, USA, Prentice Hall.

Jonkman, J., S. Butterfield, W. Musial and G. Scott (2009). *Definition of a 5-MW Reference Wind Turbine for Offshore System Development* National Renewable Energy Laboratory.

Juang, J.-N. (1994). *Applied System Identification*. New Jersey, USA, Prentice Hall Englewood Cliffs.

Kármán, T. v. (1948). *Progress in the statistical theory of turbulence*. Proceedings of the National Academy of Science of the United States of America **34**: 530-539.

Kuhn, M. J. (2001). *Dynamics and Design Optimisation of Offshore Wind Energy Conversion Systems*. PhD thesis, Delft University of Technology.

Kvittem, M. I. and T. Moan (2015). *Time domain analysis procedures for fatigue assessment of a semi-submersible wind turbine*. Marine Structures **40**: 38-59.

Larsen, T. J. and A. M. Hansen (2007). *How 2 HAWC2, the user's manual*.

LeBlanc, C. and N. J. Tarp-Johansen (2011). *Monopile in sand, stiffness and damping*. Oral Presentation, EWEA Conference. Brussels, Belgium.

Li, Z.-q., S.-j. Chen, H. Ma and T. Feng (2013). *Design defect of wind turbine operating in typhoon activity zone*. Engineering Failure Analysis(27): 165-172.

Liu, W., B. Tang and Y. Jiang (2010a). *Status and problems of wind turbine structural health monitoring techniques in China*. Renewable Energy **35**(7): 1414-1418.

Liu, W., B. Tang and Y. Jiang (2010b). *Status and problems of wind turbine structural health monitoring techniques in China*. Renewable Energy(35): 1414-1418.

Liu, W. Y., B. P. Tang, J. G. Han, X. N. Lu, N. N. Hu and Z. Z. He (2015). *The structure healthy condition monitoring and fault diagnosis methods in wind turbines: A review*. Renewable and Sustainable Energy Reviews **44**: 466-472.

Loraux, C. and E. Brühwiler (2015). *Realistic examination of the fatigue life of a wind turbine tower using data from long term monitoring*. IABSE Conference – Structural Engineering: Providing Solutions to Global Challenges. Geneva, Switzerland.

LORC. (2012a). *The Jacket - A Path to Deeper Waters*. 2013, from http://www.lorc.dk/offshore-wind/foundations/jackets#post-piling.

LORC. (2012b). *The Monopile - Close to a Monopole*. 2013, from http://www.lorc.dk/offshore-wind/foundations/monopiles.

LORC. (2012c). *Tripile - Three Monopiles in One*. 2013, from http://www.lorc.dk/offshore-wind/foundations/tripiles.

Lundsager, P., S. Frandsen and C. J. Christensen (1980). *Analysis of Data from the Gedser Wind turbine 1977-1979*. Riso-M-2242. Roskilde, Denmark, Riso National Laboratory.

Madsen, P. H., S. Frandsen, W. E. Holley and J. C. Hansen (1984). *Dynamics and Fatigue Damage of Wind Turbine Rotors during Steady Operation*. Riso-R-512. Roskilde, Denmark, Riso National Laboratory.

Magalhães, F. (2010). *Operational Modal Analysis for Testing and Monitoring of Bridges and Special Structures*. PhD thesis, Faculdade de Engenharia da Universidade do Porto.

Magalhães, F. and Á. Cunha (2011). *Explaining operational modal analysis with data from an arch bridge*. Mechanical Systems and Signal Processing **25**: 1431-1450.

Magalhães, F., A. Cunha and E. Caetano (2012). *Vibration based structural health monitoring of an arch bridge: From automated OMA to damage detection*. Mechanical Systems and Signal Processing **28**(0): 212-228.

Magalhães, F., Á. Cunha and E. Caetano (2009). *Online automatic identification of the modal parameters of a long span arch bridge*. Mechanical Systems and Signal Processing **23**(2): 316-329.

Magalhães, F., Á. Cunha, E. Caetano and R. Brincker (2010). *Damping estimation using free decays and ambient vibration tests*. Mechanical Systems and Signal Processing **24**(5): 1274-1290.

Main(e) International Consulting LLC (2012). *Floating Offshore Wind Foundations: Industry Consortia and Projects in the United States, Europe and Japan - An Overview*.

Manwell, J. F., J. G. McGowan and A. L. Rogers (2010). *Wind Energy Explained - Theory, Design and Application*, John Wiley & Sons.

Manzato, S., C. Devriendt, W. Weijtjens, E. Di Lorenzo, B. Peeters and P. Guillaume (2014). *Removing the Influence of Rotor Harmonics for Improved Monitoring of Offshore Wind Turbines*. Dynamics of Civil Structures, Volume 4. F. N. Catbas, Springer International Publishing**:** 299-312.

Manzato, S., J. R. White, B. LeBlanc, B. Peeters and K. Janssens (2013). *Advanced identification techniques for operational wind turbine data*. XXXI International Modal Analysis Conference (IMAC), California, USA.

Marinone, T., D. Cloutier, B. LeBlanc, T. Carne and P. Andersen (2014). *Artificial and Natural Excitation Testing of SWiFT Vestas V27 Wind Turbines*. XXXII International Modal Analysis Conference (IMAC). Florida, USA.

Marulo, F., G. Petrone, E. D. Lorenzo and A. Cutolo (2015). *Operational modal analysis for SHM of a wind turbine blade*. 7th International Conference on Structural Health Monitoring. Torino, Italy.

MathWorks (2012). *Matlab*. **R2012b**.

McMillan, D. and G. W. Ault (2007). *Quantification of Condition Monitoring Benefit for Offshore Wind Turbines*. Wind Engineering **31**(4): 267-285.

Mevel, L., A. Benveniste, M. Bassevillea, M. Goursatb, B. Peetersd, H. V. d. Auweraerd and A. Vecchiod (2006). *Input/Output Versus Output-Only Data Processing for Structural Identification—Application to In-Flight Data Analysis*. Journal of Sound and Vibration(295): 531-552.

Molenaar, D. (2003). *Experimental Modal Analysis of a 750 kW Wind Turbine for Structural Model Validation*. 41st AIAA Aerospace Sciences Meeting and Exhibit. Nevada, USA.

Montgomery, D. C. (2009). *Statistical quality control : a modern introduction*. New York, John Wiley & Sons.

Morthorst, P. E. and H. Jacobsen (2004). *Wind Energy - The Facts*, European Commission (EC) European Wind Energy Association (EWEA). **Volume 2 - Costs & Prices**.

Moser, P. and B. Moaveni (2011). *Environmental effects on the identified natural frequencies of the Dowling Hall Footbridge*. Mechanical Systems and Signal Processing **25**(7): 2336-2357.

Murtagh, P. J., B. Basu and B. M. Broderick (2005). *Along-wind response of a wind turbine tower with blade coupling subjected to rotationally sampled wind loading*. Engineering Structures **27**(8): 1209-1219.

Musial, W., S. Butterfield and A. Boone (2004). *Feasibility of Floating Platform Systems for Wind Turbines*. 23rd ASME Wind Energy Symposium. Nevada, USA, Nationa Renewable Energy Laboratory (NREL).

Musial, W. and B. Ram (2010). *Large-Scale Offshore Wind Power in the United States - Assessment of Opportunities and Barriers*, National Renweable Energy Laboratory (NREL).

Naess, A. and T. Moan (2012). *Stochastic Dynamics of Marine Structures*. USA, Cambridge University Press.

Naguleswaran, S. (1994). *Lateral Vibration of a Centrifugally Tensioned Uniform Euler-Bernoulli Beam*. Journal of Sound and Vibration **176**(5): 613-624.

Nielsen, J. J. and J. D. Sørensen (2011). *On risk-based operation and maintenance of offshore wind turbine components*. Reliability Engineering and System Safety(96): 218-229.

Oliveira, G., F. Magalhães, E. Caetano and Á. Cunha (2013). *Modal Identification and FE Model Correlation of a Wind Turbine Tower*. 5th International Operational Modal Analysis Conference (IOMAC). Guimarães, Portugal.

Oliveira, G., F. Magalhães and Á. Cunha (2014). *Rotor blade extension project – Determination of the blades natural frequencies*. Porto, Portugal.

Oliveira, G., W. Weijtjens, G. D. Sitter, F. Magalhães, Á. Cunha, E. Caetano and C. Devriendt (2014). *Dynamic Monitoring of wind turbines: case studies on- and off-shore*. 1st International Conference on Renewable Energies Offshore. Lisboa, Portugal.

Osgood, R. (2001). *Dynamic Characterization Testing of Wind Turbines*. Colorado, USA, National Renewable Energy Laboratory (NREL).

Osgood, R., G. Bir, H. Mutha, B. Peeters, M. Luczak and G. Sablon (2010). *Full-scale modal wind turbine tests: comparing shaker excitation with wind excitation*. XXVIII International Modal Analysis Conference (IMAC). Florida, USA.

Overschee, P. V. and B. D. Moor (1996). *Subspace Identification for Linear Systems - Theory, Implementation, Applications*, Kluwer Academinc Publishers.

Ozbek, M., F. Meng and D. J. Rixen (2013). *Challenges in testing and monitoring the in-operation vibration characteristics of wind turbines*. Mechanical Systems and Signal Processing.

Ozbek, M. and D. J. Rixen (2012). *Operational modal analysis of a 2.5 MW wind turbine using optical measurement techniques and strain gauges*. Wind Energy(16).

Ozbek, M., D. J. Rixen, O. Erne and G. Sanowb (2010). *Feasibility of monitoring large wind turbines using photogrammetry*. Energy **35**: 4802-4811.

Pappa, R. S., G. H. J. III and D. C. Zimmerman (1997). *Autonomous modal identification of the Space Shuttle tail rudder*. Virginia, USA, National Aeronautics and Space Administration (NASA).

Peeters, B. (2000). *System Identification and Damage Detection in Civil Engineering*. PhD thesis, Katholieke Universiteit Leuven.

Peeters, B. and H. V. d. Auweraer (2005). *PolyMax: a Revolution in Operational Modal Analysis*. 1st International Operational Modal Analysi Conference (IOMAC). Copenhagen, Denmark.

Peeters, B., R. Cornelius, K. Janssens and H. V. d. Auweraer (2007). *Removing Disturbing Harmonics in Operational Modal Analysis*. 2nd International Operational Modal Analysis Conference (IOMAC). Copenhagen, Denmark.

Peeters, B., H. Van der Auweraer, P. Guillaume and J. Leuridan (2004). *The PolyMAX Frequency-Domain Method: A New Standard for Modal Parameter Estimation?* Shock and Vibration **11**(3-4): 395-409.

Pelayo, F., M. López-Aenlle, A. Fernández-Canteli and R. Cantieni (2011). *Operational modal analysis of two wind turbines with foundation problems*. 4th International Operational Modal Analysis Conference. Istanbul, Turkey.

Pierson, W. and L. Moskowitz (1964). *A proposed spectral form of fully developed wind seas based on the similarity theory of S. A. Kitaigorodskii*. Journal of Geophysical Research **69**(4): 5181-5190.

Pollino, M. and A. Huckelbridge (2012). *In-situ Measurements of Fatigue Demands on a Wind Turbine Support Structure*. IEEE Energy Tech 2012. Ohio, USA.

Portuguese Renewable Energy Association (APREN). (2015). *Produção de Electricidade por Fonte em Portugal em 2015*. Retrieved 05/01/2016, from http://www.apren.pt/pt/dados-tecnicos-3/dados-nacionais-2/producao-2/a-producao-de-electricidade-em-portugal-2/fontes-de-producao-de-eletricidade/.

Prendergast, L. J., K. Gavin and P. Doherty (2015). *An investigation into the effect of scour on the natural frequency of an offshore wind turbine*. Ocean Engineering **101**: 1-11.

Putter, S. and H. Manor (1978). *Natural Frequencies of Radial Rotating Beams*. Journal of Sound and Vibration **52**(2): 175-185.

Quilter, J. (2013). *World's largest blade begins journey to Scotland*. 2013, from http://www.windpowermonthly.com/article/1191655/picture-gallery---worlds-largest-blade-begins-journey-scotland?DCMP=EMC-CONWindpowerWeekly&bulletin=windpower-weekly.

Ramírez, O., D. Tcherniak and G. Larsen (2015). *Comparative study of OMA applied to experimental and simulated data from an operating Vestas V27 wind turbine*. 6th International Operational Modal Analysis Conference (IOMAC). Gijón, Spain.

Ramler, J. R. and R. M. Donovan (1979). *Wind turbines for Electric Utilities: Development Status and Economisc*. N. T.-. DOE/NASA/1028-79/23, AIAA-79-0965.

Randall, R. B. and N. Sawalhi (2011). *A New Method for Separating Discrete Components from a Signal*. Sound & Vibration **45**(5): 6 - 9.

Rankine, W. J. M. (1865). *On the Mechanical Principles of the Action of Propellers*, Transactions of the Institution of Naval Architects.

Reynders, E. (2009). *System Identification and Modal analysis in Structural Mechanics*. PhD Thesis, K. U. Leuven.

Reynders, E., J. Houbrechts and G. De Roeck (2012). *Fully automated (operational) modal analysis*. Mechanical Systems and Signal Processing **29**(0): 228-250.

Rodrigues, J. (2004). *Identificação Modal Estocástica. Métodos de análise e aplicações em estruturas de engenharia civil*. PhD thesis, Faculdade de Engenharia da Universidade do Porto (FEUP) Laboratório Nacional de Engenharia Civil (LNEC).

Rücker, W. (2007). *Offshore wind energy plants – Problems and possible solutions*. Experimental Vibration Analysis for Civil Engineering Structures (EVACES). Porto, Portugal.

Rytter, A. (1993). *Vibrational Based Inspection of Civil Engineering Structures*. PhD thesis, Aalborg University.

Salavessa, R. (2014). *Improving instead of repowering is a technical, ecological and economic solution. Prototype - Rotor Blade Extension*. European Wind Energy Association (EWEA) 2014 Annual Event. Barcelona, Spain.

Salzman, D. J. C. and J. v. d. Tempel (2005). *Aerodynamic Damping in the Design of Support Structures for Offshore Wind Turbines*. Copenhagen Offshore Wind 2005. Copenhagen, Denmark.

Savonius, S. J. (1931). *The S-Rotor and Its Applications*. Mechanical Engineering **53**(5): 333-338.

Schwerin, B. (2010). *Featured Invention: NASA Modeling Innovations Advance Wind-Energy Industry*. Ask Magazine**:** 22 - 24.

Scionti, M., J. Lanslots, I. Goethals, A. Vecchio, H. V. d. Auweraer, B. Peeters and B. D. Moor (2003). *Tools to improve detection of structural changes from in-flight flutter data*. 8th International Conference on Recent Advances in Structural Dynamics (ISVR). Southampton, UK.

Scionti, M. and J. P. Lanslots (2005). *Stabilisation diagrams: Pole identification using fuzzy clustering techniques*. Advances in Engineering Software **36**(11–12): 768-779.

Scots Renewables. (2011). *No-Tiree-Array Group Visit An Offshore Windfarm*. from http://www.scotsrenewables.com/blog/offshorewind/no-tiree-array-group-visit-an-offshore-windfarm/.

Sectorov, W. R. (1973). *The first aerodynamic three-phase electric power plant in Balakawa*, National Aeronautics and Space Administration (NASA).

Şeker, S., E. Ayaz and E. Türkcan (2003). *Elman's recurrent neural network applications to condition monitoring in nuclear power plant and rotating machinery*. Engineering Applications of Artificial Intelligence **16**(7–8): 647-656.

Shepherd, D. (1990). *Historical Development of the Windmill*. DOE/NASA/5266-1, National Aeronautics and Space Administration (NASA).

Shi, W., J. Shan and X. Lu (2012). *Modal identification of Shanghai World Financial Center both from free and ambient vibration response*. Engineering Structures(36): 14-26.

Shirzadeh, R., C. Devriendt, M. A. Bidakhvidi and P. Guillaume (2013). *Experimental and computational damping estimation of an offshore wind turbine on a monopile foundation*. Journal of Wind Engineering and Industrial Aerodynamics **120**: 96-106.

Skjoldan, P. F. (2011). *Aeroelastic modal dynamics of wind turbines including anisotropic effects*. Risø-PhD-Report-66. Roskilde, Denmark, Riso - DTU.

Sohn, H. (2007). *Effects of environmental and operational variability on structural health monitoring*. Philosophical Transactions of the Royal Society A: Mathematical, Physical and Engineering Sciences **365**(1851): 539-560.

Sørensen, J. D. and J. N. Sørensen (2011). *Wind Energy Systems: Optimising Design and Construction for Safe and Reliable Operation*. Cambridge, UK
Philadelphia, PA, Woodhead Publishing.

Sørensen, S. P. H. and L. B. Ibsen (2013). *Assessment of foundation design for offshore monopiles unprotected against scour*. Ocean Engineering **63**: 17-25.

Spera, D. (1994). *Wind Turbine Technology - Fundamental Concepts of Wind Turbine Engineering*, The American Society of Mechanical Engineers.

Spera, D. A. (1995). *Bibliography of NASA-Related Publications on Wind Turbine Technology 1973-1995*. DOE/NASA/5776-3 NASA CR-195462.

Sutherland, H. J. (2000). *A summary of the fatigue properties of wind turbine materials*. Wind Energy **3**(1): 1-34.

Tarp-Johansen, N. J., L. Andersen, E. D. Christensen, C. Mørch, B. Kallesøe and S. Frandsen (2009). *Comparing Sources of Damping of Cross-Wind Motion*. European Offshore Wind Conference & Exhibition. Stockholm, Sweden.

Tcherniak, D., S. Chauhan and M. H. Hansen (2010a). *Applicability Limits of Operational Modal Analysis to Operational Wind Turbines*. XXVIII International Modal Analysis Conference (IMAC). Florida, USA.

Tcherniak, D., S. Chauhan, M. Rossetti, I. Font, J. Basurko and O. Salgado (2010b). *Output-only Modal Analysis on Operating Wind Turbines: Application to Simulated Data*. European Wind Energy Conference. Warsaw, Poland.

Tegen, S., M. Hand, B. Maples, E. Lantz, P. Schwabe and A. Smith (2012). *2010 Cost of Wind Energy Review*, National Renweable Energy Laboratory (NREL).

Tempel, J. V. D. (2006). *Design of Support Structures for Offshore Wind Turbines*. PhD Thesis, Technische Universiteit Delft.

Thiele, H. M. (1984). *Growian Rotor Blades: Production Development, Construction and Test*. NASA TM-77479.

Thies, P. R., L. Johanning, V. Harnois, H. C. M. Smith and D. N. Parish (2014). *Mooring line fatigue damage evaluation for floating marine energy converters: Field measurements and prediction*. Renewable Energy **63**(0): 133-144.

Thomsen, J. H., T. Forsberg and R. Bittmer (2007). *Offshore Wind Turbine Foundations - The Cowi Experience*. 26th International Conference on Offshore Mechanics and Artic Engineering (OMAE). California, USA.

Thomsen, K., J. T. Petersen, E. Nim, S. Øye and B. Petersen (2000). *A Method for Determination of Damping for Edgewise Blade Vibrations*. Wind Energy(3): 233-246.

Thresher, R. W. and D. M. Dodge (1998). *Trends in the evolution of wind turbine generator configurations and systems*. Wind ENERGY **1**(S1): 70 - 86.

Tong, W. (2010). *Wind Power Generation and Wind Turbine Design*. Great Britain, WIT Press.

Tricklebank, A. H., P. H. Halberstadt, B. J. Magee and A. Bromage (2007). *Concrete Towers for Onshore and Offshore Wind Farms*.

U.S Energy Information Administration (2015). *Levelized Cost and Levelized Avoided Cost of New Generation Resources in the Annual Energy Outlook 2015*. Washington, DC.

Ulriksen, M. D., D. Tcherniak, P. H. Kirkegaard and L. Damkilde (2015). *EWSHM 2014: Operational modal analysis and wavelet transformation for damage identification in wind turbine blades*. Structural Health Monitoring.

van Kuik, G. A. M. (2007). *The Lanchester–Betz–Joukowsky limit*. Wind Energy **10**(3): 289-291.

Vargo, D. J. (1974). *Wind Energy Developments on the 20th Centurty*. Missouri, USA.

Veljkovic, M., C. Heistermann, W. Husson, M. Limam, M. Feldmann, J. Naumes, D. Pak, T. Faber, M. Klose, K.-U. Fruhner, L. Krutschinna, C. Baniotopoulos, I. Lavasas, A. Pontes, E. Ribeiro, M. Hadden, R. Sousa, L. d. Silva, C. Rebelo, R. Simoes, J. Henriques, R. Matos, J. Nuutinen and H. Kinnunen (2012). *High-strength tower in steel for wind turbines (Histwin)*. Luxembourg.

Ventura, C. E., W. D. L. Finn, J.-F. Lord and N. Fujita (2003). *Dynamic characteristics of a base isolated building from ambient vibration measurements and low level earthquake shaking*. Soil Dynamics and Earthquake Engineering(23): 313-322.

Verboven, P., P. Guillaume, B. Cauberghe, E. Parloo and S. Vanlanduit (2003). *Stabilization Charts and Uncertainty Bounds for Frequency-Domain Linear Least Squares Estimators*. XXI International Modal Analysis Conference (IMAC). Florida, USA.

Verboven, P., E. Parloo, P. Guillaume and M. Van Overmeire (2002). *Autonomous Structural Heath Monitoring - Part I: Modal Parameter Estimation and Tracking*. Mechanical Systems and Signal Processing **16**(4): 637-657.

Versteijlen, W. G., V. Metrikine, J. S. Hoving, E. Smid and W. E. d. Vries (2011). *Estimation of the Vibration Decrement of an Offshore Wind Turbine Support Structure Caused by its Interaction with Soil*. EWEA Offshore Conference. Amsterdam, The Netherlands.

Vestergaard, J., L. Brandstrup and R. D. G. III (2004). *A Brief History of the Wind Turbine Industries in Denmark and the United States*. Academy of International Business (Southeast USA Chapter). Knoxville, USA**:** 322-327.

Voaden, G. H. (1943). *The Smith-Putnam Wind Turbine*. Turbine Topics **1**(3): 1-6.

Vugts, J. H. (2000). *Considerations on the dynamics of support structures for an OW EC*. PhD thesis, Delft University of Technology.

Wang, Y., M. Liang and J. Xiang (2014). *Damage detection method for wind turbine blades based on dynamics analysis and mode shape difference curvature information*. Mechanical Systems and Signal Processing **48**(1–2): 351-367.

Weijtjens, W. (2014). *Advanced methods for estimating and monitoring the modal parameters of operational systems subjected to non-white excitation*. PhD thesis, Vrije Universiteit Brussel.

Weijtjens, W., A. Iliopoulos, J. Helsen and C. Devriendt (2015). *Monitoring the consumed fatigue life of wind turbines on a monopile foundation*. EWEA Offshore 2015. Copenhagen, Denmark.

Weijtjens, W., T. Verbelen, G. De Sitter and C. Devriendt (2015). *Foundation structural health monitoring of an offshore wind turbine-a full-scale case study*. Structural Health Monitoring.

White, J. R., D. E. Adams and M. A. Rumsey (2010). *Modal Analysis of CX-100 Rotor Blade and Micon 65/13 Wind Turbine*. XXVIII International Modal Analysis Conference (IMAC). Florida, USA.

Wiggelinkhuizen, E. J., S. J. Watson, J. Xiang, G. Giebel, E. J. Norton, M. C. Tipluica, A. J. Christensen and E. Becker (2007). *Conmow Final Report*. ECN-E--07-044, Energy Research Centre of the Netherlands (ECN).

Wikipedia. (2005). *Eoliennes Gaspesie*. 2013, from http://en.wikipedia.org/wiki/File:Eoliennes_Gaspesie.jpg.

Wikipedia. (2009). *NASA wind turbines*. 2013, from http://en.wikipedia.org/wiki/NASA_wind_turbines.

Wikipedia. (2012). *Tripod wind energy Brhv*. 2013, from http://commons.wikimedia.org/wiki/File:Tripod_wind_energy_Brhv.jpg.

Wilkinson, M. and B. Hendriks (2011). *Report on Wind Turbine Reliability Profiles*, Reliawind.

Wilson, R. E. and P. B. S. Lissaman (1974). *Applied Aerodynamics of Wind Power Machine*. Oregon State University.

Wind Directions (January/ February 2007). European Wind Energy Asscociation (EWEA).

Wind Power Monthly. (2003). *Wind and insurance industries head for peace treaty*. 2013, from http://www.windpowermonthly.com/article/955632/wind-insurance-industries-head-peace-treaty.

Worden, K., C. R. Farrar, G. Manson and G. Park (2007). *The fundamental axioms of structural health monitoring*. Proceedings of the Royal Society A: Mathematical, Physical and Engineering Science **463**(2082): 1639-1664.

World Energy Council (WEC) (2013). *World Energy Perspective - Cost of Energy Technologies*. London, UK.

Wymore, M. L., J. E. Van Dam, H. Ceylan and D. Qiao (2015). *A survey of health monitoring systems for wind turbines*. Renewable and Sustainable Energy Reviews **52**: 976-990.

Yang, B. and D. Sun (2013). *Testing, inspecting and monitoring technologies for wind turbine blades: A survey*. Renewable and Sustainable Energy Reviews(22): 515-526.

Yang, S. and M. S. Allen (2012). *Output-only Modal Analysis using Continuous-Scan Laser Doppler Vibrometry and applicationto a 20 kW wind turbine*. Mechanical Systems and Signal Processing **31**: 228-245.

Yang, W., P. J. Tavner, C. J. Crabtree, Y. Feng and Y. Qiu (2014). *Wind turbine condition monitoring: technical and commercial challenges*. Wind Energy(17): 673-693.

Ye, X. W., Y. Q. Ni, K. Y. Wong and J. M. Ko (2012). *Statistical analysis of stress spectra for fatigue life assessment of steel bridges with structural health monitoring data*. Engineering Structures **45**(0): 166-176.

Yoo, H. H. and S. H. Shin (1998). *Vibration Analysis of Rotating Cantilever Beam*. Journal of Sound and Vibration **212**(5): 807-828.

Yoon, S. Y., Z. Lin and P. E. Allaire (2013). *Control of Surge in Centrifugal Compressors by Active Magnetic Bearings*. London, England, Springer.

Young, W. C. and R. G. Buynas (2002). *Roark's Formulas for Stress and Strain*. The United States of America, McGraw-Hill.

Zaaijer, M., J. v. d. Tempel, P. Fish, T. Topper and A. Vos (2002). *Tripod support structure - pre-design and natural frequency assessment for the 6 MW DOWEC*. Delft, the Netherlands, TUDelft.

Zhang, L., R. Brincker and P. Andersen (2005). *An Overview of Operational Modal Analysis: Major Development and Issues*. International Operational Modal Analysis. Copenhagen, Denmark.